Production and Characterisation of Porous Carbon Nanomaterials

A thesis submitted for the partial fulfilment of the requirement for the degree of

Doctor of Philosophy

In the faculty of Science of Durham University

Stuart John Goldie

Department of Chemistry

Durham University

2021

Abstract

Three dimensional porous structures of graphene and carbon nanomaterials have many exciting uses in energy storage, as catalyst supports and for water treatment to name a few; thanks to their high surface area, record conductivity, stability and potentially abundant feedstocks. However, recent publications have highlighted the need for a greater understanding of these materials' formation and characterisation methods if they are to be optimised for these applications.

Many graphene production methods result in a polydisperse mixture of flake sizes, thickness and chemical environment and understanding this complex distribution is important for many applications. Raman spectroscopy is a versatile method of graphene analysis but single point spectra cannot resolve this distribution and, in many cases, may misrepresent a material. By recording multiple spectra a statistical dataset is produced but the size required remains an important consideration. Herein a protocol was developed, utilising the convergence of data sets and a Monte Carlo based statistical method, to investigate the size of data set required for accurate characterisation. This was successfully applied to a range of carbon nanomaterials revealing different materials require bespoke analyses for complete characterisation, and even routine analysis can require hundreds of points.

This characterisation was then applied to graphitic carbon produced from metal catalysed graphitization; whilst many studies have probed the effect of different process conditions, carbon sources and metals, here we investigate the role of different salts of the same metal, previously considered irrelevant to graphitization. By analysing the distribution of material produced from three different cobalt salts: $Co(OAc)_2$, $Co(NO_3)_2$ and $CoCl_2$; it was found the thermal stability of the metal source used is key to controlling the size of metal particle formed and thereby the pore structure and carbon produced. Such control can potentially be used to tailor the properties of carbon foams produced from low cost feedstocks.

Declaration

The work presented within was undertaken within the Department of Chemistry of the University of Durham. I confirm that no part of this work has been submitted for a degree at this or any other institution and, unless otherwise stated, is the original work of the author.

Acknowledgements

Enormous thanks must be given to Dr David Johnson for teaching me much of what I know about practical laboratory work and many late night discussions of research ideas both bad and good as I was first beginning this journey. My desire to understand the techniques we use can be traced to David, and his wide knowledge and experience was an inspiring example. I also value the support and kind advice from Dr Shan Jiang, Dr Stephen Boothroyd and Dr Dominikus Heift who kept me focussed, shared a supportive pint when required and were always willing to offer feedback. I'm also thankful to Scott Bush and Tianren Xie for their friendship and many discussions during our PhD's, often as not making it up as we went but doing so together.

I am grateful to Leon Bowen for his tuition and encouragement with scanning electron microscopy, a technique I have enjoyed using and without which this thesis would be devoid of its more appealing figures. On the subject of tuition, my own teaching has been a very rewarding distraction and time spent in the first year teaching lab was rarely unenjoyable; mostly due to Prof Jacquie Robson's enthusiasm and guidance.

Finally, my great gratitude to Karl for his wisdom and experience guiding and challenging me to better my work and produce the highest quality research possible, and for his support to follow original ideas and develop new skills; without which I would have never had the confidence to embark on the journey of programming and statistics that features prominently in my published work.

Table of Contents

Abbreviations

μ	.....	Mean
2D	.....	used for 2D materials and a Raman peak from graphitic carbon labelled 2D - usage should be clear from context
AFM	.....	Atomic Force Microscopy
BET	.....	Brunauer–Emmett–Teller Theory
BSE	.....	Backscattered Electrons
ccp	.....	Cubic Close Packed (Crystal Structure)
CVD	.....	Chemical Vapour Deposition
DMF	.....	Dimethylformamide
EDX	.....	Energy Dispersive X-Ray Spectroscopy
EELS	.....	Electron Energy Loss Spectroscopy
GC-MS	.....	Gas Chromatography - Mass Spectrometry
GNP	.....	Graphite Nanoplatelet
GO	.....	Graphene Oxide
hcp	.....	Hexagonal Close Packed (Crystal Structure)
HOPG	.....	Highly Ordered Pyrolytic Graphite
HRTEM	.....	High Resolution Transmission Electron Microscopy
I_{2D}	.....	Intensity (height) of 2D Raman Peak
I_D	.....	Intensity (height) of D Raman Peak
I_G	.....	Intensity (height) of G Raman Peak
IR	.....	Infra-Red Spectroscopy
iTO	.....	In-plane Transverse Optical (Phonon Mode)
LEED	.....	Low Energy Electron Diffraction
LO	.....	Longitudinal Optical (Phonon Mode)
MOF	.....	Metal Organic Framework
MS	.....	Mass Spectrometer/Spectrometry
MWCNT	.....	Multi-Walled Carbon Nanotube
NMP	.....	N-Methyl-2-Pyrrolidone
NPs	.....	Nanoparticles
P_{10}	.....	10th percentile (10% of data below this value)
P_{90}	.....	90th percentile (90% of data below this value)
Q_{25}	.....	Lower Quartile (25% of data below this value)
Q_{75}	.....	Upper Quartile (75% of data below this value)
RF	.....	Resorcinol-Formaldehyde
rGO	.....	Reduced Graphene Oxide
$r\chi^2$	.....	Reduced Chi-Squared
SAED	.....	Select Area Electron Diffraction
SDS	.....	Sodium Dodecyl Sulfonate
SE	.....	Secondary Electron
SEM	.....	Scanning Electron Microscopy
TEM	.....	Transmission Electron Microscopy
TGA	.....	Thermal Gravimetric Analysis
UV-vis	.....	Ultra-Violet Visible Spectroscopy
XRD	.....	X-Ray Diffraction

1. Introduction

This literature review seeks to introduce some background to graphene research focussing on the most remarkable properties and potential applications that follow from them. Different methods for the production of graphene will then be reviewed and the challenges currently faced in scaling up such methods will be discussed. Considering the different materials produced and metrologies required some applications, notably energy storage devices may be better served with related but less ordered graphitic carbon materials that can benefit from the insight provided by graphene research. These disordered graphic carbon materials and the methods by which they are produced serve as background to projects to further the analysis and understanding of functional graphene derived materials. Finally this review will conclude with emphasis on the metrology of 2D materials as this is a focus of the research included in this work

1.1 Graphene Introduction

Different allotropes of carbon have been investigated for decades due to carbons abundance and the range of remarkable properties observed;[1] however, the isolation of graphene in 2004 provided a new material on which to test fundamental physics.[2] Graphene's remarkable properties had won Novoselov and Geim the physics Nobel prize in just six years and encouraged an exponential growth in the research interest of 2D materials.[3]

1.1.1 Structure

Graphene is a monolayer of sp^2 carbon atoms bonded in a planar hexagonal array, each atom forming three in-plane σ bonds to surrounding carbon leaving one electron occupying a $2p_z$ orbital that contributes to a large delocalised π system of electron density. This carbon layer has been used as a building block to describe other allotropes; illustrated in Figure 1 a single layer of graphene can be rolled into a 0D fullerene or a 1D nanotube or sheets can be stacked to form 3D graphite.[4] Dimensionality leads to different properties, for example carbon nanotubes can be metallic or semiconductors whereas graphene is a semimetal; but there are properties common to all allotropes like strong van der Waal attractions.[5,6]

Stacking graphene sheets to form graphite can result in a number of different stacking sequences that have been extensively investigated, as this is different between sources. The most thermodynamically favourable structure of pristine graphite is a hexagonal ABAB or 'Bernal' stack. Additionally an ABCA stacking sequence with a rhombohedral unit cell is relatively common and can make up 40% of natural graphite samples,[7] finally an unusual AAA

stacking sequence has been observed.[8] These structures can affect the exfoliation of layers and on a small scale the different stacking sequences can alter the electronic structure of few-layer graphene.[9,10] Graphitic carbon materials can also contain graphene sheets with no regular stacking pattern termed turbostratic graphite; this disordered carbon has a larger interlayer spacing, > 0.342 nm compared with 0.335 nm Bernal stacked,[11] to facilitate the rotations and dislocations of different sheets. Such disordered stacks are more commonly observed from smaller few layer graphene flakes than larger crystals.

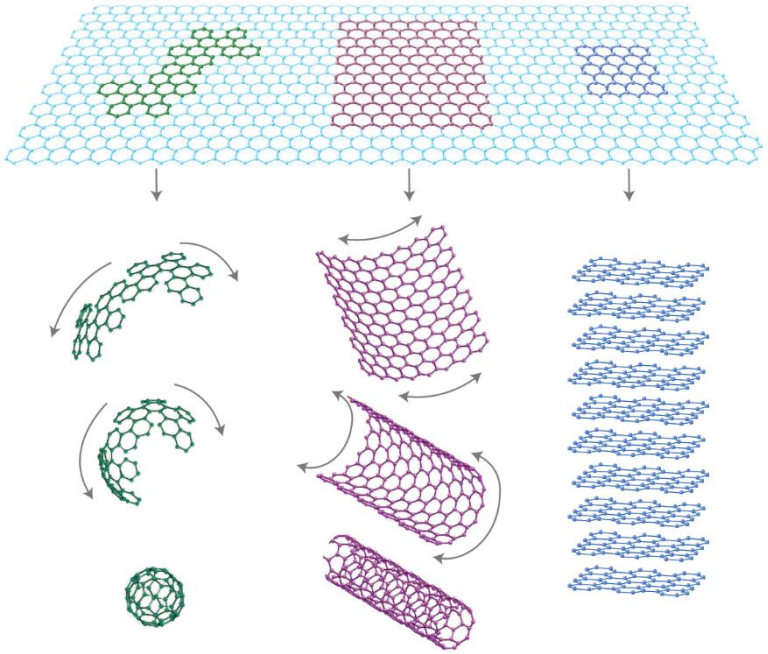

Figure 1: Graphene can be used as the starting point when modelling other allotropes of carbon. Left: rolling graphene into a C_{60} fullerene; Centre: rectangular sheets can be rolled into nanotubes; Right: graphene sheets restacking to form graphite.

Returning to graphene the number of layers is hugely important to the properties observed and as a result the ISO definition of graphene differentiates 'monolayer' graphene, containing only a single carbon layer, 'bilayer' containing two and 'few-layer' graphene containing fewer than ten layers.[12] These definitions are based on clear differences in electrical and physical properties like band structure and thermal conductivity.[4,13]

The other notable structural feature of graphene sheets is the lateral size and edges that cap the sheets; ignoring the topic of heteroatoms there are two environments edge carbon atoms can be located in: 'zig-zag' edge and 'armchair' shown in Figure 2. The armchair edges are more stable compared with zig-zag edges that have non-bonding π electrons imparting a greater chemical, electronic and magnetic activity; although, both edge types readily

scatter electrons reducing the conductivity between small flakes.[14,15] Despite the differences between these edges most materials contain a random mixture of different edge chirality's that make practically differentiating them all but impossible.[16–18]

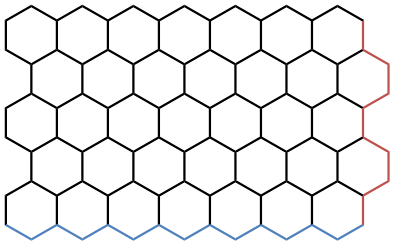

Figure 2: The skeletal structure of graphene with the armchair (red) on the right and zig-zag edges (blue) on the bottom highlighted.

Finally an introduction to other graphitic materials related to the structure of graphite is required; for a full discussion of the different materials and suggested nomenclature see an editorial in *Carbon*.[19] Many companies provide graphite nanoplates (GNPs), 2D graphite materials with a thickness and/or lateral size less than 100 nm. This is far smaller than conventional graphite powders; however, many of the quantum properties are lost when so many graphene layers are stacked together. Another common method of preparing graphene is by oxidising graphite to aid the exfoliation of different layers and then reducing the material back to a carbon sheet. Further details are provided in Section: 1.3.1 Graphene Oxide, here it should be noted that graphene oxide (GO) and reduced graphene oxide (rGO) show significant damage to the carbon framework and their properties are quite distinct from pristine graphene.

Finally graphitic carbon refers to a very broad category of materials consisting primarily of sp^2 bonded carbon but lacking the long range crystal ordering of graphite or graphene; technically graphitic does imply the existence of 3D order with some semblance of layers but lacking any formal, even rotationally disordered, stacking (cf. turbostratic).

1.1.2 Electrical Properties

The structure of graphene is important for many remarkable properties. The electronic properties that are so unusual are dominated by the behaviour of the π and π^* electrons that form the lowest unoccupied conduction band and highest occupied valence band in the band structure. At the high symmetry $\mathbf{K}$ point, located at the vertexes of the hexagonal Brillouin zone these valence and conduction bands have linear dispersions and become degenerate at a Dirac crossing as shown in Figure 3; the result of this is a metallic fermi surface at that point making graphene a semimetal. The valence and conduction bands

remain discrete bands, but there is no energy difference between them and a vanishingly small occupancy of overlapping energy states.[2,4,20–22] The lack of a band-gap in graphene makes it unsuitable as a transistor material; nevertheless, it has many other remarkable properties.

It has been shown that electrons around this crossing of valence and conduction bands at the **K** point, termed the Dirac point, behave as Dirac fermions with an effective mass of zero and capable of lossless ballistic transport; whereby charge carriers undergo no scattering events because of the low occupancy of energy levels and experience no force field from the lattice restricting their movement.[23,24] Such Dirac fermions theoretically conduct charge at relativistic speeds over microscale distances with no loss of energy. In practice long range scattering from defects in the lattice and thermal imperfections as well as doping and force fields extending from any substrates prevent such behaviour occurring perfectly.[25,26] Despite this record electron conductivities of 230,000 $cm^2\ V^{-1}\ s^{-1}$ have been obtained from pristine single layer graphene held in ultrahigh vacuum conditions.[27]

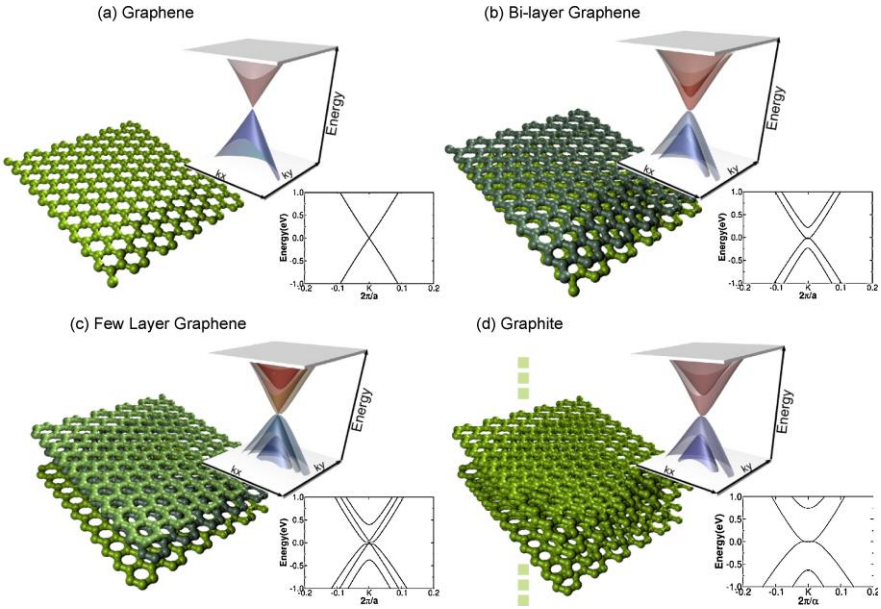

Figure 3: Illustration of increasing layer number on the band structure of graphene close to the **K** point. a) shows the characteristic Dirac point of graphene which is lost in bilayer b) and reappears in tri-layer c) whilst d) shows the semimetal character of graphite.

Ballistic transport is not the only quantum phenomenon observed in graphene at room temperature; under an applied magnetic field graphene exhibits a quantum Hall effect up to 300 K in a field of less than 20 T.[28,29] This is an unusual example of a quantum phenomenon being observed on the macro scale; previously, observing it required semi-conductors below

liquid helium temperature. Other phenomena linked to graphene are the Klein paradox whereby massless, relativistic particles will tunnel through a potential energy barrier;[30,31] and the lack of a band gap leads to the breakdown of the Born-Oppenheimer approximation.[32]

These phenomena have been linked to pristine monolayer graphene although the addition of a second layer can change these properties. The Dirac point in the band structure depends on the symmetry of the lattice, by disrupting this symmetry the band structure and electronic properties are disrupted. An extreme example is hexagonal boron nitride which can be considered a graphene lattice with two atoms present and is a semiconductor with a band gap around 5.9 eV.[33] The addition of a second graphene layer can also open a tuneable bandgap by effectively adding two additional orbitals as shown in Figure 3;[21] with control of the electric field across the layers a bandgap of 250 meV has been reported.[34]

The bandgap and other electrical properties are also strongly influenced by the stacking order. Some reports indicate the electron dispersion around the $\mathbf{K}$ point depends on ABA or ABC stacking.[7,35] In turbostratic systems the interactions between layers appear to be minimal and Raman spectra indicate layers are effectively electronically independent. Detailed discussion of the electronic properties of graphene are available in reviews on the subject, but these examples illustrate the importance of the band structure of graphene in controlling many of the most useful and interesting properties, and how influential the structure of these materials is to ensure the desired properties are obtained.[17,20,36]

1.1.3 Physical Properties

Graphene's record properties are not just electronic, the linear dispersion of energy states around the $\mathbf{K}$ point responsible for rapid electron transport also lead to ballistic phonon transport properties;[37] phonons of vibrational energy are transmitted virtually without loss through the high symmetry lattice resulting in a record thermal conductivity, reaching 5300 W/mK at room temperature.[38] Graphene also has a negative thermal expansion coefficient, this has been observed practically as graphene grown at high temperatures on a substrate expands during cooling whilst the substrate shrinks resulting in wrinkles in the graphene;[39] attempts to measure or calculate the magnitude of this effect produce a range of values around 10^{-6} K^{-1} although there is considerable uncertainty.[40,41] Theoretically this property is common to many 2D materials, caused by the dominant effect of the transverse acoustic phonon mode (ZA).[41–43] As the thermal energy increases this phonon mode increases the wavelike vibrations of the flexible carbon sheet in the *c*-axis illustrated approximately in Figure 4, this effectively pulls the edges of the sheet inwards shrinking the graphene unit cell.

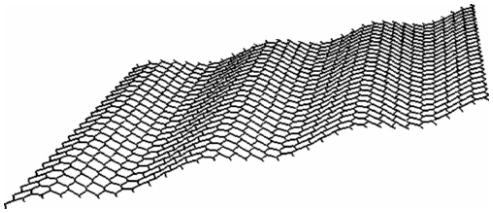

Figure 4: The ZA acoustic phonon primarily responsible for the negative thermal expansion coefficient of graphene.

The strong in-plane σ bonds and high flexibility make graphene the strongest material measured with an in-plane Young's modulus of 1.0 ± 0.1 TPa as measured by atomic force microscopy (AFM).[44] This covalent network is impermeable to gases including helium and being only one atom thick is also the thinnest material known with a large theoretical surface area of 2630 m^2/g.[45,46] The high strength provided by the in-plane bonds and flexibility of the 2D sheet appears to be a common feature of other 2D materials with monolayer MoS_2 being reported to have a Young's modulus of 270 GPa in comparison to bulk 238 GPa.[47]

The combination of such remarkable properties clearly makes graphene a versatile and useful material in a wide range of applications as discussed in the next section. First though, it is necessary to highlight the difference between perfect monolayer graphene that requires painstaking micromechanical exfoliation to prepare, and graphene produced by industrially scalable methods. The incredible electron mobility was only possible from a pristine single layer, suspended 150 nm over a SiO_2 substrate in ultrahigh vacuum conditions at 5 K after thermal annealing to remove contaminants.[27] Likewise less than a year before the record 1 TPa Young's modulus was recorded by Lee et al. a very similar measurement on graphene from Kish graphite only achieved 0.5 TPa.[44,48]

Fortunately most applications do not actually require graphene's full potential; polymer composites can be strengthened with small processable graphite platelets and many electrical devices have been investigated using conductive inks. The next section will introduce a few applications of graphene materials before considering the different production methods and challenges still to overcome but the fundamental studies of graphene have allowed such applications and provided great insight to other 2D materials that are being developed with many useful properties distinct from graphene.[49,50]

1.2 Applications of Graphene

With so many useful properties detailed in the previous section, graphene has been linked to a great variety of potential applications.[4,51–54] Here a few examples will be given and graphene formulations and energy storage applications will be discussed in greater detail since the requirements of such devices are relevant to the research undertaken.

The record thermal conductivity of graphene makes it ideal for next generation cooling systems in microelectronics;[55] also in microelectronics the high conductivity, flexibility and relative transparency of few-layer graphene make bendable screens and electronic devices theoretically possible.[56] The barrier properties of graphene could be used in future protective barrier coatings and selective membranes;[57] the quantum Hall effect would allow room temperature resistance standards with high accuracy and the strength of graphene sheets can be used in polymer composites to improve the strength and conductivity of high performance polymers.[58,59] This is a very small selection of devices that have been proposed with graphene in mind; but to date relatively few have been commercially realised.

1.2.1 Graphene Formulations

By processing graphene as a liquid reagent it can be easily integrated into existing manufacturing processes and many applications would benefit from strong highly conductive graphene flakes; as such the process of formulating stable graphene dispersions that can be added into polymer composites or printed to form electrical devices was among the first industrial projects undertaken.[60–62] Conductive graphene inks can be used to cheaply prepare new electrical devices like RF ID tags and wireless components, example shown in Figure 5, and the potential for transparent conductive tracks allows transparent heaters, displays, sensors, OLEDs and organic photovoltaic devices.[63–69]

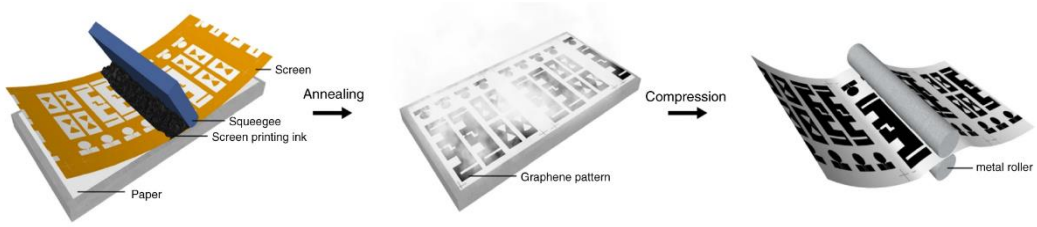

Figure 5: Graphene antenna fabrication using screen printing technology: patterning graphene ink via exposed screen and squeegee, annealing printed patterns and compressing dried pattern with steel rolling machine.

Reproduced from Pan, K. et al.; *Nat. Commun.* **2018**, 9 (1), 5197.

Conductive inks for printable electronics and 3D printing have been researched for some time. Metal nanoparticles provide excellent electrical conductivity, unfortunately the high cost of silver and gold is a barrier to cheap device production and cheaper metals like copper and nickel suffer from oxidative decay. Conductive polymers on the other hand do not achieve the electrical conductivity required.[70] Graphene is potentially a low cost highly conductive material for inks if current problems with stability and concentration are overcome.

Most research to date has used GNPs in place of pristine graphene and whilst the conductivity is effective the concentrations are too low requiring multiple layers to be printed.[71] Graphene oxide, the production of which is discussed in detail later, is also used because of the higher concentration and stability in water that can be achieved. Unfortunately GO has a low conductivity requiring post-printing reduction that is not compatible with most flexible substrates. The main barrier to graphene based inks is the concentration that can be stability dispersed in a solvent suitable for printing; and the production of such material at scale.[69–71] Currently liquid exfoliated graphene uses high boiling solvents that are not compatible with printing methods.[72] A method has been reported to exfoliate graphene in DMF, a good solvent for graphene, and then use distillation to transfer the graphene into terpineol, a good solvent for printing. Whilst effective, this is a complex and costly process not amenable to scale.[73]

Graphene composites can also benefit from stable formulations, common methods for the introduction of graphene into polymers use melt processing to blend the polymer when molten. The wetting of the highly hydrophobic graphene by the polymer can be problematic for the creation of strong composites if the adhesion between filler and polymer is poor.[74] To solve this problem functionalised graphene, that is graphene flakes chemically modified to alter their wettability, are used to improve the adhesion.[75] In many circumstances the composite is improved more by small graphite flakes than true graphene but the production of graphene like material in stable liquid dispersions remains a very topical area of research.

1.2.2 Energy Applications

Graphene is very commonly proposed for energy storage materials and other renewable energy related applications because of the high electrical conductivity, low density and relative abundance of carbon; however, the actual properties of monolayer graphene are unsuitable for many energy storage devices. Lithium ion batteries, currently the most energy dense storage devices, rely on the reversible intercalation of Li^+ between the sheets of the

graphite anode which clearly would not be possible if the graphene layers were separated. Li^+ ions are known to adsorb to the surface of graphene sheets hinting at the possibility of pure graphene battery electrodes; unfortunately, their stability is severely limited.[76] Within conventional Li-ion batteries it has been suggested the graphene based materials could improve performance by better controlling the morphology of the anodes; utilising small sheet sizes to aid the transport of Li^+ ions or by encapsulating electrode materials to aid activity with a flexible support that can handle the expansion and contraction during charge/discharge cycles.[77–80]

1.2.2.1 Sodium Ion Batteries

Alternative sodium ion batteries have recently gained traction after being left behind when the rocking chair Li-ion battery was widely commercialised. The advantage of Na-ion batteries is the abundance of sodium and electrode materials in comparison with Li based batteries; but currently a major challenge in Na-ion battery design is the anode.[81,82] Whilst viable cathodes have been tested the conventional graphite anode found in Li-ion cells does not perform comparably. The larger ionic radii of Na^+ makes intercalation thermodynamically unfavourable but Na^+ is known to adsorb onto graphene sheets, especially doped or defect sites on the surfaces.[81,83,84] Graphene, or more accurately reduced graphene oxide, has been investigated as a potential anode but most recent reports use it as a support structure for other active materials.[85,86] In August 2020 only 213 articles on "sodium ion battery" and "rGO" were found.* The characterisation of layer stacking and sp^2 carbon environments are relevant but 'hard carbon' is more viable for batteries.

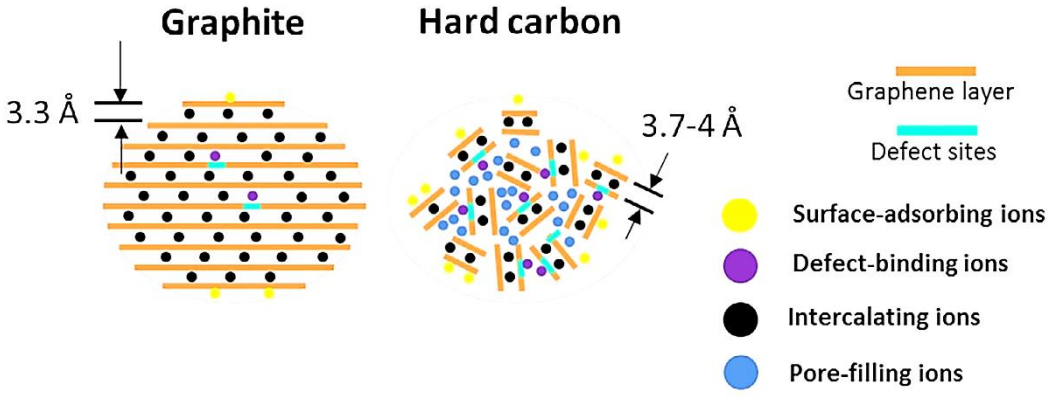

Figure 6: Schematic illustration of the differences in ion storage between graphite and hard carbon.

Adapted with permission from: Xiao, B; Rojo, T; Li, X; *ChemSusChem*, 12, 133-144, **2018**. Copyright John Wiley and Sons 2018.

* *SciFinder* search on 17/08/2020; search parameters: Topic = "sodium ion battery" AND "rGO", English language, Letters and Journals, dated from 2010 onwards only.

Hard carbon is a type of non-graphitizable carbon with a complex structure at the molecular level, many graphitic regions nanometres in size are randomly bound together with no long range order or stacking.[83,84] For the purpose of understanding ion storage in such materials a "house of cards" model is often employed with graphitic domains lying on top of one another and producing micropores in between; generally formed at high temperatures as existing graphenic domains gain sufficient thermal energy to rotate and 'collapse' onto other graphenic sheets forming very localised small graphitic stacks.[87] These materials are thought to provide three main ion-storage sites illustrated in Figure 6: intercalation between the turbostratic graphitic sheets, storage in closed micropores and surface adsorption aided by defects and dopants. There remains debate on the exact sequence by which Na^+ storage takes place and this literature introduction does not intend to review such evidence; but the importance of the carbon structure for battery performance is very clear.[83,88,89]

In brief, the interlayer spacing of turbostratic graphite should be increased to facilitate better Na^+ intercalation and improve capacity without increasing the layer spacing such that exfoliation becomes an issue.[90] The capacity can also be increased by increasing the micro porosity; unfortunately open and accessible surfaces react with the electrolyte and sodium during the first cycle, which reduces performance. Finally the introduction of dopants and defects in the graphene sheets increases sodium adhesion and interlayer spacing; unfortunately the localised nature of Na^+ adsorption repels further cations and reduces capacity. In essence battery technology is likely to benefit from graphene science due to better characterization and structural understanding but pristine graphene is of little interest for battery research.[83,91]

1.2.2.2 Supercapacitors

Graphene related materials have also been suggested for supercapacitors, devices that functionally sit between batteries and capacitors with intermediate energy and power densities. Numerous applications have been proposed but whilst a few commercial examples exist, improvements to gravimetric capacitance and device stability are required.[92] Very briefly supercapacitors store energy through two main mechanisms: electric double layer and pseudo-capacitance.[93] Electric double layer capacitance refers to the storage of electrical potential energy in the layer of charged particles attracted to the oppositely charged surface of an electrode.[94] Pseudo-capacitance stores electrical energy through redox reactions but unlike a battery the redox reactions take place between an electrode and electrolyte, rather than between two electrodes.

Graphene and related carbon materials may have the perfect properties with high surface areas, high conductivity, low weight and excellent chemical and mechanical stability; but to exploit these properties better understanding of the production and characterization of the carbon is required.[76,92,95–97] For a detailed discussion of graphene supercapacitors see the aforementioned reviews on the subject, but the primary limitation is control over structure. In both double layer and pseudo capacitor devices a high, accessible, surface area is required with good electrical conductivity and ionic diffusion characteristics; this requires hierarchically porous materials with a mixture of pore sizes. Generally cheap activated carbons do not meet all of these requirement whilst templated materials based on graphene and carbon nanotubes perform better but at hugely increased costs.[96,98–100]

The best device performances appear to be when using conductive carbon foams as a structural support for redox active particles, shown in Figure 7. These particles increase the capacitance and prevent reaggregation of the graphitic material whilst the carbon provides greater stability during repeated charge/discharge cycles and aid the conductive interface between the current collector and active electrode.[76,92,101–103] The most common material trialled for this application is rGO because of its ease of handling although other carbon foams have improved surface areas or conductivity depending on production.[95,104]

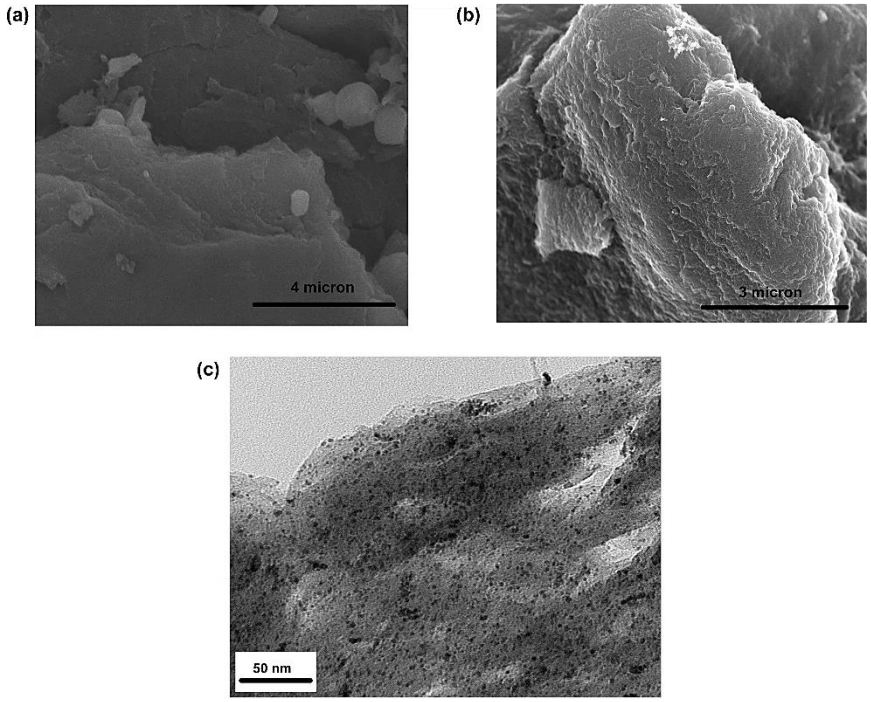

Figure 7: Images of dried graphene sheets and Pt nanoparticle separated graphene sheets. (a) SEM of dried graphene sheets, layered structure is observed. (b) SEM image of dried Pt−graphene sheets. (c) TEM image of thin slice of dried Pt−graphene sheets, black dots are Pt nanoparticles.

The electrical conductivity and relatively inert behaviour of graphene has also been applied for catalyst supports for both electrocatalysis and photocatalysis; reduced graphene oxide is commonly used because of its ease of handling and device preparation but other carbon foams have been applied. When using a pure carbon material the carbon foam provides a porous support to catalytically active nanoparticles for water splitting or waste water treatment.[105–108] But other systems have been trialled using doped graphene or alternative 2D materials with a substantial band-gap;[109–113] required for the excited state whether it be photoexcited electron-holes or electrically excited species to do chemical work.[114]

1.2.3 Commercial Devices

Whilst remarkable many of these applications are still firmly research ideas. Nevertheless, a number of commercial products containing graphene have been produced. The first was a printed security tag using graphene ink supplied by Vorbeck in 2012. This was followed by the HEAD tennis racquet in 2013 and skis in 2014 using graphene nanoplatelets from Applied Graphene Materials, and more recently in 2018 graphene enhanced golf balls from Callaway. By far the most common use of graphene is in high end sporting equipment where graphene is added to the composite to purportedly improve strength whilst reducing weight. In 2015 Graphene Lighting Plc released an LED with a printed graphene component and in 2017 Team Group announced a solid state computer drive with a graphene and copper foil cooling system. This list in not exhaustive; however, in contrast to many of the remarkable applications proposed above there still remains a discrepancy between commercially realised graphene and the theoretical possibility.

Some of these are fundamental limitations in device design and in some cases the relevant industries require time consuming testing and validation before new products can be launched like aerospace and biomedical applications.[115] Another very significant issue is the scalable production and characterization of graphene materials suitable for the proposed applications. Since different production methods result in graphene related materials with different properties, the manufacture and quality control should be tailored.[116]

1.3 Graphene Production

The seminal paper on the isolation of single layer graphene utilised micromechanical exfoliation with sticky tape to repeatedly exfoliate graphene layers from a highly ordered graphite sample.[2] This is a very reliable method of pristine monolayer graphene production but such a labour intense approach can never be scaled up. Many other approaches for the

production of graphene have now been investigated with different advantages and disadvantages; and this section aims to provide an overview of these approaches with consideration to the properties required by applications. Broadly all methods of graphene production are described as 'bottom-up' or 'top-down' as illustrate in Figure 8: bottom-up refers to the construction of graphene sheets from atomic carbon building blocks whilst 'top-down' refers to the extraction of graphene layers from graphite.[117]

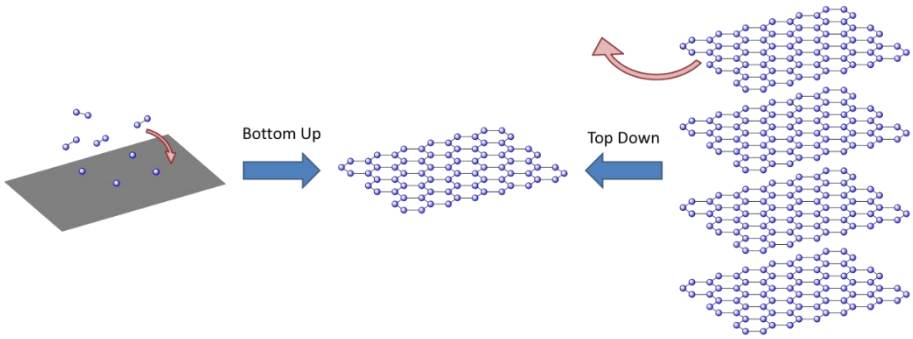

Figure 8: Schematic describing the two primary approaches to the synthesis of graphene. Bottom up synthetic techniques from vapour phase carbon atoms shown as blue spheres and the top down approach by exfoliating graphite layers.

1.3.1 Graphene Oxide

Before pristine graphene was isolated the oxidation of graphite into a water processable form was known, and the Hummers method, published in 1958, remains the predominant method of graphene oxide (GO) production.[118] GO is formed by the oxidation of graphite using strong oxidising agents, specifically permanganate, nitrate and sulfuric acid; this disrupts the sp^2 network and decorates the surface with hydrophilic functional groups. The exact structure is still debated although hydroxyl, carbonyl, epoxide, carboxylic anhydride and carboxylate groups have all been found.[119–121] The oxidised graphite is then exfoliated in water producing the graphene and centrifuged to separate residual graphite from the GO.

The ease of processing in aqueous media makes GO popular for research but the stability is a result of functional groups which also disrupt the sp^2 conjugated network; this disruption of the structure reduces the conductivity and strength of the sheet and destroys all the unusual quantum properties that make graphene so useful.[119,122] It is possible to reduce GO, forming reduced graphene oxide (rGO) but it has not been possible to completely repair the conjugated network once destroyed.[123,124] In most cases reduction removes the oxygen containing functional groups leaving holes in the graphene sheet.[125] Nevertheless high conductivity values have been recorded from rGO and the chemical processability of the starting GO has facilitated hybrid materials with nanoparticles attached to graphene sheets

for supercapacitors and other functional devices.[80,126–129] The high surface area and hydrophobic character also makes rGO an ideal candidate for waste treatment by the facile adsorption of organic pollutants from waste water streams.[130,131]

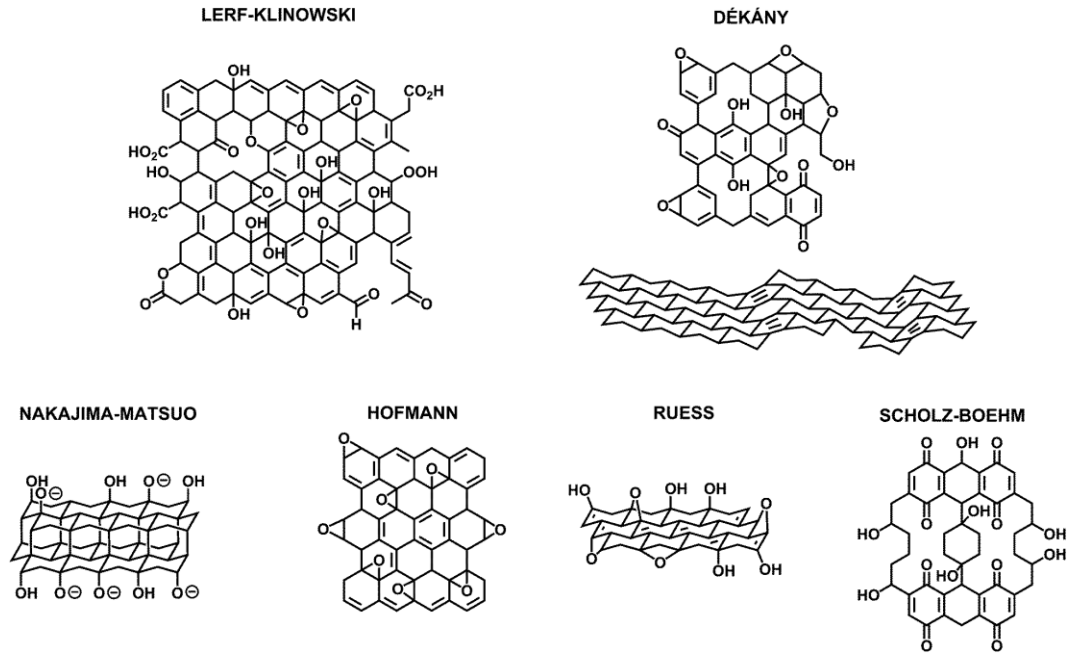

Figure 9: Structural models of GO, the Lerf-Klinowski model is more commonly accepted but there is still debate over the nature of the GO structure.

Reproduced from D. R. Dreyer, A. D. Todd and C. W. Bielawski, *Chem. Soc. Rev.*, **2014**, 43, 5288–5301 with permission from the Royal Society of Chemistry.

Applications of GO are limited by the poor properties compared with pristine graphene. GO conductive inks have too low concentration for viable printing and pollutant remediation is more cheaply done with activated carbon or other high surface area materials.[132] Despite these limitations over 70,000 papers have been published, as of November 2020, on the topic of graphene oxide† and the overwhelming majority claim GO to be the most scalable method of graphene production. That claim does appear to be rather unfounded; the widely adopted Hummer's method requires multiple high energy purification and washing steps and results in a large volume of waste. Analysis of a recent paper on improving graphene oxide production[133] results in an E-factor, a green chemistry metric of process efficiency,[134] of ~1330. That is two orders of magnitude higher than the pharmaceutical industry and four orders of magnitude higher than the petrochemical industry; and whilst a direct comparison between industrially optimised processes and lab scale research is perhaps unfair it is clear the material requirements for GO production, even before any reduction, are immense.

† Clarivate Analytics through WebofScience; search parameters: Topic = "graphene oxide", English language, Articles or Letters on 11/11/2020

It must also be noted that unlike other carbon materials derived from renewable sources GO still requires natural graphite; which is itself in great demand as global battery requirements increase.[135] Graphene oxide has been an excellent experimental platform that is easy to handle and integrate into other chemical reactions, and may have an industrial utility. Nevertheless, the large discrepancy between the properties achieved for the cost of production may explain why it has failed to find a commercially viable application to date.

1.3.2 Expanded Graphite

Expanded graphite is distinct from graphene since the flakes are still hundreds of nanometres thick; although it has been used to produce small, processable graphite flakes for over a century.[136,137] The process is relatively simple, a graphite intercalation compound is prepared with ions or small molecules trapped between the graphene layers increasing the spacing and disturbing the van der Waal forces holding the graphite together. The material is then heated or subject to mechanical force causing the intercalated stack to expand forcing small graphite flakes apart as illustrated in Figure 10.[138] Electron micrographs show the original material is made from dense graphite flakes but after the intercalated sulphate was removed the material forms a low density collection of thinner films.

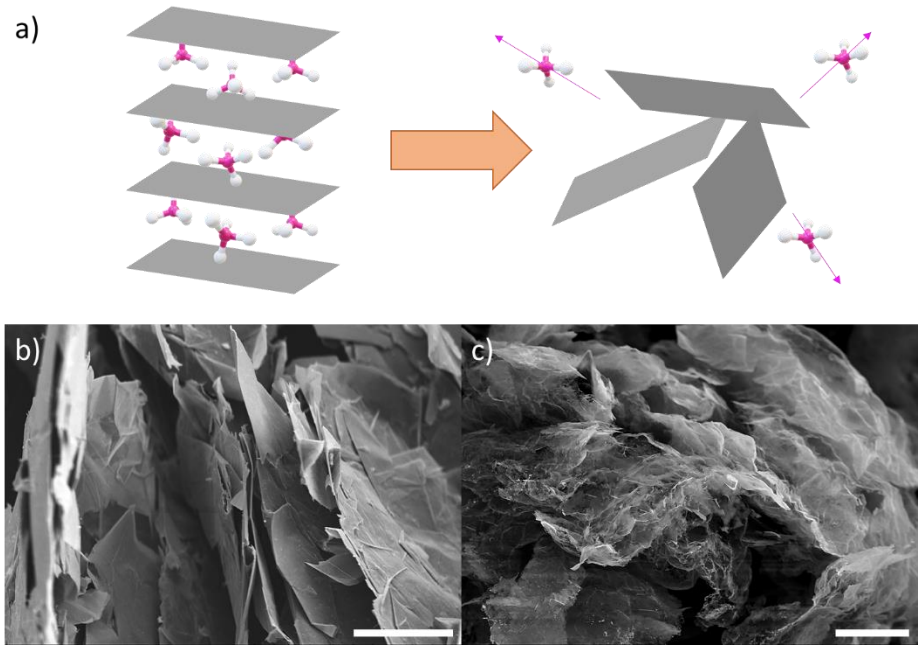

Figure 10: Graphite intercalation compounds can be thermally expanded; a) shows an illustration of ions intercalated between graphene sheets and the expanded disordered structure after heating. SEM micrographs of b) a sulfate intercalated expandable sample and c) shows the expanded graphite; scale bars 25 µm in both cases.

Expanded graphite materials have been used as lubricants in gaskets, in seals, thermal insulators, conductive resins, electrodes and adsorption substrates.[138] Recently with an

renewed interested in graphene and nanosized graphite materials expanded graphite is often subject to mechanical exfoliation to produce graphene nanoplatelets (GNPs).[139] Depending on the production method such materials often contain more defects than graphene exfoliated from pristine graphite but the small flake sizes are more stable to sedimentation and aggregation.

The most common intercalated species is sulphate because it is easy to produce from sulfuric acid and remains relatively stable to air and moisture.[140,141] Other systems have been reported including $FeCl_3$, K^+, Ca^{2+}, ClO_4^- with different properties;[142] potassium intercalated graphite in particular is commonly used to covalently functionalise graphene sheets. Although the difficulty of handling such materials restricts such an approach to the research lab.[143–145]

1.3.3 Liquid Phase Exfoliation

Exfoliation of single layer graphene from graphite represents a promising route to high quality graphene sheets at a large scale. This has resulted in significant research, much of it based on work done with carbon nanotubes,[146] to exfoliate graphene materials in the liquid phase resulting in graphene dispersions. Many different systems of solvent, graphite treatment, exfoliation methodology and stabilising agents have been trialled and comprehensive reviews are available.[147–149]

1.3.3.1 Exfoliation Techniques

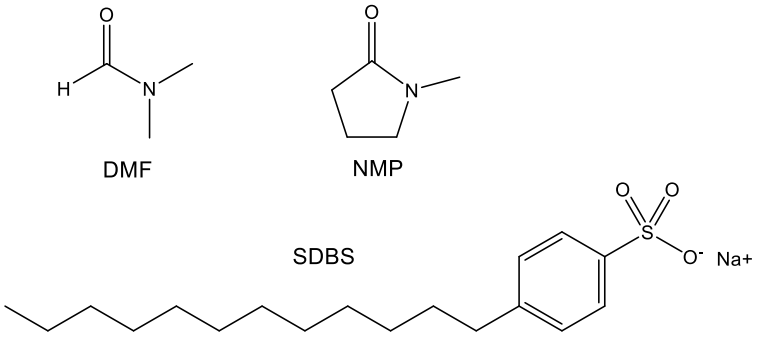

Figure 11: Chemical structures of solvents NMP (N-methyl-2-pyrrolidone) and DMF (dimethylformamide); and surfactant SDBS (sodium dodecylbenzene sulfonate) used for the exfoliation of graphene.

Early work exfoliating graphene followed similar approaches found to be successful with carbon nanotubes, using high power sonication in the organic solvents N-methyl-2-pyrrolidone (NMP) and dimethylformamide (DMF) carbon concentrations of 0.01 mg ml^{-1} were achieved.[150,151] The efficiency of graphene exfoliation from the bulk graphite was measured using microscopy which confirmed the successful production of monolayer

graphene with few defects. The exfoliation of graphene with water and sodium dodecylbenzene sulfonate (SDBS) surfactant was reported shortly after; achieving 67% of flakes less than five layers and a concentration of 0.05 mg mL^{-1}.[152] Further efforts to improve the method with solvent selection and mixed solvent systems, processing conditions and graphite treatment have been trialled; since solvent considerations are common to all liquid exfoliation the key results are discussed later; but using sonication concentrations of 63 mg mL^{-1} have been reported.[153]

The exfoliation of graphene flakes by sonication is attributed to the massive amounts of localised energy imparted by the collapse of cavities generated by ultrasound waves.[154] Very recently this mechanism has been further investigated by Li et al. who monitored the effect sonication had on large graphite flakes over very short time periods combined with computational modelling and careful microscale analysis of the graphite structure.[155] They propose a three stage exfoliation mechanism shown in Figure 12; firstly large graphite flakes are rapidly split by the propagating sound waves causing cracks to form and expand along the graphite flakes. The sound waves produce kink and twist defects on the surface of the graphite flakes, these shallow defects cause the material between them to break off, effectively exfoliating narrow graphite strips from the larger parent flake. These small flakes are too small for kinks and twist defects to be localised on the surface and instead the high energies cause sheets to slip and become dislodged from the flake.

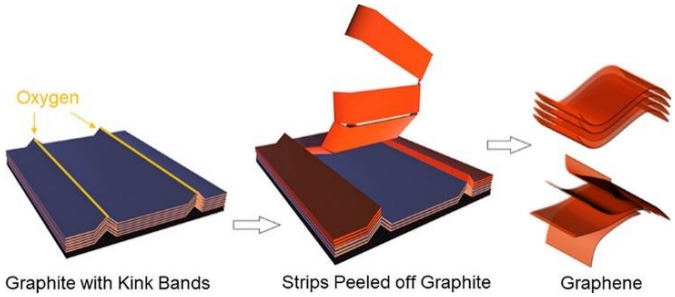

Figure 12: Graphene exfoliation proceeds via three stages, first large flakes are split and defects form. These defects facilitate the removal of smaller graphite flakes which are exfoliated into graphene.

Familiarity with the technique and relative ease has led to high power sonication in organic solvents, aqueous surfactant systems and polymer stabilised systems becoming widespread for the preparation of graphene dispersions. The main drawback to sonication is the small scale of production. Following this success wet ball milling was found to produce graphene dispersions in both DMF and SDS aqueous media.[156,157] It has since been used to produce and

functionalise graphene sheets in wet and dry systems; the disadvantage to ball milling is the long processing time required, in excess of 24 hours.[158] Required because ball milling produces two forces, impact forces directed normal to the graphene sheets and shear forces that slide graphene sheets laterally off the graphite stack. To maximise the shear forces responsible for graphite delamination longer, lower energy milling is required and even then defect formation and damage to the graphene sheets is unavoidable.

Shear mixing for graphene exfoliation was first reported in 2014 by Paton *et al.*[159]; it combines a high speed rotating mixer head - a rotor, and a stationary component - a stator, to generate a large difference in fluid velocity between them. The velocity gradient combined with the turbulent flow through the drain holes in the stator subject the liquid and any particles suspended within to strong forces as shown in Figure 13. It was initially assumed that shear mixing would require very high energy turbulent flow to replicate the energetic collisions induced by sonication,[160] fortunately this turbulent flow is not actually required and the limiting requirement is a minimum shear rate of 10^4 s^{-1}.[159]

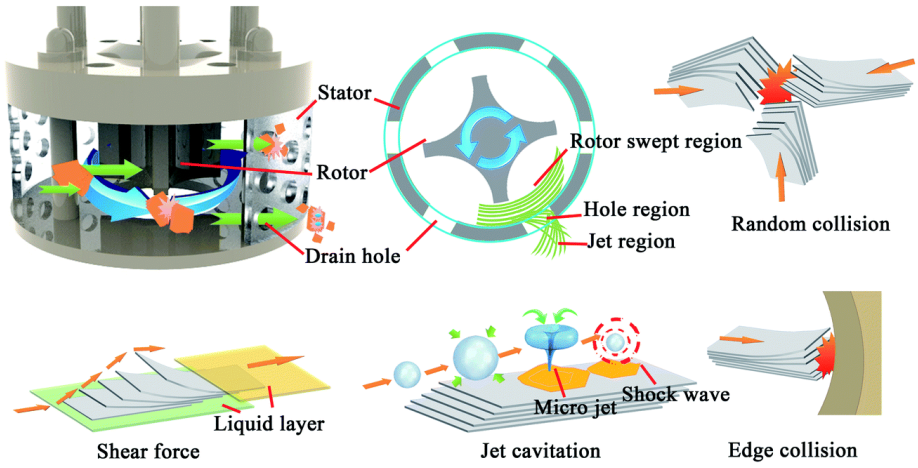

Figure 13: A diagram showing the design and process of high shear mixer typical for graphene exfoliation. Top left: 3D sectional drawing of the high shear generator and a top down section view of the main energy dissipation regions. Common energy dissipation events shown: random collisions, shear forces, jet cavitation and edge collisions.
Adapted from Ref. [160] with permission from the Royal Society of Chemistry.

The graphene produced was comparable to that produced by sonication with a concentration of 0.07 mg mL^{-1} in sodium cholate solution. Shear mixing also has similar solvent dependencies as other exfoliation methods, original testing used NMP and sodium cholate. The greatest strength of shear mixing is the scale of production, the rotor and stator can be increased in size for industrial production and even with engineering constraints it was estimated that 100 g h^{-1} could be possible in a 10 m^3 tank.

Finally the most recent method for mechanical exfoliation is microfluidization; a technique for the preparation of homogeneous dispersions of small particles by forcing fluid to flow through microscale channels (< 100 µm) under extremely high pressure (up to 207 MPa). This generates high shear forces applied to the entire fluid volume in contrast to previous techniques discussed that applied the shear forces locally. In a report from Karagiannidis et al. graphite was passed through a microfluidizer in an aqueous dispersion stabilised with carboxymethylcellulose sodium salt to produce graphite nanoplatelets approximately 10 mg/mL in concentration, although this included graphite flakes up to 200 layers in thickness.[161] Each additional pass through the channel clearly resulted in smaller flakes with lateral sizes decreasing from 0 – 20 µm after one cycle to the majority of flakes less than 2 µm after 100 cycles, although much of the material was thicker than few layer graphene.

These initial results show graphene production is possible but repeated cycles are likely required to produce small graphene flakes. Another study using sodium cholate in water found after 20 cycles and centrifugation to remove the largest unexfoliated material a concentration of 0.3 mg/mL, approximately 3% of the starting graphite material.[162] This in contrast with the original report of 100% yield achieved by including all carbon material passed through the fluidizer including flakes 70 nm thick.

The exfoliation of graphene layers from crystalline graphite is considered a promising method for large scale production. Sonication is most common in research laboratories where small volumes are required, but this is difficult to scale up. Ball milling can generate highly reactive species and may be ideal for functionalising graphene, but the damage caused to the conjugated network is sub-optimal. Shear mixing and microfluidization by contrast show more promise for scale up; indeed Thomas Swan currently sell graphene flakes produced by shear mixing following the seminal work by Paton *et al.*

1.3.3.2 Stability of Dispersions

As well as different exfoliation methods the solvent system used to stabilise the graphene dispersion must also be considered. It is unclear exactly how significant different solvents are to the mechanism of exfoliation;[155,163] however, they must be capable of stabilising the graphene flakes for delamination to occur and prevent reaggregation. The large surface area of graphene sheets provides a significant van der Waal attractive force driving aggregation, estimated to be approximately 0.04 mJ cm^{-2} per monolayer.[164–166] This must be overcome by either steric repulsion in the case of non-ionic surfactants and large polymers or the electric double layer stabilisation of colloidal graphene platelets.[152,167,168]

The solvent system must also facilitate the exfoliation event itself; the production of a new graphene sheet creates a new high energy interface between the graphene and solvent shown in Figure 14. To minimise the energy cost the interaction between the graphene and solvent should be close in energy to the solvent-solvent interactions it replaces.[150] Intuitively the use of aromatic solvents with π systems similar to graphene were investigated to minimise this interface energy, unfortunately these were generally found to be unstable.[169] A better measure is thought to be the surface energy match between the solvent and graphene surface, using the surface energy as a proxy for the interaction energy.[150]

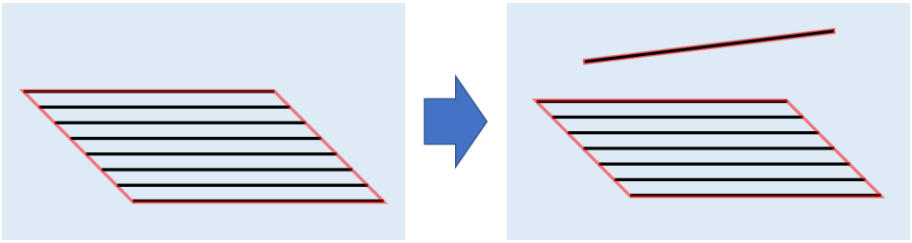

Figure 14: The high energy interface (red) between the graphite and solvent increases as a new graphene sheet is exfoliated from the parent graphite.

Refining this model further, the interactions between the solvent and graphene can be described by Hansen solubility parameters[170] and groups have attempted to use these to find new hybrid solvent systems for graphene exfoliation.[160,171,172] Hansen solubility parameters are a measure of the energy required to remove a unit volume of molecules from their neighbours to infinite separation; crucially Hansen parameters are divided into the energy contributions from polar, dispersive and hydrogen bonding components. In theory a match in all three components between the graphene and solvent would indicate a good interaction and very low surface energy at the interface. Unfortunately those values are known for very few solvents so surface energies remain commonly used as a proxy.

Matching the surface energy of solvents with the surface energy of graphene, the best solvent systems have surface tensions in the range 40 – 50 mJ m^{-2} consistent with many of the best solvents tested to date like NMP, γ-butyrolactone and DMF; for a full discussion of graphene solvent systems see comprehensive reviews.[72,147–149,158] This approach has also led to mixed solvent systems being trialled for graphene dispersions, by mixing high and low surface energy solvents it is possible to produce a mixture with the desired surface tension and improved properties for many applications.

1.3.3.3 Scalability of Graphene Inks

Liquid phase exfoliation that produces stable dispersions of graphene in a solvent system is clearly ideal for graphene based conductive inks that could be produced requiring relatively little further processing before printing. Currently limitations on concentration and rheology of graphene dispersions have prevented their widespread use and many attempts to improve the concentration result in other problems. The best solvents are thought to have high surface energies to facilitate exfoliation but these also have very high boiling points, making them difficult to evaporate after printing. NMP and DFM are also toxic so any industrially scalable graphene production must avoid such systems. O'Neill *et al.* compared the concentration of graphene dispersions in these high boiling solvents with common low boiling point solvents, specifically chloroform and isopropanol but found they could only achieve 50% the concentration of the high boiling solvents.[171]

Another method to introduce lower boiling point solvents is to add ethanol or propanol to water, reducing the surface tension. Unfortunately this approach has produced very low concentrations of graphene around 0.05 mg mL^{-1} compared with 1 mg mL^{-1} achieved with NMP.[9,173] Mixing solvents in surfactant systems has also been investigated, a blend of surfactant-ethanol-water was found to be more effective than the water-surfactant mixture achieving a concentration of 1 mg mL^{-1} without using toxic NMP.[163,174]

These are just a small sample of the approaches taken to improve the concentration of graphene dispersions in low boiling, environmentally benign solvent systems. As well as different concentrations reported, many result in different levels of exfoliation and flake sizes. Unfortunately individual micrographs and Raman spectra are poor metrics of overall material properties; so comparisons between different techniques is very difficult. However, the many different exfoliation conditions introduced can all be expected to produce different distributions of graphene thickness, flake size, defect density and surface functionalisation that will be better suited to different applications.

1.3.4 Chemical Vapour Deposition

The production methods discussed above were all 'top down', separating graphite layers into graphene. Chemical vapour deposition, or CVD, is a 'bottom up' technique that grows graphene from a carbon vapour, usually hydrocarbon gasses. Many different substrates have been trialled but transition metals are commonly used because of the favourable interactions between the metal and carbon catalysing the decomposition of hydrocarbons. Graphene layers on metal surfaces have been known for decades following LEED patterns of

carbon observed on Pt,[175] and many early studies of graphene growth focussed on epitaxial growth by matching the metal surface with the graphene structure.[176–178] This is possible for many metals but matching the crystal structure of substrate and graphene is complex.[179]

Graphene growth on polycrystalline surfaces represents a much easier method of graphene growth and is dominant for CVD graphene production. Initial reports used copper and nickel surfaces, proving graphene could be grown over metal grain boundaries and form larger graphene films; although only the copper surface produced single layer graphene.[180–182] The comparison of different metal substrates for graphene growth has been extensively reviewed elsewhere.[179,183–185] In summary, two growth mechanisms dominate: the precipitation of graphene from metals with high carbon solubilities at high temperatures and the surface growth from metals with relatively low carbon solubility.

1.3.4.1 Segregation Growth

Many transition metals with partially filled d-shells in their electron configuration show affinity for carbon and will readily form solid solutions at high temperatures, when the temperature decreases this carbon precipitates into graphene.[186–188] Ni, Co and Fe are typical of this although other metals have been investigated.[179,184] The disadvantage is the lack of thickness control, it is difficult to limit the amount of carbon dissolved into the metal which then precipitates to form multi-layered graphene. This is particularly pronounced at grain boundaries where meta-stable carbides can preferentially form, promoting greater precipitation.[180] Attempts to avoid multilayer growth have used less carbon precursor, slower cooling and controlling the thickness of metal films.[189]

Table 1: Summary of lattice constants and carbon solubility in some metals that have been used for graphene growth,[179] and the calculated equilibrium distance between the graphene layer and metal surface with the binding energy per atom of removing a graphene sheet from the metal surface.[190] (* Data for iron calculated from phase diagram using the γ phase[191]. ‡ The equilibrium distance and binding energy for cobalt were calculated from the (111) cubic face.)

	In Plane Lattice Constant / Å	Carbon Solubility at 1000°C / at.%	Equilibrium Distance / Å	Binding Energy per atom / eV
Graphite	2.46	N/A	N/A	N/A
Fe (111)*	2.86	7.26	*Data not available*	
Co (0001)	2.52	3.41	2.05‡	0.160‡
Ni (111)	2.49	2.03	2.05	0.125
Cu (111)	2.56	0.04	3.26	0.033
Pd (111)	2.75	5.98	2.30	0.084
Pt (111)	2.77	1.76	3.30	0.038

Nickel has the closest lattice match to graphene and forms a strong bond to carbon as shown in Table 1. Despite this strong interaction, the complete coverage of graphene films grown over grain boundaries is readily achieved at atmospheric pressures. By annealing the metal or increasing the deposition temperature larger grains of Ni(111) are formed which improves graphene film quality; to limit the thickness it is necessary to minimise the growth time during which carbon is available.[192–194] In a significant report Chae *et al.* optimised the growth conditions using 1000 °C, a short growth time of 5 min and gas ratio (C_2H_2 / H_2) of 2 / 45 to produce crystalline few-layer graphene coverage of polycrystalline Ni.[195]

The electron configuration of Fe ([Ar] $3d^6 4s^2$) makes it most reactive with carbon, a trend of decreasing affinity being observed as the d orbitals become progressively filled.[186] This affinity for carbon makes Fe very active for dissolution, unfortunately upon cooling metastable Fe_3C has been known to form, whereas Ni and Co precipitate graphene sheets.[196] Because of these difficulties graphene CVD on Fe has not been as extensively investigated despite advantages in cost and low toxicity; although, graphene and carbon nanotubes have been grown selectively on Fe depending on the thickness of the metal film.[197]

Completing the top row of transition metals commonly used for graphene growth is Co, which interacts more strongly with carbon than Cu and Ni (Table 1). Despite the carbon solubility in Co the graphene growth generally produces inhomogeneous, patchy coverage when polycrystalline Co was used, deposited on SiO_2/Si . [184,198] In contrast, using a templated Co(0001) surface deposited on W produced graphene comparable to Ni(111).[199] Following that Co (0001) was grown on a sapphire substrate producing a high quality monolayer.[200]

1.3.4.2 Surface Mediated Growth

Copper, with a full d-shell of electrons, has a weaker interaction with carbon and the poor solubility facilitates self-limiting graphene growth and growth over domain boundaries. In contrast to the dissolution precipitation mechanism, graphene growth on Cu is a surface phenomenon. At high temperatures the vapour carbon source, commonly CH_4 or gaseous hydrocarbon, decomposes on the metal surface leaving the carbon atom bound to the metal where it can migrate and join the growing graphene flake. Once the surface is covered there is no available metal for hydrocarbon decomposition preventing further growth. Additional flakes can nucleate underneath the existing graphene and bilayer graphene has been formed with multiple growth stages depending on the layers relative growth rates.[201]

The weaker interaction between graphene and surface allows easy growth over steps and boundaries.[179] In one example, CVD with CH_4 produced a large area film covering grain

boundaries in 10 mins.[182] Unfortunately these rotationally disordered graphene domains grow simultaneously; such boundaries within graphene can scatter ballistic electrons and reduce its strength. This is exacerbated as the nucleation density increases with no shared orientation. Most key improvements to process conditions have therefore reduced the nucleation density,[184] for example annealing copper under an inert atmosphere prevents etching producing a smoother foil, resulting in large graphene flakes shown in Figure 15.[202]

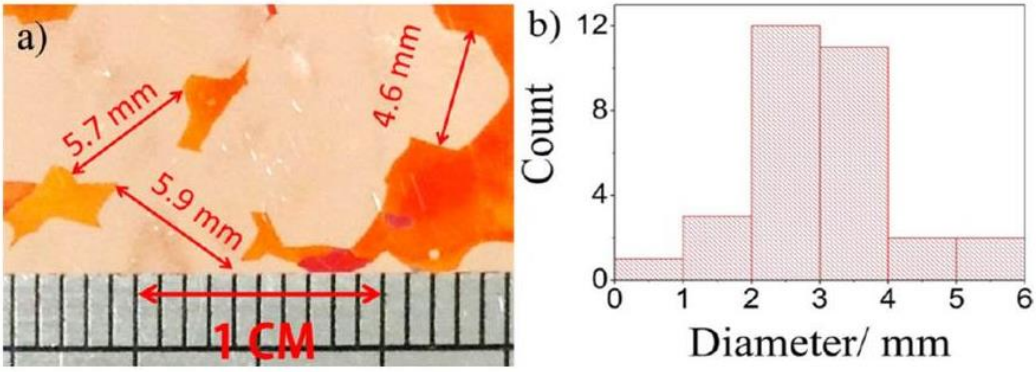

Figure 15: Single crystal graphene domains grown on copper and a histogram showing the distribution of domain sizes.[202]

Traditional approaches to the control of nucleation have been reviewed elsewhere including electropolishing, annealing and growth conditions.[184,186,203] Generally the higher the temperature the higher quality the graphene produced, although monolayer graphene growth at temperatures as low as 800°C has been observed.[204] Further evidence of the flexibility and tolerance is provided by the successful growth of graphene from copper pre-coated with carbon precursors like polymethyl methacrylate and even solid 'waste' carbon precursors like food and insects (specifically a cockroach leg) placed on the backside of the copper foil and heated to 1050 °C under H_2/Ar flow.[205]

Control over the nucleation density has been effective but it is not possible to eliminate all grain boundaries with such an approach. It is possible to grow large area graphene films with no boundaries using a single crystal substrate and this has been realised with a 5 × 50 cm^2 graphene sheet exhibiting > 99% oriented grains grown on a metre-sized single-crystal Cu(111) foil as substrate.[206] These are just a few examples of the attempts to achieve graphene growth suitable for industry, but further investigations are required.[203]

1.3.4.3 CVD on 3D Substrates

The growth of graphene films is now routinely achieved on metal foils and whilst some improvements are required this appears well suited to flexible screens, photovoltaics and transparent heaters. Many applications, however, require 3D porous structures, notable

examples being energy storage supercapacitors and battery devices.[207,208] Reduced graphene oxide is known to self-assemble into porous structures but the electrical and mechanical properties of these foams are often significantly worse than expected from high quality graphene sheets.[209] The growth of high quality graphene materials on 3D substrates by CVD is therefore of great interest as an alternative.

The first report of this was from Chen et al. reporting CVD growth of graphene on a commercial Ni foam using a conventional CVD procedure at 1000 °C with dilute CH_4 and H_2 in Ar.[210] The thermal expansion caused significant wrinkling of the sheets but few layer graphene was achieved over the entire structure, forming a free standing graphene foam once the metal was removed by acid etch to leave a flexible, highly conducing foam with a high surface area of ~850 m^2/g and porosity of ~97%. Arguably most impressive was the robustness of the foam structure that held its shape, as seen in the SEM images in Figure 16, throughout every process step. A good proof of concept, this material nevertheless suffers from very large pore sizes unsuitable for energy applications. To improve the pore structure Yoon et al. used silica nanoparticles (NPs) to template a Fe structure that was annealed and used for graphene growth.[211] By far the simplest method for producing porous metals is the reduction and subsequent annealing of a powdered precursor, specifically $NiCl_2$ to form a dense template with much larger grains than commercial Ni foams but smaller pores.[212]

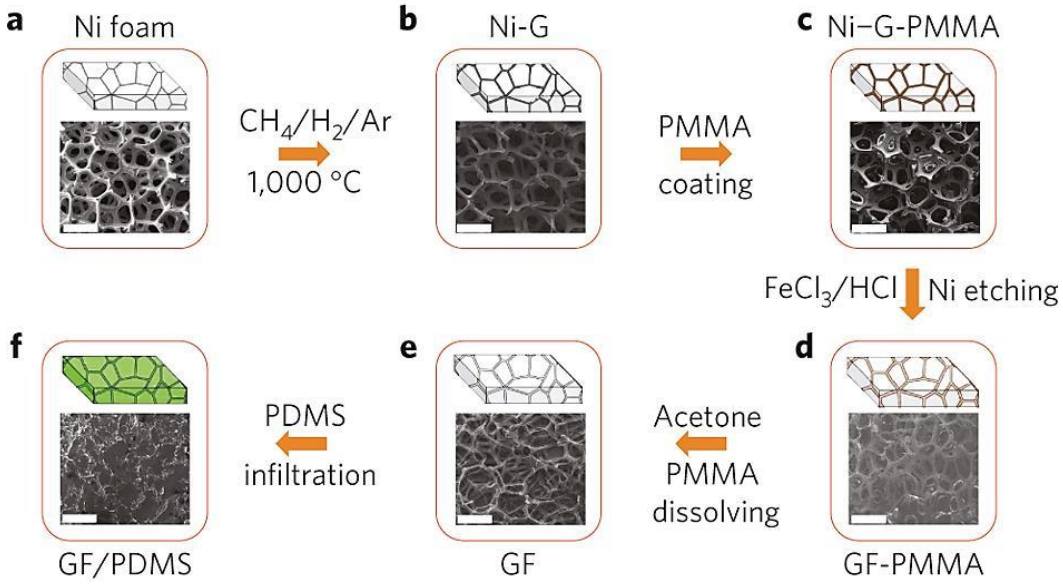

Figure 16: Diagrams and SEM images of a graphene foam structure production, graphene was grown on a commercial foam, protected with PMMA for removal of the metal and then isolated.

Nickel is commonly used for CVD on 3D structures because of the thicker graphene growth generally achieved. Whilst growth on copper can spread over different domains and crystallites the thin monolayer produced is often insufficient for freestanding structures.[210] Nevertheless CVD on a copper foam has been demonstrated; metallic powders of Ni and Cu were annealed with carbonate blowing agents producing a foam with sub-50 µm particles.[213] The Cu supported single layer growth over the metal grains resulting in a free standing foam, in comparison Ni produced thicker few layer graphene. Despite this success, the process to prepare metal foams then grow graphene and finally wash the metals from the graphene is costly. Attempting to reduce this cost graphene has been grown on bio-templates, specifically seashells and cuttlefish; whilst carbon deposition was achieved the material was more defective than graphene obtained from metals.[214,215]

A comprehensive review of this topic is provided by Chen et al.[216] as many approaches to template metal foams and different metal systems have been used for graphene production than the few highlighted here. A common aspect of CVD graphene production is the high cost, often multiple heating and reaction stages are required followed by removal of the metal template to isolate the freestanding graphene structure. Offsetting this is the unique few-layer defect free graphene foams that can be produced with these techniques.

1.4 High Temperature Graphitization

The most important considerations for graphene production are the properties required. Whilst CVD foams are often linked with energy storage devices effective charge storage requires high surface areas with micro and meso porosity, good diffusion properties and, for ion storage, graphitic stacking. These are generally lacking in CVD foams although graphitization of carbon materials is known to produce many of these properties.

1.4.1 Synthetic Graphite

Converting carbon materials into crystalline graphite has been known for over a century, and detailed studies on the formation and properties of graphite began in earnest for neutron moderation during the harnessing of nuclear fission.[217,218] Synthetic graphite can be formed by the high temperature, typically in excess of 2500 ^{o}C, rearrangement of carbon atoms into the more thermodynamically favourable graphite lattice.[219] Graphitizable carbons, materials with lamellar carbon layers already present, like coke and petrochemical feedstocks, undergo such rearrangements easily. Other carbon sources with disordered, isotropic structures such as those derived from wood or polymer resins less readily graphitize.[188]

To reduce the temperature and use a greater variety of feedstocks, graphitization catalysts can be used. Transition metals are found to be most effective by dissolving and precipitating carbon, the same mechanism responsible for CVD growth.[196] This facilitates lower temperatures, around 1000 °C, and is effective at converting non-graphitizable carbon with disordered structures. The dissolution stage provides a low energy barrier and the stability of the graphite means the process has a negative free energy change, becoming more favourable the more disordered the starting material. Reviews comparing different elements and alloys for graphitization have been published.[188,220]

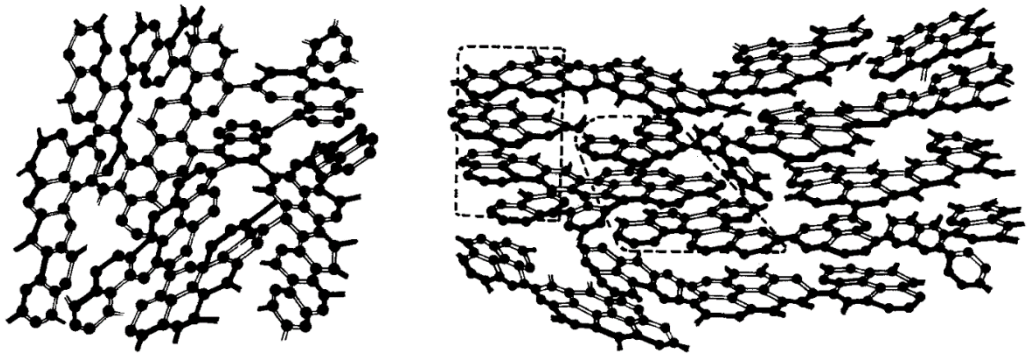

Figure 17: Diagrams of structures of a) isotropic carbon and b) graphitizable carbon. The existing layered structures are highlighted with dashed boxes.

1.4.2 Porous Carbon

Porous graphitized carbons are generally made with structural templates and metal precursors to control the porosity and graphitization respectively, often porous carbon materials are used as templates in the first instance with soluble transition metal salts that undergo in-situ reduction to form catalytically active metal particles. Templates take two main forms, hard and soft and it is important to emphasise the distinction in role between structural templates and metal particles acting as graphitization catalysis.[221,222] Although it is possible to use metal particles as structural templates.

Soft templating refers to the self-assembly of amphiphilic molecules, generally surfactants or polymers, that control the structure as in Figure 18. The advantage of soft templating is their easy removal by washing or burning but their thermal instability means the template can be destroyed before graphitizing into rigid carbon. An early example used a block

copolymer system to template the polymerisation of resorcinol-formaldehyde into a film with hexagonal columns which were maintained upon graphitization.[223]

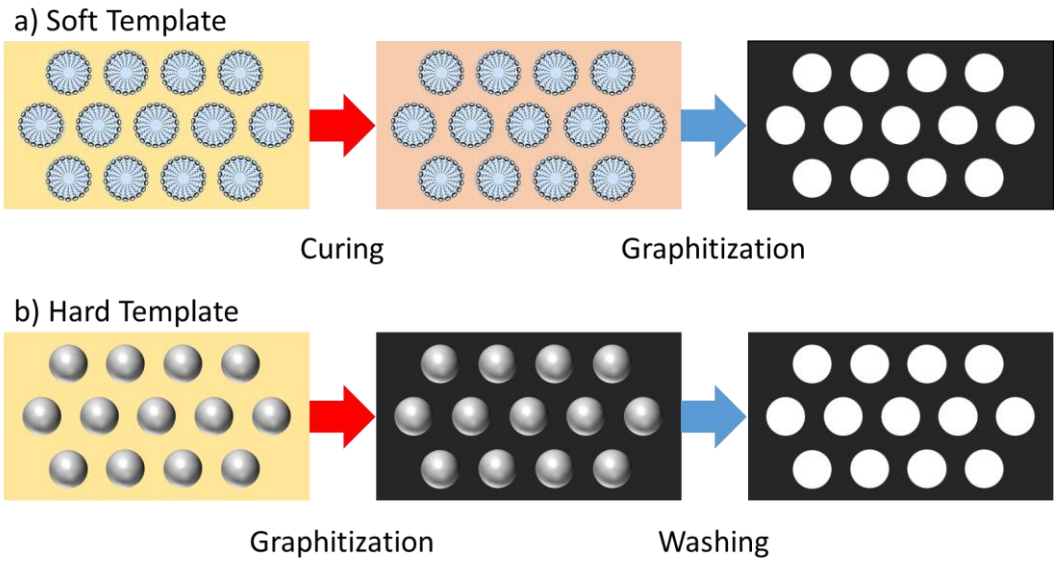

Figure 18: Example soft and hard templating approaches for carbon foam formation. a) mixed phase emulsion is formed to template holes in a polymer structure which is graphitized maintaining the holes and removing surfactant. b) Hard particles can be used to template the graphitization of soft carbon round them, before the solid particles are washed out.

Hard templating uses solid porous structures that can be coated or filled with a reagent that is processed into graphitic carbon. Nanoparticles, solid ceramics or metal foams are common hard templates and have the advantage that such robust supports are very tolerant to processing. Their stability, however, makes complete removal of the template difficult, often requiring harsh chemical treatment. One of the first reports on the graphitization of carbon precursors using a hard template utilised Y zeolite, graphitizing poly(acrylonitrile) and poly(furfuryl alcohol) within the zeolite channels. The zeolite was then removed with HF and HCl washing leaving porous carbon with a surface area as high as 2000 m^2/g.[224]

Early research focussed on using zeolites as mesoporous templates with carbon precursors including: poly(vinylchloride), poly(furfuryl alcohol), sucrose and acenaphthene being infiltrated into the zeolite structure and then heated around 700 – 900 ^oC.[225–229] An alternative to solid zeolite templates was the use of silica NPs, these can be prepared in-situ by sol-gel synthesis to produce a carbon coating,[230,231] or prepared and combined with the carbon as done with hot pitch and a silica nanoparticle colloid resulting in clearly templated voids in the carbon structure after graphitization in Figure 19a,b.[232–234]

Silica was an effective template - after removal the mesopores were intact as shown in Figure 19b-d, and surface areas of 400 m^2/g,[232] 1000 m^2/g and 2000 m^2/g were reported.[224,231]

Nevertheless, the relatively low temperatures resulted in carbon more comparable with activated carbon than graphene foams; exhibiting a clear graphitic XRD peak but the Raman spectra, when reported, is usually indicative of layered but defective sp^2 carbon. It was possible to improve the quality of the carbon with a greatly increased graphitization temperature of 2300 ^oC but that resulted in a drop in surface area.[225]

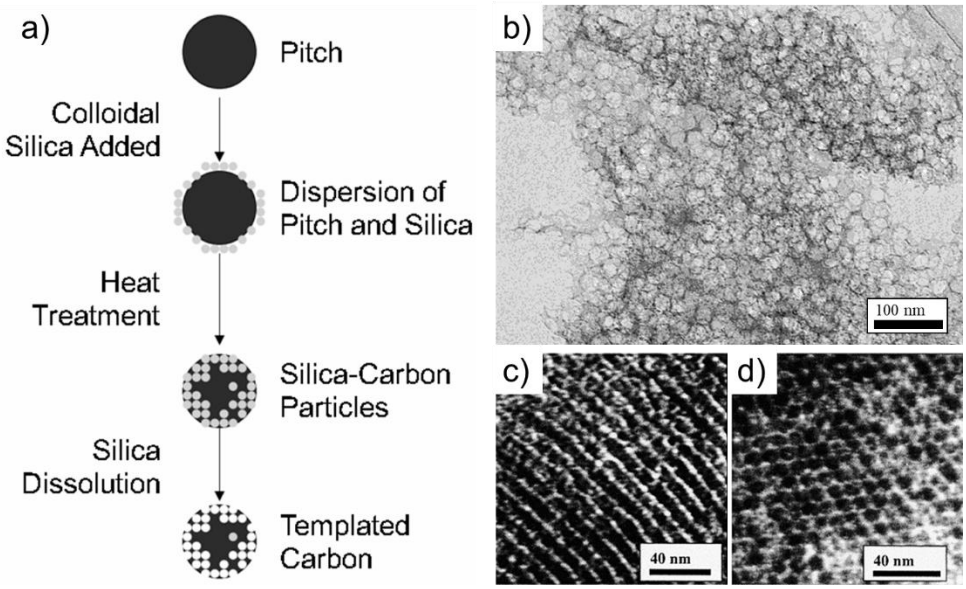

Figure 19: a) Schematic of colloidal impregnation of carbon pitch particles and processing to produce porous carbon material; b) TEM image of the resulting carbon foam following silica particle removal. c) & d) TEM images of carbon templated from zeolites.

a & b: Adapted with permission from Li, Z.; Jaroniec, M. *J. Am. Chem. Soc.* **2001**, *123* (37), 9208–9209. Copyright 2001 American Chemical Society.
c & d: Adapted from Carbon, 42, A B. Fuertes, S Alvarez, Graphitic mesoporous carbons synthesised through mesostructured silica templates, 3049-3055, Copyright 2004, with permission from Elsevier.

The other major disadvantage to using a hard template is the complex production and washing required, most silica templates themselves required a templated synthesis to form and washing was done with harsh chemicals, either HF or concentrated $NaOH_{(aq)}$. As a result, whilst effective at controlling the structure this approach to templating porous carbon is rarely utilised. This discussion of hard templates has also neglected the role of catalytic metals on the graphitization. This is because, whilst a few groups combined cobalt and nickel salts with silica particle templated graphitization, the use of transition metals or other graphitization catalysts with hard templating methods was less common.[235,236] The notable exception being CVD growth of graphene on hard metal foams, discussed previously.

By contrast soft templating is easily combined with soluble metal salts and using carbon templates simplifies any washing. A comprehensive review of all the polymers, biomolecules and other organic building blocks used to template porous carbons is beyond the scope of

this work, however, mention will be made to resorcinol-formaldehyde (RF) polymer foams. Reported since 1989,[237] they have been used extensively as precursors to carbon foams for many applications and studies.[238] Initially the porous polymer monoliths were graphitized in their pure form to produce vitreous carbon with high surface areas: 600 – 800 m^2/g.[239]

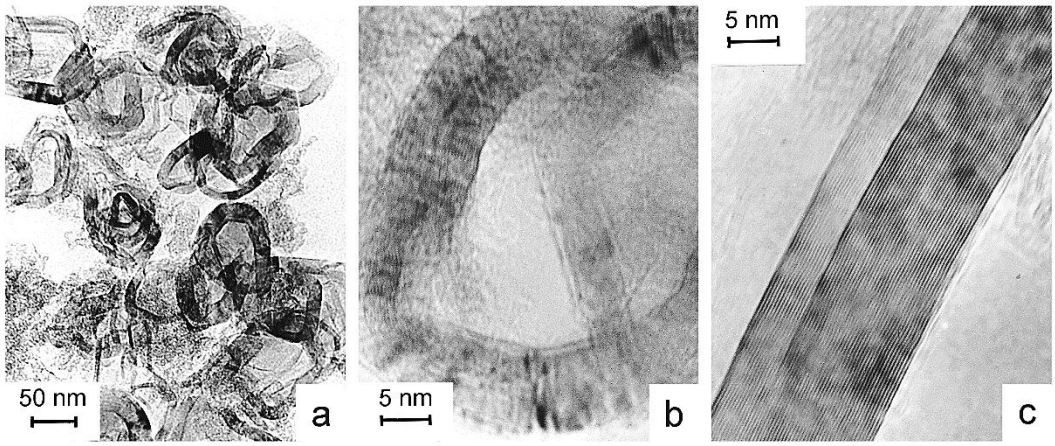

Figure 20: HRTEM micrographs of carbon aerogels showing the graphitic layers and circular patterns formed around metal particles. Images taken from different preparation conditions to illustrate graphitic carbon formation; a) formed at 1000 °C with Ni, b) 1400 °C with Co, c) 1800 °C with Ni.

To produce more conductive graphitic carbon Maldonado-Hódar et al. added 1 wt.% soluble salts of Cr, Ni, Fe and Co – specifically acetate salts except for $Cr(NO_3)_3$ – to the aqueous mixture before polymerisation and heating to 500 – 1800 °C.[240] This study demonstrated the possibility of using metals to form graphitic carbon confirmed by the C (*002*) reflection in the XRD pattern and TEM images of carbon layers, a selection of which are shown in Figure 20, and Raman spectra with graphitic carbon peaks. The template shrank during graphitization but the pore structure was maintained with specific surface areas of 300 – 400 m^2/g. The different metals did effect the pore size distribution, Fe and Cr both resulting in large pores whereas Co and Ni produced well-defined 100 nm diameter pores. Morphology can also be controlled with the formulation of the initial polymer and the metal particles leave void space after washing;[241,242] additionally the effect of graphitic carbon formation is often to reduce the surface area relative to microporous amorphous carbon.[243–246]

In addition to synthetic polymer systems; biomaterials that form gels have been investigated with soluble metal salts. Polypeptides like gelatin are ideal as they naturally form wet gels that can be freeze dried into solid foam structures and the abundance of functional groups ensures an even distribution of metal.[247–249] Neutron scattering, UV-vis and IR of metal ions within a wet gel has confirmed the ions bind to the polymer chains. These interactions have

been shown to have a significant impact on the foaming process that templates the final carbon; alongside the pH and temperature at which the gel is dried. For example nitrate salts cause more foaming than other metal salts.[250] Rapid freeze drying is also known to increase the surface area and produce smaller particles compared to hot drying.[248]

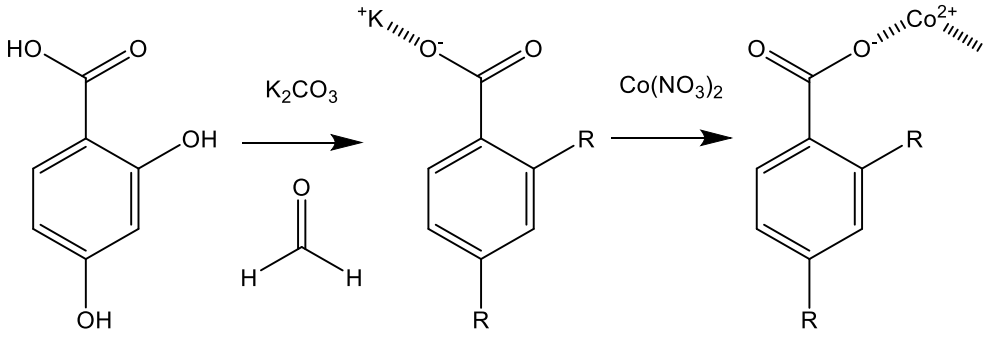

Figure 21: Example of ion exchange of metal ions into polymeric structures; in this case dihydroxybenzoic acid and formaldehyde gel polymerised with potassium carbonate followed by cobalt nitrate ion exchange. (R = polymer chain)

Strong interactions between the polymer chains and metal ions have been achieved with synthetic polymers, formaldehyde based polymer gels were produced under basic conditions resulting in K^+ counter ions attached to carboxylate groups; these were then exchanged for Co^{2+} and Ni^{2+}.[243,251] After graphitization these systems were observed to produce small metal NPs, the size of which were determined by the carbonization temperature. These closely bonded systems, however, are not required and the soaking of biomass with metal ion solutions has produced graphitized carbon via the same process.[244,252]

There are a huge variety of methods for producing porous carbon materials that can be heated to form graphitic carbon. The use of biomass or other waste carbon is obviously preferable to expensive polymer systems but controlling their pore structure can be challenging. As previously discussed many applications of porous carbon materials require a balance between micro and meso porosity and whilst many polymer foams can be optimised to provide the required morphology before graphitization, hence the interest in RF foams,[238] this is harder to achieve with biopolymers. Nevertheless it has been demonstrated that transition metal salts, in addition to enhancing graphitization, can provide some control over gel formation and metal NPs enhance mesoporosity once removed.[253]

1.4.3 Metals for Catalytic Graphitization

Metal catalysts facilitate graphitization of most carbon materials at reduced temperatures but the mechanism varies depending on the metal electron structure as summarised in Table

2. Fundamentally they provide a low energy path to the destruction and reconstruction of the carbon structure into graphitic layers. Group 4 to 7 metals with mostly vacant d-shells form strong bonds with carbon forming stable carbides, these carbides are known to catalyse the formation of graphitic carbon by dissolution of carbon into the carbide at high temperatures before precipitation as the carbide cools.[187,188,196] Metals with mostly full d-shells undergo little change in energy levels when forming weaker bonds with carbon, they are effective at catalysing the decomposition of hydrocarbons and forming a solid solution of carbon which precipitates. Finally metals with full d-shells and some heavy metals with partially full d-shells have been used for CVD growth but these metals have proved ineffective for catalytic graphitization of bulk carbon.[184,188,254]

Table 2: Section of periodic table showing electron configuration; colour coded for graphitization activity: blue - strongly carbide forming, red - good carbon solubility, yellow - weak interaction with carbon.[179,188]

3	4	5	6	7	8	9	10	11	12
Sc $3d^1\ 4s^2$	Ti $3d^2\ 4s^2$	V $3d^3\ 4s^2$	Cr $3d^4\ 4s^2$	Mn $3d^5\ 4s^2$	Fe $3d^6\ 4s^2$	Co $3d^7\ 4s^2$	Ni $3d^8\ 4s^2$	Cu $3d^{10}\ 4s^1$	Zn $3d^{10}\ 4s^2$
Y $4d^1\ 5s^2$	Zr $4d^2\ 5s^2$	Nb $4d^4\ 5s^2$	Mo $4d^5\ 5s^2$	Tc $4d^5\ 5s^2$	Ru $4d^6\ 5s^2$	Rh $4d^7\ 5s^2$	Pd $4d^8\ 5s^2$	Ag $4d^{10}\ 5s^1$	Cd $4d^{10}\ 5s^2$
La $5d^1\ 6s^2$	Hf $5d^2\ 6s^2$	Ta $5d^5\ 6s^2$	W $5d^6\ 6s^2$	Re $5d^5\ 6s^2$	Os $5d^6\ 6s^2$	Ir $5d^7\ 6s^2$	Pt $5d^8\ 6s^2$	Au $5d^{10}\ 6s^1$	Hg $5d^{10}\ 6s^2$

Group 12 metals with a complete electron configuration were not thought to be active for graphite formation due to the poor interaction with carbon; recently however, Zn has been combined with glucose for graphitic carbon formation.[255] The resulting material contained many sp^3 defect sites in common with other graphitization products. The mechanism by which zinc forms the graphitic carbon is still unknown; it's been suggested the melting and evaporation of volatile Zn into the glucose forms a zinc-char matrix that delaminates into π-π stacked lamellar fragments. Unfortunately there is little evidence presented for this complex sequence other than EDX images confirming the zinc is well dispersed. An alternative hypothesis could be A-effect graphitization; metals like Ca and Mg are known to react and preferentially etch disordered carbon regions in such chars, leaving more ordered lamellar structures that are easily graphitized.[256,257]

Group 11 metals, in particular Cu, are known to be effective catalysts for CVD growth of pristine graphene but their graphitization activity is low. Attempts to form graphitic carbon have been made with $Cu(NO_3)_2$ and $Cu_2(OH)_2CO_3$ incorporated into polymers.[252,258] Despite

some limited evidence from TEM of graphitic layers being present in select areas, overall analysis of such materials generally finds no graphitic XRD peak and Raman spectra are more consistent with amorphous carbons. The porosity of these materials was also low, 88 m^2/g reported from $Co(NO_3)_2$ in lignin. Another report using a Cu based MOF to template the structure reported disordered stacks of carbon materials observed from TEM images and SAED rings, however, XRD and Raman data was insufficient to prove graphitization.[259] The structural control permitted by the MOF was much greater than with polymer structures, the crystalline particles were maintained after heating and porosity within the structure was observed by SEM shown in Figure 22.

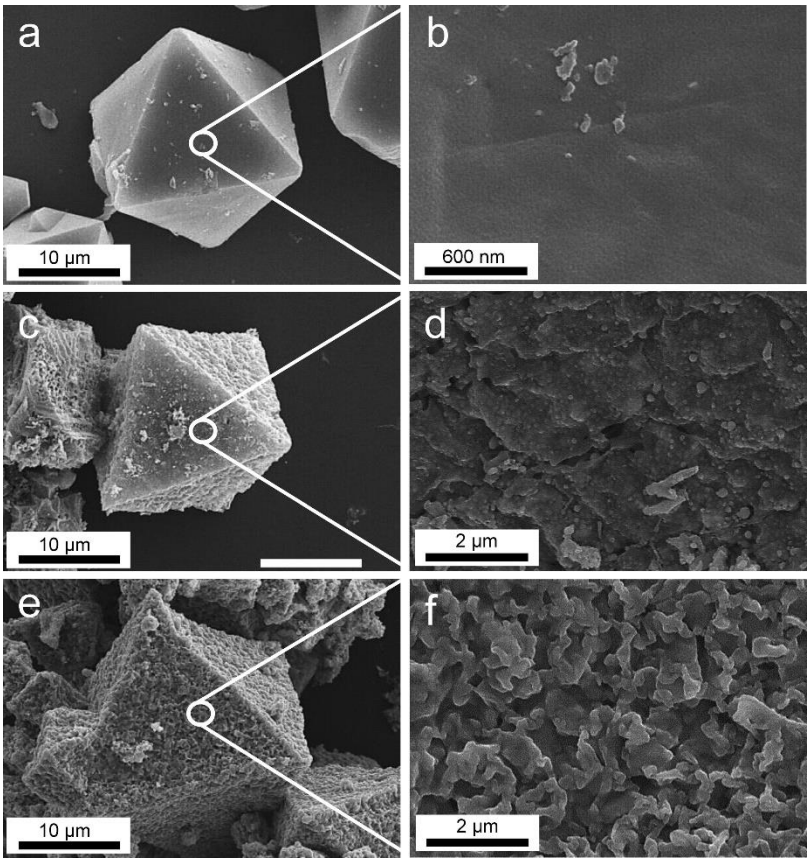

Figure 22: SEM images of a) and b) crystals of Cu based MOF, c) and d) carbonized MOF, e) and f) after oxygen treatment to oxidise copper at a), c), and e) low and b), d), and f) high magnification.

1.4.3.1 Nickel

Because Ni is effective for CVD and carbon has a high solubility when hot,[184] it is ideal for the dissolution-precipitation growth of graphene layers and has been extensively investigated. An early comparison of Ni with Fe, Co and Cr revealed Ni to be less effective but still active

for graphitic carbon formation; although few layer graphene was observed in TEM images from every metal.[240] Other early studies using $Ni(NO_3)_2$ soaked into sawdust and saccharides reported higher temperatures were preferable, although graphitic carbon was formed at both 900 and 1000 °C.[244,245] Micrographs revealed a difference in morphology of carbon with "nanocoils" produced from Ni and "nanopipes" from Fe shown in Figure 23. It is also noteworthy the optimal metal was apparently different for each carbon source.

Growth of tightly curved graphene layers around small metal NPs formed in-situ from the reduction of metal salts is commonly observed. At the high temperatures needed for graphitization metal particles would usually anneal but the carbon matrix prevents this. That phenomenon was used to produce carefully controlled graphene spheres on 175, 375 and 500 nm Ni NPs - by pre-treating the NPs with a carbon source, specifically polyol, at 250 °C agglomeration was prevented during graphitization at 500 °C.[260] TEM micrographs show few-layer graphene approximately 8 layers thick around the metal NPs. Graphitized carbon has also been prepared using powdered Ni metal with much larger particles 2 – 3 μm in diameter; sucrose solution was mixed with the powdered metal, pressed into a pellet and graphitized at 1000 °C. TGA analysis and XRD are consistent with crystalline graphite as expected from large metal particles with excess carbon.[261] Unfortunately this approach does result in low surface area materials since the graphite lacks micro and meso porosity.

Using other Ni templates higher surfaces areas have been achieved, but never the 2000 m^2/g of activated carbon.[262] A thermoset resin polymerised with a Ni organometallic monomer produced a SSA of 120 – 200 m^2/g, depending on amorphous carbon content;[263] and a comparable surface area of 115 m^2/g was achieved with $Ni(NO_3)_2$ added dropwise to a THF lignin system.[252] With a foaming agent, Na_2CO_3, added to a wood sample soaked in lignin and $NiCl_2$ the graphitized foam had a SSA of 729 m^2/g.[264]

To understand the process of graphitic carbon formation Sevilla et al. used XRD collected at different temperatures to identify the Ni reduction process; they propose the Ni salt first decomposes into NiO NPs around 300 °C, these slowly transition into Ni metal by 700 °C.[247] Thermal analysis with in-situ mass spectrometry of kraft lignin rather than saccharides reported the decomposition of $Ni(NO_3)_2$ at 200 °C,[265] which is consistent with NiO observed in XRD at 300 °C. Finally in-situ TEM and XRD, also studying $Ni(NO_3)_2$, reported reduction was completed under 500 °C and a graphite 002 XRD peak was observed around 800 °C, with HRTEM showing signs of graphene layers as low as 500 °C.[266]

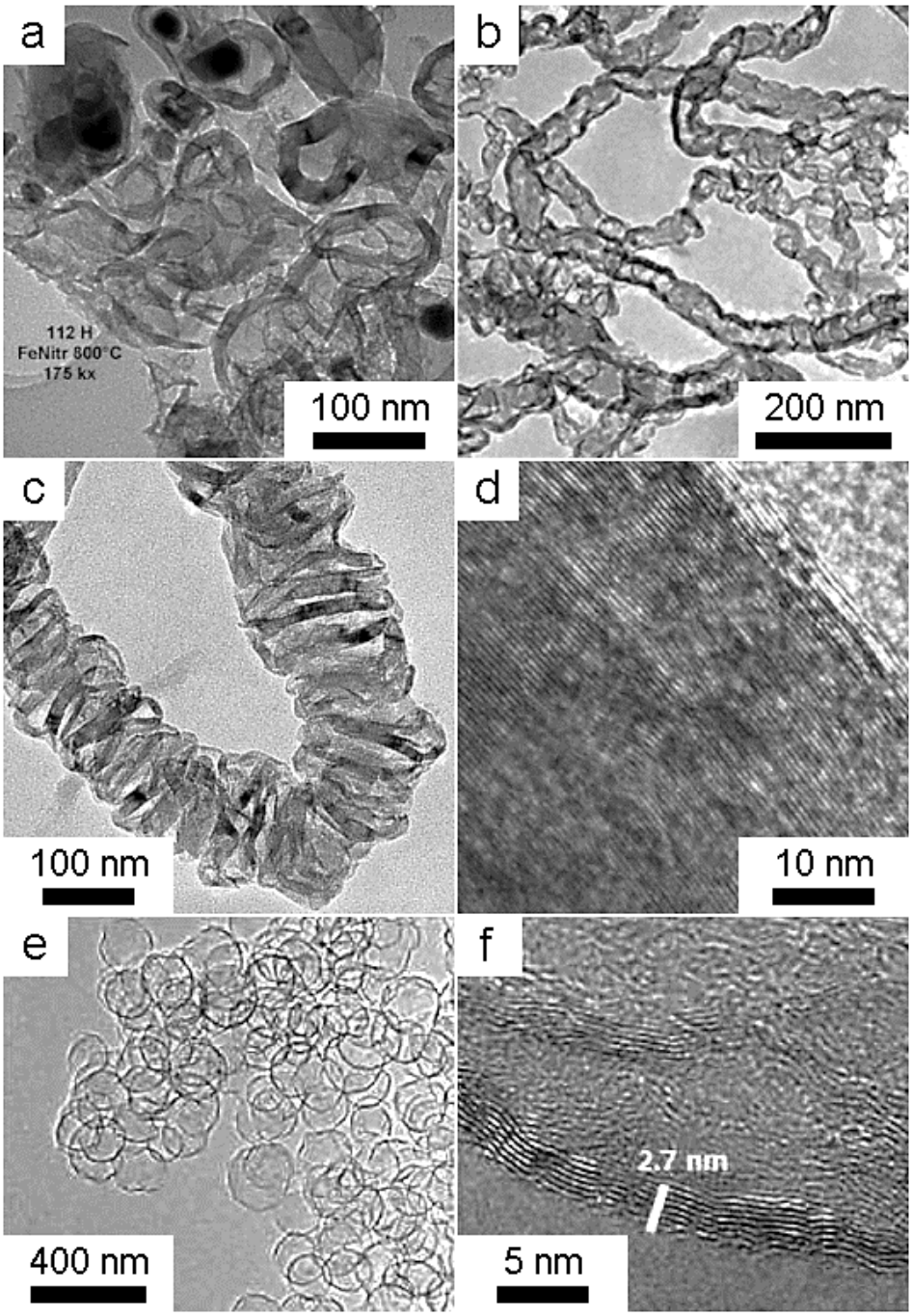

Figure 23: Series of TEM images of different carbon morphologies produced by metal catalysed graphitization. a) Large graphitic shells obtained from graphitization of Fe loaded carbon beads at 800 °C; b) carbon "nanopipes" produced from Fe particles in glucose at 900 °C; c & d) "nanocoils" obtained from sucrose and Ni NPs, d) is HRTEM image of the same sample; e & f) graphitic carbon balls produced by controlled graphitization and segregation from Ni NPs after all metal is removed, f) is a HRTEM image of the carbon ball.

1.4.3.2 Cobalt

Utilising $Co(NO_3)_2$ and $CoCl_2$ as graphitization catalysts results in similar graphene around metal particles as Ni.[243,251,267] Graphene layers around Co particles can be observed with HRTEM and examples of carbon ribbons running through carbon have been observed. Investigations of $Co(NO_3)_2$ integrated into carbon foams and probed at different temperatures suggest metal particles form at temperatures as low as 450 °C with graphene layers formed from 600 °C and further heating only serving to increase the size of the NPs.[251] There is some discrepancy, however, with other reports suggesting Co is only fully reduced at 570 °C forming thin graphite shells analogously to Ni above 700 °C.[266] One noteworthy difference between the Co and Ni particles is the remarkably small size of Co NPs, as small as 2 nm in diameter illustrated in the micrographs in Figure 24.[243,251] To optimise the structure produced, a Co containing MOF has also been graphitized resulting in regular crystals that maintained their shape following heating at 900 °C.[268]

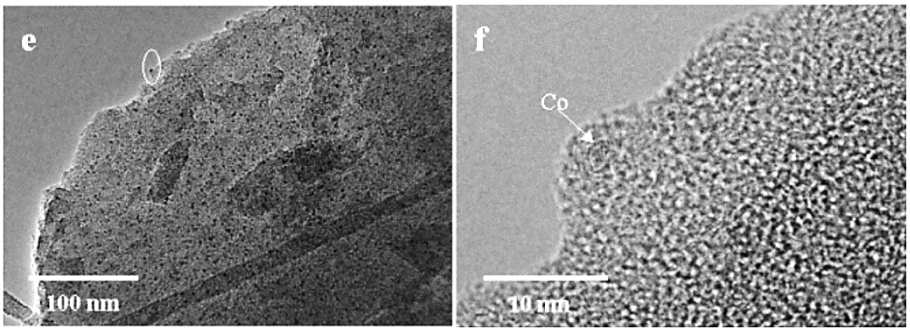

Figure 24: TEM of graphitic carbon prepared at 700 °C containing small cobalt NPs evenly spread throughout the material.

1.4.3.3 Iron

In comparison with other metals Fe is advantageous because it is abundant and non-toxic. It's low uptake for CVD systems is due to the high carbon solubility and stable carbide formation, coupled with a preference for carbon nanotube formation over few or single layer graphene.[197] Regardless Fe has been successfully used for catalytic graphitization in biomaterials and polymer systems, performing comparably to other transition metals.[244,245,252] When directly compared Fe appears to be slightly more active; for example Ni and Fe in lignin were reported to have surface areas of 115 and 108 m^2/g respectively and I_D/I_G values of 1.39 and 1.29; although, variation between process conditions and starting materials is generally greater than the difference between metals.

The greater uncertainty when using Fe for graphitization is the role of iron carbide. Many reports of Fe based catalysts for graphitic carbon formation report the presence of crystalline cementite, Fe_3C, in XRD patterns with graphene growth around iron containing particles.[252,265] These results have suggested that iron carbide is a viable catalyst for graphitic carbon formation, despite early reports that Fe was unsuitable because of the stable carbide formation.[196] Further evidence comes from the graphitization of biomass with $Fe(NO_3)_3$; electron micrographs show the Fe_3C particles migrating through the carbon structure forming tubular graphitic carbon.[269] The authors postulate that different forms of Fe, most notably metallic Fe and Fe_3C are responsible for different carbon morphologies although in this case the XRD pattern showed crystalline Fe_3C only.

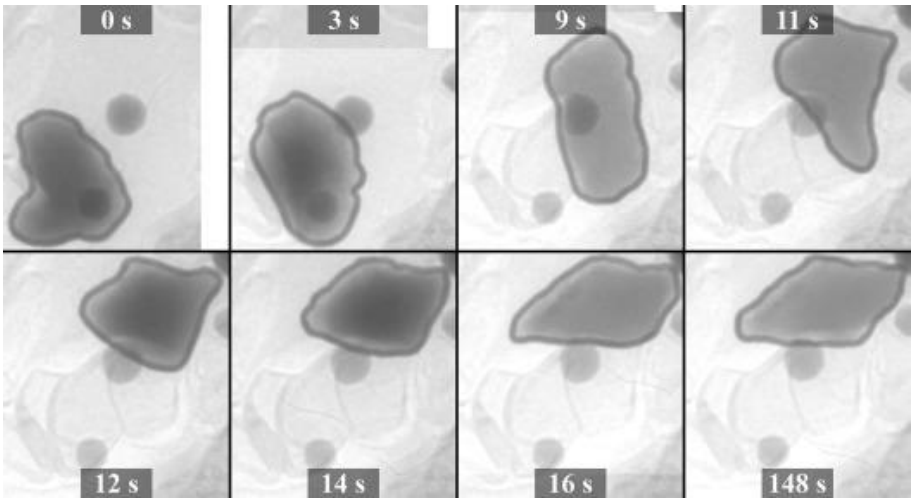

Figure 25: Frames taken from an in situ TEM video depicting the initially fast movement of the 50–200 nm iron–carbon droplets which comes to an abrupt halt when the particle is surrounded by already graphitized areas.

Adapted with permission from: Glatzel, S.; Schnepp, Z.; Giordano, C. *Angew. Chemie Int. Ed*. **2013**, 52 (8), 2355–2358. Copyright John Wiley and Sons 2013.

Another report using a different biomass further investigated the effect of varying the Fe^{2+} concentration, as more Fe^{2+} was added a Raman metric recorded a more ordered and crystalline graphitic carbon as the metal content was increased from 5% to 15%.[265] This report also found low levels of Fe^{2+} produced exclusively metal NPs but Fe_3C was observed, in XRD patterns, at Fe^{2+} content greater than 7.5%. The carbon morphology was imaged in more detail when printing $Fe(NO_3)_3$ inks onto cellulose paper for patterned electrodes.[270] When heated the paper and $Fe(NO_3)_3$ decomposed rapidly into carbon and FeO which underwent reduction to Fe_3C. TEM showed these 50 – 200 nm NPs freely migrating through the amorphous carbon leaving graphitized ribbons behind, seen in Figure 25. Images of a

molten particle also show the apparent inability of these molten iron carbide particles to migrate through graphitic carbon.

The transition temperatures between phases are still unclear; in an investigation of cellulose carbothermal reduction of FeO was reported around 600 °C. When investigating carbon monoliths supported by SiO_2 however, no Fe_3C was produced which was attributed to the instability of Fe_3C at 700 °C when the FeO reduced.[271] In a different study $Fe(NO_3)_2$ was reported to convert into Fe_3O_4 which reduced to FeO and then finally to Fe at 715 °C.[266] This was also remarked to be distinct from other metals which form metallic particles at much lower temperatures, but are not catalytically active until the temperature increases.

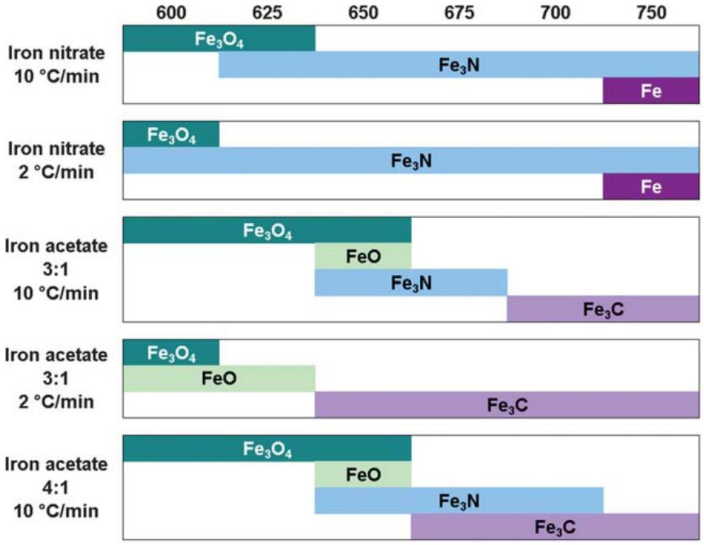

Figure 26: Summary of crystalline phases formed during calcination of gelatin/iron precursor mixtures. When using $Fe(NO_3)_2$ the Fe_3N phase remained stable for a wider temperature range before forming the metal whereas $Fe(OAc)_2$ precursors formed a FeO and Fe_3N mixture before decomposition to Fe_3C.

Reproduced from Ref. [248] with permission from The Royal Society of Chemistry.

Unfortunately, different heating rates and carbon materials used make clear conclusions difficult to draw. Although, an investigation by Schnepp et al. into the production of Fe_3N nanostructures provides significant insight into Fe_3C and Fe particles within a carbon matrix.[248] When heating iron salts in amorphous carbon the salt was observed to decompose into Fe_2O_3 at 600 °C, this was sometimes followed by the production of metastable Fe_3N which then decomposed under further heating into Fe_3C or Fe. It was observed that $Fe(NO_3)_2$ produced metallic iron particle whereas $Fe(OAc)_2$ formed the carbide. The formation of metallic or carbide particles was attributed to the surface area of the nitride intermediate; this in turn was determined by the thermal stability of the initial salt precursor.

1.4.3.4 Summary

The catalytic production of graphitic carbon for various applications is dominated by first row transition metals due to the high reactivity and relatively low cost and toxicity of these elements. Copper, whilst effective for CVD growth of monolayer graphene is generally poor at converting amorphous carbon into graphitic due to the low solubility and thus inability to reform the carbon structure. Ni and Co interact more strongly with the carbon, dissolving it and precipitating graphitic carbon whilst the dissolution into iron appears to form stable carbides that are still active graphitization catalysts. In addition to these, Mo and Cr have also been trialled for graphitization. Cr was found to perform comparably to other carbide forming metals, notably Ni and Fe, however, the removal of the stable chromium carbide was reported to be more challenging that other metals.[240,272] Mo, applied as a solution of $(NH_4)_6Mo_7O_{24}$, was found to be less effective for graphitization.[252] In addition using Mo is complicated by the chemistry involved in the decomposition of the more complex salt required for solubility and the inert and hard nature of Mo_2C make it unattractive.

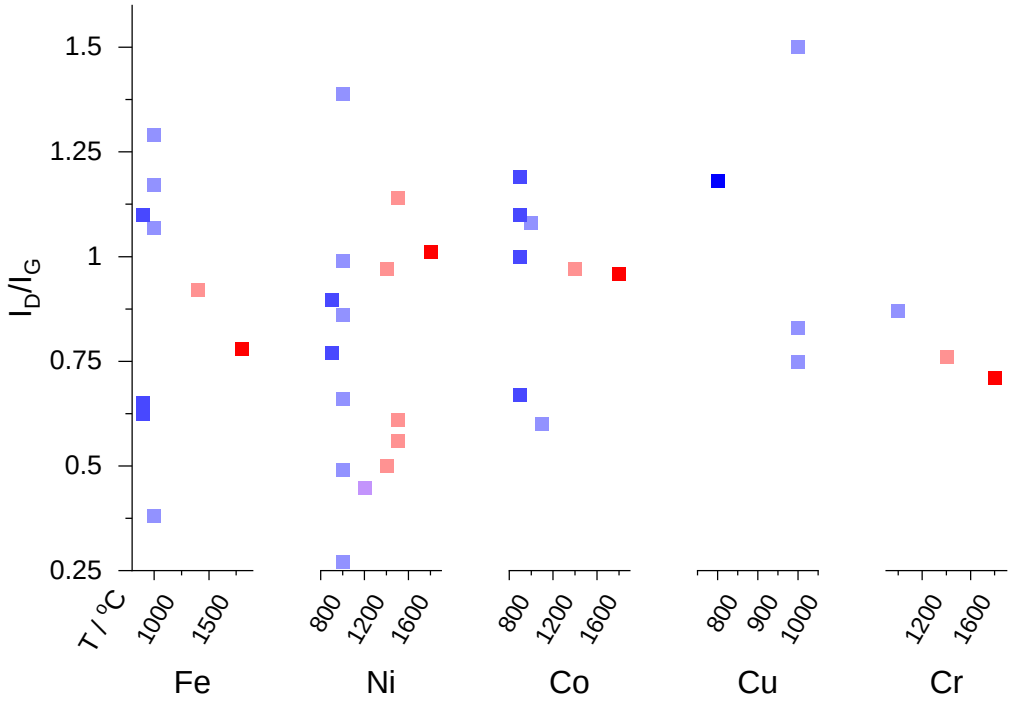

Figure 27: Summary of Raman I_D/I_G metric values from literature reports using different metal catalysts at different temperatures; the metals are grouped and temperature plotted along the x-axis for each metal. Temperature is also denoted by colours from blue to red. Data taken from literature references: [240,244,268,272–279,252,258–261,264,265,267].

Despite effort being focussed on the behaviour of different metals, the remarkable disparity of results obtained from the same metal due to processing conditions, starting carbon and other additives is illustrated by Figure 27. This comparison is made using I_D/I_G, the intensity

ratio of two Raman signals recorded from graphitic carbon commonly associated with lateral flake size and defects in the aromatic structure. A more detailed description of this metric and its interpretation is included in chapter 3. Whilst I_D/I_G is an imperfect metric due to flake size and curvature, it nevertheless highlights that the difference in carbon material obtained from the same metal is actually far greater than the differences observed between metals. Broadly the interactions between metal and carbon, and the basic growth mechanism as discussed in the next section are the same across Cr, Mn, Fe, Co and Ni.

1.4.4 Mechanism of Graphitization with Metals

Whilst different metals have broadly the same graphitization mechanism there are still thought to be important differences induced by the particle size and environment. Ōya and Marsh summarised these different growth types as G, T_s, T_n and A effect graphitization.[188]

G effect graphitization refers to dissolution-precipitation in bulk metal particles, greater than 100 nm, although often microns in scale. The carbon is isothermally reformed into the more thermodynamically stable graphite by the metal, or in some cases the stable carbide as known from SiC and Fe_3C.[254] The presence of carbide particles suggests that both metal and carbide are active for carbon graphitization and the relative stability determines the dominant species.[280] G-effect carbon is generally observed to have a single sharp peak in the XRD pattern from the 002 reflection of graphite, and a broad background from the amorphous carbon that did not contact the metal particles shown in Figure 28a. Metal particles are known to migrate through carbon structures by dissolving carbon in front and precipitating the graphitic region behind the migrating particle. In some cases these large particles decrease in size as metal or carbide is deposited; eventually producing smaller metal particles that follow the description of T_s effect graphitization.

T_s effect graphitization in contrast generally produces a much wider 002 peak at lower 2θ from the disordered turbostratic graphite formed. T_s effect graphitization is generally observed from very small, finely divided catalyst particles 10s of nm in size heated with non-graphitizable carbon. These small particles are thought to react with the surrounding carbon and form molten droplets of metal-carbide; domains of carbon floating on the surface of these droplets then coalesce together forming the more disordered turbostratic graphitic carbon observed. Alternatively the dissolution of carbon into the small NPs followed by precipitation of graphitic carbon has been proposed; but the clearly disordered turbostratic material produced is more likely to result from disparate carbon domains on the particle surface than the precipitation of very small amounts of carbon from nanoparticles.

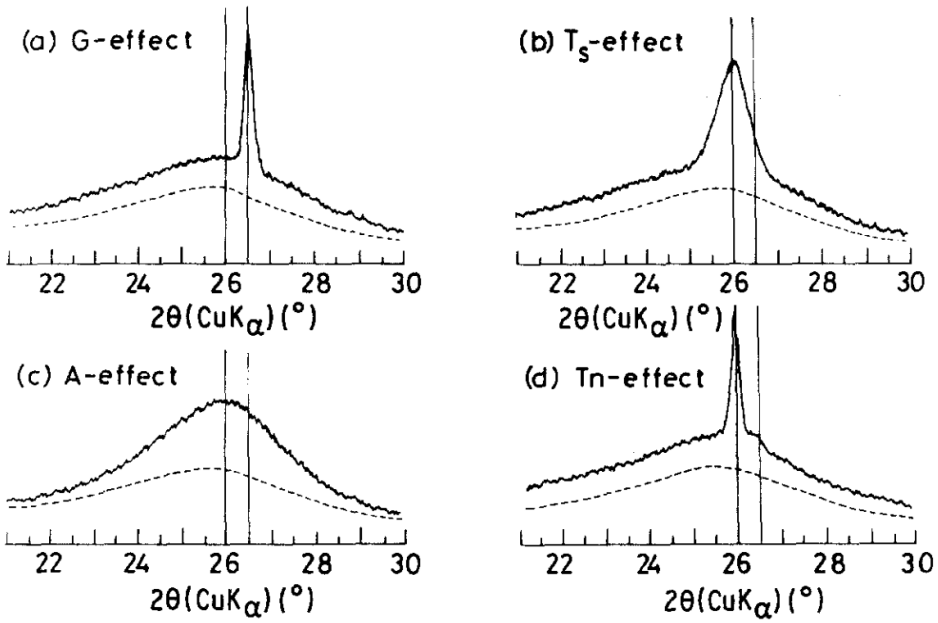

Figure 28: X-ray diffraction profiles of the carbon *(002)* peaks from different graphitization models.

Finally A and T_n effect graphitization are the same mechanism, but differ in the extent of graphitization. A-effect graphitization results in a broad amorphous carbon XRD pattern whilst T_n-effect graphitization is much more effective and produces a sharp 002 peak, seen in Figure 28c,d. The essence of this graphitization mechanism is the removal of thermally stable cross-linked structures that prevent re-arrangement of carbon materials; this has been achieved with O_2, CO_2, Ca, Mg and B doping as well as other metal vapours.[255,256,281]

The role of metal particles as templates for porosity is very intuitive; additionally, the size and shape is also linked to the mechanism observed. It may be possible to use small metal particles to both control the structure of carbon foams, inducing meso-porosity, whilst also influencing the extent of graphitization. The graphitization in turn influences properties like conductivity and strength; but a lack of graphitic carbon can also contribute much needed micropores for energy storage. Whilst pristine graphene formation is a fascinating subject for electrical devices and optical applications such materials remain expensive. Catalytic graphitization is a potential route to functional carbon foams produced from biomass and other waste or low cost materials. Examples thus far include: sawdust,[255,255] kraft lignin,[252,265] saccharides,[255,257] peanut shells,[282] whey protein,[279] poplar wood,[264] cellulose paper,[270] polypeptides,[259,253] and heavy hydrocarbon waste.[283,284]

1.5 Metrology of Graphene Materials

Thus far we have considered potential applications of graphene materials and methods of production; finally methods of analysing these materials are introduced. Specifically this section will discuss the statistics and processing to comprehensively analyse bulk samples as prepared by scalable methods and will not discuss the scientific principles behind each technique; where appropriate such details will be discussed in Chapter 3.

1.5.1 Industrial Graphene

The number of companies producing and using graphene has expanded rapidly with at least 102 different raw graphene manufacturers not including formulation suppliers in November 2020;[285] many using different manufacturing routes and producing a range of materials with irregular shapes, sizes and chemical functionality.[72] These differences in properties mean that no commercial graphene could reliably be used as a straightforward replacement for another without extensive testing. This could refer to device performance: strength, conductivity or charge storage. Given the huge number of variables involved in processing such devices, however, key metrics of the actual graphene would allow direct comparisons between the raw feedstock. Investigating the scale of the potential problem, characterization of graphene from 60 different suppliers has shown that most companies are in fact producing GNPs with a wider range of properties than the description 'graphene' would suggest.[286] As previously discussed for some applications, in particular composite materials, GNPs may be preferable to pristine graphene and matching the material with the application is important.[59] But this does still require robust characterization.

When attempts have been made at robust characterization it has also become apparent how insufficient single figure metrics are at describing such a complex nanomaterial. In proposing a classification framework Wick et al. suggested a three dimensional description of graphene materials using: lateral size, thickness and carbon to oxygen ratio.[287] Whilst comprehensive this approach would be impractical due to the difficulty in accurately measuring these three parameters from graphene materials at scale. Additionally many real materials have a distribution of flakes and environments that are more complex than a single summary statistic. Attempts to use Raman spectroscopy to probe graphene properties have found the distribution of I_D/I_G values actually measured did not reliably follow a gaussian distribution, which means any statement of mean or standard deviation has very little meaning.[288,289] The solution for this and best practice analysis is the collection of many data points to establish

the comprehensive distribution of whatever is being measured; and reporting the full distribution of parameters as a histogram or other graphical format.[289–293]

This has been highlighted,[286,294–296] with a few proposed high throughput quality control techniques for graphene materials including static light scattering, surface area measurements and wide area optical contrast images.[294,297] Unfortunately whilst many of these techniques serve one specific manufacturing route they cannot be applied to a material without prior knowledge of its origins. For example wide angle contrast images are effective for individual graphene flakes grown on a flat substrate but for dispersions or powdered materials it would not be possible to extract any useful information. It should also be stressed that graphene has experienced these difficulties because it is the most developed 2D material for applications, however, other 2D materials like h-BN and Mo_2S that are produced with similar techniques have the same potential pitfalls, as seen in Figure 29.[298]

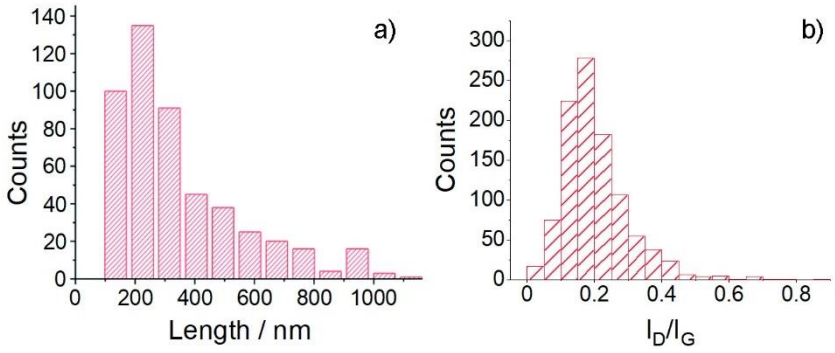

Figure 29: Example distributions of 2D material properties; a) taken from literature report of h-BN and b) from an investigation of exfoliated graphene. Adapted from [288].

1.5.2 Measuring Graphene Dispersions

Transmission electron microscopy is arguably the highest standard of graphene analysis as sheet size, shape and thickness can all be unambiguously determined from well prepared samples; and even the number of layers can be counted by imaging edges where the graphene sheets fold. In studies of graphite exfoliation TEM images are commonly used to validate claims of graphene production by showing both thickness and size of flakes produced.[146,150,152,156,161,299,300] TEM has also been used to image defects and the basal plane of graphene oxide and functionalised graphene.[123,127,301,302] Despite this great utility, the disadvantage of TEM is the time consuming and costly process of collecting images that typically are focussed on a single sheet or small cluster. For research purposes therefore TEM offers unique insight to the structure of graphene flakes but for large scale characterization of bulk samples the number of images required makes TEM impractical.

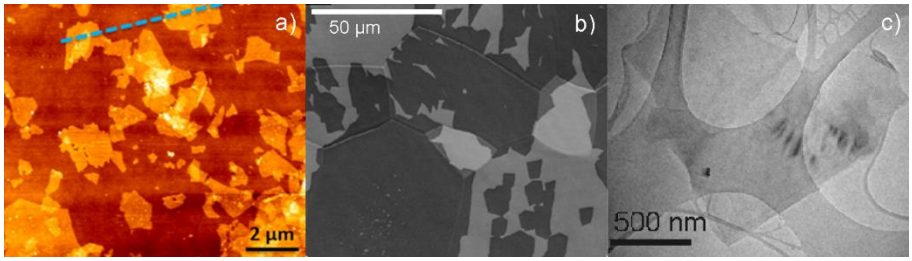

Figure 30: Example micrographs from a) AFM, b) SEM and c) TEM for graphene samples. a) & c) from liquid phase exfoliation and b) from CVD growth.

Adapted with permission from: Shinde, D. B. et al. *Langmuir,* **2016**, 32 (14), 3552–3559; Weatherup, R. S. et al. *Nano Lett.*, **2016**, 16 (10), 6196–6206; Lotya, M et al. *J. Am. Chem. Soc.* **2009**, 131 (10), 3611–3620. Copyright 2009 & 2016 American Chemical Society.

Atomic force microscopy can also be used to measure the lateral dimensions and thickness of flakes simultaneously, wider areas can be scanned and flake size statistics can be extracted more rapidly than from TEM.[288] Caution must be employed, however, when using images of many flakes because there is no absolute relationship between height as measured by AFM and number of layers.[303] In principle SEM can also image graphene layers deposited on a flat surface, and flake size statistics extracted from such images.[162] This is rarely done in practice, however, because of the poor contrast between the substrate and very thin carbon which will appear mostly transparent to the high energy electrons.

These microscopy techniques for the analysis of lateral sizes and exfoliation require stable dispersions of individualised flakes in suitable solvents, usually an alcohol or other low boiling organic. If large aggregates and bundles are present it is not possible to differentiate individual flakes, and therefore impossible to measure the lateral size or thickness.[304] This is generally achieved by sonicating the graphene material in a suitable solvent, followed by high speed centrifugation to remove large aggregates and this stable dispersion is then rapidly drop cast or spin coated onto the substrate for analysis. Since such preparation must remove all large bundles and unexfoliated material by design; this can make microscopy unsuitable for measuring samples that are not intended to be used following the same rigorous dilution and centrifugation to sediment larger particles.

Optical spectroscopy is a fast and easy method of analysing an entire dispersion, commonly used to measure the concentration of graphene in conducting inks and liquid exfoliated graphene. Applying the Beer-Lambert law optical absorption coefficients of graphene have been calculated, with an average value of 2700 mg^{-1} mL m^{-1}, this has a standard deviation of ± 1000 mg^{-1} mL m^{-1} and the full distribution is shown in Figure 31. The large variation is most likely due to light scattering from the carbon particles and the difference in graphene thickness and morphology that is not accounted for by the Beer-Lambert law.[305]

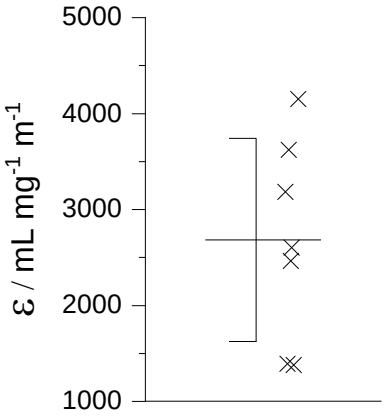

Figure 31: Distribution of optical extinction coefficients of graphene reported at 660 nm, data points are literature values, mean and standard deviation also marked. Ref: [9,150,152,163,173,299,306]

Attempts to minimise scattering have been undertaken by reducing the concentration before measurement and selecting a high wavelength of light, specifically 660 nm.[150] Nevertheless it is not possible to account for the different graphene thickness between samples. It is reported that each carbon layer absorbs approximately 2.3 ± 0.1 % of the incident light.[307] Assuming pure few-layer graphene every layer of carbon can contribute to the absorbance equally and the mass of carbon will be accurate; however, if a single flake is thicker than 134 nm, all light passing through such graphite flakes will be effectively blocked, ~0.01% transmission. This means a mass of carbon is present but excluded from the measurement. Despite this limitation UV-vis can be an effective method of measuring graphene dispersion concentrations, although, it is important that any new sample is calibrated and the extinction coefficient calculated if any change in flake thickness, size or morphology is suspected.

1.5.3 Measuring Bulk Samples

Graphene dispersions are versatile and attractive for many applications but not every production method or end use requires liquid dispersions; analysing graphene as a powdered sample can avoid many size selection issues. Often analytical tools for powdered samples are bulk techniques that do not require multiple images or measurements to be taken to achieve a statistical picture of all the graphene flakes; the disadvantage of this is the averaged nature of the data often limits information on the distribution of properties.

X-ray diffraction is a routine solid state analysis tool widely applied to graphite, the regular carbon layers provide a very strong Bragg peak that can be used to measure the interlayer spacing, stacking disorder within the material such as turbostratic graphite and the size of coherent scattering domains. Whilst a very powerful method to probe the structure of

graphitic materials with a regular stack of carbon layers present, graphene by definition has no interlayer Bragg peak making XRD unsuitable for graphene metrology.

Thermal gravimetric analysis (TGA) is in principle a very simple analytical technique; by heating the sample and monitoring the mass change any decomposition or combustion can be measured. Since different carbon phases have different thermal stabilities this can be used to identify the carbon phase present. Taking this analysis further Shtein et al. proposed a method of identifying different combustion events within a single sample that corresponded to different sized graphene nanoplatelets; by comparing the relative mass of each fraction and the temperature of combustion they were able to identify the polydispersity of GNP samples using a single analysis.[308] This process is illustrated in Figure 32 which showcases a manufactured mixture of two different graphene materials with different combustion temperatures; the thermal analysis of the mixture matched the separate thermal analyses of the GNP components. The information provided by thermal analysis is limited in scope, being unable to directly identify flake sizes or chemical environment, however, its ability to monitor polydispersity with a single measurement of a bulk sample would be ideal for some quality control processes.

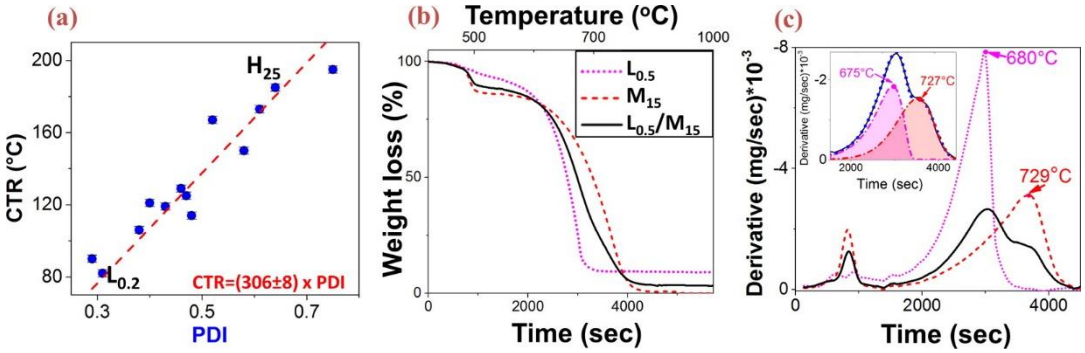

Figure 32: (a) The combustion temperature range vs the polydispersity index extracted from TEM of selected GnPs and their linear fit; (b) normalized thermogravimetric curves; (c) DTG curve of the GnP mixture ($L_{0.5}/M_{15}$) and its pure constituents ($L_{0.5}$ and M_{15}). Inset: the log-normal deconvolution of the $L_{0.5}/M_{15}$ DTG curve shows an excellent match.

Raman spectroscopy is commonly suggested for graphene metrology because it is relatively simple, but provides detailed information on the physical and chemical structure.[295,297,309] The biggest disadvantage in comparison with other bulk scale techniques is the requirement to collect multiple spectra to produce a statistically significant analysis. When undertaking Raman microscopy, a sample can be automatically moved under a fixed microscope through which the Raman signal is focussed and collected to generate these data sets; although this

can be time consuming. Raman data sets have nevertheless been effective in research environments; for example the statistical analysis of covalently functionalised graphene and CVD growth of graphene on a metal foam.[292,310]

Collecting large Raman maps in this manner also includes spatial data of the distribution of Raman spectra at different locations. This has been used to great effect on static flakes bonded to, or grown on, controlled surfaces. For example probing graphene growth on copper [111] surfaces by overlaying spatial Raman map data with microscale crystallographic data, or epitaxially growth on SiC by mapping the height profile.[311,312] The localisation of graphene flakes on a surface for Raman measurements has also probed fundamental properties of the material like thermal conductivity, the strain response of graphene flakes and confirmed the enhanced reactivity of wrinkles and highly curved edges.[313–315] Whilst powerful, these insights all rely on immobilised graphene flakes prepared in such a way that the spatial distribution is significant and meaningfully linked to other properties.

Irrespective of spatial data, simple collecting large data sets and undertaking statistical analysis on the distribution observed has been applied to commercially produced graphene, highlighting the current issue with many manufactured samples.[286] The wide applicability and information possible from Raman spectroscopy make it appealing for common standards across different manufacturing routes with minimal modification to sample preparation. Other optical imaging methods have been proposed for CVD graphene films of metal substrates, using optical contrast or back scattering from harmonic modes but such techniques tend to be very specialised towards individual flakes grown on metal foils and, therefore, not suitable for graphene powders produced at greater scale.[297,316,317]

Finally, light scattering techniques that measure the particle size of graphene flakes have been suggested for the characterization of liquid exfoliated graphene.[294] These methods are well established but most models rely on randomly tumbling particles like proteins and polymers; graphene in contrast is a more ridged 2D flake. Despite this it is possible to correlate the hydrodynamic radius with changes in flake size following shear exfoliation. Light scattering can also measure larger aggregates and unexfoliated material that the centrifugation processing, required for microscopy, excludes. Despite these benefits, light scattering to measure graphene flake size is still limited by the averaged hydrodynamic radius measured and cannot accurately measure sheet thickness, much less different chemical functionalities or defects within the aromatic structure.

1.6 Conclusion

Since the isolation of graphene its remarkable strength, conductivity and inert nature have generated enormous interest and excitement for possible uses; graphene has been linked to supercapacitors, battery electrodes, photocatalysis, conductive ink, flexible screens and optoelectrical devices, transparent electrical components, high strength composites, barrier coatings, functional fluids and coolants and quantum Hall based resistance standards. Despite this potential many devices actually require different combinations of graphene's properties, and in many cases other graphenic carbon materials; for example Na^+ batteries require disordered stacks and layers of graphitic carbon rather than isolated single layers.

Different requirements may be fulfilled by the equally diverse production methods developed for graphene and related materials. The primary concern for many applications and devices is the cost and scalability of manufacture. CVD grown pristine graphene may be ideal for high end electrical devices but the limited scale of production make CVD unappealing for larger volume products. A larger scale production technique, liquid phase exfoliation has received much interest recently for its potential production of low cost graphene inks that can be used in additive manufacturing processes. Although, exfoliating graphite still requires the highly crystalline graphite starting material.

Catalytic graphitization, the process whereby low cost carbon feedstocks are converted into nanostructured graphitic carbon materials using transition metal catalysts, does not require crystalline graphite and has been proposed for energy storage applications. The combination of high surface area, relatively inert and highly conductive foams are ideal for battery electrodes and supercapacitors. The different graphitization methods, starting materials and catalysts used have thus far produced a wide range of different carbon materials with different degrees of conjugated carbon structures, surface area and pore structures. Of note, these differences are generally greater within the same metal than between different metals indicating the process is highly depended on processing conditions and more tolerant to metal chemistry than supposed. The size of metal particles and distribution of transition metal salts are known to influence the final carbon but a clear understanding of the formation of graphitic carbon formation is still elusive.

More generally a greater understanding of graphene metrology and a process whereby it can be analysed and codified is required for it to be more widely utilised by industry. [286,294–296] Currently the lack of any harmonised system prevents different materials from being used in similar processes without significant prior investigations. Whilst this discussion has focussed

on graphene as the most developed 2D material closest to applications; such considerations apply to other developing 2D materials with desirable properties for other industries. The production of Mo_2S based semi-conducting inks have the potential to simplify electrical device manufacture, however, many of the same concerns over scalability of production methods and reliable quality control that currently exist for graphene will equally apply.

Overall some key challenges remain for graphene utilisation. Robust and reliable analytical tools must be developed to enable graphene producers and device manufacturers to clearly communicate material properties; this should combine high throughput analysis with rigorous characterization of an entire material distribution. Unfortunately common graphene analytical tools to date have failed in one of these requirements. Additionally low cost, scalable production methods for graphene based materials should be developed capable of producing materials that may be very distinct from pristine graphene but that meet the requirements of the desired applications. Together these two topics form the primary focus of the research discussed herein: developing a statistical method for metrology and understanding the graphitization process of converting low cost feedstocks into potentially useful carbon materials.

2. Aims and Objectives

The challenges remaining for graphene development are complex. Underpinning many is the need for greater understanding and characterization of the inhomogeneous nature of 2D nanomaterials. Unlike conventional chemical systems graphene is not a uniform molecular system but a mixture of flakes with different sizes and thickness, a greater understanding of the analysis of this mixture is required for reliable metrology to develop.

Despite the different techniques that have been trialled, introduced in Chapter 1, no reliable high throughput method has emerged to meet the requirements of quality control standards. A detailed discussion of the characterisation techniques applied in this work is the focus of Chapter 3. It is possible the lack of a widespread, rapid analytical technique is because no such perfect technique exists and other more time consuming methods must be applied. Identifying the minimum characterisation required for a mixture of graphene flakes may inform developments in metrology and bridge the gap. Focussing on Raman spectroscopy because of its versatility and depth of information, the statistics of large sample sizes is investigated in Chapter 4. Using a wide selection of graphene related materials, large Raman data sets are collected and subjected to statistical analysis to understand the distribution of the graphene material; but also to understand the development of the data as it is collected. The key question to be answered is what scale of Raman spectroscopy is required to have confidence in the analysis of a graphene material.

Detailed analysis will also be used to understand the process of catalytic graphitization, aiming to control the resulting porosity and conductivity of graphitic carbon. Such materials have been obtained from biomass and other low cost carbon sources, this makes catalytic graphitization an appealing process for the manufacture of electrodes and energy storage devices. Recent developments have focussed on the production of carbon foams and their integration to devices such as supercapacitors and alkali metal batteries. Despite this mechanistic models for the conversion of carbon into porous graphitic materials have rarely been postulated since the seminal work by Ōya and Marsh.

Utilising the statistical insight on graphene analysis and other solid state characterisation methods; Chapter 5 discusses the production and characterisation of graphitic foams from a selection of different cobalt salts; aiming to identify how such materials can be produced in a controlled method in the future. The performance of such materials will not be tested in any real devices since the properties required for good capacitance and energy density are well known. Instead the processes that form the microstructure will be investigated.

3. Characterisation of Graphene

3.1 Raman Spectroscopy

Raman spectroscopy uses the phenomenon of light scattering to probe vibrational states. Scattering can be either elastic, changing direction but not energy in a process known as Rayleigh scattering or inelastic in which energy is transferred (Figure 33). This inelastic scattering was first observed by Sir C V Raman in 1928 using sunlight and a filter,[318] but the requirement for high intensity monochromatic light meant the technique did not find widespread use until the introduction of laser sources in the 1960s. Raman spectroscopy has since become a powerful tool for probing a wide range of substances from the vibrational states of small molecules to the band structure and phonon modes in solid state materials.

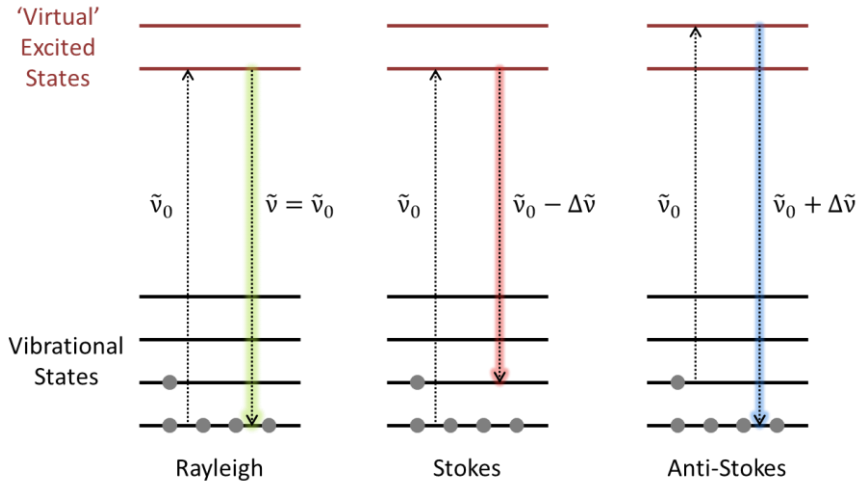

Figure 33: Schematic illustrating the three main scattering processes; the incident photon is absorbed shown on the left with energy $\tilde{\nu}_0$ placing the system in an excited state. The system will decay from this state back to a real energy level, emitting a photon with a different wavelength in the case of Raman scattering.

In a classical model a molecule has a vibrational potential described as a harmonic oscillator with a number of evenly spaced energy levels. During Raman scattering the molecule is said to be excited into a 'virtual excited state' from which it relaxes into a different vibrational level to the one it initially occupied. The energy difference between vibrational levels causes the change in photon energy measured by Raman spectroscopy. A red-shift is caused by excitation of a molecule into a higher energy level, known as a Stokes shift, whilst the blue-shift caused by a loss in energy of the system is known as anti-Stokes. Since higher energy levels are less populated than the ground state in accordance with the Boltzmann distribution the Stokes lines are more intense than the anti-Stokes.

The vibrational modes that contribute to a Raman spectrum are determined by selection rules that require a change is polarizability of the molecule during the Raman scattering process. A rigorous treatment of this can be found elsewhere;[319] however, this model is generally insufficient to explain the phenomena observed when measuring carbon nanomaterials. This complexity is what makes Raman spectroscopy such a powerful tool for characterising carbon nanomaterials; allowing the discrimination of graphene, graphite and carbon nanotubes as well as investigating their size and the presence of functional groups.

3.1.1 Graphitic Carbon Raman Features

The Raman spectrum of sp^2 carbon materials can mainly be considered in terms of three spectral features, a D, G and 2D peak although they may not all be observed from every material. There are additional smaller peaks as shown in Figure 34 but these are generally less useful for analysis.

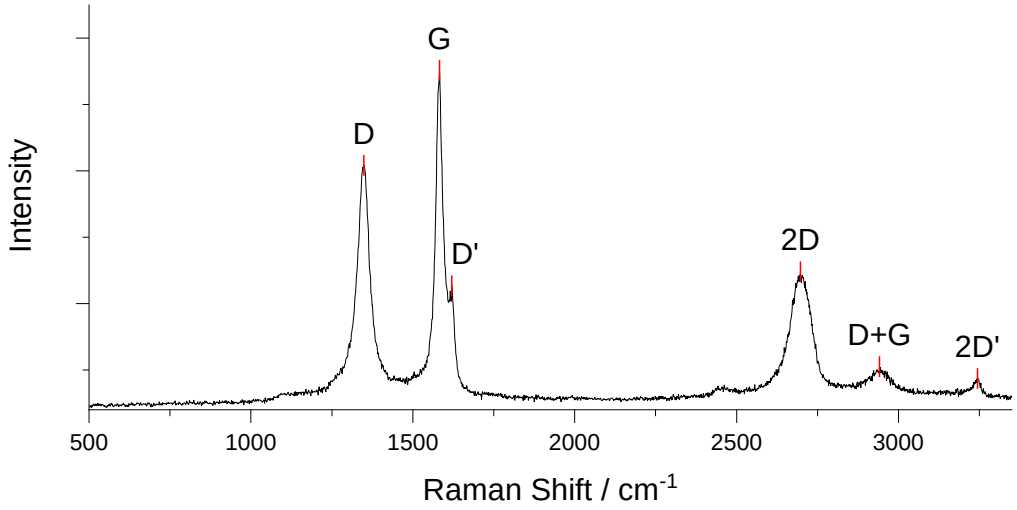

Figure 34: An example Raman spectrum with significant peaks labelled. This was collected from functionalised graphite using a 633 nm laser.

G Peak – 1580 cm^{-1}

Usually the most intense feature, the G peak can be considered a signature of sp^2 carbon in a material and as such is often used as a reference peak for comparing the intensities of other peaks. In a molecular picture this is the E_{2g} doubly degenerate asymmetric stretching mode of a benzene ring; when the picture is expanded to a solid carbon material this E_{2g} symmetry refers to the degenerate iTO (in-plane transverse optical) and LO (longitudinal optical) phonon modes (Figure 35) of the carbon plane lattice.

This scattering process is a conventional first order transition in which the electromagnetic field of the photon interacts with the material, generating a photoexcited state. This excited

state emits a phonon and the remaining energy is emitted as a scattered photon.[11] Unlike conventional Raman spectroscopy the excited state is an energy level described by the band structure close to the high symmetry **K** point, and the similarity in energy of the photons and transitions make the process resonant, improving the intensity of the Raman signal.[320] In graphite and related materials the continuous band structure means a range of wavelengths meet the resonance condition, although laser wavelengths around 532nm are commonly used as the laser source for resonance Raman spectroscopy.

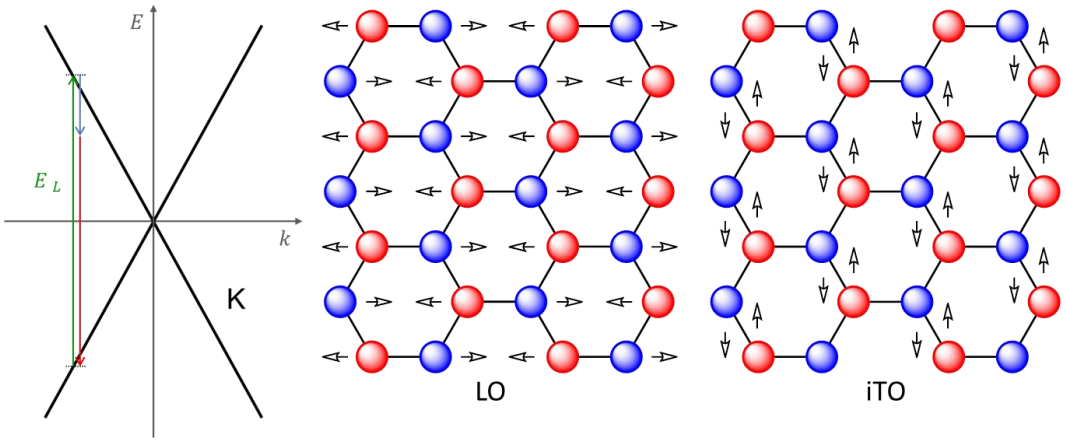

Figure 35: Schematic of the Raman scattering process of the G peak. Left: absorption of laser light of energy (E_L) shown in green followed by inelastic scattering and emission of a Raman photon indicated in red. Right: lattice vibration modes responsible for the inelastic scattering.

D Peak – 1350 cm^{-1}

When the Raman spectra of sp^2 carbon materials were first studied structural and chemical defects were quickly linked to the D peak; although, the actual scattering mechanism underwent numerous iterations. It is now described as a second order double resonance process, see Figure 36, in which the defects 'activate' the Raman process.[321]

1. The incident photon is absorbed by the material producing a photoexcited electron-hole pair occupying "real" energy levels within the band structure
2. The excited state emits a iTO phonon to release energy, however, in this case there is also a significant change in the system momentum formally denoted as a change in k-space from near the high symmetry **K** point to **K'**.
3. The photoexcited electron undergoes a scattering event from a defect in the lattice, which converts the system momentum back to the original state. Thus the overall process is said to be 'activated' by defects.
4. The photoexcited electron and hole can recombine, emitting a scattered photon of reduced energy

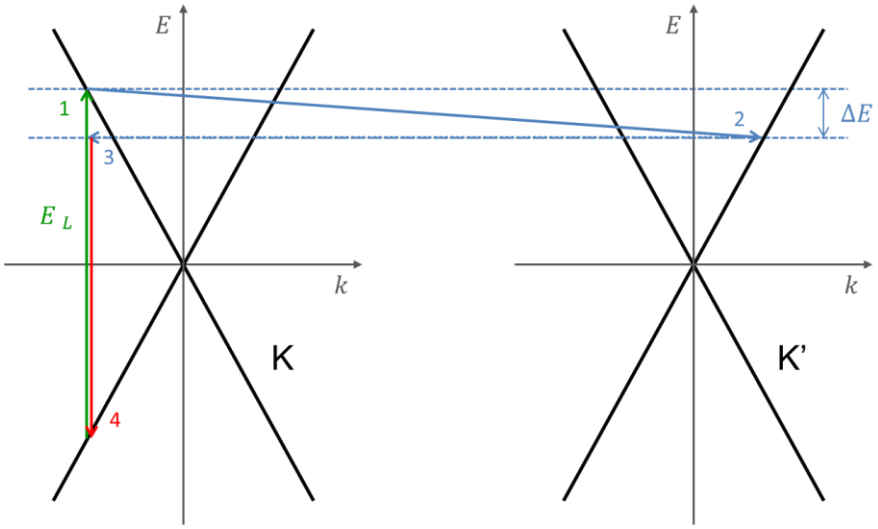

Figure 36: Schematic of the inter-valley scattering process responsible for the D band activation. The initial absorption is shown in green, followed by photoexcited electron transitions in blue before the final emission shown in red.

A double resonance process is one in which the transitions involved in the scattering process correspond to the incident and emitted photons making the signal intensity significantly higher than expected. Additionally it makes the signals observed from these double resonance processes slightly unusual compared to conventional Raman signals. Firstly the D peak is dispersive; this means the wavenumber of the Raman signal changes as the laser source energy changes by $\sim 50\ cm^{-1}\ /\ eV$;[15] secondly the intensity of the signal does not follow the expected $I \propto \tilde{\nu}^4$ relationship whilst the G peak does.[322,323] The effect of this is that only the G peak will get smaller when a lower energy laser source is used, making all double resonant peaks including the D peak appear larger by comparison as illustrated by Figure 37.

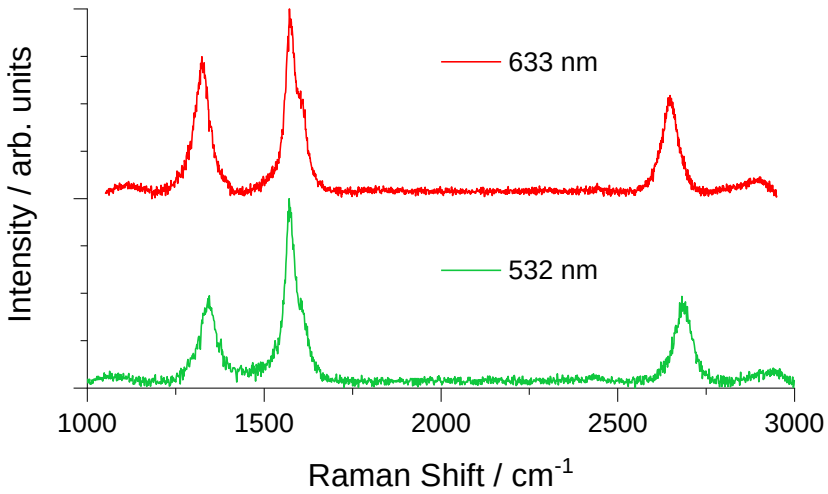

Figure 37: Raman spectra of an identical sample with different lasers demonstrating the changing peak position and relative intensity of the D and 2D peaks. The green spectrum was recorded with a 532nm laser source whilst the red spectrum was recorded with a 633 nm laser.

D' Peak – 1620 cm^{-1}

The D' peak is also activated by defects within the material and has very similar properties to the D peak described above. The scattering mechanism in this case, however, goes via an intra-valley scattering process between energy levels close to the **K** point rather than the significant change in momentum observed for the D peak. Practically the most significant difference is the relatively low intensity and close proximity of the D' peak to the G peak means that it is often difficult to resolve.

2D Peak – 2700 cm^{-1}

This is generally the second most prominent peak in graphitic samples, and was historically labelled G' but the scattering process involves the zone centre phonons, like the D peak, hence the current notation of 2D. Two different fourth order models, a double resonant and triple resonant have been proposed to explain this transition.[11,320,324] Both models rely on many of the same processes of photoexcitation followed by inelastic scattering; however, the conservation of momentum in this process is fulfilled by electron and hole scattering creating lattice vibrations rather than defects in the material.

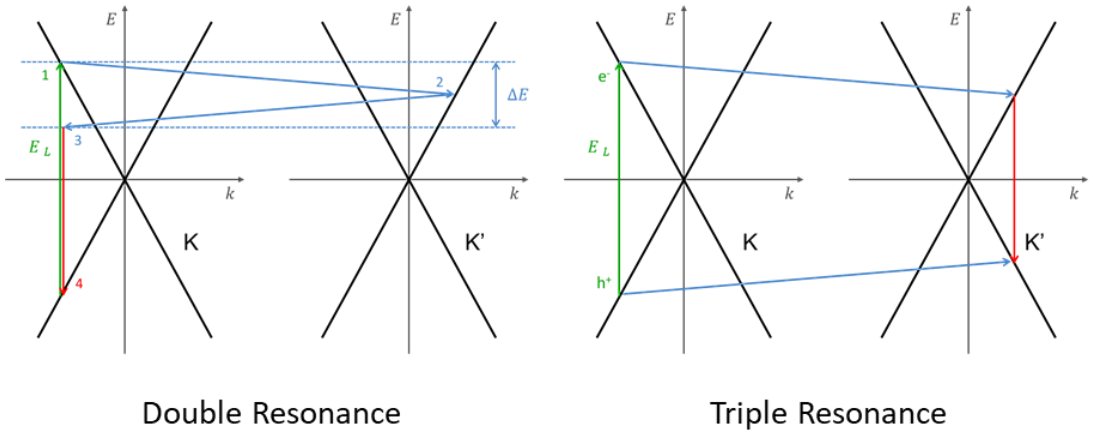

Figure 38: The two models proposed to explain the Raman scattering process responsible for the 2D peak; absorption of the incident light (of energy E_L) shown in green and emission of the scattered light in red.

The stages proposed for the scattering are:

1. Absorption of light to produce a photoexcited electron-hole pair.
2. Inelastic electron-phonon scattering, losing energy to the vibrational mode and changing momentum (**q**) about the high symmetry **K** point to the **K'** point.
3. Further inelastic scattering with an exchanged momentum (**-q**) that conserves the system momentum through this Raman scattering process.
4. Recombination of the photoexcited electron and hole by emission of a photon.

The double and triple resonance processes involve the same phonons, specifically the iTO phonons about the **K** or **K'** point. In the case of triple resonance, however, both the photoexcited electron and hole are scattered resulting in occupation of "real" energy levels following every transition, whilst in the double resonance model only the electron is scattered, and recombination and photon emission occurs from a "virtual" energy level.

Since the D and 2D peaks both originate from the same phonon modes around the **K** point both have a dispersive wavenumber, for the 2D peak that varies by $\sim 95\ cm^{-1}\ /\ eV$ and a relative intensity ratio (I_{2D}/I_G) that changes with laser wavelength (Figure 37).[324] The resonance condition makes the 2D peak especially sensitive to any changes in the materials band structure since distortions to the distribution of energy levels will alter the energy and intensity of the Raman scattering process. Such distortions can be caused by doping or exfoliation, making the 2D peak a valuable tool for probing graphene flakes.

Nanotube Radial Breathing Modes – 100s cm^{-1}

The peculiar nature of nanotubes leads to specific properties in their Raman spectra compared to other materials. The change in dimensionality to 1D has a significant effect on the band structure, producing quantised energy levels in the density of states plot. In addition carbon nanotubes have Raman spectral features in the range of only a few hundred wavenumbers. These peaks are attributed to the completely symmetrical A_1 stretching of carbon atoms away from the centre of the tube causing the nanotube to expand and shrink in diameter. These peaks can be linked to the diameter and chirality of the nanotubes; for further information see the rigorous review from Saito *et. al*.[320]

3.1.2 Effects of Layer Stacking

When analysing graphene materials one of the most important properties is layer stacking. The band structure of monolayer graphene has a single conduction band and a single valence band caused by the bonding and antibonding combinations of the carbon p_z orbitals; this produces a single sharp 2D peak. The addition of a second carbon layer to form bilayer graphene also introduces two additional bands of slightly different energy to the system and thereby increases the number of possible transitions to four as shown in Figure 39.[13,21] The different exchanges of momentum labelled **q** are all conserved during the overall Raman scattering process, however, the energy lost to phonon excitation is subtly different giving rise to the four different wavelengths of Raman scattered light from bilayer graphene.

This dramatic change in shape of the 2D band continues for three layer graphene, which theoretically has nine transitions although five peaks are sufficient to fit the measured signal

due to degeneracies.[324] Whilst these subtle changes can be expected to continue until the number of layers effectively becomes infinite, the differences become less significant after approximately four layers.[11] As shown in Figure 40 the Raman spectrum of HOPG is described by just two Lorentzian peaks. Whilst this change in shape is a powerful tool for investigating the fundamental properties of graphene the complexity inherent in fitting such models makes this impractical for large scale analysis undertaken on inhomogeneous samples.

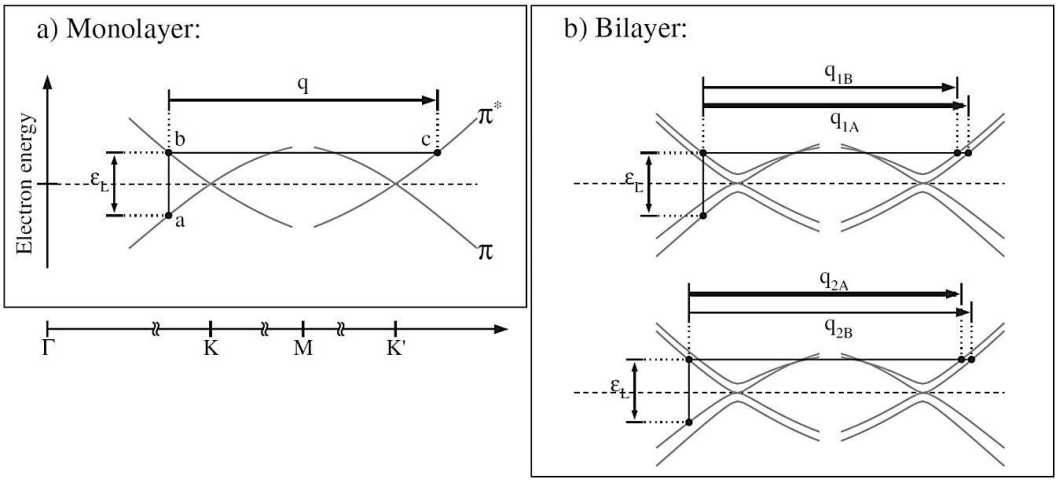

Figure 39: a) Band structure of monolayer graphene with the 2D Raman transitions indicated; q is the exchanged phonon momentum and ε_L is the laser energy. b) Bilayer graphene band structure with the four different transitions shown. (The top and bottom bands are identical but only two transitions are shown on each for clarity)

The number of graphene layers is not the only consideration, the alignment of the layers must also be considered and misalignments and rotations of the graphene sheets can be detected in the 2D peak. As the stacking orientation changes, the structural symmetry and nearest neighbours change which alters the Fermi surface of the carbon material; since the position and gradient of the electronic bands are altered the energy change measured by Raman spectroscopy is also altered. [290,325–327] In the case of turbostratic graphite, in which layers are stacked directly on top of each other, the 2D peak maintains the same intensity as hexagonal stacked graphite but has only a single peak and not the asymmetric peak of HOPG.

This change in energy is also manifest in the variation of the 2D peak position;[324] as graphite becomes few layer graphene the peak is redshifted although the magnitude of this has been linked to substrate interactions.[328] Whilst this change in Raman wavenumber is commonly reported it is important to consider the difficulties that arise when trying to extract the exact wavenumber of a very asymmetric Raman signal.

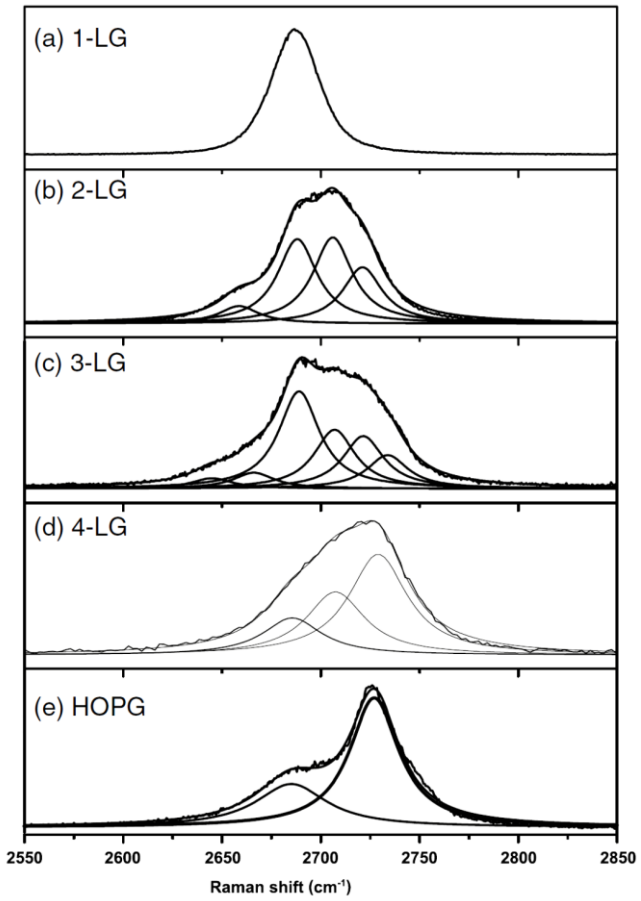

Figure 40: A series showing the evolution of the Raman 2D peak as the number of layers increases, the multiple Lorentzian peaks fitted to the observed peak are shown underneath.

Finally the most significant difference between the Raman spectrum of bulk graphite and monolayer graphene is the intensity of the 2D peak, usually a fraction of the height of the G peak in graphite the 2D peak is observed to be many times higher than the G in monolayer graphene.[13] This difference is due to the highly resonant origin of the 2D peak and the relatively high number of energy levels within the materials band structure involved in the Raman scattering process. The 2D peak intensity is determined by the electron scattering rate but relies on both electrons and holes getting scattered; monolayer graphene lacks any interactions between sheets so there are fewer incoherent scattering events incompatible with the Raman emission criteria, therefore more incident photons are Raman scattered.

The clear difference in relative intensities of the 2D and G peak between graphene and graphite is commonly used when analysing graphene and usually reported as I_{2D}/I_G.[329] This ratio changes dramatically for single and bilayer samples compared to graphite and even small amounts of exfoliated material in a bulk sample can produce subtle increases in I_{2D}/I_G.

Care must be employed when comparing data from different laser sources though; as already stated the G peak obeys the standard $I \propto \tilde{\nu}^4$ relation expected in Raman spectroscopy whilst the other peaks from graphitic carbon do not. This means the relative peak heights will change as the laser energy changes.

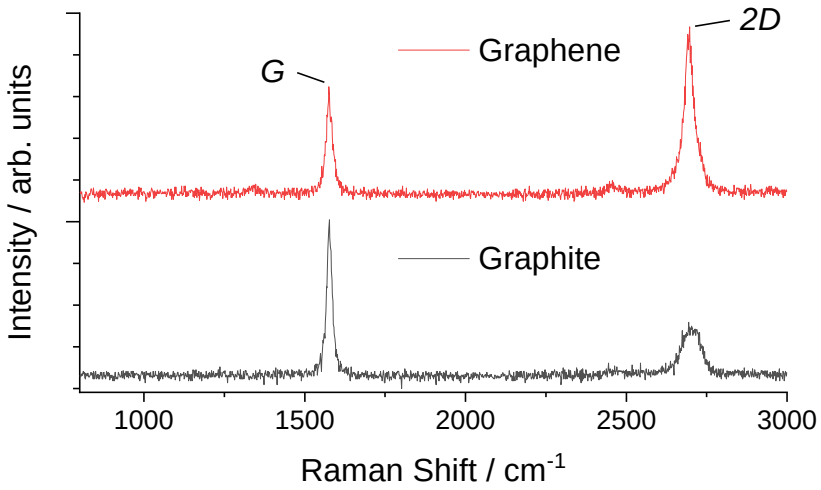

Figure 41: Raman spectra of graphene and graphite recorded with a 532 nm green laser.

3.1.3 Defects in the sp^2 Network

In addition to examining the thickness of graphene flakes; because the D peak is caused by breaks in the six-fold symmetry surrounding sp^2 carbon rings it can be very powerful for probing lattice defects and sheet edges, where other functional groups or atoms are bonded next to the aromatic region of graphitic carbon. To explore this effect further single layer graphene can provide an ideal experimental platform and by bombarding a graphene sheet with Ar^+ ions Lucchese et al. were able to probe specific densities of random defects.[330]

As more defects were formed the relative height of the D peak, I_D/I_G, increased. Fitting this trend the authors proposed a "local activation model" to explain the increase in D peak intensity; this model suggests every point defect induced by ion bombardment is described by a small area of structurally disordered carbon (shown in red in Figure 42) that cannot contribute to the Raman spectrum. The disordered area does, however, 'activate' the aromatic carbon around it (shown in green in Figure 42) by allowing the exchange of momentum required for the D peak. As the defect density increases a greater proportion of graphitic carbon becomes 'activated' and emits Raman scattered photons at both 1580 cm^{-1} and ~1350 cm^{-1} contributing to the increasing I_D/I_G metric. This increase is limited, however, by the availability for new defects to form; as shown in Figure 42e when the defect density becomes too high there is actually a decrease in carbon capable of Raman scattering.

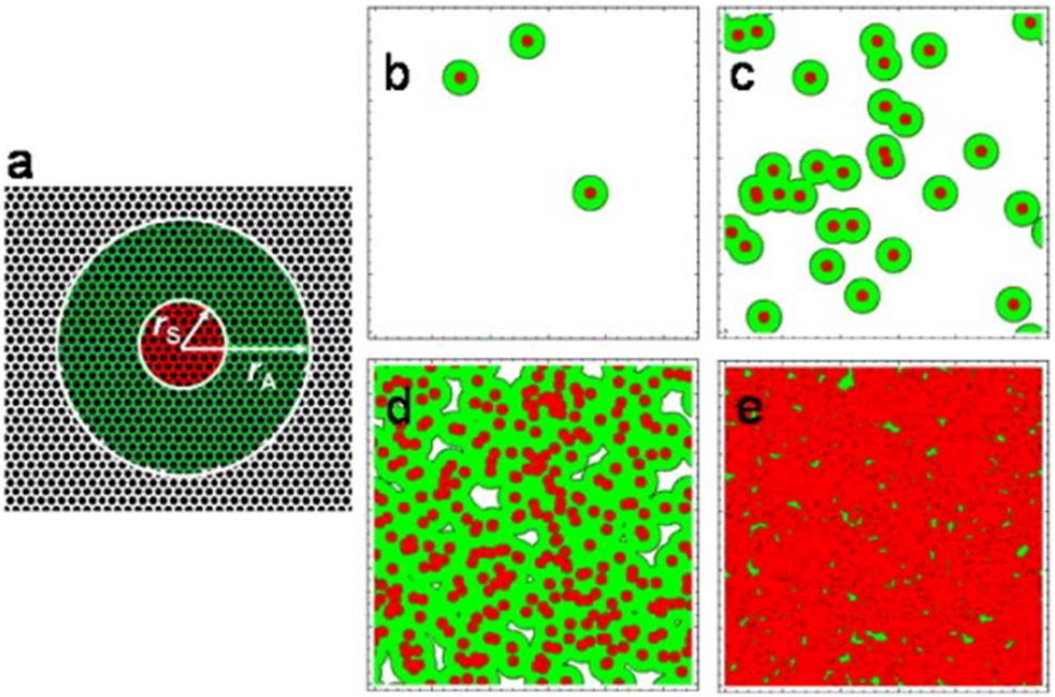

Figure 42: a) Definition of the "*activated*" (green) and "*structurally-disordered*" (red) regions. b–e) shows 55 × 55 nm portions of the graphene simulation cell, with snapshots of the structural evolution of the graphene sheet for increasing defect concentrations.

Whilst powerful this model is limited by the assumption that all defects are randomly distributed over the graphene sheet. In reality, TEM investigations of GO and rGO have shown that defects tend to increase the reactivity of the surrounding carbon leading to the formation of 'islands' of highly functionalised carbon surrounded by relatively pristine graphene, seen clearly in Figure 43.[302,331] Despite this limitation the main trends observed with the model system are consistently observed from graphite oxide, chemically functionalised graphene and synthetic graphite samples.

In a discussion on the topic Ferrari refers to an 'amorphization trajectory' of increasing I_D/I_G from graphite into nanocrystalline graphite but then a decrease in D peak intensity as the material becomes more related to amorphous carbon with significant sp^3 content.[321] In addition, real materials often exhibit peak broadening as they become more disordered; it is possible this is caused by greater scattering of phonons within the material causing the photoexcited electrons and holes responsible for Raman scattering to lose coherence.[332,333] Alternatively the range of different groups and defect sites may all have subtly different effects on the band structure thereby producing a wider range of Raman shift energies than observed from pristine systems.

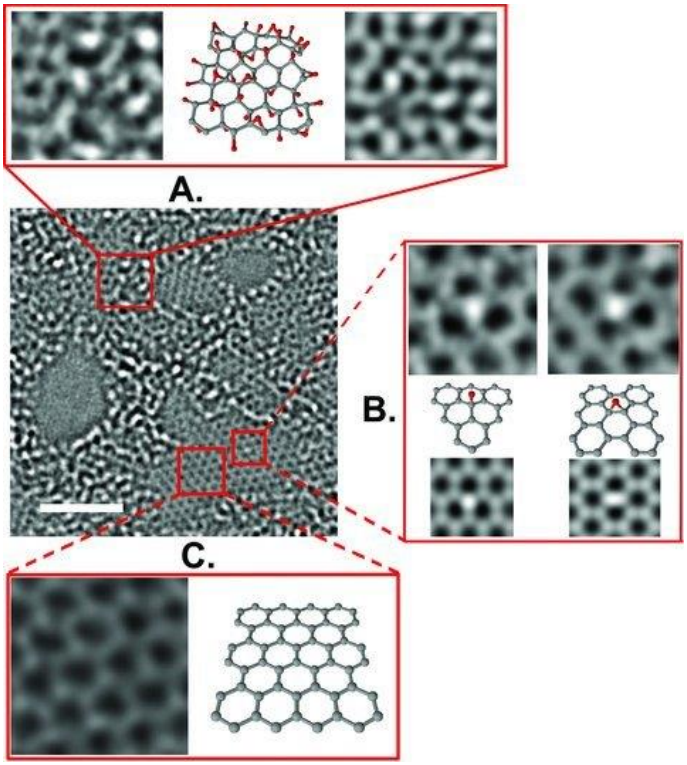

Figure 43: Aberration-corrected TEM micrograph of suspended GO, scale bar is 2 nm. Expansions A-C show proposed local structures. This image clearly shows the different regions of highly crystalline graphite and disordered amorphous carbon with no random defects apparent.

This peak broadening is known to have a very significant effect on highly functionalised material like GO; because the intensity of the D' peak becomes more significant and the width of both the G and D' peaks become larger it is commonly observed for the two to merge into a single wide peak centred around 1600 cm^{-1}.[321,334,335] This peak, sometimes referred to as G-apparent or G_{app}, has the dispersive properties of the D' signal but significant width and asymmetry from the G peak. These highly disordered systems also highlight the reduction in 2D peak intensity as the aromatic carbon structure is lost,[133] in the case of graphite and graphene oxide it is common to observe no 2D peak at all and only with harsh reduction can the 2D signal be observed.

Considering these trends illustrated in Figure 44, it is clear models like Ar^+ bombardment as introduced above can provide significant insight to the Raman scattering mechanisms of graphitic carbon materials. Caution is needed, however, when attempting to draw direct relationships or proportionality from these ideal models without consideration of defect type and local electronic environment.[336]

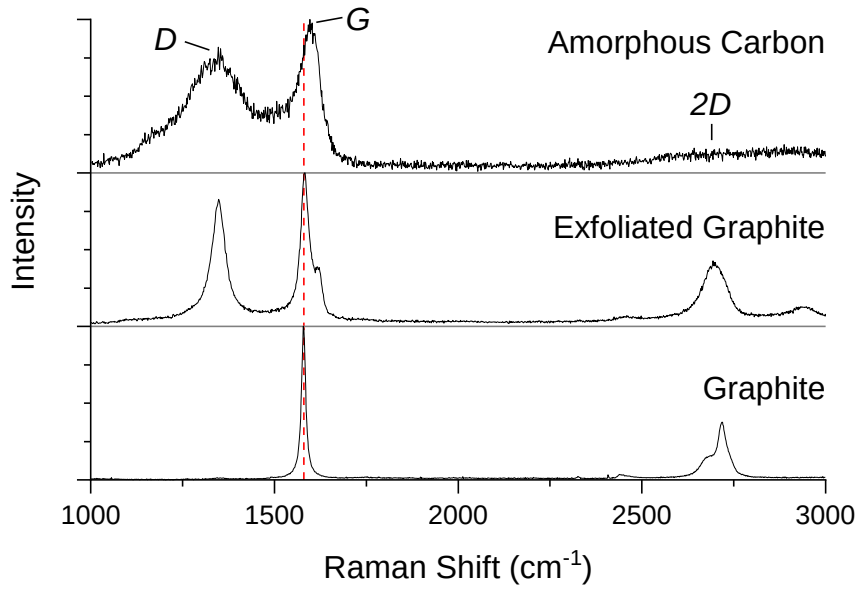

Figure 44: Example Raman spectra of different graphite derived materials showing the evolution of the D and D' peaks. The bottom is pristine graphite and more defects are present moving up the figure, all spectra were recorded using a 532 nm laser.

3.1.4 The Effect of Graphene Sheet Sizes

Thus far discussion of defects has focussed on point defects caused by chemical functionalisation or damage to the basal plane; however, the same symmetry breaking mechanism applies to sheet edges. The loss of six-fold symmetry along the sheet edge allows photoexcited electrons to scatter and recombine to emit the Raman scattered photon; so a region of 'activated' carbon would be expected to extend into the graphene sheet from the edges. This has been confirmed experimentally with a combination of ion bombardment and high temperature annealing of amorphous carbon.[337]

Since graphene sheet edges contribute to the D peak intensity, it follows that smaller flakes with a greater proportion of edge to crystalline basal plane will have a greater I_D/I_G value; a relationship which could in principle be used to measure the size of graphene flakes. Historically an inverse relationship to do precisely that was proposed by Tuinstra et al. stating that the average crystallite size is inversely proportional to I_D/I_G;[338,339] the appealing simplicity of this relationship means it is still found in modern literature as a measure of graphene flake size. Unfortunately the original analysis is based on the assumption that the D peak is entirely the product of graphene flake size; specifically a vibrational mode that would not induce any change in polarizability and therefore be Raman inactive in large flakes becomes Raman active in small sheets. As discussed above, experimental and modelling investigations of graphene have shown the origin of the D peak to be symmetry breaking defects.

It clearly still follows that smaller flakes have a greater proportion of edges and therefore a higher D peak signal, but without knowing the shape of a flake or chemical functionality it would be inaccurate to identify a meaningful average flake size.[321] It has recently been suggested that point defects commonly associated with functional groups can be deconvoluted from the edge signals generally linked to flake size by also considering the peak widths.[337] Even in this case caution is needed, average crystallite size is merely an averaged value derived from the prevalence of edge sites to basal plane carbon, and without understanding the shape of flakes these cannot be perfectly linked as indicated in Figure 45. Comparison of such values before and after physical or chemical processing would likely be a meaningful indication of changes to the graphite flake sizes but attempting to claim a universally meaningful metric from such an averaged value seems disingenuous.

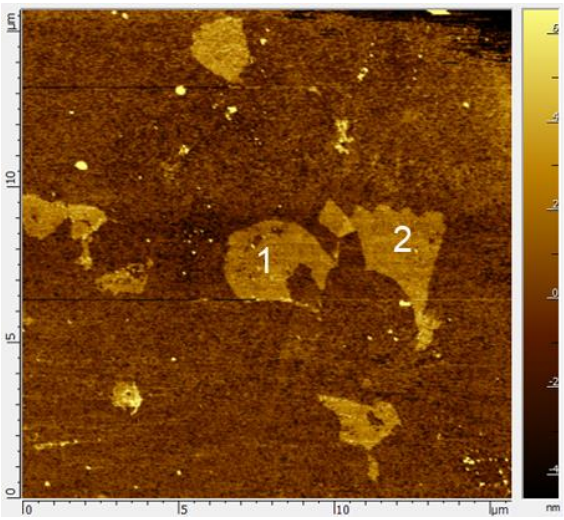

	1	2
Area / µm^2	26	28
Perimeter / µm	24	29
Ratio	0.93	1.05

Figure 45: AFM height profile of solvent exfoliated graphene, with key size metrics from two typical flakes shown. Despite being very comparable in size their ratio of flake edge is clearly different.

3.1.5 Summary

Raman spectroscopy is a very powerful technique for the analysis of carbon nanomaterials; data collection is generally easier and less costly than microscopy whilst providing detailed information about the material under analysis. Much of this is down to the close link between the Raman signals and the material structure. The G peak is a signature of aromatic carbon observed from molecular systems as a well as graphite and graphene which makes it ideal as a reference peak; in contrast the D peak is not always observed since it requires a structural defect to activate. The D' peak, close in energy to the G peak, is caused by a similar mechanism to the D peak but it is usually lower in intensity and harder to resolve. The D' peak width is sometimes used as a measure of defect homogeneity; in the case of very

disordered systems with many different defects present the D' is often lost into the G peak whilst the D peak grows in intensity.

The final large peak observed from graphitic carbon systems is the 2D peak; the highly resonant nature makes it highly sensitive to layer stacking and graphene exfoliation. The signal intensity and line shape change dramatically as layer number increases from single layer graphene to bi-layer but these changes become less significant as the layer number increases further. These changes are commonly used to probe exfoliation of graphene from graphite and to monitor few layer graphene growth on a variety of substrates.

To monitor changes in structural disordered within the basal plane, including chemical functionalisation and changes to graphene flake size, the D peak is generally used. Whilst exact interpretations are often difficult general trends can be very informative for understanding processing or comparing similar materials. Generally the higher the D peak the more "defect" sites present. Whether they are edges due to decreased flake size, functional groups bonded to the graphene surface or damage to the basal plane caused by high energy processing is more challenging to determine. Wider peaks generally indicate many different types of defect, commonly found from amorphous graphitic carbon or graphite oxide whilst sharp peaks are usually caused by a single defect like uniform edges.

3.2 Thermal Analysis

To compliment the myriad microscale analytical techniques commonly applied to nanomaterials, methods that probe macroscale bulk quantities of sample are needed. Thermogravimetric analysis is possibly the most conceptually simple of these techniques; the mass of a substance is monitored whilst the temperature is changed at a controlled rate in a controlled atmosphere. Plotting the mass as a function of temperature or time indicates the temperature at which any changes that alter the mass of sample take place, such as combustion or decomposition. To understand these changes further the exhaust gas can be passed through an infrared spectrometer (IR), mass spectrometer (MS) or gas-chromatograph coupled to a mass spectrometer (GC-MS).[340]

To compare the gravimetric plots between samples, metrics are used. The most common are the extrapolated onset temperature, described by ISO as the "point of intersection of extrapolated baseline and tangent drawn at point of inflection of step" and the temperature or time of maximum mass loss, often referred to as an inflection point and calculated from peaks in the first derivative plot.

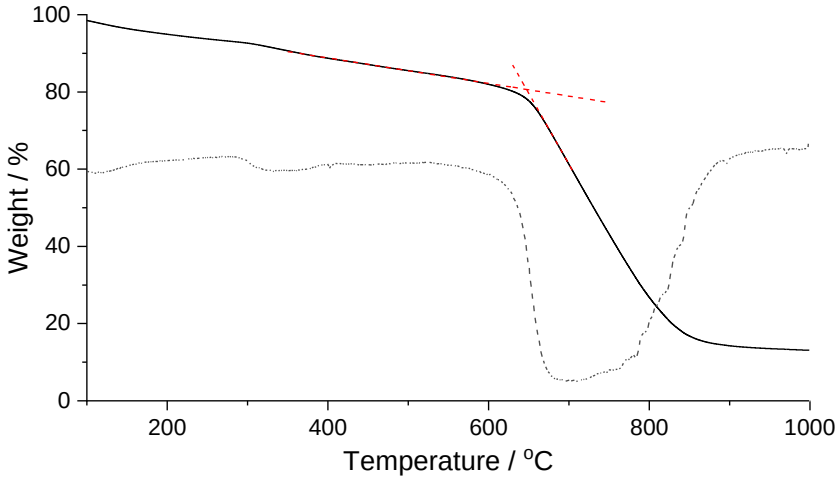

Figure 46: Example thermal analysis plot showing change in weight (black line) and derivative plot showing the rate of change of weight (dashed line). The extrapolated baseline and tangent are shown in red dashed lines, the onset is found at the intersection of the red dashed lines.

3.2.1 Analysing Carbon

The most intuitive comparison to make between different forms of carbon is their combustion temperatures; generally carbon materials with reactive sites combust at lower temperatures whilst more stable systems like graphite and carbon nanotubes combust at higher; approximate onset temperatures from common samples are shown in Table 3.

Table 3: Onset temperatures for the combustion of different carbon materials, measured at 1 °C/min under a flow of air.[341,342]

Compound	Onset of Thermal Decomposition / °C
Graphite	644
Soot	565
Diamond	629
C_{60}	444
Nanotubes	695

Unfortunately exact onset temperatures are known to vary with sample preparation and treatment. Testing a loose powder compared to a large chunk of material alters the surface area available to the atmosphere which can reduce the measured combustion temperature. The rate of heating is also known to have a huge influence; this is mostly due to a slight lag between the sample reaching temperature and sufficient sample undergoing combustion to actually record a mass change. A comparison using buckminsterfullerene has shown this effect for faster heating rates with a temperature of maximum mass loss of 444 °C recorded at 1 °C/min increasing to 545 °C at 10 °C/min and even reaching 600 °C at 20 °C/min.[341]

This variability in absolute combustion temperature makes using these values as unique identifiers difficult; although perfectly possible with good analytical technique, and comparisons between samples are readily achieved. Additionally, it is possible to identify different phases within a mixed material from multiple, distinct combustion temperatures observed.[308] Defective or highly strained phases may undergo combustion at a lower temperature with a distinct inflection point before the more thermally stable material burns. This approach has even been used to purify a mixed carbon matrix by undertaking a controlled burn at a temperature sufficient to burn all amorphous carbon whilst leaving the graphitic carbon behind.[263]

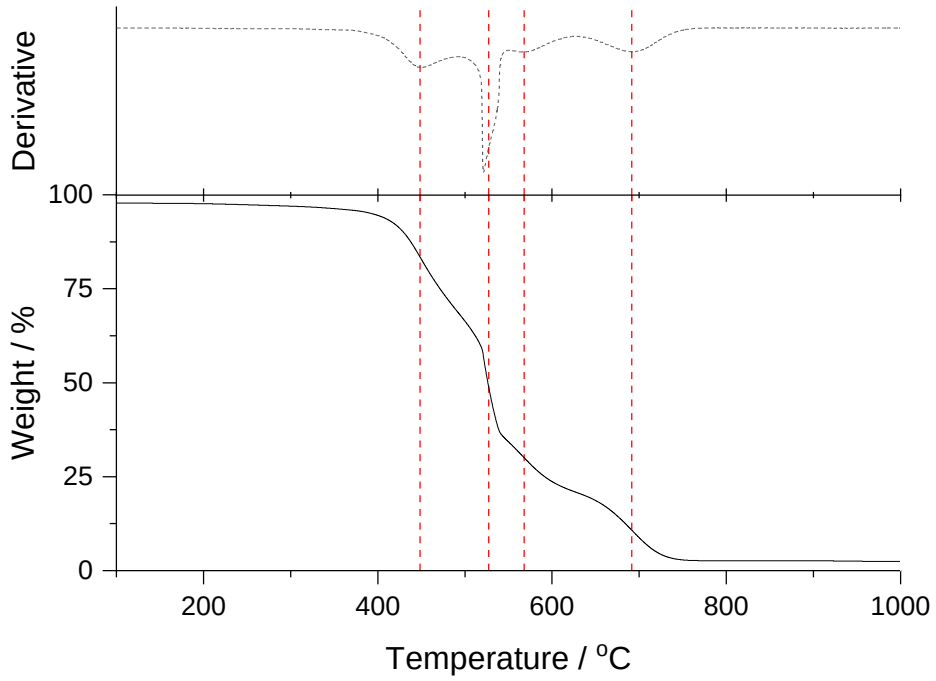

Figure 47: Thermal analysis plot with multiple weight loss events highlighted with red dashed lines. The derivative plot is used to identify these different events with peaks in the rate of weight loss corresponding to the maximum gradient of percentage weight.

3.2.2 Inert Atmospheres

Mass loss profiles recorded under inert atmosphere are also valuable to identify any functional groups or meta-stable phases within a material. Whilst carbon materials will not combust under inert gas flow oxidised carbon is commonly observed to loose mass as the less stable organic functional groups decompose into carbon dioxide, carbon monoxide and water. In this way inert gases and air used in tandem can identify the difference between material that has undergone chemical functionalisation and material that has suffered

structural defects; chemical groups will exhibit mass loss under any atmosphere whereas defective regions will combust at a lower temperature in air; but show no change under inert.

3.3 Electron Microscopy

Electron microscopy is very powerful for nanomaterial analysis due to the high magnification and range of signals that can be collected. Microscope systems are limited by diffraction and the smallest object that can be theoretically resolved depends on the wavelength according to Abbe's Law; optical microscope systems can achieve resolutions ~ 150 nm obeying this limit and whilst some techniques capable of circumventing the diffraction limit have been developed;[343] these systems cannot truly image nanomaterials with high resolution. A high energy electron beam in contrast has a much smaller de Broglie wavelength and correspondingly smaller diffraction limit; assuming a perfect system a 10 keV electron beam has a theoretical limiting resolution around 0.005 nm.

Using electrons requires physical lenses be replaced with magnetic, and most systems are operated at high vacuum to minimise electron scattering. Interactions between electrons and matter also provide a variety of additional experiments that can be completed in the microscope; inelastic scattering of electrons produces information on composition and electronic structure whilst characteristic x-rays allow elemental analysis on a microscopic scale. The next section will outline the basic principles of scanning and transmission electron microscopy (SEM and TEM), with particular reference to techniques done within this work. The two primarily differ in their image collection process; whilst a TEM images the electrons that pass through very thin samples a SEM collects electrons scattered back from a sample surface. This allows greater flexibility in samples but SEMs achieve lower resolutions.

3.3.1 Scanning Electron Microscopy

The electron beam is produced from an electron gun; commonly field emission guns, which use a large potential between the tip and extraction anode to remove electrons from the source and accelerate them down the microscope column. Once accelerated the electron beam is focussed into a tight circle on the sample surface using a series of magnetic lenses and apertures. A typical SEM layout is shown in Figure 48 although it should be noted the exact layout of these lenses varies from system to system.

The electron beam will generally pass through condenser lenses to collimate the electrons into a parallel stream and then an objective lens will provide the final focussing and demagnification of the beam into the desired spot size. Apertures are used to exclude

electrons that are significantly divergent from the main parallel beam, thus reducing noise. The image is generated using scanning coils which raster the focussed beam back and forth across the sample surface and the signal emitted from the surface is detected and used to generate the desired image. Unlike other microscopes the magnification is not actually produced by the lenses but rather the length scale the electron beam is moved on the surface. High resolution images, however, are only possible with very small spot sizes.

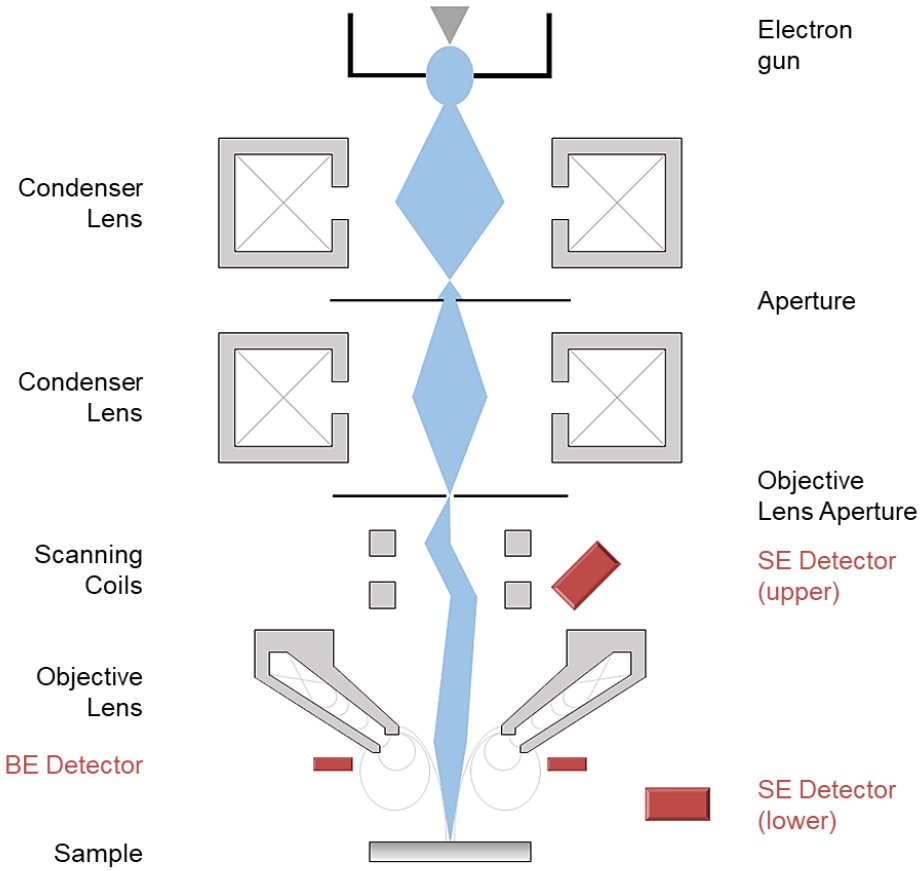

Figure 48: Basic schematic of key components and magnetics lenses of a SEM with a snorkel configuration of objective lens shown. The electron beam is shown in pale blue whilst common electron detectors are shown in approximate positions in red.

3.3.1.1 Detected Signals

As the electron beam impacts the surface the incident, or primary, electrons undergo elastic and inelastic collisions. The subsequent electrons produced by these processes are detected and used to produce electron micrographs. Most commonly used are secondary electrons (SE), low energy electrons released as the primary beam excites core and valence electrons from the sample. After overcoming the work function, these are low in energy and weakly penetrating so can only be detected from within a few nanometres of the surface.

Backscattered electrons (BSE) are higher energy electrons produced from the scattering of primary electrons back out of the sample. These electrons have a higher energy and can travel from further within the material proving information on composition and other features within the sample as well as limited topography. Compositional information is provided because elements with a higher atomic number backscatter more strongly.

In addition to the electrons emitted from the material when it is impacted by the electron beam, it is possible for the high energy electrons to produce characteristic x-ray radiation. Incident electrons can ionize a core shell electron causing a valence shell electron to fill the vacancy; this decrease in energy produces a photon characteristic of the electron energy difference. In addition to these signals: Auger electrons, cathodoluminescence and a background x-ray continuum can all be generated from samples under SEM conditions, but they are less commonly used and will not be discussed further.

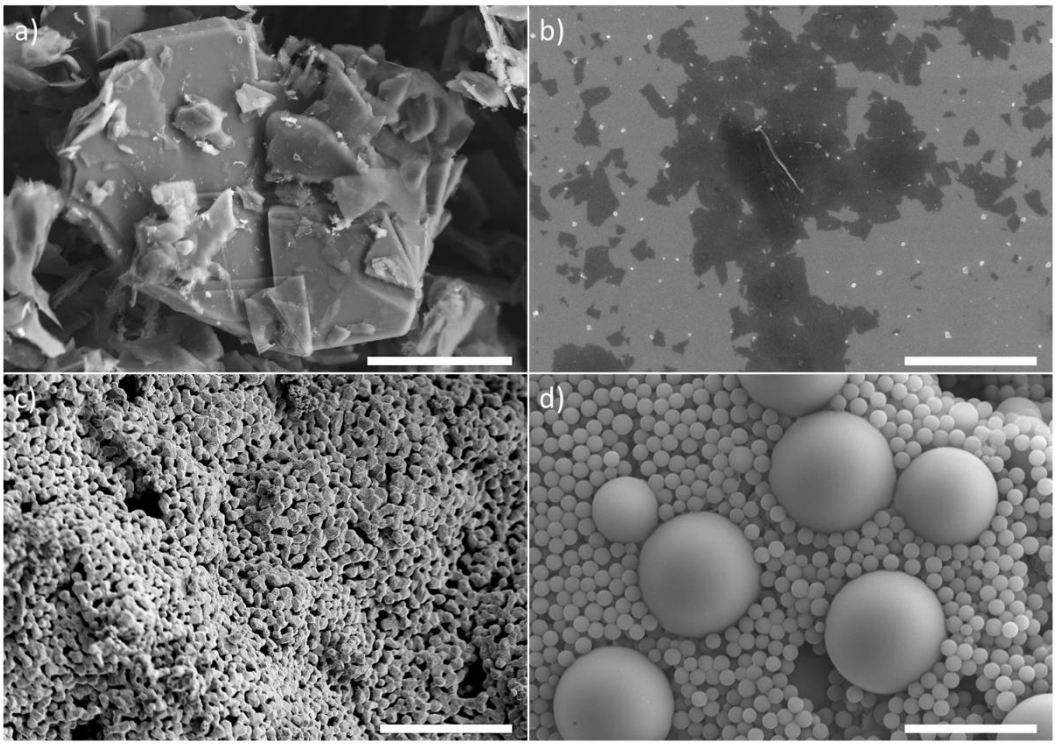

Figure 49: Example SE micrographs from a range of materials. a) Graphite flake with multiple crystalline domains and smaller flakes present on the surface; recorded at 5 kV, scale bar = 5 µm. b) Graphene oxide flakes deposited on a silicon wafer, the dark regions are graphene flakes distributed over the surface; recorded at 3 kV, scale bar = 4 µm. c) Cobalt metal foam, seen to have a microstructure made from small particles partially annealed together; recorded at 6 kV, scale bar = 40 µm. d) Polystyrene beads produced from mixed phase polymerisation; recorded at 8 kV with a 20 nm gold coating, scale bar = 4 µm.

Secondary electrons are popular because of the intuitive images of surface features, morphologies and particles. The wide depth of field and surface resolution make SE images

ideal to examine the morphology of porous materials as done extensively when looking at graphene based carbon foams. SE can also be used to visualise graphene flakes deposited on surfaces due to the contrast difference between the substrate and graphene, although TEM and AFM remain better choices to examine the distribution of flake size and thickness.

Typical SE micrographs from a range of materials are shown in Figure 49; a) shows a graphite flake with different crystalline domains and smaller flakes on the surface. b) graphene oxide flakes shown as dark patches dispersed on silicon; whilst the thickness of these flakes cannot be gauged from SEM the lateral flake sizes can be measured. Considering 3D porous structures, c) reveals that a cobalt metal foam produced from high temperature reduction is actually formed from many small metal particles, 2-3 µm in size, partially agglomerated together leaving a network of channels through the material. The final example, d) shows a series of polystyrene latex beads from oil in water polymerisation that clearly produced two very distinct particle sizes. Some larger beads, microns in size, were found randomly scattered whilst a very large number of polymer particles 100s nm across were formed.

The primary use of backscattered electron images in this work was to highlight metal particles distributed within foams. In Figure 50 copper particles known to be present in the sample are clearly visible as white dots throughout the material. The copper is highlighted relative to the bulk carbon because it is a larger atom with more electrons, so it more strongly backscatters electrons making a more intense signal. In comparison to the SE image of the same area on the left, the greater penetration of BSE is illustrated by the many indistinct surface features whilst subsurface features are now visible. Whilst useful for thick samples the elemental contrast is very low from monolayers.

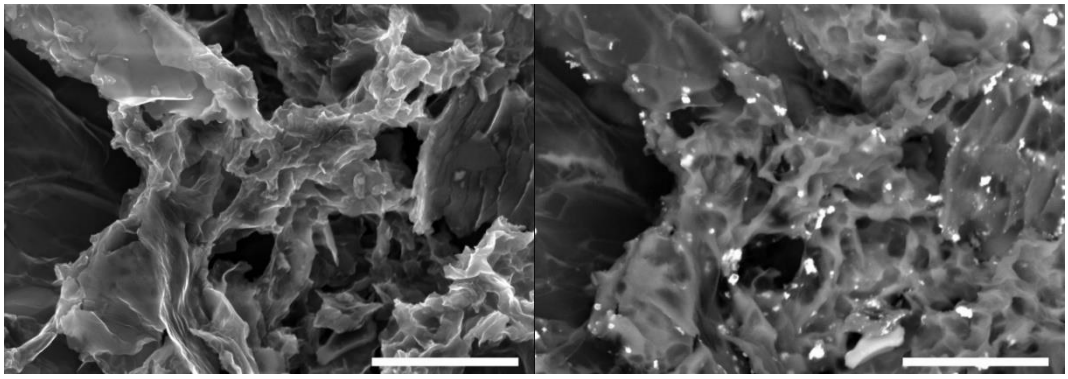

Figure 50: SE and BSE image of a carbon foam containing copper particles; both images were recorded from the same point for comparison, recorded at 10 kV scale bar = 10 µm.

Characteristic x-ray signals can be used to determine the identity and location of elements within a sample under analysis and even produce an elemental map of an area that can be

compared with electron images to gain deeper understanding. The electron beam, however, must have sufficient energy to ionize core shell electrons for these x-rays to be produced and such high energy electrons can penetrate the sample, causing damage and generating x-rays from sub-surface features.

3.3.1.2 Interaction Volume

As already seen, electron micrographs are versatile but the depth from which the signal is generated is an important consideration. The primary electrons incident on a surface will randomly scatter and spread in a teardrop shape from the impact point shown in Figure 51; material in this entire volume will be affected by high energy electrons and emit all types of radiation described above. However, whilst x-rays emitted from 100s nm inside the sample may still reach the detector, low energy SEs lack the penetration to exit the sample and cannot be detected from anything other than the top few nanometres of sample. This interaction volume is important for carbon materials and porous structures because many signals will pass through thin carbon layers, and x-ray and BSE analysis will often reveal features hidden below the surface. Nanoparticles may also be difficult to resolve if their size becomes comparable to the interaction volume and thin, especially monolayer, materials may have very poor contrast since the background signal being emitted from the substrate will often dwarf the difference in signal caused by the monolayer deposited on top.

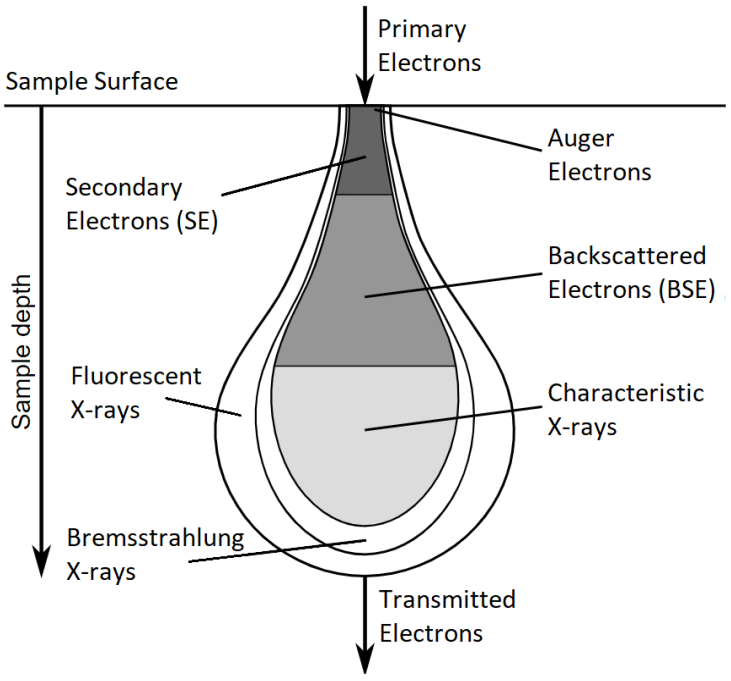

Figure 51: The teardrop shape of the electron interaction volume. The lighter colours show the maximum depth from which each signal type, labelled, can be detected.

3.3.1.3 Sample Preparation

Overall SEM is powerful for imaging porous materials that have micro and nanoscale structures because of the range of information that can be extracted from a very flexible range of sample types. There is no requirement for the samples to be thin or flat as common with other microscopy techniques and the depth of field possible allows exquisite images to be recorded of highly textured materials that even optical microscopy cannot achieve. Despite this the main limitation of the technique is the ability of the sample to withstand a high energy electron beam without suffering significant damage, or more commonly building a significant electrical charge on the surface that interacts with the incident beam. This process, commonly known as charging, is common on insulating samples like polymers and must be overcome before images can be collected. It is possible to establish experimental conditions in which the incident electrons are balanced by the charge leaving the sample and high quality images can be produced. It is more common, however, for insulating samples to be sputter coated with a thin layer of conductive material, often carbon or gold, which allows all electrical charge to dissipate rapidly and high quality images can be achieved.

3.3.2 Transmission Electron Microscopy

The significant difference between transmission and scanning electron microscopes is where a SEM measures the electrons reflected from the surface under electron irradiation, a TEM measures the electrons that pass through very thin samples. This means a much higher energy electron beam can be used since there is no build-up of charge on the material surface; using higher energy electrons allows a more focussed beam. TEM can achieve much higher magnifications than SEM but sample preparation can be more complex, since samples thinner than 100 nm are generally required.

The high resolution images made possible with TEM promoted a large interest in nanomaterials; carbon nanotubes were imaged with electron microscopy before evidence was collected from other analytical methods and allowed researchers to actually see the structure.[1,344,345] However, the electron energies required for high resolution images can damage the materials under analysis, particularly fragile carbon structures.[346] The introduction of spherical aberration correction in TEMs provided a method of achieving atomic resolution without the damaging high energy beams.[347,348]

The possibility of achieving atomic resolution with 80 keV electron beams allowed a huge amount of information to be gathered about the structure of graphene and related materials including the distribution of defects, the chirality of sheet edges and the roughness and

folding of sheets.[349–351] The structure of graphene as established from these studies has been discussed in the introduction and will not be repeated here. In this work, the utility of imaging atomic scale defects is low since we are more interested in bulk materials, however, TEM can still be very powerful for gaining understanding of the material produced.

3.3.2.1 High Resolution Images

In many cases the most important parameter is the graphene layer number and the most direct method for measuring the number of layers is to count them. With high resolution TEM it is possible to resolve the edge of graphene flakes, where they fold over or roll up into a scroll to reduce the number of dangling bonds and capping groups. As the layers fold over on themselves there is a significant number of carbon atoms presented parallel with the electron beam. This effect is illustrated in Figure 52d with a schematic of two layers folding producing a dark fringe seen in a TEM shown in 5b.[352] These edges can be counted, providing direct evidence of the layer number. There are reports that single and bi-layer graphene may be difficult to resolve but thicker layers are very clearly visible.[353]

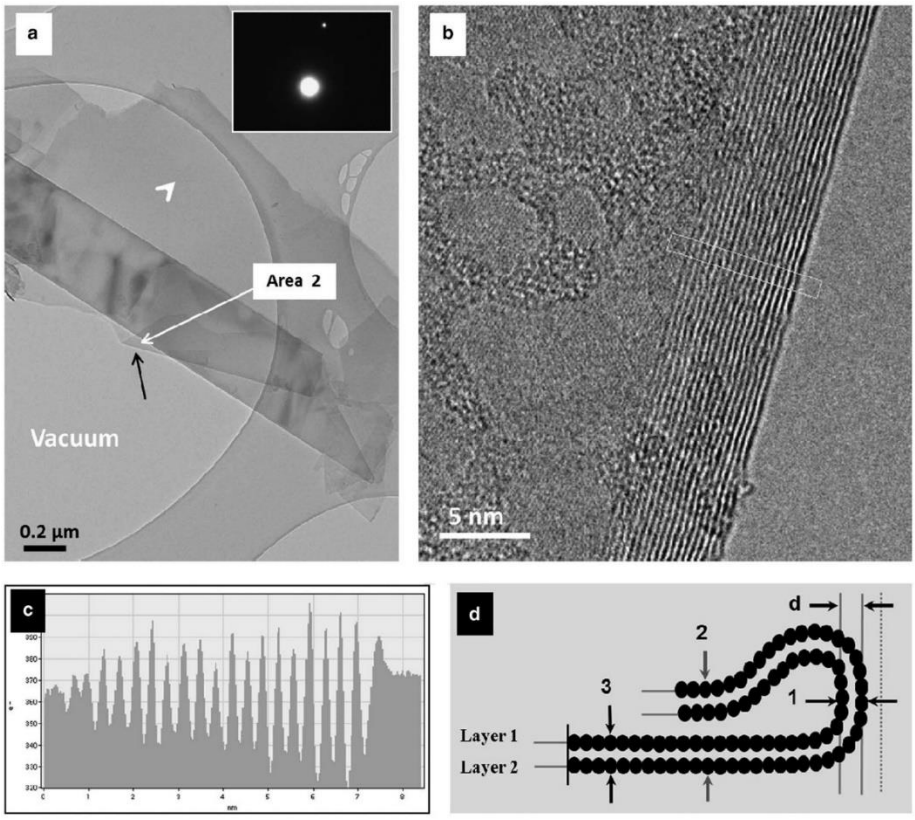

Figure 52: **a**) bright-field TEM image of one-folded ultrasound-assisted graphene flake. The inset is a SAED pattern at the orientation away from the zone axis taken from the unfolded part of the flake (indicated by white arrow head); **b**) high-resolution image of the folded edge of the flake taken from the indicated area in **a**) (black arrow). The flake is 17–18 layers thick here, as indicated by the intensity profile in **c**); (**d**) the drawing of the folded edge of the flake shows how **c**-planes become parallel to the incident beam of electrons and appear in the image.

Dark lines caused by carbon layers are commonly observed from nanotubes and fullerenes as well; the number of layers in multiwalled carbon nanotubes can often be counted and concentric circles may be observed if the nanotube is aligned with the electron beam. Such circles have also been observed from spherical carbon particles dubbed nano onions.[354]

3.3.2.2 Selected Area Electron Diffraction

In addition to directly imaging materials the focused electron beams allows other experiments to be completed on materials with a high degree of spatial resolution. One of the most powerful of these techniques is specified area electron diffraction (SAED); the parallel beam of high energy electrons passing through the material have a wavelength approximately two orders of magnitude smaller than atomic spacings. The electrons passing through should therefore be treated as waves that produce a diffraction pattern. This diffraction pattern is caused by the arrangement of the atoms so crystalline lattices produce clear spots, each corresponding to different Bragg reflections analogous to XRD.

Inside the TEM it is possible to select a specific area of material based on the electron images, allowing diffracted electrons only from the specified region to be detected and analysed. In this way, detailed information about the crystal structure of micro-scale regions of the sample can be collected and compared, either with other regions of the same sample or referenced to patterns predicted from crystal structures.[355] If multiple crystal domains are present with different relative orientations multiple sets of diffraction spots will be produced, slightly rotated in relation with each other. This can be useful to determine a small number of rotated crystal domains, although, a large number of such domains will produce many diffraction spots that become impossible to distinguish.

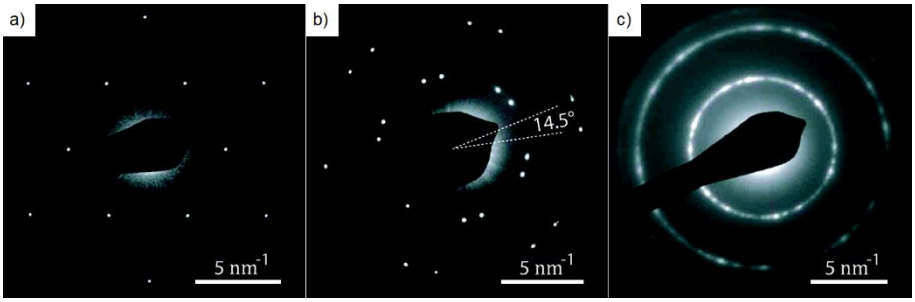

Figure 53: SAED patterns from a single layer of graphene oxide (a), two overlapping layers of GO (b) and a thick film of graphene oxide (c). The increasing thickness is accompanied with more spots at offset rotations that result in disks in the thick multilayer sample.

The hexagonal lattice of graphene makes this technique a powerful method of analysing carbon films, both to compare crystalline graphite with amorphous carbon and to analyse the stacking and orientation of graphene layers.[301,356,357] The significant difference between the diffraction peaks from graphite and graphene is the absence of the (002) interlayer reflection only possible from the stacked sheets in graphite. Single layer and bi-layer graphene have also been distinguished due to the presence of the second layer of carbon. Such analyses are reserved for crystalline materials with large grain sizes well distributed on TEM grids. In many cases a large number of different graphene grains will be present close together; this is commonly observed as a disk of overlapping spots in the diffraction pattern.

3.3.2.3 Elemental Analysis

Other experiments that can be run in a TEM allow for highly localised elemental analysis, identifying the composition of samples and the distribution of elements within them. Energy dispersive x-ray spectroscopy (EDX) and electron energy loss spectroscopy (EELS) are the most common elemental analysis tools. Much like in an SEM, the EDX measures the characteristic x-rays produced by elements under high electron energy irradiation; since TEM's operate at much higher potentials there is sufficient signal to excite core shell electrons from even heavy elements. These x-rays can be reabsorbed by other elements present within the sample with comparable energy levels, and is especially significant for light elements.[358] EELS is an alternative elemental analysis tool with a greater spatial resolution and signal to noise from light elements that measures the energy lost in the inelastic forward scattering of the electron beam, and thereby the atoms in the sample can be identified. The intensity of this signal is less dependent on the atomic number and absorption by other atoms within the sample.[355]

Atom number contrast can also be achieved with the brightness of the electron image. In the case of bright-field images the electrons that pass through empty or low density space are shown as bright or white areas whilst the denser samples block the electron beam and are shown as dark regions. In this way, the distribution of heavy electron blocking domains and lighter areas can be easily visualised; however, the elemental composition cannot be determined from the brightness. Dark-field images are the opposite of light field and show the scattered electrons, effectively highlighting dense areas capable of scatting more electrons whilst empty space appears dark since there are no electrons being scattered.

3.4 X-ray Diffraction

A mainstay of solid state analysis, x-ray diffraction (XRD) probes the atomic arrangement in crystalline materials including atomic spacing, unit cell size and symmetry, defects and dislocations. At its most fundamental x-ray diffraction is described by Bragg's Law which relates the angle of constructive interference to the spacing between parallel crystal planes reflecting x-rays illustrated in Figure 54. Such crystal planes are well described by Miller indices (hkl), and since the constructive interference measured by XRD requires the additional pathlength, shown in blue, to be an integer multiple of the x-ray wavelength the interlayer spacing can be calculated from basic trigonometry as $2d_{hkl} \sin\theta = \lambda$.[359]

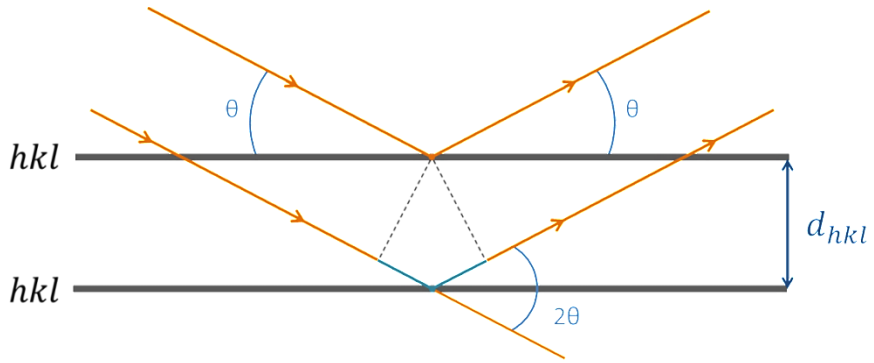

Figure 54: Schematic of parallel crystal planes and the reflection of x-rays shown in orange; Bragg's Law derived since the additional pathlength shown in blue must be equal to an integer multiple of the wavelength.

Whilst powerful for the analysis of x-ray diffraction patterns this approach simplifies the diffraction process by modelling planes of atoms. In reality x-rays interact with electron clouds within the material, exciting electrons that become new wave sources; these emitted x-rays undergo interference with each other and as such the diffraction pattern is formally a Fourier transform of the electron density distribution of the material in real space. However, such a complex discussion of all possible parameters that can affect the electron distribution is not required for this work. It should also be clarified that whilst single crystal x-ray diffraction is capable of elucidating the crystal structure of new materials, it is not possible to isolate large single crystals of graphitic carbon materials and powder XRD is utilised. Rather than collecting a 3D diffraction pattern of spots on a screen, powder XRD rotates an x-ray source and detector around the sample deposited as a flat surface measuring the x-ray intensity as the 2θ angle changes. It is not possible to resolve crystal structures ab initio from powder diffraction data but this is not a concern for graphitic carbon analysis.

In the x-ray source high energy electrons impact a target and produce a continuous spectrum of Bremsstrahlung (deceleration) radiation. Additionally core shell electrons are ejected

causing outer shell electrons to drop down in energy to fill the vacancy, releasing excess energy as x-ray photons with a wavelength characteristic of the element. A filter can then remove the continuous spectrum to produce the monochromatic x-rays required for XRD. A very common target is Cu producing Kα radiation with a weighted average wavelength of 1.5418 Å.[360] Unfortunately this is very close to the $K\beta_5$ transitions of Co, 1.6089 Å, resulting in strong fluorescence when Co samples are irradiated with Cu Kα x-rays. To prevent the fluorescent background a Mo source was used which has a shorter wavelength of 0.7108 Å.

In addition to the 2θ values used to calculate the unit cell parameters from Bragg's Law, the width of the measured peaks can be linked to the size of coherent scattering domains within powdered samples. This is known as the Scherrer equation, and arises because the number of unit cells present in sub-micron crystallites is finite.[361] A crude picture is a stack of crystal planes such as used for Bragg's Law, for angles very close to the Bragg scattering angle the surface layers are emitting x-rays very similar in phase and the destructive interference responsible for the low signal originates from deep within the sample. In small sub-micron crystallites these layers may not be present, resulting in a measurable intensity at angles close to the Bragg scattering angle; the smaller the crystallite the wider the peak observed.

3.4.1 Graphite XRD

Graphite has a relatively strong x-ray diffraction intensity for a light carbon material from the (002) interlayer reflection condition due to the ordered electron cloud in the plane of the graphene sheets, with an interlayer spacing in crystalline graphite of 3.356 ± 0.002 Å.[362] The (002) peak therefore dominates discussion of graphite XRD patterns and is commonly used to calculate the interlayer spacing, crystallite size and presence of intercalated species.

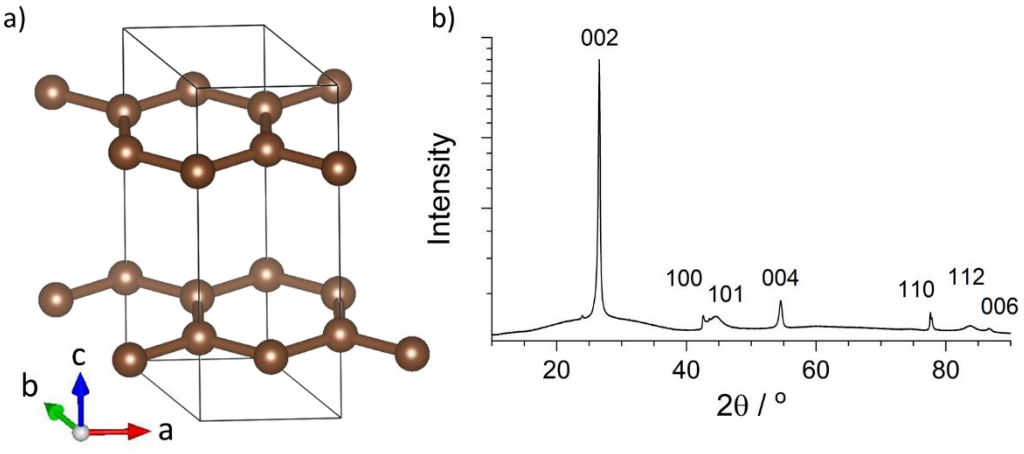

Figure 55: a) Graphite unit cell. b) Example XRD pattern of flake graphite, note the intensity is plotted on a square root scale to better show the low intensity peaks.

Despite the large (002) intensity the other peaks, shown in Figure 55, can be insightful for graphite XRD analysis when present, for example the (100) and (101) peak width is indicative of the lateral flake size. Unfortunately the strong (002) intensity and preferred orientation of graphite flakes generally make resolving other Bragg reflections challenging. Commonly this results in the (002) peak position being used to calculate interlayer spacing without any possible correction for zero-shift error; such values are then utilised to infer changes to the graphite structure despite the potential error.[363]

3.4.2 Graphitic Carbon Materials

When analysing graphitic carbon materials the XRD pattern is complicated by the different scattering domains that are not well described by the ideal unit cell of graphite. Using the hard carbon model introduced in Chapter 1 we can consider small regions of low strain graphite regions, or coherent scattering domains, within a larger structure of amorphous carbon. The carbon in between graphite domains is thought to be sp^3 carbon or very buckled and strained graphene layers, the diffraction profile is then modelled by the graphite peak with a width related to the size of the coherent scattering domains, note this is very different to the particle size.[363] This model, illustrated in Figure 56 also accounts for stacking faults within the graphite domains; with a probability of every layer being stacked as Bernal ABAB graphite or dislocated into ABCA rhombohedral graphite or a random turbostratic graphite material. Fitting models have been proposed for detailed analysis of graphite, however, such an involved approach is not required for the comparison between materials.

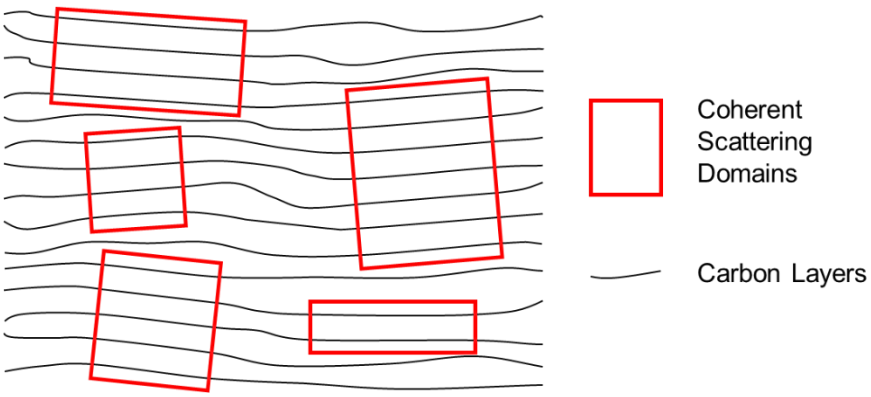

Figure 56: Schematic of coherent scattering domains in amorphous carbon material.

Generally wider XRD peaks are linked to more disordered graphitic materials with smaller and less regular graphite domains within the material; unfortunately, the precise calculation of particle sizes is difficult because of the presence of adjacent carbon within the material.[364] Unlike the conventional application of XRD peak widths, most graphitic domains do not have a clear boundary but rather a region of increasing spacing and rotationally mismatched

graphitic layers. Despite this apparent complexity an analysis of different synthetic nuclear graphite materials, linking various XRD parameters with structural properties, found the averaged interlayer spacing, $\langle d_{002} \rangle$, is the most efficient indicator of graphitization and order within the structure.[365] Such values are ideally calculated from multiple peaks to ensure suitable zero-shift correction but this is often error prone because of the low signal intensities.

3.5 Gas Sorption and Surface Area

Physisorption of particles is used to measure the surface area and probe the pore structure of many materials. If the size of the adsorbed particle is known and the number of particles, commonly gas molecules, attached to the surface are known the surface area can be calculated. The most widespread method is the Brunauer–Emmett–Teller (BET) theory, named after its authors.[366] Whilst very commonly applied, this method does make some fundamental assumptions that are unsuitable for micro and meso porous carbons. Most notably BET theory assumes identical binding sites and cannot account for different functional groups on the carbon surface, assumes no interactions between adsorbed molecules within the layers and that the heat of adsorption onto a layer of adsorbed molecules is the same as condensation.[367,368]

In a microporous material the surface potentials responsible for attracting gas molecules can overlap creating very strong binding sites within the material, theoretically filling these sites can produce unrealistic surface areas. Mesopores also suffer with overlapping potentials and often result in condensation of large liquid phases within internal volumes significantly below the condensation point, this is easily observed as hysteresis in gas sorption isotherms.

Despite these limitations isothermal nitrogen sorption is commonly used to measure the surface area of carbon materials.[240–243,252,263,265,268] The many failings of the method when applied to carbon materials containing a mixture of domains and pore sizes make absolute surface area measurements unreliable; so statements of surface area will herein be confined to like for like comparisons between very similar materials.

4. Raman Statistical Analysis

4.1 Introduction

Since the landmark isolation of single layer graphene there have been many investigations into its record properties, summarised in the introduction, which are all highly desirable in many real world devices and applications.[53] Despite this interest, commercial products utilising graphene are still rare and recent publications have pointed to the lack of robust metrology and standards by which graphene and related carbon materials can be measured and compared.[19,51,286,287,294–297,309] The lack of a widely adopted, high-throughput, low cost, simple and rigorous analytical method may in-fact indicate that such a singular approach does not exist; instead a compromise between rapid screening and detailed analysis may be required to ensure quality control measures can meet minimum standards. What such minimum standards are will remain a question for key stakeholders.

Here is presented a statistical method for identifying when detailed micro scale measurements can be considered representative of a macroscale material; thereby answering 'How close can we get to high-throughput?'. Specifically we focus on Raman spectroscopy; among many techniques for graphene analysis Raman remains the most versatile due to the depth of information that can be readily extracted with very little sample preparation required; including exfoliation efficiency, particle size, layer number and chemical functionalization.

Whilst Raman analysis is comprehensive, the laser spot sizes are commonly of the order of a micron and therefore, in common with other micro-scale techniques a single spectrum cannot be generalised to an entire material. Whilst it is common for a representative Raman spectrum of a carbon sample to be reported,[156,369–371] this is undesirable due to the variations likely to be present. To highlight this point Figure 57a shows three different Raman spectra from the same material. Based on the evidence of only one spectrum this could be highly oxidised graphite, shown at the top in blue, or few layer graphene in the middle in red, whereas in reality the sample is mostly graphitized carbon shown at the bottom in green. A better picture of this material is possible from the 3D bivariate histogram shown in Figure 57b; such plots calculate the population of bins defined by two parameters simultaneously, the size of the bin is given by the x and y axis in the same way a standard histogram's bins are defined by the x-axis for the single parameter being plotted. The population is shown as a heat map from blue with lowest population extending to yellow for the most populated bin. The highly populated bin is an indication of the key peak parameters present across

many spectra recorded and therefore is more representative of the bulk material. The spread and width also visualises information about the homogeneity of the material under study.

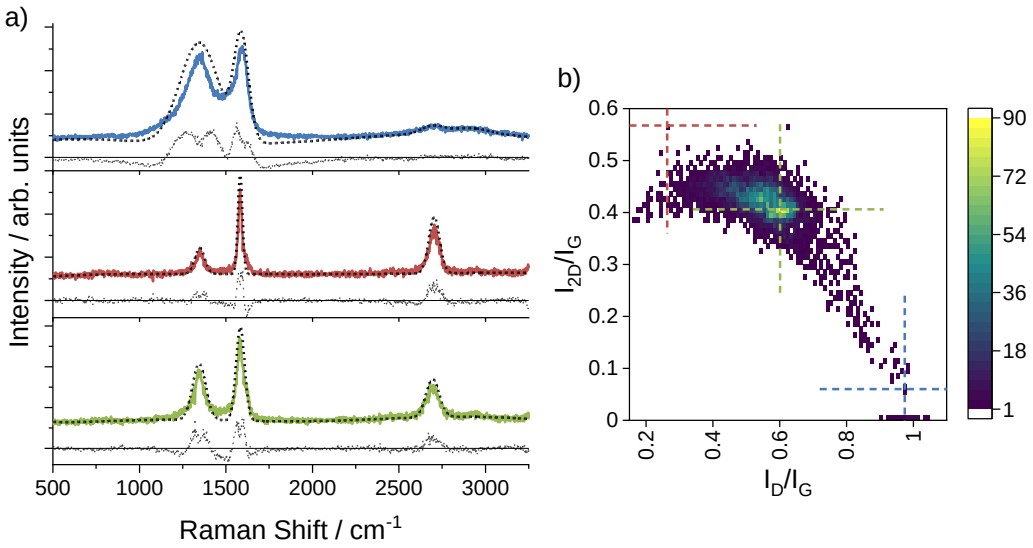

Figure 57: a) A selection of spectra from high temperature carbonized material, illustrating how poorly one spectrum represents the overall distribution. The fitted models are shown as dotted lines with the residual value in grey. b) Distribution shown as a bivariate histogram; the population of bins denoted as a colour map and bins defined by both the I_D/I_G ratio (x-axis) and I_{2D}/I_G ratio (y-axis). Coloured crosshairs link example bins to a typical spectrum with those features.

The histogram is only possible by recording multiple spectra; this is effective and the method we propose for robust quality control measures.[289–291] But such an approach is time consuming. It is therefore beneficial to consider how many data points are actually required. This question has never been considered before for graphene analysis, and the application of statistical methods to understand and justify the scale of analysis undertaken is a new addition for graphene metrology. This work introduces a statistical method for justifying the size of data sets required for reliable and reproducible nanomaterial analysis using microscale probes. Focussing on graphene metrology using Raman spectroscopy, the size of data sets required for different industrially relevant graphene related materials are discussed. In addition to the statistical method, this also required the development of a spectral fitting procedure and consideration of the role of signal to noise on data set sizes.

It is unlikely that any one technique can meet all the disparate demands from a field as broad as graphene. Raman spectroscopy can be a non-destructive, relatively straightforward technique that requires little specialist experience and instrument time. It must be noted some practical experience is still desired and samples can be damaged by high laser powers; most carbon nanomaterials strongly absorb visible light and the focused spots used for micro-Raman spectroscopy can rapidly increase the local temperature. Nevertheless, Raman is relatively simple whilst providing a high level of information; in contrast to microscopy

techniques like AFM and TEM that provide a wealth of information but are costly, time consuming and require experienced operators.[304] The time needed to capture the required number of Raman data points can be significant it must be acknowledged, but there is a balance to be struck between analysis that is impractical and analysis that is ineffective.

4.2 Methodology of Statistical Analysis

A selection of graphene related materials have been prepared and analysed using 1024 Raman spectra collected from powder samples following the workflow in Figure 58. The samples were chosen to cover a range of interesting and topical materials, specifically: graphite, liquid exfoliated graphene, reduced graphene oxide and high temperature graphitized carbon; additionally two commercial GNP samples and a commercial MWCNT sample were analysed. The powders were pressed directly into crude pellets, thereby ensuring no size selection in the sample preparation as could be expected if making liquid dispersions. Pressing samples by applying uniaxial pressure in this way could result in the preferred orientation of the graphene sheets, and should probably be avoided if analysing a crystalline graphitic material that is known to form ordered surfaces. In this case, point spectra recorded from unpressed powders were consistent with the distributions measured from the pressed samples, so this is not thought to be significant.

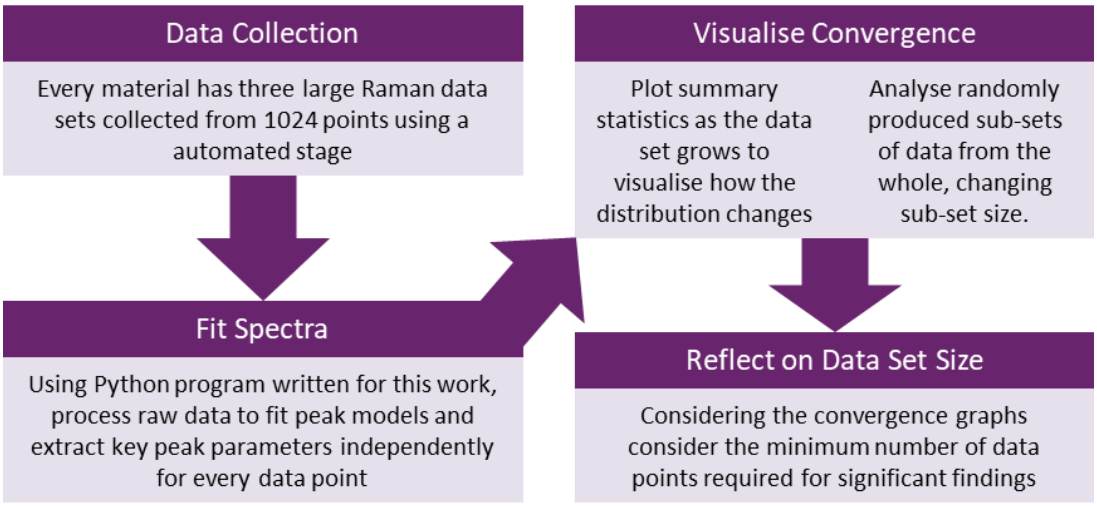

Figure 58: Flowchart of the statistical analysis procedure used for the analysis of nanomaterials.

Independent Raman spectra were then collected from points 2.5 µm apart over an area covering 80 x 80 μm^2 at a low laser power; these maps generally took around 16 hours to acquire the 1024 points. This was repeated at least three times for every sample. 16 hours was considered the limit since the aim was to identify the smallest map size, and thereby the shortest time, for analysis and 16 hours or more per sample is not feasible for most users.

These spectra were fitted using a computer code discussed later in this chapter; this returned key peak parameters known to link to physical properties as explained in Section 3.1. For this statistical work the key parameters of interest will be the I_D/I_G peak height ratios that link to the flake size and presence of defects and the I_{2D}/I_G ratio which links to the exfoliation and graphene thickness.

The parameters returned from each map are then analysed according to the workflow in Figure 58, initially for data convergence as the map was collected. Data convergence refers to the trend of a data set towards a consistent distribution as more data points are included; in the case of independent random variables this is the central limit theorem. Initially with few data points it would be expected that every new, additional data point may have a significant effect on the distribution produced. As the data set gets larger each new point becomes less significant; if the complete distribution is being accurately sampled, a sample size is reached beyond which the distribution remains unchanged by any new data points. The method introduced here looks at the entire distribution, making no assumptions about statistical models, visualising how key summary statistics vary as more points are added to the map. The summary statistics chosen were mean, interquartile range and 10th and 90th percentiles, plotted as a function of sample size. This visualises the change in the distribution of data as more Raman spectra are collected and the approximate value at which the distribution stops changing, at this point the data set could be considered to have converged.

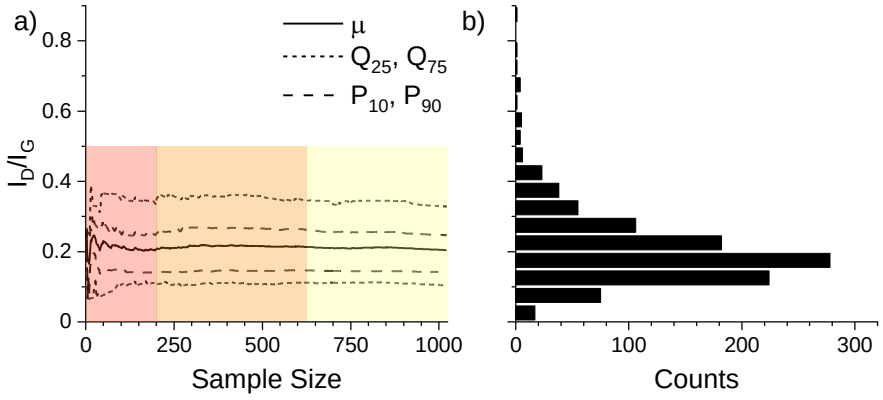

Figure 59: A convergence plot (a) showing the floating I_D/I_G mean, quartiles and percentiles as the sample size changes; the coloured regions denote approximate regions of increasing convergence from left to right. The histogram (b) shares the y-axis and displays the full I_D/I_G distribution with all 1000 points. The convergence plot illustrates the variability of summary statistics as the size of the data changes and the final distribution is typical of such materials that do not follow a normal distribution.

Figure 59 demonstrates the change in summary statistics as new points are added, which is initially very dramatic before becoming smoother. In the example shown the left (red) region

highlights highly variable data where any analysis undertaken with so few data points will be unreliable and dependent on the exact points measured. The middle (orange) region shows where the data is starting to converge although noise is observed and the right area (yellow) shows where the data has converged within error and new data points make relatively little difference. After this convergence there is little to be gained by collecting further spectra other than to increase the resolution of the distribution, but collecting fewer data points could result in erroneous distributions. The tolerance to errors in the Raman analysis will depend on its purpose; if one simply wished to look for significant changes to a material following some treatment or process far fewer points could be collected, whereas identifying minor phases and impurities in bulk powder requires a more comprehensive data set.

The majority of studies that use microscopic techniques; whether that is Raman microanalysis, electron microscopy or scanning probe microscopy generally report a mean and standard deviation assuming the graphene material follows a Gaussian model.[153,162,372] Unfortunately this model is rarely applicable to graphene materials, seen in the distribution of Figure 59 and shown from careful analysis of flake sizes by Kouroupis-Agalou et al.[288,373] This requirement for flexibility to deal with different data sets that do not always follow well behaved statistics is the main motivating factor for using graphical convergence testing and summary statistics in the way done here rather than using more traditional statistical testing.

Aside from a normal distribution, a log-normal is often suitable for samples prepared from exfoliation methods; during these processes the graphite sheets undergo random fission events to produce smaller or thinner sheets. This is a multiplicative process. Assuming the probability of a splitting event remains constant the probability of multiple fission events reduces rapidly, for a ½ chance of a flake ripping there is only a ⅛ chance of it splitting three times. Another common distribution is a bimodal system: large flakes sediment during processing and remain unchanged whilst a population of very small or chemically altered graphene flakes may be extensively changed.

In addition many important properties can be heavily influenced by minority fractions within a material.[374,375] The same exciting properties like nanoparticle size, shape and complex chemical environment that promise the most remarkable applications require similarly complex characterization, thereby prohibiting the use of single averaged values. Rather than finding another distribution model, it is easier and more reliable to report the entire distribution of values measured or at least compare a range of summary statistics like mean (μ), upper and lower quartiles (Q_{75}, Q_{25}) and 10% and 90% percentiles (P_{10}, P_{90}).

In addition to the convergence plots described above a method known as bootstrapping was used to better understand the effect of under-analysing a material. This method analyses small sub-samples of the original distribution and by randomly generating different sub-samples for analysis; can be used to analyse the scatter in these smaller sub-samples about the 'true' value of the larger population distribution.[376] This is done using a Monte Carlo type method to randomly select values from the large data set and place them into a smaller sub-sample; this can be analysed to find the mean or even full distribution of that sub-sample before repeating the process to generate and analyse another random sub-sample. As the sub-sample increases in size, closer to the size of the full sample data set, the mean and distribution is expected to more closely resemble the sample distribution as illustrated in Figure 60. Conversely, the variation and noise in smaller sub-samples is indicative of the analysis that would result from only collecting smaller Raman data sets.

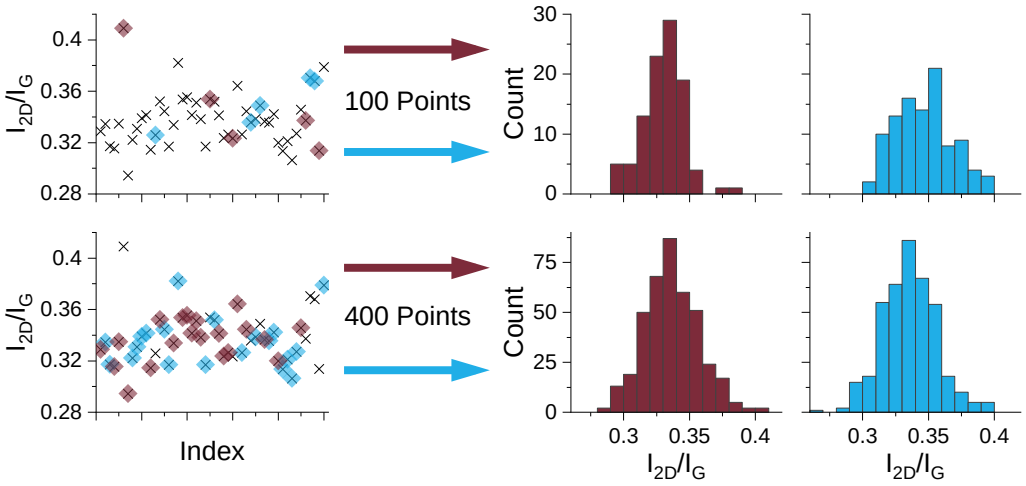

Figure 60: Illustration of the Monte Carlo based Bootstrap analysis. The scatter plots show a number of I_{2D}/I_G data points with two sets of random values highlighted in red and blue. The distributions of these sub-samples are shown in the histograms to the right; note the difference between histograms when the smaller sub-sample is used. This data was taken from 1024 points recorded from GNPs, the scatter plots only show a small fraction of these data points for clarity in the schematic.

Here a quick clarifying note on terminology is useful. The 'true' or 'population' distribution is the theoretical complete distribution from measuring an infinite number of Raman spectra from a material; the 'sample' distribution is the data set collected from 1024 points from a material. The 'sub-sample' is a smaller set of q data points taken randomly from the measured 'sample' data set and used for bootstrap analysis. The difference between the 'true population' distribution and measured 'sample' distribution is assumed to be minimal; this was checked by recording three different 'sample' distributions from different points on the same material and these were found to be similar to each other such that any differences between the 'sample' distribution and 'population' distribution is considered ignorable.

In this work a pseudo random number generator (using system parameters as a seed to ensure no repeat sequences) was used to select data points at random from the large number of Raman spectra collected by means of Raman mapping. The peak intensity ratios I_D/I_G and I_{2D}/I_G were extracted from each random point and from these the sub-samples were produced; these ratios were used as the simplest set of metrics that represented the entire spectrum. 400 sub-samples of each size q were produced for analysis.

To visualise this data meaningfully two plots were produced for each full data set, examples given in Figure 61. One plot is a panel of line histograms comparing the distribution of sub-samples; each histogram for a specific size of sub-samples with multiple random sub-samples of the same size plotted with differently coloured lines. These plots provide an easy way of visualising how the distribution of I_D/I_G or I_{2D}/I_G peak parameters change with increasing sample size. With very small sample sizes there is a significant variation between analyses as shown with the mis-match of lines. In the example shown with only 10 data points in the sub-sample, one random sub-sample plotted in green contains a lot of high I_{2D}/I_G values, hence the green line histogram showing peaks to the right of many other sub-sample histograms where other sub-samples of 10 points show no data points. With sub-samples of 250 points, however, the different lines align almost perfectly and the different distributions are almost indistinguishable. This shows that 250 points is sufficient for any random combination to produce a very similar distribution.

Above we consider each sub-sample as a complete distribution, sub-samples can also be described by the mean value of data points within. The mean values from 400 of these sub-samples of the same size are then considered as a distribution of mean values. This meta-distribution of mean values can be described as summary statistics and plotted as a convergence plot (Figure 61b), showing how the mean values extracted from a series of randomly produced sub-samples tend uniformly towards the mean of the full distribution. Whilst not immediately intuitive, this plot indicates the difference likely to be observed from different random data sets of the sample material for a given size; in the example shown below 100 data points it is possible for the mean values of two analyses to differ by 0.01. Whilst small in magnitude, this is only the difference in mean. If considering the entire distributions used for phase purity analysis such a small shift could be very significant.

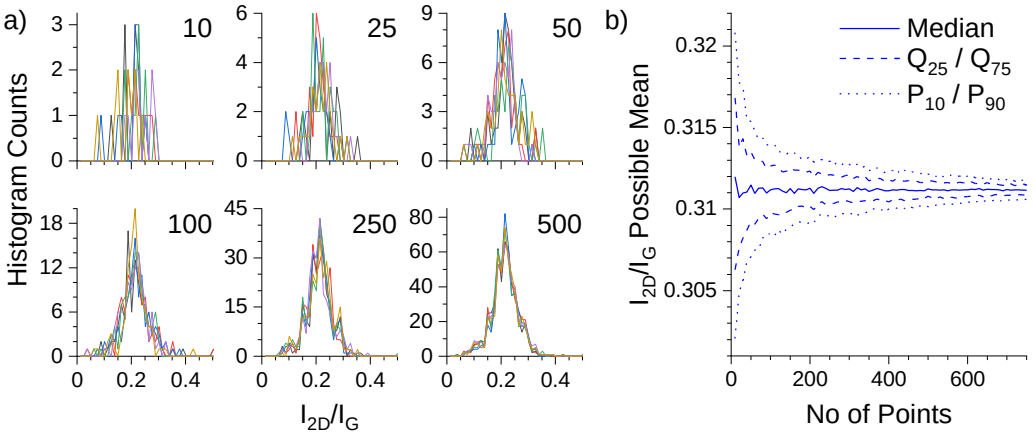

Figure 61: Example plots from bootstrap analysis, a) shows a panel plot of line histograms of sub-samples containing different numbers of data points (labelled) randomly selected. Different coloured lines are different sub-samples. b) shows the convergence of the mean values calculated from 400 sub-samples of every size; since there are 400 means for each size these produce a distribution. This meta-distribution of mean values provides the summary statistics shown here.

Such processing is complex but the core aim is simple. By analysing sub-samples generated at random it is possible to approximate what would happen were one to only measure q points taken at random from a wide area. It is hoped these plots make clear the effect of under analysing a material and the diminishing return from measuring more points than necessary. Randomly sampling in this way does assume a random distribution of points over a material surface whereas in reality there are localized regions with common spectra. If a smaller sample was taken over a small area a faster convergence could be observed. However, as we shall see from the example materials discussed in detail it is often desirable to collect multiple spectra, from many different points over the sample surface, chosen at random to ensure all components are included in the analysis.

4.3 Raman Spectra Fitting Procedure

The statistical analysis outlined above requires the Raman spectra to be fitted, producing single value peak parameters like height and position from each point that has been analysed. This is undertaken with a bespoke computer program specifically written for the fitting of Raman spectra from carbon materials. This program is freely available on GitHub (https://github.com/SGoldie4/RamanMapAnalysis). Spectra are all independently fitted with a 6th order polynomial background model (Eqn.1) and Lorentzian peak shapes (Eqn.2). The order of the polynomial background is mostly arbitrary. Simple trial and error with higher orders of background produced errors overfitting simple spectra, whilst lower order background functions could fail to account for unexpected steps sometimes recorded due to fluorescence or other high intensity background reflection. This optimisation was untaken

assuming a large background range from 500 cm^{-1} to above 3000 cm^{-1}; this ensures sufficient background above and below the peaks expected from carbon. Were a smaller background range used, it could result in an overfit of the background since fewer data points are used to constrain the same number of free variables.

$$y = c_0 + c_1 x + c_2 x^2 + \cdots + c_6 x^6 + \sum_n^{G,D,2D,D+G,D'} f(x|A_n, \sigma_n, \mu_n) \qquad \text{(Eqn.1)}$$

$$f(x|A_n, \sigma_n, \mu_n) = \frac{A}{\pi} \cdot \frac{\sigma}{(x-\mu)^2 + \sigma^2} \qquad \text{(Eqn.2)}$$

Where $c_n$are coefficients to the polynomial terms, A is the peak amplitude (note this is distinct from peak height), μ is the peak position in cm^{-1} and σ is the half width at half max.

The use of an exclusively Lorentzian peak shape is based on the guidance published by Pollard et al. on Raman spectroscopy for graphene analysis.[295] They argue that the different underlying processes that contribute to the Raman spectrum of graphitic carbon materials make the actual peak shapes obtained irregular; but found that Lorentzian peaks are most reliable of the common peaks used for spectral analysis. Some trials conducted in this work supports this recommendation; even when mixing Gaussian and Lorentzian functions in a true Voigt fit the residual was smallest for a pure Lorentzian model, shown in Figure S 219.

The fitting was done taking each spectrum independently and using a freely available non-linear least squares minimisation program, *lmfit*, to optimise the parameters of the model stated above;[377] this returns the fitted peak parameters and estimates the uncertainty of every parameter for further analysis. The exact model applied to each spectrum is flexible depending on the result of the fitting as discussed later. The Raman peaks possible are: G, D, 2D, D+G and D' which covers all major peaks, shown in Figure 62, observed from graphitic carbon. Radial breathing modes from nanotubes are not currently included in the model due to the complexity in deconvoluting different radial breathing modes from a mixed powder containing different sizes and chiralities of nanotubes.

In addition to fitting peak shapes to the data set the program also determines the signal to noise and produces a goodness of fit metric to allow easy quality checking of large Raman maps and to highlight any outliers or anomalous points. These require an estimate of the noise or variance of the spectrum, in this case this is achieved by using regions of known background with no peaks present; specifically the intensity data before 1200 cm^{-1}, between 1700 cm^{-1} – 2550 cm^{-1} and after 3050 cm^{-1}. This assumes the intensity of the 2D' peak is negligible which is generally true for most common materials. This region is used to

approximate a single error value used for signal analysis of the spectrum; this is derived by repeatedly taking the standard deviation of eleven sequential data points and then averaging all these deviation values to provide the mean standard deviation $SD(y)$. Whilst crude, the assumption is that eleven sequential points in regions containing no peaks are close together and therefore could be expected to have the same value; thus any deviation is considered noise. By averaging these standard deviation values from across the system any minor bumps or outliers are negated to estimate the average scatter of points around the 'true' value expected. This approach is preferred over the use of fitted background functions because of the involvement of signal to noise parameters in such a fitting procedure.

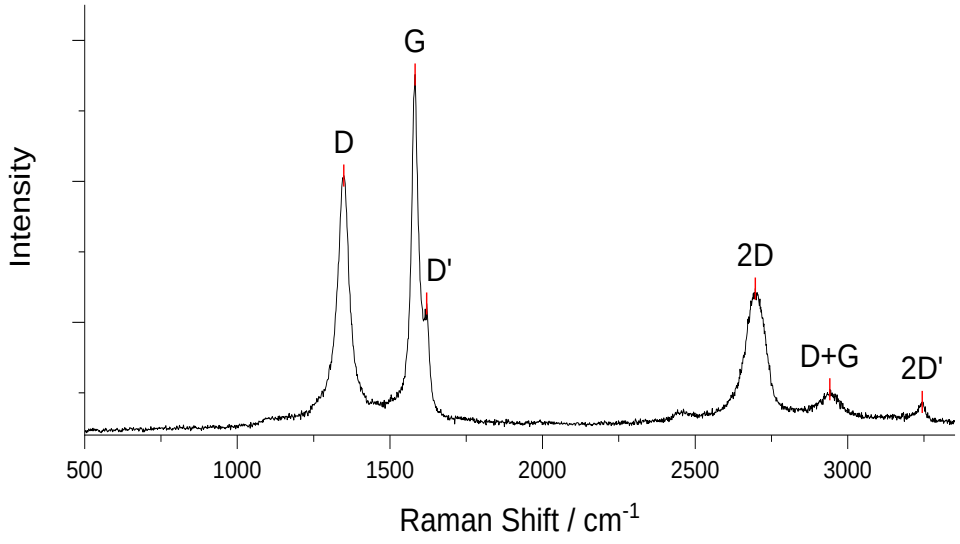

Figure 62: An example Raman spectrum of exfoliated graphene with all key peaks labelled. Not all peaks will be present in every material.

The signal to noise parameter reported is calculated from the fitted signal intensity of the G peak using a relationship reported elsewhere;[378] the peak height has the average signal intensity from the same background region subtracted as denoted by μ_y.

$$\frac{S}{N} = \frac{I_G - \mu_y}{SD(y)} \qquad \text{(Eqn.3)}$$

The least squares fitting process minimises the difference between model and experimental data, calculated as the reduced chi squared value given in (Eqn.4), where M is the number of data points; y_{calc} is the calculated value, y_{meas} is the measured value, $SD(y)$ is the standard deviation of the y counts, M_{free} is the number of free variables in the fitting.

$$\chi_v{}^2 = \frac{\sum_x^N (y_{calc} - y_{meas})^2}{SD(y) \cdot (M - M_{free})} \qquad \text{(Eqn.4)}$$

To ensure robust signal fitting the program runs through a complex algorithm that sequentially adds peaks to the model and then quantifies the improvement that extra peak has produced; the $r\chi^2$ values with and without the new peak are compared and any peak failing to improve the quality of fit by greater than 2.5% is rejected following the principle of Occam's razor. The requirement of 2.5% was decided following a series of trials on noisy data sets; below this value poorly defined peaks are included in the model which results in instability and errors. A limit greater than 2.5% risks excluding valid peaks from the analysis.

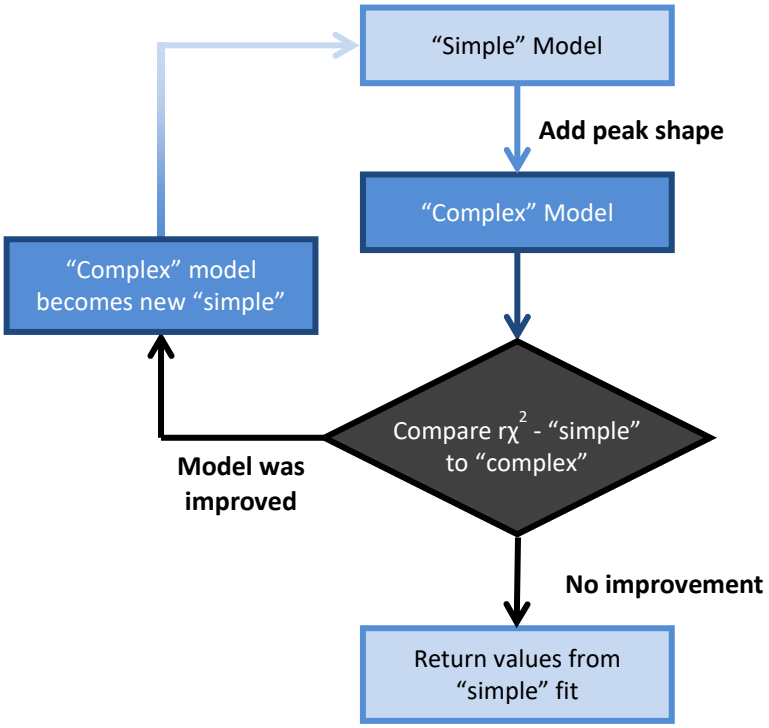

Figure 63: Diagram indicating the sequence used during fitting to ensure the model remains valid as more peaks are added. The D' and D+G peaks are only added following using input, although these are still validated using the workflow.

A simplified flow diagram is shown in Figure 63, in essence a logical progression can be identified and followed based on the physical origin of peaks that become interdependent on each other. It is for this reason that the first test is to apply a G peak to a polynomial background, if there is no discernible G peak present then graphitic carbon cannot be detected and attempting to fit other graphitic carbon peaks would be a waste of computer resource. By treating every spectrum completely independently there is no risk to an entire data set from single points of high noise or poor focus since these spectra will be discounted from the final output. This minimises the pre-treatment required and adds a more statistically robust approach to filter data points that, due to experimental conditions, contain insufficient carbon Raman signal for meaningful analysis. These are sometimes encountered when automatically collecting data over a wide area of inhomogeneous sample.

It must be noted this approach can also produce a phenomenon of splitting low intensity peaks into a false bimodal distribution with peak intensity ratios (I_D/I_G or I_{2D}/I_G) pigeon holed into exactly zero and real values as illustrated in Figure 64. This is commonly observed from graphite due to the low intensity of the D band due to the low number of edges and defect sites to break the symmetry required to activate the D peak. This low intensity D band can become lost in the noise and therefore the algorithm comparing the goodness of fit cannot find a significant difference between including or excluding the D peak. Under that circumstance the D peak is automatically excluded from the model, returning an apparent height of zero. In many cases this is an accurate result from pristine graphite as there is no D peak but low D peaks can also become lost in the noise, appearing to distort the distribution.

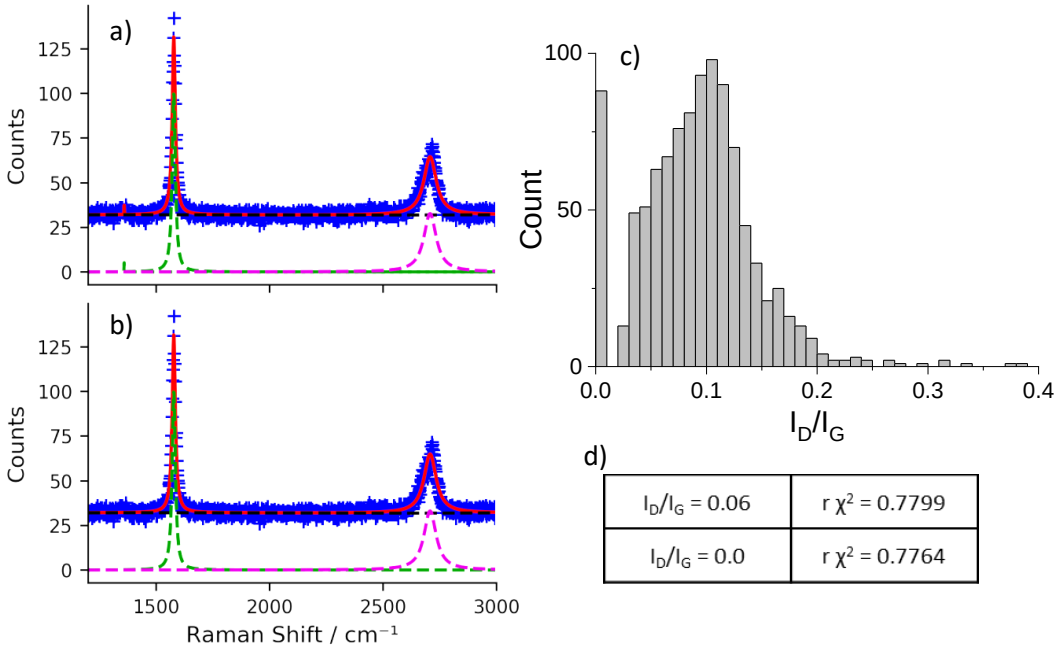

Figure 64: Illustration of spectra containing peaks that cannot be reliably fitted taken from graphite as an example. Both a) and b) show experimental data in blue, fitted model in red and individual peak shapes in green and purple; a) includes the D peak whilst b) does not include the D peak fit. The effect of this pigeon holing effect is illustrated by the histogram in c) with the unoccupied bin between zero and the main distribution, fitting outputs shown in table d).

This effect is necessary to maintain the integrity of the fitted parameters and uncertainly estimates, and will only be significant with low quality or noisy data. If additional degrees of freedom are allowed in the model with insufficient data to support their inclusion the non-linear regression, and in particular the co-variance matrix required for uncertainty estimates, becomes unstable. For further information see *lmfit* documents. In brief during the fitting process the program maps out an approximation of how every parameter varies in relation to other parameters and how these impact the residual being minimised. In this way the model parameters that produce the lowest residual, or best fit, can be identified. In addition,

an estimate of the uncertainty in these values can be found from the range these best-fit values could be varied by, allowing other parameters to change, whilst keeping the overall residual within one standard deviation of the optimum. If additional parameters are included without the physical data to constrain them i.e. a significant peak to fit, these correlations become too variable and no error estimates can be returned. Thus to maintain the rigorous analysis of significant peaks within the data, small peaks too difficult to determine from random noise are excluded and the final output reports them as exactly zero.

4.4 Results and Discussion

This detailed statistical consideration of nanomaterial analysis is important because of the variability present within samples of seemingly identical material. As demonstrated in the following section there is a significant difference between single point spectra and full data sets. Extreme examples of this were two commercial graphene nanoplatelets. Whilst the materials tested were marketed as different grades, they were clearly labelled graphene powder and technical specifications included very similar Raman spectra showing a clear G and 2D peak with little D peak present indicating a high quality material with few defects.

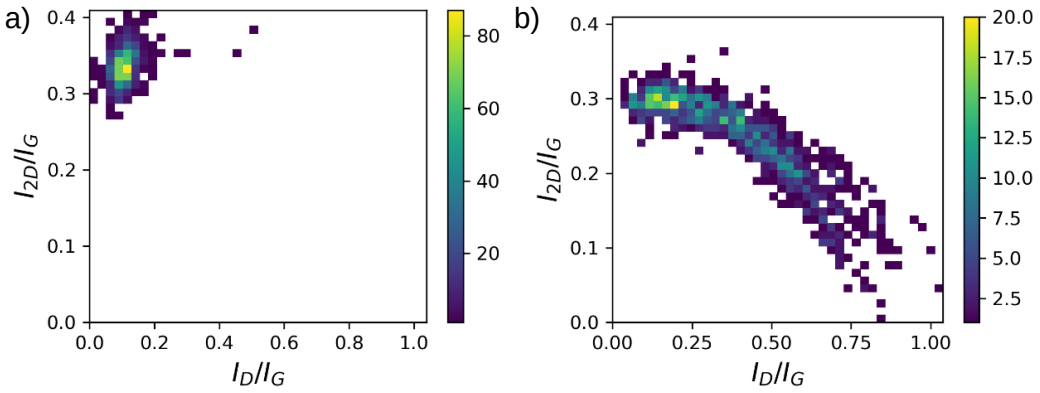

Figure 65: 3D bivariate histograms illustrating the dramatic difference between the two samples of graphite nanoplatelets – labelled for convenience as “high quality” a), and “low quality” as b).

These single spectra reported in technical data sheets were consistent with spectra measured in this analysis and yet the total distribution, as shown in Figure 65, clearly reveals a much more complex mixture present. Whilst one material could reasonably be described by the single Raman data point reported in the specification with a I_D/I_G around 0.1, hereafter referred to as “high quality” for simplicity, the other material is far more polydisperse. The spread of data points around the most populated bin in the left histogram is expected from random noise in a large data set. In contrast the very significant population of data points

with higher I_D/I_G values and decreasing I_{2D}/I_G present in the right histogram from the "low quality" material reveal there is a huge range of particle sizes and chemical defects.

This material also illustrates the utility of visualising the entire distribution in place of aggregated mean values that do not apply to such an asymmetric data set. Whilst the mean values, listed in Table 4, do capture the increase in defective material from the lower quality material this poorly reflects the reality of graphene flakes mixed with highly defective carbon. In essence, a full analysis should be completed to establish the distribution of peak parameters present before single value metrics are employed.

Table 4: Aggregated mean values with deviations from the two different samples of graphene nanoplatelets. It should be noted that the asymmetrical distribution of the lower quality material is unsuitable for averages.

		Mean	Standard Deviation	Standard Error
I_D/I_G	"High Quality"	0.1087	0.04	0.0008
	"Low Quality"	0.352	0.2	0.004
I_{2D}/I_G	"High Quality"	0.3317	0.02	0.0004
	"Low Quality"	0.255	0.06	0.001

4.4.1 Shear Exfoliated Graphene

The utility of a statistically meaningful data set was also proved when comparing graphite with shear exfoliated graphite, a commonly reported method for graphene production. Whilst high shear forces have proved capable of exfoliating carbon layers from graphite crystals to produce single layer graphene, the efficiency and yield of this process is low and the graphene produced is generally mixed with a large concentration of bulk graphite flakes. Such graphite flakes dominated the Raman analysis but careful consideration of the large data set does reveal a subtle shift in key metrics I_{2D}/I_G and I_D/I_G.

A sample of natural flake graphite was exfoliated in sodium cholate surfactant and three different data sets were collected from both the starting graphite and exfoliated material and analysed separately as shown in the box plot in Figure 66. The most noticeable change is the increase in I_D/I_G ratio and significant increase in width of the distribution. This is consistent with the decrease in flake size expected during such processing and clearly shows the material is undergoing change. I_{2D}/I_G is more usually linked to the exfoliation efficiency as few layer graphene has a larger 2D peak intensity relative to graphite; in this experiment there is a slight increase in I_{2D}/I_G observed following shear mixing, although the difference is minimal.

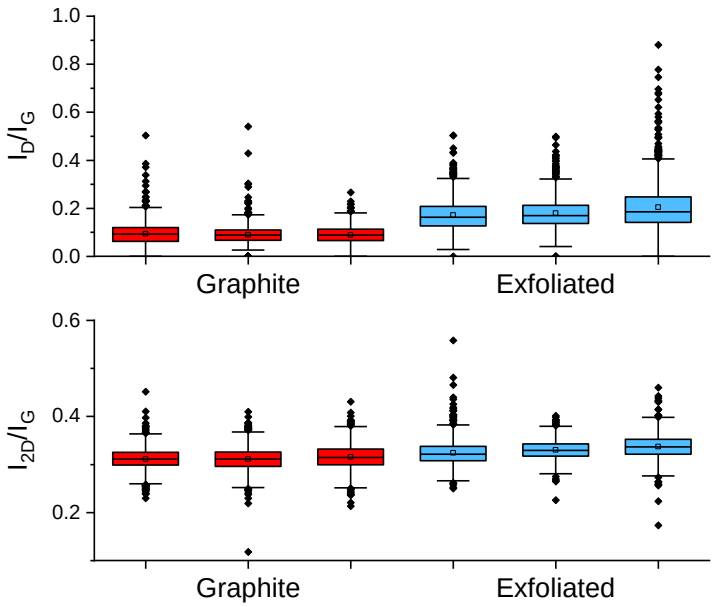

Figure 66: Box plot comparing the distribution of key peak parameters from the graphite and exfoliated materials, three independent data sets were collected and analysed for each material.

Such a minor change is not unexpected; fluid phase shear mixing is capable of exfoliating carbon layers from graphite but the efficiency of the technique is often poor, with a very significant amount of the graphite remaining unexfoliated.[72,159,161] There are methods known to separate this bulk graphite from the exfoliated graphene; unfortunately, such steps are complex and often not suitable for industrial production.[379] As such, the powder was analysed as produced for any change following shear mixing. In this context it is likely that the small increase in 2D peak height is caused by a small number of graphene flakes mixed with a lot of unexfoliated graphite. Such a change would be very difficult to observe from single spectra due to the noise and variability inherent in Raman spectroscopy and nanomaterials.

The 3D histograms in Figure 67 which show both peak parameters simultaneously makes this shift more noticeable; it is clear that in comparison to the starting graphite the increase in I_D/I_G caused by flakes decreasing in lateral size is directly related to the increase in I_{2D}/I_G caused by the exfoliation of carbon layers. Whilst this understanding of the exfoliation process is not novel and such mechanisms have been proved by other groups investigating shear exfoliation;[155] the ability to detect such changes from Raman data sets without the need for comprehensive and costly microscopies is a new approach. In the case of novel materials or genuinely new mechanisms, it would be undesirable to rely exclusively on a single technique. For the purpose of quality control of a known material, however, such depth of information could be very valuable.

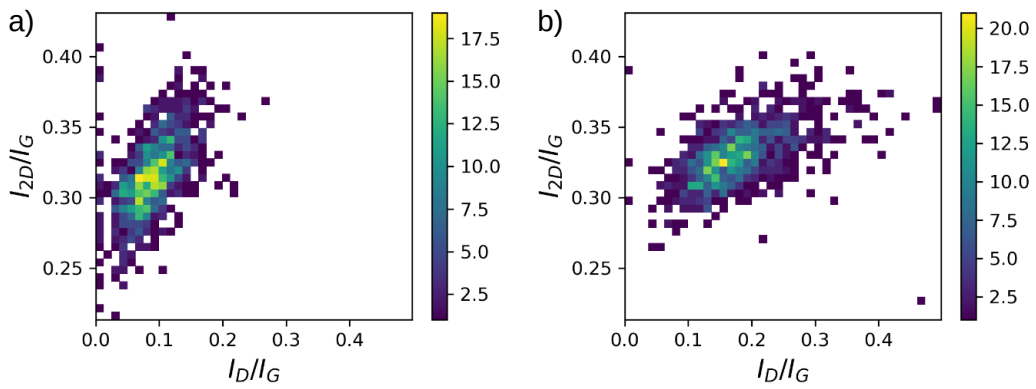

Figure 67: 3D bivariate histograms from a) graphite; b) exfoliated graphite. Key peak parameters are shown on the axes whilst bin occupancy is shown as a heat map.

When collecting large Raman data sets in this way the spatial distribution can also be considered, and indeed has been to great effect for graphene immobilised on surfaces as discussed in Chapter 1. On the other hand, it is expected that shear mixing graphite would produce a bulk powder randomly disordered at the length scale of Raman spots; containing no spatial information. Therefore each point collected in this experiment can be considered effectively random. Although this condition cannot be assumed for all materials, for example high temperature graphitized samples as discussed in more detail later; for shear mixed graphene this random distribution is shown in Figure 68. The best practice as undertaken here would be to visualise the spatial pattern, easily enabled by most commercial Raman micro-spectrometers, and in the case of random noise further consideration of spatial trends can be disregarded.

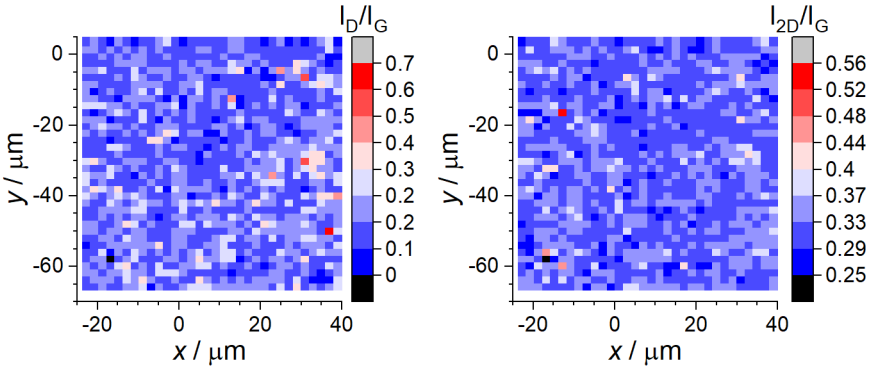

Figure 68: The spatial distribution of key Raman metrics I_D/I_G and I_{2D}/I_G, shown as a heat map, from a lightly pressed pellet of exfoliated graphite. The shear mixing has produced a random mixture.

It is hoped the utility and importance of complete data sets from microscale analyses of nanomaterials has thus been justified. The question then becomes one of pragmatism; how many data points are required for such analysis without wasting instrument time.

To investigate this the change in key summary statistics as more data points were collected are plotted as well as bootstrap plots that are useful for indicating the extent of error possible from under resolving materials. As an example the convergence of I_{2D}/I_G data from graphite, a homogeneous control material, is shown in Figure 69. As expected random noise causes some instability from the first data points collected but this rapidly stabilised and the summary statistics plotted remained constant after around 300 points. In this case it would be expected that whilst tens of spectra could be relied upon to produce an estimate of the mean of such a distribution, around 100 points would be needed for an accurate mean. The full distribution, based on the 10th and 90th percentiles, require even more points, around 300, even for a material as reliable as graphite.

It could be tempting at this stage to consider the changes in summary statistics observed irrelevant for most analysis and within the error of the experiment given the natural variation in Raman spectra. Whilst this is valid for a material like graphite that is known to be homogeneous, the power of establishing a constant and unchanging distribution is the confidence to know whether a secondary phase is present in low levels.

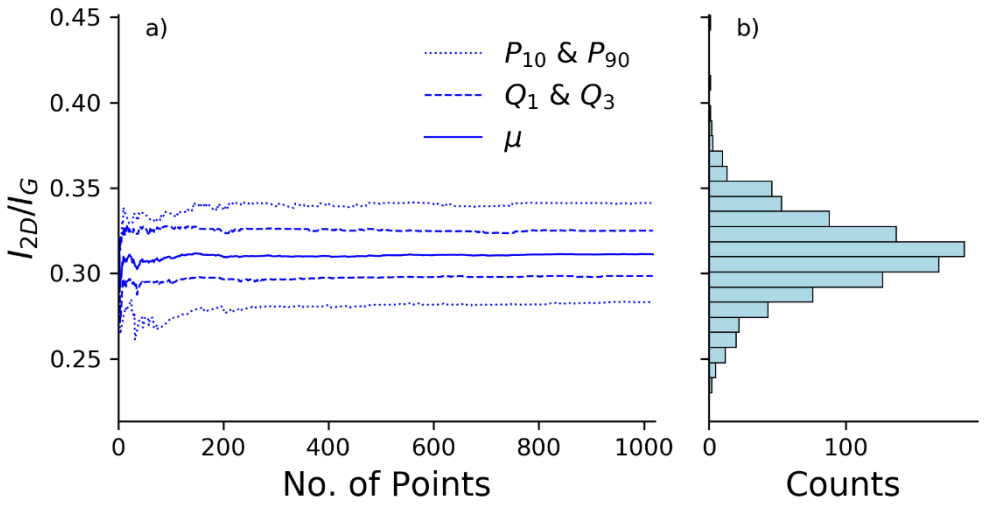

Figure 69: Convergence plot from a graphite data set showing a) the change in summary statistics of I_{2D}/I_G as more data points are added to the analysis. b) The final distribution histogram.

The convergence plots for the exfoliated graphite, a material with a wider distribution of peak parameters, was unsurprisingly found to be less stable requiring more points to complete the distribution. Whilst the modal peak in the distribution was established rapidly the significant tail caused by the exfoliated material required more data to reliably establish. To visualise the effect of under analysing the material by only collecting a small number of data points, bootstrap plots are used. An example for exfoliated graphite is shown in Figure

70; whilst the distribution plotted from a large data set is consistent with the expected pattern from the histogram of the complete data set, the different distributions shown in different colours from smaller data sets are radically different to one another.

In essence each colour represents a distribution containing only the number of data points labelled, randomly selected from the total larger data set recorded. When that sample size is over 250 the distributions are consistent within some noise and the tail is clearly defined. For smaller sample sizes, however, most data sets only find one or two data points of higher I_D/I_G and fail to truly describe the tailed asymmetric distribution found from this material. Indeed in many cases having only recorded 25 points the higher peak ratios indicative of exfoliated materials would probably be discounted as outliers.

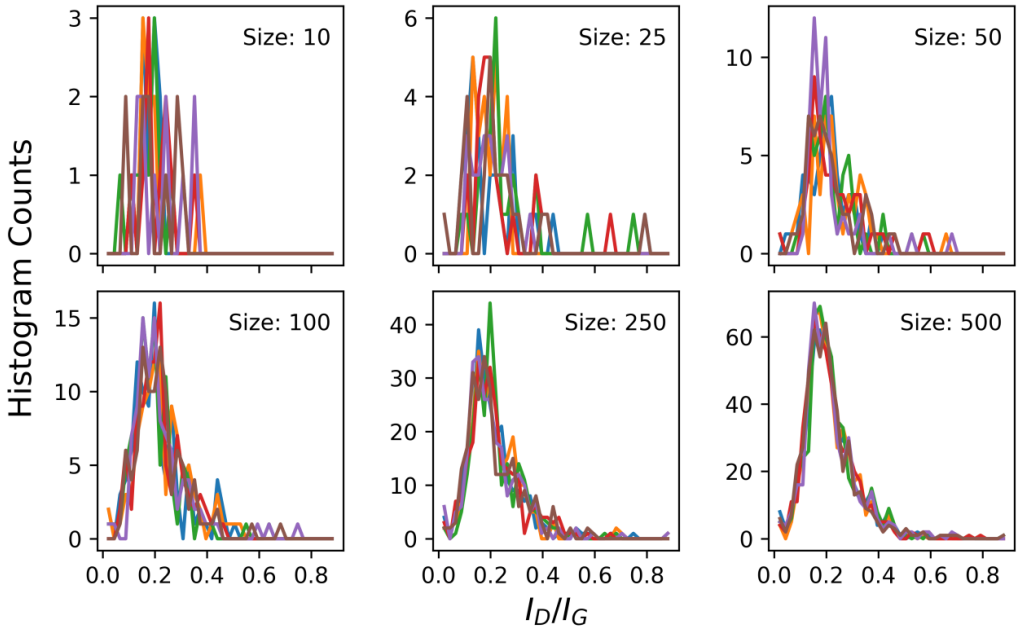

Figure 70: Panel showing result of bootstrap analysis of exfoliated graphite. Each panel shows five examples, shown in different colours, of distributions of I_D/I_G produced from sub-samples; the size of these is labelled and the x-axis is common across all I_D/I_G panel plots.

4.4.2 Graphene Nanoplatelets

It is clear that different materials require bespoke analyses that also reflect the purpose of that analysis. Considering the graphene nanoplatelets previously discussed, the “high quality” sample has a very reliable Raman spectrum that would require a relatively small sample size. In contrast, the polydisperse “low quality” sample requires a much larger data set to approach complete characterisation. These effects are illustrated in Figure 71 where key bootstrap and convergence line plots from the two materials are shown. The monodisperse sample has a much sharper distribution in the bootstrap plots (Figure 71b)

even with a small sample size; if only 100 Raman spectra were recorded there could be some uncertainty due to the shift in mean and intensity between the yellow line and much shallower green line. The general trend, however, is consistent and with 300 data points the different sub-samples are practically indistinguishable from each other.

The convergence plot (Figure 71a) shows the same trends; with less than 200 data points the mean and distribution width is changing substantially as new spectra are included. After this point the distribution becomes more established; although there are still some changes to the mean value after this sample size. In contrast the other "low quality" GNP sample has a much wider range of I_D/I_G values that cause significant variation even after hundreds of points have been recorded; indeed 500 points are required before the interquartile range and mean become stable as shown in the convergence plot (Figure 71c). The most obvious feature in the bootstrap line plots is the asymmetrical shape of the distributions of "low quality" sample with a significant tail as the fraction of small flakes with a large I_D/I_G ratio is smaller but still significant to the overall material.

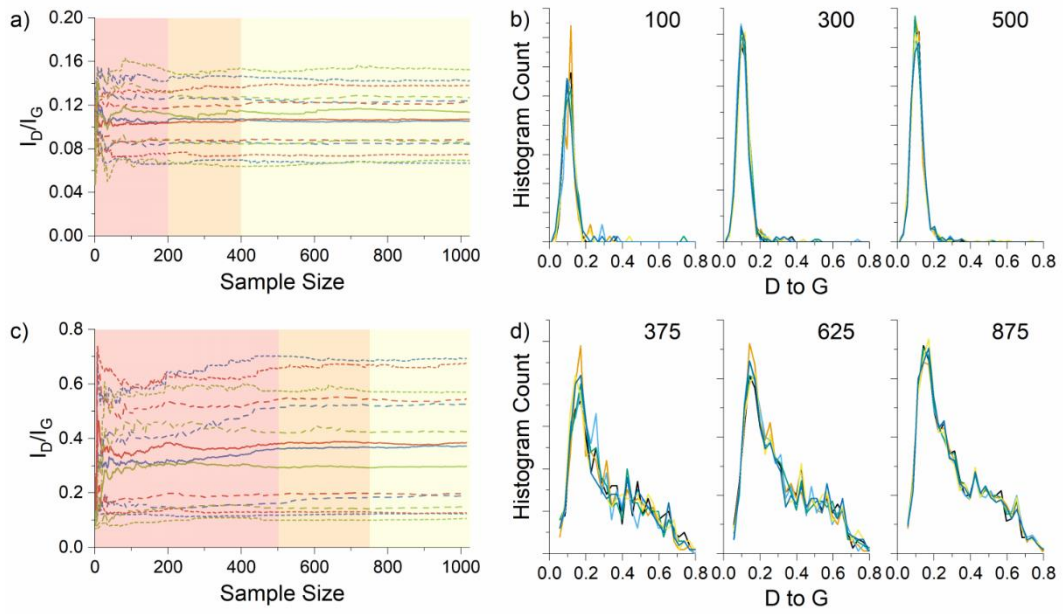

Figure 71: Analysis of data sets collected from the two GNP samples; a) & b) are from the "high quality" sample whilst c) & d) show data from the "low quality". Plots a) & c) show convergence data of key statistics with increasing data stability highlighted in red, orange to yellow, whilst b) & d) show the bootstrap analysis of distributions from sub-samples, the size of which is labelled.

It is clear the different samples have very different properties and would behave differently during analysis; this therefore means that different and bespoke analysis procedures would be preferable for each material. Unfortunately such an approach would be very costly. The best approach may be to tailor the analysis to the level of detailed understanding required; for quick snap-shots of a material it is usually reliable to measure 10s of spectra. If more

information is required then a larger scale analysis to justify the number of data points would be advisable to ensure that minor fractions or chemically distinct regions have been included.

Thus far analysis of top-down graphene produced from various methods of exfoliating graphite have been considered as examples. It could be expected that other methods of graphene formation would produce materials with different chemical environments, that would be detected by Raman spectroscopy. One example is reduced graphene oxide. Detailed analysis of oxidised graphitic material was not undertaken in this study because the nature of information that can be extracted is very limited as discussed in the introduction. Such extensive chemical functionalisation and damage to the carbon network produces very wide D and G peaks with no 2D Raman signal; conclusions beyond simply confirming the material has been oxidised are not possible without additional techniques. However, extensive reduction can repair the aromatic structure of the carbon sufficiently to detect the 2D peak; thereby allowing some measure of reduction efficiency.

4.4.3 Reduced Graphene Oxide

Following chemical reduction with hydrazine the rGO examined in this study regained a distinct 2D peak indicative of a partially repaired conjugated network vital for conductivity, with a I_{2D}/I_G = 0.09 and a very narrow distribution, albeit slightly asymmetric. The D peak is more variable spectrum to spectrum as represented by the wider and unstable I_D/I_G distribution shown in Figure 72, but this is expected since that peak is dependent on both peak size and presence of defects and functional groups. Decoupling these effects is not attempted in this work, but it is clear that the I_D/I_G ratios measured from the large number of Raman spectra do not follow a simple normal distribution and a second phase of material is present. Whilst the most common value of I_D/I_G as seen from the histogram, Figure 72, is around 1.3 there is a significant tail to the distribution descending below 1.2.

As with other samples the convergence plot of summary statistics changing over sample size is useful for identifying how many points are required to stabilise the distribution. It was assumed that chemical reduction would produce a more homogeneous material with a normal distribution of random noise in peak parameters but this was not observed. It was found that a crude convergence of the centre of the distribution is achieved after approximately 100 points, although 600 points are required to remove most of the noise from the analysis. This instability is caused by the ‘tail’ present in the distribution caused by points with lower relative peak intensities.

The bootstrap plots in Figure 72a clearly show this, when the size of the sub-sample in the bootstrap plot is large, specifically 500 data points, the different sub-samples are almost indistinguishable from each other. However, when the sub-sample size is only 50 data points there is a lot of noise in the tail and many sub-samples do not include any such data points. Were the material to be analysed with only 50 points, it is possible the very significant tail of lower peak intensities would be missed.

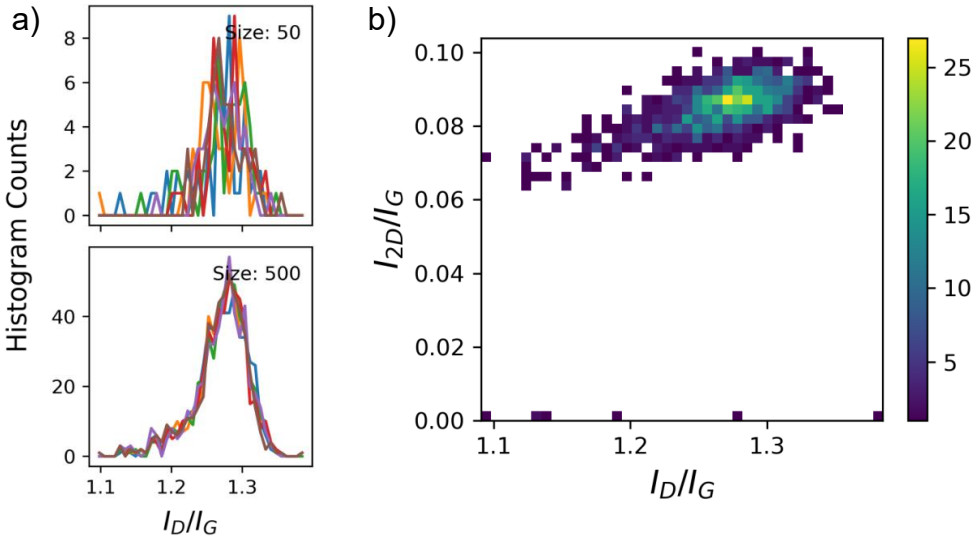

Figure 72: Example data set of reduced graphene oxide; a) shows two extreme cases from bootstrap analysis before and after data convergence and b) a 3D bivariate histogram showing the complete data set.

Data points with a lower intensity were not artefacts of fitting or signal to noise, a topic discussed in more detail later in this section. It is likely these spectra are caused by a minor fraction of carbonaceous material heavily functionalized by the oxidation process; the reduction may have been sufficient to repair some aromatic sp^2 domains with a clear G peak but insufficient to regenerate enough structure to produce D or 2D peaks. Such trends where the D peak intensity increases in line with conductivity have been reported in other work investigating the reduction of graphene oxide materials; and islands of graphitic material surrounded by regions of amorphous carbon are usually attributed as the cause.[123,124]

4.4.4 Graphitized Polymer

In addition to top-down approaches for graphene preparation, we have also considered bottom-up techniques; techniques that grow graphene from carbon building blocks. The process of high-temperature graphitization has been studied by many groups, however, comprehensive statistical Raman analysis is rarely, if ever, utilised. The graphene sample analysed was prepared from a two phase aqueous in oil polymerisation to produce a porous

polymer (resorcinol-formaldehyde resin) containing iron(III) chloride; when heated the iron reduces to form metal particles which grow graphene on their surface. It has been found that large data sets can be effectively applied and these materials also highlight that complementary characterization and understanding is often required.

More data sets were collected from this material, to account for the macroscale structural features that are known to be present within the material from other studies of graphene prepared in this manner. In total six Raman data sets, each covering an area 80 x 80 μm^2, were collected and the combined distribution, shown in Figure 73, produced a clear picture of a material predominately made from well graphitized carbon with a significant fraction of amorphous carbon.

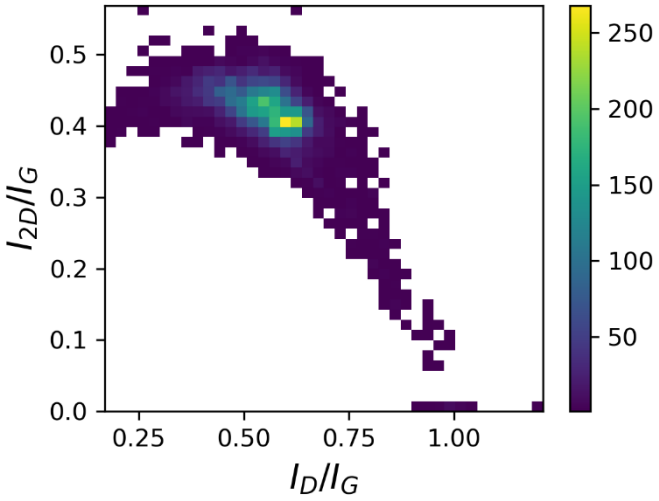

Figure 73: 3D bivariate histogram of the combined data sets collected from the carbonized sample; the large number of points makes the distribution very well resolved.

Overall the data set was consistent with the expected literature results although many of the individual Raman maps did not fully reflect this material. In this case the spatial maps of the Raman mapping did show more structure than those of randomly mixed powders. This is attributed to difficulties grinding and preparing powder samples from the very hard carbon material without damaging it, on account of it containing crystalline metal and metal carbide particles. This produces larger crystallites of graphitic carbon that generally have a length scale greater than the 2.5 µm step size between different Raman spectra and this can be seen in the bottom left corner of the spatial map data in Figure 74.

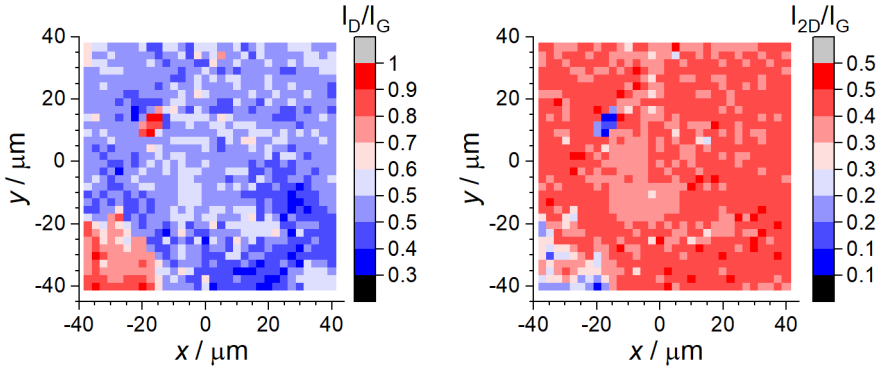

Figure 74: Raman map data from high temperature graphitized polymer showing the spatial distribution of Raman parameters against the stage coordinates. The distinctly different region in the bottom left corner is a collection of more amorphous material that could not be mixed.

These larger domains contributed to structure and sudden changes seen in the convergence plots and summary statistics from this material, Figure 75, showing a sudden dramatic decrease in the upper quartile and saw-tooth pattern attributed to the measurement collected by rastering back and forth across the sample surface. After completing one row of the map, spectra are collected from the distinctly different area resulting in a large jump in the summary statistics. Small spikes less dramatic than this can be seen in other materials at low data set size but are usually the result of focussing a large map onto a rough or sloped surface. If one edge is more or less out of focus, it may either produce a more exactly average Raman spectrum if defocused, or a more extreme side of a distribution if very tightly focussed. In the case of the iron carbonized sample, however, this saw-tooth pattern is much stronger and results from the spatial ordering of the data. This reinforces the importance of complementary analysis of unknown materials; but large Raman data sets will still play a role.

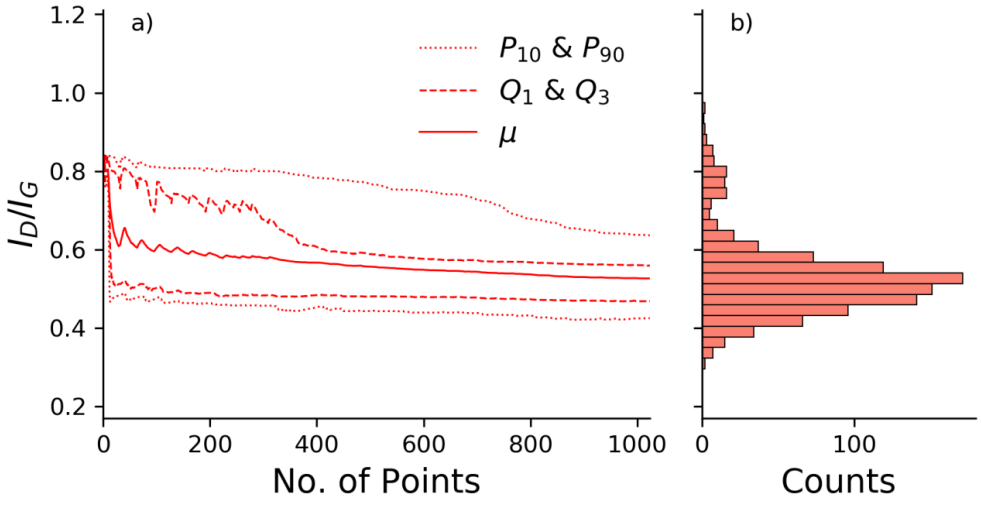

Figure 75: Convergence plot of I_D/I_G demonstrating the sudden changes in ratio from one small map on a specific area of material when the material has structure greater than the length scale of the measurement.

When analysing materials with such spatial ordering it is clearly beneficial to cover a large area by sampling from many places, either randomly selected or controlled to ensure complete representative coverage. In this way, many small Raman data sets can be combined to produce a more comprehensive understanding of the material. Conclusions regarding the crystallite size will require analysis of the spatial distribution whilst the relative fraction of one material to another would require a more holistic analysis of the entire distribution as introduced here. Specifically the distribution being evolved from multiple different maps should be analysed for changes as new points and new maps are added; to ensure the measurement taken is still representative. In this specific case, the D peak was far more variable and the overall distribution across all map data shows an asymmetric distribution with a small but notable population of more defective carbon around 0.8; however, these regions were more localised and only found on a few maps. The combined data set and bootstrap analysis, which is different to the very localised map shown above in Figure 75, indicates that around 250-300 points is sufficient to identify the main phase of the material, although these points should be collected over a much wider area than the 80 x 80 μm^2 area used in each small map; further discussion and data provided in Appendix 9.1.7.

4.4.5 Multiwalled Carbon Nanotubes

Multiple data sets were also needed to analyse the commercial sample of multi-walled carbon nanotubes investigated. Six data sets were recorded which together produced an approximately normal distribution of key peak parameters; however, two data sets were found to have slightly more extreme distributions when compared with the other individual data sets. The summary statistics of all data sets for the I_D/I_G metric are shown in Figure 76; it is clear that most are clustered around a central narrow distribution with a combined mean value of 1.25 but there are two data sets with very different values of the peak height ratio. Specifically the 3rd data set with an average of 1.12 and the 4th data set with an average of 1.36. It should also be noted that these data sets are much wider than the other sets and there is overlap between the quartiles and percentiles of those different data sets.

The 2D peak height ratio shows a similarly confused set of overlapping distributions from different data sets. By combining the data sets together and randomising the order, to remove artificial structure, a random distribution is produced. This has a very standard frequency distribution for I_D/I_G, and a flat topped distribution from I_{2D}/I_G that produces a slight bimodal trend in the 3D histogram heat map. The exact cause of these differences between different samples taken at random from the bulk container – a 1kg tin of

commercially supplied nanotubes; cannot be ascertained using only the Raman data collected here. Additional investigation using electron microscopies, thermal analysis and an understanding of the production and packaging process may explain many of these differences however such detailed study is not necessary for establishing the utility of collecting a larger data set over many areas of the sample.

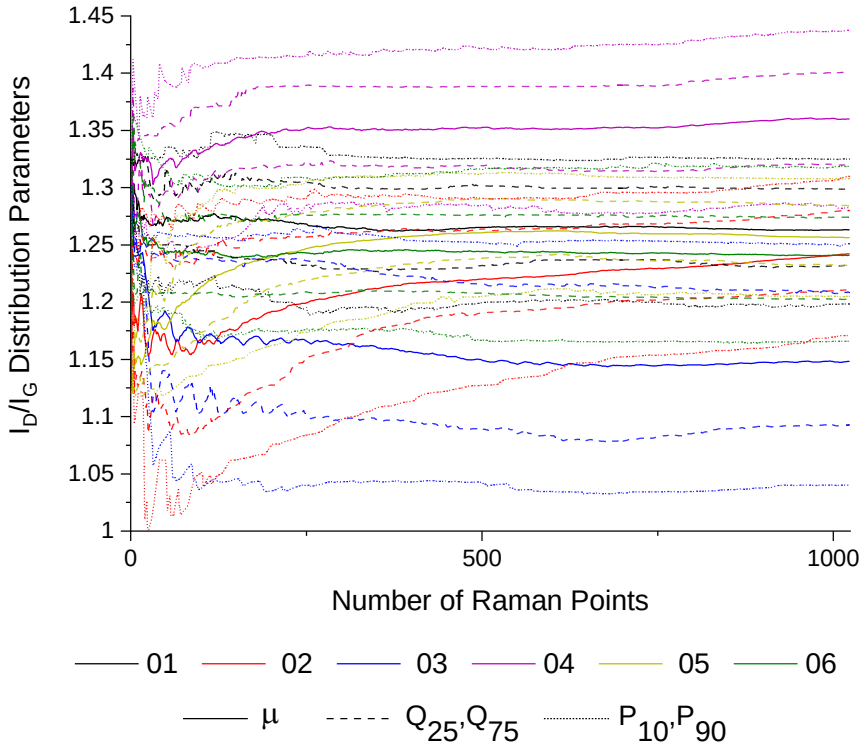

Figure 76: Summary statistics showing the change in I_D/I_G as the data set size increases. Different data sets shown in different colours – the significant outliers are 03 at the bottom and 04 at the top.

The convergence plots from this commercial material show many of the same trends, although there are some slight differences that point to the inhomogeneity of the bulk sample. Using the combined data it appears that over a thousand points would be required before the distribution was completely described and these points should be collected from a wide area of the material as for the carbonized sample discussed above. The convergence plots from the individual data sets, Figure 76, appear to converge more rapidly but there are clearly different spatial regions causing the difference between spectra recorded from different points on the sample surface. These large differences can influence the mean and quartiles of the data even when hundreds of points have already been measured.

In this case a more nuanced analysis of the nanotubes would be desirable to understand the different features identified, however, the level of this analysis will also depend on application, balancing thorough analysis with efficient use of time. Example spectra from

every data set are shown in Figure 77 for context of the difference between data sets. Whilst the exact peak heights are subtly different the overall character of the Raman spectra are very similar. It could reasonably be argued that a sample with a very defined chemical composition and defect density would benefit from understanding the differences between the peak ratios discussed. In contrast a sample of crude carbon nanotubes of mixed chirality, size and elemental purity would probably be expected to vary batch to batch. In such a case, detailed analysis of the extent discussed here would be wasteful.

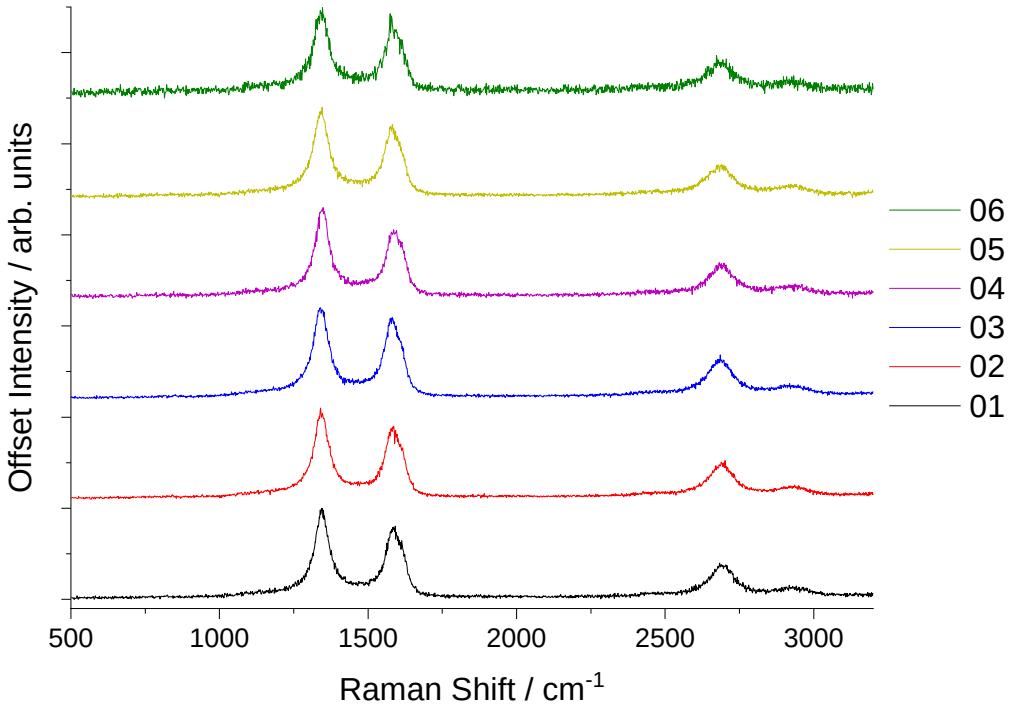

Figure 77: Example spectra from all data sets of MWCNTs; each spectrum is selected to be representative of the modal peak parameters from each sample distribution; no processing further than the normalisation of signal intensity has been applied.

Raman spectroscopy clearly has great utility in analysing carbon nanomaterials and rewarding insights are possible from suitably rigorous analysis using multiple data points. More fundamentally, the importance of justifying the sample size collected when analysing nanomaterials of any sort has been stated. The natural variation in these materials makes single point measurements very unreliable and bulk techniques often suffer from crude averaging that fails to account for the mixture of different environments that are actually present. The use of 3D histograms is very effective for carbon nanomaterials because of the ubiquity of the two metrics I_{2D}/I_G and I_D/I_G; more generally, plotting histograms to understand the true shape of the data set must be a first step for nanomaterial analysis.

Visualising complete distributions and not just aggregate mean values is very important because it has been repeatedly observed that most manufacturing and chemical processes do not result in random error. More structured data sets are often encountered that require a more nuanced discussion that is most easily facilitated with a complete distribution in the first instance. It is acknowledged that for the comparison of different samples a more succinct method is required, and for this summary statistics have been used successfully, especially in justifying the sample sizes required. However, such simplifications and summaries should follow careful consideration of larger data sets to understand a material's characteristics; and cannot be justified following a single point spectrum.

4.4 Investigating Signal to Noise

Understanding the effect of signal to noise on Raman spectra is very important when attempting to provide guidance for analysis protocols since different experimental conditions will record data of varying signal intensity. To understand these effects a large model data set was produced based on the same mathematical model used to fit Raman spectra; although, the model data set was created independently. It was then fitted with the same Python program used for Raman map analysis. This map was based on a single model spectrum, to which random noise was added to produce different spectra that were nevertheless all derived from the same peak shapes with identical heights, positions and widths. The model spectrum was based on a high quality spectrum recorded from reduced graphene oxide, selected because of its high D peak and low 2D peak allowing both extremes to be investigated simultaneously. Real peak parameters were used in a model combining a 4th order polynomial with Lorentzian line shapes (Eqn.2).

$$y = c_0 + c_1 x + c_2 x^2 + c_3 x^3 + c_4 x^4 + \sum_n^{G\,,D\,,2D\,,D+G} f(x|A_n, \sigma_n \mu_n) \qquad \text{(Eqn.5)}$$

Where A is the peak amplitude (this is distinct from height), μ is the peak position in cm^{-1} and σ is the half width at half max. The specific parameters used are listed below in Table 5.

Table 5: All parameters used in the above equations to generate the model spectrum.

Background	c_0	-12
	c_1	0.145
	c_2	-1.39 x10^{-4}
	c_3	5.35 x10^{-8}
	c_4	-7.0 x 10^{-12}

G Peak	A_G	25500
	μ_G	1577
	σ_G	31.8
D Peak	A_D	46000
	μ_D	1345
	σ_D	43
2D Peak	A_{2D}	7513
	μ_{2D}	2677
	σ_{2D}	87
D+G Peak	A_{D+G}	5415
	μ_{D+G}	2921
	σ_{D+G}	65

Once the model spectrum was established a pseudo random number generator, based on the Mersenne Twister algorithm, was used to create random noise. By repeating this process multiple spectra could be created with the same fundamental peak parameters and level of noise but remaining unique. The noise added was based on a normal distribution probability density function (Eqn.6) since this was shown to be an effective approximation of real experimental noise; every intensity (y) value was recalculated from the expected value (μ). Controlling the standard deviation (σ) meant a controlled level of noise can be applied.

$$PDF(x|\mu,\sigma) = \frac{1}{\sqrt{2\pi\sigma^2}} \cdot e^{\frac{-(x-\mu)^2}{2\sigma^2}} \quad \text{(Eqn.6)}$$

This approach was used to generate a model 'map' containing 500 individual spectra based on the same model with controlled noise added; this entire process was then repeated to produce another 'map' containing 500 points with increased noise. By increasing the standard deviation for each 'map' used in the PDF in integers a sequence of model maps were produced with steadily increasing levels of noise, example spectra shown in Figure 78 for high and low extremes. Here it should be noted, the standard deviation was used in the random number generator to control the level of noise being simulated but further discussion of distributions and deviations refers to statistical analysis of the fitted data sets.

The model maps thus created were subjected to the same fitting and convergence analysis as real data sets. In this case, however, since the fundamental spectrum was the same, any deviation can be attributed to noise within the data rather than sample polydispersity or

other experimental effects. The fitted output parameters from all 500 spectra were then analysed.

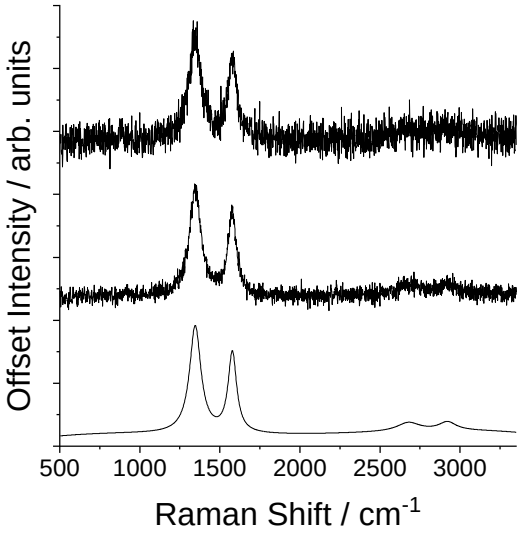

Figure 78: Example spectra produced by adding random noise to a model spectrum, shown at the bottom with a standard deviation of 0. The middle spectrum is an example produced with a standard deviation about the expected value of 15, and the top spectrum is the noisy extreme produced with a standard deviation of 30.

When considering the signal to noise, it is important to control for the different heights of the D and 2D peaks. To control for this all subsequent analysis will use the convention that the signal to noise values are normalised, relative to the lowest peak (Eqn.7) within the parameter of interest. In practice the I_D/I_G signal to noise is determined by the G peak height whilst the I_{2D}/I_G signal to noise is determined by the much lower 2D peak. This also allows a wider range of values to be modelled within the same map data.

$$\frac{S_G}{N} \times \frac{I_{2D}}{I_G} = \frac{S_{2D}}{N} \qquad \text{(Eqn.7)}$$

Considering I_D/I_G the most obvious finding was the rapid increase in distribution width as the noise increased (Figure 79). Whilst the variation in measured ratios was far more varied as noise increased this distribution remained well described by a normal curve; and within the limit of good signal to noise ratios, the mean was not observed to change very significantly. As shown in Figure 80 this trend remains reasonably constant until the noise becomes comparable to around 10% of the signal strength; at this point it is supposed that the background correction becomes unstable and peak intensity becomes lost to fractionally increased polynomial functions attempting to correct for the increased noise. Attempting detailed analysis on data of insufficient signal will likely provide erroneous results, although

the difference between signal to noise levels of 64 compared with 1024 is actually relatively minor and faster data acquisition will often be acceptable for routine analysis.

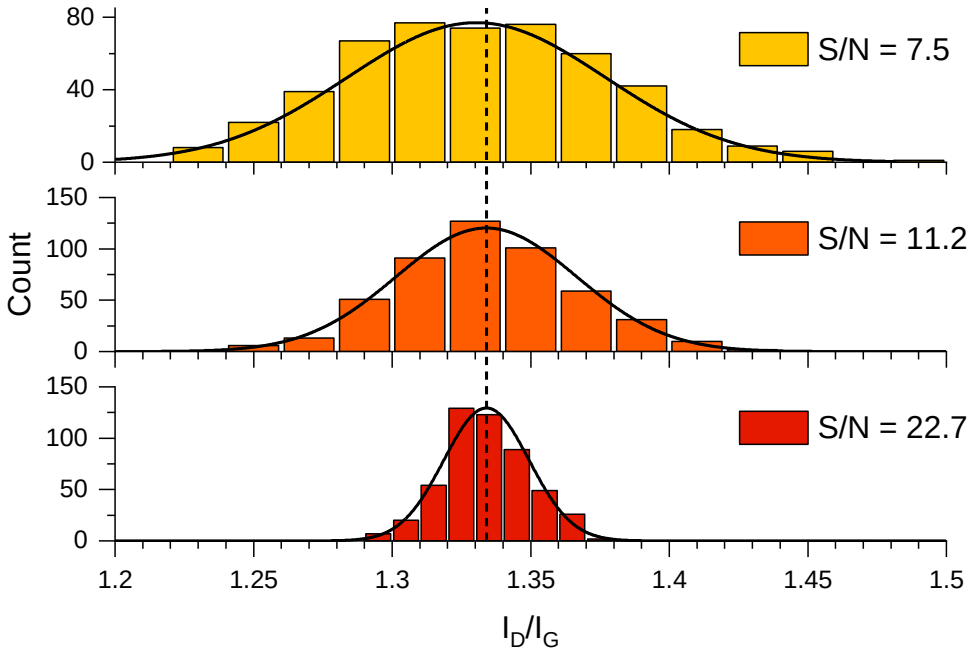

Figure 79: I_D/I_G values measured from the model data sets, each distribution of ratios was modelled as a normal distribution shown in black. The expected I_D/I_G from the model data = 1.334 highlighted with the dashed line. The signal to noise is shown in the legend.

To understand the relationship between the standard deviation of the 500 model spectra and the signal to noise level calculated, a scatter plot showing the coefficient of variation, defined as the deviation normalised to the peak height, compared with the normalised noise level were produced. The coefficient of variation allows comparisons of both I_{2D}/I_G and I_D/I_G despite their difference in magnitude. Figure 80c effectively shows the percentage deviation from the expectation value of 500 data points that only differ in the random noise added, plotted against the signal to noise.

$$\frac{\sigma_x}{\mu_x} = Coefficient\ of\ Deviation$$

Figure 80c shows there is a strong linear relationship between the average noise level within a set of data and the random noise to be expected in the fitted output. This normally distributed noise is unavoidable when using real data sets, however, it is also clear that the standard deviation will remain below 5% for a good signal to noise level. Real materials often produce significantly wider and less defined distributions and this can reasonably be attributed to polydispersity within the sample.

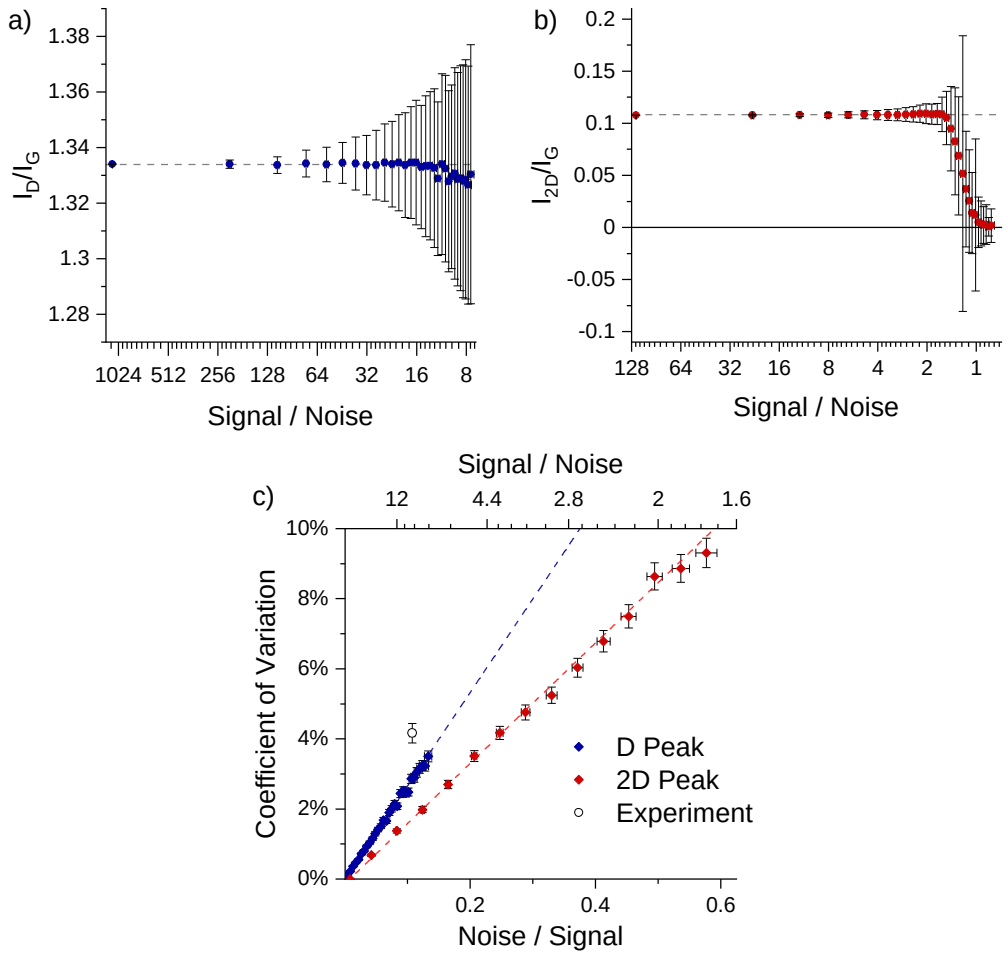

Figure 80: Mean values from a) I_D/I_G and b) I_{2D}/I_G from 500 spectra against the mean signal to noise; in both cases square root x-axes have been used to better show the data. c) The relationship between the standard deviation and noise level, all normalised to the height of the lowest peak with linear trend lines shown, experiment data was taken from a graphite control.

These linear trends were observed to breakdown as the signal intensity of the lowest peak, in this model data set the 2D peak, approaches the noise present within the background. As the I_{2D}/I_G ratio decreases the standard deviation is seen to vary significantly because of the non-continuous distribution of peak ratios produced, these regions are shown in Figure 81. As the signal intensity becomes too small for reliable fitting the peak is simply considered to be zero, this results in a region where the I_{2D}/I_G data contains a number of unevenly distributed values with a significant population of zero values. This causes a rapid decrease in the mean value and a sudden increase in the standard distribution measured. In this limit, normalising the standard deviation produces very high values due to the denominator approaching zero; once the sudden change is complete the standard deviation would actually be expected to decrease as more data points are reported as exactly zero.

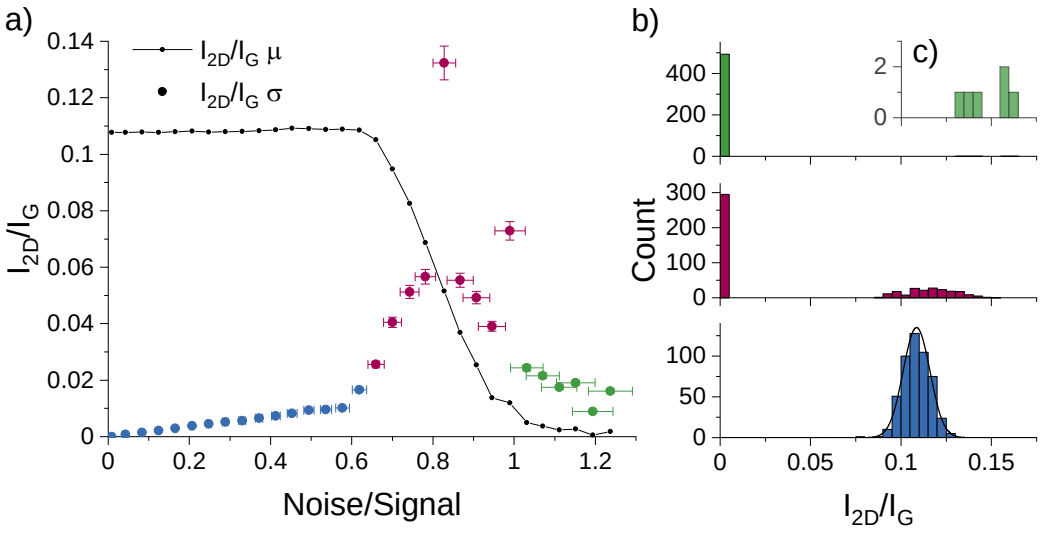

Figure 81: The effect of noise on peaks with low signal intensity is very significant. a) shows the mean I_{2D}/I_G values from the 500 fitted model spectra and the standard deviation values as coloured spots whilst b) shows typical distributions of the I_{2D}/I_G ratios at different noise levels (N/S = 0.413, 0.828, 1.24 from bottom to top); insert c) shows the low population I_{2D}/I_G ratios, the x-axis is consistent with other plots but the y-axis is significantly zoomed. The different colours highlight the different regions: blue when the signal intensity is sufficient for accurate fitting; red when the signal intensity is low and the distribution is very wide containing zero values and fitted peaks; green shows where the signal intensity is so low the distribution is dominated by zero values.

In this limit the analysis and peak fitting become unstable as the peak height becomes lost in noise, occurring at signal to noise values around 1.5, suggesting that this represents the limit of usability for extracting even vague average values from Raman map data. Signal to noise ratios greater than two can be used to estimate mean values for material properties, conditional on large Raman data sets hundreds of points in size. At this signal to noise, however, the scatter in data is significant and signal to noise values of the lowest spectral feature should be above twenty if probing the polydispersity of a nanomaterial powder.

Modelling the effect of noise in this way was also intended to probe the effect of noise on the convergence of data sets. Whilst these model data sets produce a normal distribution that could be reliably subjected to statistical methods like a t-test the same graphical tests for convergence were utilised to ensure consistent findings between the real samples and model data. The resulting plots are complex in appearance but the broad trends in convergence are maintained, despite the increasing noise and scatter within the data sets shown in Figure 82. The most obvious feature is the width of the distributions as the noise level increases, yet looking closely even the lower noise data sets show significant variation before eventually converging to consistent values. Considering the most noisy data set shown in red with the widest distribution, it is clear there is substantial variation in the summary statistics as the lines shift up and down until reaching an approximate convergence

around 350 points. Considering the data sets with little noise, shown in blue, the same vertical variation is observed with low samples sizes even if the magnitude is lower.

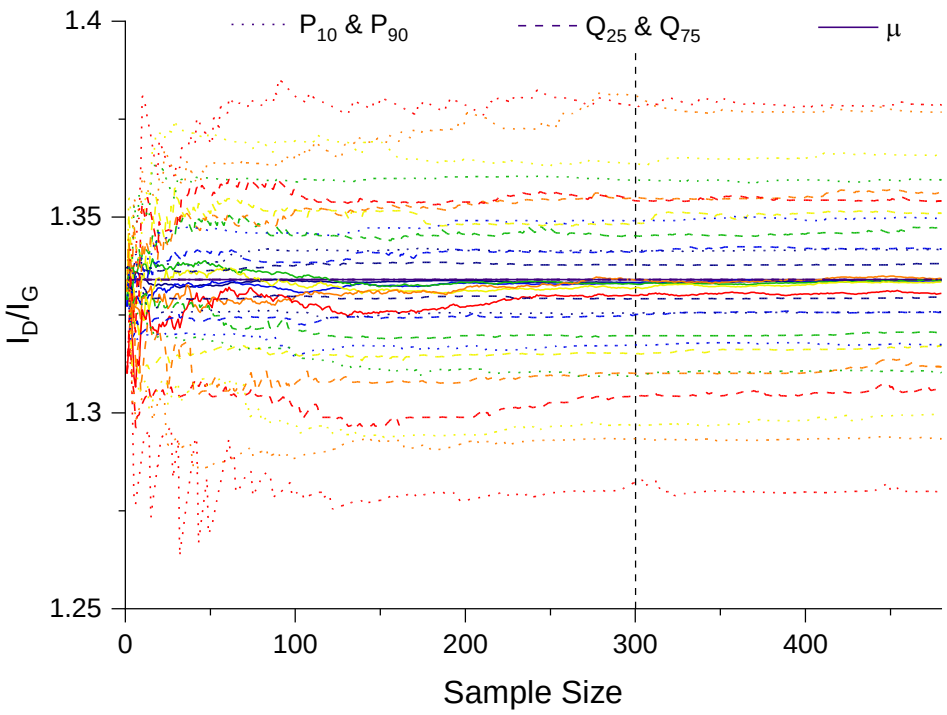

Figure 82: Convergence plot of summary statistics describing the distributions of model data sets. The colours denote increasing noise following a rainbow colour scheme from blue to red. Whilst complex this plot shows that increasing noise causes greater spread but crucially the rate of convergence remains comparable across the model data sets.

To better illustrate this, the variability of the lower quartile (Q_{25}) is shown in Figure 83. The Q_{25} was compared to the final value producing a percentage variation, the greater this percentage variation the further that data point is from the final converged value from the entire data set. The key finding is the significant change in variation for all noise levels which abruptly decreases, the lines becoming flatter and smoother, around 350 data points. Considering the red line from high noise model data, this is variable at low sample sizes with new data points causing substantial shifts to Q_{25}; but after around 350 data points they converge and the Q_{25} measured from 350 points remains the same as the Q_{25} measured from 500 points. This trend is the same from the low noise model in blue, this also shows variation with fewer than 350 points until the data converges.

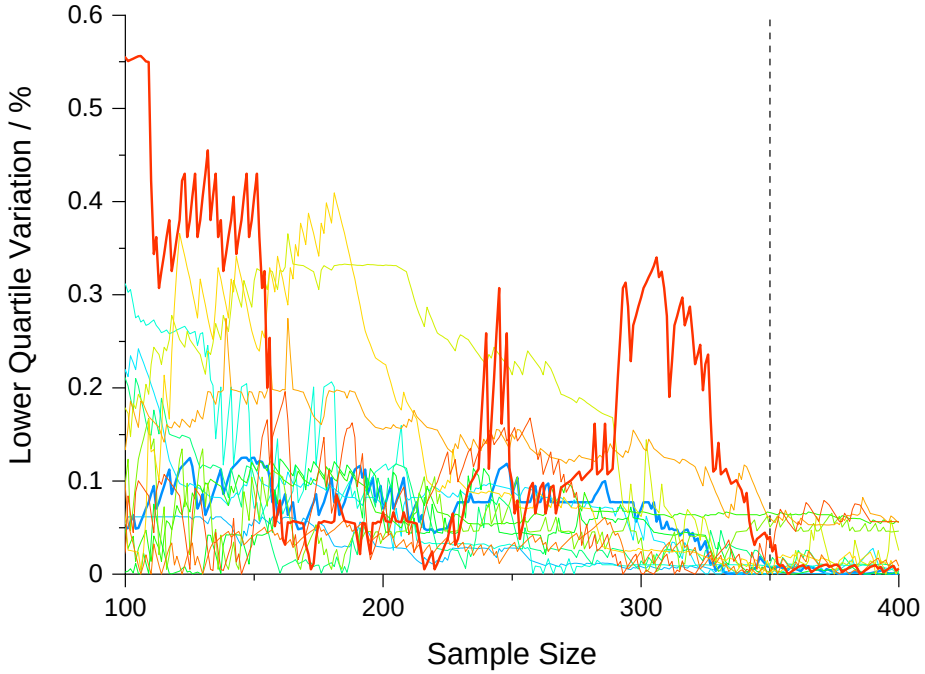

Figure 83: The convergence of the lower quartile (Q_{25}) relative to the final converged value of each data set. The colours indicate increasing noise following a rainbow colour scheme from blue to red; by displaying each data set as a percentage the relatively low variation in maps with little noise becomes visible and the crucial convergence rate is observed to remain steady, all data sets show significant variation before converging around 350.

The important finding is not the magnitude of variation with increasing noise, but rather the rate of convergence since this influences the number of spectra that should be measured from real samples. Here it is shown that signal to noise levels do not have a significant effect on the rate of convergence; therefore any data collected on the convergence of different real materials will remain valid regardless of noise, assuming the limits discussed above are considered.

4.5 Conclusions

This work was motivated primarily by difficulties encountered when characterising carbon nanomaterials due to their highly diverse properties. Such difficulties have been widely reported and could be expected from many other topical nanomaterials that also exhibit subtle differences in size, shape and chemistry. Considering the carbon nanomaterials investigated it is clear that a single spectrum, as traditionally reported, is unlikely to be representative of the entire material and many other interesting and important features may be missed. Statistically meaningful and robust analyses are required if a reliable nanomaterial metrology can be established to further the commercial utility of these diverse

materials. To this end the methodology developed here can be used to make claims on the validity and robustness of future nanomaterial analysis.

Furthermore the highly diverse range of properties and characteristics resulting from different production methods means that simple gaussian distribution models can rarely be applied to nanomaterials. Instead nuanced consideration of each material is needed and analytical methods may benefit from being tailored as required. One possible approach was exemplified in this investigation, by using summary statistics as proxies for the complete distribution the change in data as more points are added can be visualised. This allows a much greater understanding of the development and behaviour of the analysis, potentially leading to better methodologies being proposed and justified. Whilst this example has focussed exclusively on Raman analysis there is no reason why such an approach cannot be applied to any other analytical technique that uses single point measurements to sample from a bulk material.

To facilitate this detailed analysis of large Raman data sets, a bespoke computer program for precisely fitting the peaks produced by carbon materials was developed and applied. This was of benefit since it was possible to include an algorithm to systematically check the validity of increasingly complex models using goodness of fit parameters and this program is made freely available at GitHub (https://github.com/SGoldie4/RamanMapAnalysis).

Comprehensive discussion of various carbon materials has revealed the diverse nature of these materials and the behaviour of large data sets whilst also illustrating the value in the detail made possible. Commercial samples, nominally sold with the same name were found to be vastly different in quality and homogeneity, although such findings could easily be missed from single point analysis. Differences in materials following chemical and physical processing were also detected from the reduction of graphene oxide and the exfoliation of graphite. The methodology was applied to synthetic graphene from high temperature growth and carbon nanotubes, although in both cases the need for a nuanced consideration of the material was required. These materials were found to contain some structure at the length scale of the microscope used and therefore required a change in approach following the initial analysis. Such flexibility will likely be required for the metrology of other carbon nanomaterials and is not considered a weakness of the technique.

Finally, the effect of signal to noise was probed. Probably more pertinent to Raman spectroscopy than other techniques, it is important to consider the effect on statistical distributions and the behaviour of data sets as the noise level increases. Whilst perfect

spectra collected over very long time scales are ideal for precise peak fitting that is not feasible for many settings and especially not for any industrial quality control process. Modelling random noise was found to increase the width of the distribution but had little influence on the convergence observed. This is important because the detection of secondary phases and other features of interest often depend on the data set establishing a regular distribution - unchanged as new data points are added. The increased width of such distributions is potentially problematic. Fortunately, it was observed that this usually followed a normal distribution as expected from the random noise between different spectra. Furthermore, the magnitude of this spread in data points was generally found to be less than the distribution of real spectra measured from materials. It is therefore concluded that wide distributions can reliably be attributed to material properties rather than noisy data.

An accepted standard level of nanomaterial analysis has yet to be established, and the level of information required for various quality control purposes must be agreed by many stakeholders. This work aims to inform such efforts and suggests a possible method of analysis. It is hoped a diverse range of properties and characteristics has been well documented and the requirement for such nuanced discussion is clear; and the statistical approaches can be used to further the discussion around nanomaterial metrology and harmonised global standards.

5. Catalytic Graphitization Study

5.1 Introduction

Despite graphene's huge potential, a reliable low cost method of production suitable for real devices is still elusive. Considering exclusively three-dimensional graphene architectures notable applications are energy storage devices such as supercapacitors and battery electrodes or photo and electro-catalysts. [107,114,380,381] The low density, high surface area and high conductivity of graphitic carbon foams are ideal for these applications;[209] unfortunately the controlled production of pore size and graphitic carbon content has not been fully realised. As discussed in chapter 1, self-assembly and growth of 3D graphene foams on metal templates are unsuitable for such applications due to the mismatch of properties, generally poor mesoporosity from CVD graphene foams and reduced conductivity and scalability from self-assembled rGO. The approach focussed on here, that predates the isolation of single layer graphene, uses wet chemistry to self-assemble or otherwise form aerogels containing both carbon and catalyst, which can react under certain conditions to form graphitic carbon.

The metal catalyst can both template the pore structure and graphitic carbon formation. Generally soluble metal salts are used as precursors that are easily mixed with the carbon foam and then undergo carbothermal reduction at high temperatures to form metal particles. Graphitic carbon grows on the metal particles via dissolution-precipitation and by removing the metal from the foam, pores are left in the carbon matrix.[196,252] Previous studies have mixed many different metal salts and carbon precursors but no complete understanding of the foam production has been achieved. As highlighted in the literature review transition metals like Fe, Ni, Co, Cr and Mn all perform very similar roles, producing carbon that is more variable within each metal than between the metals.

Considering the carbon precursors used, almost any carbon based material can in principle be graphitized but the most common approaches make either a dried polymer gel from emulsion polymerisation or related technique as a porous template,[235,236,243,246,251,272] or use biomass based feedstock.[244,247,252,265,269] The use of biomass feedstock in particular is advantageous for scaled up production of functional carbon materials by this method. For relevant devices greater control over the pore structure and morphology must be obtained. The graphitization of biomass foams with metal salts still leaves amorphous carbon unconverted if the catalyst is not completely dispersed throughout the starting foam. This amorphous carbon is responsible for much of the surface area and hierarchical structure, and after oxidative washing nitrogen adsorption was observed to lose hysteresis.[244] Similarly

reduced metal loads were found to increase the surface area but reduce the graphitic carbon content of a fuel cell electrode.[235] This trade-off is significant because energy storage devices like supercapacitors require hierarchical porous structures with both micropores (smaller than 2 nm) to provide high surface areas for charge storage, and meso (>2 nm, <50 nm) and macro pores (>50 nm) to allow electrolyte infiltration and diffusion.[99]

The typical preparation of these materials can be broadly described in three stages: 1) production of a carbon material to be graphitized usually containing catalyst, 2) heat treatment to decompose and graphitize the carbon, 3) washing to remove residual catalyst or other impurities. We have previously demonstrated a wet chemistry approach to preparing a surfactant and sugar based gel that could be burnt and reduced to form a clean metal foam for CVD graphene production.[310] To minimise the complex processing required, it is possible to reduce this carbon based gel in one step, forming metal particles and graphitizing the sugar. This method is therefore used to investigate the role of the metal precursor on the graphitization process; it is hoped that a greater understanding of the role of the metal precursor and reduction process can provide better control of the graphitized material than investigations focussed on the reduced metal chemistry have achieved. Many transition metals are effective at catalysing graphene growth in this way but cobalt nanoparticles are interesting for other applications including water splitting electrocatalysts.[382]

5.2 Results and Discussion

An aqueous dextran/TritonX^{TM}-45/cobalt gel was prepared and freeze dried to form a porous sticky material. This was heated in a mildly reducing atmosphere to generate a carbon and metal foam and then washed with HCl to isolate the final graphene based foam. A dextran based gel was chosen as a starting point because it is simple to produce and the high oxygen content has been linked to an even distribution of cations throughout the structure.[247,383] Hydrated $Co(OAc)_2$, $CoCl_2$ and $Co(NO_3)_2$ were chosen for their availability and high water solubility.

5.2.1 Probing the Carbon Produced

The powder XRD and Raman micro-spectroscopy recorded over a random area of the carbonized materials clearly show the significant effect the cobalt has; the metal free control is exclusively amorphous carbon as shown by the broad XRD scattering centred around 10.5° in Figure 84, with no clear peak discernible and lack of a 2D Raman peak in Figure 85.[364] In

contrast the cobalt containing materials show signs of graphitic domains within the structure giving rise to the strong 002 in-plane reflection in the XRD pattern and a 2D Raman signal, attributed to the resonant scattering from the sp^2 network in graphene sheets.[384] Despite this, the carbon materials produced using different cobalt salts as catalyst precursors have different degrees of graphitization. The XRD patterns (Figure 84) show some common features but the differences between the carbon produced remains clear; the common features across all diffraction patterns are the broad 002 and 004 reflections around 11° and 20° measured with a Mo source, λ = 0.7093 Å. It can be concluded that all materials have formed layers at high temperatures even without metals but these layers lack long range order and regular stacking, causing the broad diffraction signal. The inclusion of the metal salts produces much more crystalline graphene layers seen by the sharp reflections observed from those samples.

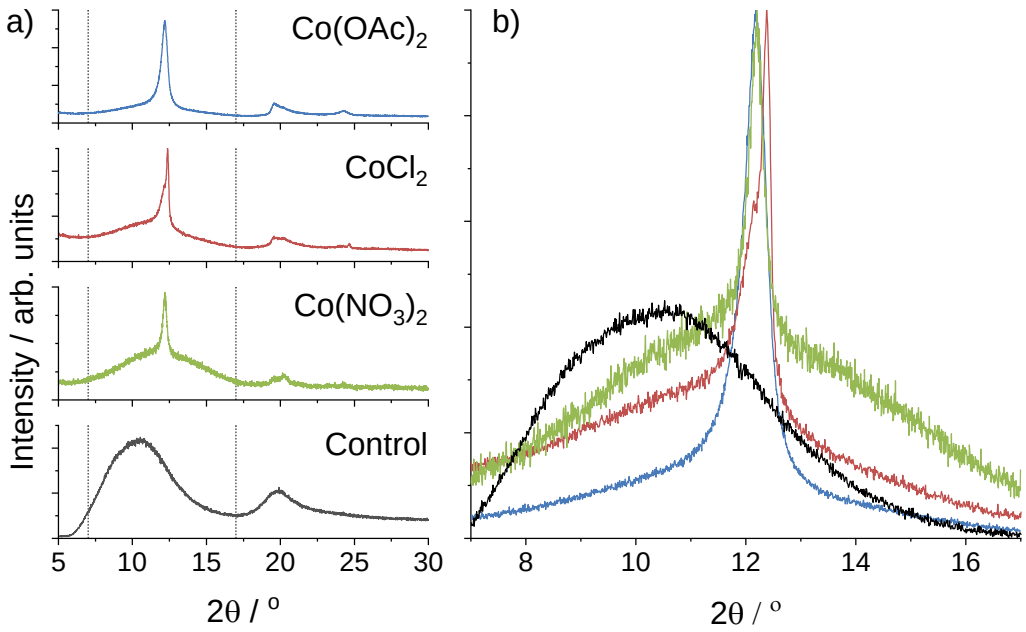

Figure 84: Powder XRD data from the carbonized materials recorded with a Mo source (λ = 0.7093 Å) showing crystalline graphite; a) shows full range diffraction patterns from the carbonized materials following acid washing to remove metal. The dotted lines denote the region of the 002 carbon peak. Data from this region is shown in b) taken from the material before acid washing focussed on the graphite 002 peak. Peak intensities have been normalised, whilst the metal free control is shown with reduced intensity for clarity.

Whilst these signals from the metal catalysed graphitized carbon are sharp in comparison to amorphous carbon, this diffraction reflection is still relatively wide indicating disordered crystallites of graphite layers. This relative width and poor signal to noise prevents any useful information from being realistically extracted from the 004 peak but the 002 peak still provides information on the carbon formation. It should be noted the $Co(OAc)_2$ and $Co(NO_3)_2$

catalyst precursor samples have a single peak whereas the reflection condition observed from the $CoCl_2$ derived sample appears to contain the same wide reflection but also a sharper peak at slightly higher 2θ.

To understand the XRD profiles of the different carbon materials produced it is useful to consider the work on graphitization models summarized by Ōya and Marsh and discussed in detail in the introduction. The $Co(OAc)_2$ and $Co(NO_3)_2$ derived samples produced materials that can be easily described by the T_s-effect graphitization. This is a model of graphene growth from very small finely distributed metal particles tens of nanometers in size. The exact growth mechanism from these particles is uncertain although it is likely dissolution-precipitation of the carbon, at high temperatures, is responsible for the growth of turbostratic carbon on their surface. This graphite lacks three-dimensional order, instead forming layers of graphene material that do not have any consistent stacking with the surrounding matrix. This form of graphite growth is reported to exhibit a wider XRD profile with a larger apparent interlayer spacing than graphite formed from G-effect.

G-effect graphitization is generally found in multi-phase carbon materials in which crystalline graphite is formed on the surface of larger metal particles within a matrix of disordered carbon. This growth mechanism is reported from particles larger than 100 nm and has an XRD profile with a sharper graphite 002 peak due to the ordered stacking, and is generally observed at a slightly smaller apparent interlayer spacing. Considering these trends in XRD profile, the carbon produced by high temperature carbonization with no metal present is described as amorphous carbon with no long range order or layer stacking, preventing a clear peak being detected from the powder diffraction pattern. The other samples prepared with metal present during the graphitization process have a higher background around the 002 reflection, but it does not match the amorphous signal. All three samples do, however, show the wider 002 reflection expected from the T_s-effect graphitization where some graphitic material is formed. This signal clearly dominates in the $Co(OAc)_2$ and $Co(NO_3)_2$ sample whilst the $CoCl_2$ derived sample has another sharper reflection 0.2^o greater than the other wider peak. This is attributed to the G-effect graphitization, the difference in peak position of 0.2^o as measured with a Mo x-ray source (0.7093 Å), while small, agrees with the reported shift of 0.5^o when measured with Cu radiation (1.5406 Å).

This data suggests the metal formed from the initial salt is necessary for the graphitization process although different salts form different carbon phases. The $Co(OAc)_2$ and $Co(NO_3)_2$ derived samples contain domains of turbostratic carbon but regular graphitization. In

contrast the $CoCl_2$ is expected to be a mixed phase material with some more disordered carbon and some high quality graphite domains grown on larger metal particles.[188]

These different graphitization models also fit with the Raman data measured, shown as 3D bivariate histograms in Figure 85. These histograms show the distribution of two key metrics derived from the peak intensity ratios. I_D/I_G is indicative of the defects present in the material since the D peak is activated by breaks in the aromatic carbon structure and I_{2D}/I_G is indicative of the long range order of the system and graphene thickness. The 3D histogram shows the relative population of different peak ratios, light colours indicating more populated bins so the peak ratios described by both axes were very common whilst the dark regions indicate very few spectra with such a combination of peak heights.

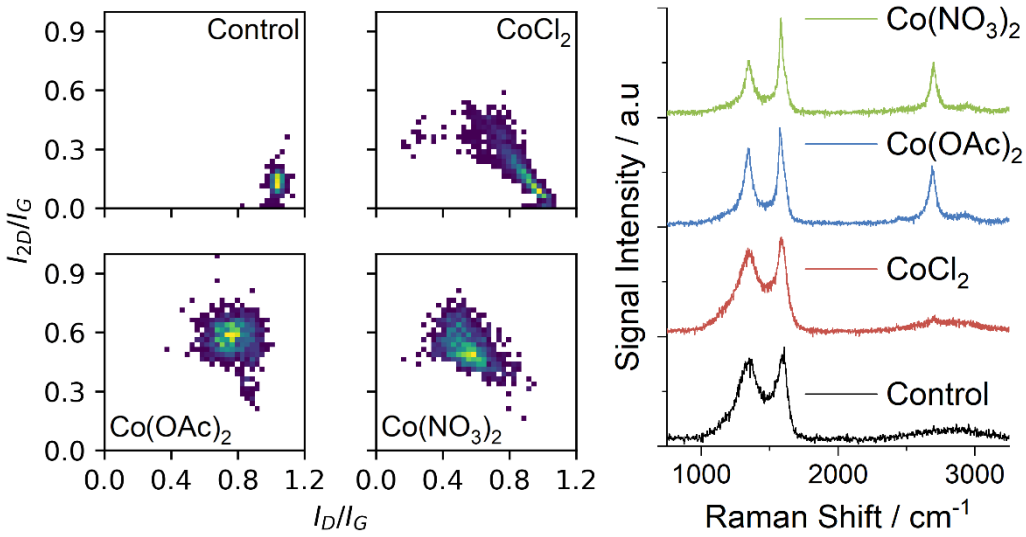

Figure 85: 3D bivariate histograms displaying Raman map data from carbonized samples derived from salts labelled; graphitic I_D/I_G and I_{2D}/I_G peak intensity ratios are shown on each axis and frequency shown as heat map. Representative spectra taken from the most populated area of the histograms are shown to the right.

The amorphous carbon produced from carbonization with no metal present has a high I_D/I_G ratio of 1.0 indicating there are aromatic rings present but many defect sites are bonded to them and they lack any long range order hence the very low 2D signal, producing a histogram entirely populated in the bottom right corner of the plot. A representative spectrum is also shown in Figure 85, which is consistent with the most populated bin in the histogram, and this clearly shows the wide D and G peaks as expected from amorphous carbon whilst the 2D peak is part of the wide feature to the right of the spectrum. This broad hump is actually a result of the wide 2D peak and D+G peaks combining together; but this feature is also why the 3D histogram shows a very small I_{2D}/I_G ratio despite there being no distinct 2D peak present in the spectra shown.

The $CoCl_2$ derived sample also has a large population with the same characteristics, I_D/I_G around 1.0 and a very low 2D peak but there are a small number of spectra more consistent with graphite visible. Graphite is expected to have a I_{2D}/I_G value around 0.4 and a lower I_D/I_G depending on the crystallinity of graphite flakes. These spectra were unusual in the large data set collected, but a clear concentration of purple bins indicating low numbers of spectra with those features were recorded. The presence of a minor fraction of graphite is in keeping with the G-effect graphitization suggested, where large metal crystals aid the formation of quality graphite around themselves whilst leaving the carbon matrix largely unaffected.

In contrast the $Co(OAc)_2$ and $Co(NO_3)_2$ derived materials have a much more homogenous distribution of spectral features seen from the more symmetrical shapes in the 3D histogram. These plots, in particular the $Co(NO_3)_2$ sample, also highlight the utility of viewing both peak ratios simultaneously, the symmetrical shapes mean that conventional 2D histograms for that material would follow normal distributions indicating random scatter; where in fact there is a slight inverse correlation between the relative intensity of the D peak and the 2D peak. This is entirely expected given the nature of the material being measured, it would be expected that some regions contain smaller flakes with more defects disrupting the sp^2 network and producing smaller I_{2D}/I_G and higher I_D/I_G values whilst other regions are more graphitized and have the opposite trend. Overall the spectra from the $Co(OAc)_2$ and $Co(NO_3)_2$ derived samples are consistent with defective and strained graphene like materials and typical spectra of these samples are also shown in Figure 85. The I_D/I_G is substantially lower than amorphous carbon for both salts whilst the I_{2D}/I_G is higher than would be expected from graphite suggesting the graphene layers produced are thinner than bulk graphite materials. This production of small but well graphitized domains within the material is consistent across both the XRD and Raman analysis.

Thermal gravimetric analysis further supports these findings of different carbon phases from samples with different salt precursors. TGA was completed in an inert nitrogen atmosphere and air, the air is most informative since the combustion temperature of carbon materials depends on the crystallinity and aromaticity, more defective materials combust more readily than crystalline graphitic carbon. TGA in an inert atmosphere can be used to identify functional groups or sorbates that can are not thermally stable; in this case every sample was dried in a vacuum oven before analysis to minimise the mass loss caused by water. Upon heating under nitrogen all samples had very little mass loss even at 1000 ^oC as shown in Figure 86b; this confirms the production of pure carbon materials with very few functional groups present since oxygen, nitrogen or chloride containing groups would not be thermally

stable to high temperatures. The approximately 10% mass loss observed from any samples is attributed to residual air and water within the material and trace functional groups.

Table 6: Thermal gravimetric analysis data in an air flow showing the combustion onset temperature and maximum combustion rate temperature for each sample. For further information on the calculation of these parameters see Chapter 3 and derivative plots in Figure S 223.

Sample	Onset Temperature / °C	Inflection Point / °C
$Co(OAc)_2$	625	675
$CoCl_2$ amorphous	580	625
$CoCl_2$ crystalline	650	700
$Co(NO_3)_2$	350	625
Metal Free	580	645

Thermal stability with respect to combustion is more informative for the carbon material produced and the key parameters are summarised in Table 6. The metal free control samples produced amorphous carbon with combustion consistent with reports of sooty carbon.[341] The $CoCl_2$ derived sample shows two distinct phases as expected from the Raman and XRD data, one an excellent match with the amorphous carbon control as seen from the two very close lines in Figure 86a and almost identical onset temperature around 580 °C and similar inflection point at 625 °C; the second phase present from the $CoCl_2$ sample can be seen as a tail on the TGA plot, this is also shown more closely in the insert, and is a good match with the graphitic carbon formed from the $Co(OAc)_2$ precursor. The carbon produced from the $Co(OAc)_2$ precursor exhibits a single clean combustion process, whilst lower temperature than graphite this is higher than amorphous carbon and entirely consistent with small domains of graphitic carbon.[341,342]

The minor fraction of graphite formed from the $CoCl_2$ precursor is more stable than the few layer graphitic domains produced from the other salts as would be expected from high quality graphite. The small tail visible only represents 9% of the mass burnt, however, the onset temperature of 650 °C and inflection point of 700 °C is higher than the other materials. Finally the carbon produced from the $Co(NO_3)_2$ would be expected to perform similarly to the $Co(OAc)_2$ since both sets of data have been very consistent and predict very similar growth mechanisms. Unfortunately this sample still contains nanoparticles that could not be removed with washing. These account for the 5% mass remaining after combustion and were

confirmed with electron microscopy; more significantly for thermal analysis these residual nanoparticles are known to catalytically aid the combustion of carbon materials which leads to the early onset.[243] Whilst the nanoparticles reduce the onset temperature the inflection point, or rate of maximum combustion is more consistent with the graphitic carbon formed from the $Co(OAc)_2$ salt.

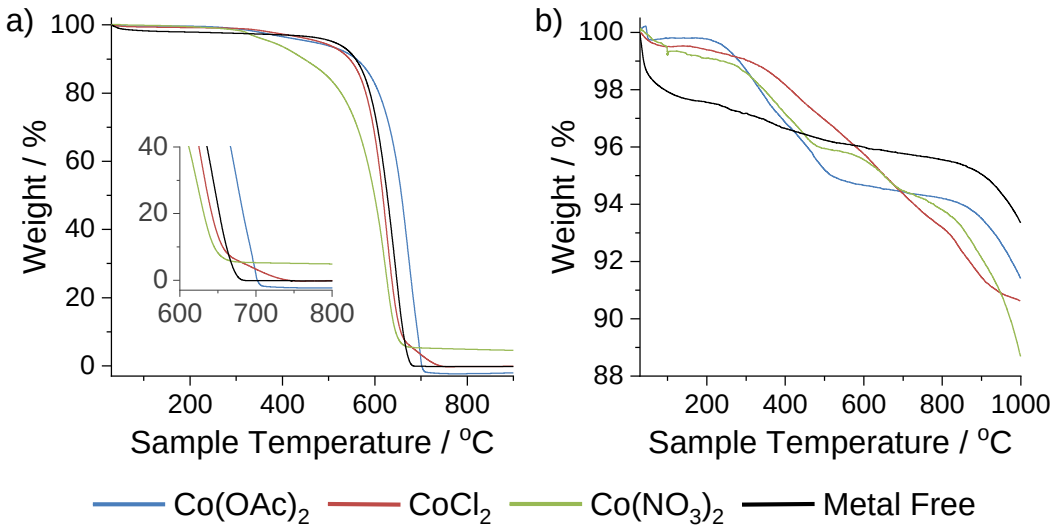

Figure 86: TGA mass loss profiles of all carbon foams, after acid washing, produced by graphitization with the metal salt listed in the legend, a) recorded in air showing combustion of carbon with a zoomed insert of the final combustion process, b) recorded in nitrogen showing decomposition of functional groups. Samples were pressed into pellets and heated at 10 °C/min.

5.2.2 Viewing the Metal Particles

The previous section discussed the formation of graphitic carbon at high temperatures around metal particles. These metal particles are formed by the carbothermal reduction of the salts dissolved into the sugar gel, however, the actual metal particles formed are different in every case.[246,248,269] Electron micrographs of the carbonized materials show these differences very clearly. When $CoCl_2$ is used as a precursor the metal is found in large, highly crystalline particles microns in size, far larger than the 100 nm reported to be the threshold for G-effect graphitization. These are decorated over the surface from which graphite layers can grow following a dissolution-precipitation mechanism.[196] EDX mapping (Figure 87b) highlights the metal content concentrated into the crystals whose sharp edges and regular shapes indicate high crystallinity, a feature supported by the clear XRD pattern (Figure 88) obtained from the carbonized material before acid washing. Further imaging after acid washing (Figure 87c & 4d) reveals the carbon shells grown on the metal surface can actually maintain their structure even after the metal is removed from inside. Furthermore these images show the crystallinity and thin nature of the graphite grown; even after removal of

the metal sharp edges and smooth surfaces can be seen. At higher beam energy there is also significant electron transmission observed through the thin carbon; it is not possible to resolve truly few layer graphene as the contrast would be too small in SEM imaging of this nature, however, the translucent appearance indicates the carbon grown form the metal is likely 100s of nanometres thick.[385]

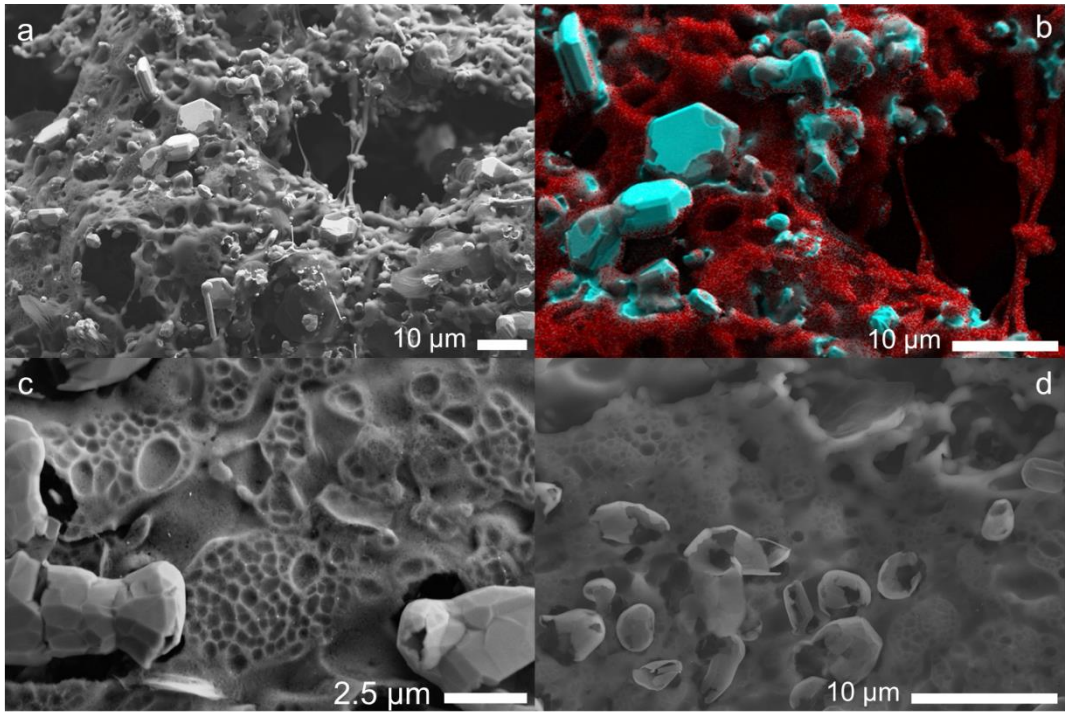

Figure 87: Scanning electron micrographs of $CoCl_2$ derived foam after carbonization. a) Carbonized foam before acid washing showing metal particles; b) composite SE image and EDX map showing cobalt (blue) and carbon (red) distribution; c) SE image after acid washing showing carbon shells (imaged at 4 kV); d) SE image after acid washing showing carbon shells, the higher energy electrons partially transmit through the thin graphite shells producing the translucence appearance.

It might be expected that a complete carbon coating of the metal would protect it from reacting with the acid but this was shown not to be the case. XRD diffraction patterns contained no peaks from Co (Figure 84) and thermal analysis produced no residual mass from metal oxide (Figure 86). The carbon growth, even on highly crystalline metal particles, is therefore a combination of different crystallites, probably growing simultaneously on every face and producing a series of cracks and joins between them. The cracks and gaps observed by SEM in the carbon shell support this incomplete carbon growth from the metal that allows acid penetration and removal of the metal particles.

Powder XRD was also used before the carbonized materials were acid washed, when they still contained the metal particles, to probe the different environments the metals are found in (Figure 88). The indexing was confirmed by Rietveld refinement of the XRD data, shown in

Figure S 220 - 222. The first observation is the difference in signal intensity between the different samples; the Bragg intensities being correlated to the amount of crystalline material present. While samples were not prepared for quantitative analysis, this suggests the $CoCl_2$ derived sample contains more crystalline metal than the $Co(NO_3)_2$ derived foams. Approximately the same quantity of material was packed into the capillaries used for each measurement, and in every case the powder was prepared by grinding the solid free standing foam in acetone before drying and pouring into the capillaries. This observation is consistent with observations from handing the samples, the $Co(NO_3)_2$ derived carbon foam was a lower density material whilst the other samples handled more like conventional powders.

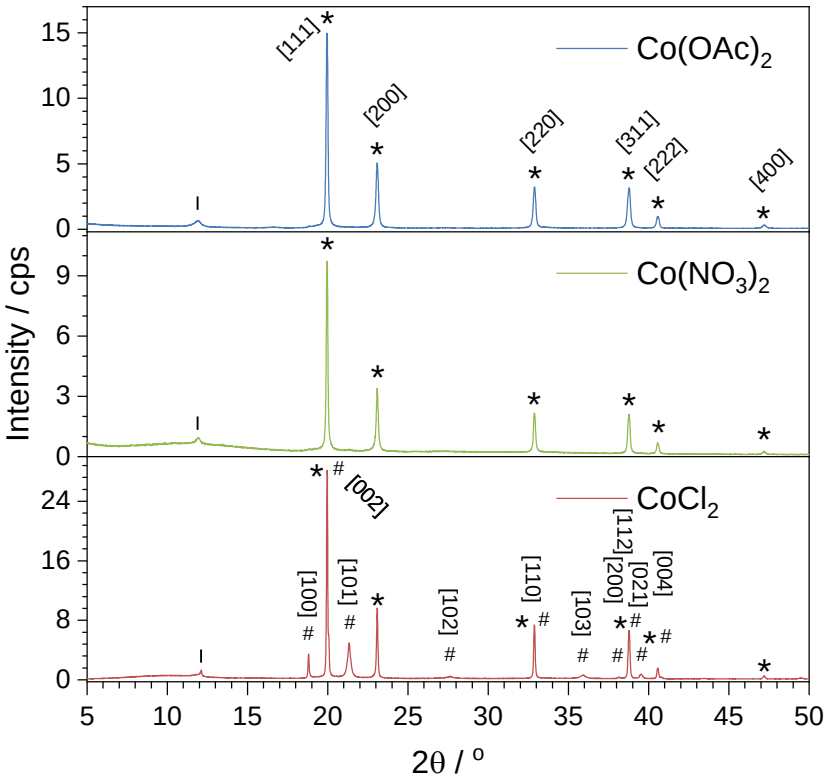

Figure 88: Powder XRD patterns of carbonized foams containing Co metal produced in-situ; $Co(OAc)_2$ and $Co(NO_3)_2$ salts produced metal with exclusively ccp reflections (*) indexed in the top pattern. The $CoCl_2$ salt produced both hcp (#) and ccp (*) phases with only hcp peaks indexed.

Considering the metal formed from the $CoCl_2$ precursor, this sample produced sharp peaks in the diffraction pattern from both hexagonal and cubic crystal systems whereas the cobalt formed from the in-situ reduction of $Co(OAc)_2$ and $Co(NO_3)_2$ is only found with the face centred cubic structure. Published investigations on the reduction and crystal structure of cobalt metals have found that reduction from cobalt salts generally goes through CoO which then reduces into the metal and anneals into crystals at elevated temperatures.[386–388] The crystal system the metal adopts is dependent on the particle size; at high temperatures the

cubic ccp structure is the most thermodynamically stable but as the metal cools the hcp structure becomes more favourable. In contrast, small particles such as those found suspended in a supporting matrix maintain the ccp structure;[386–389] this phenomenon has been observed from cobalt foams[389] and nanoparticles deposited on alumina structures.[387]

Using electron microscopy to investigate the microstructure of the carbon materials produced from the $Co(OAc)_2$ and $Co(NO_3)_2$ metal precursors supports these conclusions as seen in Figure 91; metal nanoparticles are found to be evenly distributed throughout the carbon matrix hence the ccp crystal structure detected by XRD. This is also consistent with the T_s graphitization mechanism predicted from the carbon analysis. In contrast the $CoCl_2$ derived sample contained both hcp and ccp metal found from small particles supported by the carbon matrix; but also large crystalline metal particles of sufficient size to anneal and revert to the more thermodynamically stable hexagonal form. These large particles would be expected to exhibit G-effect graphitization as observed from this sample.

SEM images show some small nanoparticles decorated over the wispy carbon produced from the $Co(NO_3)_2$ sample, which are confirmed to be cobalt with EDX mapping, although no nanoparticles were clear on the $Co(OAc)_2$ sample because of the resolution limit of the SEM. 10 kV electrons are required to excite core shell electrons and produce a x-ray signal from the cobalt, unfortunately the interaction volume at this energy is larger than the smallest nanoparticles. TEM does show spherical nanoparticles of uniform size present throughout the carbon material as well as empty spaces of very similar sizes (Figure 91d). Analysing multiple images reveal a consistent distribution of nanoparticle diameters, the images used are in Appendix 9.2.3. The nanoparticle sizes from the $Co(OAc)_2$ sample are shown in Figure 89; these particles formed within the carbon matrix are around 1.5 – 4.5 nm in diameter.

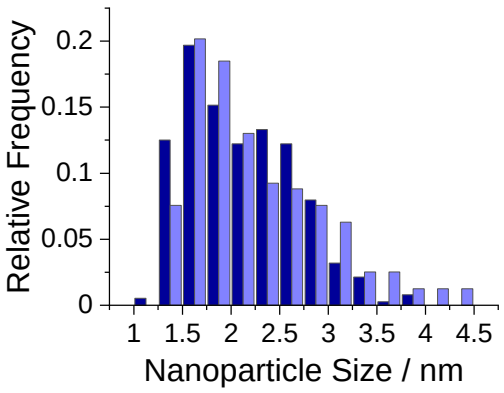

Figure 89: Histogram of the particle size distribution as measured by transmission electron microscopy showing the particle size measured from the sample derived from $Co(OAc)_2$.

The $Co(NO_3)_2$ reduced into larger particles as expected from the SEM images and TEM analysis revealed two different types of nanoparticles formed. Spherical particles very similar to those found from the $Co(OAc)_2$, only slightly larger, and a number of much larger nanoparticles around 60 nm in diameter of irregular size. The size distributions of these are shown in Figure 90. Whilst these particles were observed to be different sizes, the majority remained below the 100 nm approximate size at which G-effect graphitization occurs.

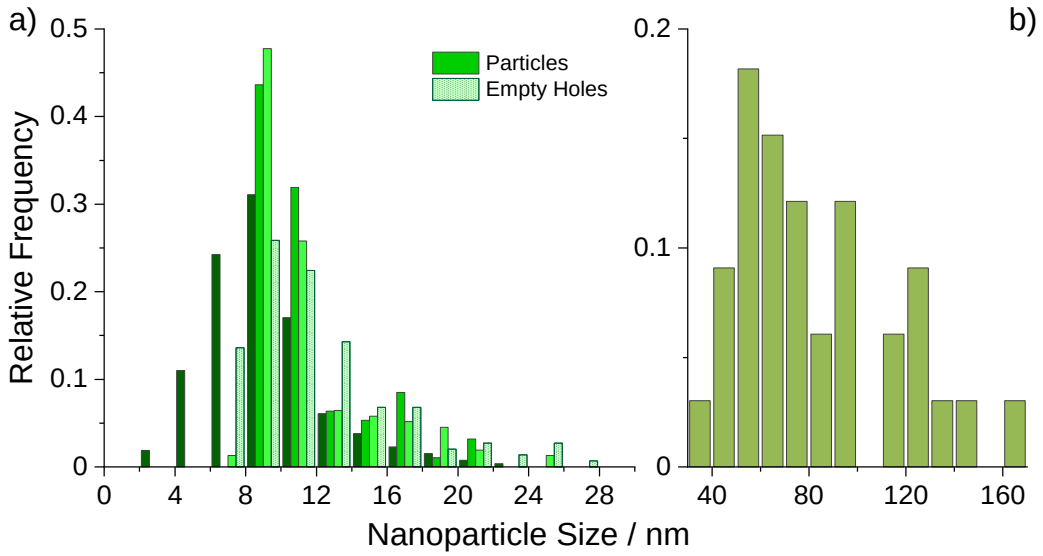

Figure 90: Histograms of the particle size distribution as measured by transmission electron microscopy from the sample derived from $Co(NO_3)_2$. a) Smaller nanoparticles and the empty voids left after washing whilst b) shows larger nanoparticles from a different image.

The impact of these nanoparticles on carbon graphitization has been studied and generally the same dissolution/precipitation mechanism is thought to be responsible for carbon growth on both large metal surfaces and smaller metal particles. The significant curvature of the metal nanoparticles, however, can induce strain in the graphite sheets or cause incomplete coverage.[196,251] The HRTEM images of the carbon around these particles and left behind after removal support these conclusions (Figure 91d); lines are observed in circles around the particle sites indicating graphite layers grown outwards before forming a larger matrix of graphitic carbon domains crosslinked together. Similar patterns have been observed from other systems and the term 'carbon onions' has been proposed to describe these smaller layered spheres of carbon grown from small particles.[390] Carbon nanotubes grown as the metal particles migrated through the carbon, leaving the nanotube extruded behind, would also be expected from a system of this nature. Whilst no nanotubes were observed from the EM images studied, and Raman analysis revealed no low Raman shift signals characteristic of nanotubes their presence cannot be completely discounted.

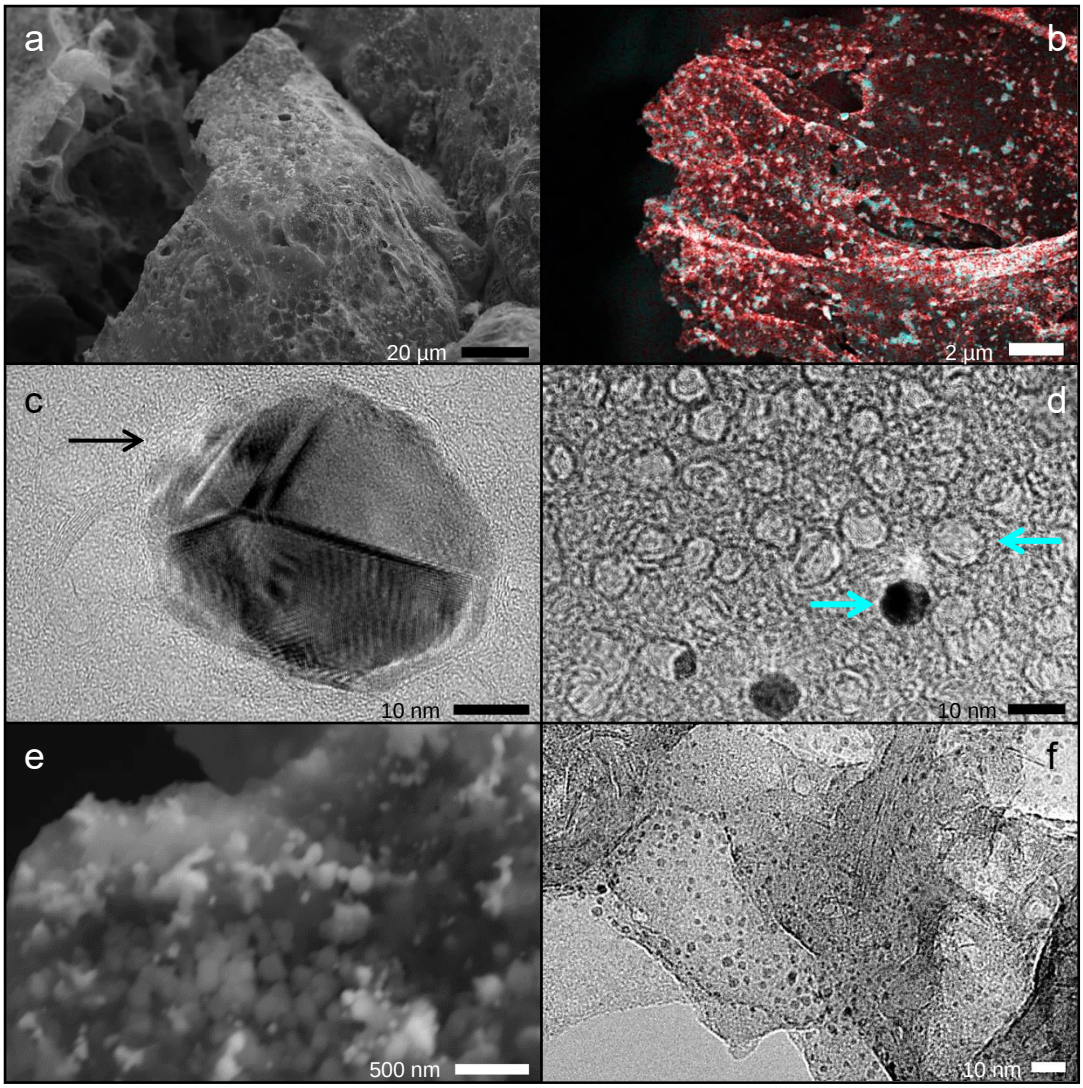

Figure 91: Electron micrographs of the carbonized foams produced from: a-d) $Co(NO_3)_2$ and e-f) $Co(OAc)_2$ salts. a) SEM with metal present, b) composite secondary electron image and EDX map showing cobalt (blue) and carbon (red) distribution, c) HRTEM image of a single metal particle with carbon growth visible around the edge, d) HRTEM image showing nanoparticles and the vacant sites left by other particles highlighted with arrows, e) SEM image of carbon surface with metal present, f) TEM of carbon sheets with nanoparticle observed on the surface.

The tight curvature of the carbon onions produced and small particle size prevented any accurate layer counting. Discrete lines were observed around the larger metal crystals but considering the highly crystalline nature of those structures the fringes observed may be a result of the electron beam undergoing diffraction through the metal crystal. The clear dark lines and wavy pattern within the metal particle on Figure 91c are a clear example of this effect and the fringes highlighted with the arrow are more likely diffraction fringes than carbon layers. To investigate the crystallinity of the carbon produced around these particles a selected area electron diffraction (SAED) pattern was collected from the acid washed sample, $Co(NO_3)_2$, to prevent the interference of metal. SAED collects the diffracted electrons

passing through a specified area of the sample, in this case the carbon region shown in Figure 92. The diffracted electrons can then be indexed according to Bragg's Law. The pattern produced shows clear rings that can be indexed to the [002], [101] and [110] diffraction angles of graphite; with a very faint hexagonal pattern of spots visible. The spots indicate that crystalline graphite layers are present but the clearer and more significant diffuse rings are caused by randomly oriented graphite crystallites. They collectively diffract electrons with a specific angle from the electron beam, producing a circle on the detector, but the random orientation of the crystallites causes the diffuse rings in place of well-defined spots.

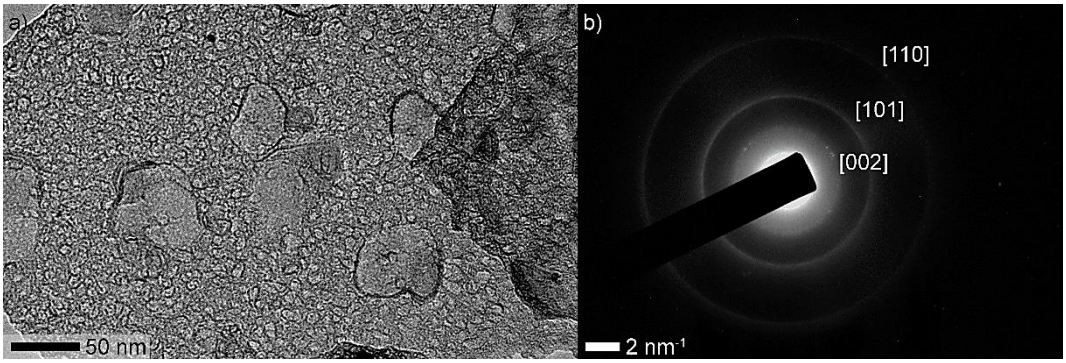

Figure 92: a) Electron micrograph of graphene growth around metal nanoparticles removed by acid wash from $Co(NO_3)_2$ sample and b) the SAED pattern in the region shown with three rings visible and indexed to graphite.

5.2.3 Analysis of Surface Area

The overall morphology of the carbonized materials is also expected to vary with the cobalt salt used to form the catalytic metal particles since the carbon growth and handling characteristics of each material were distinct. SEM images of the foam taken with a lower magnification viewing a wider sample area show this clearly; the carbon produced from the $CoCl_2$ sample seen in Figure 87 is formed from porous amorphous carbon with large metal crystals decorated over the surface. Curiously at low magnification the carbon from the $Co(OAc)_2$ precursor appears to be a very similar irregular mass of carbon with large pores visible 10 s to 100s of microns in size running through the carbon , shown in Figure 93. The $Co(NO_3)_2$ salt reduced into metal particles, however, the carbon produced is much lower density, containing many fibrous elements holding a much more open structure together.

It was expected that coverage of the metals by inert carbon would impede their removal by mineral acids. However, the foam produced from the reduction of $CoCl_2$ was not impacted due to cracks and gaps within the carbon; in contrast the $Co(NO_3)_2$ precursor formed smaller nanoparticles that were completely covered. This protected some of the nanoparticles from the acid wash; there was a 8 wt.% difference between the expected cobalt content and actual

mass reduction following HCl washing. In addition even after acid washing metal particles were observed in the TEM images (Figure 91d) and the thermal analysis shows a 3.8% residue at 1000 °C (Figure 86) and catalytic combustion at lower temperatures.[243,263] The discrepancy in mass is likely due to slight water content in the thermal analysis increasing the original measured mass and reducing the relative proportion of metal. In contrast the $Co(OAc)_2$ reduction produced very small nanoparticles that could freely migrate out of the structure; gentle dispersion in ethanol was sufficient to remove these and TEM found the otherwise clean carbon grid decorated with metal nanoparticles.

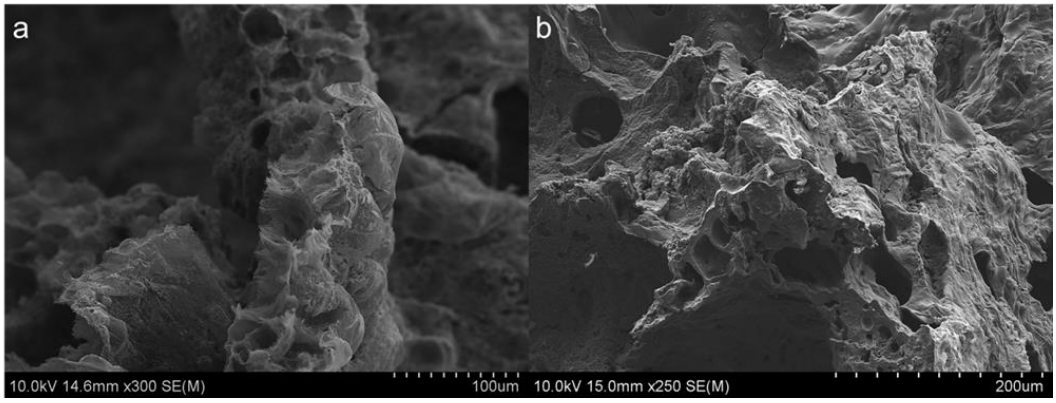

Figure 93: Low magnification SEM images of a) $Co(NO_3)_2$ based foam and b) $Co(OAc)_2$ based foam showing the difference in morphology.

To probe the microstructure produced in these carbon materials gas sorption analysis was performed with isotherms shown in Figure 94. The small nanoparticles and porous structure of the $Co(OAc)_2$ has the highest BET specific surface area as measured by N_2 adsorption (Table 7), although the anomalously high reading before any washing was probably caused by removal of the nanoparticles during the sample preparation, which required gentle crushing of the bulk material in ethanol to produce uniform powders. It was hoped this would make internal pore space equally accessible across all samples, given the $Co(NO_3)_2$ sample was brittle and crumbled during routine preparation. The free migration of particles from the $Co(OAc)_2$ derived carbon before acid washing was in contrast to $Co(NO_3)_2$ with a BET surface area of 39.18 $m^2 g^{-1}$ before washing but increased substantially to 103.3 $m^2 g^{-1}$ after, despite the wash step being insufficient to removal all the nanoparticles. The smallest change upon removal of the metal was the $CoCl_2$ sample, probably due to the large nanoparticles covered in smooth graphite crystallites that will contribute less to the surface area than the amorphous regions.

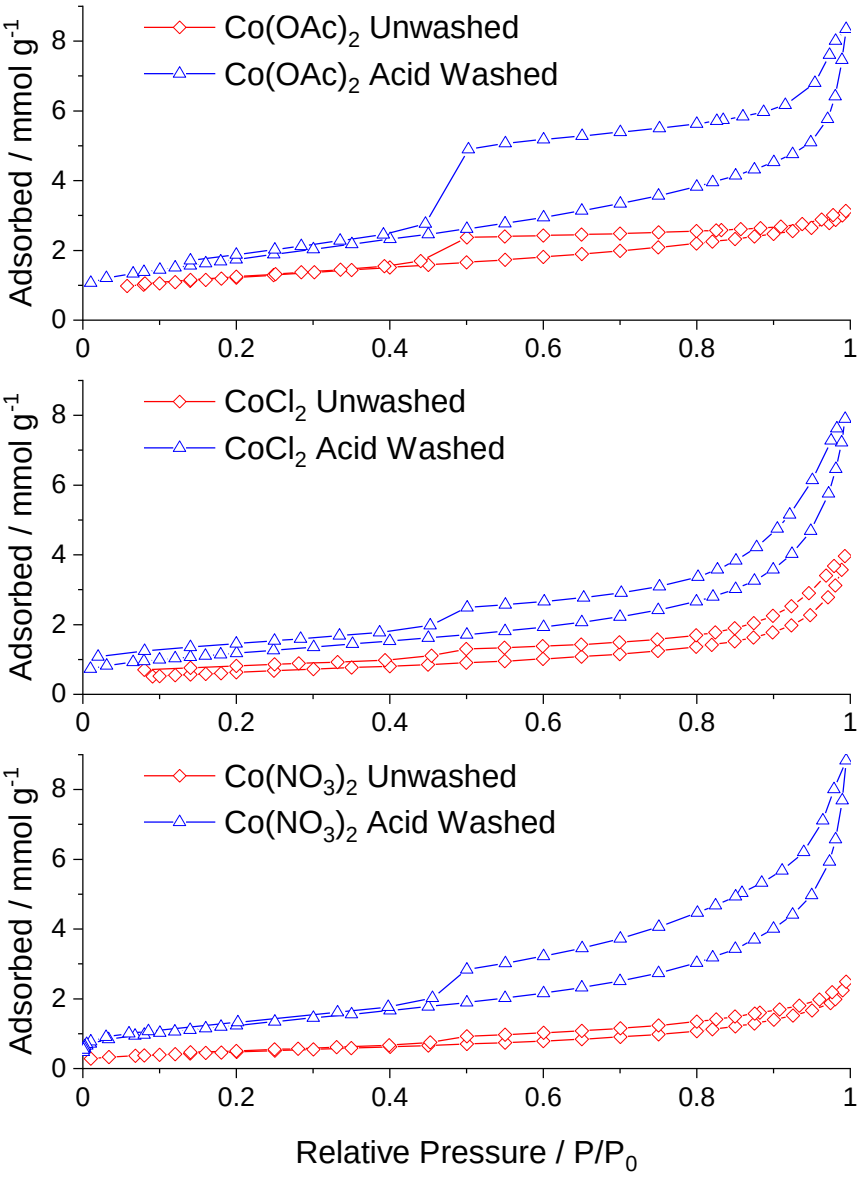

Figure 94: N_2 isotherms of all three materials before acid and after washing in 6M HCl.

The N_2 isotherms show a significant hysteresis in every case, although this effect is greatest in the $Co(OAc)_2$ derived sample. This hysteresis is consistent with liquid nitrogen trapped in internal pore areas accessible through narrow channels, likely produced by the nanoparticles within the carbon matrix. These internal pore spaces hold nitrogen which cannot escape even as the pressure decreases because of the capillary force of the liquid nitrogen in the access channels. Eventually the pressure decreases sufficiently to overcome the capillary forces and the entire internal volume of nitrogen is released. The hysteresis of the $Co(NO_3)_2$ sample is less and the SEM images show a more fibrous network with metal particles trapped in the carbon (Figure 91b), consistent with a small internal surface area. Nitrogen sorption of the amorphous carbon produced with no metal present failed to stabilize because the

volume of nitrogen adsorbed onto the surface was too low. Whilst Raman data indicates the $CoCl_2$ derived samples also contains a significant fraction of very similar amorphous carbon, there is a clear porosity and slight hysteresis in contrast to the smooth glassy carbon formed without the metal present.

Table 7: BET surface areas of the different foams produced from carbonization and the same foams after washing in HCl, fitted with BET model from nitrogen adsorption data.

Cobalt Precursor	**Surface Area / m^2 g^{-1}**	
	Carbon & Metal	Acid Washed
$Co(OAc)_2$	96	144
$CoCl_2$	52	96
$Co(NO_3)_2$	39	103

Combining the numerous methods of analysis focused on the carbon produced, metal particles and overall morphology of the carbonized carbon, clear conclusions can be drawn about the nature of the graphitization in each case. With no metal present the dextran decomposes into amorphous carbon, there is no order to the structures formed and the Raman spectra are consistent with aromatic domains randomly spread throughout the material. This randomly disordered carbon has no micro-porosity and the SEM images show a smooth glassy carbon. The addition of $Co(OAc)_2$ produces nanoparticles of crystalline cobalt, around 2 nm in diameter randomly distributed throughout the carbon matrix. These promote graphitization around themselves, producing a graphitic carbon that lacks substantial long range order but has a distinct 002 layer stacking XRD reflection. These nanoparticles produce narrow channels through the material with high specific surface area.

The $Co(NO_3)_2$ salt resulted in a very similar structure of nanoparticles scattered throughout the material; these produced a very similar graphitization of smaller strained graphite crystallites with little long range ordering. The nanoparticles from this salt were larger, however, and the carbon morphology was quite different. Fibrous carbon interlinked and produced a macro-porous structure as seen with the SEM but containing fewer micro-pores and small channels. Finally the $CoCl_2$ produced larger highly crystalline metal particles that grew large graphite flakes across their surface; these graphite flakes were still thin and disordered with respect to their neighbours but the layer stacking and crystalline domains were much more like graphite. Despite these large graphite flakes dominating, evidence of some smaller nanoparticles within the structure can be inferred from the XRD pattern

consistent with both G-effect and T_s-effect graphitization and the specific surface area measured form the $CoCl_2$ derived sample.

5.2.3 Role of Metal Reduction

To explain the difference in material properties from graphitized dextran using different cobalt precursors dissolved in the gel, the reduction of the cobalt salts in a mixed hydrogen-argon atmosphere was investigated with thermal analysis (Figure 95) coupled to mass spectrometry. The exact ratio used for the thermal analysis (5% H_2) was not the same as the gas mixture used for graphitization (1% H_2) but this difference in gas composition was not thought to be significant. The influence of hydrogen concentration is reported to only be significant approaching a pure H_2 gas flow, and in both cases here the H_2 remained diluted.[388] It was also not possible to replicate the complex carbon environment, in practice the reduction of the metal salts is likely to occur via a carbothermal reduction with the surrounding carbon acting as a reducing agent. Despite these limitations significant insight to the reduction process of these metal salts can be achieved.

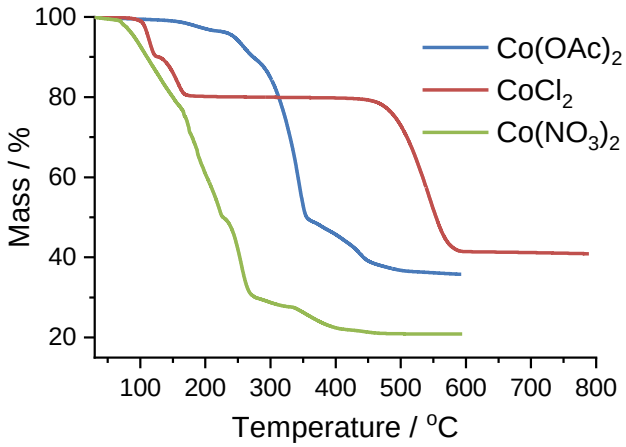

Figure 95: Thermal analysis of metal salts used in preparation of carbon foams, completed in a reducing atmosphere.

$CoCl_2$ is a very stable salt, upon heating the first process is the loss of water in two steps (20% mass) followed by a prolonged stable phase before the reduction of the salt rapidly in the temperature range 450°C – 600°C (39%). The initial loss of water is difficult to stoichiometrically account for exactly. The hexahydrate salt was dried in a vacuum oven into the dihydrate salt before analysis but since sample handling and preparation was not undertaken under a protective atmosphere; some additional moisture would be expected given the hygroscopic nature of $CoCl_2$. During the higher temperature rapid mass loss a

significant spike is observed for ions of mass 36 u ($H^{35}Cl$) and 38 u ($H^{37}Cl$) in the waste gas flow indicating that the salt reduces directly into elemental metal and HCl gas.[391]

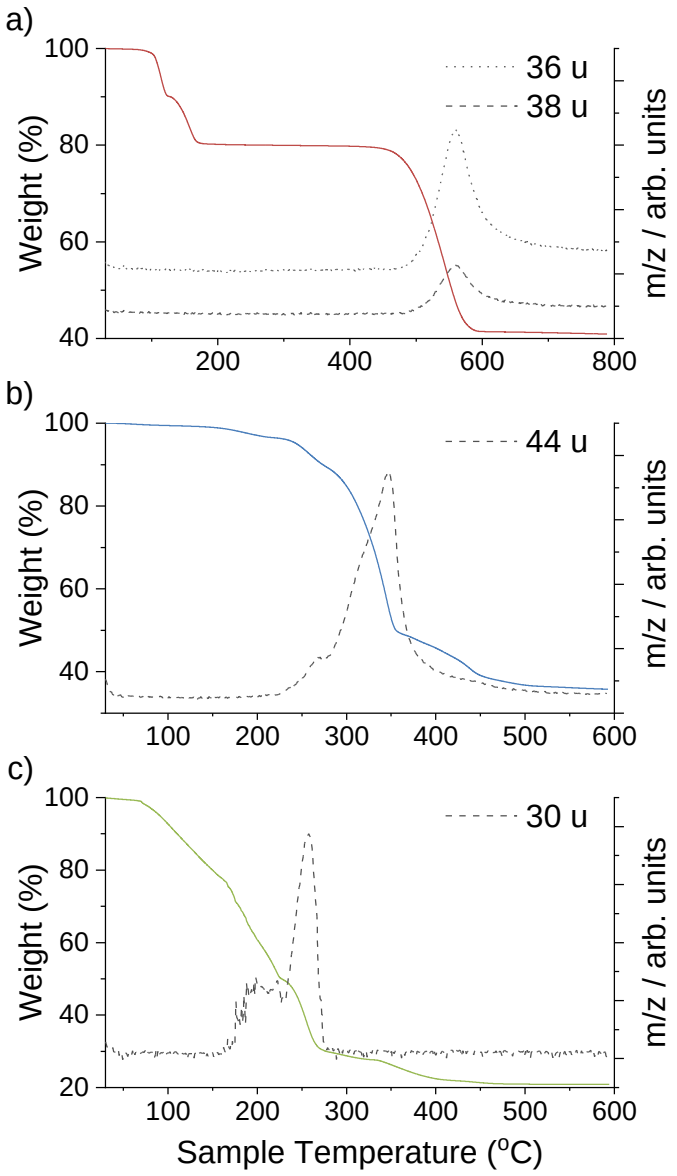

Figure 96: Thermal gravimetric analysis in a 5% H_2 atmosphere of the three cobalt salts studied shown as solid lines; mass spectrometry intensity of specific mass ions in the waste stream shown as dashed and dotted lines. a) $CoCl_2$, b) $Co(OAc)_2$ and c) $Co(NO_3)_2$; 36 u = $H^{35}Cl$, 38 = $H^{37}Cl$, 44 u = CO_2, 30 u = NO.

$Co(OAc)_2$ undergoes a straightforward reduction with an onset around 250°C and a peak mass loss at 350°C producing a corresponding signal for ions of mass 44 u (CO_2) and forming a residue 36% of the initial mass, consistent with almost total reduction to cobalt metal as reported elsewhere.[392] This data suggests the salt rapidly decomposes into gaseous by-products and the reduced metal. The reduction of $Co(NO_3)_2{\cdot}6H_2O$ is a more complex process, initially the salt melts with the loss of water starting at 55°C, seen as the first sharp decrease

in weight, this is followed by the loss of the nitrogen at 165°C-265°C producing NO as shown by the mass trace of 30 u. Following the loss of the nitrogen there is a further mass loss, the final reduction of cobalt oxide into the metallic cobalt metal (21% mass) at 400°C.[393]

The presence of reactive gases generated inside the foam material may explain some of the morphology observed from the carbon. Significant concentrations of oxidizing NO_x gases from the $Co(NO_3)_2$ may oxidatively etch some of the carbon leaving a more open structure as observed with SEM and reducing the percentage mass remaining after the carbonization process, Table 8. In contrast the CO_2 and related by-products from the $Co(OAc)_2$ do not cause additional mass loss compared with the salt free control and the SEM shows a more dense, solid structure at low magnification levels (Figure 93).

It is tempting to attribute the increase in mass from the chloride to functionalization of the carbon structure with heavy chloride groups, however, neither thermal analysis (Figure 86b) nor EDX spectra (Figure 97) reveal any chlorine remaining in the carbon foam. It is possible that any functional groups that did form were removed during the high temperature anneal under the hydrogen flow; alternatively all functional groups in the carbon foam may have been reduced by the gas flow before the decomposition of the $CoCl_2$.

Table 8: Mass remaining from all dried, solid material after carbonization process; carbon remaining calculated from the carbon in the initial gel compared to the ratio of mass after acid washing of the final product.

Sample	All Solid Remaining / %	Carbon Remaining / %
Control	10.865(4)	
$Co(OAc)_2$	24.610(2)	17.32(3)
$CoCl_2$	28.934(3)	20.02(4)
$Co(NO_3)_2$	17.799(3)	9.19(2)

During the graphitization process it was also observed that thick oil was produced and condensed on the inside of the quartz tube; this oil was extracted and washed in acetone before being concentrated and analysed with GC-MS. The chromatography traces contained a large number of different compounds, however, many had common mass fragments and were identified as various derivatives of the starting TritonX™-45 that had undergone decomposition. Even tightly bound into clay structures TritonX™ is known to completely desorb and vaporize by 500°C;[394] this suggests the vapours and derivatives had condensed

before reacting with the HCl gas produced by the reduction of the $CoCl_2$. In contrast the CO_x produced by the reduction of $Co(OAc)_2$ and the NO_x from the $Co(NO_3)_2$ salt would react with the volatile TritonX™ vapours.

The decomposition of the $Co(NO_3)_2$ and oxidizing gases released appear to reduce the chain length of the organic fragments observed in the oily residue, in most cases cleaving the ether chain of the surfactant producing lighter hydrocarbons with alcohol groups terminating the ends of the ether chain. This suggest the nitrate salt has an oxidizing effect on the carbon present during the reduction process. The $Co(OAc)_2$ decomposition is not expected to oxidise the carbon present and the chromatography trace reveals many of the same heavier fragments as the control reduction without metal present. Finally the $CoCl_2$ reduction is known to produce HCl which can undergo an elimination reaction with alcohol groups terminating the TritanX™ hydrophilic tail. GC-MS clearly shows this happening with multiple fragments found in both halogenated and alcohol form within the oil extracted, shown in Figure 98. At the temperature the HCl is produced, however, the TritonX™ fragments are expected to have vaporised and condensed outside the hot area, so the vapour phase reaction is unlikely to affect the solid carbon material remaining. This lack of chloride functional groups in the final graphitized material is supported by the TGA and EDX data.

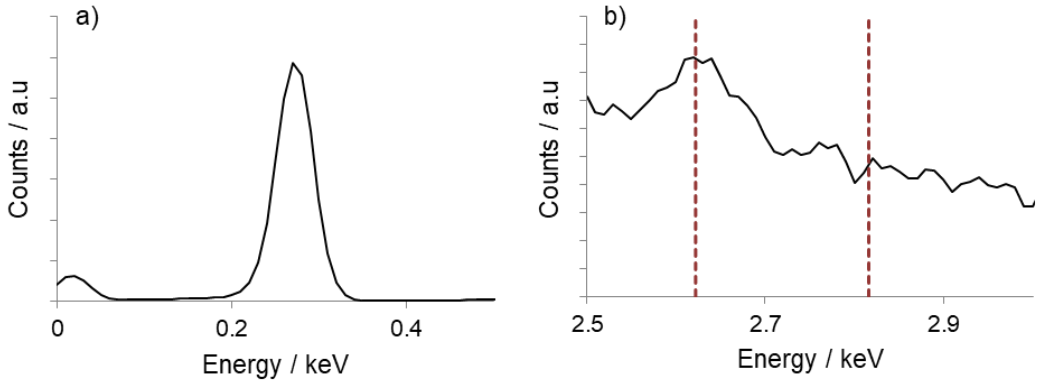

Figure 97: EDX spectra from the $CoCl_2$ derived sample. a) x-ray counts from carbon $K_{\alpha 1}$ emission; b) x-rays counts in the region expected from Cl $K_{\alpha 1,2}$ with the expected energies shown by the dashed lines.

These reaction trends are supported by the percentage of carbon remaining after the graphitization process. When using $Co(NO_3)_2$ as a metal precursor with a significant amount of oxidizing gas produced the carbon remaining is less than found from the metal free control. When using the non-oxidising metal precursors, in this context the chloride is not considered oxidising because it is produced at too high a temperature, the carbon remaining

is substantially higher because of the catalytic effect on graphitization to produce thermally stable aromatic carbon.

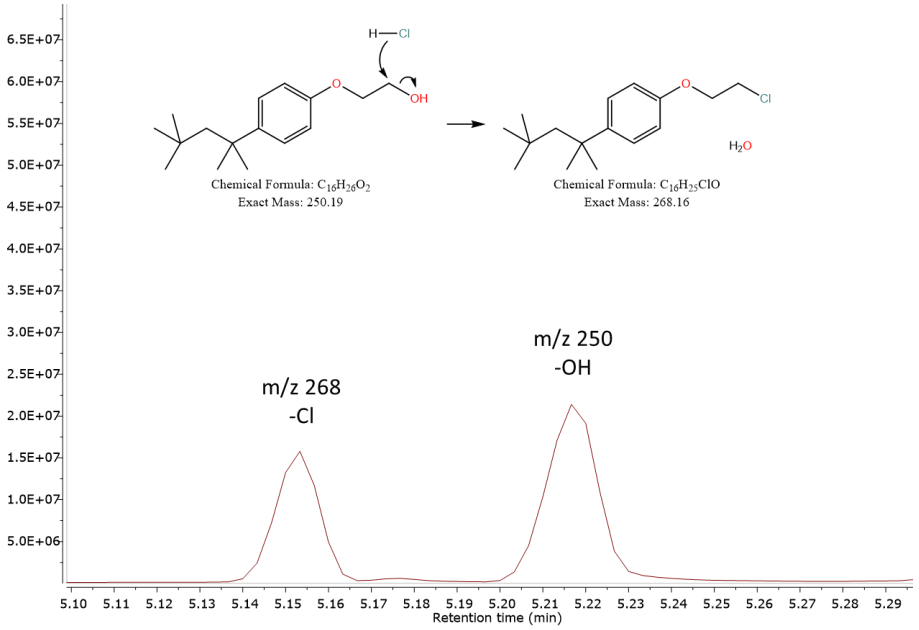

Figure 98: Partial GC trace from the oil extracted from $CoCl_2$ sample; the molecular mass peak present for the compound isolated at each retention time is labelled. These peaks represent the conversion of the alcohol terminated chain to the chloride terminated chain as shown in the reaction scheme at the top.

Beyond the observation from the $Co(NO_3)_2$ there is limited evidence for any reaction between the gases produced and the solid graphitic carbon produced. Given that, it is logical to suggest the temperature of reduction and carbon environment influences the size and distribution of the metal nanoparticles produced; and thus these nanoparticles are the key to determining the graphitization process that follows at higher temperatures.

Considering the carbon foam produced with $CoCl_2$ as a catalyst precursor, previous studies suggest that sugar based carbon undergoes pyrolysis into amorphous carbon between 300 ^oC – 600 ^oC which would be before any of the salt underwent reduction.[245,247] It follows that this would produce an open pore structure of amorphous carbon that allows significant migration of the cobalt at high temperature to anneal into micron sized crystalline particles. These large particles then graphitize the carbon around them in a highly ordered manner leaving more disordered carbon in the rest of the structure, consistent with the G model of catalytic graphitization. Some of the metal produced would be unable to migrate and anneal so a small fraction of nanoparticle would likely be formed, contributing to the T_s-effect graphitization and cubic cobalt observed from the XRD pattern. Nevertheless the large crystallites would dominate the structure, as has been observed.

The $Co(OAc)_2$ and $Co(NO_3)_2$ salts both decompose at lower temperatures when the carbon foam will still contain many functional groups and retain much of its original structure. The large number of oxygen functional groups may aid in evenly dispersing the cobalt salt which, combined with the regular structure, results in localized nanoparticles that are trapped inside the carbon matrix and mostly unable to anneal into larger particles. This hypothesis is fully consistent with the microscopy and XRD data collected and would cause the T_s model graphitization observed from these samples. In a previous study with polymer aerogels Fu et. al found that cobalt nanoparticles began forming from $Co(NO_3)_2$ ion exchanged into a charged polymer matrix at 450 °C but carbon layers were not observed until 600 °C.[251] Whilst the carbon structure's interactions with the charged cobalt cations are very different between our materials, the finding of different temperatures influencing nanoparticle formation is clearly significant.

The difference between the $Co(NO_3)_2$ and $Co(OAc)_2$ salts can be explained by a mixture of temperature and reactive gas formation, the lower melting temperature of the $Co(NO_3)_2$ followed by etching of the carbon matrix by NO_x allows the cobalt particles to coalesce to a greater extend forming the larger nanoparticles within the structure. The $Co(OAc)_2$ in contrast does not have this space to migrate into and therefore is trapped in very small nanoparticles distributed throughout the structure, close enough together that channels form between them. In this way the graphene formation is almost uniform on account of the regular presence of cobalt nanoparticles, although the highly curved surface of the nanoparticle produced strained graphene sheets with the significant I_D/I_G ratio observed.[384]

5.3 Conclusion

Mesoporous graphene foams have been produced in a single step reduction of dextran, TritonX-45™ and three common cobalt salts. The cobalt salts are shown to reduce in-situ to form catalytic cobalt nanoparticles; however, the different salts result in very different forms of carbon in the final product. Following analysis of the carbon and by-products formed to understand the process, this difference is attributed to the differing thermal stability of the transition metal salts used.

When thermally stable salts are used the carbon matrix decomposes first, removing functional groups that may bind the metal ions and forming large pore spaces and amorphous carbon. As the temperature rises and the metal cations reduce to the elemental metal, the temperature and space is sufficient for large metal particles to anneal and form within the carbon matrix. This was observed from the $CoCl_2$ sample with XRD and SEM

revealing highly crystalline particles microns in size decorated over the carbon. These large metal particles are ideal for the dissolution/precipitation of carbon forming crystalline graphite templated by the metal surface known as G-effect graphitization; however, this is not sufficient to graphitize the bulk of the amorphous carbon support. These two different phases were clearly distinguishable with Raman spectroscopy recorded over a large number of points. The 3D histogram shows a high population of spectra consistent with amorphous graphitized carbon but there was evidence of graphite also seen in the sharp x-ray diffraction peak from the bulk powder and two phases in the TGA of pressed powder.

In contrast to the thermally stable salts, when metal precursors are used that reduce at lower temperatures the metal formation occurs before the carbon matrix completely decomposes and loses functional groups. The lack of open pore space and relatively low mobility of the metal ions produces much smaller nanoparticles trapped within the carbon, in the case of the $Co(OAc)_2$ sample nanoparticles less than 4 nm in size were produced which is remarkably small. These nanoparticles also catalyse the graphitization of carbon through the same dissolution/precipitation mechanism. Despite this the graphite flakes produced have distinct properties because of the greater strain on the flakes and smaller sizes caused by the small nanoparticles. This is known as T_s-effect graphitization from literature studies of the phenomenon and the Raman, thermal analysis and XRD all confirmed the strained nature of the graphite formed.

The Raman analysis shows a more homogenous sample containing a single phase; with I_{2D}/I_G ratios higher than expected from graphite but a large I_D/I_G consistent with the growth of strained graphene layers around the small curved nanoparticles. The XRD peaks were also broader suggesting smaller coherent scattering domains and the SAED pattern supports the presence of graphene layers randomly orientated with respect to each other. This lack of long range 3D structuring makes the material comparable to a graphene foam with many of the material properties controllable by tailoring the stability of the salts.

The primary application of porous graphitic carbon is in energy storage devices like supercapacitors where the conductivity and high surface area can be used for rapid charge storage and discharging. Gas sorption measurements confirm the presence of internal pore volumes that are accessed through narrow channels; $CoCl_2$, the more thermally stable metal precursor, had a lower surface area due to the smooth nature of the graphite crystallites formed whilst the $Co(OAc)_2$ sample produced the larger surface area. The very small nanoparticles in that sample were also able to freely migrate out of the structure with many

nanoparticles observed outside the carbon matrix in TEM images and the smallest improvement in surface areas following acid washing.

In summary, the thermal stability of the soluble metal precursor used when forming the gel determines the size of the metal particles formed within the carbon matrix, which in turn dictates the graphitization process observed. The influence of reactive gasses produced during the reduction process was also investigated but limited evidence of genuine functionalisation was found. The HCl produced was found to react with the oily volatile products condensed on the furnace tube but if any halogenation of the carbon occurred the high temperature processing removed such functional groups. Trace doping of the graphene structure may be observed, especially when using nitrogen containing salts, however, there was no significant difference detected. Furthermore recent work on graphene doping has shown that almost any level of trace doping can subtly improve the conductivity of the graphene sheets; but this effect is too low to reliably be used to improve real devices when compared with many other performance limiting factions like device fabrication.[395]

The use of the nitrate salt did produce one noticeable effect on the morphology of the carbon due to the oxidising nature of the gasses produced by its reduction. These appear to have etched some of the carbon resulting in a more open porous structure with space for large nanoparticle to anneal. By combining these effects it is proposed that greater control over the carbon morphology can be achieved; currently much is known about the initial carbon structure and chemical environment to control the porous carbon produced but utilising the thermal stability of the salt has not been considered.

6. Conclusions and Outlooks

The analysis of graphene and related materials and the process of graphitic carbon formation has been discussed. The current problems with graphene metrology have been introduced and the case for a more versatile and scalable analytical method made. Raman spectroscopy is already widely employed because of its depth of information and ease of analysis but the question asked here was the scale of analysis required for confidence in the characterisation.

By analysing three independent large data sets generated from a variety of graphene materials, both commercially sourced and synthetic, the behaviour of such data sets and the analysis process has been obtained. Unsurprisingly, when the number of spectra collected were small, each new spectrum had the potential for significant change to the distribution and understanding of material properties; as more data points were included this potential was reduced. The number of points required for this impact to be negligible was variable for different materials. In the first instance to undertake the analysis of many Raman spectra a computer program was written for the sequential fitting of the most common peaks observed in the Raman spectra of carbon materials; the sequential fitting enable each new peak to be validated as a suitable model for the spectra being fitted and this method was successfully applied to all carbon materials tested.

The different carbon samples were found to require different scales of analysis because the distribution of graphene flake sizes, chemical functional groups, layer numbers and defect densities as indicated from the I_{2D}/I_G and I_D/I_G metrics were distinct across different materials. The distributions of these parameters were also confirmed to defy conventional statistical models in many cases, as similarly indicated by other researchers. The result of these irregular distributions is that conventional statistical tests cannot reliably be applied to all materials. To overcome this problem graphical methods have been developed, by plotting summary statistics of the distributions as the size of data sets increased it was possible to visually observe the effect of the increasing sample size. In addition random re-sampling of sub-samples taken from the large analysis graphically illustrates the effect of under resolving materials. These graphical methods can be applied to materials irrespective of the distribution model and allow users to justify the scale of analysis required for different materials.

To demonstrate the methodology: graphite, exfoliated graphene, reduced graphene oxide, high temperature graphitized carbon and commercial samples of graphene nanoplatelets and multiwalled carbon nanotubes were all tested and the scale of analysis required justified.

The specific number of data points required for the specific materials tested here is not the key finding, rather the graphical method for understanding and justifying the number of data points that should be measured from heterogeneous nanomaterials is more widely applicable. Demonstrated here for graphene there is no obvious reason why this methodology cannot be applied to other 2D materials.

Indeed a promising future project may be the application of this method to other 2D materials like hexagonal boron nitride, black phosphorene and molybdenum sulfide. In addition, the program written to accurately fit the Raman spectra of carbon materials could benefit from further optimisation to improve speed and efficiency as currently the time required to fit large data sets of highly defective materials can be measured in hours.

The other focus was to update understanding of catalytic graphitization, a topical process for the ability to convert waste carbon feedstocks and biomass into high value porous carbon. Porous, conductive carbon materials are promising for energy storage applications but still suffer from poor control over the graphitic carbon structure and porosity. The specific system investigated was a dextran gel prepared containing different cobalt salts that underwent carbothermal reduction to form metal particles that catalyse graphitization. By extensive analysis of the structure, chemistry and waste by-products a new mechanism of decomposition and graphitic carbon formation has been proposed. More significant than the metal chemistry, the thermal stability of the metal precursors used has been shown to determine the nature of the carbon formed in this system.

When metal precursors with low thermal stability are used they undergo rapid reduction whilst still trapped in the carbon matrix, forming small nanoparticles and uniform graphene onions grown around these small particles. In contrast when thermally stable precursors are used the carbon foam decomposes first, leaving large spaces for the metal to anneal and large crystalline graphite to grow from the crystalline metal particles microns in size. The detailed analysis of the carbon formed was largely dependent on the large Raman data sets analysed using the insight gained from the previous section, and such large data sets enabled the different graphitic carbon phases to be identified; and electron micrographs clearly displayed the different metal and carbon growth, supported by additional analyses.

Whilst the cobalt nanoparticles formed in this work do have potential applications as catalysts, for example water splitting, the greater impact is hoped to be gained from the new mechanistic understanding of graphitic carbon growth. As demonstrated in Chapter 1 other studies have shown greater variation within metals than between so it is expected these

trends remain true for other transition metals with the same dissolution-precipitation growth process. Producing graphitic carbon foams with other, low cost transition metals is the obvious next step for this research area as well as investigating the possibility of mixing different salts with different thermal stabilities to generate hierarchical porous structure for applications in energy storage.

7. Experimental Details

7.1 Raman Mapping

7.1.1 Raman Spectroscopy

Raman spectra were recorded with a Horiba LabRam Evolution using a 532 nm laser (17.2 mW, M^2 <1.1, Beam Divergence <0.45 mRad) and x50 long working distance objective lens (Leica HCX PL FLUOTAR, WD = 8mm, NA = 0.55); samples were ground to a fine powder and pressed into pellets to provide a smooth, flat surface to focus onto. Three samples were taken from each type of material and automatic Raman maps were collected over a 80 x 80 μm^2 square at 2.5 µm intervals to produce a total data set of 1024 points, acquisition time and number of repeat scans was varied according to sample to maximize the signal to noise possible. The instrument was calibrated to the 520.7 cm^{-1} Raman signal of silicon before every map was recorded.

7.1.2 Materials

325 mesh natural flake graphite, iron(III) chloride reagent grade (97%), resorcinol reagent plus (99%), furfural (99%), sodium cholate hydrate BioXtra (>99%), hydrazine monohydrate reagent grade (98%), potassium permanganate ACS reagent grade (≥99.0%), sodium nitrate ACS reagent grade (≥99.0%) and polystyrene (average Mw ~350,000, average Mn ~170,000) were purchased from Sigma Aldrich and used as received. Methanol analytical reagent grade (>99.9%) was purchased from Fisher Scientific. Pureshield argon (99.998%) and hydrogen (99.995%) were used as provided by BOC. 6 M hydrochloric acid was prepared from hydrochloric acid S.G 1.18 purchased from Fisher Scientific. Hydrogen peroxide (27% sol. stabilised in H_2O) was purchased from Alfa Asar. All chemicals were used as purchased.

Commercial samples were sourced from different companies and analysed as received; the use of 'high' and 'low' quality labels to differentiate the two graphite nanoplatelet samples was based on the marketing materials of the products from their manufactures.

7.1.3 Sample Preparation

7.1.3.1 Exfoliation

Graphite (25 g) and sodium cholate hydrate (2.5 g) were mixed in distilled water (500 mL) in a jacked glass vessel. A L5M Silverson high shear mixer equipped with a 32 mm rotor and a 96 2 mm x 2 mm square hole stator (rotor stator gap is 136 µm) was run at 8,000 rpm for 90 minutes whilst cooling the dispersion to 0 °C.

The resulting dispersion is centrifuged at 500 rpm (32 g) for 45 min and supernatant collected to remove the unexfoliated graphite. Supernatant centrifuged at 1,000 rpm (129 g) for 45 minutes and then the supernatant from this is further centrifuged at 10,000 rpm (12857 g) for 45 min, to remove tiny fragments, and the sediment collected. The sediment was dispersed in water and filtered (0.2 µm polycarbonate), 3 L of distilled water is then used to remove the residual sodium cholate, followed by 100 mL of ethanol and acetone. The filter paper was dried in a vacuum oven (~1 Pa, 60 ^{o}C) for 24 hours and few layer graphene is removed.

7.1.3.2 Graphitization

Graphitic foam produced following similar method to Kiciński et al.;[246] resorcinol (2.5 g) and iron(III) chloride (8.3 g) were dissolved in a mixture of water (23 mL) and methanol (24 mL) to which furfural (5.0 g) was added. This mixture was placed in a centrifuge tube and mixed with a vortex mixture, then placed in an oven for 24 hs at 60 ^{o}C for polymerization. Following a further 3 days to dry the solid polymer was placed in an alumina boat for high temperature processing. The alumina boat was placed inside a quartz worktube (I.D 29 mm) inside a Carbolite tube furnace (MTF 12/38/400); the system was purged with argon (150 mL min^{-1}) for 30 min then hydrogen (8.72 mL min^{-1}) was added to the flow at atmospheric pressure, argon gas flow measured by volumetric flow meter whilst hydrogen controlled by a Brooks 5850 TR series mass flow controller in totalizer mode. The furnace was heated to 1050 ^{o}C at 10 ^{o}C and held at this temperature for 2 hrs. Following high temperature processing the graphitized foam is washed in 6M HCl for 48 hs before filtering (0.2 µm, polycarbonate) and washed with copious water until washings were neutral.

7.1.3.3 Chemically Reduced GO

Graphite oxide was produced using the Hummers method;[118] typically sodium nitrate (5 g) was dissolved in sulfuric acid (230 mL) at 0^{o}C before graphite (10 g) is added followed by the slow addition of potassium permanganate (30 g), ensuring the temperature does not exceed 10^{o}C. The mixture is then heated to 35^{o}C for 2 hours after which ice cold deionized water (460 mL) was slowly added to quench the reaction and the brown solution was further diluted (1.4 L) and hydrogen peroxide added until effervescence stops. The acidic solution is centrifuge washed until neutral, with a subsequent 6M HCl wash and neutralization.

20 mL of the graphite oxide solution is then sonicated (20 min, 30% amplitude, 5 s pulse) using a 750 W Cole palmer Ultrasonic Processor. This mixture was centrifuged at 1000 rpm for 30 minutes and then the supernatant was freeze dried (SP Scientific BenchTop Pro). The

graphene oxide (40 mg) thus prepared was dispersed into water (50 mL) and reduced by the addition of hydrazine monohydrate (20 µL) and heating to 60 °C for 24 hours; the resulting black dispersion was filtered (0.2 µm Nylon) and re-dispersed by gentle sonication into water (20 mL) and freeze dried (SP Scientific BenchTop Pro).

7.2 Dextran – Cobalt Graphitization

7.2.1 Materials

Cobalt(II) nitrate hexahydrate ACS reagent ≥ 98%, cobalt(II) acetate tetrahydrate ACS reagent ≥ 98.0%, dextran from Leuconostoc mesenteroides (average mol. wt. 1,500,000-2,800,000) and Triton™ X-45 were all used as purchased from Sigma Aldrich. Cobalt(II) chloride hexahydrate was used as purchased from Alfa Aesar. Pureshield argon (99.998%) and hydrogen (99.995%) were used as provided by BOC. 6M hydrochloric acid was prepared from hydrochloric acid S.G 1.18 purchased from Fisher Scientific. Furnace tube washing and waste oil analysis was done with acetone AR (99.5%) from Fisher Scientific.

7.2.2 Synthesis

7.2.2.1 Wet Dextran Gel

Gels were prepared in similar fashion to Khan and Mann;[383] dextran was gently stirred into water with the salt to form a viscous liquid to which Triton™ X-45 was added and the mixture then stirred with a mechanical stirrer at 600 rpm to form a homogeneous mixture. In every case 4 g of salt was used and the other reagents were added to maintain a consistent mass ratio (1:2:2) between the cobalt metal, dextran and Triton™ respectively; water was added to keep a constant ratio (1:2.5) between sugar and water respectively. The wet gel was placed into an alumina boat and freeze dried (SP Scientific BenchTop Pro) for at least 24 hs at ~4 Pa to produce a hard foam.

7.2.2.2 Synthesis of graphene foam

The alumina boat containing the foam was placed inside a quartz worktube (I.D 29 mm) inside a Carbolite tube furnace (MTF 12/38/400). The system was purged with argon (800 mL min^{-1}) for 30 min then hydrogen (8.72 mL min^{-1}) was added to the flow all at atmospheric pressure; argon gas flow measured by volumetric flow meter whilst hydrogen controlled by a Brooks 5850 TR Series mass controller in totalizer mode. The furnace was heated to 1000 °C at 10 °C min^{-1} and held at this temperature for one hour before it was allowed to cool.

7.2.2.3 Extraction and Washing

Both the quartz worktube and resulting carbonized foam were washed with acetone (~200 mL) to remove oily residues then vacuum filtered and air dried. The oily by-product was isolated by removal of solvent *in vacuo* and then re-dissolved in acetone (10 µL mL^{-1}) for GC-MS analysis. The carbonized foam was washed with 6M hydrochloric acid for 42 h before being filtered through a 0.02 µm membrane and washed with copious high purity water until washings were neutral; these were diluted into one litre of high purity water using a volumetric flask for ICP analysis. Before any analysis of solid material all samples were dried in a vacuum oven (60 °C, < 1 mbar) for at least 24 hs.

7.2.3 Characterization

7.2.3.1 Raman Spectroscopy

Raman spectra were recorded with a Horiba LabRam Evolution using a 532 nm, 1 mW laser and a x50 long working distance objective lens. The instrument was calibrated against the 520.7 cm^{-1} Raman signal of silicon. Samples were ground up and pressed into flat disks for Raman mapping to generate a significant number of points for analysis that were representative of the whole material; maps were fitted with a six order polynomial background and Lorentzian line shapes using a custom Python program, details in supporting information.

7.2.3.2 Thermo-gravimetric analysis (TGA)

TGA was carried out with a Perkin Elmer TGA 8000 heating from ambient temperature to 1000 °C at 10 °C/min under either air or nitrogen gas flow (30 mL/min); all samples were compressed to form crude pellets. Thermal analysis with in-situ mass spectrometry was done with a Perkin Elmer Pyris 1 TGA heating from ambient temperature at 10 °C/min under a 100 mL/min gas flow of 5% H_2/Ar mixed speciality gas from BOC. All cobalt salts were dried under vacuum (room temperature, < 1 mbar) and analysed in powder form. MS analysis was done with a Hiden HPR-20, initially running a full range scan to identify key peaks before the measurement was repeated scanning specific mass ranges in 5 s windows.

7.2.3.3 X-ray diffraction (XRD)

Powder XRD patterns of cobalt foam samples were collected with a Bruker d8 Advance diffractometer using a Mo Kα source (λ = 0.7093 Å) operating at 50 kV and 40 mA. The foam was ground into a fine powder and packed into a 1.0 mm glass capillary which was rotated at 40 rpm during the measurement; XRD fitting was done with GSASII software using *.cif* files of hcp and ccp cobalt taken from the ICSD.[389,396]

7.2.3.4 Electron microscopy (EM)

SEM images were collected with a Hitachi SU-70 FEG SEM and EDX data was collected with an Oxford Instruments EDX system (X-MaxN 50 Silicon Drift Detector), data analysed with the proprietary AZtec software. All samples were imaged uncoated at 10 kV, unless otherwise stated in the caption, and stuck onto an adhesive carbon pad.

TEM images were acquired using a JEOL 2100F FEG TEM operating at 80 kV. Samples were dispersed in ethanol solution then dropped onto holey carbon on a 300 mesh copper grid. Particle sizes were measured using ImageJ software.[397]

7.2.3.5 Gas sorption analysis

Gas sorption measurements were taken using a Micromeritics ASAP 2020 nitrogen porosimeter using 1/2 inch glassware fitted with a filler rod, sealed frit and isothermal jacket. The Brunauer–Emmett–Teller (BET) model was used to calculate specific surface areas from nitrogen adsorption data at 77 K in the P/P_0 range 0.05 – 0.25.

7.2.3.6 Inductively coupled plasma optical emission spectroscopy (ICP-OES)

ICP-OES analysis was done on a Yobin Yvon Horiba Ultima 2 instrument with a radial torch and sequential monochromator; Co ICP-OES standards (0, 100, 300, 500 ppm) were used for calibration. Six measurements were taken per sample at each wavelength (350.228 nm and 356.038 nm) and averaged to give the final measured concentration of cobalt.

7.2.3.7 Gas-chromatography-mass spectrometry (GCMS)

Waste oils were analysed using a Shimadzu QP2010-Ultra; Rxi-17Sil MS column (0.15 µm x 10 m x 0.15 mm) with 0.41 mL min^{-1} helium carrier gas and a temperature gradient of 50 ^{o}C/min to 300 ^{o}C; 0.5 µL samples were injected for low resolution electrospray mass spectrometry in positive ion mode (ES+).

8. References

1 S. Iijima, *Nature*, 1991, **354**, 56–58.
2 K. S. Novoselov, A. K. Geim, S. V Morozov, D. Jiang, Y. Zhang, S. V Dubonos, I. V Grigorieva and A. A. Firsov, *Science (80-.).*, 2004, **306**, 666 LP – 669.
3 E. P. Randviir, D. A. C. Brownson and C. E. Banks, *Mater. Today*, 2014, **17**, 426–432.
4 A. K. Geim and K. S. Novoselov, *Nat Mater*, 2007, **6**, 183–191.
5 R. A. Jishi, D. Inomata, K. Nakao, M. S. Dresselhaus and G. Dresselhaus, *J. Phys. Soc. Japan*, 1994, **63**, 2252–2260.
6 M. Terrones, A. R. Botello-Méndez, J. Campos-Delgado, F. López-Urías, Y. I. Vega-Cantú, F. J. Rodríguez-Macías, A. L. Elías, E. Muñoz-Sandoval, A. G. Cano-Márquez and J.-C. Charlier, *Nano Today*, 2010, **5**, 351–372.
7 K. F. Mak, J. Shan and T. F. Heinz, *Phys. Rev. Lett.*, 2010, **104**, 176404.
8 J.-C. Charlier, J.-P. Michenaud and X. Gonze, *Phys. Rev. B*, 1992, **46**, 4531–4539.
9 F. Mori, M. Kubouchi and Y. Arao, *J. Mater. Sci.*, 2018, **53**, 12807–12815.
10 S. D. Costa, J. E. Weis, O. Frank, M. Fridrichová and M. Kalbac, *2D Mater.*, 2016, **3**, 25022.
11 L. M. M. Malard, M. A. A. Pimenta, G. Dresselhaus and M. S. S. Dresselhaus, *Phys. Rep.*, 2009, **473**, 51–87.
12 International Organization for Standardization, *Nanotechnologies — Vocabulary — Part 13: Graphene and related two-dimensional (2D) materials*, 2017.
13 A. C. Ferrari, J. C. Meyer, V. Scardaci, C. Casiraghi, M. Lazzeri, F. Mauri, S. Piscanec, D. Jiang, K. S. Novoselov, S. Roth and A. K. Geim, *Phys. Rev. Lett.*, 2006, **97**, 187401.
14 T. Enoki, S. Fujii and K. Takai, *Carbon N. Y.*, 2012, **50**, 3141–3145.
15 C. Casiraghi, A. Hartschuh, H. Qian, S. Piscanec, C. Georgi, A. Fasoli, K. S. Novoselov, D. M. Basko and A. C. Ferrari, *Nano Lett.*, 2009, **9**, 1433–1441.
16 Y.-W. Son, M. L. Cohen and S. G. Louie, *Phys. Rev. Lett.*, 2006, **97**, 216803.
17 S. Dutta and S. K. Pati, *J. Mater. Chem.*, 2010, **20**, 8207–8223.
18 K. Wakabayashi and S. Dutta, *Solid State Commun.*, 2012, **152**, 1420–1430.
19 A. Bianco, H.-M. Cheng, T. Enoki, Y. Gogotsi, R. H. Hurt, N. Koratkar, T. Kyotani, M. Monthioux, C. R. Park, J. M. D. Tascon and J. Zhang, *Carbon N. Y.*, 2013, **65**, 1–6.
20 A. H. Castro Neto, F. Guinea, N. M. R. Peres, K. S. Novoselov and A. K. Geim, *Rev. Mod. Phys.*, 2009, **81**, 109–162.
21 T. Ohta, A. Bostwick, T. Seyller, K. Horn and E. Rotenberg, *Science (80-.).*, 2006, **313**, 951–954.
22 P. R. Wallace, *Phys. Rev.*, 1947, **71**, 622–634.
23 J. Tworzydło, B. Trauzettel, M. Titov, A. Rycerz and C. W. J. Beenakker, *Phys. Rev. Lett.*, 2006, **96**, 246802.
24 K. S. Novoselov, A. K. Geim, S. V Morozov, D. Jiang, M. I. Katsnelson, I. V Grigorieva, S. V Dubonos and A. A. Firsov, *Nature*, 2005, **438**, 197–200.
25 X. Du, I. Skachko, A. Barker and E. Y. Andrei, *Nat. Nanotechnol.*, 2008, **3**, 491–495.
26 S. V. Morozov, K. S. Novoselov, M. I. Katsnelson, F. Schedin, D. C. Elias, J. A. Jaszczak and A. K. Geim, *Phys. Rev. Lett.*, 2008, **100**, 016602.
27 K. I. Bolotin, K. J. Sikes, Z. Jiang, M. Klima, G. Fudenberg, J. Hone, P. Kim and H. L. Stormer, *Solid State Commun.*, 2008, **146**, 351–355.
28 K. S. Novoselov, Z. Jiang, Y. Zhang, S. V. Morozov, H. L. Stormer, U. Zeitler, J. C. Maan, G. S. Boebinger, P. Kim and A. K. Geim, *Science (80-.).*, 2007, **315**, 1379–1379.
29 C. Berger, Z. M. Song, T. B. Li, X. B. Li, A. Y. Ogbazghi, R. Feng, Z. T. Dai, A. N. Marchenkov, E. H. Conrad, P. N. First and W. A. de Heer, *J. Phys. Chem. B*, 2004, **108**, 19912–19916.
30 C. Bai and X. Zhang, *Phys. Rev. B*, 2007, **76**, 75430.

31 D. Dragoman, *Phys. Scr.*, 2009, **79**, 15003.
32 S. Pisana, M. Lazzeri, C. Casiraghi, K. S. Novoselov, A. K. Geim, A. C. Ferrari and F. Mauri, *Nat Mater*, 2007, **6**, 198–201.
33 G. Cassabois, P. Valvin and B. Gil, *Nat. Photonics*, 2016, **10**, 262–266.
34 Y. Zhang, T.-T. Tang, C. Girit, Z. Hao, M. C. Martin, A. Zettl, M. F. Crommie, Y. R. Shen and F. Wang, *Nature*, 2009, **459**, 820–823.
35 P. Anees, M. C. Valsakumar, S. Chandra and B. K. Panigrahi, *Model. Simul. Mater. Sci. Eng.*, 2014, **22**, 035016.
36 G. Yang, L. Li, W. B. Lee and M. C. Ng, *Sci. Technol. Adv. Mater.*, 2018, **19**, 613–648.
37 K. Saito, J. Nakamura and A. Natori, *Phys. Rev. B*, 2007, **76**, 115409.
38 A. A. Balandin, S. Ghosh, W. Bao, I. Calizo, D. Teweldebrhan, F. Miao and C. N. Lau, *Nano Lett.*, 2008, **8**, 902–907.
39 B. Deng, Y. Hou, Y. Liu, T. Khodkov, S. Goossens, J. Tang, Y. Wang, R. Yan, Y. Du, F. H. L. Koppens, X. Wei, Z. Zhang, Z. Liu and H. Peng, *Nano Lett.*, , DOI:10.1021/acs.nanolett.0c02785.
40 W. Bao, F. Miao, Z. Chen, H. Zhang, W. Jang, C. Dames and C. N. Lau, *Nat Nano*, 2009, **4**, 562–566.
41 S. Mann, R. Kumar and V. K. Jindal, *RSC Adv.*, 2017, **7**, 22378–22387.
42 N. Mounet and N. Marzari, *Phys. Rev. B*, 2005, **71**, 205214.
43 M. Pozzo, D. Alfè, P. Lacovig, P. Hofmann, S. Lizzit and A. Baraldi, *Phys. Rev. Lett.*, 2011, **106**, 135501.
44 C. Lee, X. Wei, J. W. Kysar and J. Hone, *Science (80-.).*, 2008, **321**, 385–388.
45 A. Peigney, C. Laurent, E. Flahaut, R. R. Bacsa and A. Rousset, *Carbon N. Y.*, 2001, **39**, 507–514.
46 J. S. Bunch, S. S. Verbridge, J. S. Alden, A. M. van der Zande, J. M. Parpia, H. G. Craighead and P. L. McEuen, *Nano Lett.*, 2008, **8**, 2458–2462.
47 S. Bertolazzi, J. Brivio and A. Kis, *ACS Nano*, 2011, **5**, 9703–9709.
48 I. W. Frank, D. M. Tanenbaum, A. M. van der Zande and P. L. McEuen, *J. Vac. Sci. Technol. B Microelectron. Nanom. Struct.*, 2007, **25**, 2558.
49 C. Tan, X. Cao, X.-J. Wu, Q. He, J. Yang, X. Zhang, J. Chen, W. Zhao, S. Han, G.-H. Nam, M. Sindoro and H. Zhang, *Chem. Rev.*, 2017, **117**, 6225–6331.
50 K. F. Mak and J. Shan, *Nat. Photonics*, 2016, **10**, 216–226.
51 Y. Zhu, H. Ji, H.-M. Cheng and R. S. Ruoff, *Natl. Sci. Rev.*, 2017, **5**, 90–101.
52 C. Soldano, A. Mahmood and E. Dujardin, *Carbon N. Y.*, 2010, **48**, 2127–2150.
53 K. S. Novoselov, V. I. Fal'ko, L. Colombo, P. R. Gellert, M. G. Schwab and K. Kim, *Nature*, 2012, **490**, 192–200.
54 D. A. C. Brownson and C. E. Banks, *Analyst*, 2010, **135**, 2768–2778.
55 A. A. Balandin, *Nat. Mater.*, 2011, **10**, 569–581.
56 Y. Song, W. Fang, R. Brenes and J. Kong, *Nano Today*, 2015, **10**, 681–700.
57 V. Berry, *Carbon N. Y.*, 2013, **62**, 1–10.
58 X. Huang, X. Qi, F. Boey and H. Zhang, *Chem. Soc. Rev.*, 2012, **41**, 666–686.
59 J. Du and H.-M. Cheng, *Macromol. Chem. Phys.*, 2012, **213**, 1060–1077.
60 S. Wang, P. K. Ang, Z. Wang, A. L. L. Tang, J. T. L. Thong and K. P. Loh, *Nano Lett.*, 2010, **10**, 92–98.
61 G. Eda, G. Fanchini and M. Chhowalla, *Nat. Nanotechnol.*, 2008, **3**, 270–274.
62 D. Parviz, S. Das, H. S. T. Ahmed, F. Irin, S. Bhattacharia and M. J. Green, *ACS Nano*, 2012, **6**, 8857–8867.
63 Stevens Institute of Technology, USA; United States Dept. of the Army ., *U.S. Pat. Appl. Publ.*, 2012, 12 pp.
64 Siemens Aktiengesellschaft, Germany; Siemens Concentrated Solar Power Ltd. ., *PCT Int. Appl.*, 2014, 18pp.

65 BASF SE, Germany; BASF China Company Limited ., *PCT Int. Appl.*, 2014, 21pp.
66 Nanotek Instruments, Inc., USA ., *U.S. Pat. Appl. Publ.*, 2010, 13 pp.
67 US2011042813, 2012.
68 K. Pan, Y. Fan, T. Leng, J. Li, Z. Xin, J. Zhang, L. Hao, J. Gallop, K. S. Novoselov and Z. Hu, *Nat. Commun.*, 2018, **9**, 5197.
69 D. Li, W.-Y. Lai, Y.-Z. Zhang and W. Huang, *Adv. Mater.*, 2018, **30**, 1704738.
70 D. S. Saidina, N. Eawwiboonthanakit, M. Mariatti, S. Fontana and C. Hérold, *J. Electron. Mater.*, 2019, **48**, 3428–3450.
71 A. Kamyshny and S. Magdassi, *Chem. Soc. Rev.*, 2019, **48**, 1712–1740.
72 D. W. Johnson, B. P. Dobson and K. S. Coleman, *Curr. Opin. Colloid Interface Sci.*, 2015, **20**, 367–382.
73 J. Li, F. Ye, S. Vaziri, M. Muhammed, M. C. Lemme and M. Östling, *Adv. Mater.*, 2013, **25**, 3985–3992.
74 V. B. Mohan, K. Lau, D. Hui and D. Bhattacharyya, *Compos. Part B-Engineering*, 2018, **142**, 200–220.
75 N. Saravanan, R. Rajasekar, S. Mahalakshmi, T. P. Sathishkumar, K. S. K. Sasikumar and S. Sahoo, *J. Reinf. Plast. Compos.*, 2014, **33**, 1158–1180.
76 Y. Sun, Q. Wu and G. Shi, *Energy Environ. Sci.*, 2011, **4**, 1113–1132.
77 C. Uthaisar and V. Barone, *Nano Lett.*, 2010, **10**, 2838–2842.
78 S.-L. Chou, J.-Z. Wang, M. Choucair, H.-K. Liu, J. A. Stride and S.-X. Dou, *Electrochem. commun.*, 2010, **12**, 303–306.
79 J.-Y. Liu, X.-X. Li, J.-R. Huang, J.-J. Li, P. Zhou, J.-H. Liu and X.-J. Huang, *J. Mater. Chem. A*, 2017, **5**, 5977–5994.
80 X. Jiang, X. Yang, Y. Zhu, H. Jiang, Y. Yao, P. Zhao and C. Li, *J. Mater. Chem. A*, 2014, **2**, 11124.
81 J.-Y. Hwang, S.-T. Myung and Y.-K. Sun, *Chem. Soc. Rev.*, 2017, **46**, 3529–3614.
82 N. Yabuuchi, K. Kubota, M. Dahbi and S. Komaba, *Chem. Rev.*, 2014, **114**, 11636–11682.
83 B. Xiao, T. Rojo and X. Li, *ChemSusChem*, 2019, **12**, 133–144.
84 D. A. Stevens and J. R. Dahn, *J. Electrochem. Soc.*, 2000, **147**, 1271.
85 L. Zhao, L. Wang, S. Zeng, Q. Liu, W. Yan, M. Liu, H. Gong and J. Zhang, *J. Mater. Sci.*, 2020, **55**, 14491–14500.
86 J. Liu, Y.-G. Xu and L.-B. Kong, *Solid State Ionics*, 2020, **355**, 115416.
87 J. R. Dahn, W. Xing and Y. Gao, *Carbon N. Y.*, 1997, **35**, 825–830.
88 E. Olsson, J. Cottom, H. Au, Z. Guo, A. C. S. Jensen, H. Alptekin, A. J. Drew, M.-M. Titirici and Q. Cai, *Adv. Funct. Mater.*, 2020, **30**, 1908209.
89 Y. Li, Y. Lu, Q. Meng, A. C. S. Jensen, Q. Zhang, Q. Zhang, Y. Tong, Y. Qi, L. Gu, M.-M. Titirici and Y.-S. Hu, *Adv. Energy Mater.*, 2019, **9**, 1902852.
90 Y. An, H. Fei, G. Zeng, L. Ci, B. Xi, S. Xiong and J. Feng, *J. Power Sources*, 2018, **378**, 66–72.
91 X. Dou, I. Hasa, D. Saurel, C. Vaalma, L. Wu, D. Buchholz, D. Bresser, S. Komaba and S. Passerini, *Mater. Today*, 2019, **23**, 87–104.
92 H. Jiang, P. S. Lee and C. Li, *Energy Environ. Sci.*, 2013, **6**, 41–53.
93 A. González, E. Goikolea, J. A. Barrena and R. Mysyk, *Renew. Sustain. Energy Rev.*, 2016, **58**, 1189–1206.
94 F. Belhachemi, S. Rael and B. Davat, in *Conference Record of the 2000 IEEE Industry Applications Conference. Thirty-Fifth IAS Annual Meeting and World Conference on Industrial Applications of Electrical Energy (Cat. No.00CH37129)*, IEEE, Rome, Italy, 2000, vol. 5, pp. 3069–3076.
95 J. Yan, Q. Wang, T. Wei and Z. Fan, *Adv. Energy Mater.*, , DOI:10.1002/aenm.201300816.

96 Z. Yu, L. Tetard, L. Zhai and J. Thomas, *Energy Environ. Sci.*, 2015, **8**, 702–730.
97 C. Zhong, Y. Deng, W. Hu, J. Qiao, L. Zhang and J. Zhang, *Chem. Soc. Rev.*, 2015, **44**, 7484–7539.
98 C. Liu, Z. Yu, D. Neff, A. Zhamu and B. Z. Jang, *Nano Lett.*, 2010, **10**, 4863–4868.
99 T. Liu, F. Zhang, Y. Song and Y. Li, *J. Mater. Chem. A*, 2017, **5**, 17705–17733.
100 The Regents of the University of California, USA ., *PCT Int. Appl.*, 2017, 20pp.
101 V. Hoa Nguyen and J.-J. Shim, *Mater. Lett.*, 2015, **139**, 377–381.
102 V. H. Nguyen, C. Lamiel and J.-J. Shim, *Electrochim. Acta*, 2015, **161**, 351–357.
103 Y. Si and E. T. Samulski, *Chem. Mater.*, 2008, **20**, 6792–6797.
104 M. J. and S. S. and P. S. and N. C. M. and N. H. K. and T. K. and J. H. Lee, *Nanotechnology*, 2015, **26**, 75402.
105 V. Bhatia, G. Malekshoar, A. Dhir and A. K. Ray, *J. Photochem. Photobiol. A Chem.*, 2017, **332**, 182–187.
106 X. Wang, J. Li, Y. He, T. Qian and Q. Shen, *Colloids Surfaces A Physicochem. Eng. Asp.*, 2014, **461**, 178–183.
107 V. Kumar, K.-H. Kim, J.-W. Park, J. Hong and S. Kumar, *Chem. Eng. J.*, 2017, **315**, 210–232.
108 J. Li, Z. Zhao, Y. Ma and Y. Qu, *ChemCatChem*, 2017, **9**, 1554–1568.
109 P. Chen, L.-K. Wang, G. Wang, M.-R. Gao, J. Ge, W.-J. Yuan, Y.-H. Shen, A.-J. Xie and S.-H. Yu, *Energy Environ. Sci.*, 2014, **7**, 4095–4103.
110 D. J. Martin, K. Qiu, S. A. Shevlin, A. D. Handoko, X. Chen, Z. Guo and J. Tang, *Angew. Chemie Int. Ed.*, 2014, **53**, 9240–9245.
111 S. J. A. Moniz, S. A. Shevlin, D. J. Martin, Z.-X. Guo and J. Tang, *Energy Environ. Sci.*, 2015, **8**, 731–759.
112 X. Wang, K. Maeda, A. Thomas, K. Takanabe, G. Xin, J. M. Carlsson, K. Domen and M. Antonietti, *Nat Mater*, 2009, **8**, 76–80.
113 Y. Hou, Z. Wen, S. Cui, X. Guo and J. Chen, *Adv. Mater.*, 2013, **25**, 6291–6297.
114 N. Zhang, M.-Q. Yang, S. Liu, Y. Sun and Y.-J. Xu, *Chem. Rev.*, 2015, **115**, 10307–10377.
115 G. A. Van Norman, *JACC Basic to Transl. Sci.*, 2016, **1**, 277–287.
116 R. S. Edwards and K. S. Coleman, *Nanoscale*, 2013, **5**, 38–51.
117 J. M. Tour, *Chem. Mater.*, 2014, **26**, 163–171.
118 W. S. Hummers and R. E. Offeman, *J. Am. Chem. Soc.*, 1958, **80**, 1339.
119 D. R. Dreyer, A. D. Todd and C. W. Bielawski, *Chem. Soc. Rev.*, 2014, **43**, 5288–5301.
120 D. R. Dreyer, S. Park, C. W. Bielawski and R. S. Ruoff, *Chem. Soc. Rev.*, 2010, **39**, 228–240.
121 M. Rosillo-Lopez, T. J. Lee, M. Bella, M. Hart and C. G. Salzmann, *RSC Adv.*, 2015, **5**, 104198–104202.
122 A. M. Dimiev and J. M. Tour, *ACS Nano*, 2014, **8**, 3060–3068.
123 M. T. H. Aunkor, I. M. Mahbubul, R. Saidur and H. S. C. Metselaar, *RSC Adv.*, 2016, **6**, 27807–27828.
124 S. Pei and H.-M. Cheng, *Carbon N. Y.*, 2012, **50**, 3210–3228.
125 S. Mao, H. Pu and J. Chen, *RSC Adv.*, 2012, **2**, 2643.
126 B. G. Choi, M. Yang, W. H. Hong, J. W. Choi and Y. S. Huh, *ACS Nano*, 2012, **6**, 4020–4028.
127 C. Z. and M. C. and X. X. and L. Z. and L. Z. and F. X. and X. L. and Y. L. and W. H. and J. Gao, *Nanotechnology*, 2014, **25**, 135707.
128 L. Zhao, X.-L. Sui, J.-L. Li, J.-J. Zhang, L.-M. Zhang and Z.-B. Wang, *ACS Appl. Mater. Interfaces*, 2016, **8**, 16026–16034.
129 W. Chen, S. Li, C. Chen and L. Yan, *Adv. Mater.*, 2011, **23**, 5679–5683.
130 S. Gupta and N.-H. Tai, *J. Mater. Chem. A*, 2016, **4**, 1550–1565.
131 H. Bi, X. Xie, K. Yin, Y. Zhou, S. Wan, L. He, F. Xu, F. Banhart, L. Sun and R. S. Ruoff, *Adv.*

Funct. Mater., 2012, **22**, 4421–4425.
132 S. De Gisi, G. Lofrano, M. Grassi and M. Notarnicola, *Sustain. Mater. Technol.*, 2016, **9**, 10–40.
133 D. C. Marcano, D. V Kosynkin, J. M. Berlin, A. Sinitskii, Z. Sun, A. Slesarev, L. B. Alemany, W. Lu and J. M. Tour, *ACS Nano*, 2010, **4**, 4806–4814.
134 R. A. Sheldon, *Green Chem.*, 2017, **19**, 18–43.
135 B. Ballinger, M. Stringer, D. R. Schmeda-Lopez, B. Kefford, B. Parkinson, C. Greig and S. Smart, *Appl. Energy*, 2019, **255**, 113844.
136 US1137373, 1915.
137 US1137373, 1915.
138 D. D. L. Chung, *J. Mater. Sci.*, 1987, **22**, 4190–4198.
139 J. S. Park, L. Yu, C. S. Lee, K. Shin and J. H. Han, *J. Colloid Interface Sci.*, 2014, **417**, 379–384.
140 N. Iwashita and M. Inagaki, *Synth. Met.*, 1989, **34**, 139–144.
141 R. Nishitani, Y. Sasaki and Y. Nishina, *Synth. Met.*, 1989, **34**, 315–321.
142 M. S. Dresselhaus and G. Dresselhaus, *Adv. Phys.*, 1981, **30**, 139–326.
143 G. Bepete, E. Anglaret, L. Ortolani, V. Morandi, K. Huang, A. Pénicaud and C. Drummond, *Nat Chem*, 2017, **9**, 347–352.
144 D. Dasler, R. A. Schäfer, M. B. Minameyer, J. F. Hitzenberger, F. Hauke, T. Drewello and A. Hirsch, *J. Am. Chem. Soc.*, 2017, **139**, 11760–11765.
145 C. Vallés, C. Drummond, H. Saadaoui, C. A. Furtado, M. He, O. Roubeau, L. Ortolani, M. Monthioux and A. Pénicaud, *J. Am. Chem. Soc.*, 2008, **130**, 15802–15804.
146 N. Nakashima, Y. Tomonari and H. Murakami, *Chem. Lett.*, 2002, 638–639.
147 J. N. Coleman, *Acc. Chem. Res.*, 2013, **46**, 14–22.
148 A. Amiri, M. Naraghi, G. Ahmadi, M. Soleymaniha and M. Shanbedi, *Flatchem*, 2018, **8**, 40–71.
149 Y. Xu, H. Cao, Y. Xue, B. Li and W. Cai, *Nanomaterials*, 2018, **8**, 942.
150 Y. Hernandez, V. Nicolosi, M. Lotya, F. M. Blighe, Z. Sun, S. De, M. T., B. Holland, M. Byrne, Y. K. Gun'Ko, J. J. Boland, P. Niraj, G. Duesberg, S. Krishnamurthy, R. Goodhue, J. Hutchison, V. Scardaci, A. C. Ferrari and J. N. Coleman, *Nat Nano*, 2008, **3**, 563–568.
151 P. Blake, P. D. Brimicombe, R. R. Nair, T. J. Booth, D. Jiang, F. Schedin, L. A. Ponomarenko, S. V. Morozov, H. F. Gleeson, E. W. Hill, A. K. Geim and K. S. Novoselov, *Nano Lett.*, 2008, **8**, 1704–1708.
152 M. Lotya, Y. Hernandez, P. J. King, R. J. Smith, V. Nicolosi, L. S. Karlsson, F. M. Blighe, S. De, Z. Wang, I. T. McGovern, G. S. Duesberg and J. N. Coleman, *J. Am. Chem. Soc.*, 2009, **131**, 3611–3620.
153 U. Khan, H. Porwal, A. O'Neill, K. Nawaz, P. May and J. N. Coleman, *Langmuir*, 2011, **27**, 9077–9082.
154 K. S. Suslick and G. J. Price, *Annu. Rev. Mater. Sci.*, 1999, **29**, 295–326.
155 Z. Li, R. J. Young, C. Backes, W. Zhao, X. Zhang, A. Zhukov, E. Tillotson, A. P. Conlan, F. Ding, S. J. Haigh, K. S. Novoselov and J. N. Coleman, *ACS Nano*, , DOI:10.1021/acsnano.0c03916.
156 W. Zhao, M. Fang, F. Wu, H. Wu, L. Wang and G. Chen, *J. Mater. Chem.*, 2010, **20**, 5817–5819.
157 C. Knieke, A. Berger, M. Voigt, R. N. K. Taylor, J. Röhrl and W. Peukert, *Carbon N. Y.*, 2010, **48**, 3196–3204.
158 M. Yi and Z. Shen, *J. Mater. Chem. A*, 2015, **3**, 11700–11715.
159 K. R. Paton, E. Varrla, C. Backes, R. J. Smith, U. Khan, A. O'Neill, C. Boland, M. Lotya, O. M. Istrate, P. King, T. Higgins, S. Barwich, P. May, P. Puczkarski, I. Ahmed, M. Moebius, H. Pettersson, E. Long, J. Coelho, S. E. O'Brien, E. K. McGuire, B. M. Sanchez, G. S. Duesberg, N. McEvoy, T. J. Pennycook, C. Downing, A. Crossley, V. Nicolosi and

J. N. Coleman, *Nat. Mater.*, 2014, **13**, 624–630.
160 L. Liu, Z. Shen, M. Yi, X. Zhang and S. Ma, *RSC Adv.*, 2014, **4**, 36464–36470.
161 P. G. Karagiannidis, S. A. Hodge, L. Lombardi, F. Tomarchio, N. Decorde, S. Milana, I. Goykhman, Y. Su, S. V Mesite, D. N. Johnstone, R. K. Leary, P. A. Midgley, N. M. Pugno, F. Torrisi and A. C. Ferrari, *ACS Nano*, 2017, **11**, 2742–2755.
162 K. R. Paton, J. Anderson, A. J. Pollard and T. Sainsbury, *Mater. Res. Express*, 2017, **4**, 25604.
163 C. Yeon, S. J. Yun, K.-S. Lee and J. W. Lim, *Carbon N. Y.*, 2015, **83**, 136–143.
164 W. Wang, S. Dai, X. Li, J. Yang, D. J. Srolovitz and Q. Zheng, *Nat. Commun.*, 2015, **6**, 7853.
165 X. Chen, F. Tian, C. Persson, W. Duan and N. Chen, *Sci. Rep.*, 2013, **3**, 3046.
166 R. O. Brennan, *J. Chem. Phys.*, 1952, **20**, 40–48.
167 R. J. Smith, M. Lotya and J. N. Coleman, *New J. Phys.*, 2010, **12**, 125008.
168 Y. Arao, F. Mori and M. Kubouchi, *Carbon N. Y.*, 2017, **118**, 18–24.
169 A. B. Bourlinos, V. Georgakilas, R. Zboril, T. A. Steriotis and A. K. Stubos, *Small*, 2009, **5**, 1841–1845.
170 D. B. Shinde, J. Brenker, C. D. Easton, R. F. Tabor, A. Neild and M. Majumder, *Langmuir*, 2016, **32**, 3552–3559.
171 A. O'Neill, U. Khan, P. N. Nirmalraj, J. Boland and J. N. Coleman, *J. Phys. Chem. C*, 2011, **115**, 5422–5428.
172 J. Zhang, L. Xu, B. Zhou, Y. Zhu and X. Jiang, *J. Colloid Interface Sci.*, 2018, **513**, 279–286.
173 W.-W. Liu, B.-Y. Xia, X.-X. Wang and J.-N. Wang, *Front. Mater. Sci.*, 2012, **6**, 176–182.
174 S. Wang, M. Yi, Z. Shen, X. Zhang and S. Ma, *RSC Adv.*, 2014, **4**, 25374–25378.
175 A. E. Morgan and G. A. Somorjai, *Surf. Sci.*, 1968, **12**, 405–425.
176 A. T. N'Diaye, J. Coraux, T. N. Plasa, C. Busse and T. Michely, *New J. Phys.*, , DOI:10.1088/1367-2630/10/4/043033.
177 P. W. Sutter, J.-I. Flege and E. A. Sutter, *Nat. Mater.*, 2008, **7**, 406–411.
178 E. Loginova, N. C. Bartelt, P. J. Feibelman and K. F. McCarty, *New J. Phys.*, , DOI:10.1088/1367-2630/11/6/063046.
179 M. Batzill, *Surf. Sci. Rep.*, 2012, **67**, 83–115.
180 A. Reina, S. Thiele, X. Jia, S. Bhaviripudi, M. S. Dresselhaus, J. A. Schaefer and J. Kong, *Nano Res.*, 2009, **2**, 509–516.
181 A. Reina, X. Jia, J. Ho, D. Nezich, H. Son, V. Bulovic, M. S. Dresselhaus and J. Kong, *Nano Lett.*, 2009, **9**, 30–35.
182 X. Li, W. Cai, J. An, S. Kim, J. Nah, D. Yang, R. Piner, A. Velamakanni, I. Jung, E. Tutuc, S. K. Banerjee, L. Colombo and R. S. Ruoff, *Science (80-.).*, 2009, **324**, 1312–1314.
183 Y. Zhang, L. Zhang and C. Zhou, *Acc. Chem. Res.*, 2013, **46**, 2329–2339.
184 R. S. Edwards and K. S. Coleman, *Acc. Chem. Res.*, 2013, **46**, 23–30.
185 K. Yan, L. Fu, H. Peng and Z. Liu, *Acc. Chem. Res.*, 2013, **46**, 2263–2274.
186 C. Mattevi, H. Kim and M. Chhowalla, *J. Mater. Chem.*, 2011, **21**, 3324–3334.
187 A. Ōya and S. Ōtani, *Carbon N. Y.*, 1979, **17**, 131–137.
188 A. Ōya and H. Marsh, *J. Mater. Sci.*, 1982, **17**, 309–322.
189 S. T. and A. R. and P. H. and J. K. and P. W. and P.-L. H. and C. K. and J. S. and J. Kong, *Nanotechnology*, 2010, **21**, 15601.
190 G. Giovannetti, P. A. Khomyakov, G. Brocks, V. M. Karpan, J. van den Brink and P. J. Kelly, *Phys. Rev. Lett.*, 2008, **101**, 026803.
191 Y. Xue, B. Wu, Y. Guo, L. Huang, L. Jiang, J. Chen, D. Geng, Y. Liu, W. Hu and G. Yu, *Nano Res.*, 2011, **4**, 1208–1214.
192 M.-S. Wang, Y. Cheng, L. Zhao, U. K. Gautam and D. Golberg, *ACS Nano*, 2017, **11**, 10575–10582.

193 D. Zhu, H. Gao, T. Yang, T. Yang, L. Li, G. Yin, X. Li, C. Nicklin, X. Gao, Z. Li, L. Yi and X. Li, *Carbon N. Y.*, 2015, **94**, 775–780.
194 L. L. Patera, F. Bianchini, C. Africh, C. Dri, G. Soldano, M. M. Mariscal, M. Peressi and G. Comelli, *Science (80-.).*, 2018, **359**, 1243–1246.
195 S. J. Chae, F. Guenes, K. K. Kim, E. S. Kim, G. H. Han, S. M. Kim, H.-J. Shin, S.-M. Yoon, J.-Y. Choi, M. H. Park, C. W. Yang, D. Pribat and Y. H. Lee, *Adv. Mater.*, 2009, **21**, 2328+.
196 F. J. Derbyshire, A. E. B. Presland and D. L. Trimm, *Carbon N. Y.*, 1975, **13**, 111–113.
197 D. Kondo, K. Yagi, M. Sato, M. Nihei, Y. Awano, S. Sato and N. Yokoyama, *Chem. Phys. Lett.*, 2011, **514**, 294–300.
198 M. E. Ramon, A. Gupta, C. Corbet, D. A. Ferrer, H. C. P. Movva, G. Carpenter, L. Colombo, G. Bourianoff, M. Doczy, D. Akinwande, E. Tutuc and S. K. Banerjee, *ACS Nano*, 2011, **5**, 7198–7204.
199 A. Varykhalov and O. Rader, *Phys. Rev. B*, 2009, **80**, 035437.
200 H. Ago, Y. Ito, N. Mizuta, K. Yoshida, B. Hu, C. M. Orofeo, M. Tsuji, K. Ikeda and S. Mizuno, *ACS Nano*, 2010, **4**, 7407–7414.
201 N. Yang, K. Choi, J. Robertson and H. G. Park, *2D Mater.*, 2017, **4**, 035023.
202 L. Gan and Z. Luo, *ACS Nano*, 2013, **7**, 9480–9488.
203 L. Lin, B. Deng, J. Sun, H. Peng and Z. Liu, *Chem. Rev.*, 2018, **118**, 9281–9343.
204 J. M. Wofford, S. Nie, K. F. McCarty, N. C. Bartelt and O. D. Dubon, *Nano Lett.*, 2010, **10**, 4890–4896.
205 G. Ruan, Z. Sun, Z. Peng and J. M. Tour, *ACS Nano*, 2011, **5**, 7601–7607.
206 X. Xu, Z. Zhang, J. Dong, D. Yi, J. Niu, M. Wu, L. Lin, R. Yin, M. Li, J. Zhou, S. Wang, J. Sun, X. Duan, P. Gao, Y. Jiang, X. Wu, H. Peng, R. S. Ruoff, Z. Liu, D. Yu, E. Wang, F. Ding and K. Liu, *Sci. Bull.*, 2017, **62**, 1074–1080.
207 X. Wang and G. Shi, *Energy Environ. Sci.*, 2015, **8**, 790–823.
208 M. Inagaki, J. Qiu and Q. Guo, *Carbon N. Y.*, 2015, **87**, 128–152.
209 L. Jiang and Z. Fan, *Nanoscale*, 2014, **6**, 1922–1945.
210 Z. Chen, W. Ren, L. Gao, B. Liu, S. Pei and H.-M. Cheng, *Nat Mater*, 2011, **10**, 424–428.
211 J.-C. Yoon, J.-S. Lee, S.-I. Kim, K.-H. Kim and J.-H. Jang, *Sci. Rep.*, 2013, **3**, 1788.
212 W. Li, S. Gao, L. Wu, S. Qiu, Y. Guo, X. Geng, M. Chen, S. Liao, C. Zhu, Y. Gong, M. Long, J. Xu, X. Wei, M. Sun and L. Liu, *Sci. Rep.*, 2013, **3**, 2125.
213 S. D. and M. W. and J. W. and J. V. and E. M. and B. M. B. and V. M. and L. C. and F. B. and J. A. Garrido, *2D Mater.*, 2016, **3**, 45013.
214 L. Shi, K. Chen, R. Du, A. Bachmatiuk, M. H. Rümmeli, K. Xie, Y. Huang, Y. Zhang and Z. Liu, *J. Am. Chem. Soc.*, 2016, **138**, 6360–6363.
215 K. Chen, C. Li, Z. Chen, L. Shi, S. Reddy, H. Meng, Q. Ji, Y. Zhang and Z. Liu, *Nano Res.*, 2016, **9**, 249–259.
216 K. Chen, L. Shi, Y. Zhang and Z. Liu, *Chem. Soc. Rev.*, 2018, **47**, 3018–3036.
217 US568323A, 1896.
218 W. P. Eatherly, *J. Nucl. Mater.*, 1981, **100**, 55–63.
219 M. Wissler, *J. Power Sources*, 2006, **156**, 142–150.
220 H. Marsh and A. P. Warburton, *J. Appl. Chem.*, 1970, **20**, 133–142.
221 N. D. Petkovich and A. Stein, *Chem. Soc. Rev.*, 2013, **42**, 3721–3739.
222 L. Chuenchom, R. Kraehnert and B. M. Smarsly, *Soft Matter*, 2012, **8**, 10801–10812.
223 C. Liang, K. Hong, G. A. Guiochon, J. W. Mays and S. Dai, *Angew. Chemie Int. Ed.*, 2004, **43**, 5785–5789.
224 T. Kyotani, T. Nagai, S. Inoue and A. Tomita, *Chem. Mater.*, 1997, **9**, 609–615.
225 A. B. Fuertes and S. Alvarez, *Carbon N. Y.*, 2004, **42**, 3049–3055.
226 T.-W. Kim, I.-S. Park and R. Ryoo, *Angew. Chemie Int. Ed.*, 2003, **42**, 4375–4379.
227 Z. Ma, T. Kyotani and A. Tomita, *Chem. Commun.*, 2000, 2365–2366.
228 R. Ryoo, S. H. Joo and S. Jun, *J. Phys. Chem. B*, 1999, **103**, 7743–7746.

229 S. Jun, S. H. Joo, R. Ryoo, M. Kruk, M. Jaroniec, Z. Liu, T. Ohsuna and O. Terasaki, *J. Am. Chem. Soc.*, 2000, **122**, 10712–10713.
230 D. Kawashima, T. Aihara, Y. Kobayashi, T. Kyotani and A. Tomita, *Chem. Mater.*, 2000, **12**, 3397–3401.
231 S. Han, K. Sohn and T. Hyeon, *Chem. Mater.*, 2000, **12**, 3337–3341.
232 Z. Li and M. Jaroniec, *J. Am. Chem. Soc.*, 2001, **123**, 9208–9209.
233 Z. Li, M. Jaroniec, Y.-J. Lee and L. R. Radovic, *Chem. Commun.*, 2002, 1346–1347.
234 S. B. Yoon, G. S. Chai, S. K. Kang, J.-S. Yu, K. P. Gierszal and M. Jaroniec, *J. Am. Chem. Soc.*, 2005, **127**, 4188–4189.
235 T. Hyeon, S. Han, Y.-E. Sung, K.-W. Park and Y.-W. Kim, *Angew. Chemie Int. Ed.*, 2003, **42**, 4352–4356.
236 S. Han, Y. Yun, K.-W. Park, Y.-E. Sung and T. Hyeon, *Adv. Mater.*, 2003, **15**, 1922–1925.
237 R. W. Pekala, *J. Mater. Sci.*, 1989, **24**, 3221–3227.
238 M. Kakunuri and C. S. Sharma, *J. Mater. Res.*, 2018, **33**, 1074–1087.
239 R. W. Pekala and C. T. Alviso, *MRS Proc.*, 1992, **270**, 3.
240 F. J. Maldonado-Hódar, C. Moreno-Castilla, J. Rivera-Utrilla, Y. Hanzawa and Y. Yamada, *Langmuir*, 2000, **16**, 4367–4373.
241 M. Aghabararpour, S. Motahari, Z. Sanaee and A. Ghahreman, *J. Nanoparticle Res.*, 2019, **21**, 178.
242 G. Hasegawa, K. Kanamori and K. Nakanishi, *Mater. Lett.*, 2012, **76**, 1–4.
243 A.-H. Lu, W.-C. Li, E.-L. Salabas, B. Spliethoff and F. Schüth, *Chem. Mater.*, 2006, **18**, 2086–2094.
244 M. Sevilla, C. Sanchís, T. Valdés-Solís, E. Morallón and A. B. Fuertes, *J. Phys. Chem. C*, 2007, **111**, 9749–9756.
245 M. Sevilla, C. Sanchís, T. Valdés-Solís, E. Morallón and A. B. Fuertes, *Carbon N. Y.*, 2008, **46**, 931–939.
246 W. Kiciński, M. Bystrzejewski, M. H. Rümmeli and T. Gemming, *Bull. Mater. Sci.*, 2014, **37**, 141–150.
247 M. Sevilla and A. B. Fuertes, *Mater. Chem. Phys.*, 2009, **113**, 208–214.
248 Z. Schnepp, M. Thomas, S. Glatzel, K. Schlichte, R. Palkovits and C. Giordano, *J. Mater. Chem.*, 2011, **21**, 17760–17764.
249 A. E. Danks, M. J. Hollamby, B. Hammouda, D. C. Fletcher, F. Johnston-Banks, S. E. Rogers and Z. Schnepp, *J. Mater. Chem. A*, 2017, **5**, 11644–11651.
250 Z. Schnepp, M. J. Hollamby, M. Tanaka, Y. Matsushita, Y. Xu and Y. Sakka, *Chem. Commun.*, 2014, **50**, 5364–5366.
251 R. Fu, T. F. Baumann, S. Cronin, G. Dresselhaus, M. S. Dresselhaus and J. H. Satcher, *Langmuir*, 2005, **21**, 2647–2651.
252 Q. Yan, J. Li, X. Zhang, E. B. Hassan, C. Wang, J. Zhang and Z. Cai, *J. Nanoparticle Res.*, 2018, **20**, 223.
253 Z. Schnepp, Y. Zhang, M. J. Hollamby, B. R. Pauw, M. Tanaka, Y. Matsushita and Y. Sakka, *J. Mater. Chem. A*, 2013, **1**, 13576–13581.
254 W. Weisweiler, N. Subramanian and B. Terwiesch, *Carbon N. Y.*, 1971, **9**, 755–761.
255 X.-F. Jiang, R. Li, M. Hu, Z. Hu, D. Golberg, Y. Bando and X.-B. Wang, *Adv. Mater.*, 2019, **31**, 1901186.
256 A. Ōya and S. Ōtani, *Carbon N. Y.*, 1975, **13**, 450–451.
257 A. Oya, R. Yamashita and S. Otani, *High Temp. - High Press.*, 1978, **10**, 511–520.
258 J. Zhao, Y. Jiang, H. Fan, M. Liu, O. Zhuo, X. Wang, Q. Wu, L. Yang, Y. Ma and Z. Hu, *Adv. Mater.*, 2017, **29**, 1604569.
259 A.-Y. Kim, M. K. Kim, K. Cho, J.-Y. Woo, Y. Lee, S.-H. Han, D. Byun, W. Choi and J. K. Lee, *ACS Appl. Mater. Interfaces*, 2016, **8**, 19514–19523.
260 S.-M. Yoon, W. M. Choi, H. Baik, H.-J. Shin, I. Song, M.-S. Kwon, J. J. Bae, H. Kim, Y. H.

Lee and J.-Y. Choi, *ACS Nano*, 2012, **6**, 6803–6811.
261 J. Sha, C. Gao, S.-K. Lee, Y. Li, N. Zhao and J. M. Tour, *ACS Nano*, 2016, **10**, 1411–1416.
262 K. Kaneko, C. Ishii, M. Ruike and H. kuwabara, *Carbon N. Y.*, 1992, **30**, 1075–1088.
263 J. W. Long, M. Laskoski, T. M. Keller, K. A. Pettigrew, T. N. Zimmerman, S. B. Qadri and G. W. Peterson, *Carbon N. Y.*, 2010, **48**, 501–508.
264 D. Sun, X. Yu, X. Ji, Z. Sun and D. Sun, *J. Alloys Compd.*, 2019, **805**, 327–337.
265 Q. Yan, J. Li, X. Zhang, J. Zhang and Z. Cai, *Nanomater. Nanotechnol.*, 2018, **8**, 184798041881895.
266 J. Hoekstra, A. M. Beale, F. Soulimani, M. Versluijs-Helder, J. W. Geus and L. W. Jenneskens, *J. Phys. Chem. C*, 2015, **119**, 10653–10661.
267 Z. Yan, Q. Hu, G. Yan, H. Li, K. Shih, Z. Yang, X. Li, Z. Wang and J. Wang, *Chem. Eng. J.*, 2017, **321**, 495–501.
268 J. Tang, R. R. Salunkhe, H. Zhang, V. Malgras, T. Ahamad, S. M. Alshehri, N. Kobayashi, S. Tominaka, Y. Ide, J. H. Kim and Y. Yamauchi, *Sci. Rep.*, 2016, **6**, 30295.
269 E. Thompson, A. E. Danks, L. Bourgeois and Z. Schnepp, *Green Chem.*, 2015, **17**, 551–556.
270 S. Glatzel, Z. Schnepp and C. Giordano, *Angew. Chemie Int. Ed.*, 2013, **52**, 2355–2358.
271 C. J. Thambiliyagodage, S. Ulrich, P. T. Araujo and M. G. Bakker, *Carbon N. Y.*, 2018, **134**, 452–463.
272 J. Yuan, C. Giordano and M. Antonietti, *Chem. Mater.*, 2010, **22**, 5003–5012.
273 G. Zhong, L. Ma, C. Yan, P. Zhuang and X. Ma, *Chem. Eng. J.*, 2020, **398**, 125545.
274 N. Amini, K.-F. Aguey-Zinsou and Z.-X. Guo, *Carbon N. Y.*, 2011, **49**, 3857–3864.
275 M. Pudukudy, Z. Yaakob, A. Kadier, M. S. Takriff and N. S. M. Hassan, *Int. J. Hydrogen Energy*, 2017, **42**, 16495–16513.
276 I. Major, J.-M. Pin, E. Behazin, A. Rodriguez-Uribe, M. Misra and A. Mohanty, *Green Chem.*, 2018, **20**, 2269–2278.
277 C. Chen, K. Sun, A. Wang, S. Wang and J. Jiang, *Bioresources*, 2018, **13**, 3165–3176.
278 M. Zhong, J. Yan, H. Wu, W. Shen, J. Zhang, C. Yu, L. Li, Q. Hao, F. Gao, Y. Tian, Y. Huang and S. Guo, *Fuel Process. Technol.*, 2020, **198**, 106241.
279 K. Wang, Y. Cao, X. Wang, P. R. Kharel, W. Gibbons, B. Luo, Z. Gu, Q. Fan and L. Metzger, *Energy*, 2016, **101**, 9–15.
280 W. Weisweiler, N. Subramanian and B. Terwiesch, *Carbon N. Y.*, 1971, **9**, 755–761.
281 T. Noda and M. Inagaki, *Carbon N. Y.*, 1964, **2**, 127–130.
282 T. Purkait, G. Singh, M. Singh, D. Kumar and R. S. Dey, *Sci. Rep.*, 2017, **7**, 15239.
283 O. P. Morris, X. Zang, A. Gregg, B. Keller, B. Getachew, S. Ingersoll, H. A. Elsen, M. M. Disko, N. Ferralis and J. C. Grossman, *Adv. Mater.*, 2019, **31**, 1900331.
284 X. Zang, C. Jian, S. Ingersoll, H. Li, J. J. Adams, Z. Lu, N. Ferralis and J. C. Grossman, *Sci. Adv.*, 2020, **6**, eaaz5231.
285 M. G. Ltd, Graphene producers, https://www.graphene-info.com/companies-list/graphene-producers, (accessed 11 November 2020).
286 A. P. Kauling, A. T. Seefeldt, D. P. Pisoni, R. C. Pradeep, R. Bentini, R. V. B. Oliveira, K. S. Novoselov and A. H. Castro Neto, *Adv. Mater.*, 2018, **30**, 1803784.
287 P. Wick, A. E. Louw-Gaume, M. Kucki, H. F. Krug, K. Kostarelos, B. Fadeel, K. A. Dawson, A. Salvati, E. Vázquez, L. Ballerini, M. Tretiach, F. Benfenati, E. Flahaut, L. Gauthier, M. Prato and A. Bianco, *Angew. Chemie Int. Ed.*, 2014, **53**, 7714–7718.
288 K. Kouroupis-Agalou, A. Liscio, E. Treossi, L. Ortolani, V. Morandi, N. M. Pugno and V. Palermo, *Nanoscale*, 2014, **6**, 5926–5933.
289 A. Wróblewska, A. Dużyńska, J. Judek, L. Stobiński, K. Żerańska, A. P. Gertych and M. Zdrojek, *J. Phys. Condens. Matter*, 2017, **29**, 475201.
290 M. Bayle, N. Reckinger, J.-R. Huntzinger, A. Felten, A. Bakaraki, P. Landois, J.-F. Colomer, L. Henrard, A.-A. Zahab, J.-L. Sauvajol and M. Paillet, *Phys. Status Solidi*,

2015, **252**, 2375–2379.
291 S. Eigler, *Chem. - A Eur. J.*, 2016, **22**, 7012–7027.
292 J. M. Englert, P. Vecera, K. C. Knirsch, R. A. Schäfer, F. Hauke and A. Hirsch, *ACS Nano*, 2013, **7**, 5472–5482.
293 D. L. Silva, J. L. E. Campos, T. F. D. Fernandes, J. N. Rocha, L. R. P. Machado, E. M. Soares, D. R. Miquita, H. Miranda, C. Rabelo, O. P. Vilela Neto, A. Jorio and L. G. Cançado, *Carbon N. Y.*, 2020, **161**, 181–189.
294 A. Kovtun, E. Treossi, N. Mirotta, A. Scidà, A. Liscio, M. Christian, F. Valorosi, A. Boschi, R. J. Young, C. Galiotis, I. A. Kinloch, V. Morandi and V. Palermo, *2D Mater.*, 2019, **6**, 025006.
295 A. J. Pollard, *Meas. Sci. Technol.*, 2016, **27**, 92001.
296 T. Reiss, K. Hjelt and A. C. Ferrari, *Nat. Nanotechnol.*, 2019, **14**, 907–910.
297 J. R. Kyle, C. S. Ozkan and M. Ozkan, *Nanoscale*, 2012, **4**, 3807–3819.
298 A. A. Graf, S. P. Ogilvie, H. J. Wood, C. J. Brown, M. Tripathi, A. A. K. King, A. B. Dalton and M. J. Large, *Chem. Mater.*, 2020, **32**, 6213–6221.
299 U. Khan, A. O'Neill, M. Lotya, S. De and J. N. Coleman, *Small*, 2010, **6**, 864–871.
300 Y. Hernandez, M. Lotya, D. Rickard, S. D. Bergin and J. N. Coleman, *Langmuir*, 2010, **26**, 3208–3213.
301 N. R. Wilson, P. A. Pandey, R. Beanland, R. J. Young, I. A. Kinloch, L. Gong, Z. Liu, K. Suenaga, J. P. Rourke, S. J. York and J. Sloan, *ACS Nano*, 2009, **3**, 2547–2556.
302 T. Szabó, O. Berkesi, P. Forgó, K. Josepovits, Y. Sanakis, D. Petridis and I. Dékány, *Chem. Mater.*, 2006, **18**, 2740–2749.
303 P. Nemes-Incze, Z. Osváth, K. Kamarás and L. P. Biró, *Carbon N. Y.*, 2008, **46**, 1435–1442.
304 C. Backes, T. M. Higgins, A. Kelly, C. Boland, A. Harvey, D. Hanlon and J. N. Coleman, *Chem. Mater.*, 2017, **29**, 243–255.
305 R. Su, S. F. Lin, D. Q. Chen and G. H. Chen, *J. Phys. Chem. C*, 2014, **118**, 12520–12525.
306 D. Tasis, K. Papagelis, P. Spiliopoulos and C. Galiotis, *Mater. Lett.*, 2013, **94**, 47–50.
307 R. R. Nair, P. Blake, A. N. Grigorenko, K. S. Novoselov, T. J. Booth, T. Stauber, N. M. R. Peres and A. K. Geim, *Science (80-.).*, 2008, **320**, 1308–1308.
308 M. Shtein, I. Pri-Bar, M. Varenik and O. Regev, *Anal. Chem.*, 2015, **87**, 4076–4080.
309 A. J. Pollard and D. Roy, *Spectrosc. Eur.*, 2015, **27**, 9–12.
310 M. K. Tynan, D. W. Johnson, B. P. Dobson and K. S. Coleman, *Nanoscale*, 2016, **8**, 13303–13310.
311 M. Ishihara, Y. Koga, J. Kim, K. Tsugawa and M. Hasegawa, *Mater. Lett.*, 2011, **65**, 2864–2867.
312 S. Shivaraman, M. V. S. Chandrashekhar, J. J. Boeckl and M. G. Spencer, *J. Electron. Mater.*, 2009, **38**, 725–730.
313 T. Yu, Z. Ni, C. Du, Y. You, Y. Wang and Z. Shen, *J. Phys. Chem. C*, 2008, **112**, 12602–12605.
314 S. Chen, Q. Li, Q. Zhang, Y. Qu, H. Ji, R. S. Ruoff and W. Cai, *Nanotechnology*, 2012, **23**, 365701.
315 Q. Wu, Y. Wu, Y. Hao, J. Geng, M. Charlton, S. Chen, Y. Ren, H. Ji, H. Li, D. W. Boukhvalov, R. D. Piner, C. W. Bielawski and R. S. Ruoff, *Chem. Commun.*, 2013, **49**, 677–679.
316 A. Säynätjoki, L. Karvonen, J. Riikonen, W. Kim, S. Mehravar, R. A. Norwood, N. Peyghambarian, H. Lipsanen and K. Kieu, *ACS Nano*, 2013, **7**, 8441–8446.
317 C. M. Nolen, D. Teweldebrhan, G. Denina, B. Bhanu and A. A. Balandin, *ECS Trans.*, 2019, **33**, 201–209.
318 C. Raman and K. Krishnan, *Nature*, 1928, **121**, 501–502.
319 P. Vandenabeele, *Practical Raman Spectroscopy - An Introduction*, John Wiley & Sons,

Ltd, Chichester, UK, 1st edn., 2013.
320 R. Saito, M. Hofmann, G. Dresselhaus, A. Jorio and M. S. Dresselhaus, *Adv. Phys.*, 2011, **60**, 413–550.
321 A. C. Ferrari, *Solid State Commun.*, 2007, **143**, 47–57.
322 L. G. Cançado, A. Jorio and M. A. Pimenta, *Phys. Rev. B*, 2007, **76**, 064304.
323 P. Klar, E. Lidorikis, A. Eckmann, I. A. Verzhbitskiy, A. C. Ferrari and C. Casiraghi, *Phys. Rev. B*, 2013, **87**, 205435.
324 J. S. Park, A. Reina, R. Saito, J. Kong, G. Dresselhaus and M. S. Dresselhaus, *Carbon N. Y.*, 2009, **47**, 1303–1310.
325 J.-W. Jiang, H. Tang, B.-S. Wang and Z.-B. Su, *Phys. Rev. B*, 2008, **77**, 235421.
326 Z. Ni, Y. Wang, T. Yu, Y. You and Z. Shen, *Phys. Rev. B*, 2008, **77**, 235403.
327 L. G. Cançado, K. Takai, T. Enoki, M. Endo, Y. A. Kim, H. Mizusaki, N. L. Speziali, A. Jorio and M. A. Pimenta, *Carbon N. Y.*, 2008, **46**, 272–275.
328 A. Das, B. Chakraborty and A. K. Sood, *Bull. Mater. Sci.*, 2008, **31**, 579–584.
329 D. R. Lenski and M. S. Fuhrer, *J. Appl. Phys.*, 2011, **110**, 013720.
330 M. M. Lucchese, F. Stavale, E. H. M. Ferreira, C. Vilani, M. V. O. Moutinho, R. B. Capaz, C. A. Achete and A. Jorio, *Carbon N. Y.*, 2010, **48**, 1592–1597.
331 K. Erickson, R. Erni, Z. Lee, N. Alem, W. Gannett and A. Zettl, *Adv. Mater.*, 2010, **22**, 4467–4472.
332 G. Compagnini, F. Giannazzo, S. Sonde, V. Raineri and E. Rimini, *Carbon N. Y.*, 2009, **47**, 3201–3207.
333 E. H. Martins Ferreira, M. V. O. Moutinho, F. Stavale, M. M. Lucchese, R. B. Capaz, C. A. Achete and A. Jorio, *Phys. Rev. B*, 2010, **82**, 125429.
334 A. A. K. King, B. R. Davies, N. Noorbehesht, P. Newman, T. L. Church, A. T. Harris, J. M. Razal and A. I. Minett, *Sci. Rep.*, 2016, **6**, 19491.
335 D. Teweldebrhan and A. A. Balandin, *Appl. Phys. Lett.*, 2009, **94**, 13101.
336 P. Vecera, J. C. Chacón-Torres, T. Pichler, S. Reich, H. R. Soni, A. Görling, K. Edelthalhammer, H. Peterlik, F. Hauke and A. Hirsch, *Nat. Commun.*, 2017, **8**, 15192.
337 L. G. Cançado, M. G. da Silva, E. H. M. Ferreira, F. Hof, K. Kampioti, K. Huang, A. Pénicaud, C. A. Achete, R. B. Capaz and A. Jorio, *2D Mater.*, 2017, **4**, 25039.
338 F. Tuinstra and J. L. Koenig, *J. Chem. Phys.*, 1970, **53**, 1126–1130.
339 L. G. Cançado, K. Takai, T. Enoki, M. Endo, Y. A. Kim, H. Mizusaki, A. Jorio, L. N. Coelho, R. Magalhães-Paniago and M. A. Pimenta, *Appl. Phys. Lett.*, 2006, **88**, 163106.
340 PerkinElmer, A Beginners Guide Thermogravimetric Analysis, https://www.perkinelmer.com/lab-solutions/resources/docs/FAQ_Beginners-Guide-to-Thermogravimetric-Analysis_009380C_01.pdf, (accessed 16 February 2020).
341 J. D. Saxby, S. P. Chatfield, A. J. Palmisano, A. M. Vassallo, M. A. Wilson and L. S. K. Pang, *J. Phys. Chem.*, 1992, **96**, 17–18.
342 L. S. K. Pang, J. D. Saxby and S. P. Chatfield, *J. Phys. Chem.*, 1993, **97**, 6941–6942.
343 R. Heintzmann and G. Ficz, *Briefings Funct. Genomics Proteomics*, 2006, **5**, 289–301.
344 L. V. Radushkevich and V. M. Lukyanovich, *J. Phys. Chem. Russ.*, 1952, **26**, 88–95.
345 S. Iijima and T. Ichihashi, *Nature*, 1993, **363**, 603–605.
346 J. C. Meyer, F. Eder, S. Kurasch, V. Skakalova, J. Kotakoski, H. J. Park, S. Roth, A. Chuvilin, S. Eyhusen, G. Benner, A. V Krasheninnikov and U. Kaiser, *Phys. Rev. Lett.*, 2012, **108**, 196102.
347 M. Haider, G. Braunshausen and E. Schwan, *Optik (Stuttg).*, 1995, **99**, 167–179.
348 S. Morishita, R. Ishikawa, Y. Kohno, H. Sawada, N. Shibata and Y. Ikuhara, *Microscopy*, 2017, **67**, 46–50.
349 A. Hashimoto, K. Suenaga, A. Gloter, K. Urita and S. Iijima, *Nature*, 2004, **430**, 870–873.
350 J. H. Warner, M. H. Rümmeli, T. Gemming, B. Büchner and G. A. D. Briggs, *Nano Lett.*,

2009, **9**, 102–106.
351 J. C. Meyer, A. K. Geim, M. I. Katsnelson, K. S. Novoselov, D. Obergfell, S. Roth, C. Girit and A. Zettl, *Solid State Commun.*, 2007, **143**, 101–109.
352 S. Rubino, S. Akhtar and K. Leifer, *Microsc. Microanal.*, 2016, **22**, 250–256.
353 Z. Liu, K. Suenaga, P. J. F. Harris and S. Iijima, *Phys. Rev. Lett.*, 2009, **102**, 15501.
354 Z. Czigány and L. Hultman, *Ultramicroscopy*, 2010, **110**, 815–819.
355 W. Sigle, *Annu. Rev. Mater. Res.*, 2005, **35**, 239–314.
356 S. Horiuchi, T. Gotou, M. Fujiwara, R. Sotoaka, M. Hirata, K. Kimoto, T. Asaka, T. Yokosawa, Y. Matsui, K. Watanabe and M. Sekita, *Jpn. J. Appl. Phys.*, 2003, **42**, L1073--L1076.
357 A. Bachmatiuk, J. Zhao, S. M. Gorantla, I. G. G. Martinez, J. Wiedermann, C. Lee, J. Eckert and M. H. Rummeli, *Small*, 2015, **11**, 515–542.
358 G. Cliff and G. W. Lorimer, *J. Microsc.*, 1975, **103**, 203–207.
359 W. H. Bragg and W. L. Bragg, *Proc. R. Soc. London Ser. A-Containing Pap. A Math. Phys. Character*, 1913, **88**, 428.
360 R. D. Deslattes, E. G. Kessler, P. Indelicato, L. de Billy, E. Lindroth and J. Anton, *Rev. Mod. Phys.*, 2003, **75**, 35–99.
361 U. Holzwarth and N. Gibson, *Nat. Nanotechnol.*, 2011, **6**, 534.
362 P. TRUCANO and R. CHEN, *Nature*, 1975, **258**, 136–137.
363 H. Shi, J. Reimers and J. R. Dahn, *J. Appl. Crystallogr. - J APPL CRYST*, 1993, **26**, 827–836.
364 Z. Q. Li, C. J. Lu, Z. P. Xia, Y. Zhou and Z. Luo, *Carbon N. Y.*, 2007, **45**, 1686–1695.
365 Z. Zhou, W. G. Bouwman, H. Schut and C. Pappas, *Carbon N. Y.*, 2014, **69**, 17–24.
366 S. Brunauer, P. H. Emmett and E. Teller, *J. Am. Chem. Soc.*, 1938, **60**, 309–319.
367 C. Weidenthaler, *Nanoscale*, 2011, **3**, 792–810.
368 J. Rouquerol, P. Llewellyn and F. Rouquerol, in *Characterization of Porous Solids VII*, eds. P. L. Llewellyn, F. Rodriquez-Reinoso, J. Rouqerol and N. Seaton, Elsevier, 2007, vol. 160, pp. 49–56.
369 Y. Xu, K. Sheng, C. Li and G. Shi, *J. Mater. Chem.*, 2011, **21**, 7376–7380.
370 Y. Huang, D. Wu, J. Jiang, Y. Mai, F. Zhang, H. Pan and X. Feng, *Nano Energy*, 2015, **12**, 287–295.
371 H. Wang, J. Yang, P. Zhao, A. Gölzhäuser, W. Liu, X. Chen and Z. Zheng, *Nanoscale*, 2020, **12**, 5170–5174.
372 P. Vecera, J. Holzwarth, K. F. Edelthalhammer, U. Mundloch, H. Peterlik, F. Hauke and A. Hirsch, *Nat. Commun.*, 2016, **7**, 12411.
373 A. Liscio, K. Kouroupis-Agalou, X. D. Betriu, A. Kovtun, E. Treossi, N. M. Pugno, G. De Luca, L. Giorgini and V. Palermo, *2D Mater.*, 2017, **4**, 025017.
374 A. J. Marsden, D. G. Papageorgiou, C. Vallés, A. Liscio, V. Palermo, M. A. Bissett, R. J. Young and I. A. Kinloch, *2D Mater.*, 2018, **5**, 32003.
375 J. Kim, J. Kim, S. Song, S. Zhang, J. Cha, K. Kim, H. Yoon, Y. Jung, K.-W. Paik and S. Jeon, *Carbon N. Y.*, 2017, **113**, 379–386.
376 B. Efron, *Ann. Stat.*, 1979, **7**, 1–26.
377 M. Newville, T. Stensitzki, D. B. Allen and A. Ingargiola, , DOI:10.5281/ZENODO.11813.
378 Horiba, Signal to Noise Ratio Explained, https://www.horiba.com/en_en/technology/measurement-and-control-techniques/molecular-spectroscopy/fluorescence-spectroscopy/how-to-calculate-signal-to-noise-ratio/, (accessed 23 August 2019).
379 U. Khan, A. O'Neill, H. Porwal, P. May, K. Nawaz and J. N. Coleman, *Carbon N. Y.*, 2012, **50**, 470–475.
380 D. A. C. Brownson and C. E. Banks, *Phys. Chem. Chem. Phys.*, 2012, **14**, 8264–8281.
381 C. Xu, B. Xu, Y. Gu, Z. Xiong, J. Sun and X. S. Zhao, *Energy Environ. Sci.*, 2013, **6**, 1388.

382 S.-X. Guo, Y. Liu, A. M. Bond, J. Zhang, P. Esakki Karthik, I. Maheshwaran, S. Senthil Kumar and K. L. N. Phani, *Phys. Chem. Chem. Phys.*, 2014, **16**, 19035–19045.
383 F. Khan and S. Mann, *J. Phys. Chem. C*, 2009, **113**, 19871–19874.
384 A. C. Ferrari and D. M. Basko, *Nat. Nanotechnol.*, 2013, **8**, 235–246.
385 D. C. Joy, *J. Microsc.*, 1984, **136**, 241–258.
386 O. A. Bulavchenko, S. V Cherepanova and S. V Tsybulya, *Zeitschrift Fur Krist.*, 2009, 329–334.
387 L. J. Garces, B. Hincapie, R. Zerger and S. L. Suib, *J. Phys. Chem. C*, 2015, **119**, 5484–5490.
388 O. A. Bulavchenko, S. V Cherepanova, V. V Malakhov, L. S. Dovlitova, A. V Ishchenko and S. V Tsybulya, *Kinet. Catal.*, 2009, **50**, 192–198.
389 E. A. O. and D. M. Jones, *Proc. Phys. Soc. Sect. B*, 1954, **67**, 456.
390 H. Rastegar, M. Bavand-vandchali, A. Nemati and F. Golestani-Fard, *Phys. E Low-dimensional Syst. Nanostructures*, 2018, **101**, 50–61.
391 J. R. Partington and R. P. Towndrow, *Trans. Faraday Soc.*, 1939, **35**, 553–559.
392 T. Wanjun and C. Donghua, *Chem. Pap.*, 2007, **61**, 329–332.
393 T. Cseri, S. Békássy, G. Kenessey, G. Liptay and F. Figueras, *Thermochim. Acta*, 1996, **288**, 137–154.
394 C. Breen, G. Thompson and M. Webb, *J. Mater. Chem.*, 1999, **9**, 3159–3165.
395 L. Wang, Z. Sofer and M. Pumera, *ACS Nano*, 2020, **14**, 21–25.
396 B. H. Toby and R. B. Von Dreele, *J. Appl. Crystallogr.*, 2013, **46**, 544–549.
397 C. A. Schneider, W. S. Rasband and K. W. Eliceiri, *Nat. Methods*, 2012, **9**, 671.
398 M. Paillet, R. Parret, J.-L. Sauvajol and P. Colomban, *J. Raman Spectrosc.*, 2018, **49**, 8–12.

9. Appendix – Additional Data

9.1 Raman Mapping

9.1.1 Graphite Data

Analysis of the starting graphite shows a very regular distribution of 2D peak heights and low D peak intensity as expected from crystalline graphite, this low peak intensity causes some artefacts. The regular graphite converges more swiftly than many materials although even this requires a significant number of data points before the distribution is absolutely stable. The scale of analysis requires depends greatly on the purpose, however, in this instance we find graphite converges completely around 300 data points, whilst approximately 100 data points were required to cover the core distribution parameters.

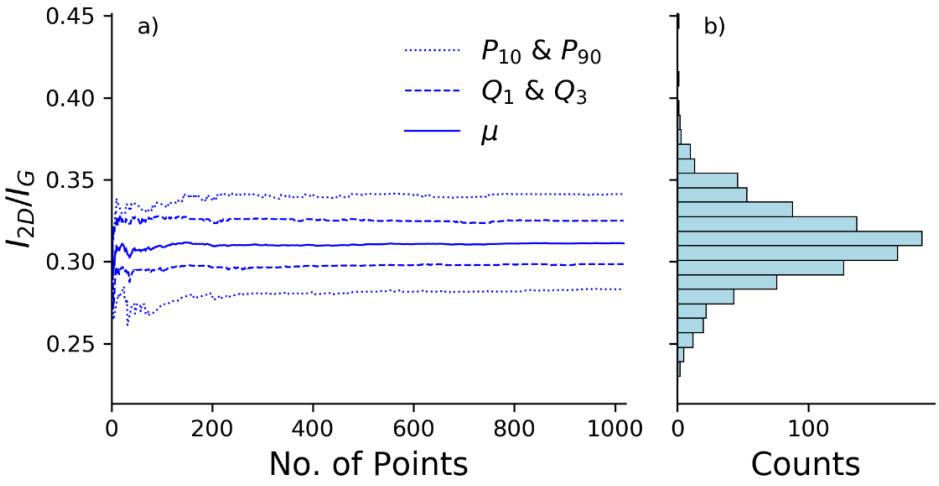

Figure S 1: Convergence plot from graphite (data set 1) showing a) the change in summary statistics of I_{2D}/I_G as more data points are added to the analysis. b) The final distribution shown as a horizontal histogram, y-axis constant across all plots showing I_{2D}/I_G convergence data from graphite sample.

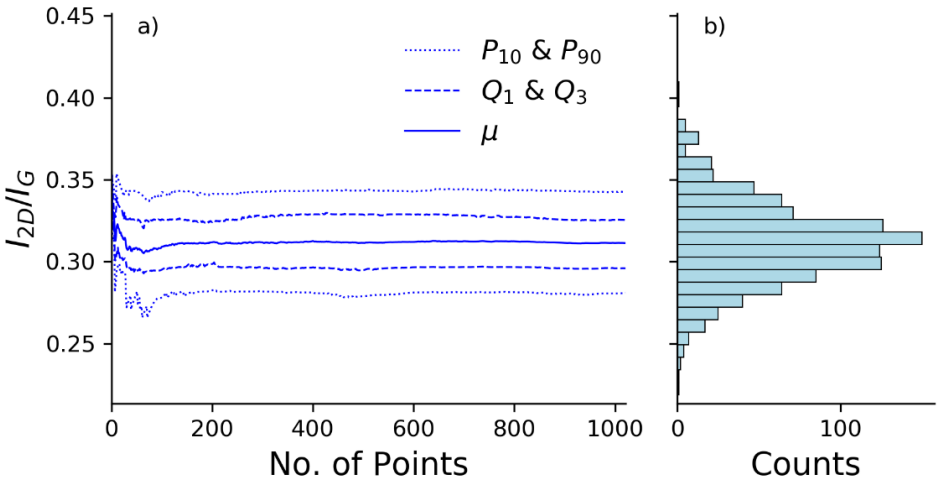

Figure S 2: Convergence plot from graphite (data set 2) described in detail above.

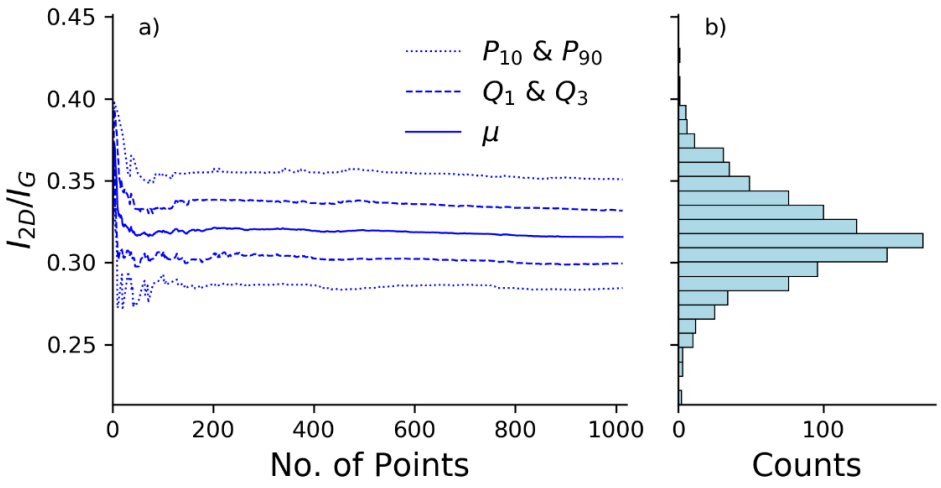

Figure S 3: Convergence plot from graphite (data set 3) described in detail above.

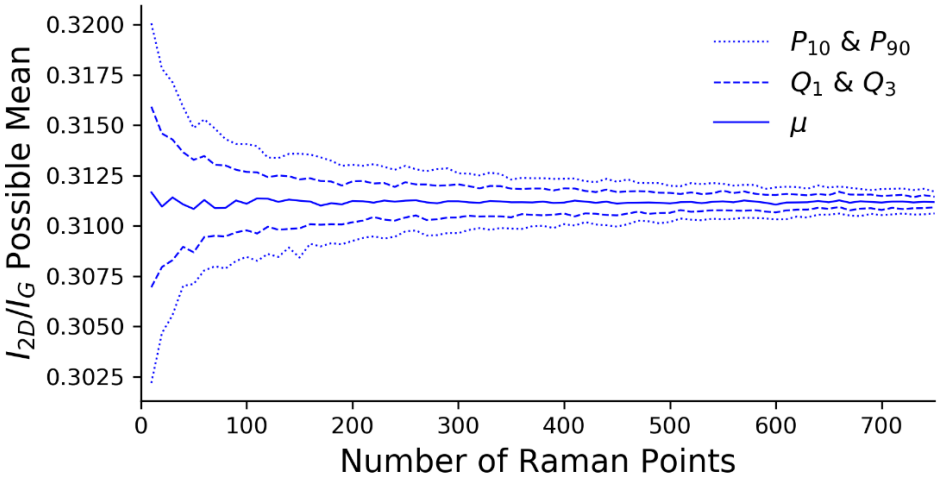

Figure S 4: Bootstrap convergence plot from graphite (data set 1); this shows the summary statistics (10th and 90th percentiles, 1st and 3rd quartiles, and mean) describing the distribution of mean values obtained from multiple analyses of smaller sub-sets of the sample size shown on the x-axis. This plot can be considered a probability distribution of possible mean values for different sample sizes.

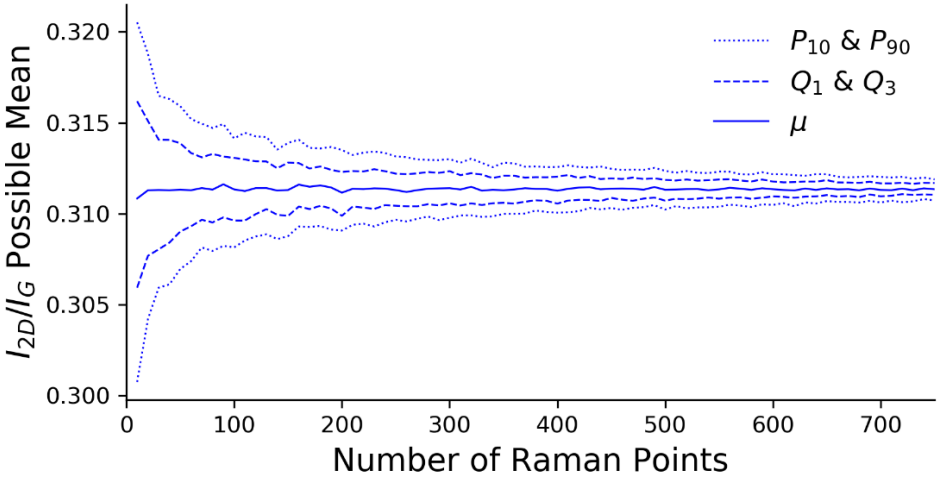

Figure S 5: Bootstrap convergence plot from graphite (data set 2), described in detail above.

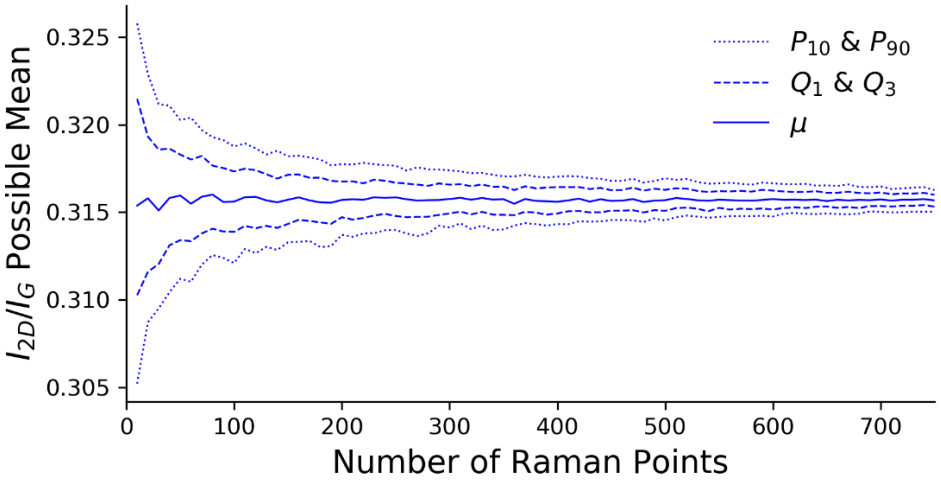

Figure S 6: Bootstrap convergence plot from graphite (data set 3), described in detail above.

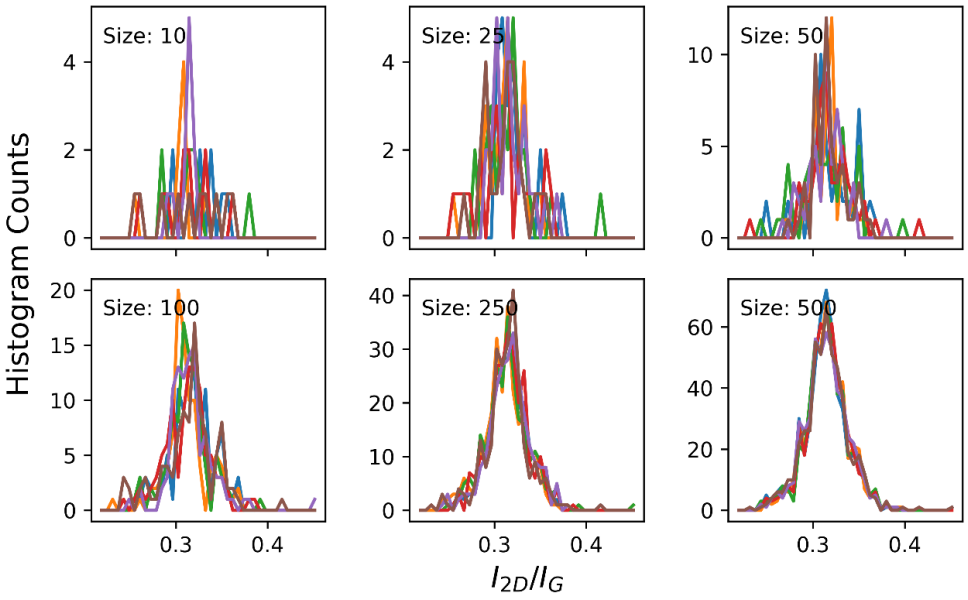

Figure S 7: Panel showing result of bootstrap analysis of graphite (data set 1). Each panel shows five examples, shown in different colors, of distributions of I_{2D}/I_G produced from sub-sets; the size of these is labelled and the x-axis is common across all I_{2D}/I_G panel plots. These show the convergence to a uniform distribution as the sub-set size increases.

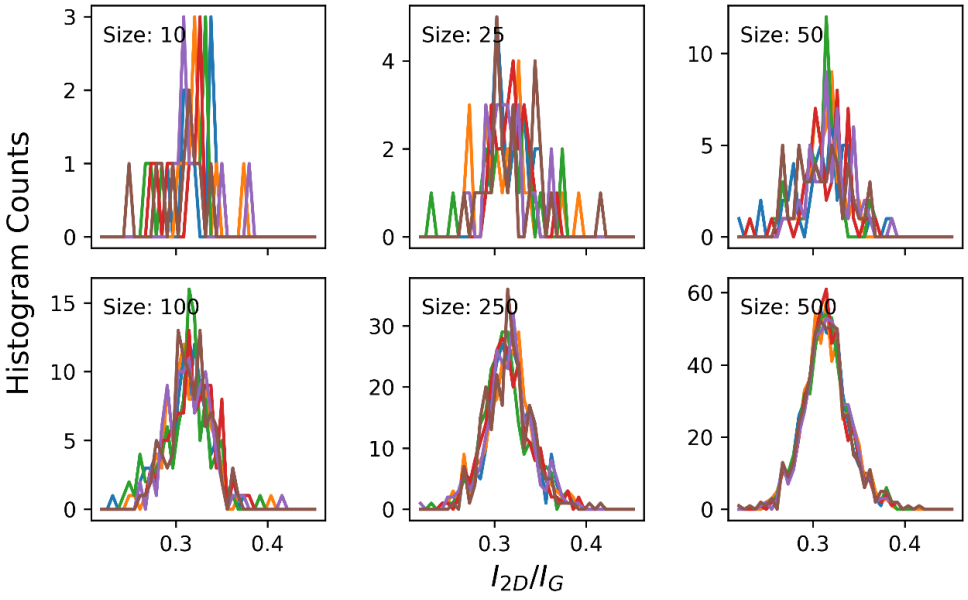

Figure S 8: Panel showing result of bootstrap analysis of graphite (data set 2), described in detail above.

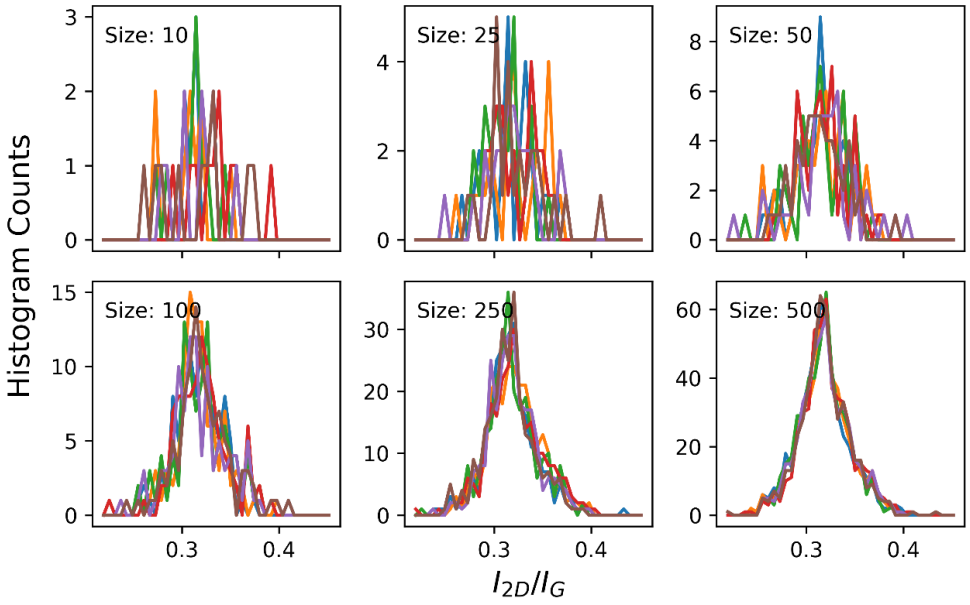

Figure S 9: Panel showing result of bootstrap analysis of graphite (data set 3), described in detail above.

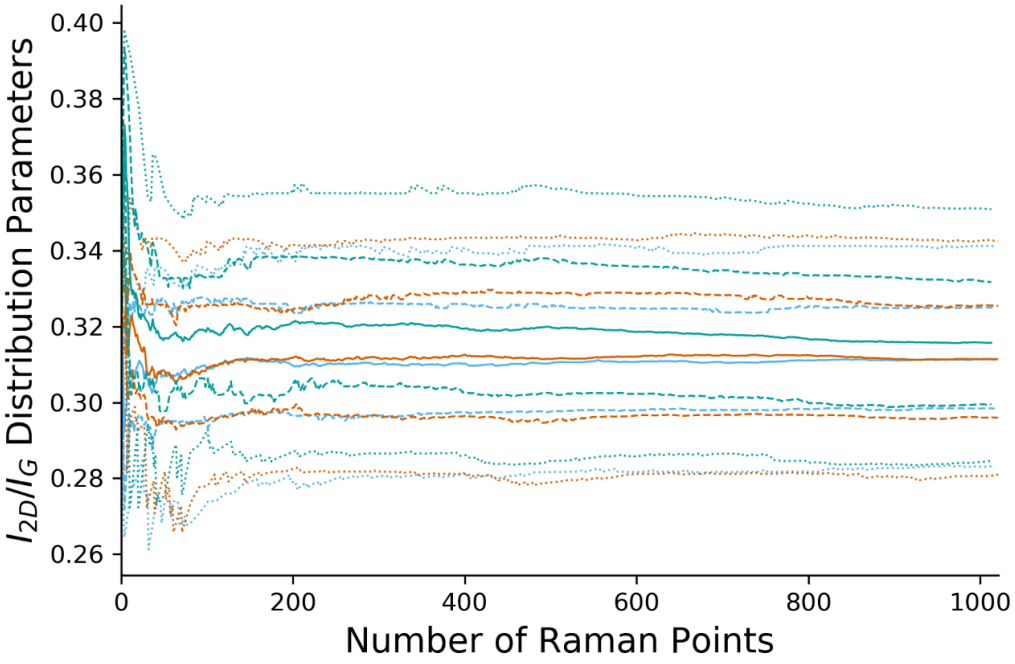

Figure S 10: Plot showing the convergence data of I_{2D}/I_G from all three graphite data sets. The dots denote the same summary statistics whilst different data sets are shown in different colors. Whilst complex this plot indicates that convergence of all three maps is consistent.

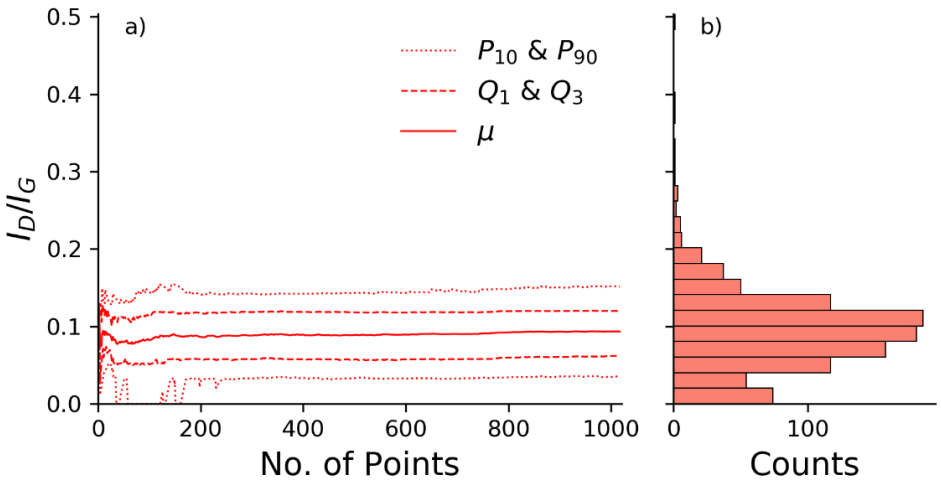

Figure S 11: Convergence plot from graphite (data set 1) showing a) the change in summary statistics of I_D/I_G as more data points are added to the analysis. b) The final distribution shown as a horizontal histogram, y-axis constant across all plots showing I_D/I_G convergence data from graphite sample.

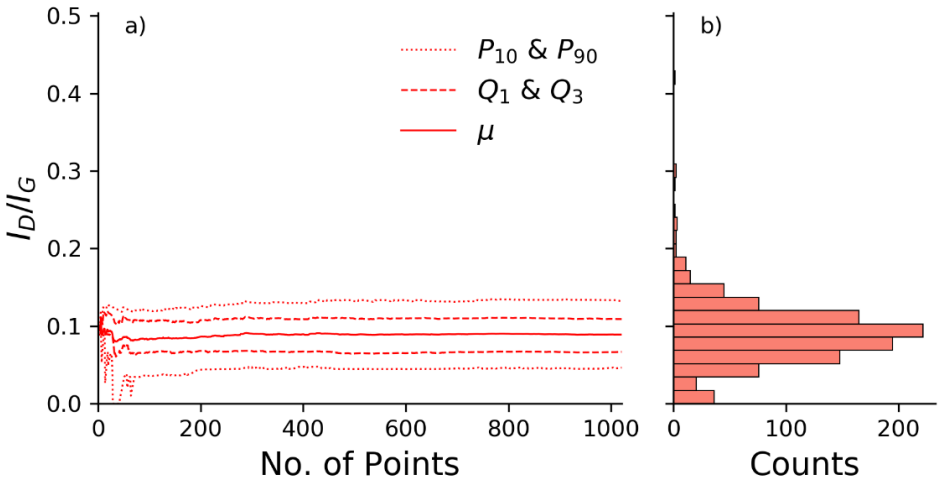

Figure S 12: Convergence plot from graphite (data set 2) described in detail above.

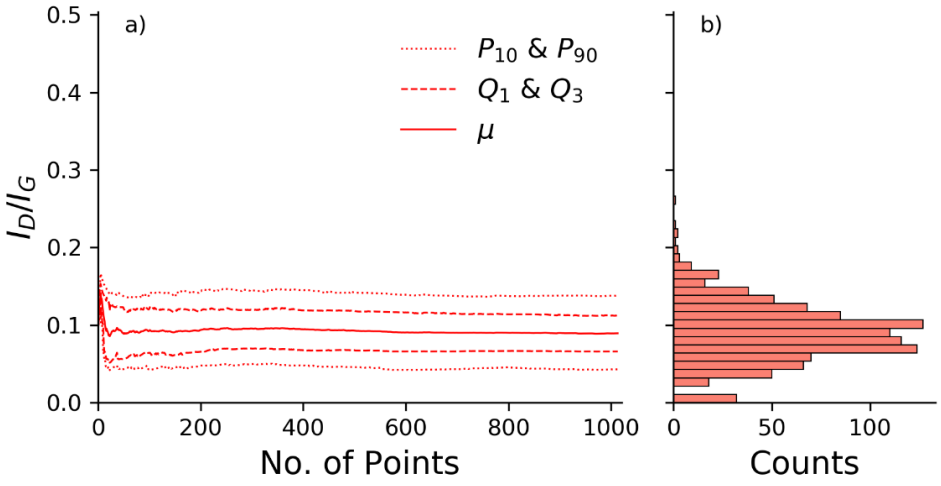

Figure S 13: Convergence plot from graphite (data set 3) described in detail above.

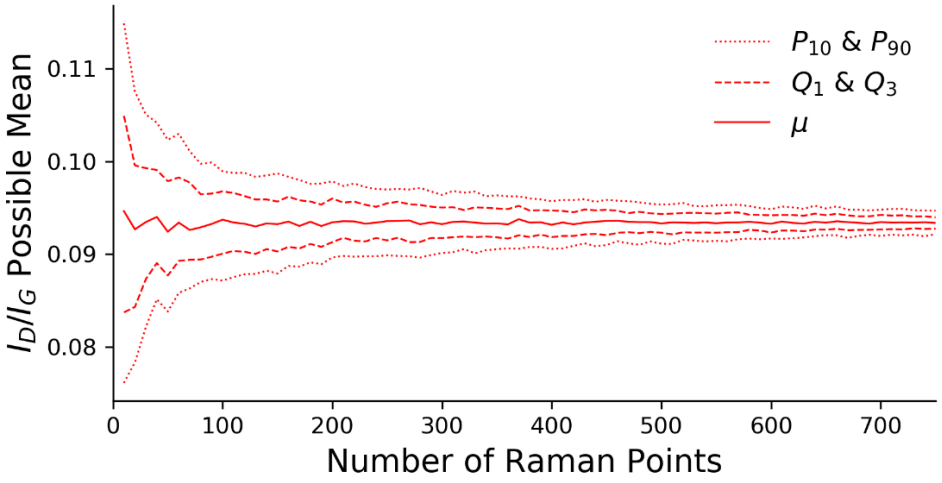

Figure S 14: Bootstrap convergence plot from graphite (data set 1); this shows the summary statistics (10th and 90th percentiles, 1st and 3rd quartiles, and mean) describing the distribution of mean values obtained from multiple analyses of smaller sub-sets of the sample size shown on the x-axis. This plot can be considered a probability distribution of possible mean values for different sample sizes.

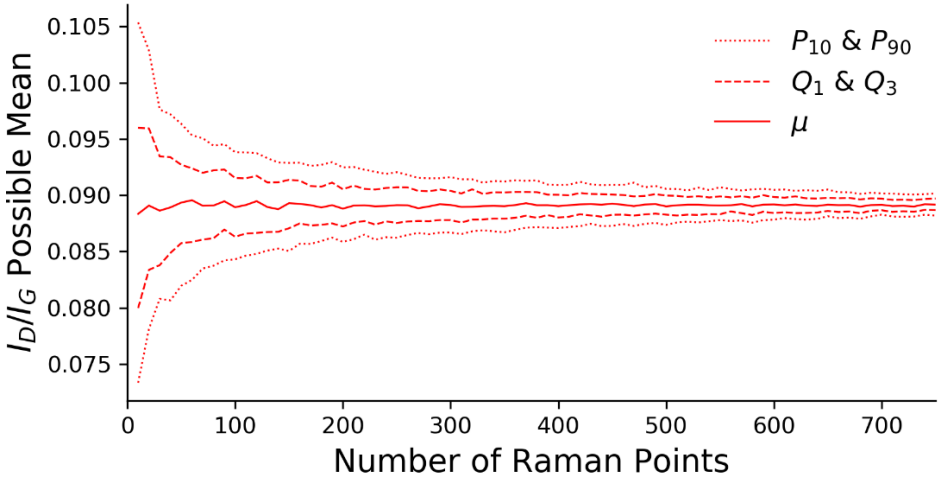

Figure S 15: Bootstrap convergence plot from graphite (data set 2), described in detail above.

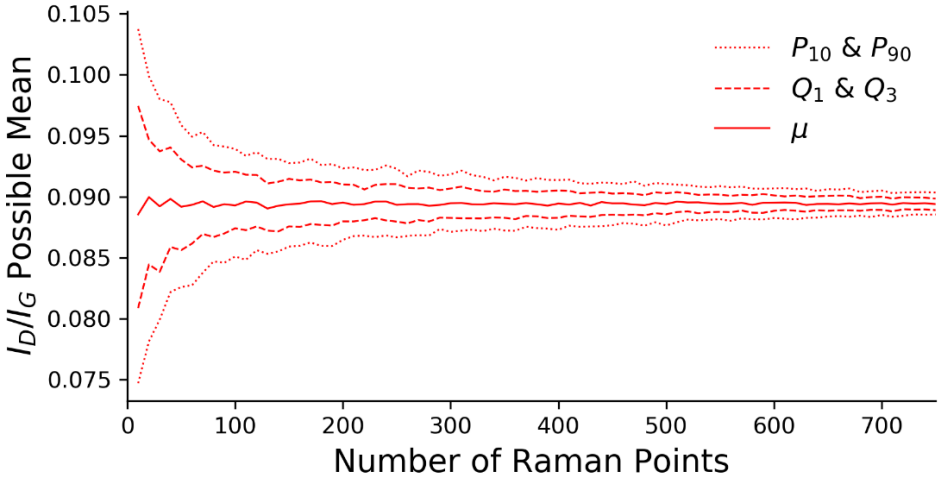

Figure S 16: Bootstrap convergence plot from graphite (data set 3), described in detail above.

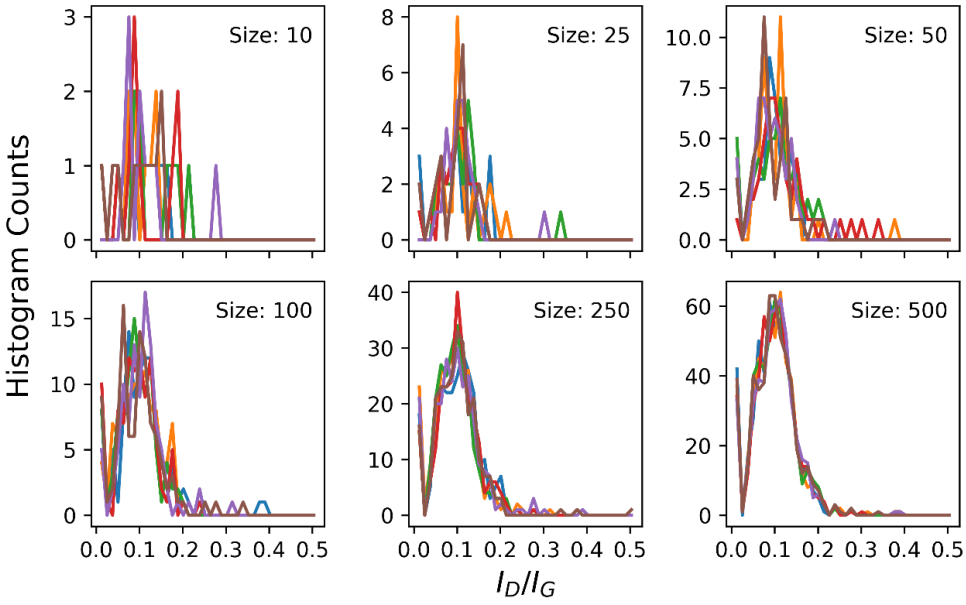

Figure S 17: Panel showing result of bootstrap analysis of graphite (data set 1). Each panel shows five examples, shown in different colors, of distributions of I_D/I_G produced from sub-sets; the size of these is labelled and the x-axis is common across all I_D/I_G panel plots. These show the convergence to a uniform distribution as the sub-set size increases.

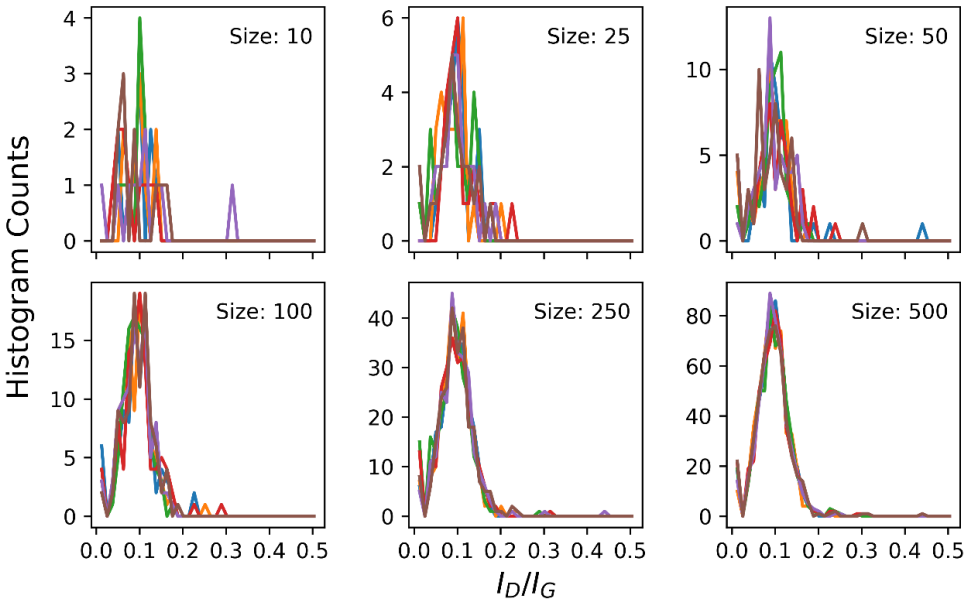

Figure S 18: Panel showing result of bootstrap analysis of graphite (data set 2), described in detail above.

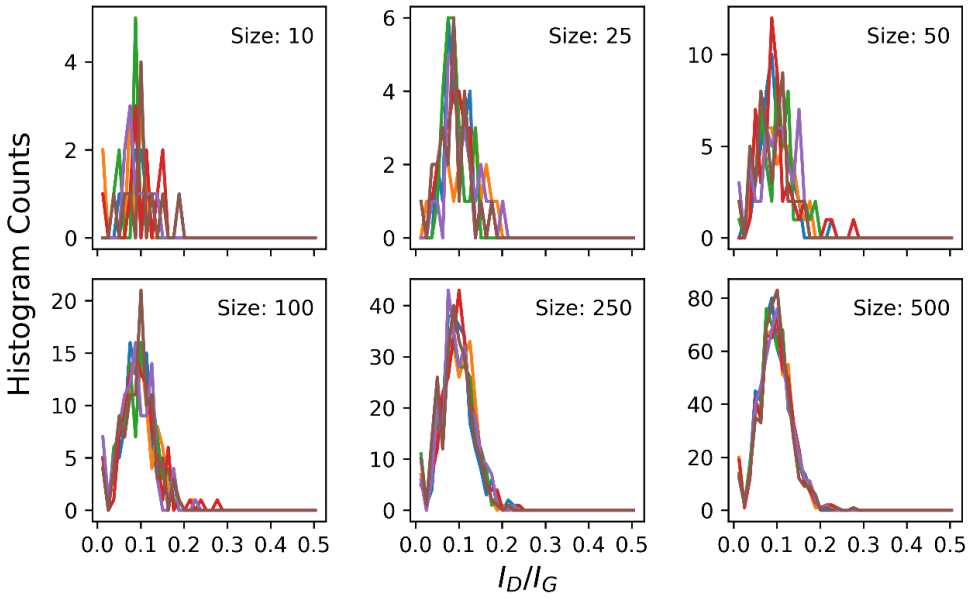

Figure S 19: Panel showing result of bootstrap analysis of graphite (data set 3), described in detail above.

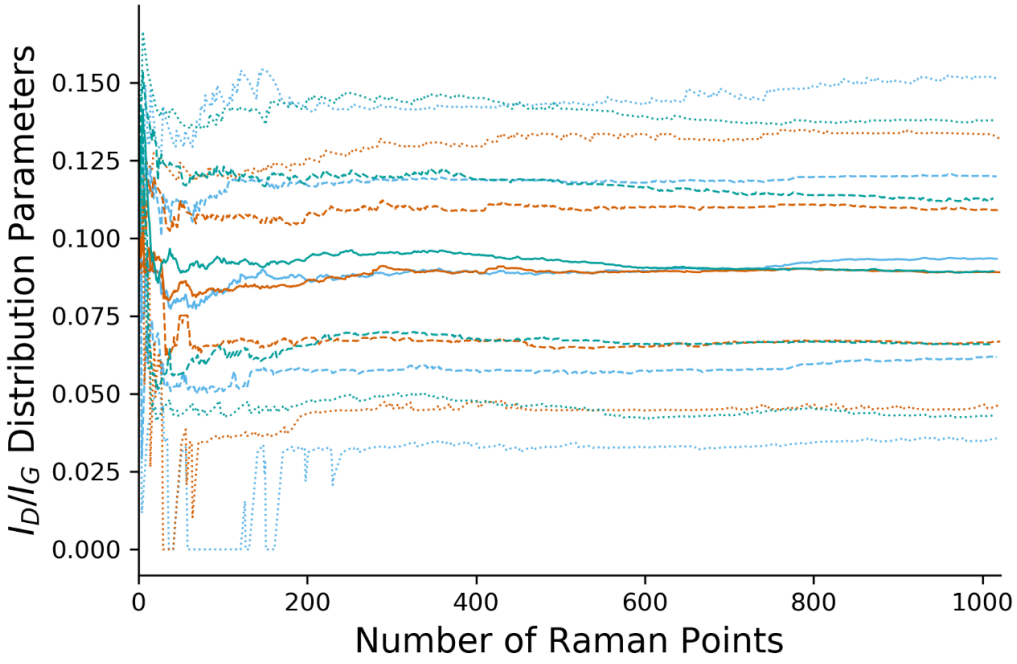

Figure S 20: Plot showing the convergence data of I_D/I_G from all three graphite data sets. The dots denote the same summary statistics whilst different data sets are shown in different colors. Whilst complex this plot indicates that convergence of all three maps is consistent.

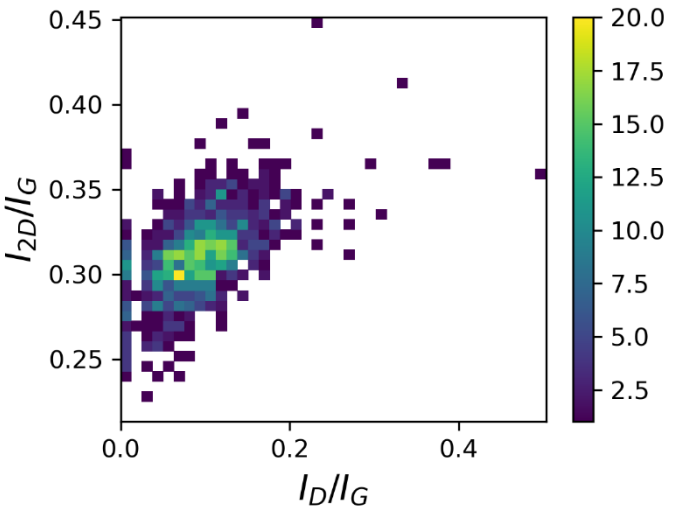

Figure S 21: 3D bivariate histogram showing the distribution of key peak ratios from graphite data (data set 1). The histogram count is shown by the colored heat map (key on right) and the bins are read simultaneously from the x and y axes which are common to all plots.

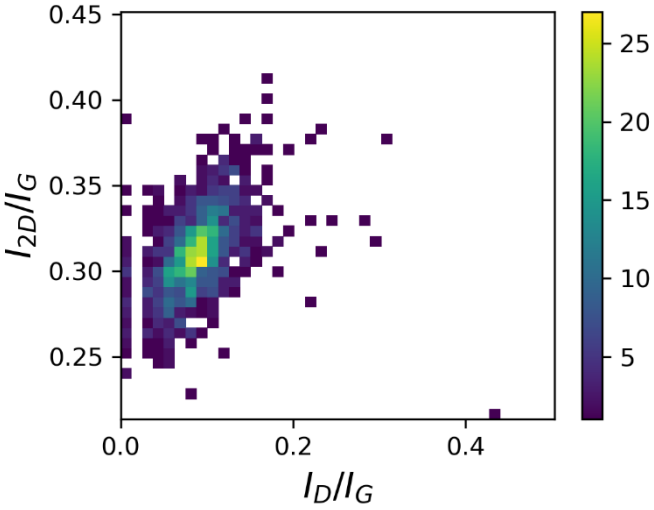

Figure S 22: 3D bivariate histogram showing the distribution of data from graphite (data set 2).

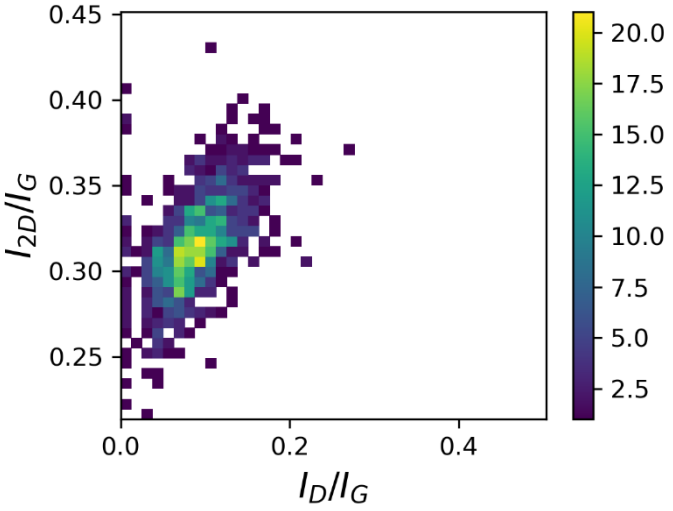

Figure S 23: 3D bivariate histogram showing the distribution of data from graphite (data set 3).

9.1.2 Exfoliated Graphene

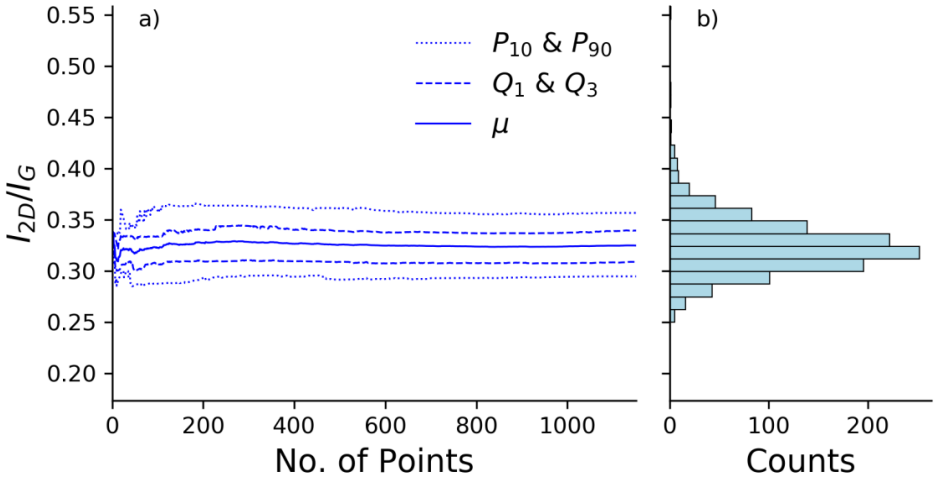

Figure S24: Convergence plot from exfoliated graphene (data set 1) showing a) the change in summary statistics of I_{2D}/I_G as more data points are added to the analysis. b) The final distribution shown as a horizontal histogram, y-axis constant across all plots showing I_{2D}/I_G convergence data from graphite sample.

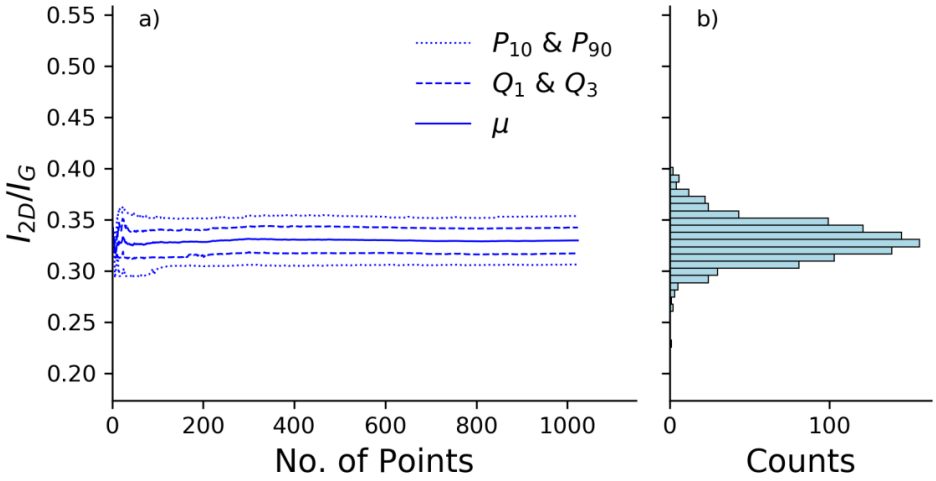

Figure S25: Convergence plot from exfoliated graphene (data set 2) described in detail above.

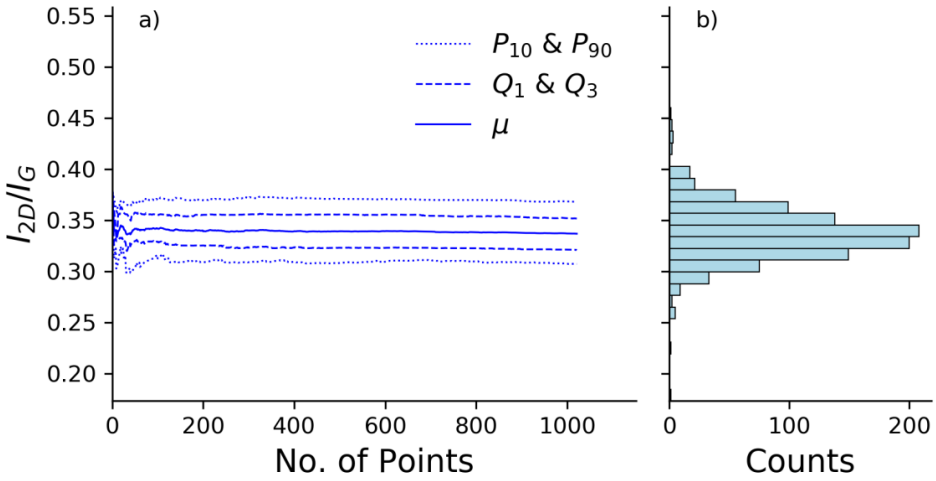

Figure S26: Convergence plot from exfoliated graphene (data set 3) described in detail above.

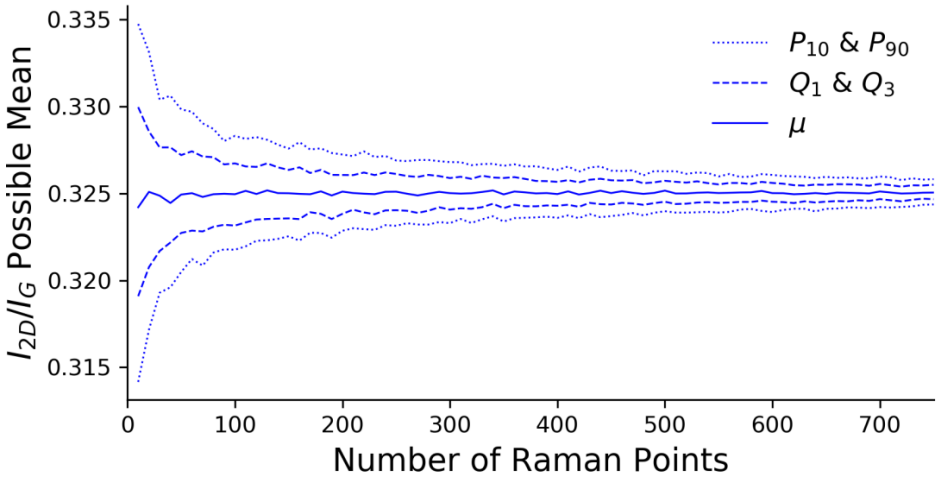

Figure S27: Bootstrap convergence plot from exfoliated graphene (data set 1); this shows the summary statistics (10th and 90th percentiles, 1st and 3rd quartiles, and mean) describing the distribution of mean values obtained from multiple analyses of smaller sub-sets of the sample size shown on the x-axis. This plot can be considered a probability distribution of possible mean values for different sample sizes.

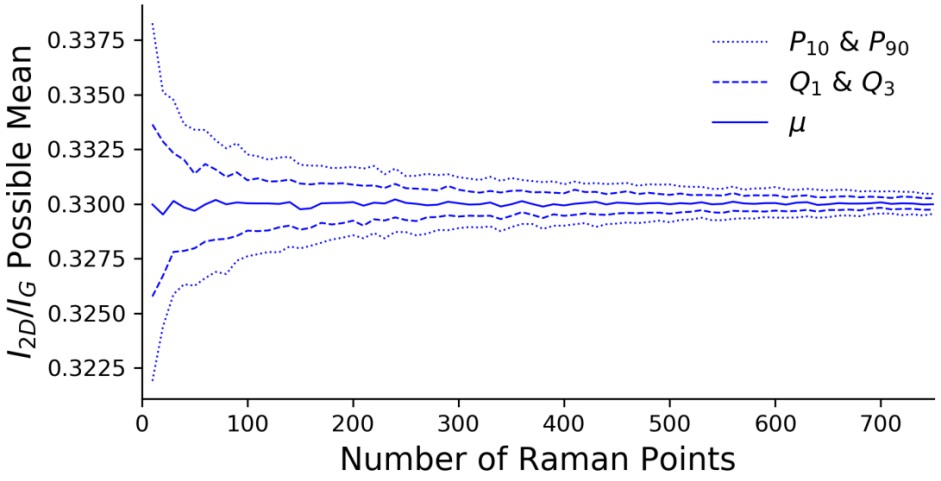

Figure S28: Bootstrap convergence plot from exfoliated graphene (data set 2), described in detail above.

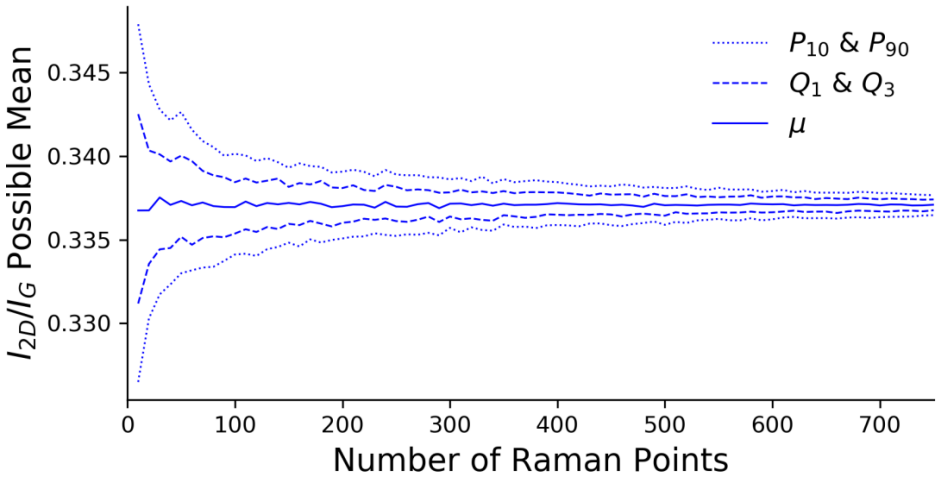

Figure S29: Bootstrap convergence plot from exfoliated graphene (data set 3), described in detail above.

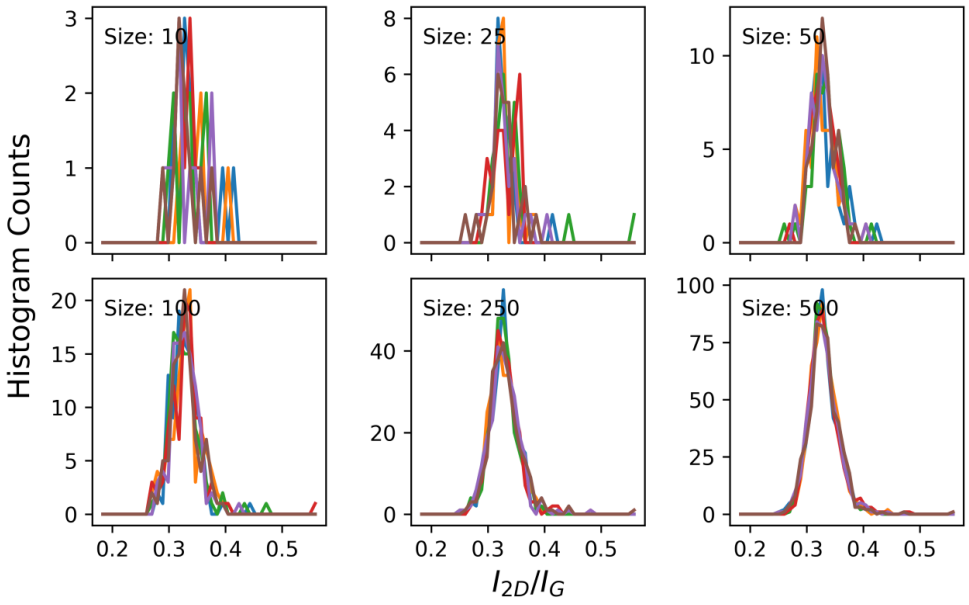

Figure S30: Panel showing result of bootstrap analysis of exfoliated graphene (data set 1). Each panel shows five examples, shown in different colors, of distributions of I_{2D}/I_G produced from sub-sets; the size of these is labelled and the x-axis is common across all I_{2D}/I_G panel plots. These show the convergence to a uniform distribution as the sub-set size increases.

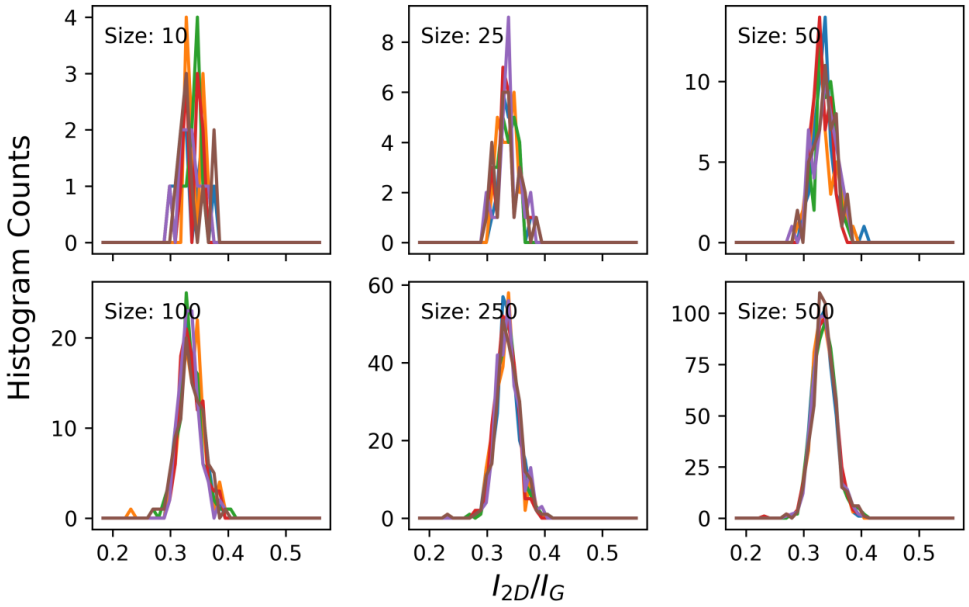

Figure S31: Panel showing result of bootstrap analysis of exfoliated graphene (data set 2), described in detail above.

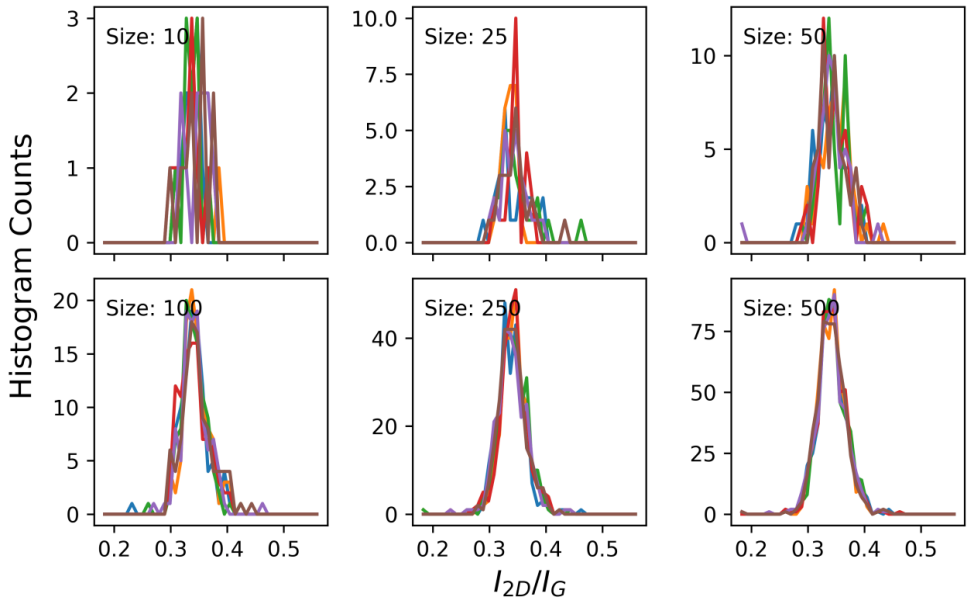

Figure S32: Panel showing result of bootstrap analysis of exfoliated graphene (data set 3), described in detail above.

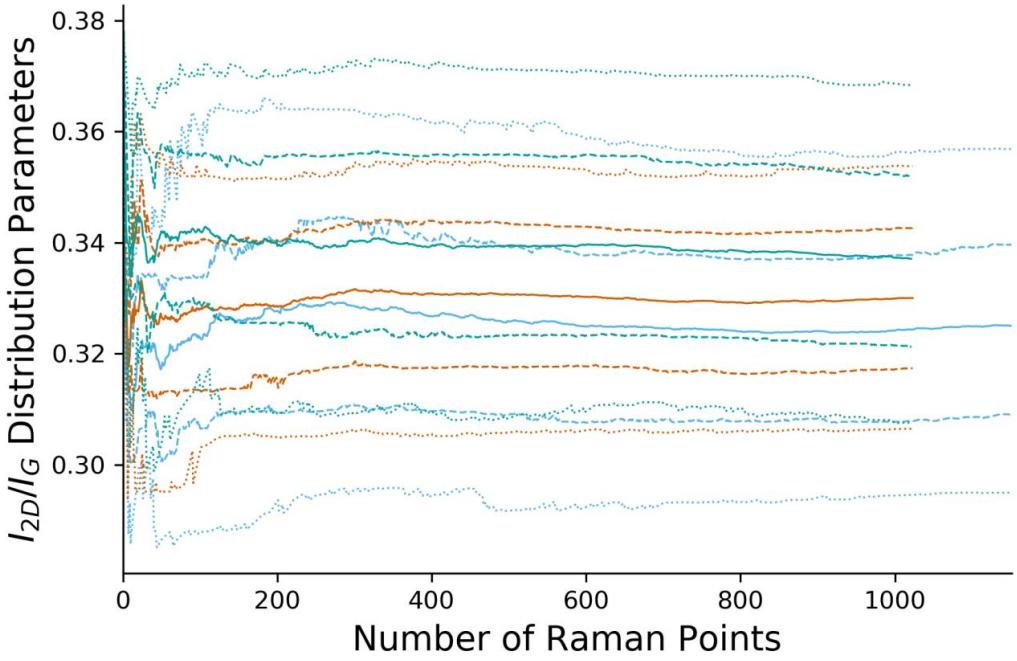

Figure S33: Plot showing the convergence data of I_{2D}/I_G from all three exfoliated graphene data sets. The dots denote the same summary statistics whilst different data sets are shown in different colors. Whilst complex this plot indicates that convergence of all three maps is consistent.

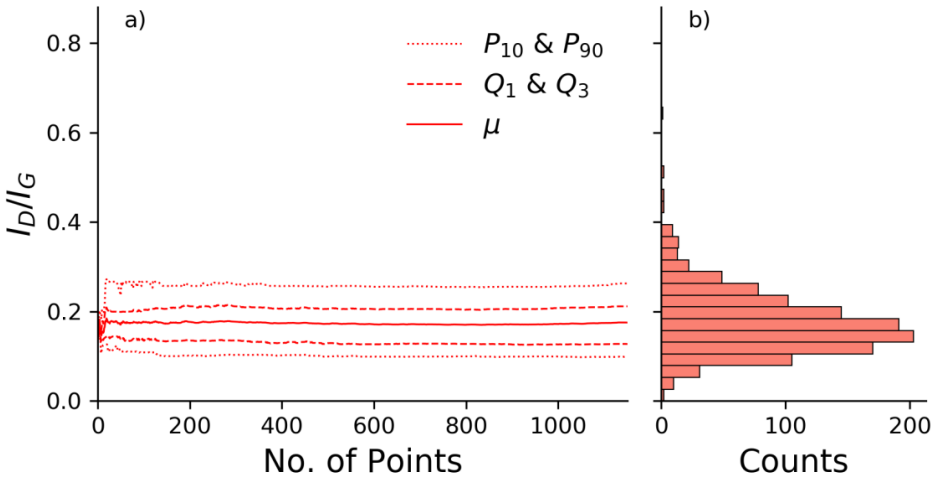

Figure S34: Convergence plot from exfoliated graphene (data set 1) showing a) the change in summary statistics of I_D/I_G as more data points are added to the analysis. b) The final distribution shown as a horizontal histogram, y-axis constant across all plots showing I_D/I_G convergence data from graphite sample.

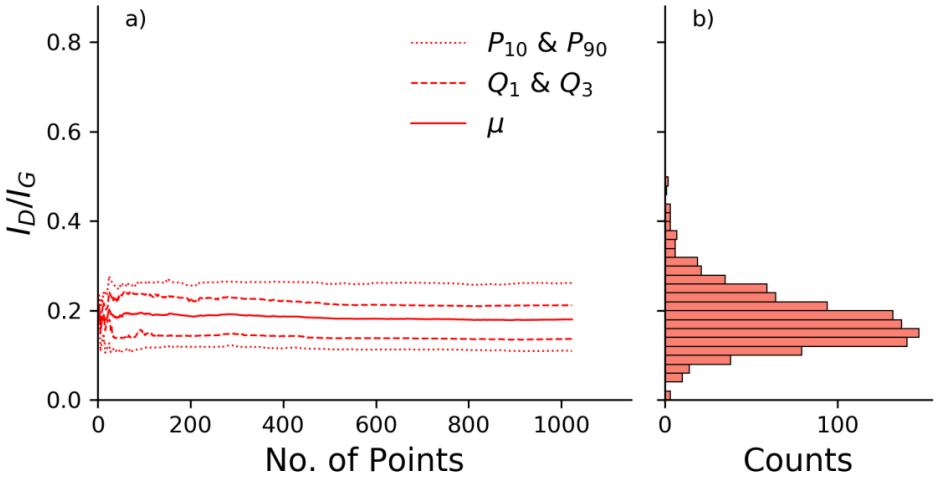

Figure S35: Convergence plot from exfoliated graphene (data set 2) described in detail above.

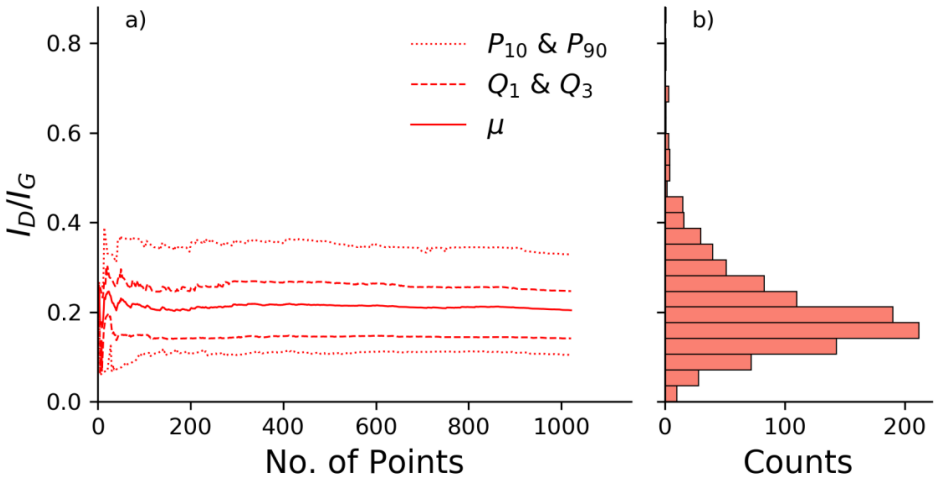

Figure S36: Convergence plot from exfoliated graphene (data set 3) described in detail above.

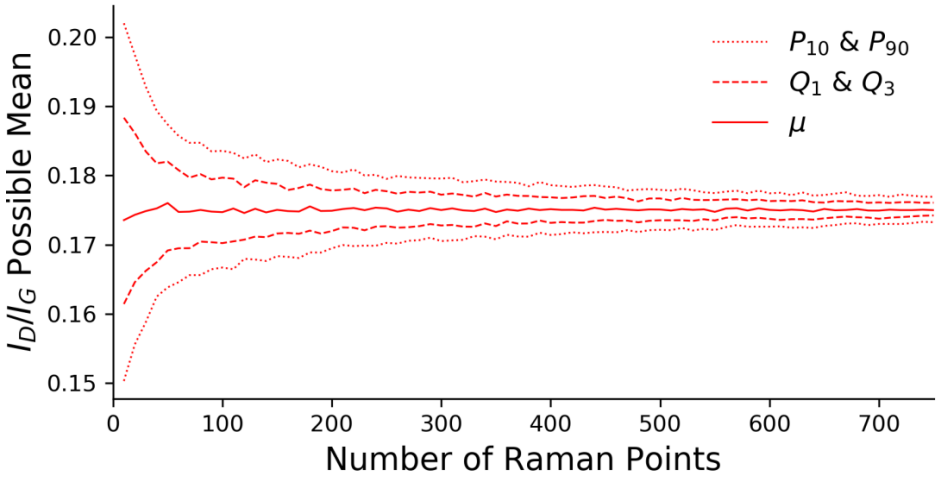

Figure S37: Bootstrap convergence plot from exfoliated graphene (data set 1); this shows the summary statistics (10th and 90th percentiles, 1st and 3rd quartiles, and mean) describing the distribution of mean values obtained from multiple analyses of smaller sub-sets of the sample size shown on the x-axis. This plot can be considered a probability distribution of possible mean values for different sample sizes.

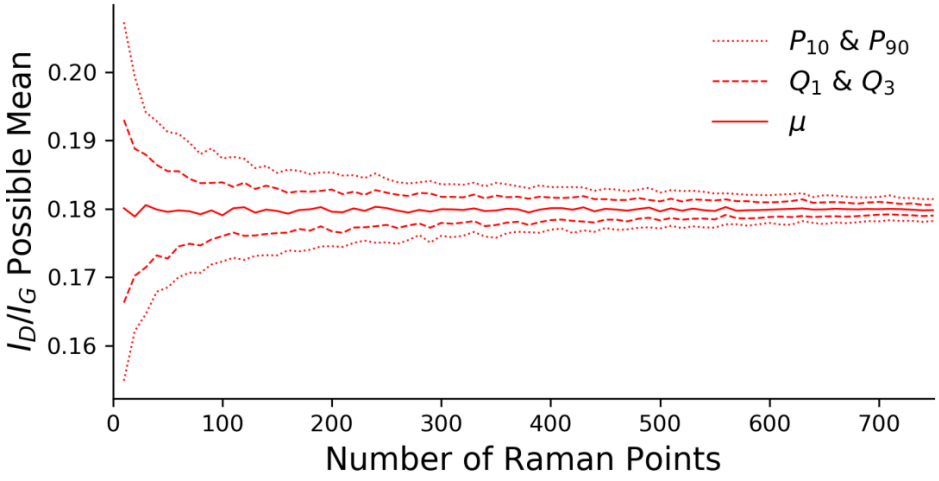

Figure S38: Bootstrap convergence plot from exfoliated graphene (data set 2), described in detail above.

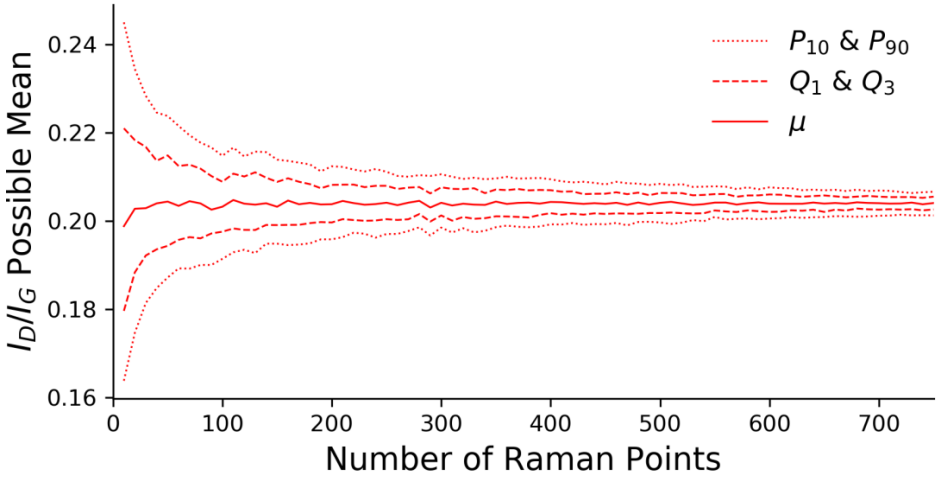

Figure S39: Bootstrap convergence plot from exfoliated graphene (data set 3), described in detail above.

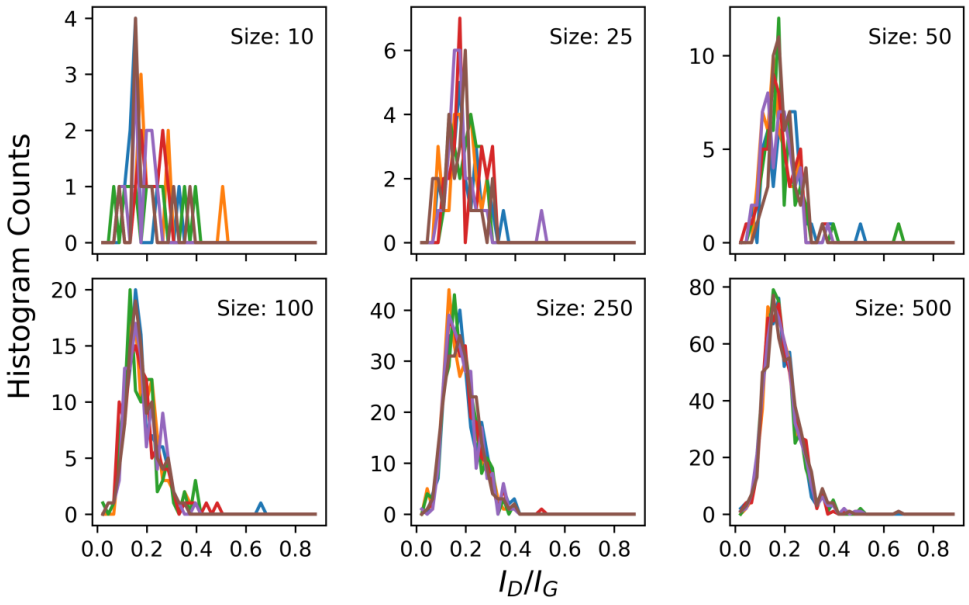

Figure S40: Panel showing result of bootstrap analysis of exfoliated graphene (data set 1). Each panel shows five examples, shown in different colors, of distributions of I_D/I_G produced from sub-sets; the size of these is labelled and the x-axis is common across all I_D/I_G panel plots. These show the convergence to a uniform distribution as the sub-set size increases.

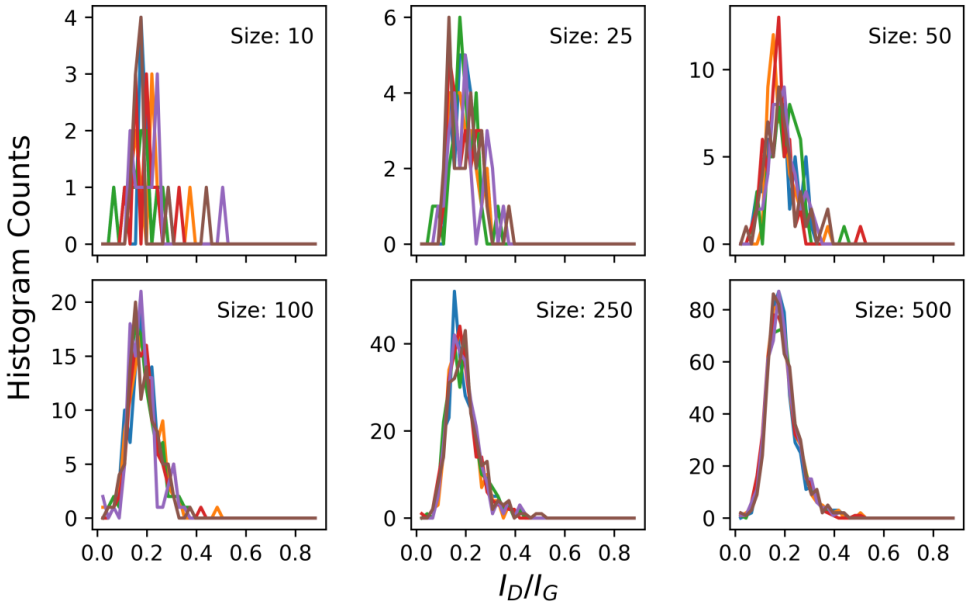

Figure S41: Panel showing result of bootstrap analysis of exfoliated graphene (data set 2), described in detail above.

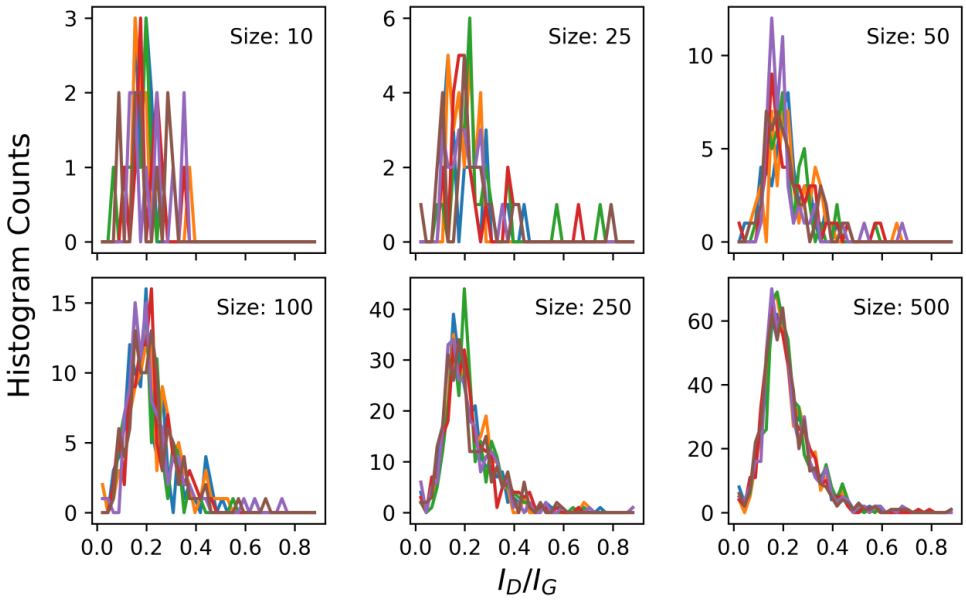

Figure S42: Panel showing result of bootstrap analysis of exfoliated graphene (data set 3), described in detail above.

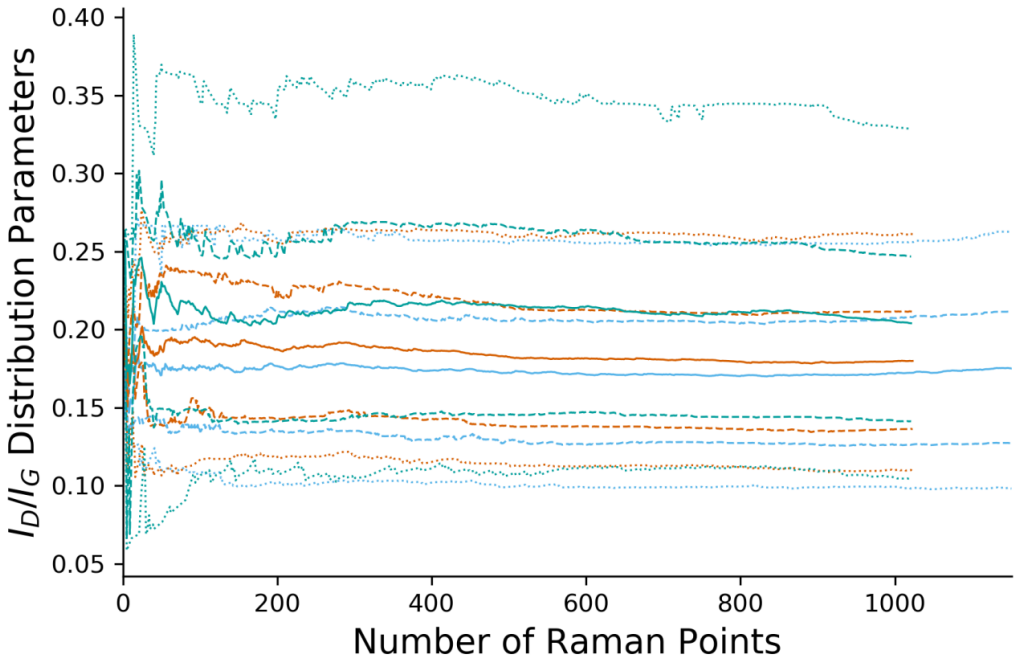

Figure S43: Plot showing the convergence data of I_D/I_G from all three exfoliated graphene data sets. The dots denote the same summary statistics whilst different data sets are shown in different colors. Whilst complex this plot indicates that convergence of all three maps is consistent.

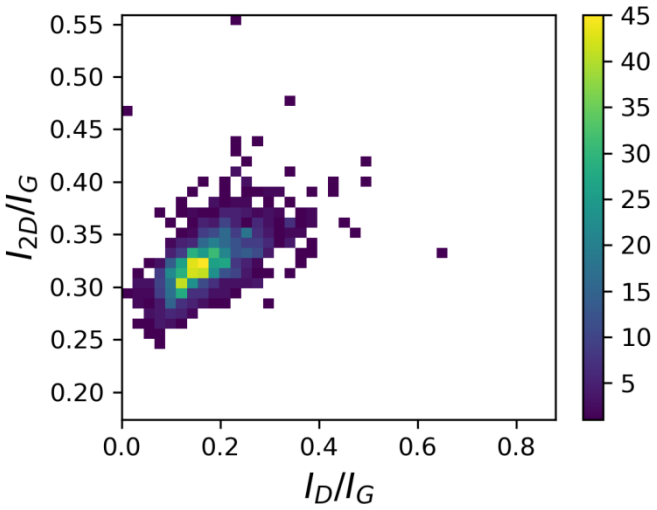

Figure S44: 3D bivariate histogram showing the distribution of key peak ratios from exfoliated graphene data (data set 1). The histogram count is shown by the colored heat map (key on right) and the bins are read simultaneously from the x and y axes which are common to all plots.

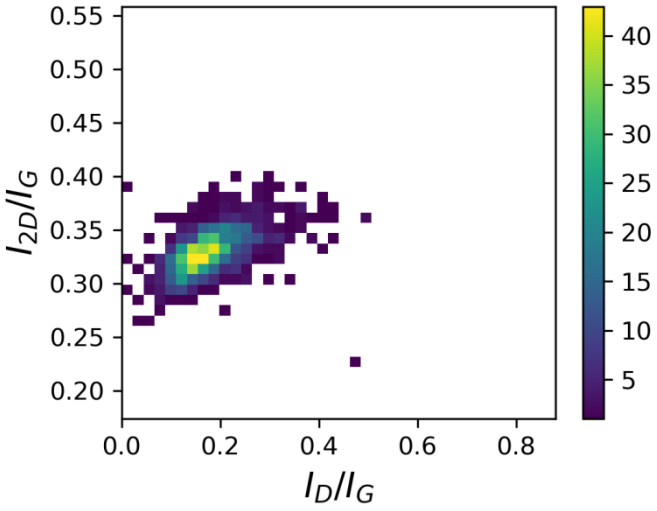

Figure S45: 3D bivariate histogram showing the distribution of data from exfoliated graphene (data set 2).

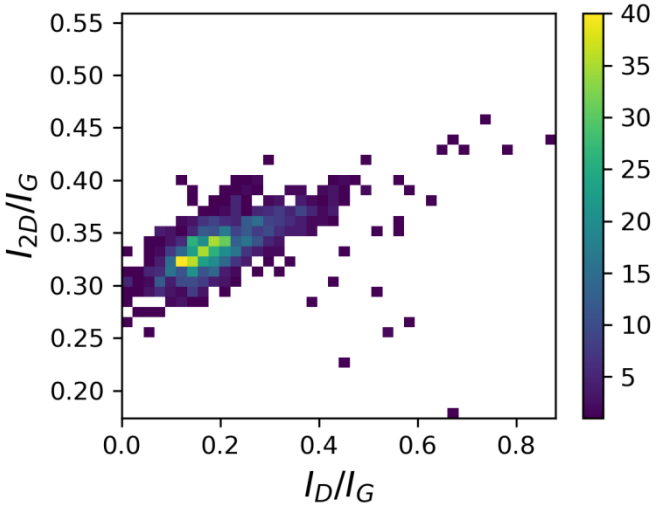

Figure S46: 3D bivariate histogram showing the distribution of data from exfoliated graphene (data set 3).

9.1.3 Graphene Nanoplatelets ‘High Quality’

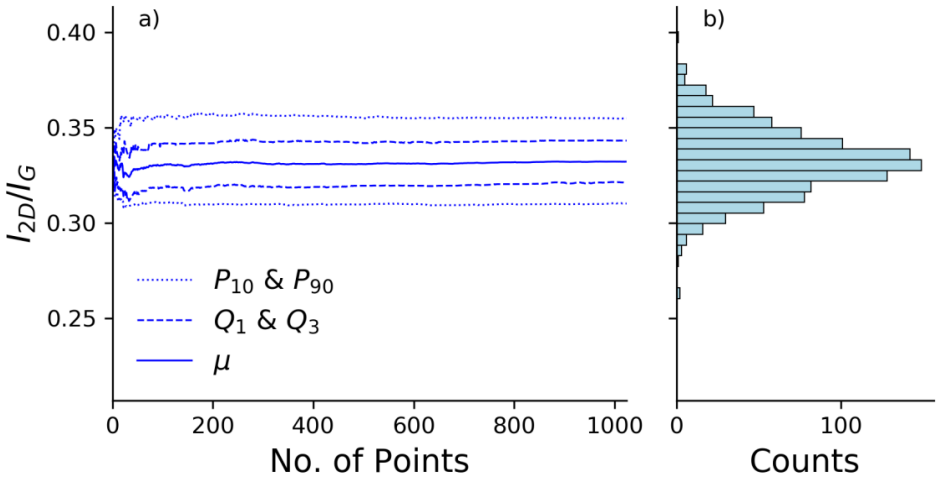

Figure S 47: Convergence plot from commercial GNPs (data set 1) showing a) the change in summary statistics of I_{2D}/I_G as more data points are added to the analysis. b) The final distribution shown as a horizontal histogram, y-axis constant across all plots showing I_{2D}/I_G convergence data from graphite sample.

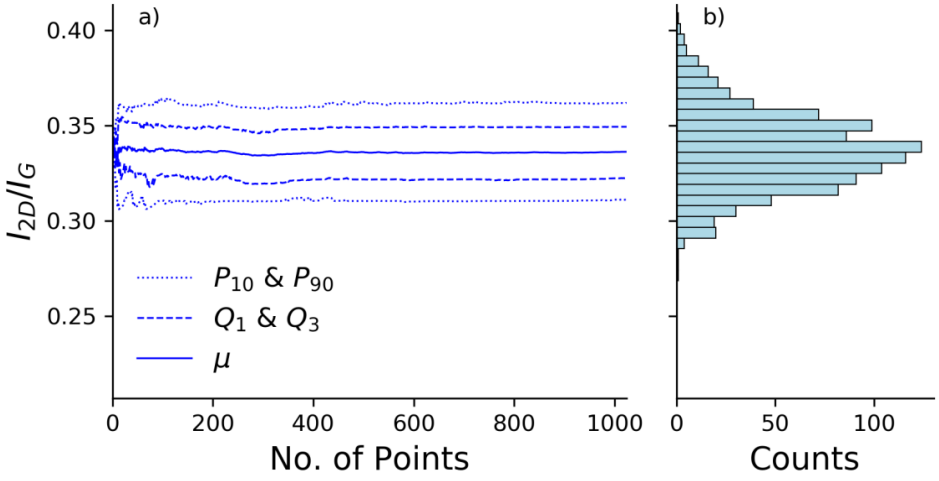

Figure S 48: Convergence plot from commercial GNP (data set 2) described in detail above.

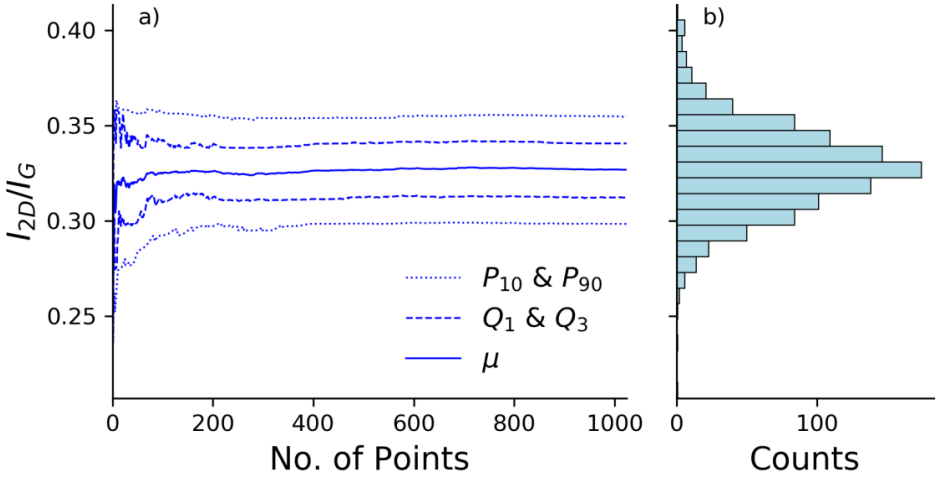

Figure S 49: Convergence plot from commercial GNP (data set 3) described in detail above.

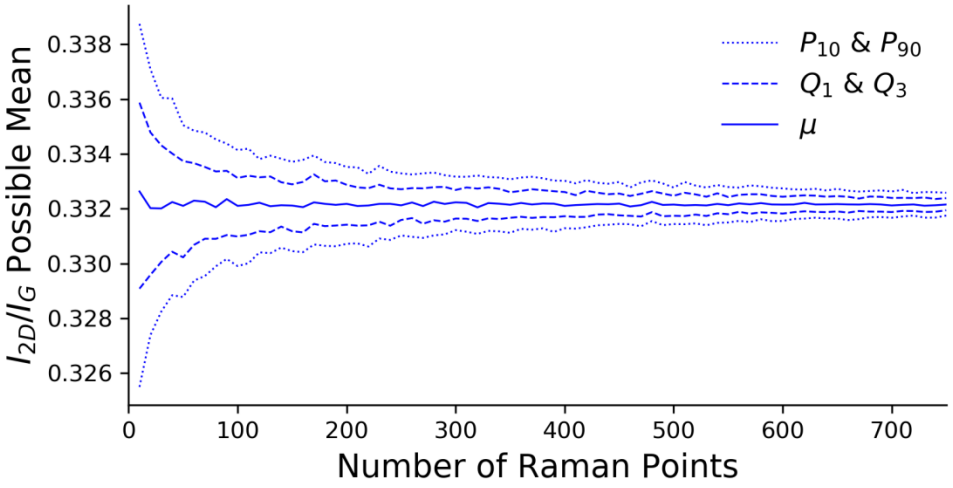

Figure S 50: Bootstrap convergence plot from commercial GNPs (data set 1); this shows the summary statistics (10th and 90th percentiles, 1st and 3rd quartiles, and mean) describing the distribution of mean values obtained from multiple analyses of smaller sub-sets of the sample size shown on the x-axis. This plot can be considered a probability distribution of possible mean values for different sample sizes.

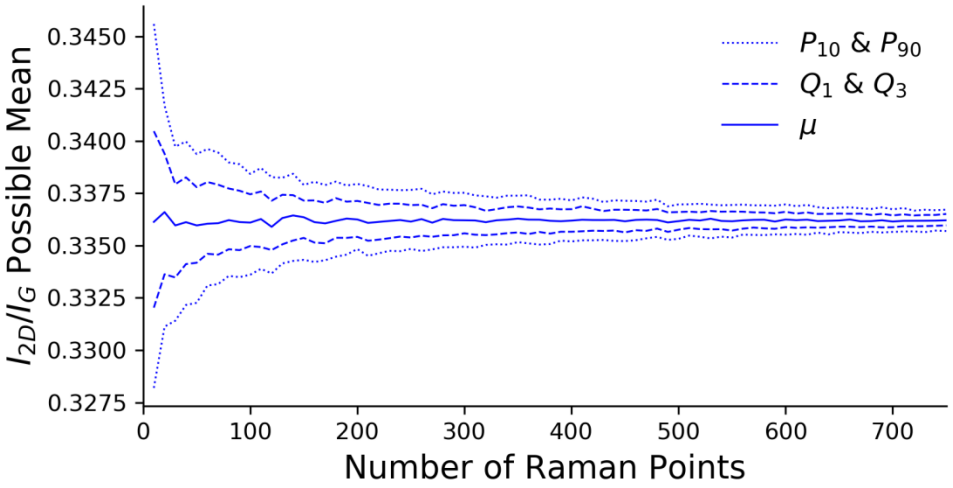

Figure S 51: Bootstrap convergence plot from commercial GNPs (data set 2), described in detail above.

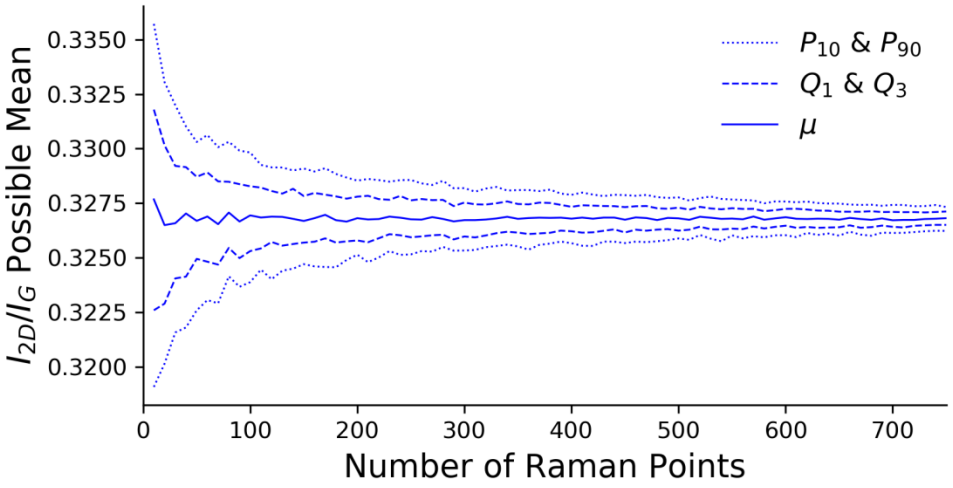

Figure S 52: Bootstrap convergence plot from commercial GNPs (data set 3), described in detail above.

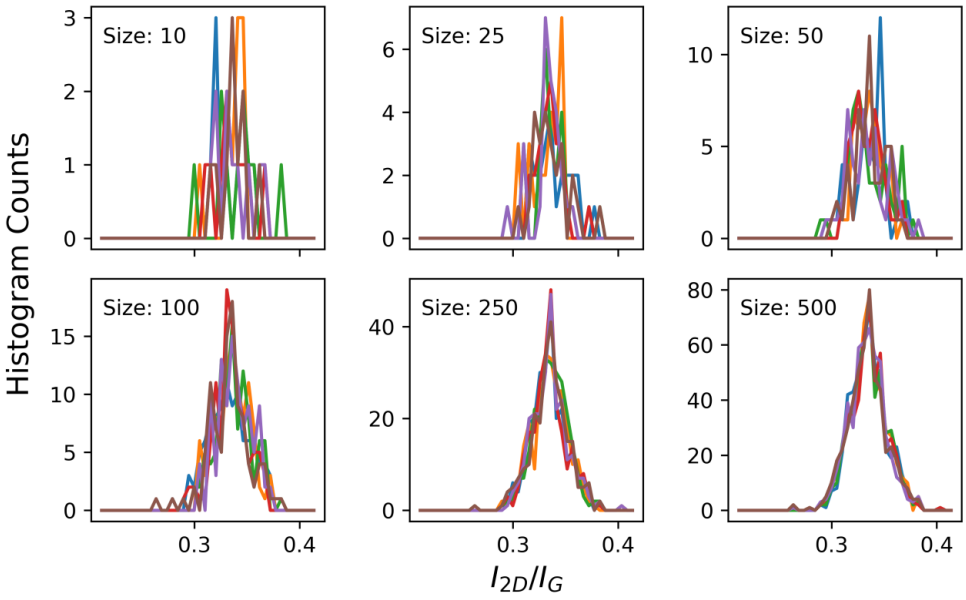

Figure S 53: Panel showing result of bootstrap analysis of commercial GNPs (data set 1). Each panel shows five examples, shown in different colors, of distributions of I_{2D}/I_G produced from sub-sets; the size of these is labelled and the x-axis is common across all I_{2D}/I_G panel plots. These show the convergence to a uniform distribution as the sub-set size increases.

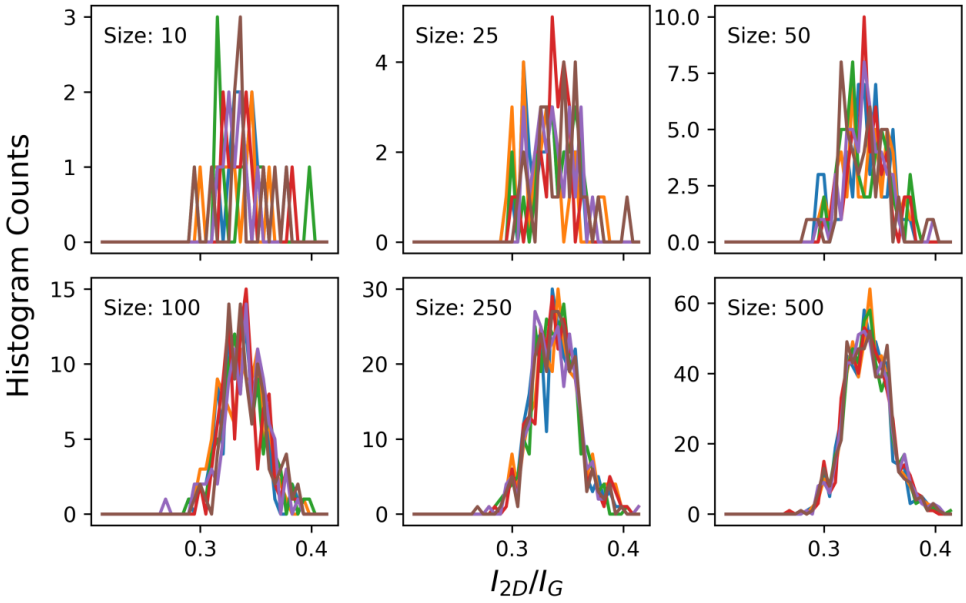

Figure S 54: Panel showing result of bootstrap analysis of commercial GNPs (data set 2), described in detail above.

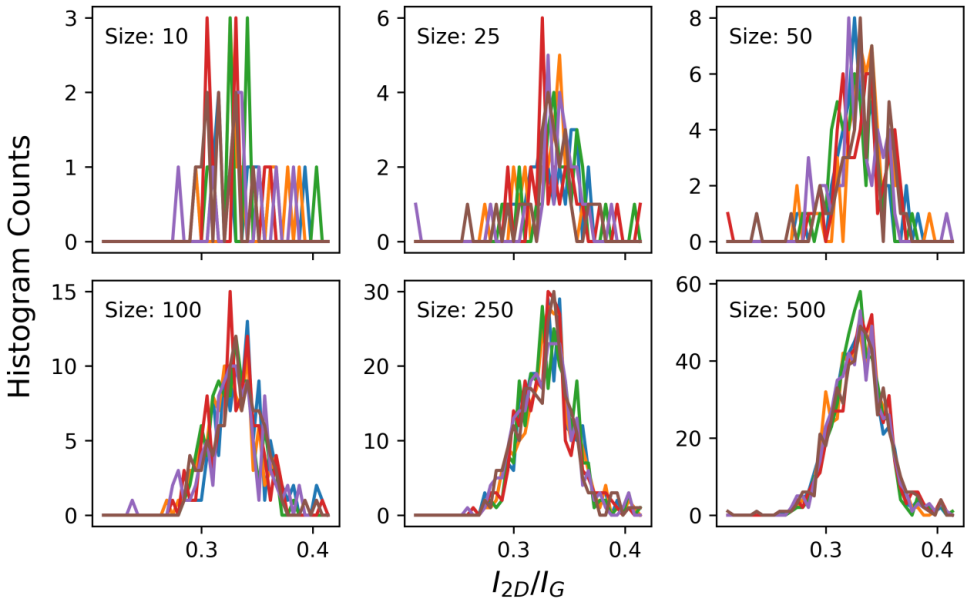

Figure S 55: Panel showing result of bootstrap analysis of commercial GNPs (data set 3), described in detail above.

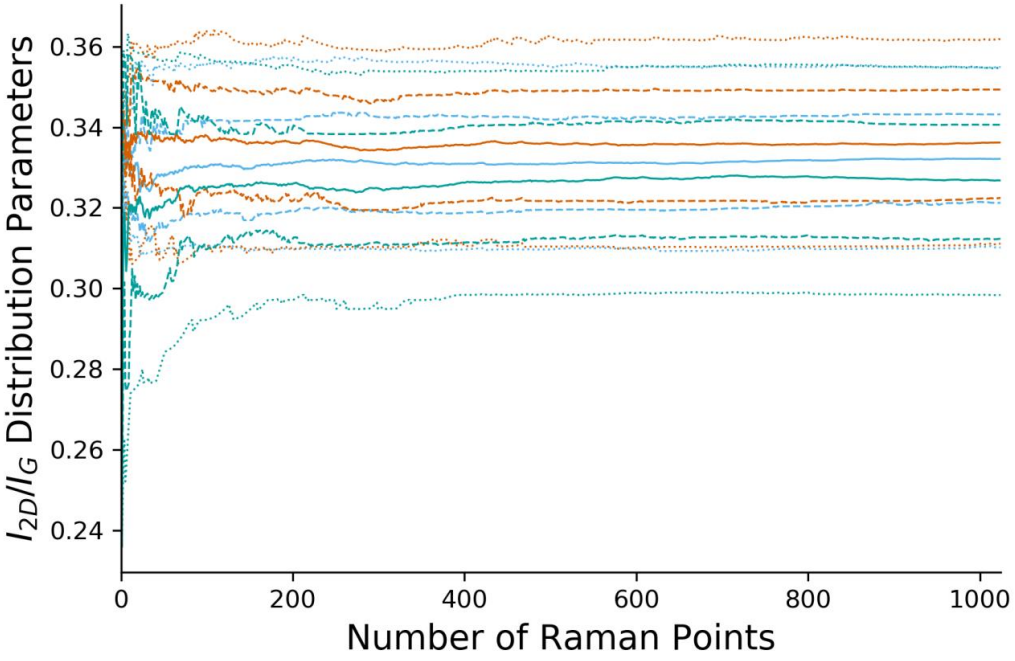

Figure S 56: Plot showing the convergence data of I_{2D}/I_G from all three commercial GNPs data sets. The dots denote the same summary statistics whilst different data sets are shown in different colors. Whilst complex this plot indicates that convergence of all three maps is consistent.

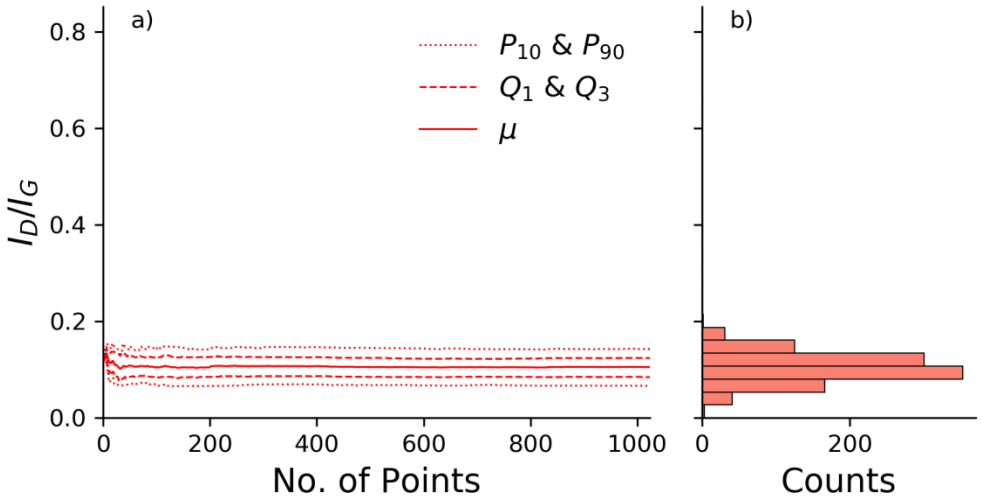

Figure S 57: Convergence plot from commercial GNPs (data set 1) showing a) the change in summary statistics of I_D/I_G as more data points are added to the analysis. b) The final distribution shown as a horizontal histogram, y-axis constant across all plots showing I_D/I_G convergence data from graphite sample.

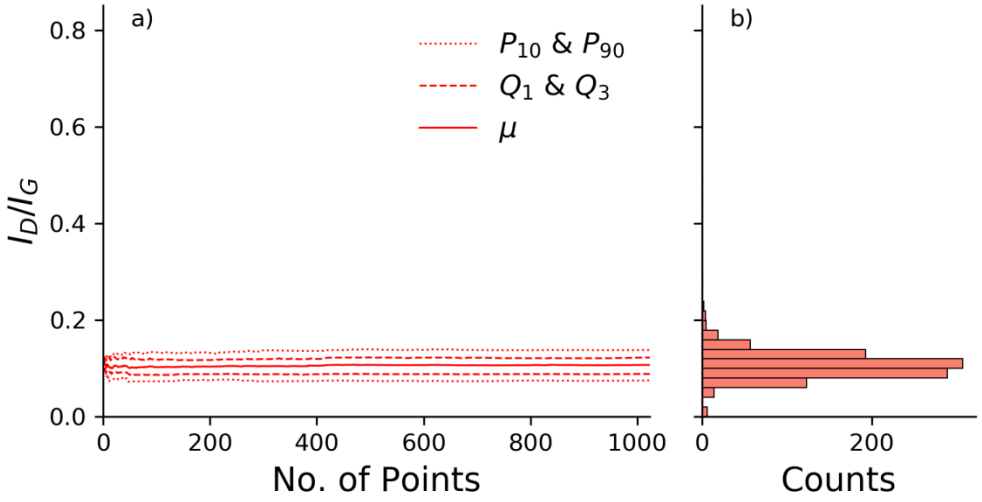

Figure S 58: Convergence plot from commercial GNPs (data set 2) described in detail above.

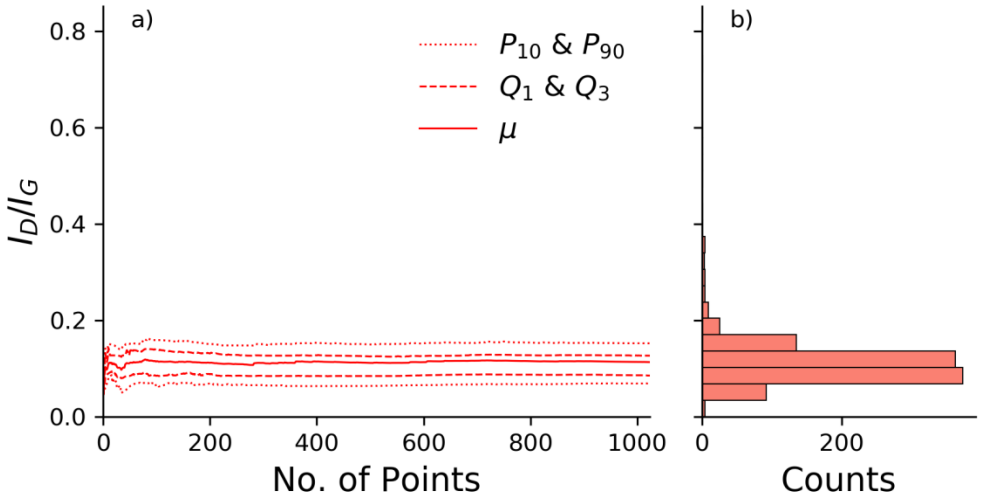

Figure S 59: Convergence plot from commercial GNPs (data set 3) described in detail above.

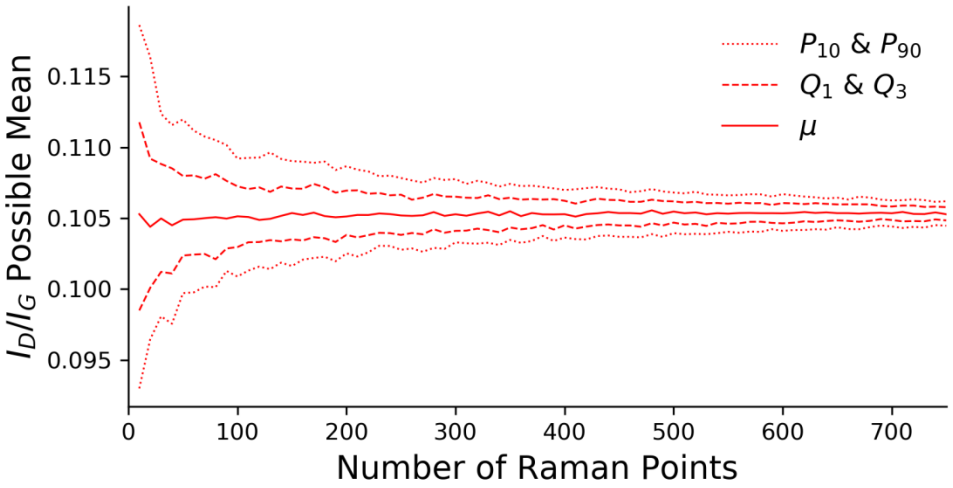

Figure S 60: Bootstrap convergence plot from commercial GNPs (data set 1); this shows the summary statistics (10th and 90th percentiles, 1st and 3rd quartiles, and mean) describing the distribution of mean values obtained from multiple analyses of smaller sub-sets of the sample size shown on the x-axis. This plot can be considered a probability distribution of possible mean values for different sample sizes.

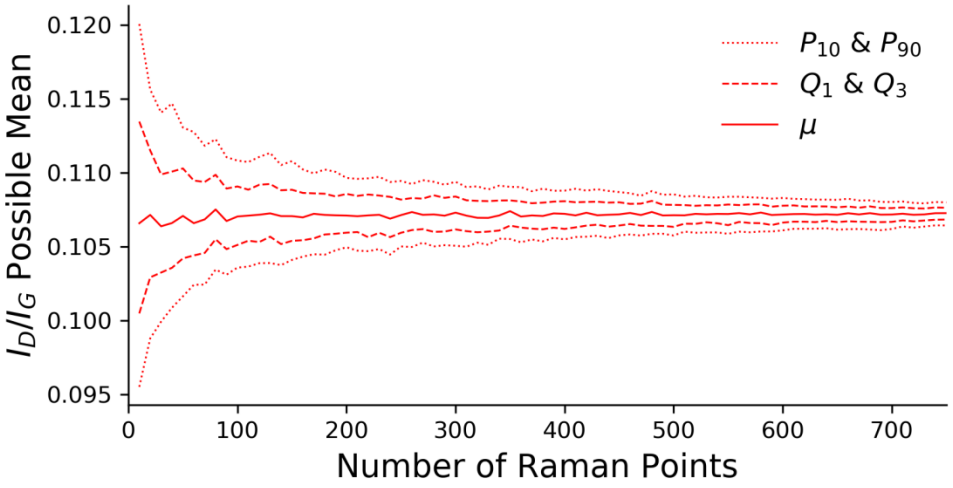

Figure S 61: Bootstrap convergence plot from commercial GNPs (data set 2), described in detail above.

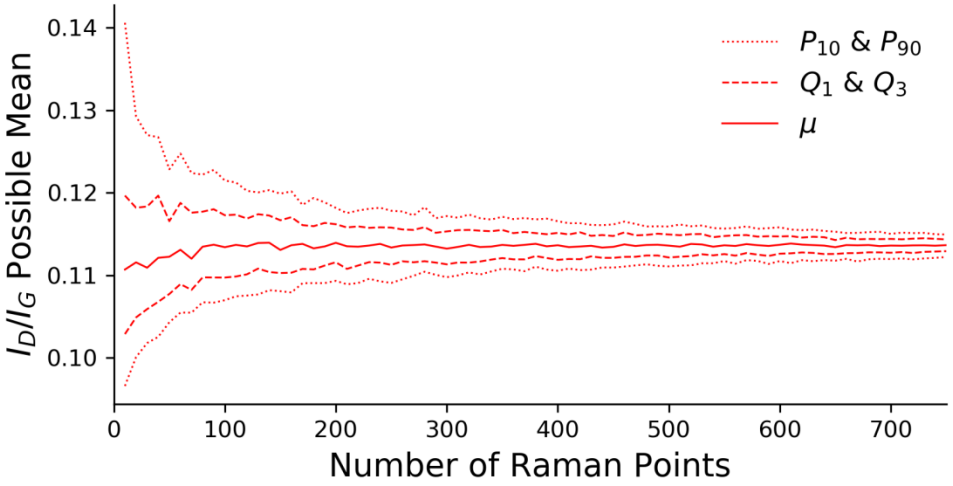

Figure S 62: Bootstrap convergence plot from commercial GNPs (data set 3), described in detail above.

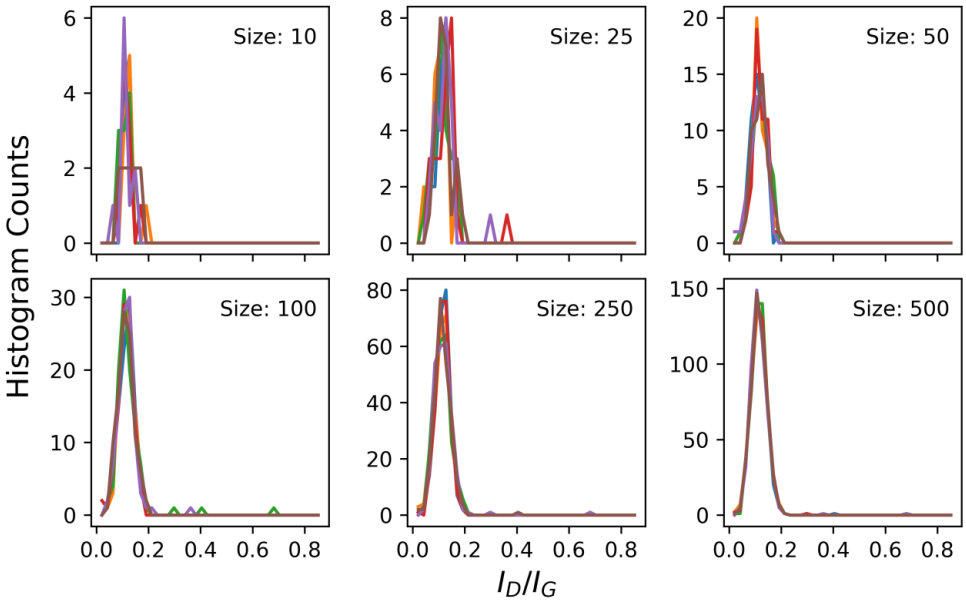

Figure S 63: Panel showing result of bootstrap analysis of commercial GNPs (data set 1). Each panel shows five examples, shown in different colors, of distributions of I_D/I_G produced from sub-sets; the size of these is labelled and the x-axis is common across all I_D/I_G panel plots. These show the convergence to a uniform distribution as the sub-set size increases.

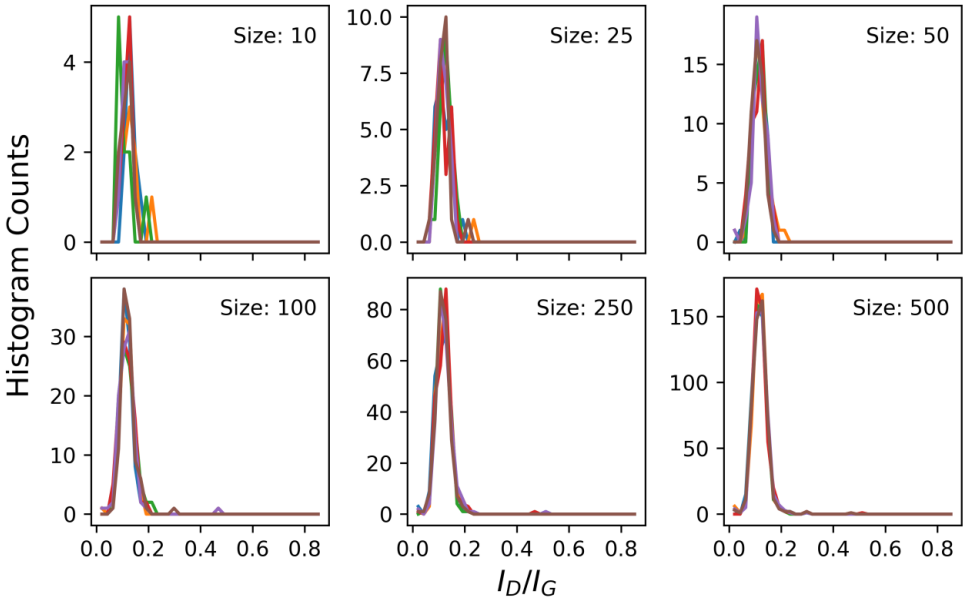

Figure S 64: Panel showing result of bootstrap analysis of commercial GNPs (data set 2), described in detail above.

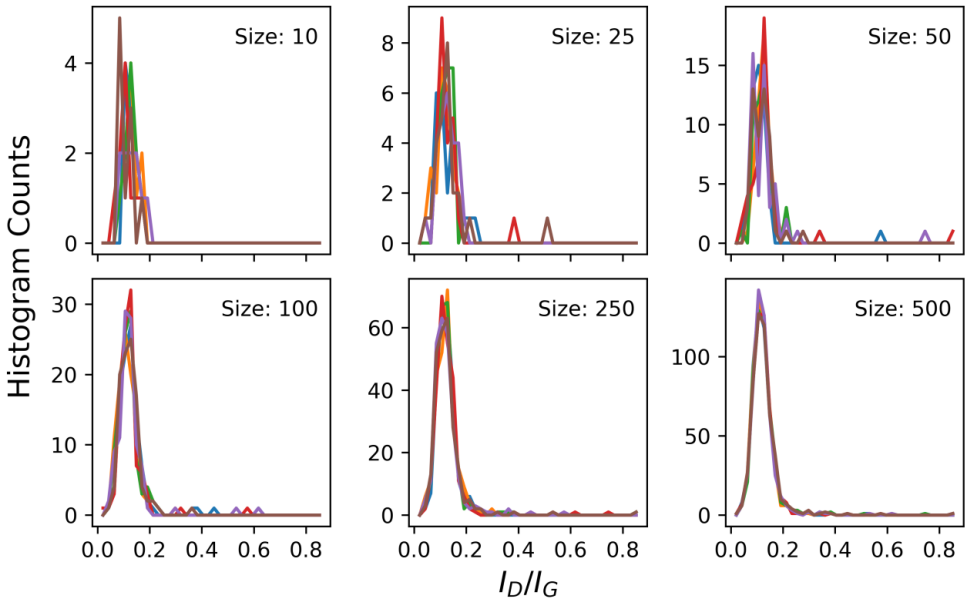

Figure S 65: Panel showing result of bootstrap analysis of commercial GNPs (data set 3), described in detail above.

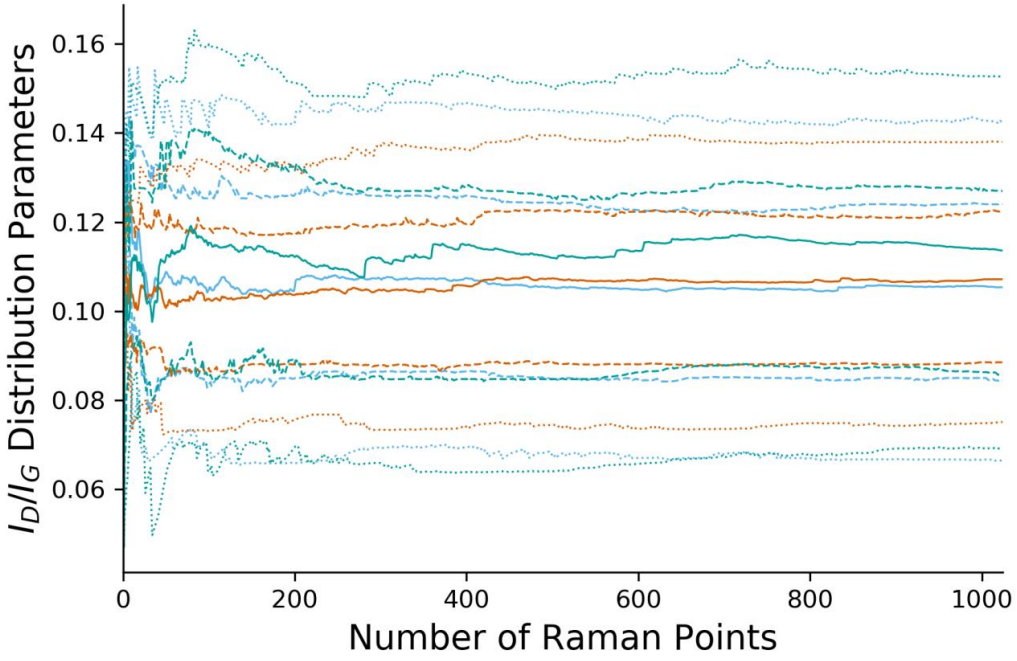

Figure S 66: Plot showing the convergence data of I_D/I_G from all three commercial GNPs data sets. The dots denote the same summary statistics whilst different data sets are shown in different colors. Whilst complex this plot indicates that convergence of all three maps is consistent.

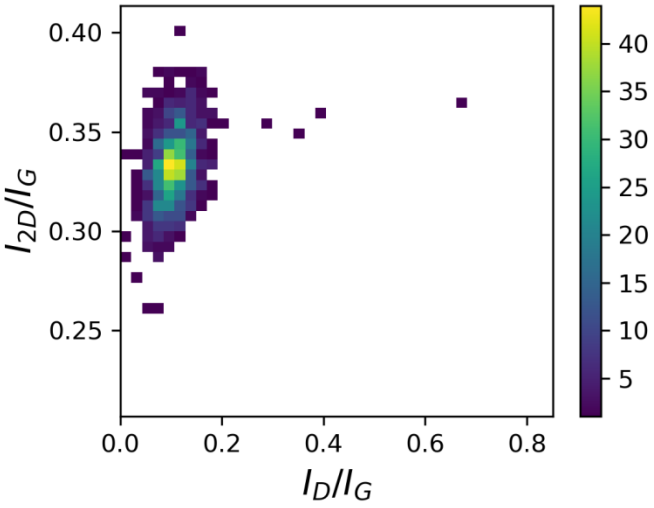

Figure S 67: 3D bivariate histogram showing the distribution of key peak ratios from commercial GNPs data (data set 1). The histogram count is shown by the colored heat map (key on right) and the bins are read simultaneously from the x and y axes which are common to all plots.

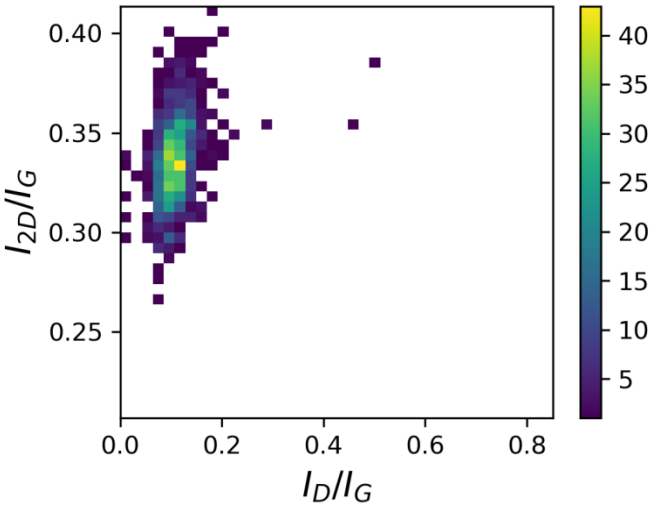

Figure S 68: 3D bivariate histogram showing the distribution of data from commercial GNPs (data set 2).

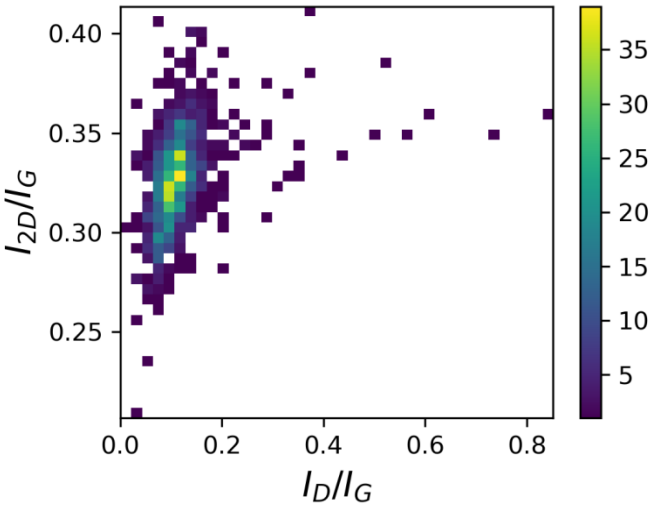

Figure S 69: 3D bivariate histogram showing the distribution of data from commercial GNPs (data set 3).

9.1.4 Graphene Nanoplatelets 'Low Quality'

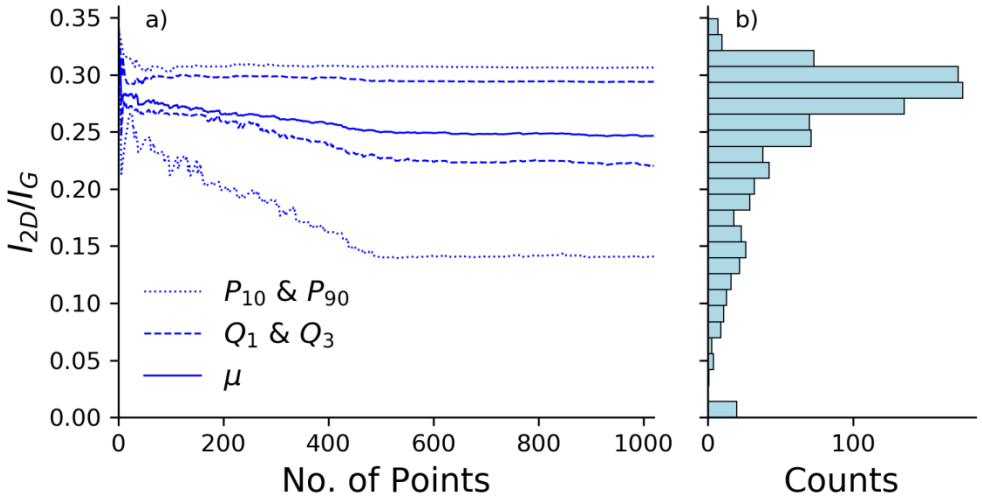

Figure S 70: Convergence plot from commercial GNPs (data set 1) showing a) the change in summary statistics of I_{2D}/I_G as more data points are added to the analysis. b) The final distribution shown as a histogram, y-axis constant across all plots showing I_{2D}/I_G convergence data from graphite sample.

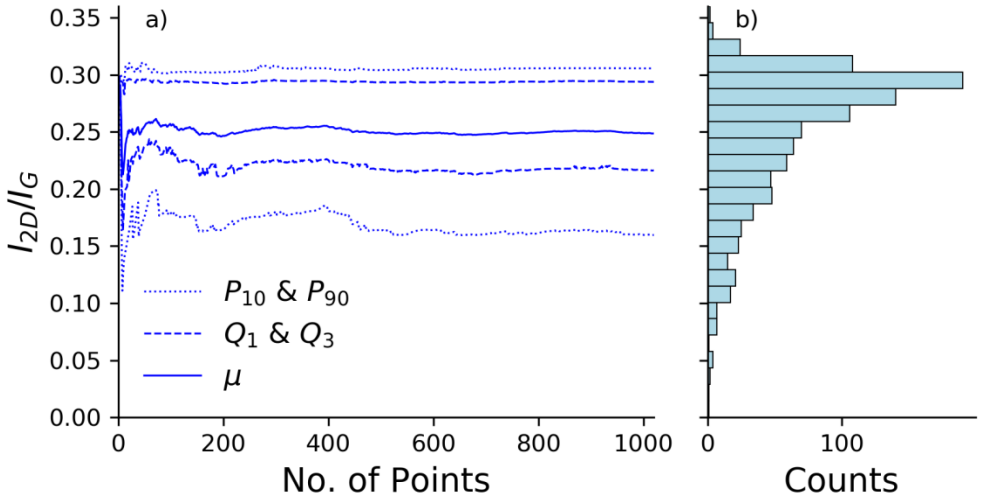

Figure S 71: Convergence plot from commercial GNPs (data set 2) described in detail above.

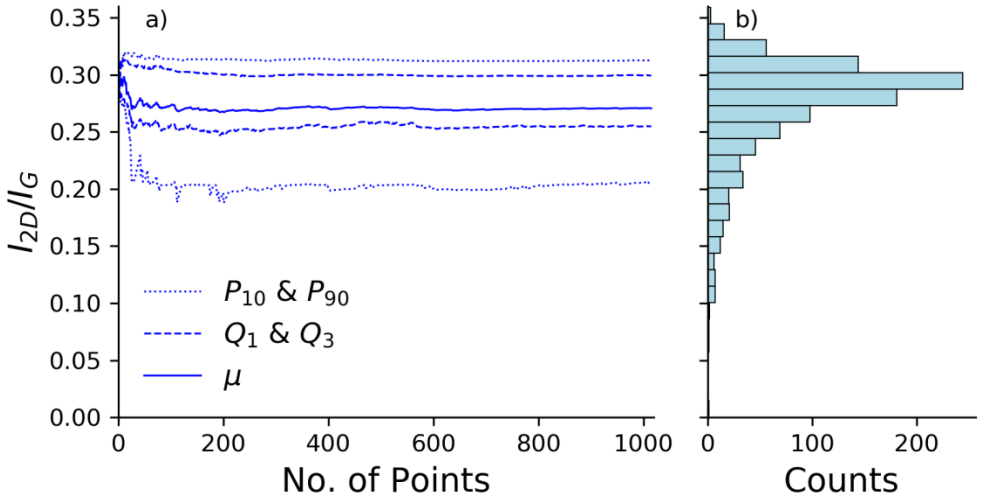

Figure S 72: Convergence plot from commercial GNPs (data set 3) described in detail above.

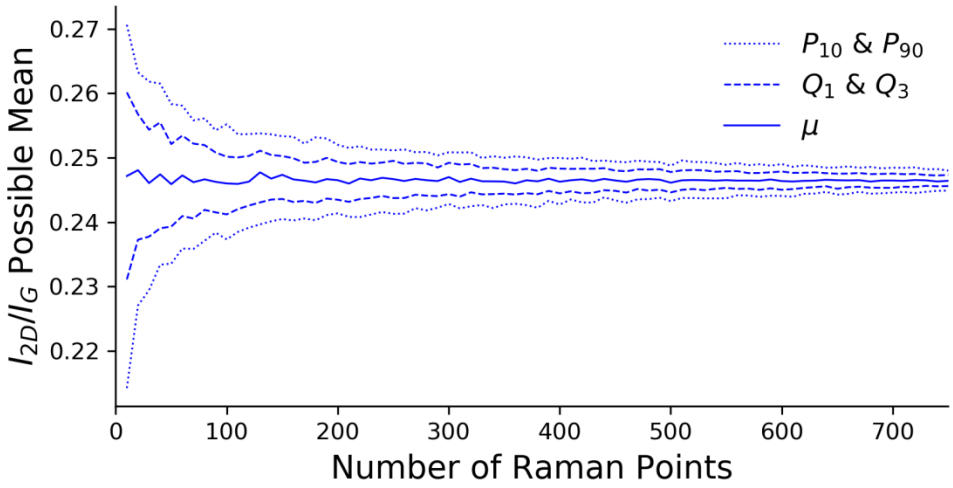

Figure S 73: Bootstrap convergence plot from commercial GNPs (data set 1); this shows the summary statistics (10th and 90th percentiles, 1st and 3rd quartiles, and mean) describing the distribution of mean values obtained from multiple analyses of smaller sub-sets of the sample size shown on the x-axis. This plot can be considered a probability distribution of possible mean values for different sample sizes.

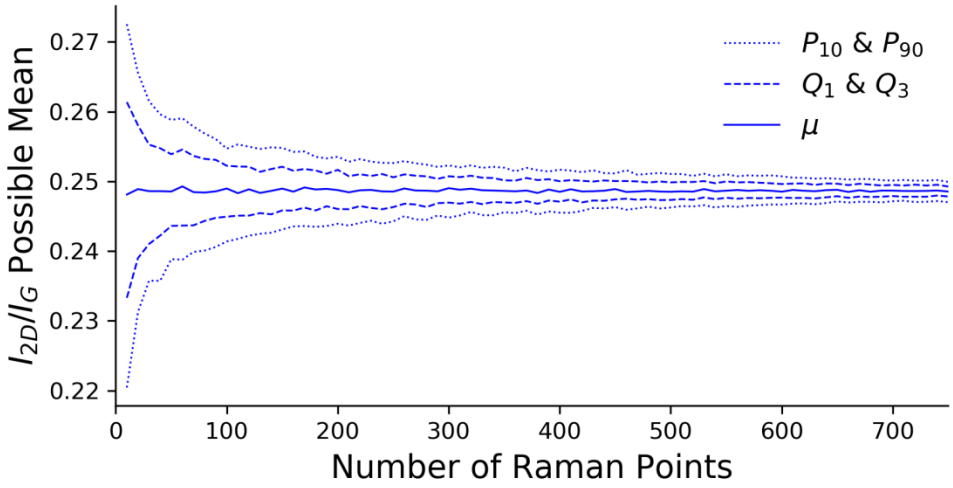

Figure S 74: Bootstrap convergence plot from commercial GNPs (data set 2), described in detail above.

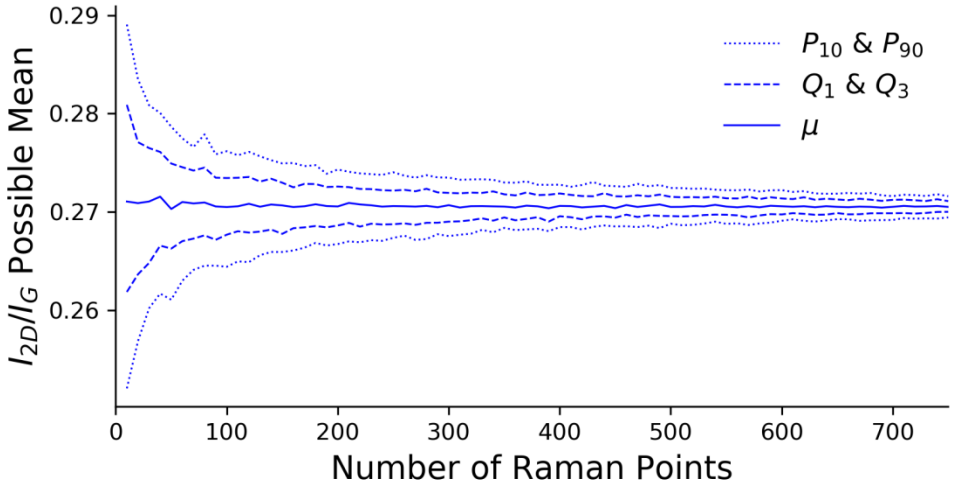

Figure S 75: Bootstrap convergence plot from commercial GNPs (data set 3), described in detail above.

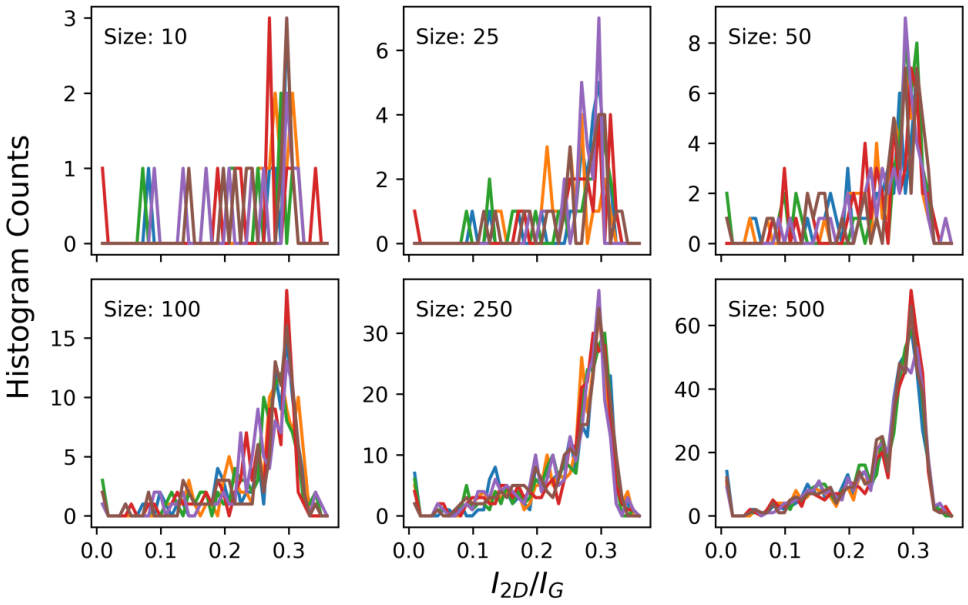

Figure S 76: Panel showing result of bootstrap analysis of commercial GNPs (data set 1). Each panel shows five examples, shown in different colors, of distributions of I_{2D}/I_G produced from sub-sets; the size of these is labelled and the x-axis is common across all I_{2D}/I_G panel plots. These show the convergence to a uniform distribution as the sub-set size increases.

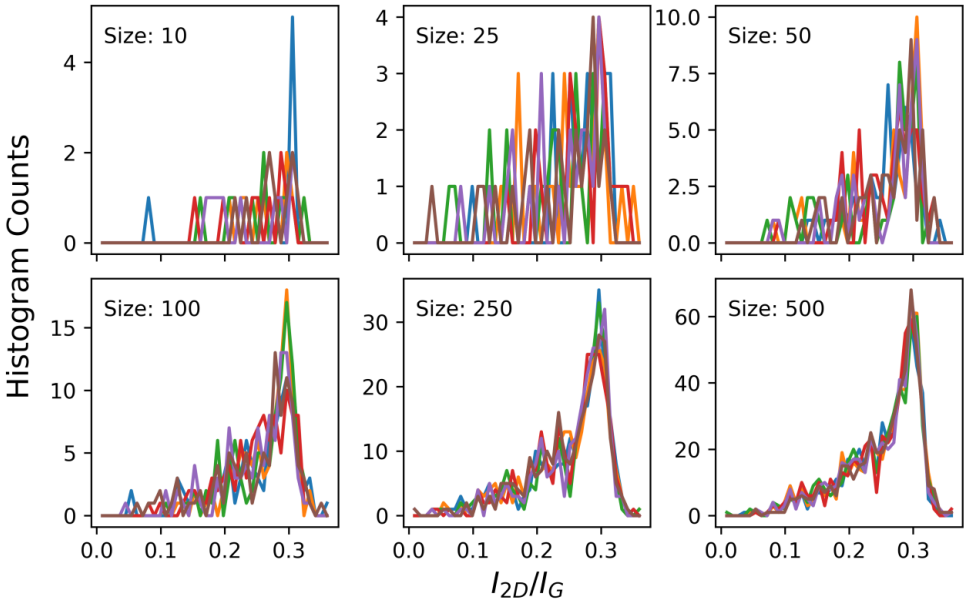

Figure S 77: Panel showing result of bootstrap analysis of commercial GNPs (data set 2), described in detail above.

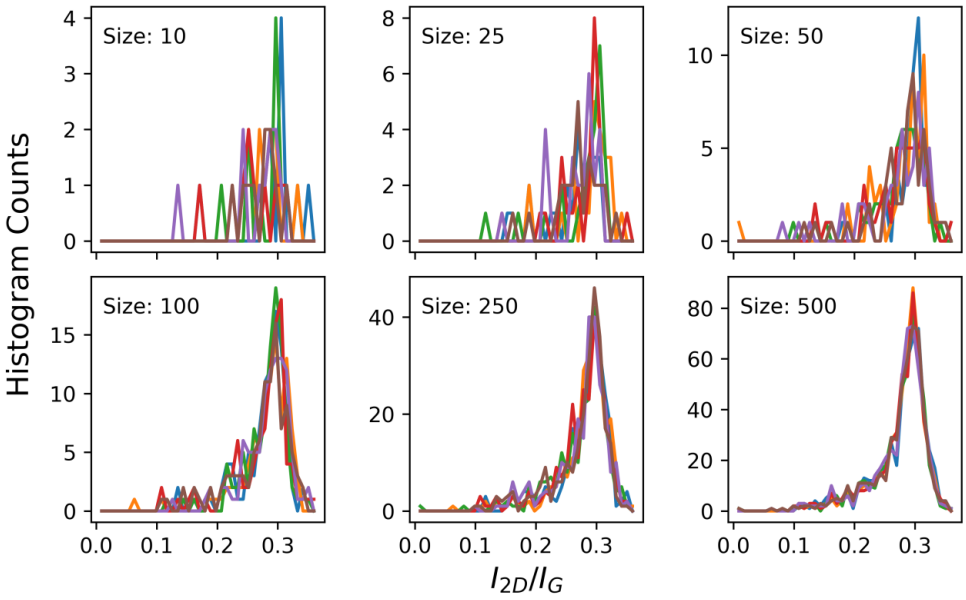

Figure S 78: Panel showing result of bootstrap analysis of commercial GNPs (data set 3), described in detail above.

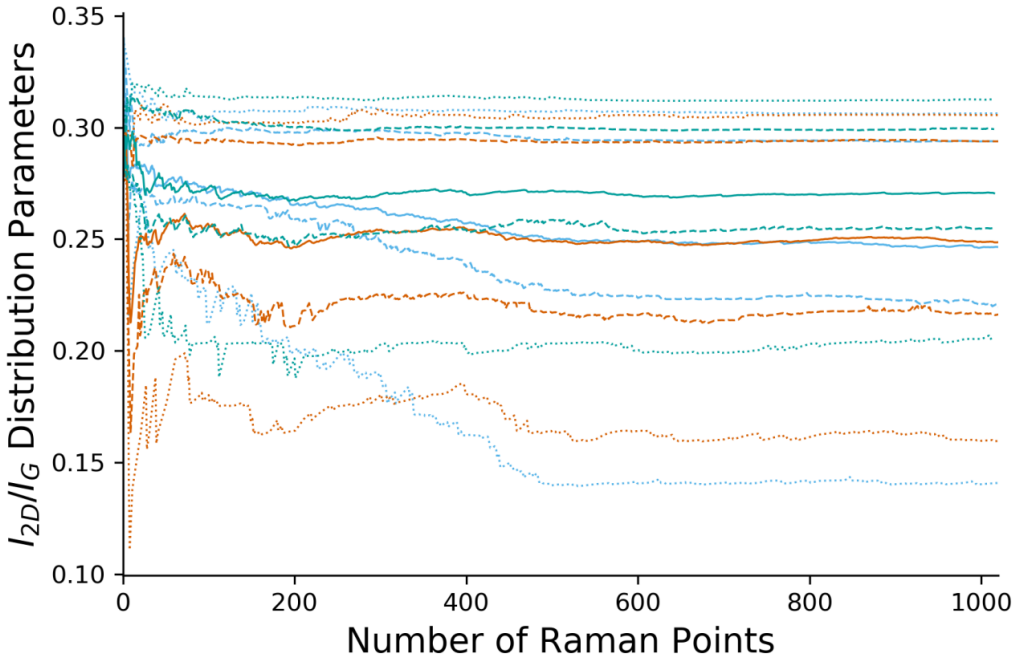

Figure S 79: Plot showing the convergence data of I_{2D}/I_G from all three commercial GNPs data sets. The dots denote the same summary statistics whilst different data sets are shown in different colors. Whilst complex this plot indicates that convergence of all three maps is consistent.

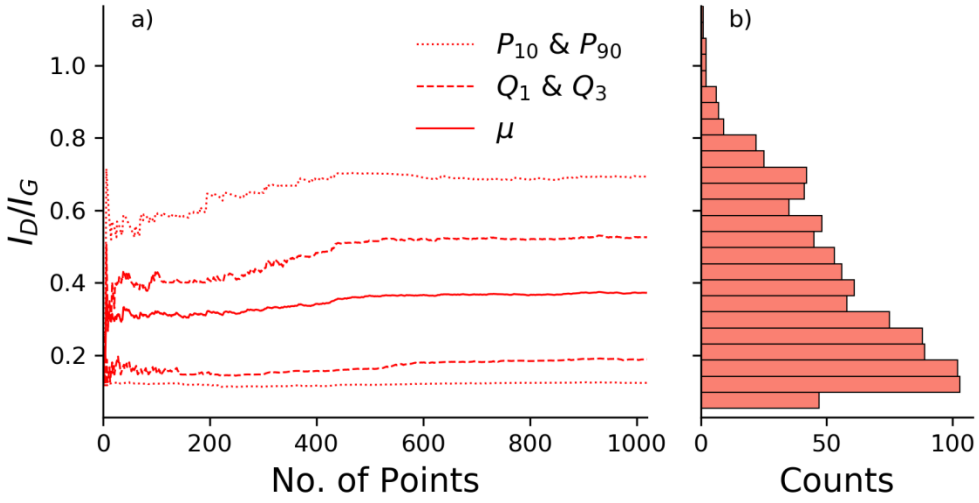

Figure S 80: Convergence plot from commercial GNPs (data set 1) showing a) the change in summary statistics of I_D/I_G as more data points are added to the analysis. b) The final distribution shown as a horizontal histogram, y-axis constant across all plots showing I_D/I_G convergence data from graphite sample.

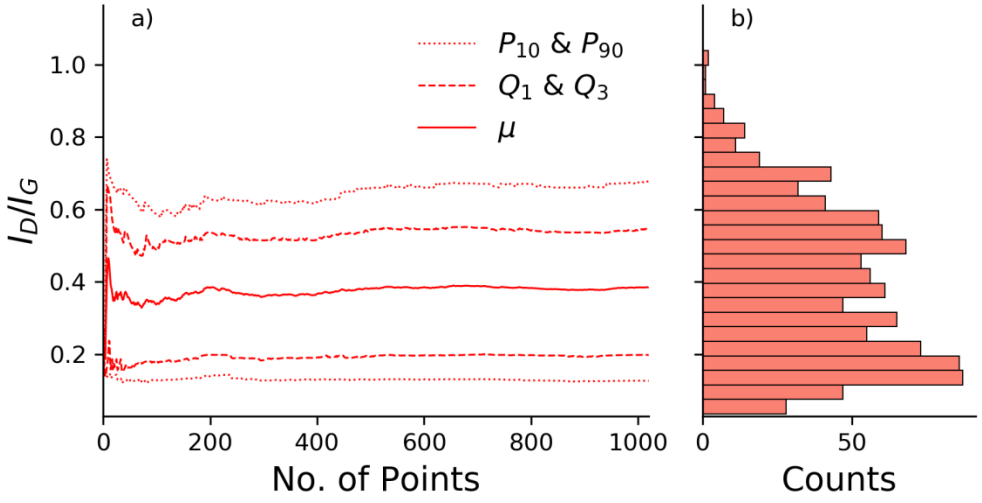

Figure S 81: Convergence plot from commercial GNPs (data set 2) described in detail above.

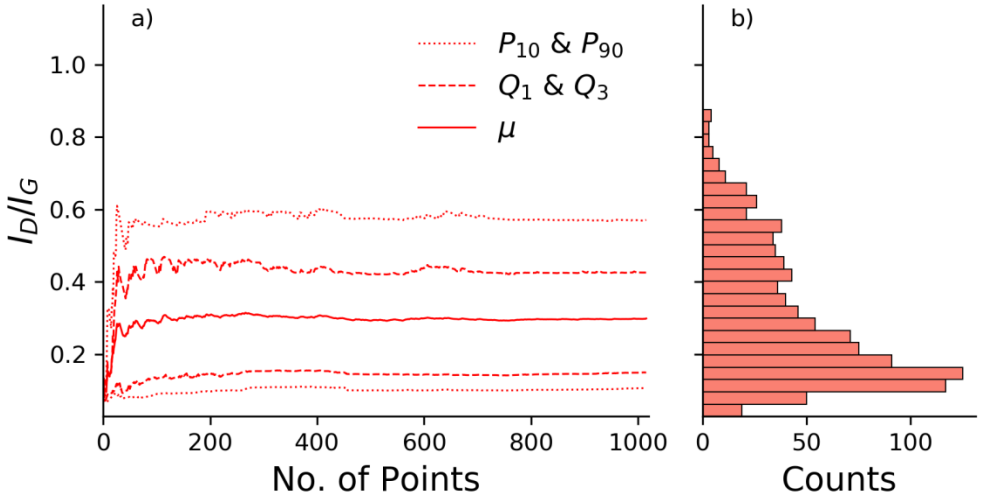

Figure S 82: Convergence plot from commercial GNPs (data set 3) described in detail above.

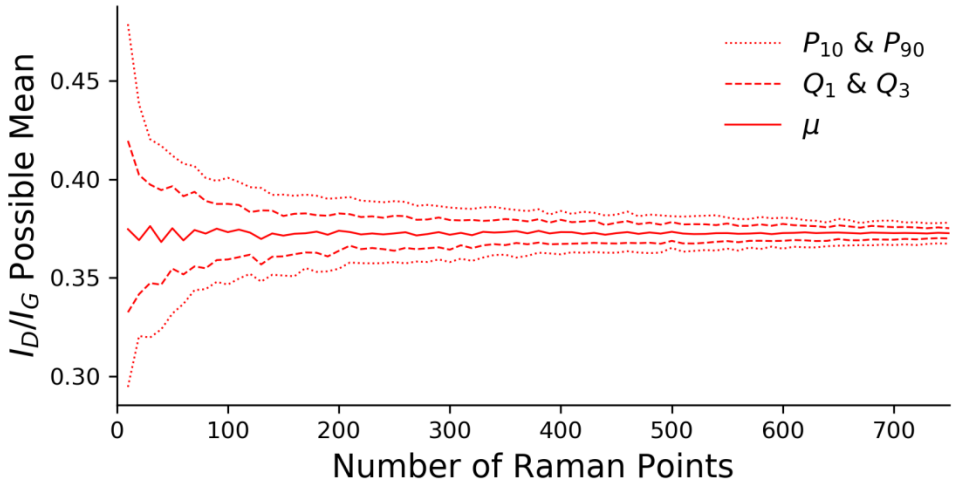

Figure S 83: Bootstrap convergence plot from commercial GNPs (data set 1); this shows the summary statistics (10th and 90th percentiles, 1st and 3rd quartiles, and mean) describing the distribution of mean values obtained from multiple analyses of smaller sub-sets of the sample size shown on the x-axis. This plot can be considered a probability distribution of possible mean values for different sample sizes.

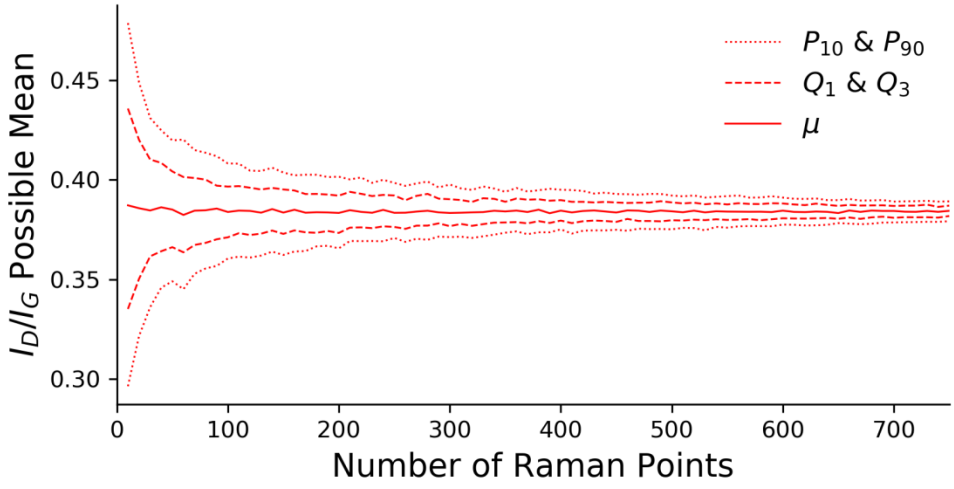

Figure S 84: Bootstrap convergence plot from commercial GNPs (data set 2), described in detail above.

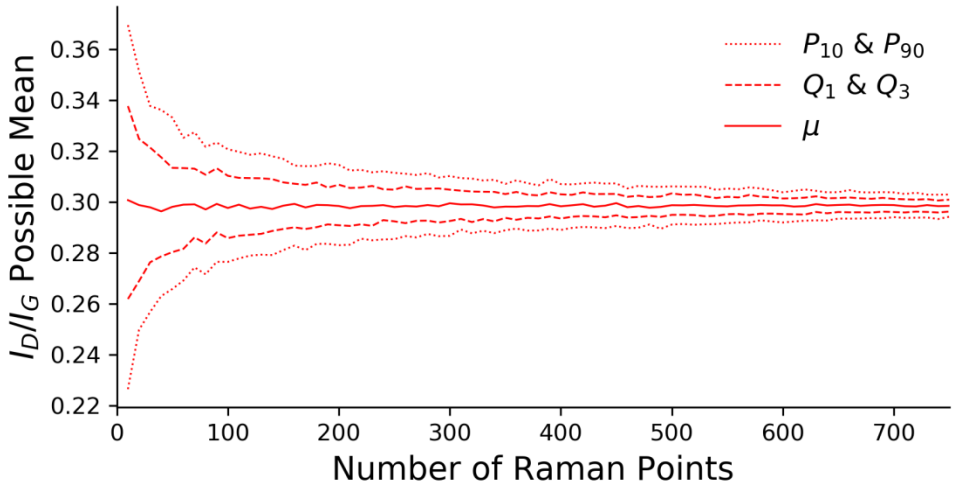

Figure S 85: Bootstrap convergence plot from commercial GNPs (data set 3), described in detail above.

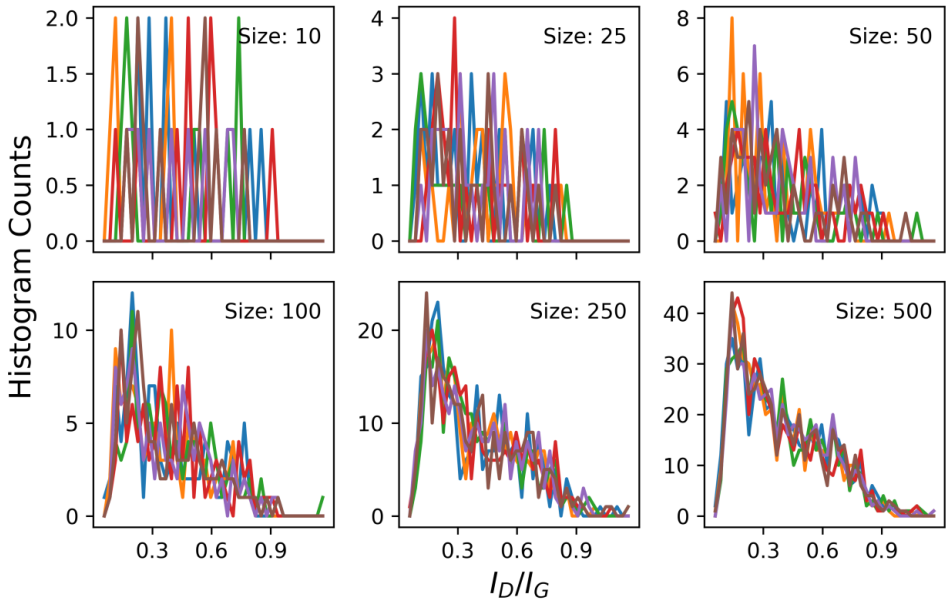

Figure S 86: Panel showing result of bootstrap analysis of commercial GNPs (data set 1). Each panel shows five examples, shown in different colors, of distributions of I_D/I_G produced from sub-sets; the size of these is labelled and the x-axis is common across all I_D/I_G panel plots. These show the convergence to a uniform distribution as the sub-set size increases.

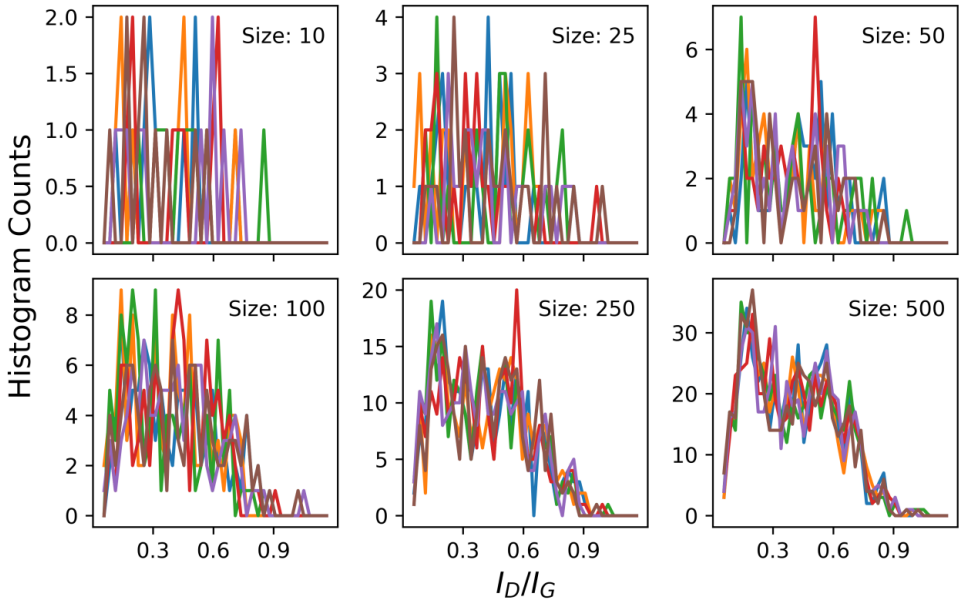

Figure S 87: Panel showing result of bootstrap analysis of commercial GNPs (data set 2), described in detail above.

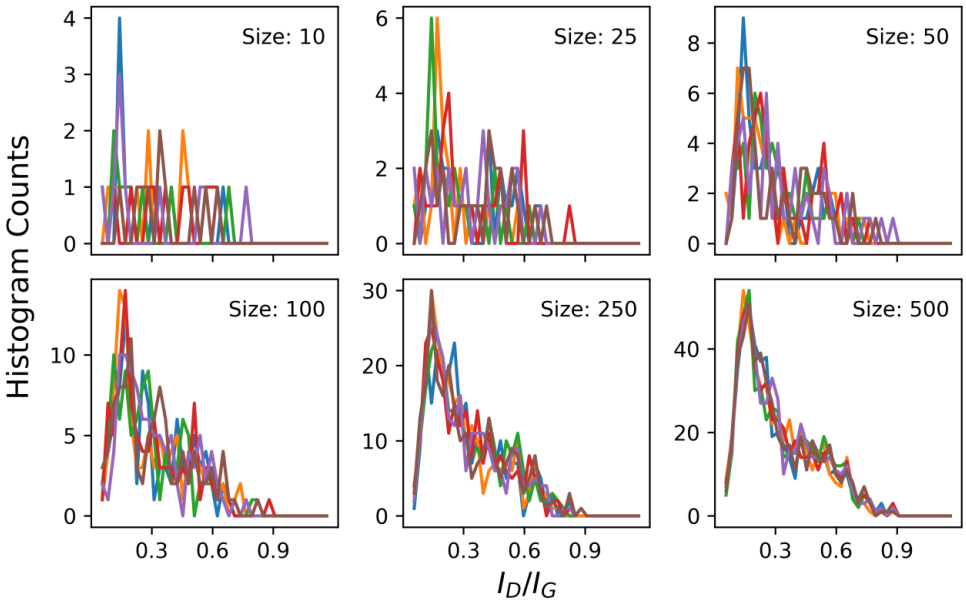

Figure S 88: Panel showing result of bootstrap analysis of commercial GNPs (data set 3), described in detail above.

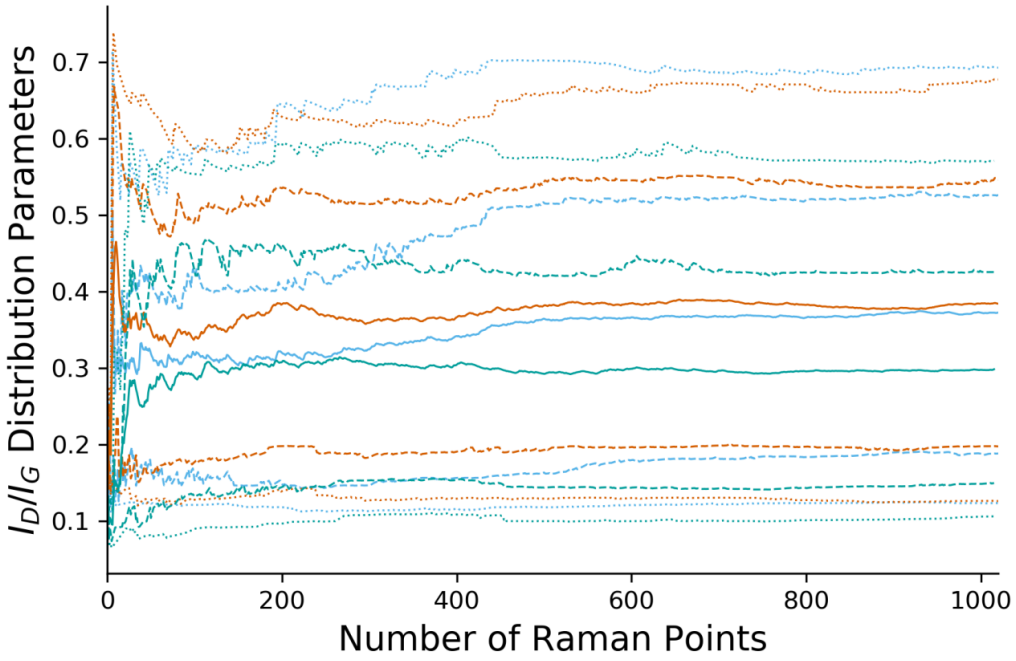

Figure S 89: Plot showing the convergence data of I_D/I_G from all three commercial GNPs data sets. The dots denote the same summary statistics whilst different data sets are shown in different colors. Whilst complex this plot indicates that convergence of all three maps is consistent.

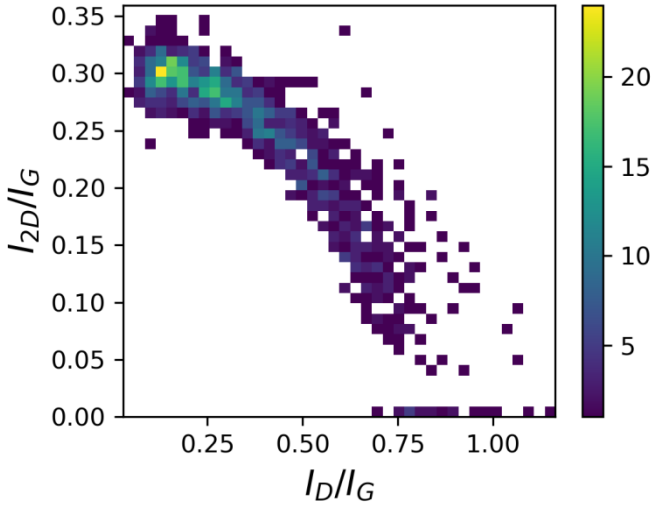

Figure S 90: 3D bivariate histogram showing the distribution of key peak ratios from commercial GNPs data (data set 1). The histogram count is shown by the colored heat map (key on right) and the bins are read simultaneously from the x and y axes which are common to all plots.

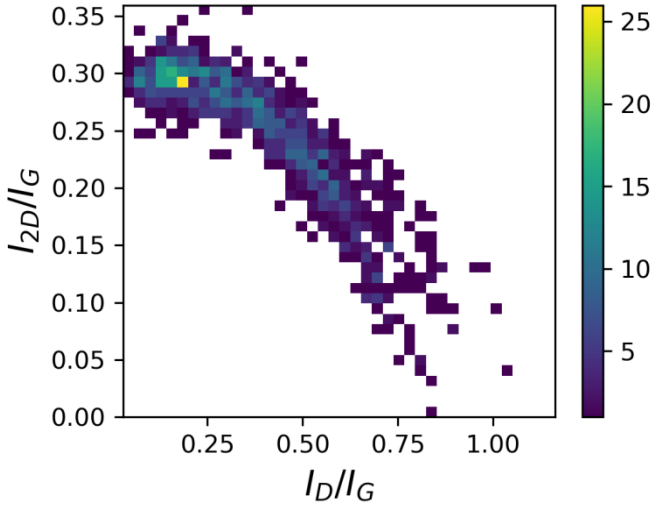

Figure S 91: 3D bivariate histogram showing the distribution of data from commercial GNPs (data set 2).

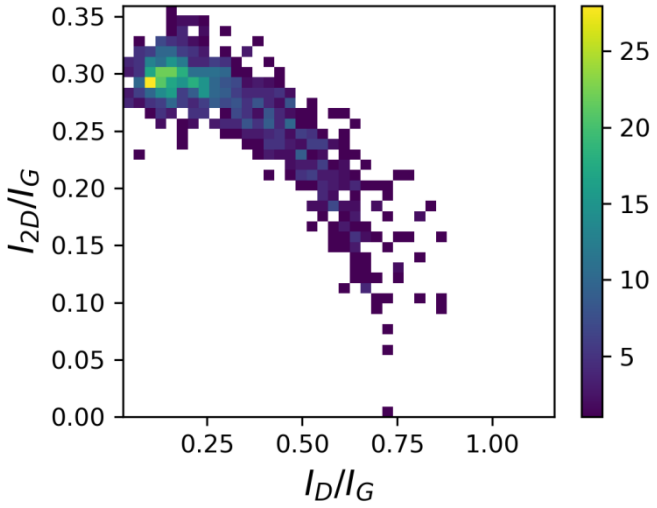

Figure S 92: 3D bivariate histogram showing the distribution of data from commercial GNPs (data set 3).

9.1.5 Commercial Multiwalled Carbon Nanotubes

Similar procedures were used to analyses the data collected from commercial multiwalled carbon nanotubes, although more data sets were collected and are displayed below including figures showing convergence of I_{2D}/I_G ratios as data points were collected, bootstrap analysis of I_{2D}/I_G, convergence plots of I_D/I_G, bootstrap plots of I_D/I_G and 3D bivariate histograms showing the distribution of both peak ratios simultaneously. More data sets were required from this material as different samples taken from the bulk - a 1 kg tub of MWCNTs, exhibited differences in their Raman character. This suggests the large volume of power was not uniform, whether this is a common issue with large volumes of nanomaterial was not thoroughly investigated, although other groups have investigated the quality of commercially sold carbon nanomaterials; it should be highlighted that only by collecting a statistically justified sample size can such anomalies be found.

The I_D/I_G ratio was variable between different acquisitions but when considering the aggregated total data set the final distribution is normal around 1.25. The 3rd data set collected was significantly lower than this average (1.12) and the 4th data set higher (1.36), there was overlap between the tails of the different distributions hence the normal distribution from the combined data set shown in Figure S 144. The cause of these different spectra from different samples of nominally the same material will not be subject to speculation here; however, the implications for the analysis of nanomaterials are that multiple data sets should be collected to ensure the quality of an entire material. Whilst it was hoped that using Raman spectroscopy with micron spaces between analysis spots would be sufficient it appears that for many materials wider sampling is required.

In this case when the different data sets were randomly recombined to remove any ordering, the convergence plots show that over a thousand points may be required to fully characterize such disordered materials but these should be recorded from many different areas of sample rather than a single large map. This effect of non-random local structure is indicated in many of the convergence plots which show structure in the data from the regular lines of laser spots used for data collection, at the end of each line the new spectra recorded would more closely resemble the material at the start of the previous; causing the sawtooth pattern visible in many of the convergence plots (Figure S104,106,124,126).

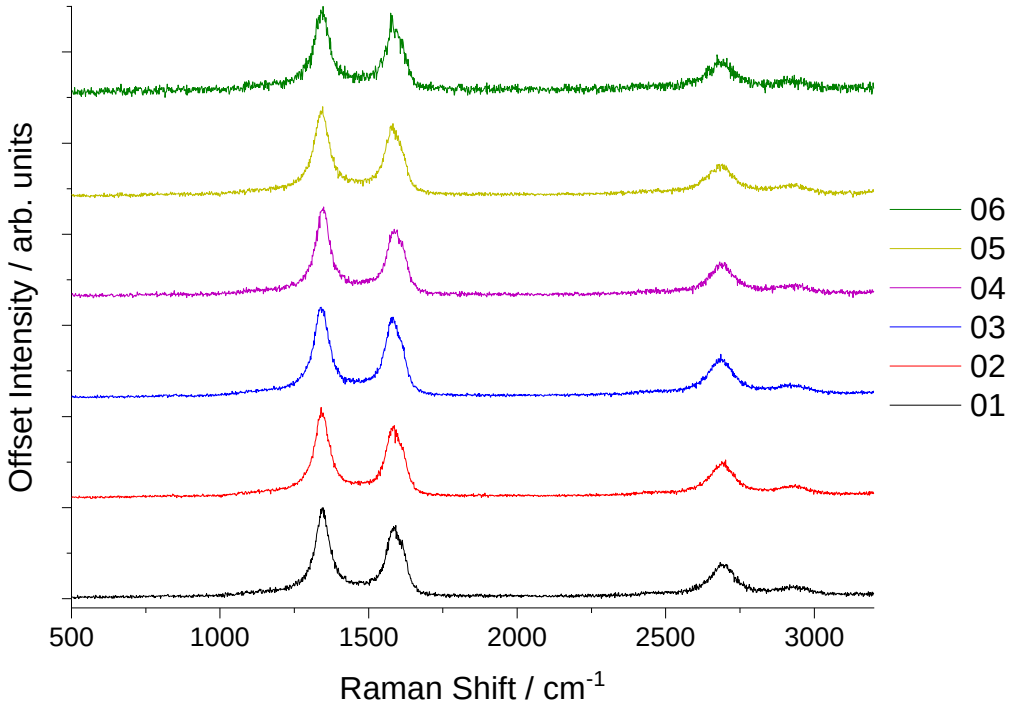

Figure S 93: Example spectra from all data sets of MWCNTs; each spectrum is selected to be representative of the modal peak parameters from each sample distribution; no processing further than the normalization of signal intensity has been applied.

It should also be stressed that statistically justified data sets are extremely powerful for identifying different phases of a material, or justifying changes to a material following processing. The absolute difference between the maps at the "extremes" of this distribution are not actually substantially different, especially when compared with some materials exhibiting huge differences between the phases present. Example spectra representative of the modal peak parameters from each distinct data set are shown in Figure S 93; these show that the distribution remains narrow enough that differences between the extremes are still very similar spectroscopically.

Thus far, discussion has focused on the D peak intensity as the key metric for understanding this nanotube sample; mostly due to the relatively large intensity and therefore defect concentration in this material. Considering now the 2D peak, this can also be linked to the crystalline quality of carbon nanotubes, albeit usually high quality single walled tubes. In this case, the 2D peak also has extreme values, however, the overall distribution tends to encompass the extremes with a very broad, flat topped distribution. Unexpectedly the 3D histogram of the combined sample does show a bimodal distribution in the I_{2D}/I_G parameters, separated by approximately 0.05. Despite this, the overall trend in convergence data is

similar to the I_D/I_G data with possibly a slightly faster convergence due to the narrower distribution and the bootstrap plots show the same flat-topped distribution.

Overall, the analysis of commercial nanotubes required a more nuanced approach to data collection; a single Raman spectrum may miss important phases or features of the material but a brute force approach to large data sets would appear to be insufficient. This work never intended to complete a full analysis of every material, especially commercial samples and hence the question of attributing peak parameters to physical properties has not been attempted. Many reviews exist in literature linking Raman spectroscopy features with physical properties of carbon nanomaterials.[11,320,398] We merely wish to highlight the power of statistically justifying sample size and analysis procedures to ensure the data truly reflects the material under analysis.

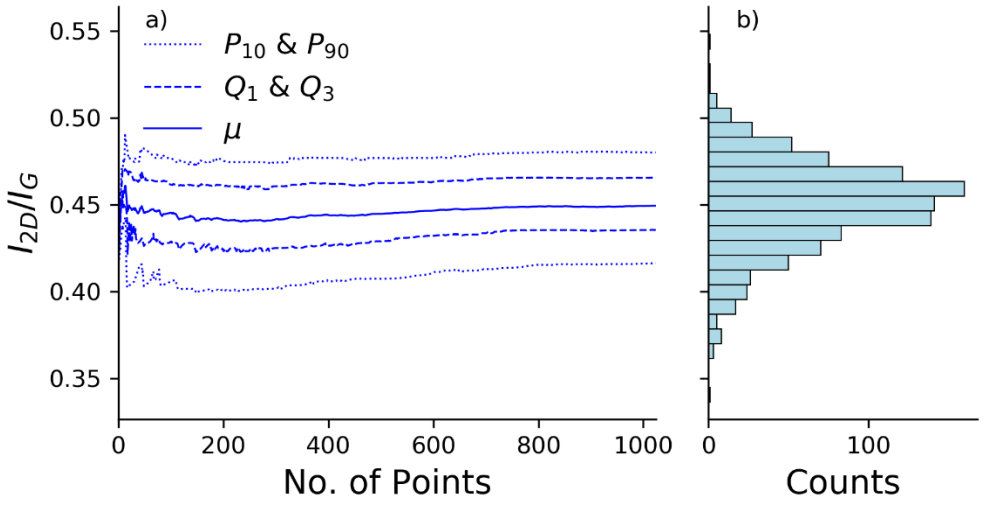

Figure S 94: Convergence plot from commercial MWCNTs (data set 1) showing a) the change in summary statistics of I_{2D}/I_G as more data points are added to the analysis. b) The final distribution shown as a horizontal histogram, y-axis constant across all plots showing I_{2D}/I_G convergence data from graphite sample.

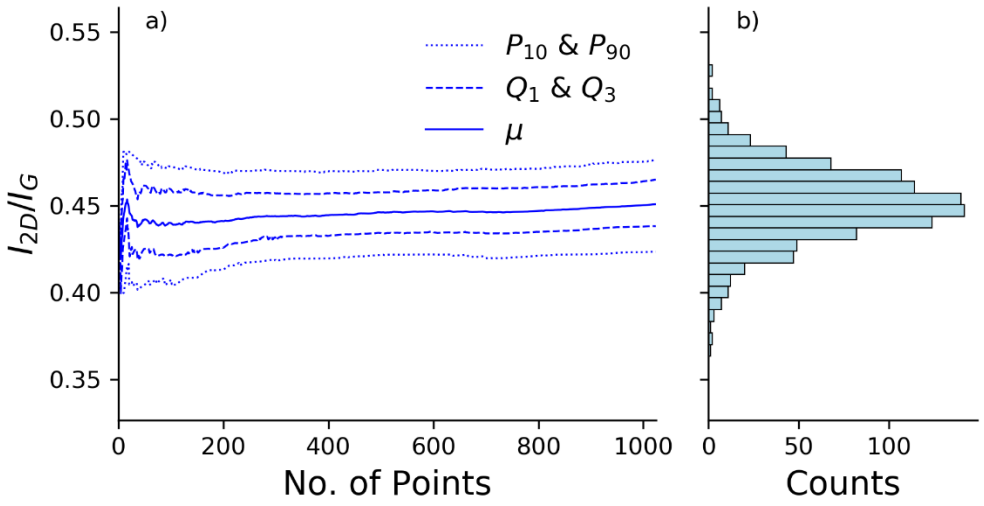

Figure S 95: Convergence plot from commercial MWCNTs (data set 2) described in detail above.

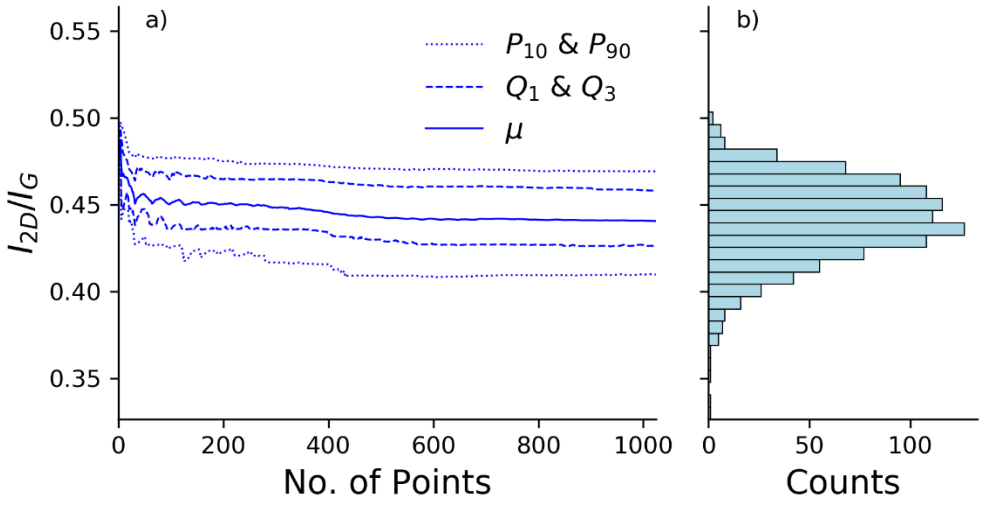

Figure S 96: Convergence plot from commercial MWCNTs (data set 3) described in detail above.

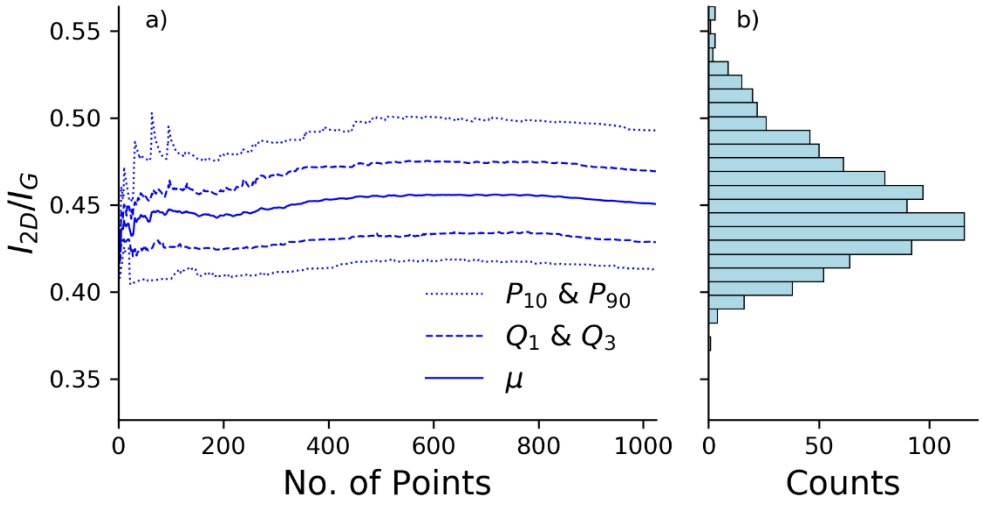

Figure S 97: Convergence plot from commercial MWCNTs (data set 4) described in detail above.

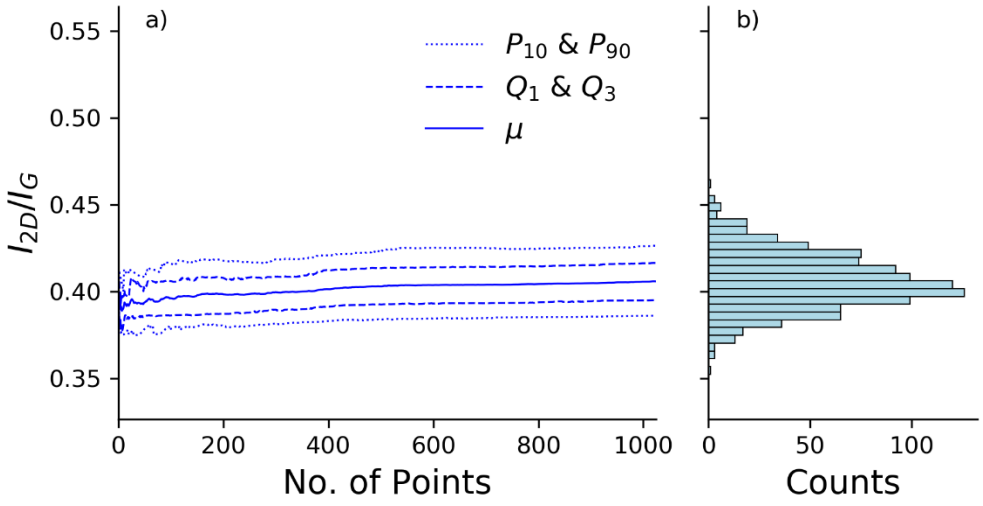

Figure S 98: Convergence plot from commercial MWCNTs (data set 5) described in detail above.

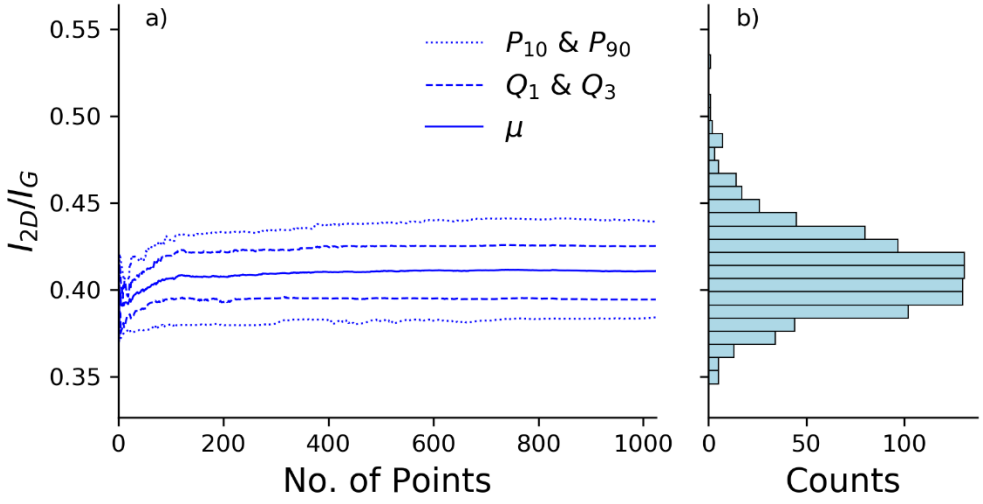

Figure S 99: Convergence plot from commercial MWCNTs (data set 6) described in detail above.

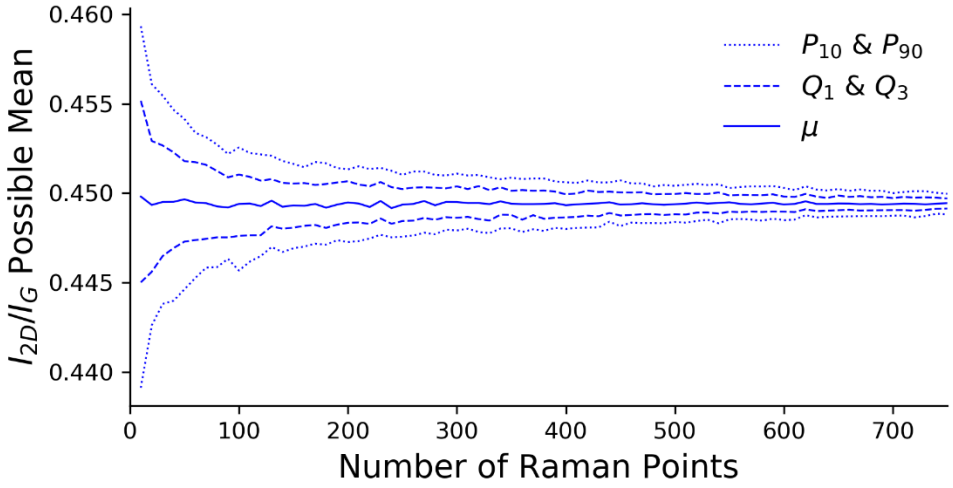

Figure S 100: Bootstrap convergence plot from commercial MWCNTs (data set 1); this shows the summary statistics (10^{th} and 90^{th} percentiles, 1^{st} and 3^{rd} quartiles, and mean) describing the distribution of mean values obtained from multiple analyses of smaller sub-sets of the sample size shown on the x-axis. This plot can be considered a probability distribution of possible mean values for different sample sizes.

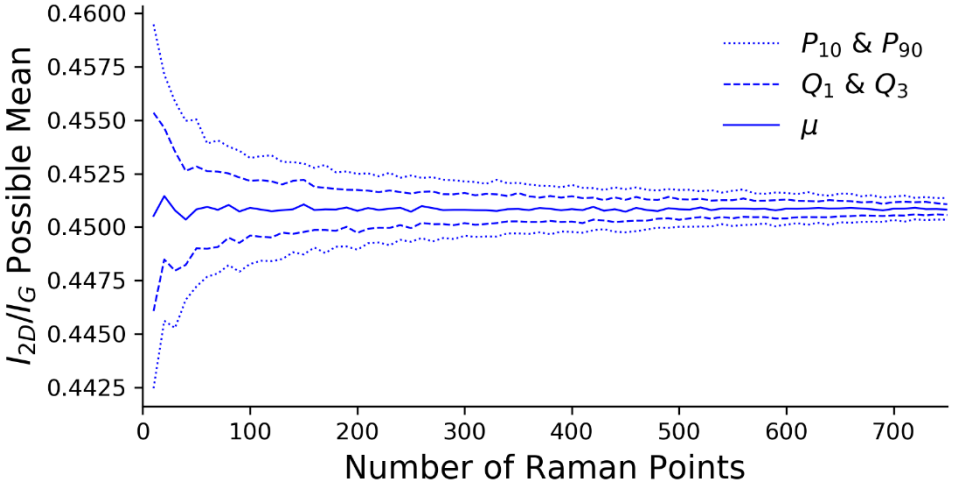

Figure S 101: Bootstrap convergence plot from commercial MWCNTs (data set 2), described in detail above.

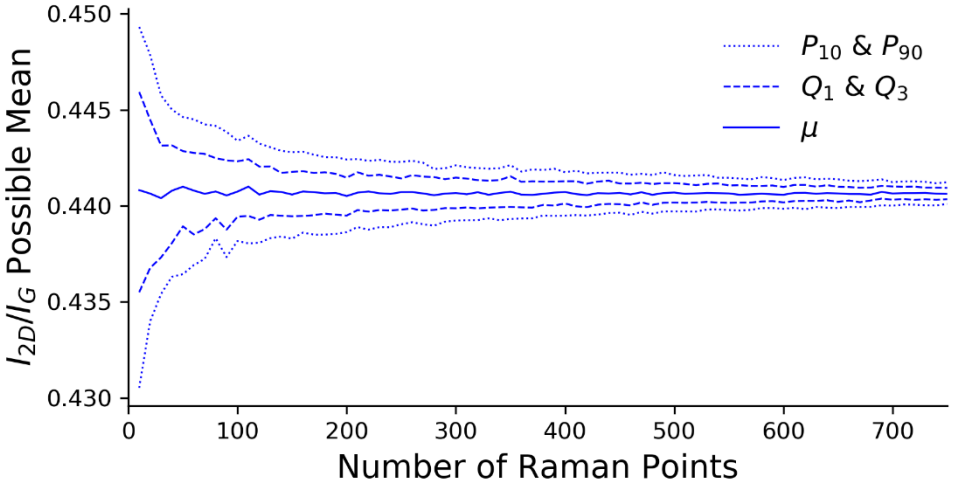

Figure S 102: Bootstrap convergence plot from commercial MWCNTs (data set 3), described in detail above.

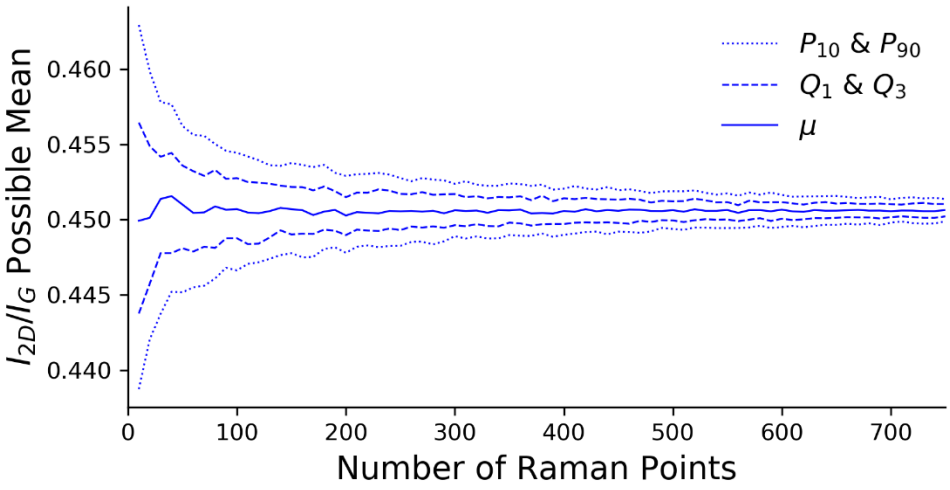

Figure S 103: Bootstrap convergence plot from commercial MWCNTs (data set 4), described in detail above.

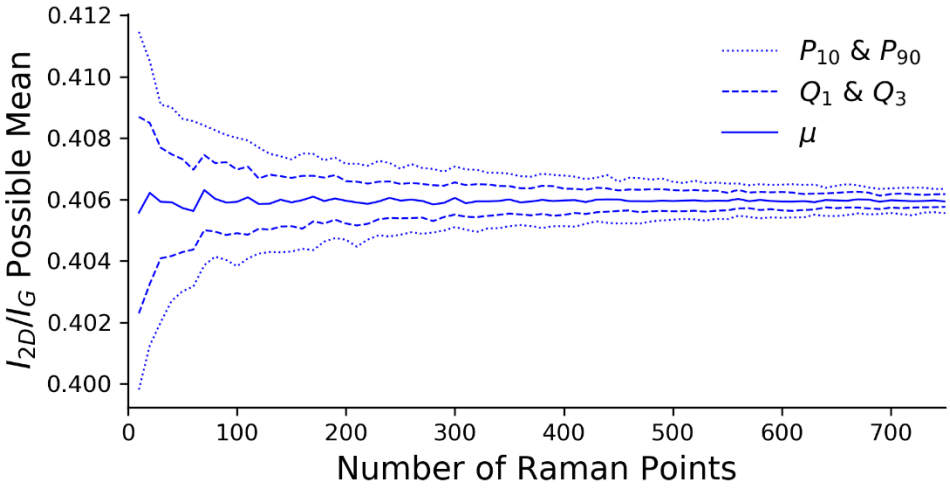

Figure S 104: Bootstrap convergence plot from commercial MWCNTs (data set 5), described in detail above.

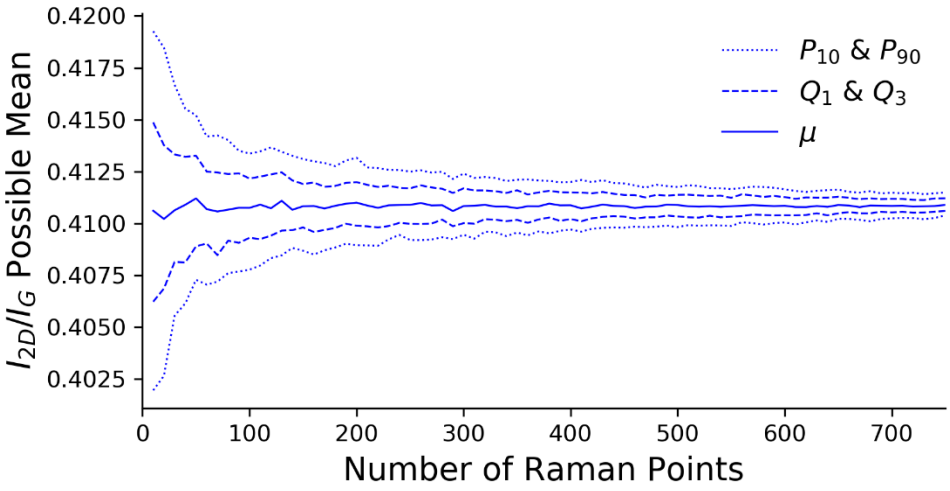

Figure S 105: Bootstrap convergence plot from commercial MWCNTs (data set 6), described in detail above.

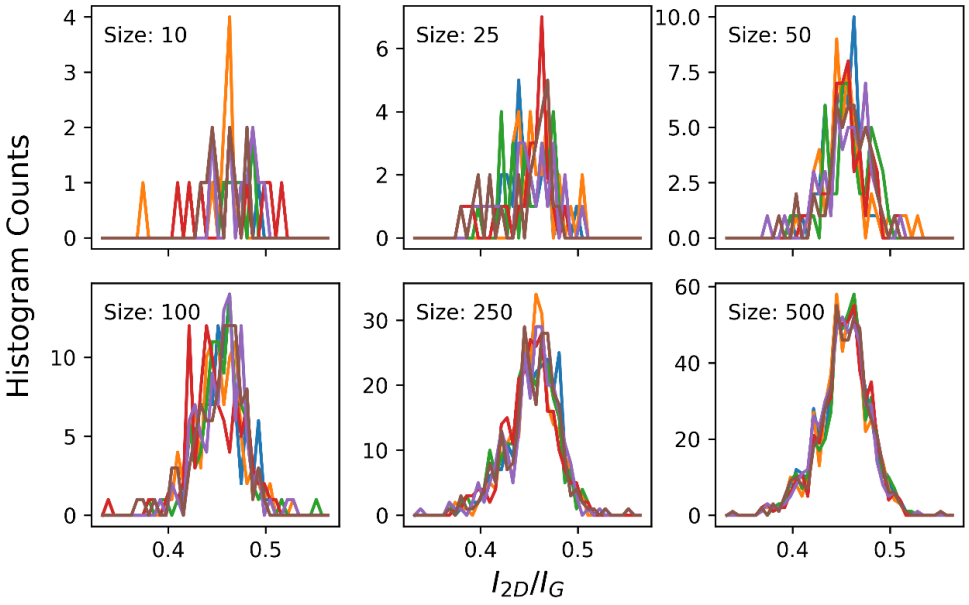

Figure S 106: Panel showing result of bootstrap analysis of commercial MWCNTs (data set 1). Each panel shows five examples, shown in different colors, of distributions of I_{2D}/I_G produced from sub-sets; the size of these is labelled and the x-axis is common across all I_{2D}/I_G panel plots. These show the convergence to a uniform distribution as the sub-set size increases.

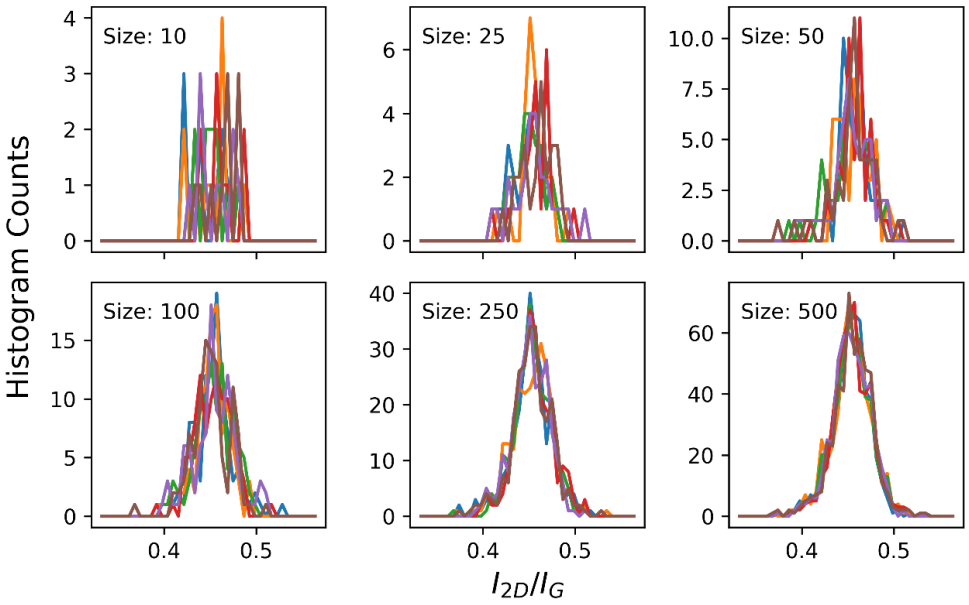

Figure S 107: Panel showing result of bootstrap analysis of commercial MWCNTs (data set 2), described in detail above.

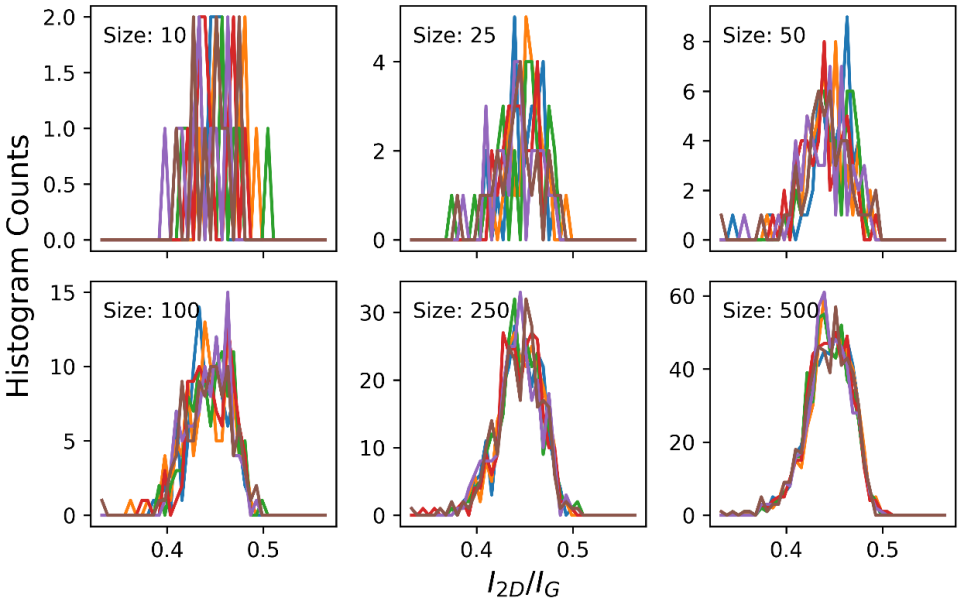

Figure S 108: Panel showing result of bootstrap analysis of commercial MWCNTs (data set 3), described in detail above.

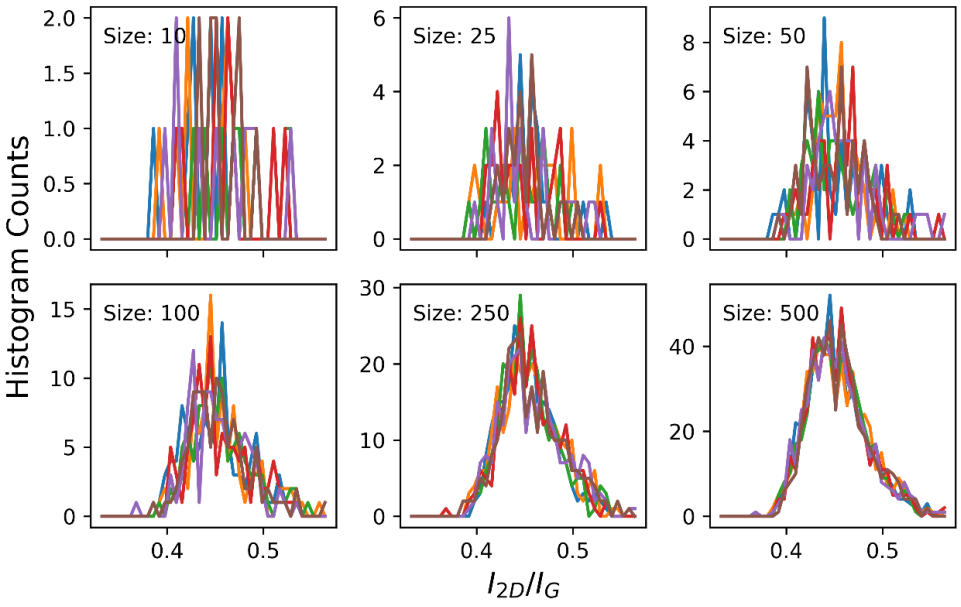

Figure S 109: Panel showing result of bootstrap analysis of commercial MWCNTs (data set 4), described in detail above.

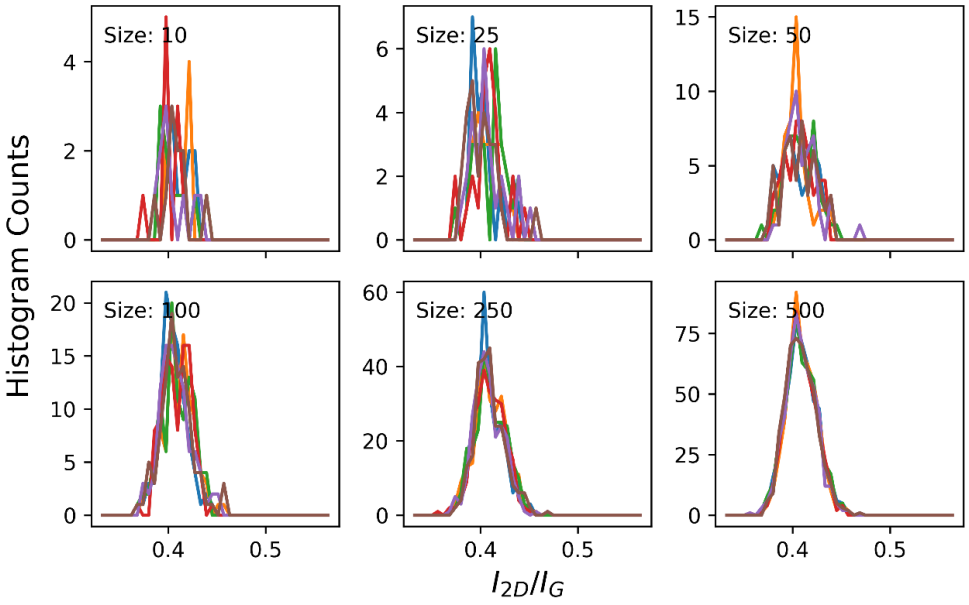

Figure S 110: Panel showing result of bootstrap analysis of commercial MWCNTs (data set 5), described in detail above.

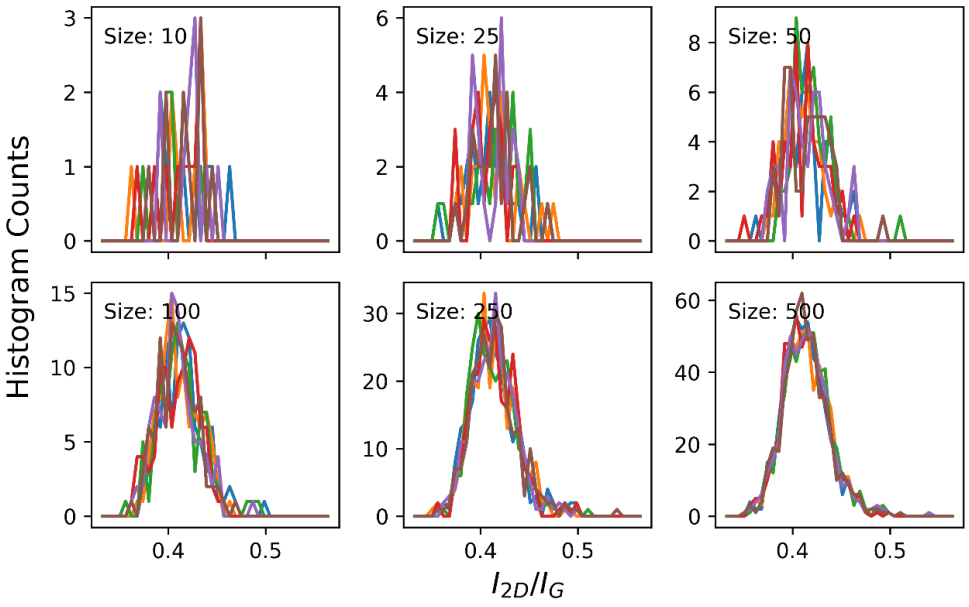

Figure S 111: Panel showing result of bootstrap analysis of commercial MWCNTs (data set 6), described in detail above.

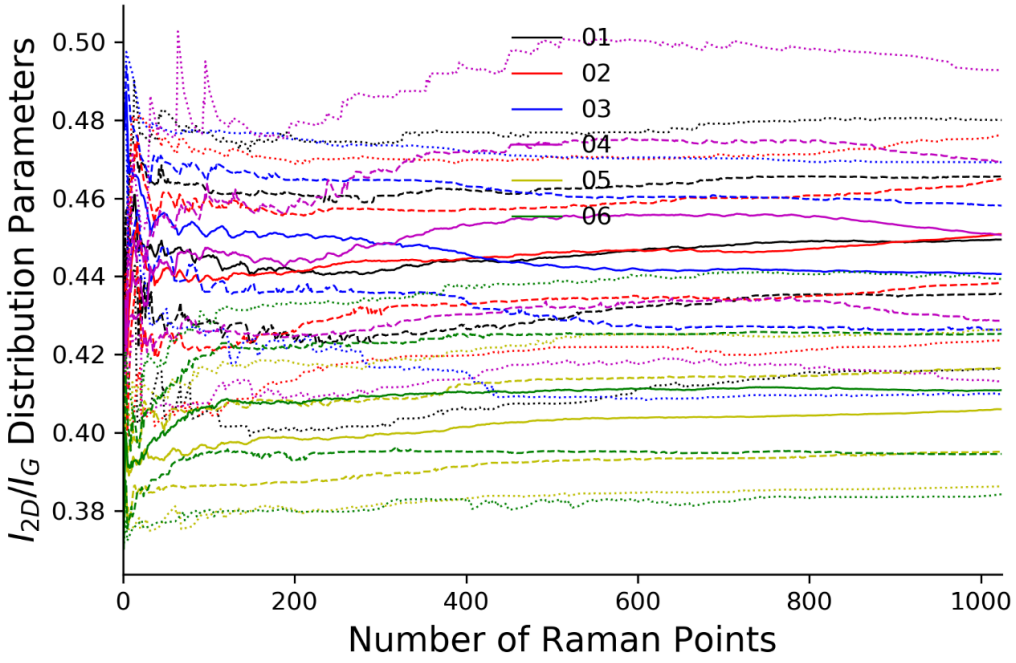

Figure S 112: Plot showing the convergence data of I_{2D}/I_G from all three commercial GNPs data sets. The dots denote the same summary statistics whilst different data sets are shown in different colors. Whilst complex this plot indicates that convergence of all three maps is consistent.

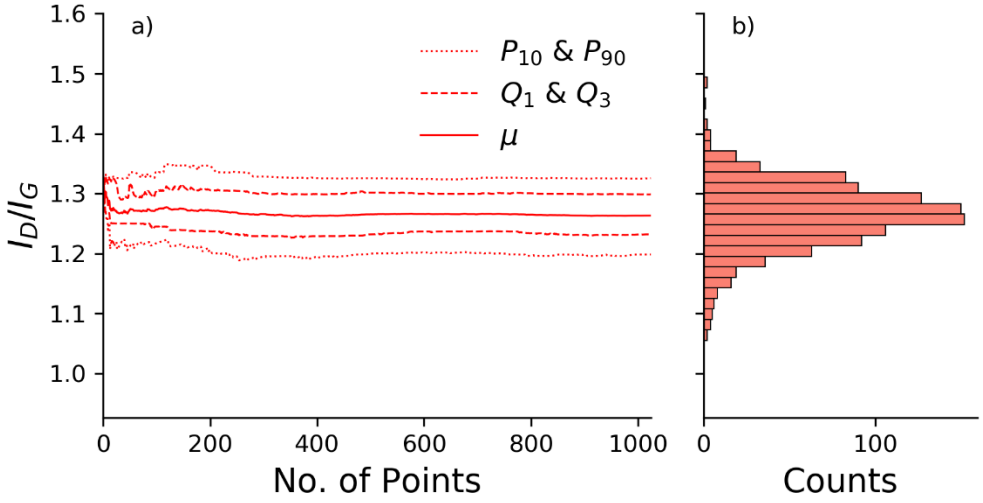

Figure S 113: Convergence plot from commercial MWCNTs (data set 1) showing a) the change in summary statistics of I_D/I_G as more data points are added to the analysis. b) The final distribution shown as a horizontal histogram, y-axis constant across all plots showing I_D/I_G convergence data from graphite sample.

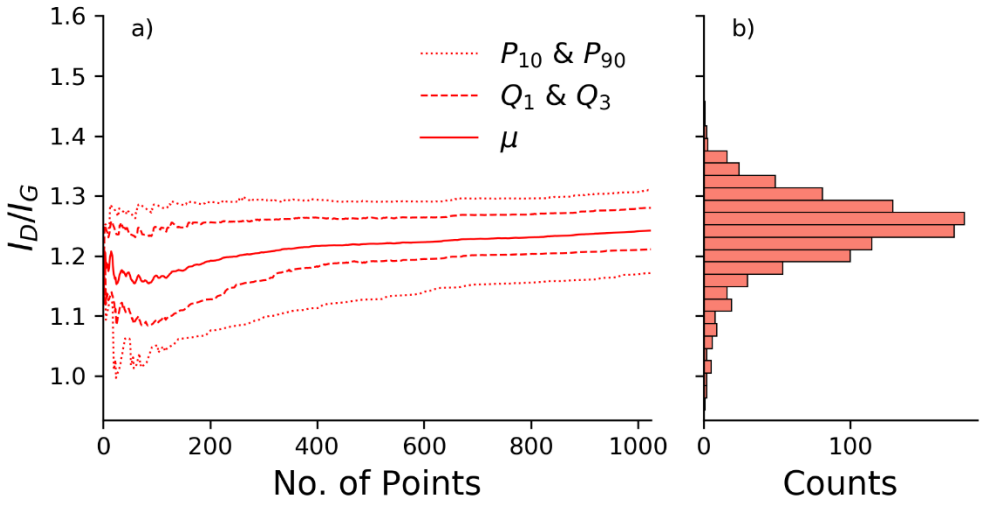

Figure S 114: Convergence plot from commercial MWCNTs (data set 2) described in detail above.

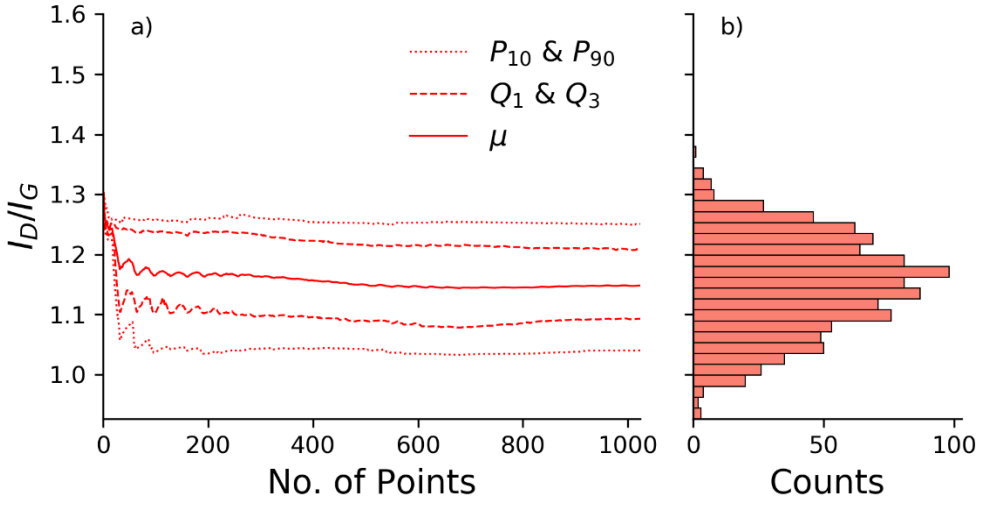

Figure S 115: Convergence plot from commercial MWCNTs (data set 3) described in detail above.

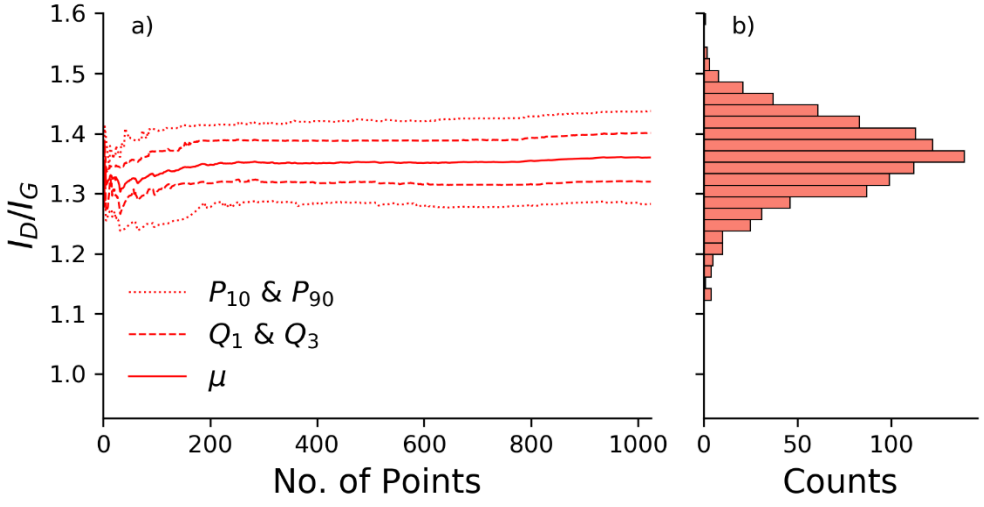

Figure S 116: Convergence plot from commercial MWCNTs (data set 4) described in detail above.

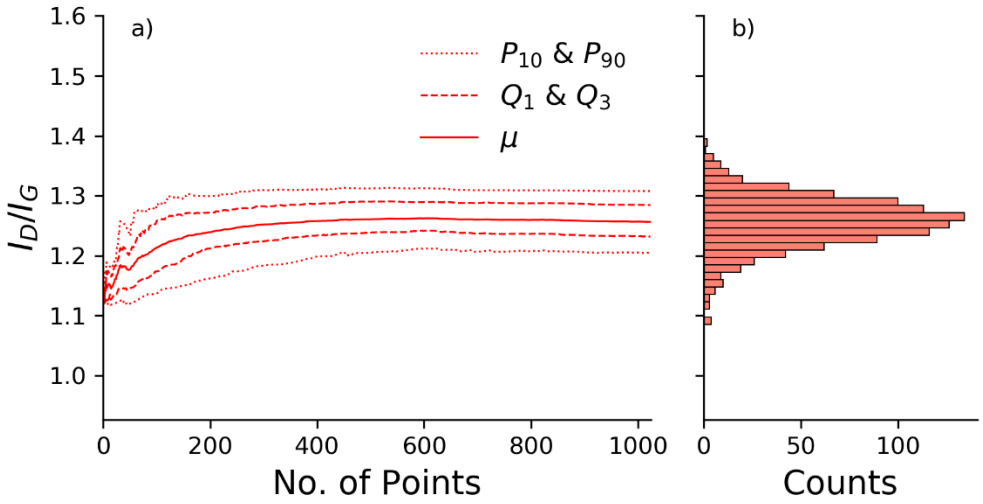

Figure S 117: Convergence plot from commercial MWCNTs (data set 5) described in detail above.

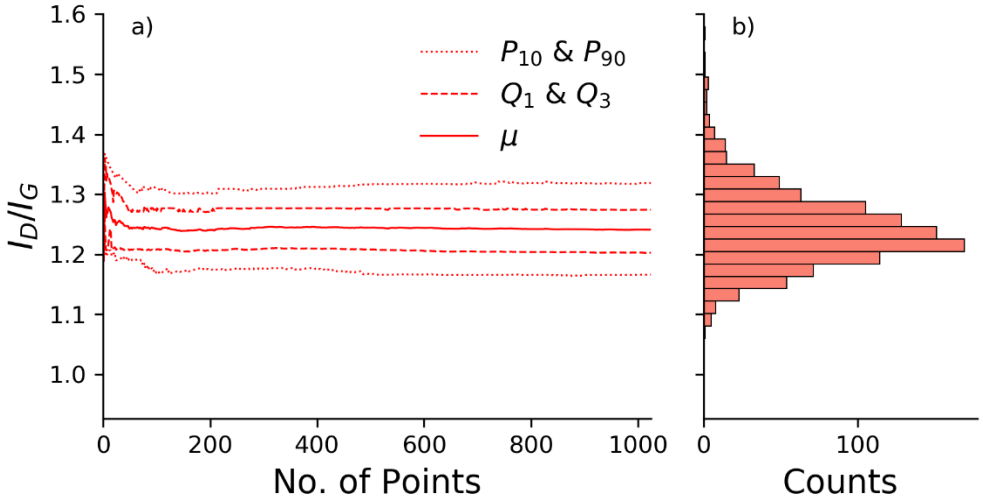

Figure S 118: Convergence plot from commercial MWCNTs (data set 6) described in detail above.

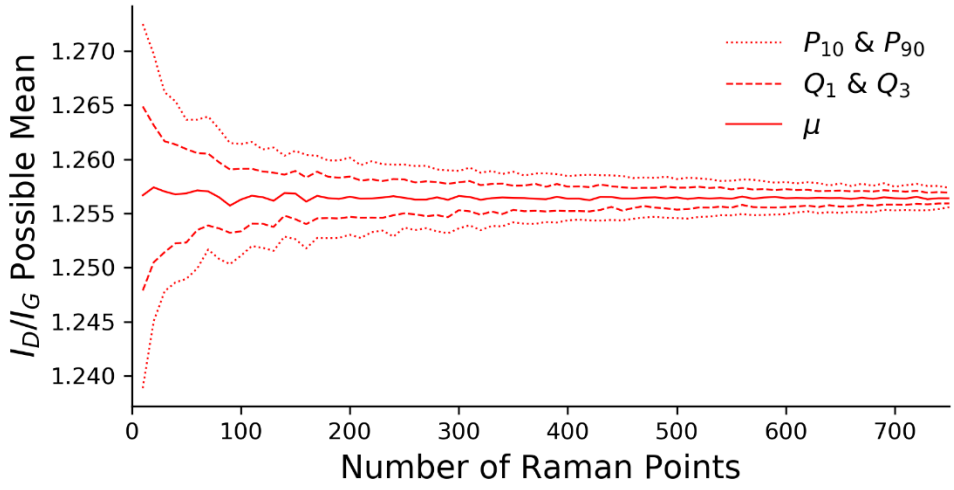

Figure S 119: Bootstrap convergence plot from commercial MWCNTs (data set 1); this shows the summary statistics (10^{th} and 90^{th} percentiles, 1^{st} and 3^{rd} quartiles, and mean) describing the distribution of mean values obtained from multiple analyses of smaller sub-sets of the sample size shown on the x-axis. This plot can be considered a probability distribution of possible mean values for different sample sizes.

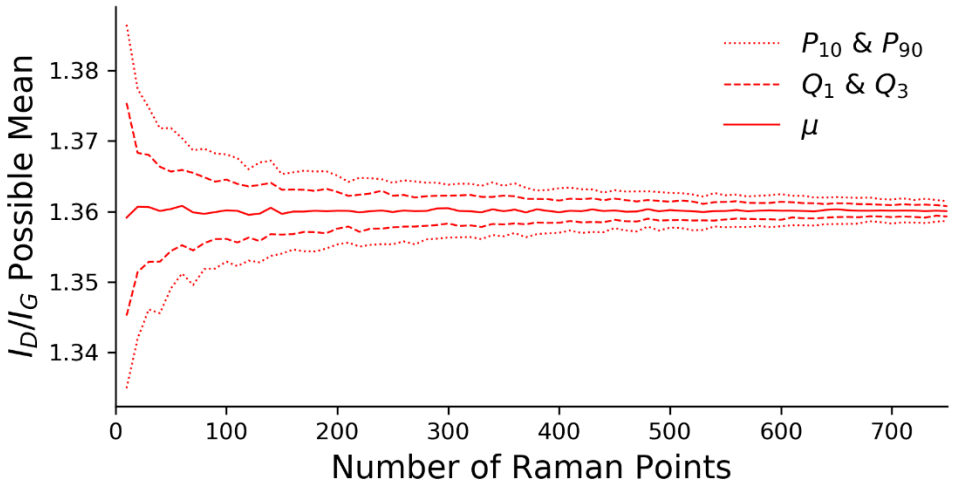

Figure S 120: Bootstrap convergence plot from commercial MWCNTs (data set 2), described in detail above.

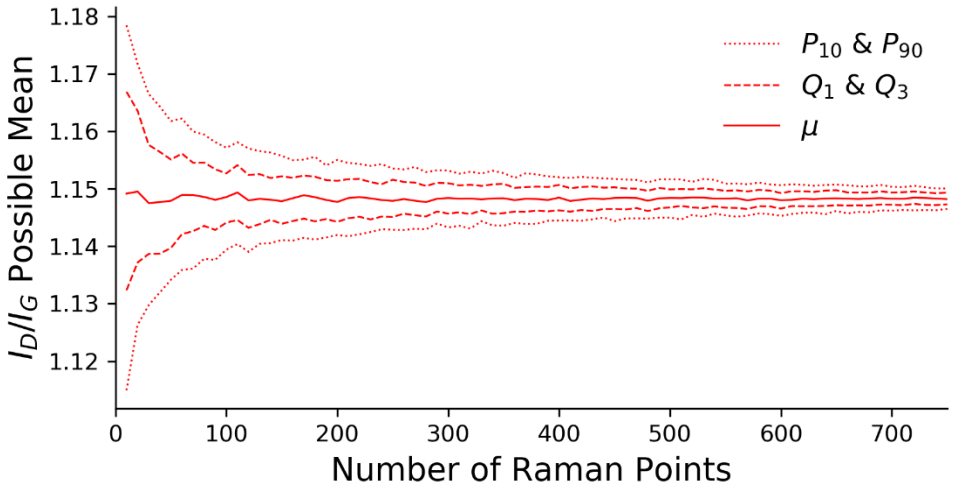

Figure S 121: Bootstrap convergence plot from commercial MWCNTs (data set 3), described in detail above.

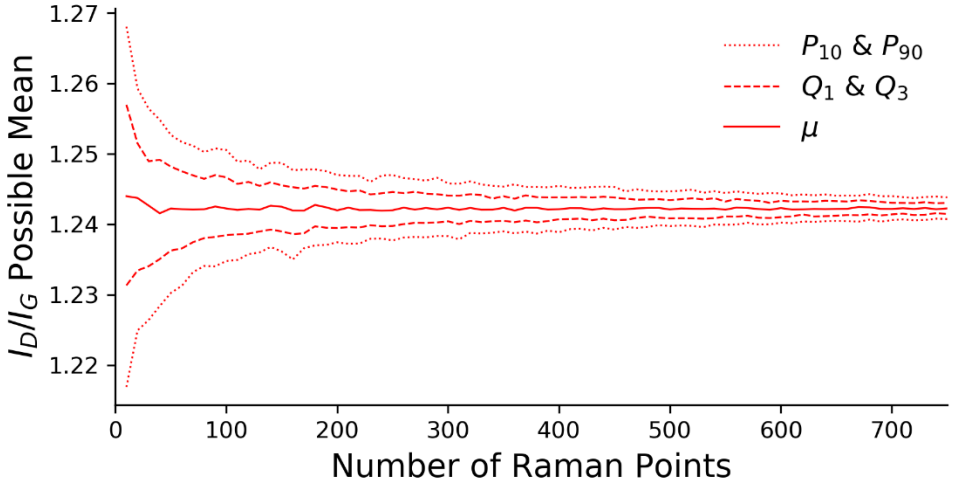

Figure S 122: Bootstrap convergence plot from commercial MWCNTs (data set 4), described in detail above.

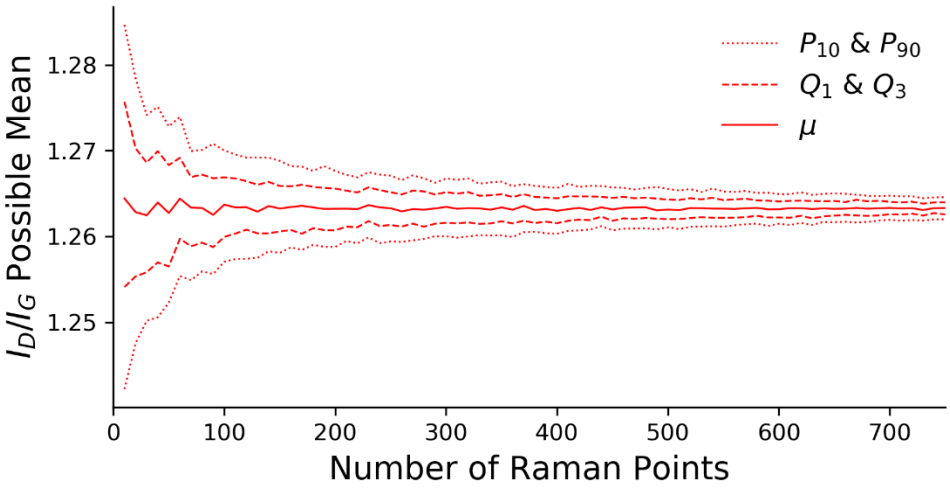

Figure S 123: Bootstrap convergence plot from commercial MWCNTs (data set 5), described in detail above.

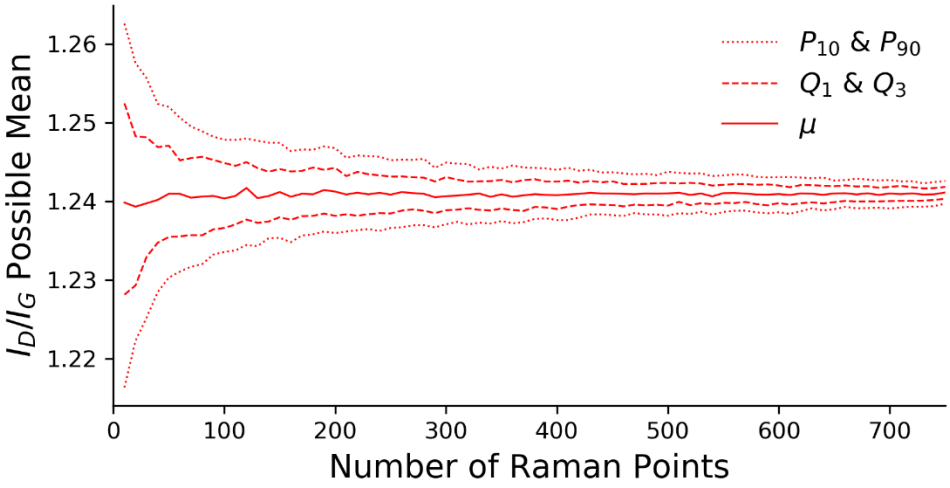

Figure S 124: Bootstrap convergence plot from commercial MWCNTs (data set 6), described in detail above.

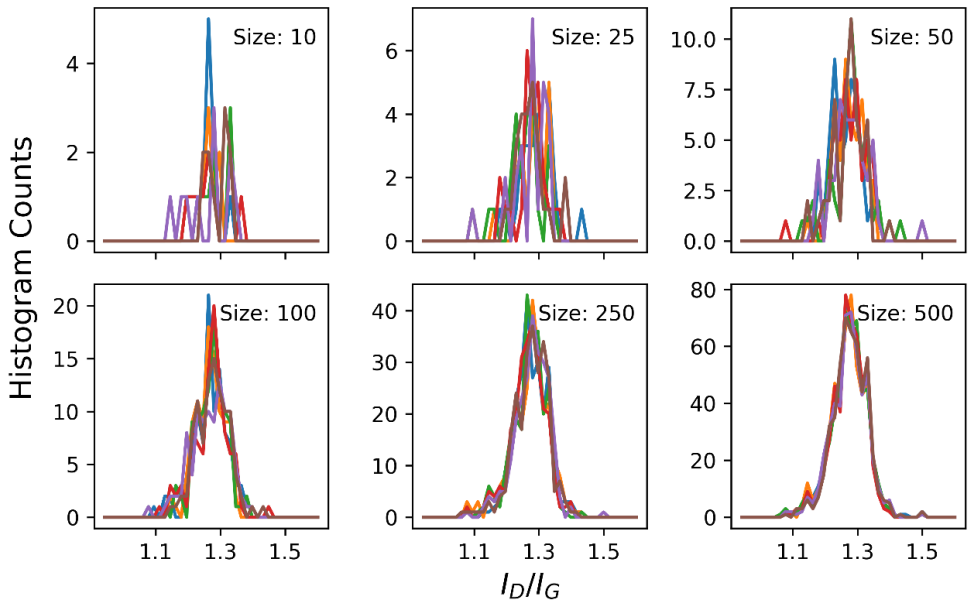

Figure S 125: Panel showing result of bootstrap analysis of commercial MWCNTs (data set 1). Each panel shows five examples, shown in different colors, of distributions of I_D/I_G produced from sub-sets; the size of these is labelled and the x-axis is common across all I_D/I_G panel plots. These show the convergence to a uniform distribution as the sub-set size increases.

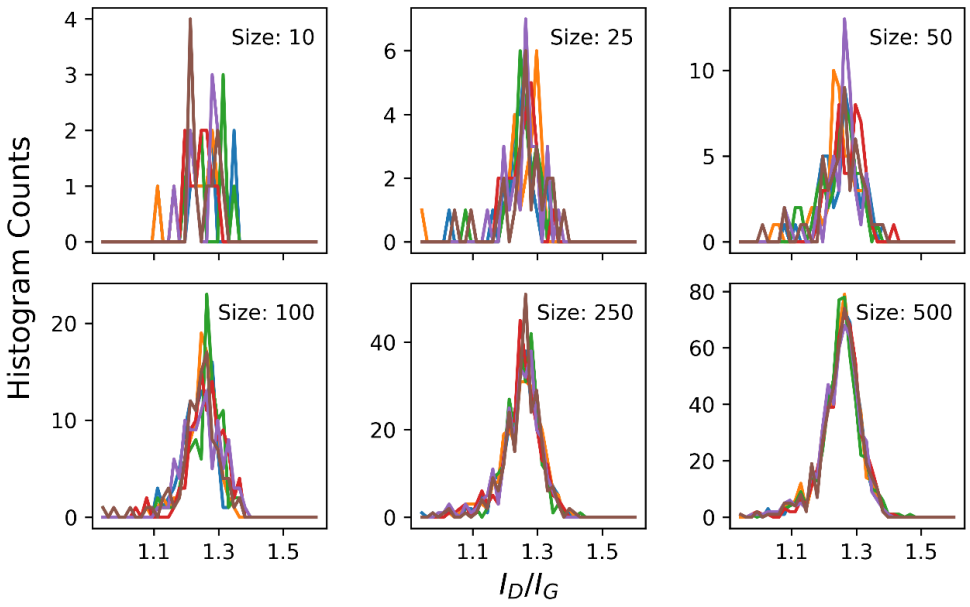

Figure S 126: Panel showing result of bootstrap analysis of commercial MWCNTs (data set 2), described in detail above.

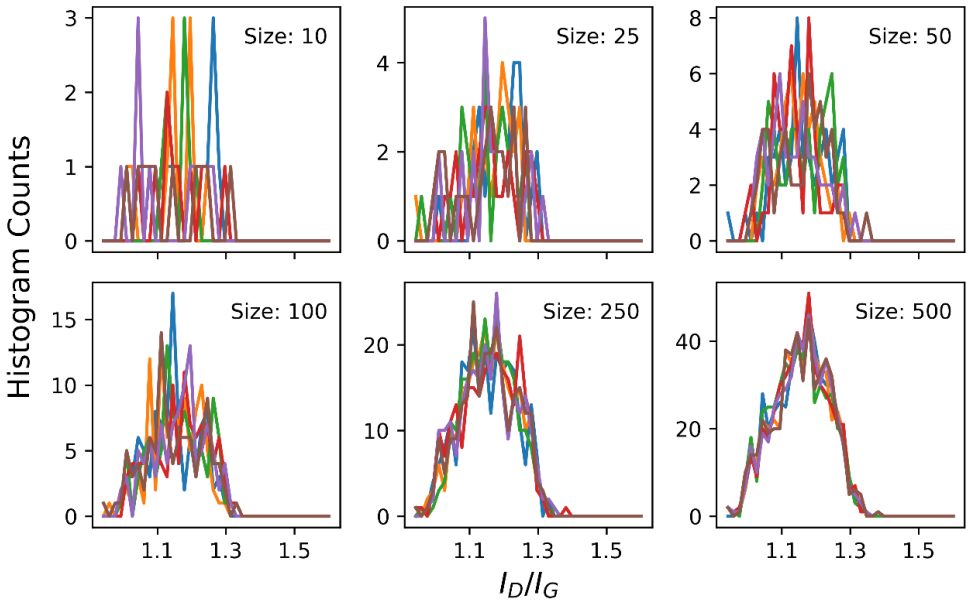

Figure S 127: Panel showing result of bootstrap analysis of commercial MWCNTs (data set 3), described in detail above.

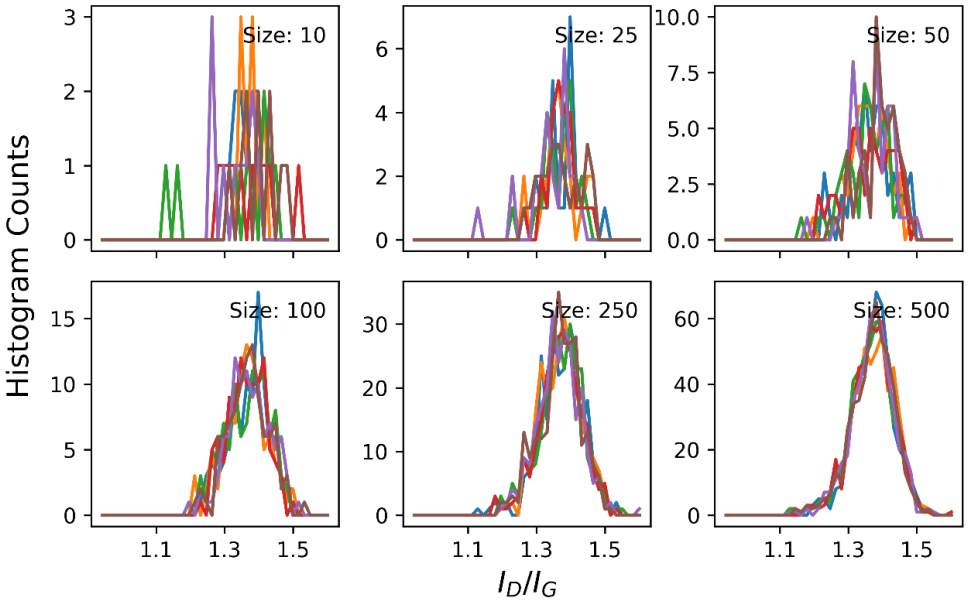

Figure S 128: Panel showing result of bootstrap analysis of commercial MWCNTs (data set 4), described in detail above.

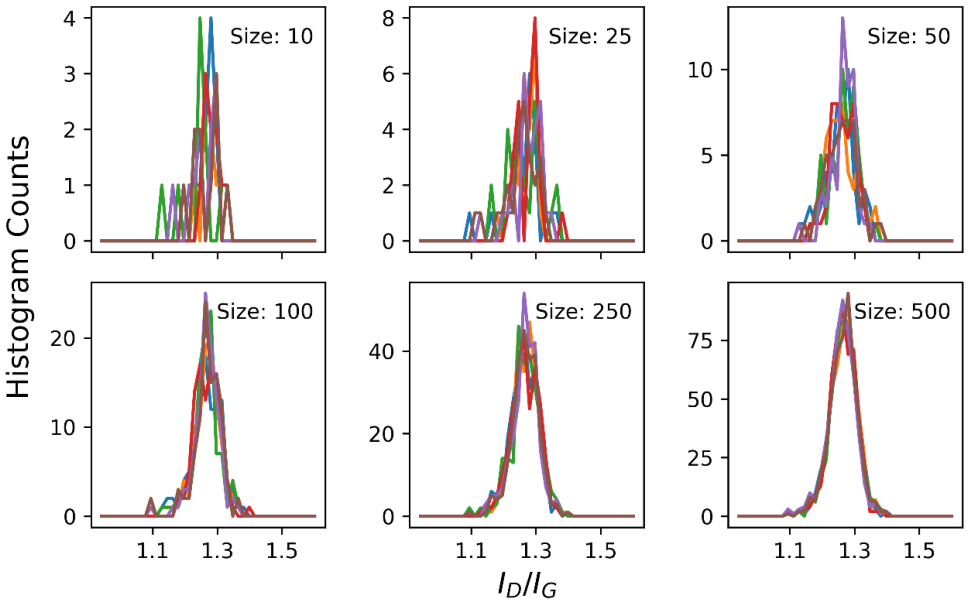

Figure S 129: Panel showing result of bootstrap analysis of commercial MWCNTs (data set 5), described in detail above.

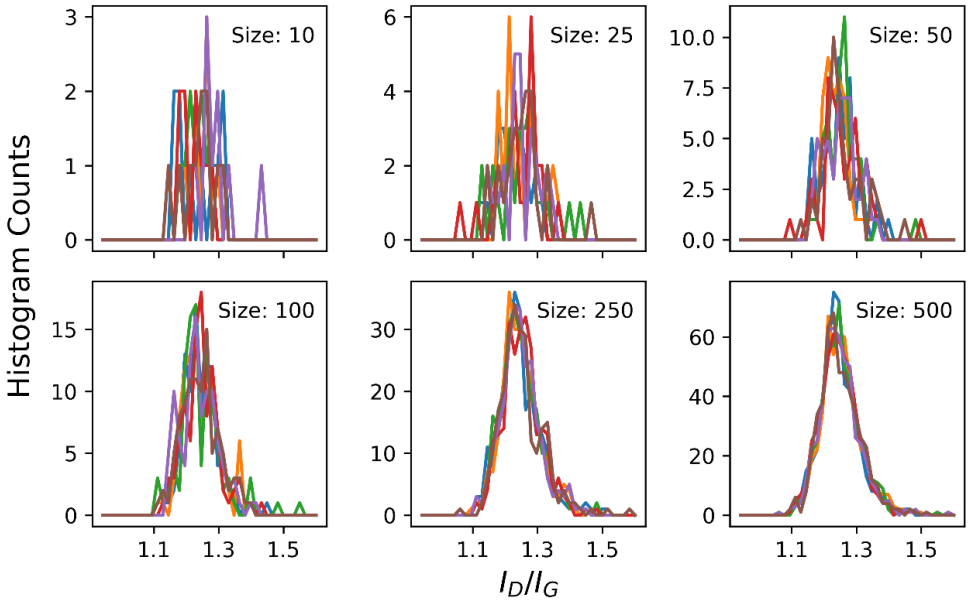

Figure S 130: Panel showing result of bootstrap analysis of commercial MWCNTs (data set 6), described in detail above.

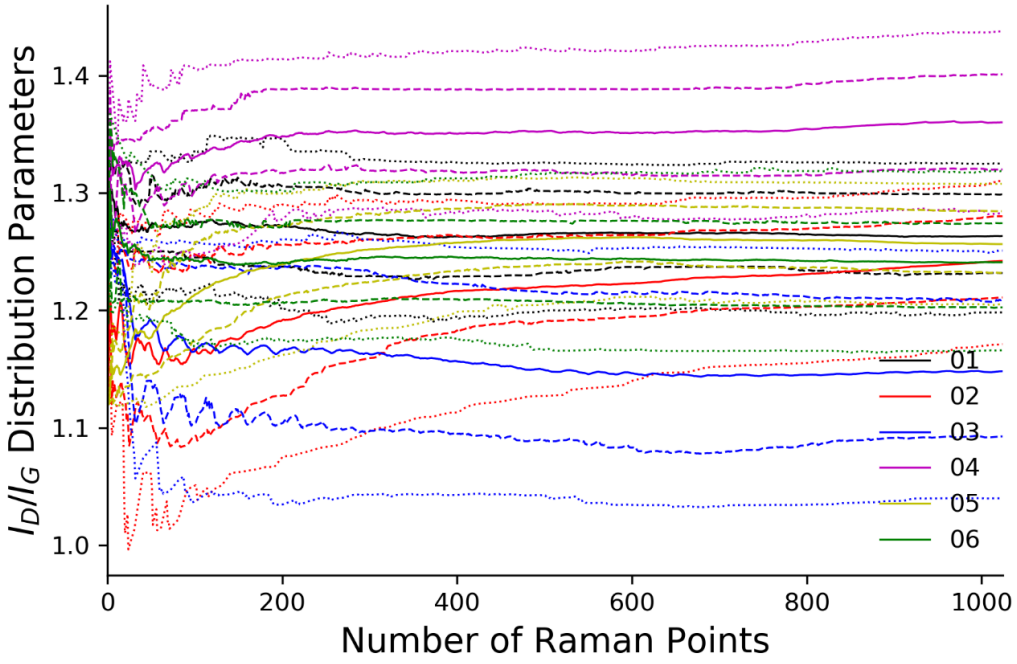

Figure S 131: Plot showing the convergence data of I_D/I_G from all three commercial GNPs data sets. The dots denote the same summary statistics whilst different data sets are shown in different colors. Whilst complex this plot indicates that convergence of all three maps is consistent.

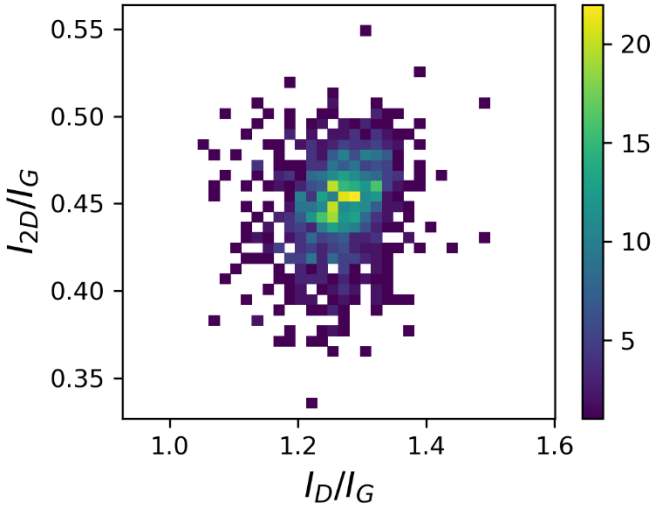

Figure S 132: 3D bivariate histogram showing the distribution of key peak ratios from MWCNTs (data set 1). The histogram count is shown by the colored heat map (key on right) and the bins are read simultaneously from the x and y axes which are common to all plots.

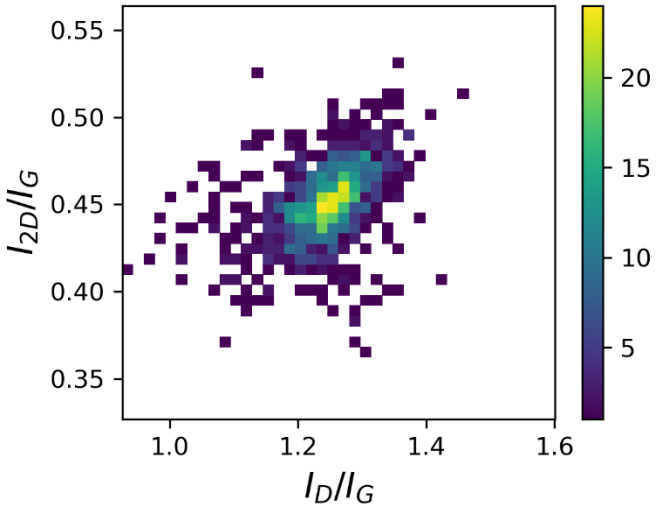

Figure S 133: 3D bivariate histogram showing the distribution of data from commercial MWCNTs (data set 2).

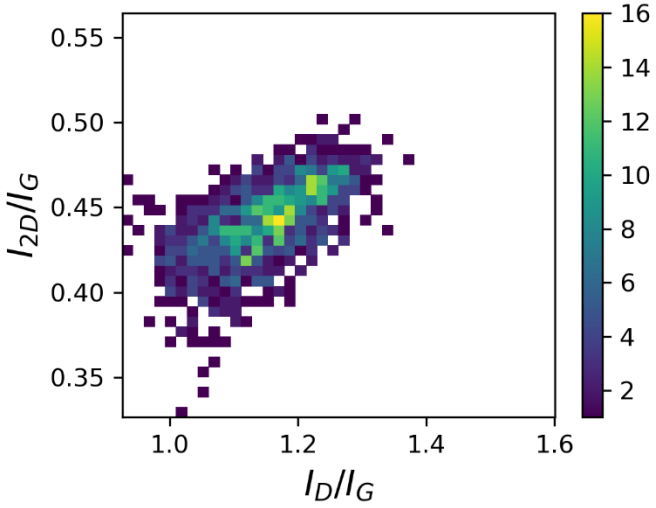

Figure S 134: 3D bivariate histogram showing the distribution of data from commercial MWCNTs (data set 3).

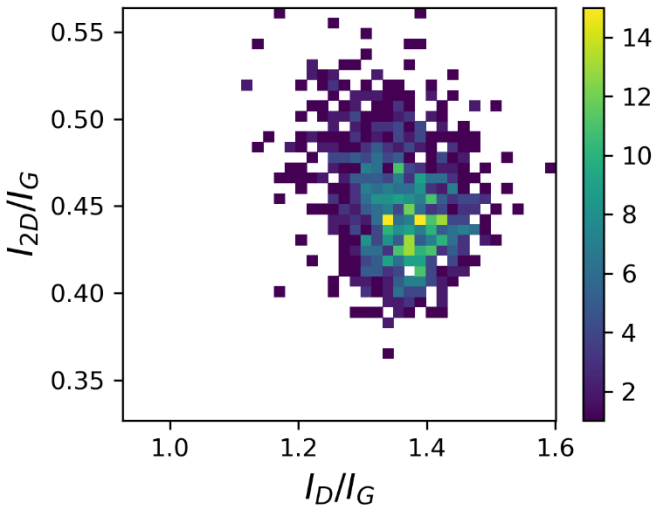

Figure S 135: 3D bivariate histogram showing the distribution of data from commercial MWCNTs (data set 4).

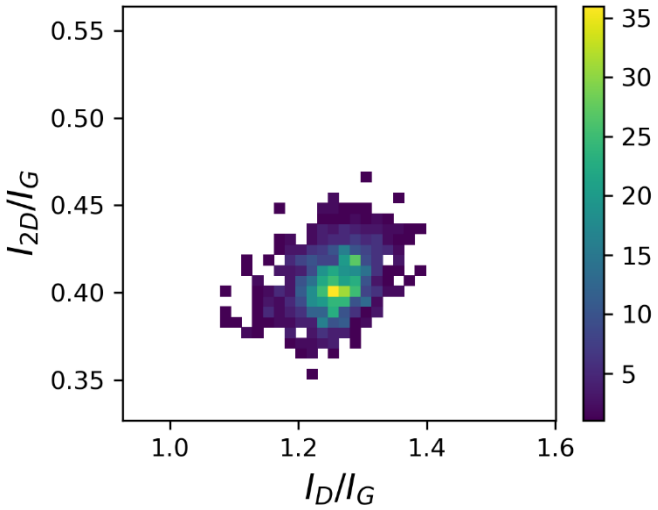

Figure S 136: 3D bivariate histogram showing the distribution of data from commercial MWCNTs (data set 5).

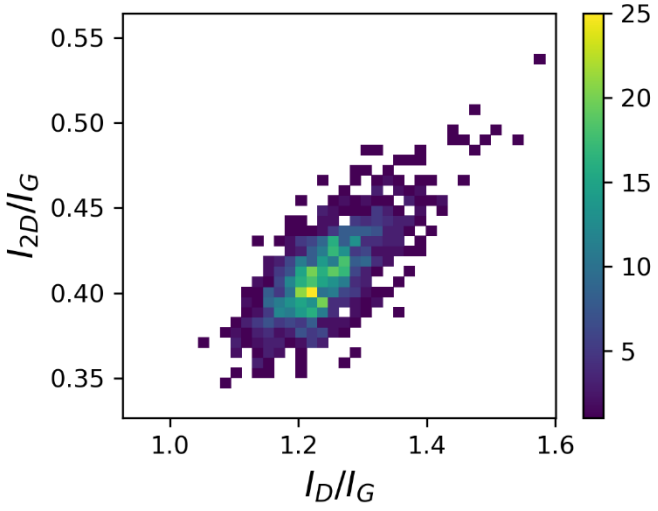

Figure S 137: 3D bivariate histogram showing the distribution of data from commercial MWCNTs (data set 6).

To consider the overall convergence and trends of the data set, the six different maps recorded from the multi-walled nanotubes were combined together and re-arranged into a random order to remove the structure inherent in the data. Whilst not representative of the real maps that would be collected from the material it is useful to ensure the overall trends measured did ultimately converge. Thus the plots below are the same style as above but show the aggregated, randomized data.

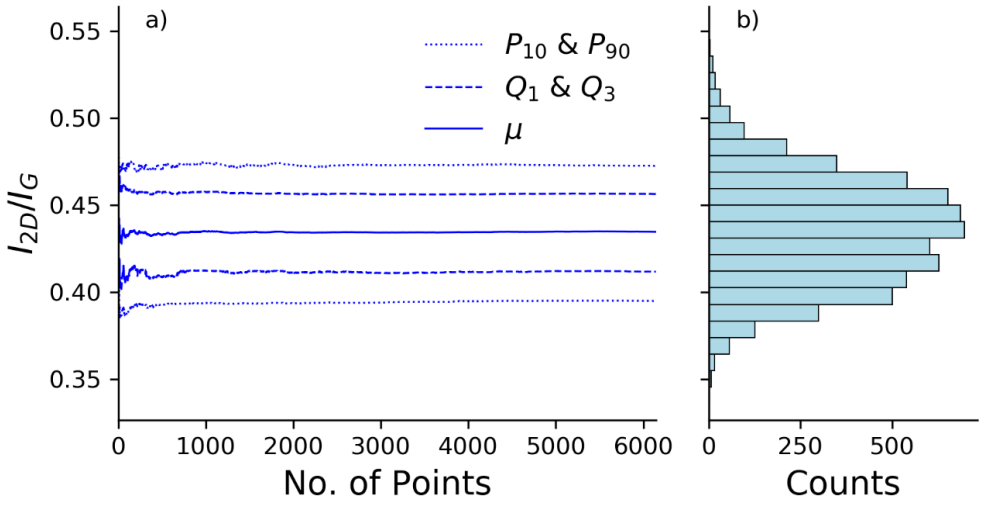

Figure S 138: Convergence plot from commercial MWCNTs (aggregated data) showing a) the change in summary statistics of I_{2D}/I_G as more data points are added to the analysis. b) The final distribution shown as a horizontal histogram.

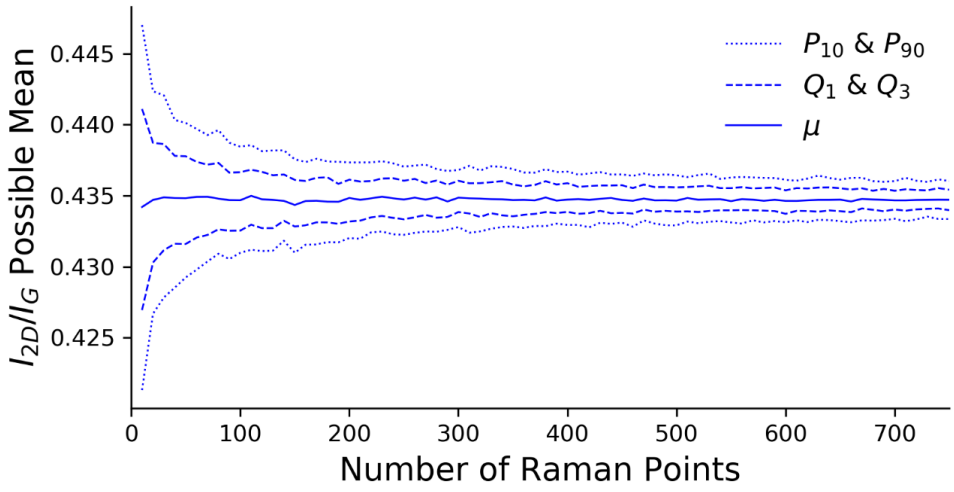

Figure S 139: Bootstrap convergence plot from commercial MWCNTs (aggregated data); this shows the summary statistics (10^{th} and 90^{th} percentiles, 1^{st} and 3^{rd} quartiles, and mean) describing the distribution of mean values obtained from multiple analyses of smaller sub-sets of the sample size shown on the x-axis. This plot can be considered a probability distribution of possible mean values for different sample sizes.

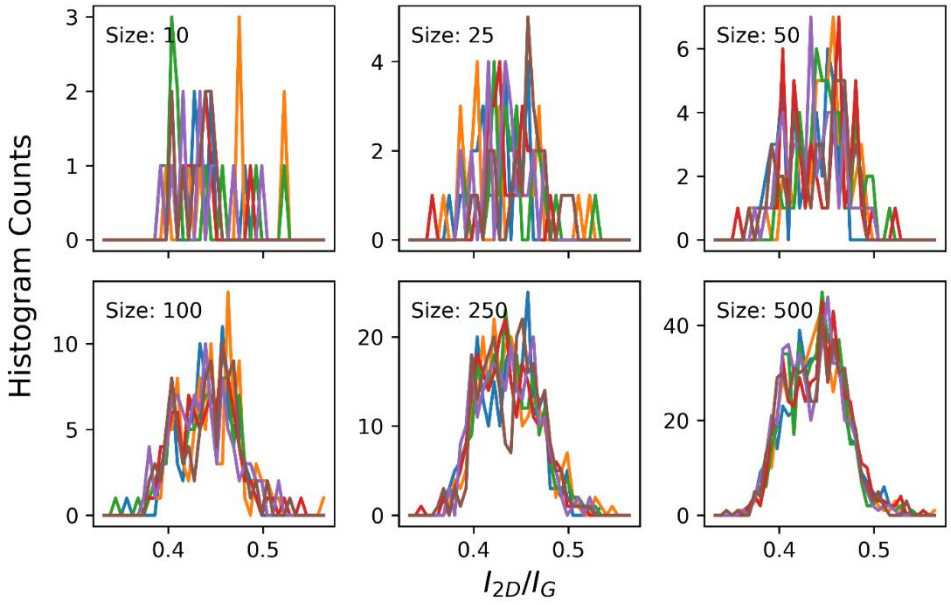

Figure S 140: Panel showing result of bootstrap analysis of commercial MWCNTs (aggregated data). Each panel shows five examples, shown in different colors, of distributions of I_{2D}/I_G produced from sub-sets; the size of these is labelled and the x-axis is common across all I_{2D}/I_G panel plots. These show the convergence to a uniform distribution as the sub-set size increases.

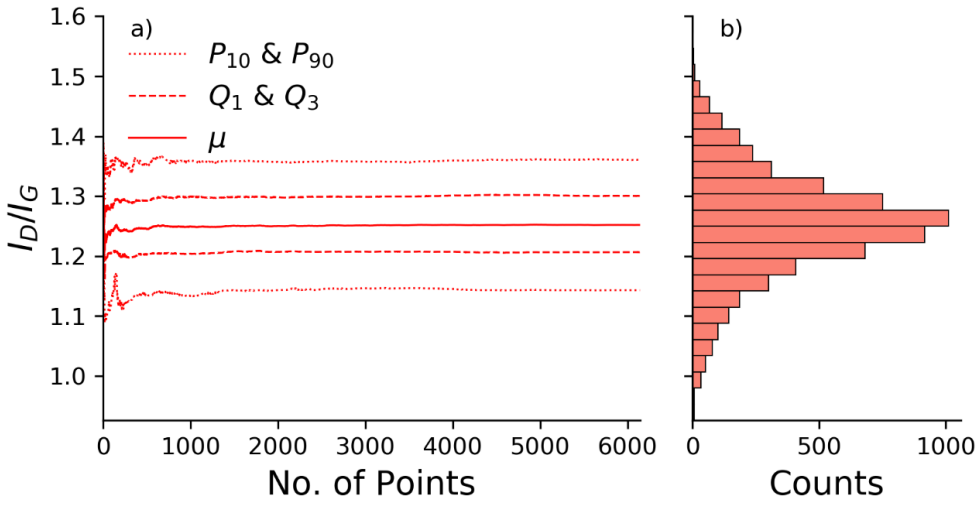

Figure S 141: Convergence plot from commercial MWCNTs (aggregated data) showing a) the change in summary statistics of I_D/I_G as more data points are added to the analysis. b) The final distribution shown as a horizontal histogram.

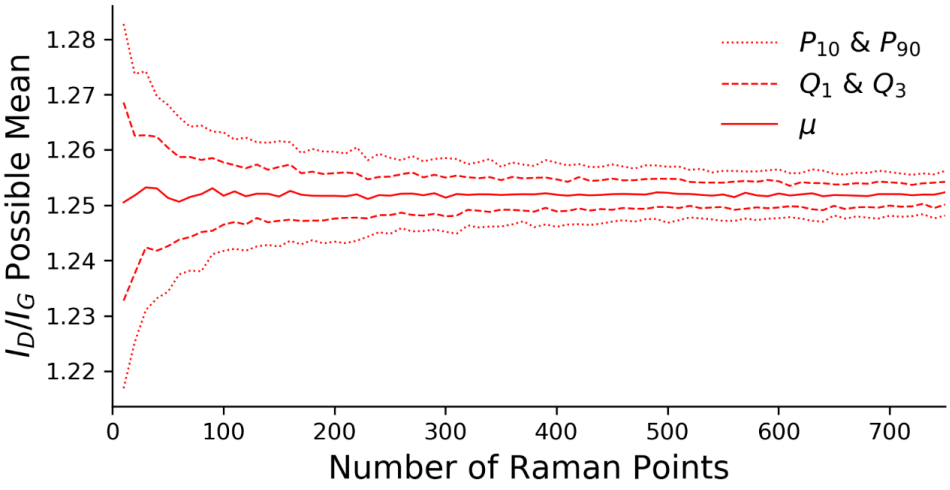

Figure S 142: Bootstrap convergence plot from commercial MWCNTs (aggregated data); this shows the summary statistics (10th and 90th percentiles, 1st and 3rd quartiles, and mean) describing the distribution of mean values obtained from multiple analyses of smaller sub-sets of the sample size shown on the x-axis. This plot can be considered a probability distribution of possible mean values for different sample sizes.

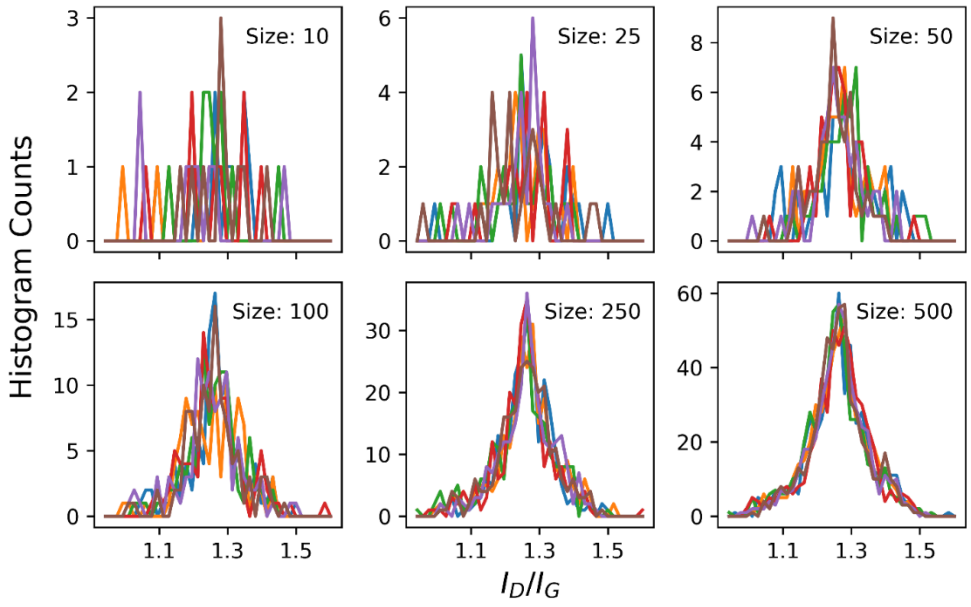

Figure S 143: Panel showing result of bootstrap analysis of commercial MWCNTs (aggregated data). Each panel shows five examples, shown in different colors, of distributions of I_D/I_G produced from sub-sets; the size of these is labelled and the x-axis is common across all I_D/I_G panel plots. These show the convergence to a uniform distribution as the sub-set size increases.

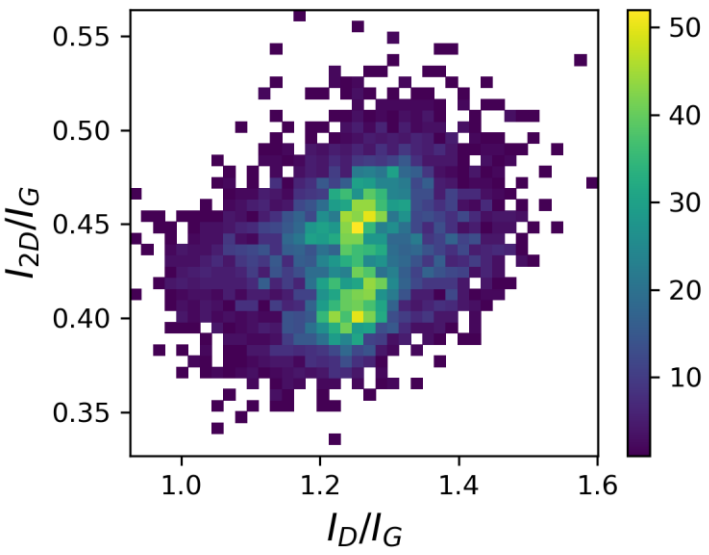

Figure S 144: 3D bivariate histogram showing the distribution of key peak ratios from commercial MWCNTs (aggregated data). The histogram count is shown by the colored heat map (key on right) and the bins are read simultaneously from the x and y axes.

9.1.6 Reduced Graphene Oxide

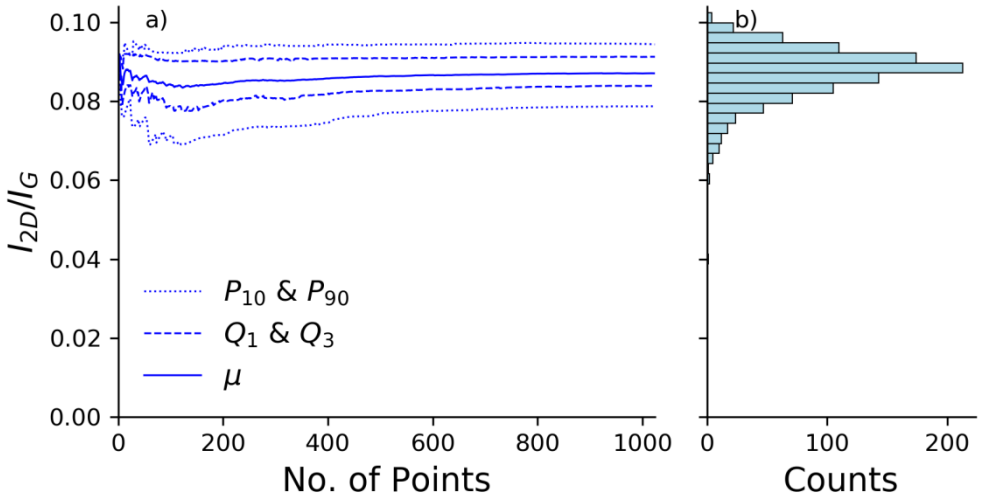

Figure S145: Convergence plot from reduced GO (data set 1) showing a) the change in summary statistics of I_{2D}/I_G as more data points are added to the analysis. b) The final distribution shown as a horizontal histogram, y-axis constant across all plots showing I_{2D}/I_G convergence data from graphite sample.

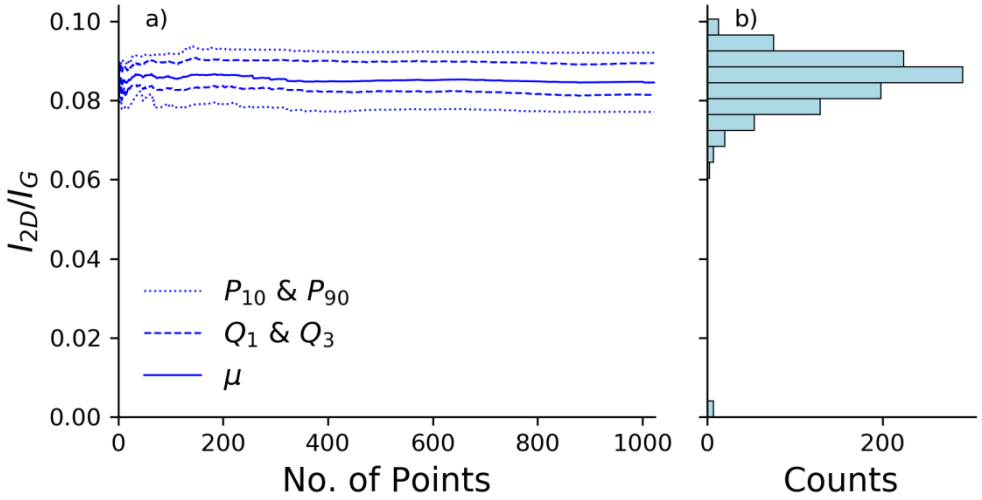

Figure S146: Convergence plot from reduced GO (data set 2) described in detail above.

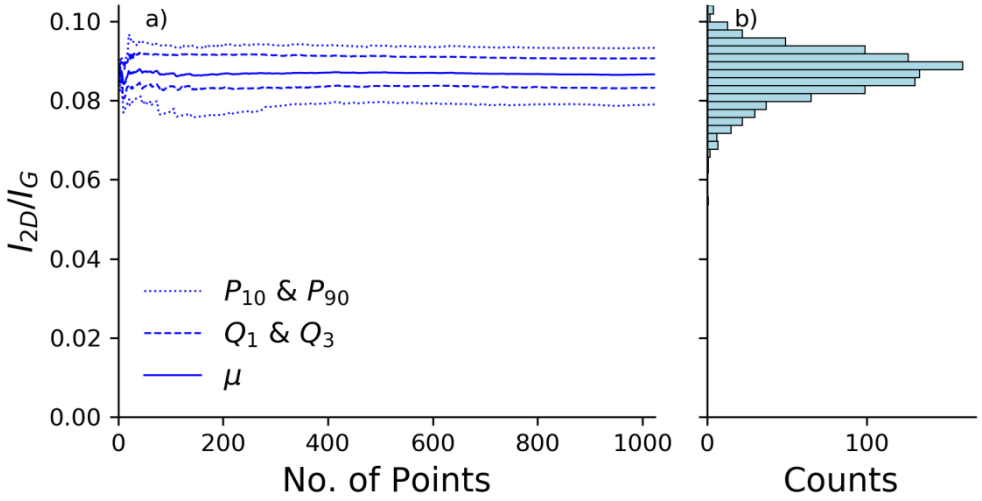

Figure S147: Convergence plot from reduced GO (data set 3) described in detail above.

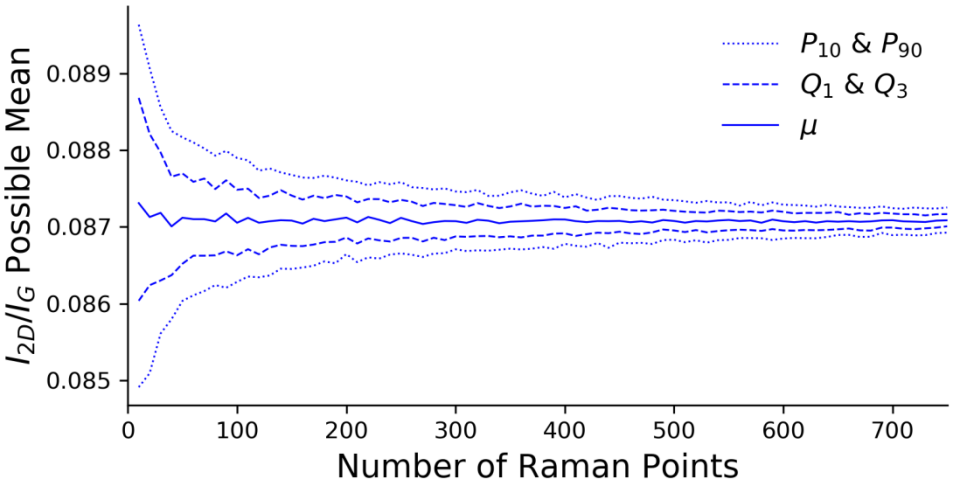

Figure S148: Bootstrap convergence plot from reduced GO (data set 1); this shows the summary statistics (10th and 90th percentiles, 1st and 3rd quartiles, and mean) describing the distribution of mean values obtained from multiple analyses of smaller sub-sets of the sample size shown on the x-axis. This plot can be considered a probability distribution of possible mean values for different sample sizes.

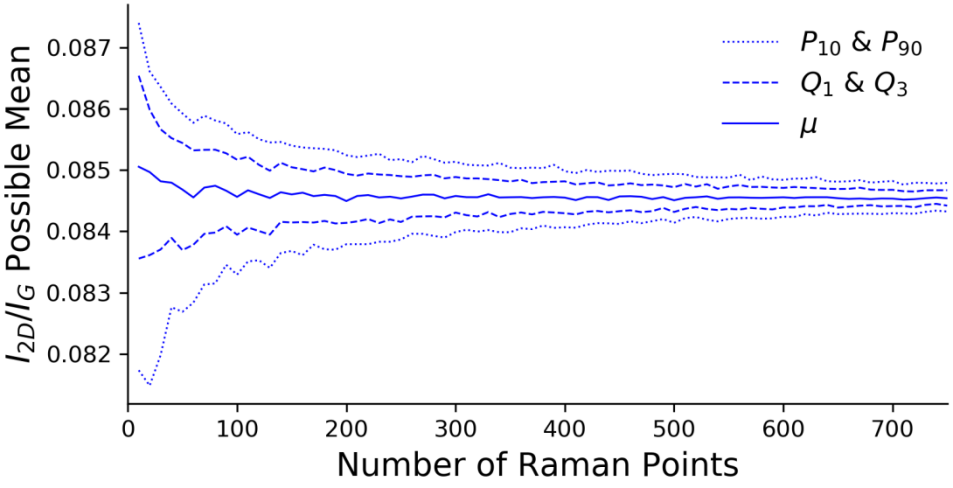

Figure S149: Bootstrap convergence plot from reduced GO (data set 2), described in detail above.

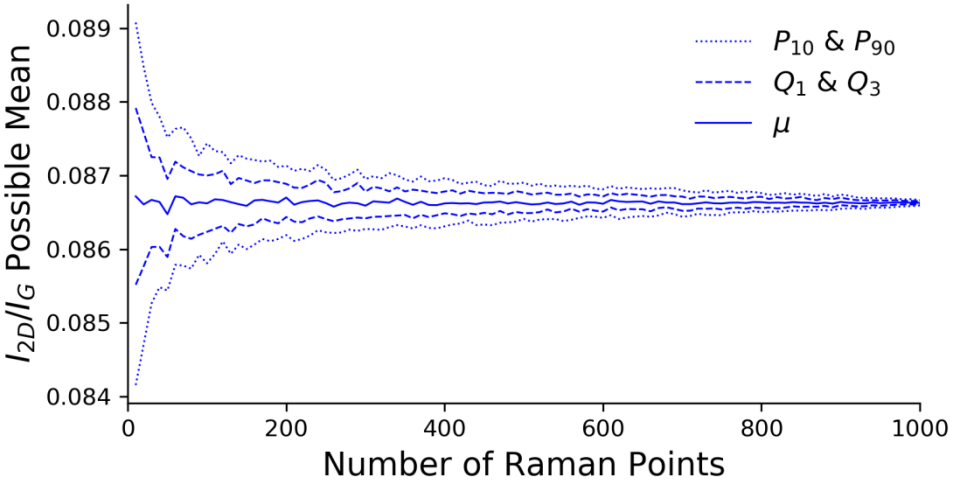

Figure S150: Bootstrap convergence plot from reduced GO (data set 3), described in detail above.

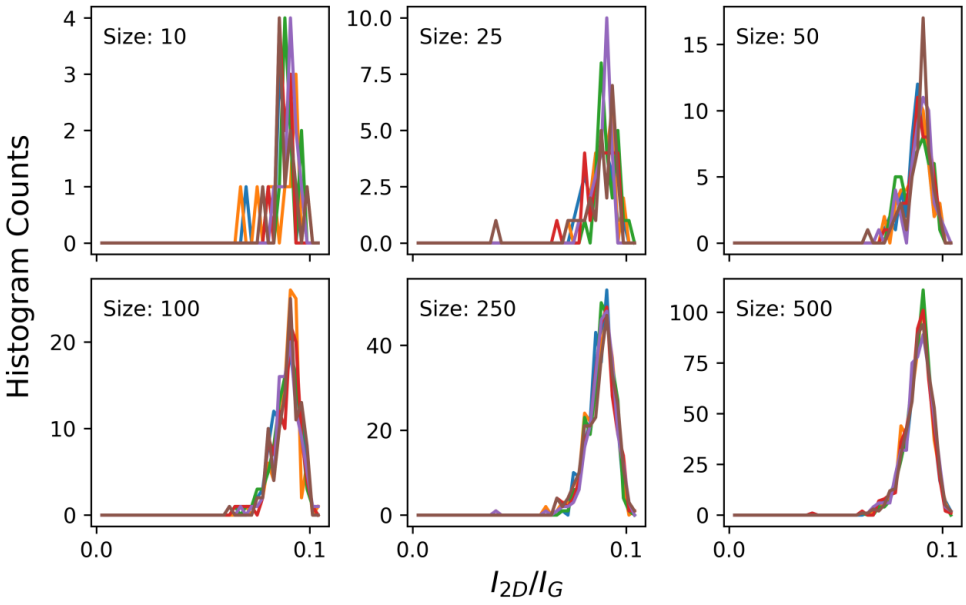

Figure S151: Panel showing result of bootstrap analysis of reduced GO (data set 1). Each panel shows five examples, shown in different colors, of distributions of I_{2D}/I_G produced from sub-sets; the size of these is labelled and the x-axis is common across all I_{2D}/I_G panel plots. These show the convergence to a uniform distribution as the sub-set size increases.

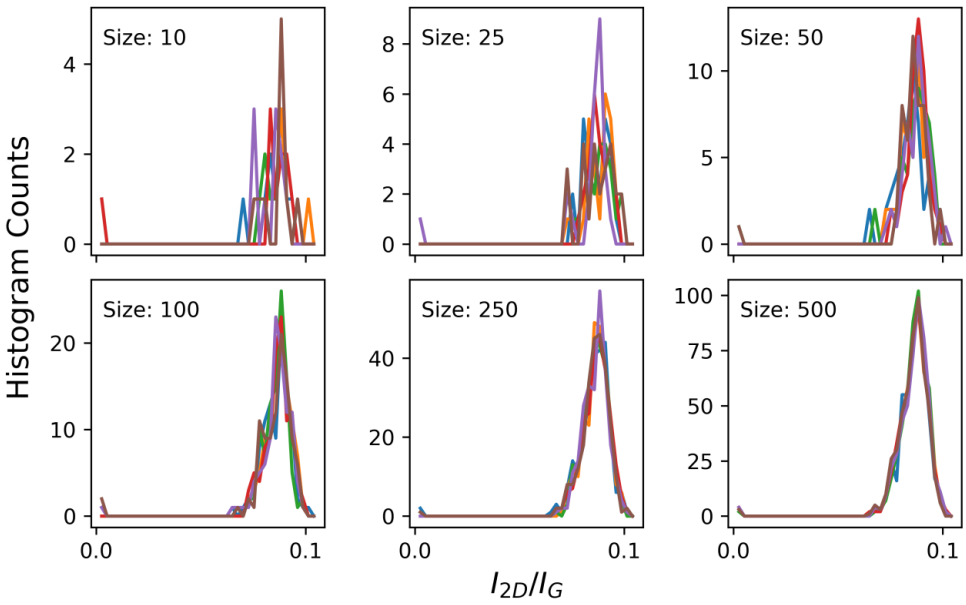

Figure S152: Panel showing result of bootstrap analysis of reduced GO (data set 2), described in detail above.

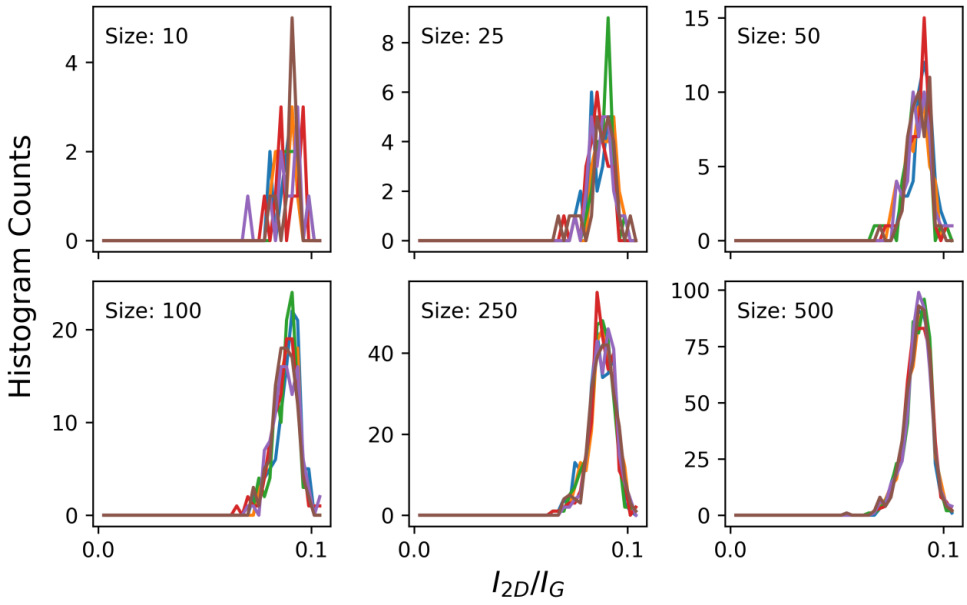

Figure S153: Panel showing result of bootstrap analysis of reduced GO (data set 3), described in detail above.

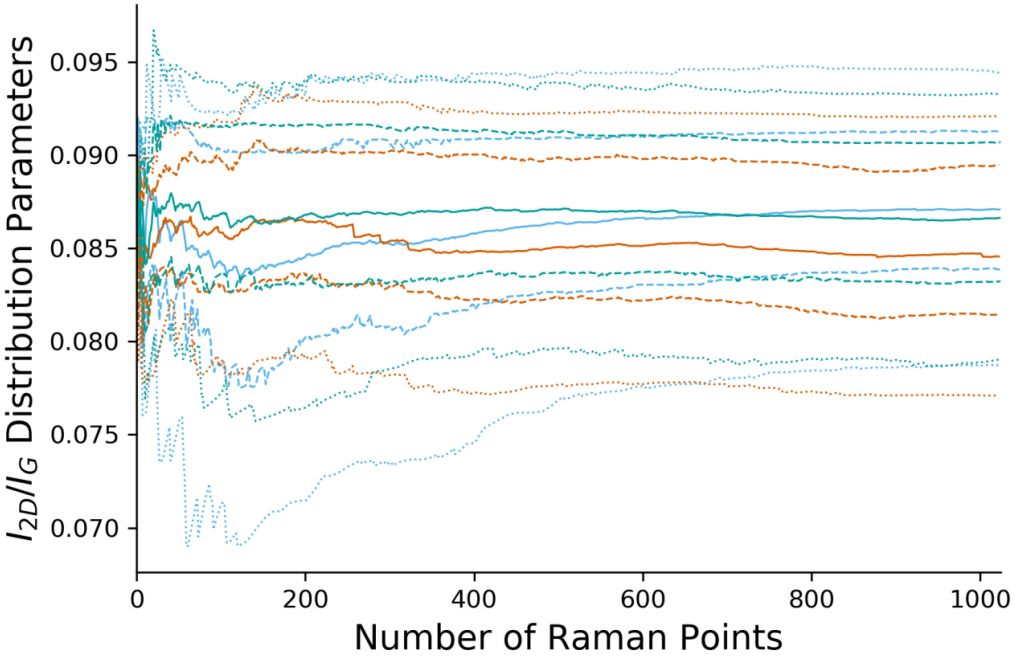

Figure S154: Plot showing the convergence data of I_{2D}/I_G from all three reduced GO data sets. The dots denote the same summary statistics whilst different data sets are shown in different colors. Whilst complex this plot indicates that convergence of all three maps is consistent.

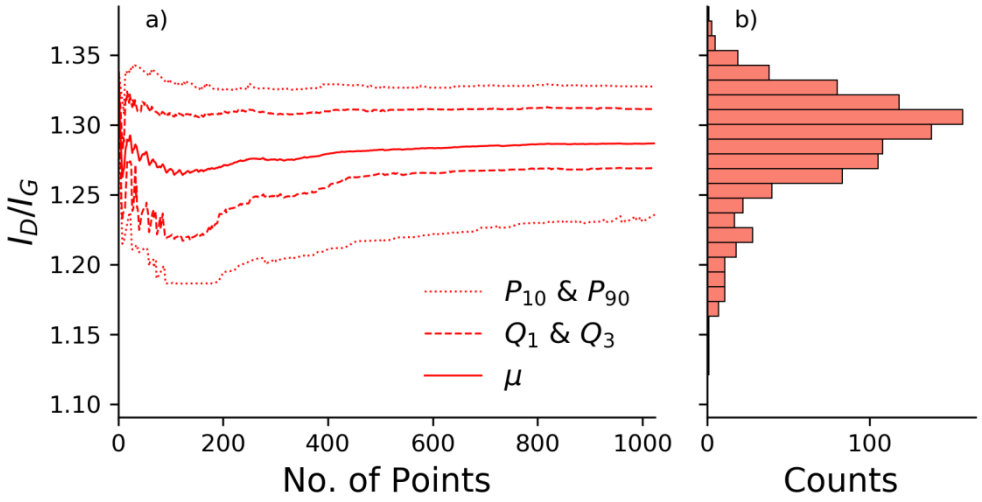

Figure S155: Convergence plot from reduced GO (data set 1) showing a) the change in summary statistics of I_D/I_G as more data points are added to the analysis. b) The final distribution shown as a horizontal histogram, y-axis constant across all plots showing I_D/I_G convergence data from graphite sample.

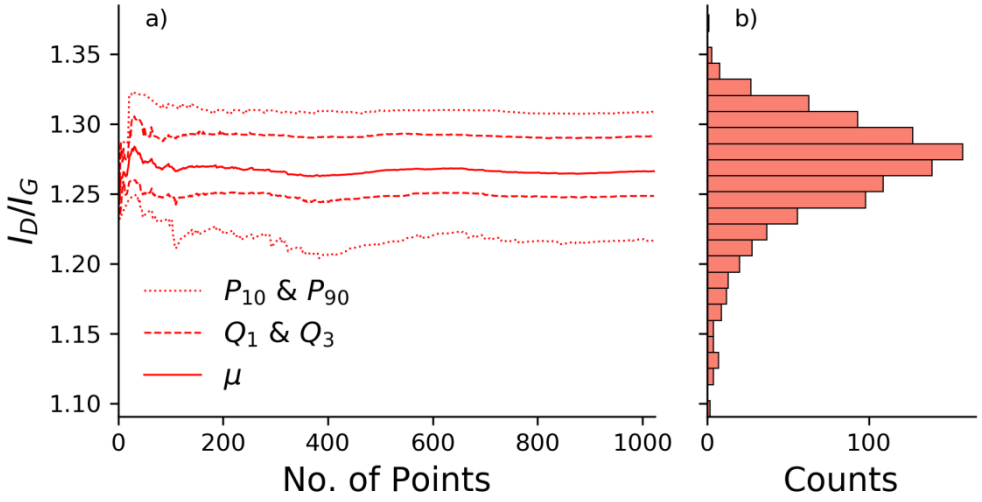

Figure S156: Convergence plot from reduced GO (data set 2) described in detail above.

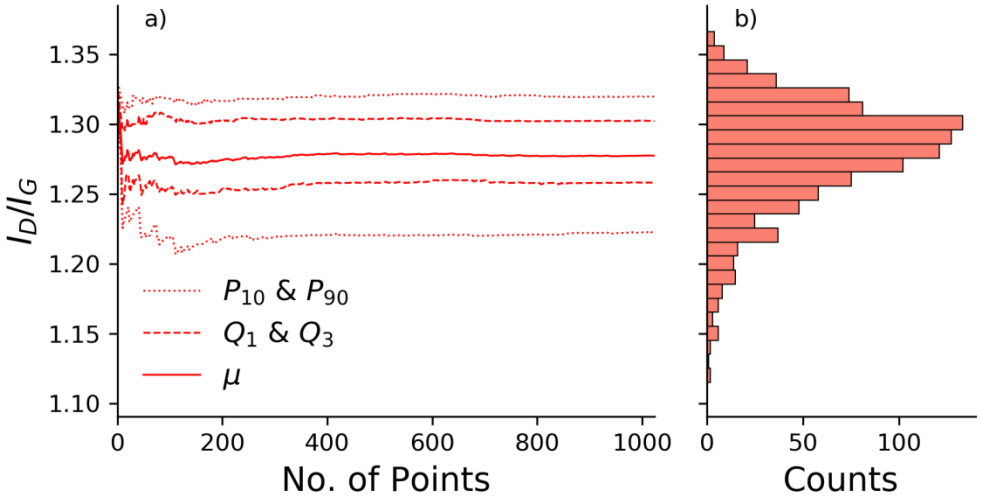

Figure S157: Convergence plot from reduced GO (data set 3) described in detail above.

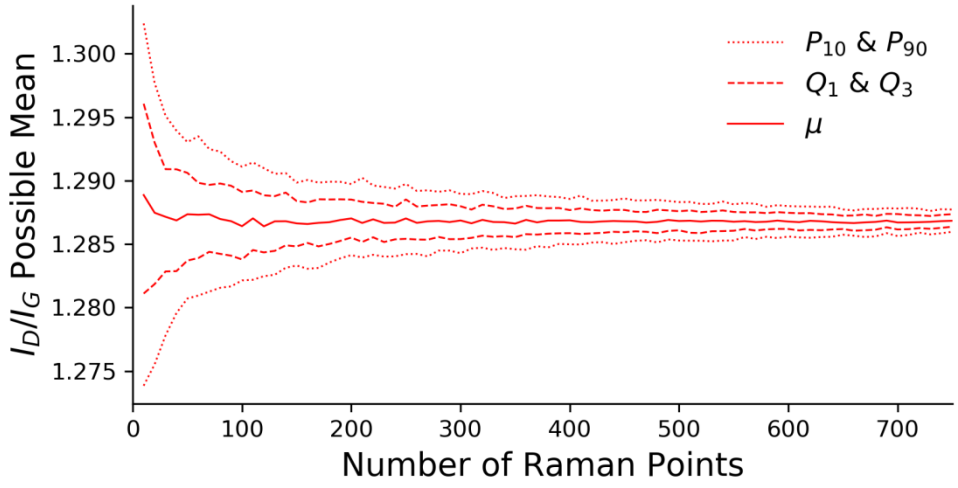

Figure S158: Bootstrap convergence plot from reduced GO (data set 1); this shows the summary statistics (10th and 90th percentiles, 1st and 3rd quartiles, and mean) describing the distribution of mean values obtained from multiple analyses of smaller sub-sets of the sample size shown on the x-axis. This plot can be considered a probability distribution of possible mean values for different sample sizes.

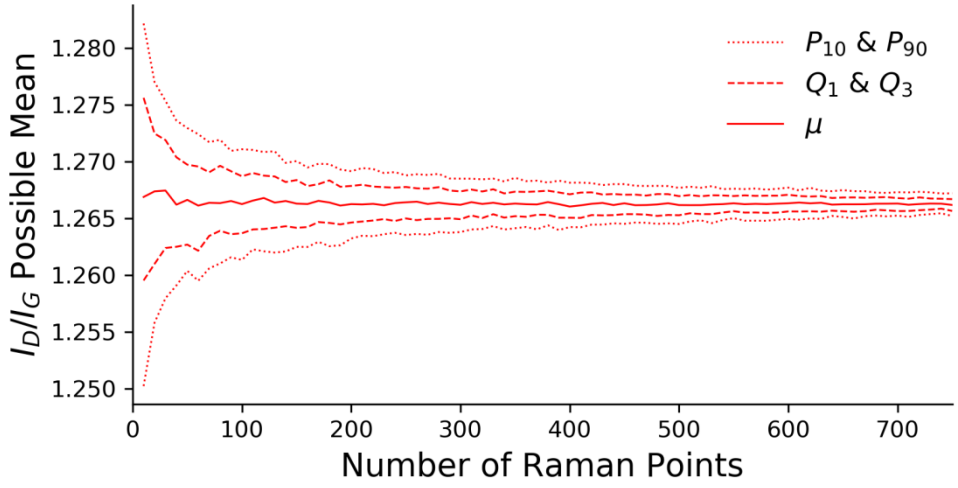

Figure S 159: Bootstrap convergence plot from reduced GO (data set 2), described in detail above.

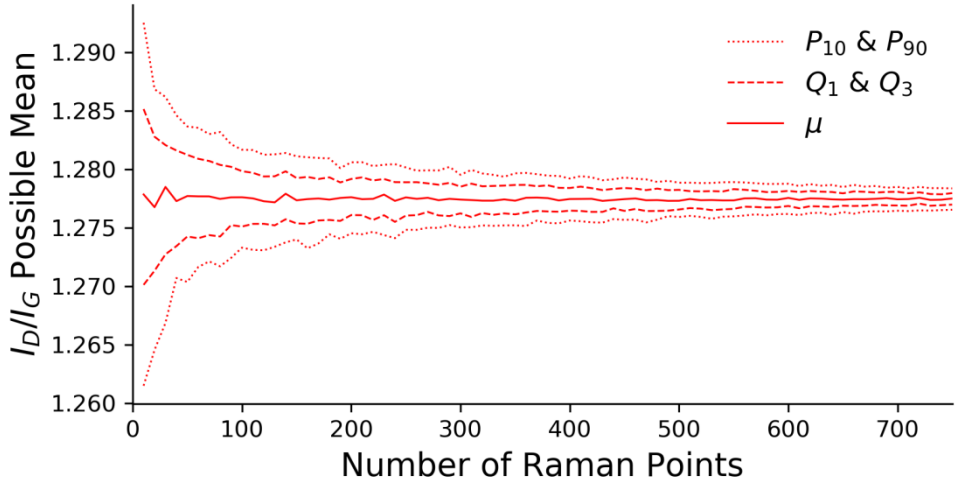

Figure S160: Bootstrap convergence plot from reduced GO (data set 3), described in detail above.

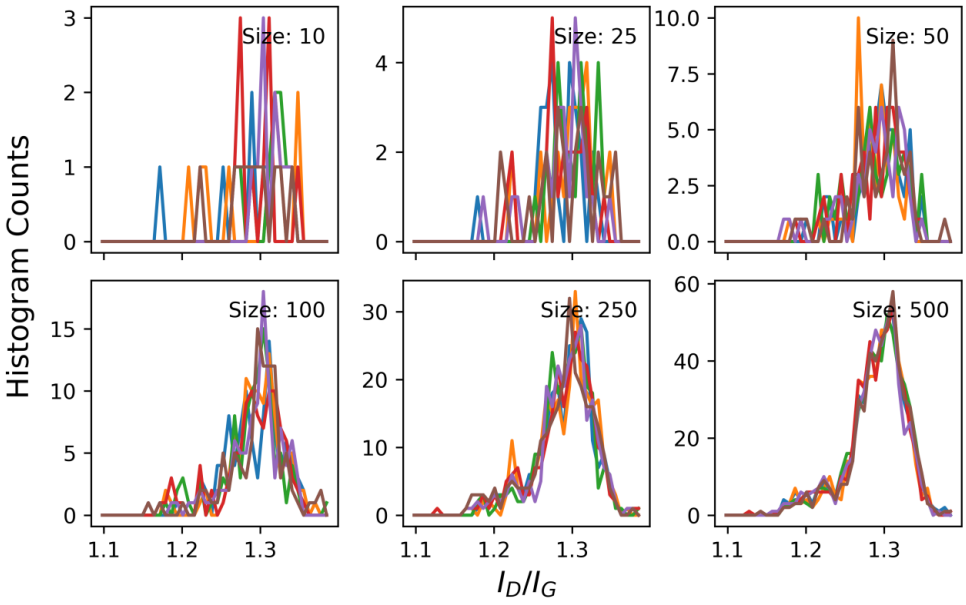

Figure S161: Panel showing result of bootstrap analysis of reduced GO (data set 1). Each panel shows five examples, shown in different colors, of distributions of I_D/I_G produced from sub-sets; the size of these is labelled and the x-axis is common across all I_D/I_G panel plots. These show the convergence to a uniform distribution as the sub-set size increases.

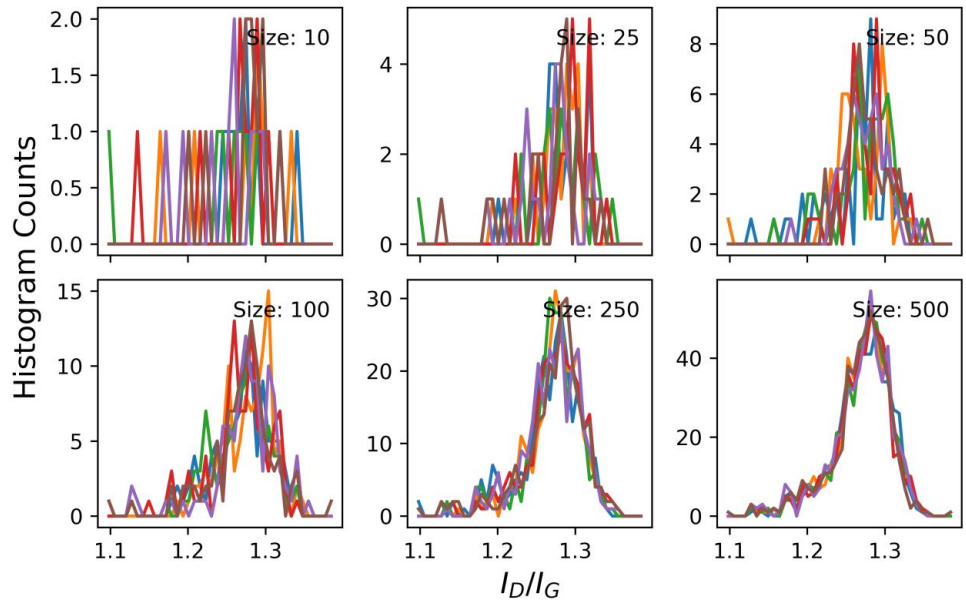

Figure S162: Panel showing result of bootstrap analysis of reduced GO (data set 2), described in detail above.

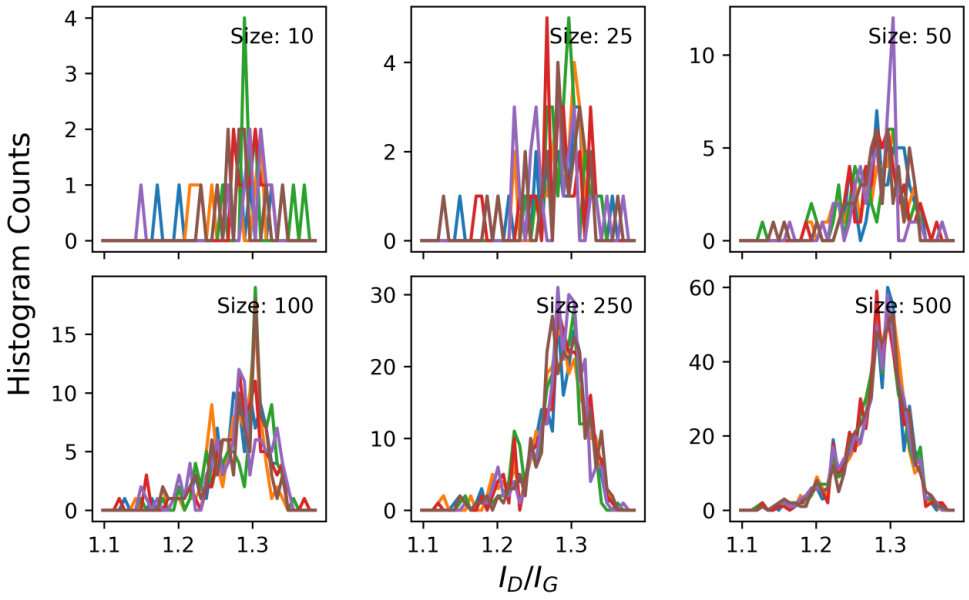

Figure S163: Panel showing result of bootstrap analysis of reduced GO (data set 3), described in detail above.

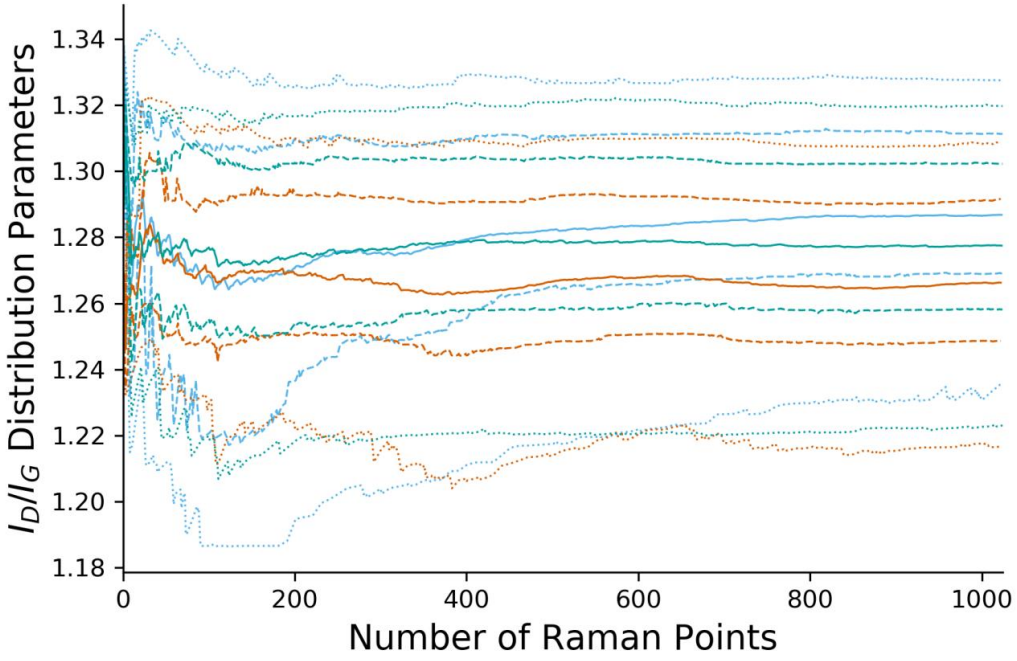

Figure S164: Plot showing the convergence data of I_D/I_G from all three reduced GO data sets. The dots denote the same summary statistics whilst different data sets are shown in different colors. Whilst complex this plot indicates that convergence of all three maps is consistent.

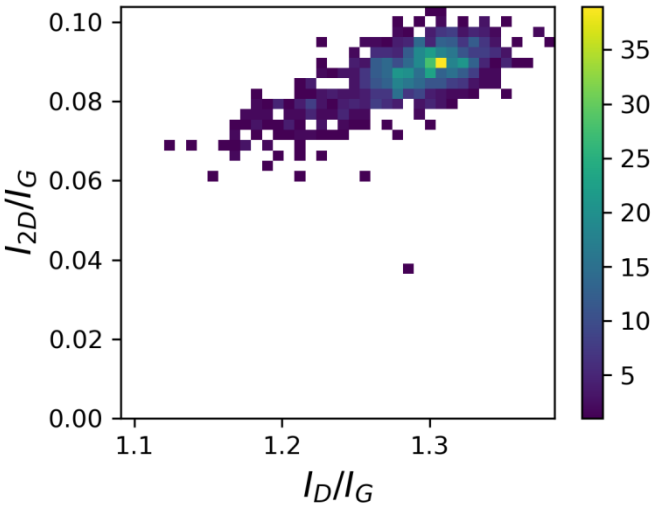

Figure S165: 3D bivariate histogram showing the distribution of key peak ratios from reduced GO data (data set 1). The histogram count is shown by the colored heat map (key on right) and the bins are read simultaneously from the x and y axes which are common to all plots.

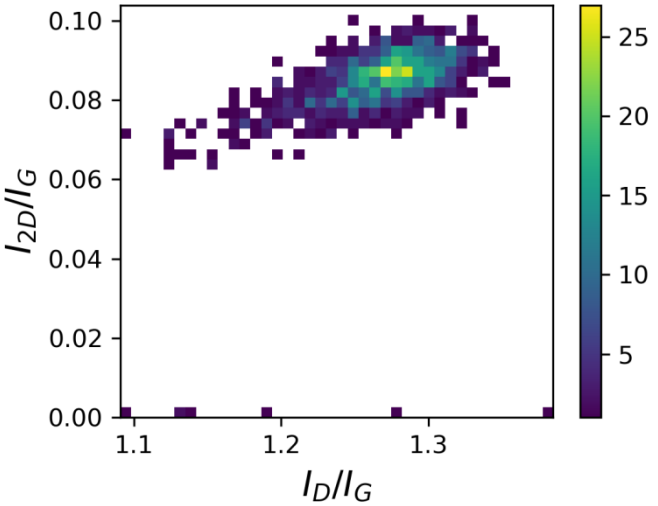

Figure S166: 3D bivariate histogram showing the distribution of data from reduced GO (data set 2).

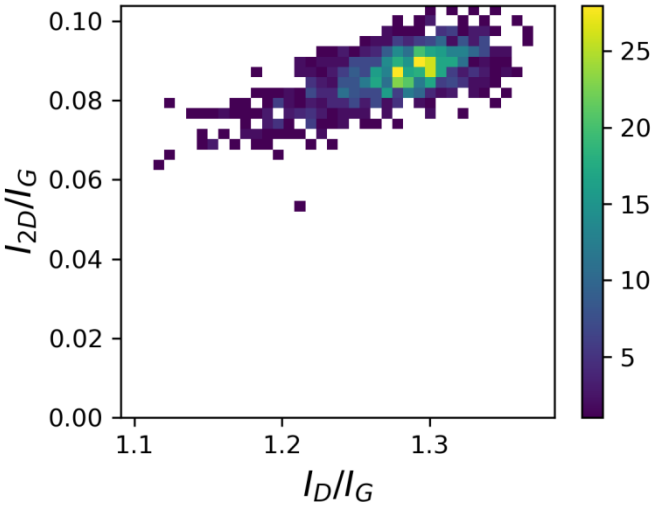

Figure S167: 3D bivariate histogram showing the distribution of data from reduced GO (data set 3).

9.1.7 High Temperature Graphitization

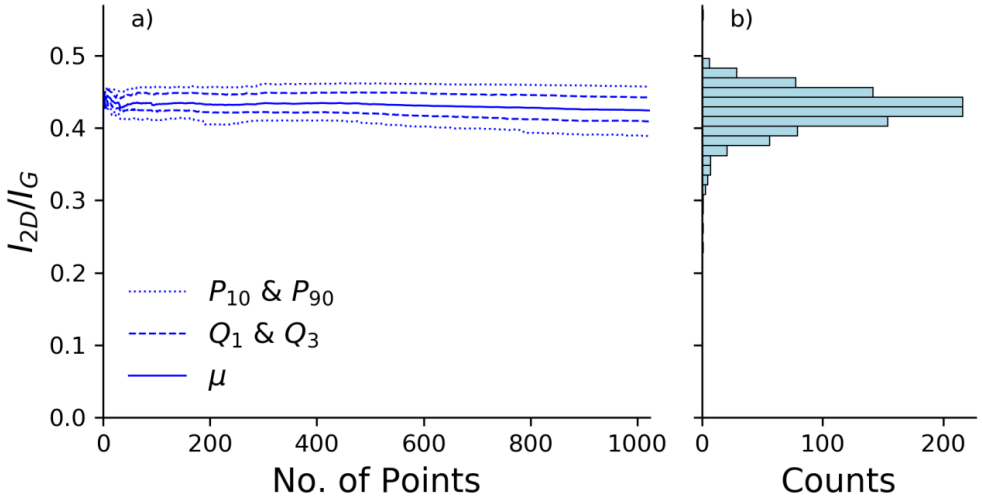

Figure S 168: Convergence plot from graphitized carbon (data set 1) showing a) the change in summary statistics of I_{2D}/I_G as more data points are added to the analysis. b) The final distribution shown as a horizontal histogram, y-axis constant across all plots showing I_{2D}/I_G convergence data from graphite sample.

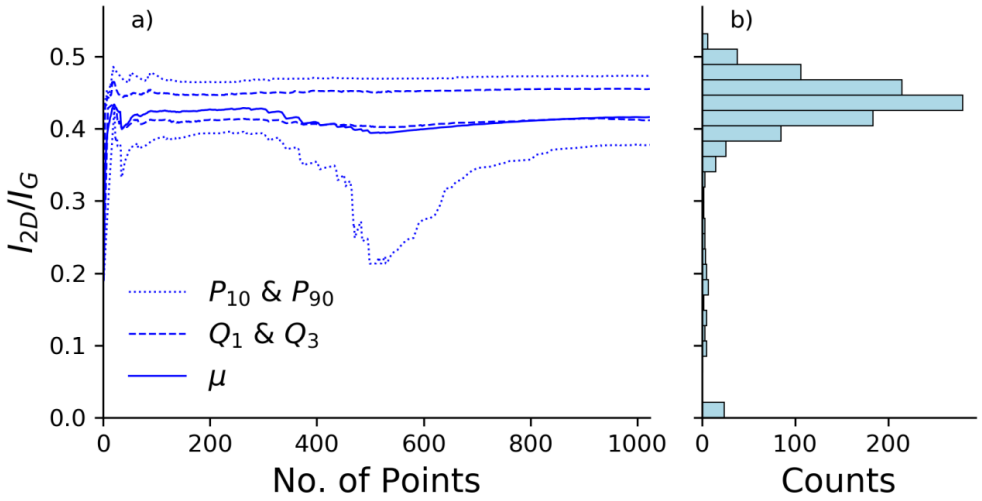

Figure S 169: Convergence plot from graphitized carbon (data set 2) described in detail above.

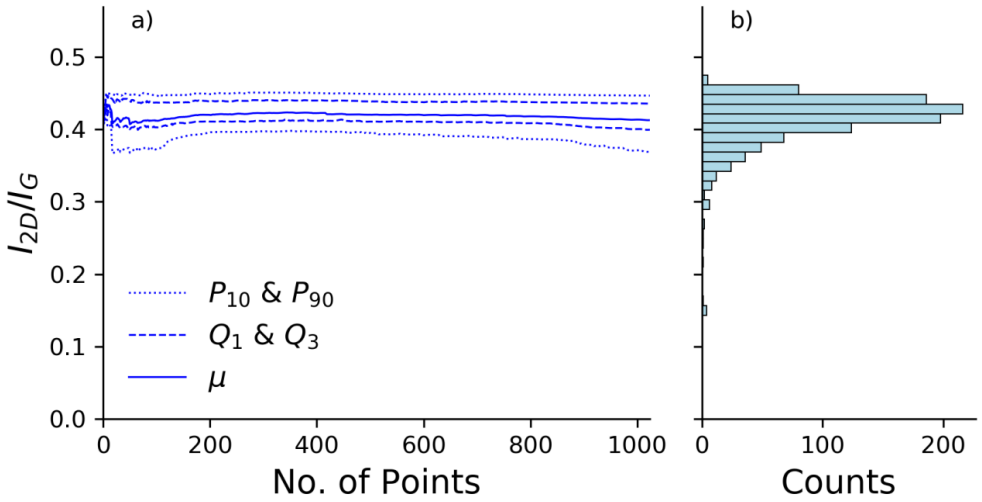

Figure S 170: Convergence plot from graphitized carbon (data set 3) described in detail above.

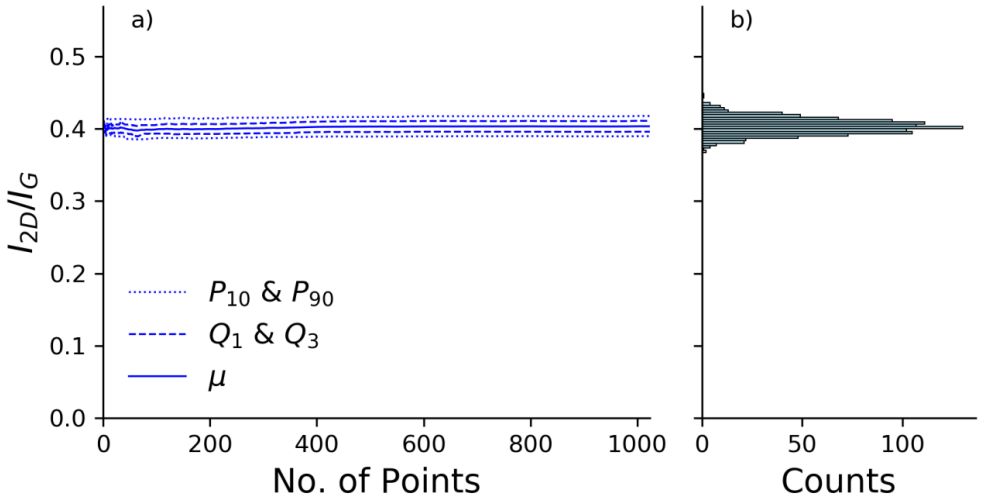

Figure S 171: Convergence plot from graphitized carbon (data set 4) described in detail above.

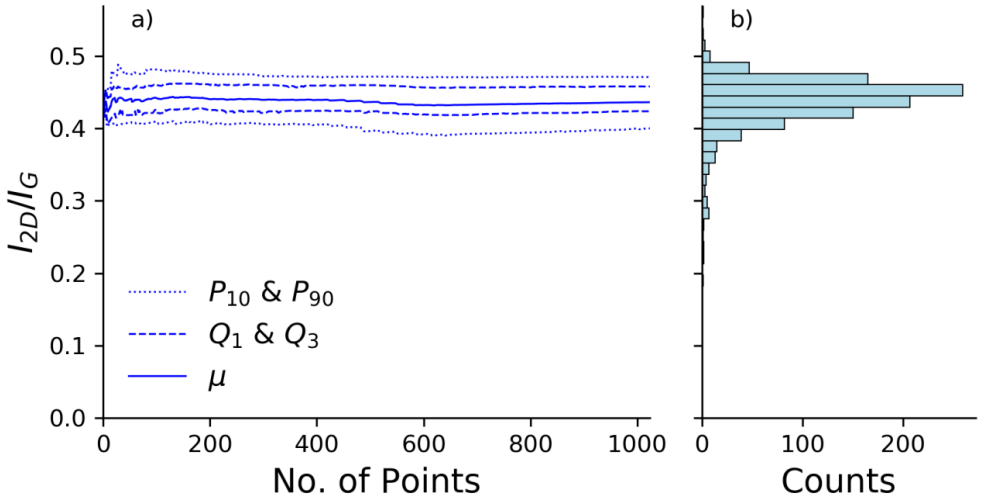

Figure S 172: Convergence plot from graphitized carbon (data set 5) described in detail above.

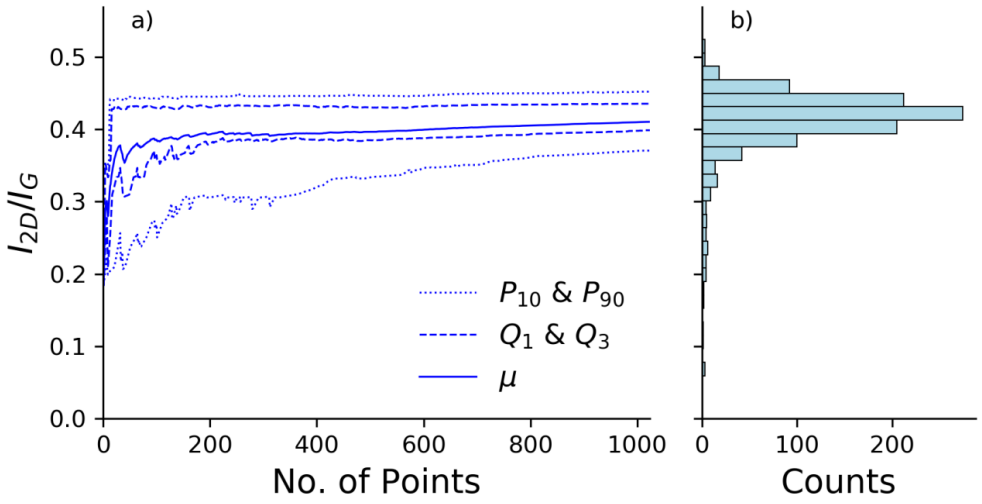

Figure S 173: Convergence plot from graphitized carbon (data set 6) described in detail above.

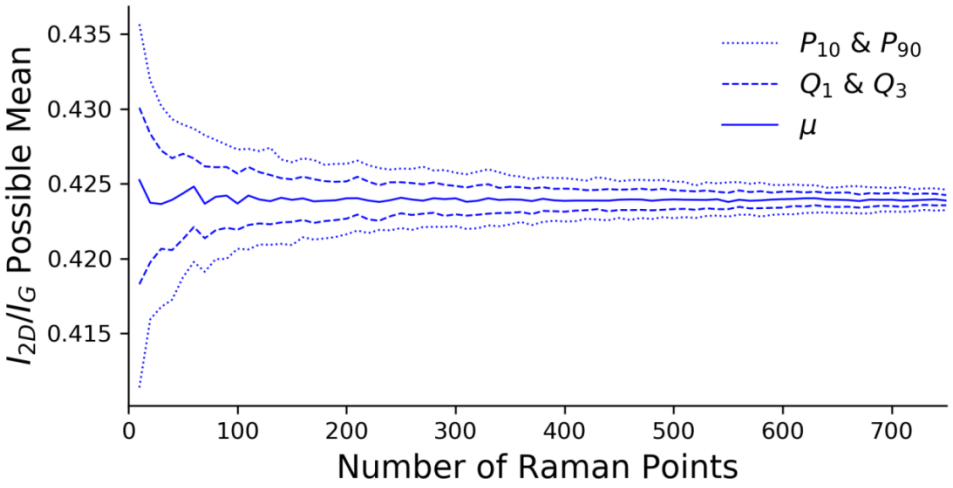

Figure S 174: Bootstrap convergence plot from graphitized carbon (data set 1); this shows the summary statistics (10th and 90th percentiles, 1st and 3rd quartiles, and mean) describing the distribution of mean values obtained from multiple analyses of smaller sub-sets of the sample size shown on the x-axis. This plot can be considered a probability distribution of possible mean values for different sample sizes.

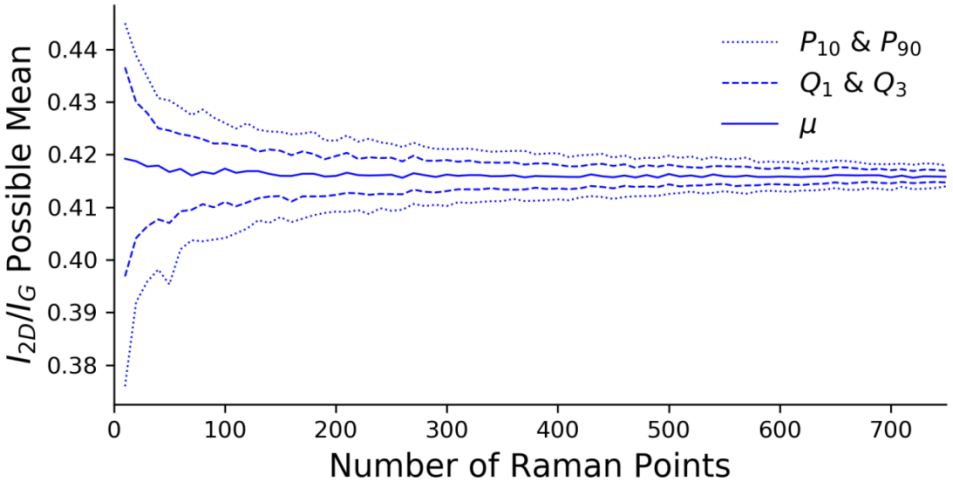

Figure S 175: Bootstrap convergence plot from graphitized carbon (data set 2), described in detail above.

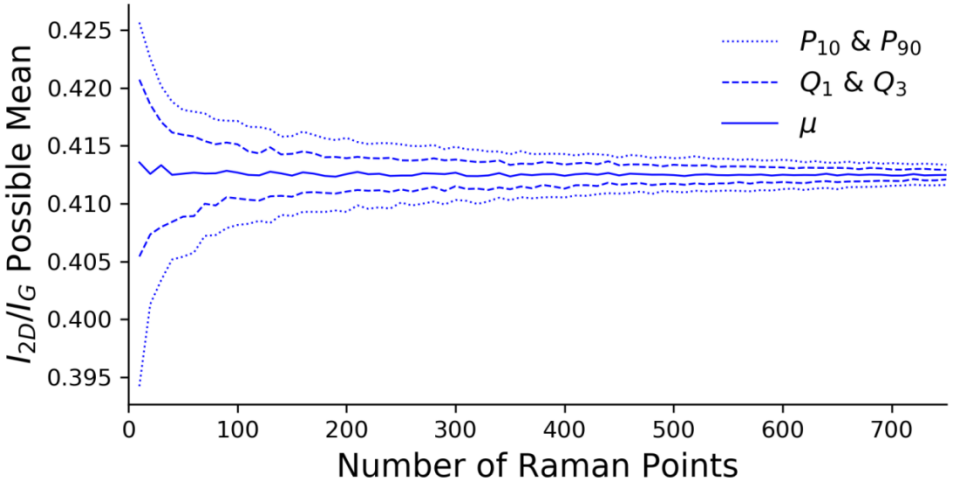

Figure S 176: Bootstrap convergence plot from graphitized carbon (data set 3), described in detail above.

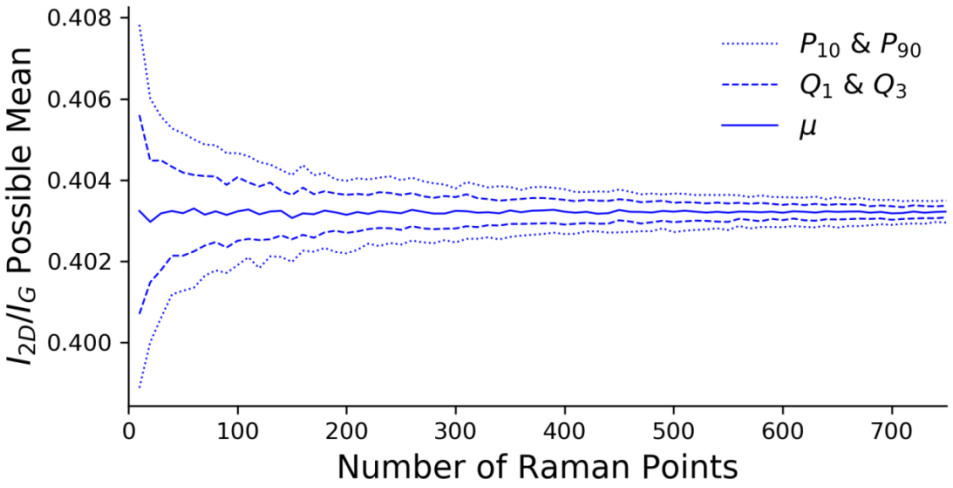

Figure S 177: Bootstrap convergence plot from graphitized carbon (data set 4), described in detail above.

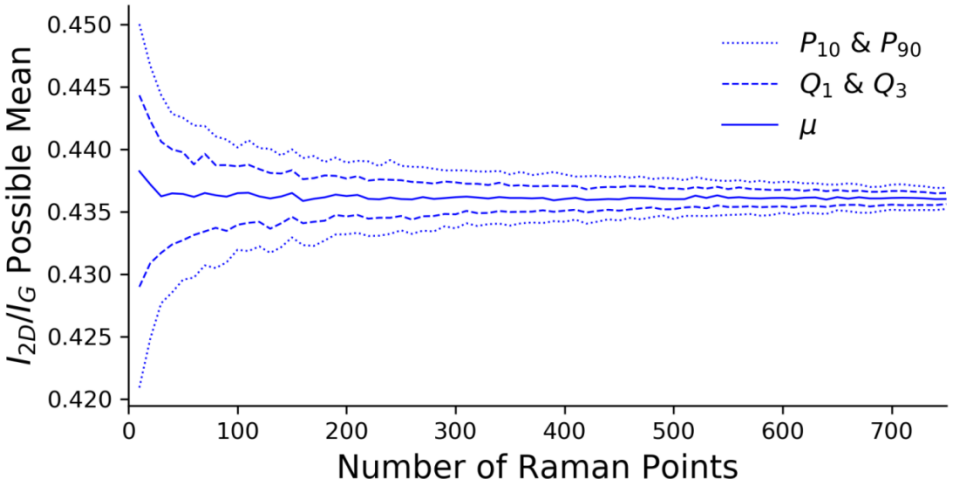

Figure S 178: Bootstrap convergence plot from graphitized carbon (data set 5), described in detail above.

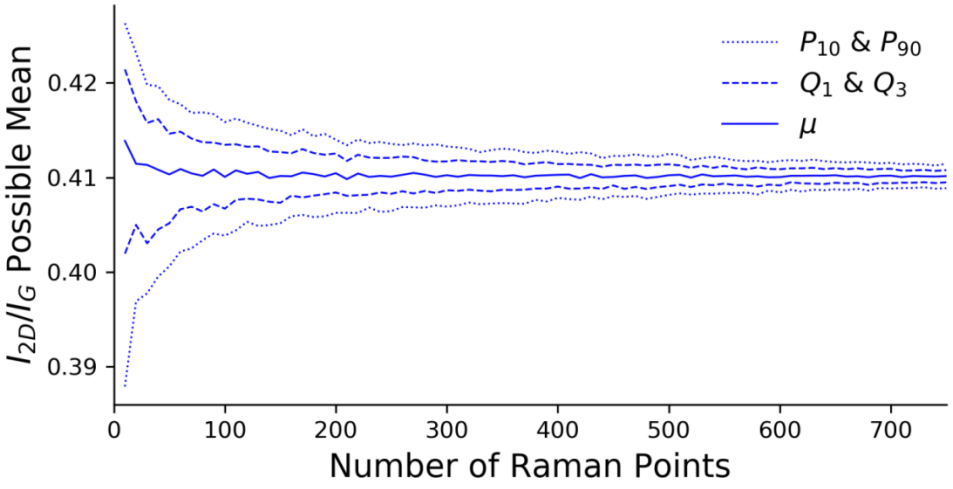

Figure S 179: Bootstrap convergence plot from graphitized carbon (data set 6), described in detail above.

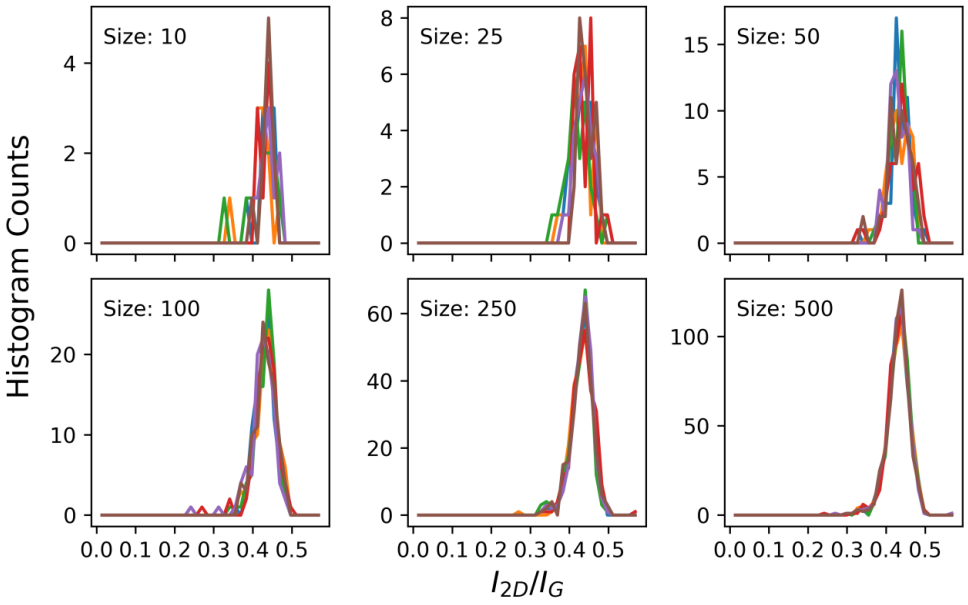

Figure S 180: Panel showing result of bootstrap analysis of graphitized carbon (data set 1). Each panel shows five examples, shown in different colors, of distributions of I_{2D}/I_G produced from sub-sets; the size of these is labelled and the x-axis is common across all I_{2D}/I_G panel plots. These show the convergence to a uniform distribution as the sub-set size increases.

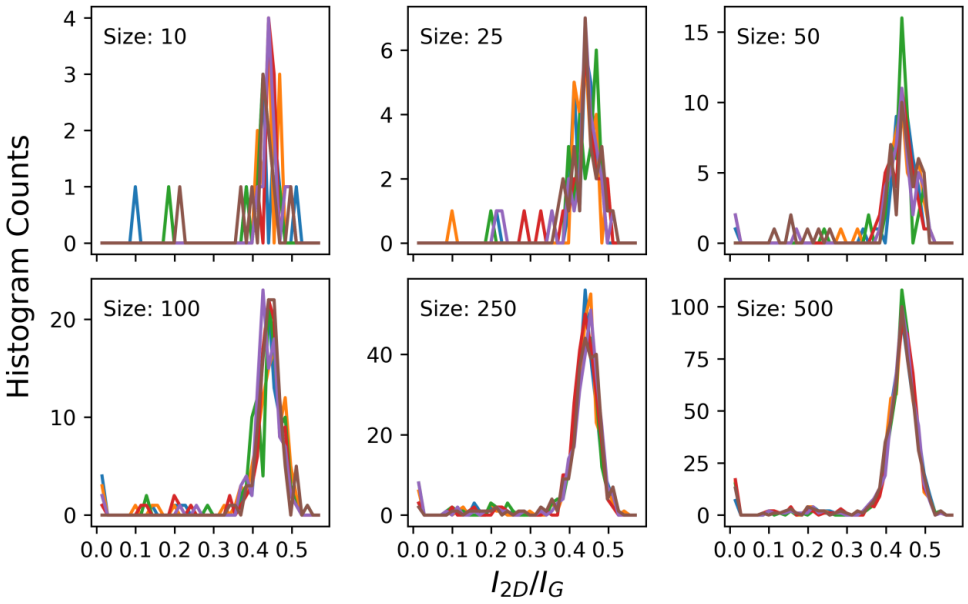

Figure S181: Panel showing result of bootstrap analysis of graphitized carbon (data set 2), described in detail above.

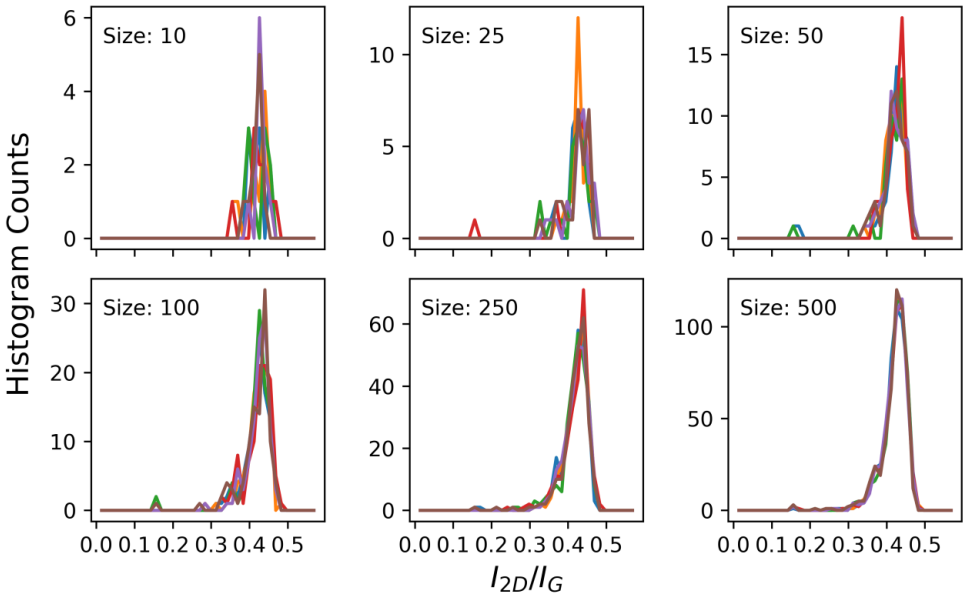

Figure S 182: Panel showing result of bootstrap analysis of graphitized carbon (data set 3), described in detail above.

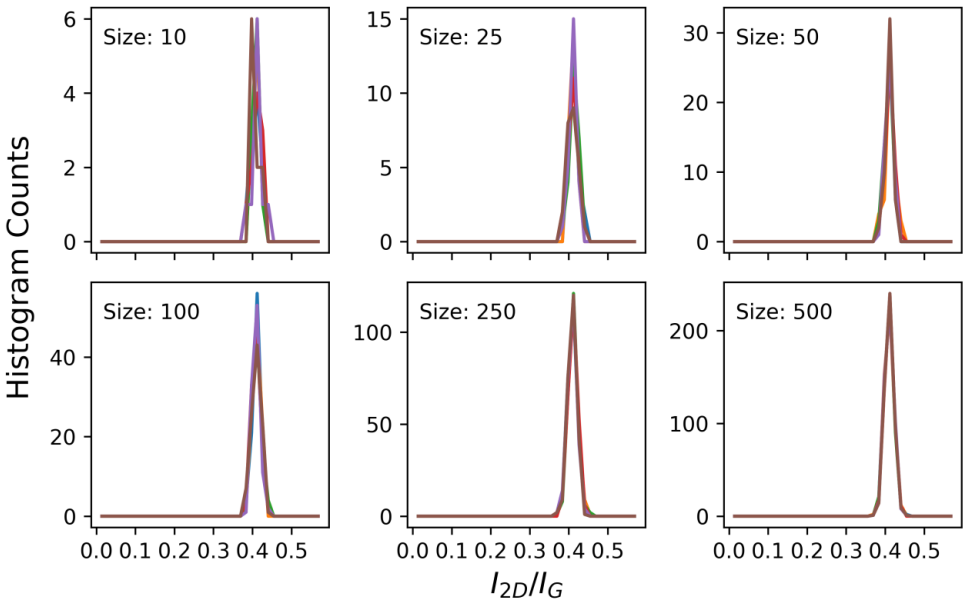

Figure S 183: Panel showing result of bootstrap analysis of graphitized carbon (data set 4), described in detail above.

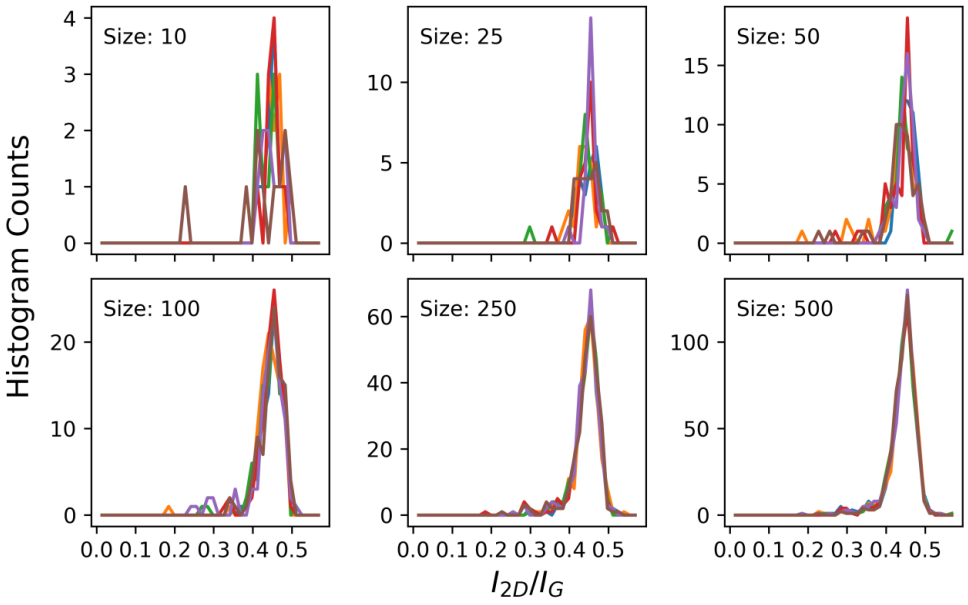

Figure S 184: Panel showing result of bootstrap analysis of graphitized carbon (data set 5), described in detail above.

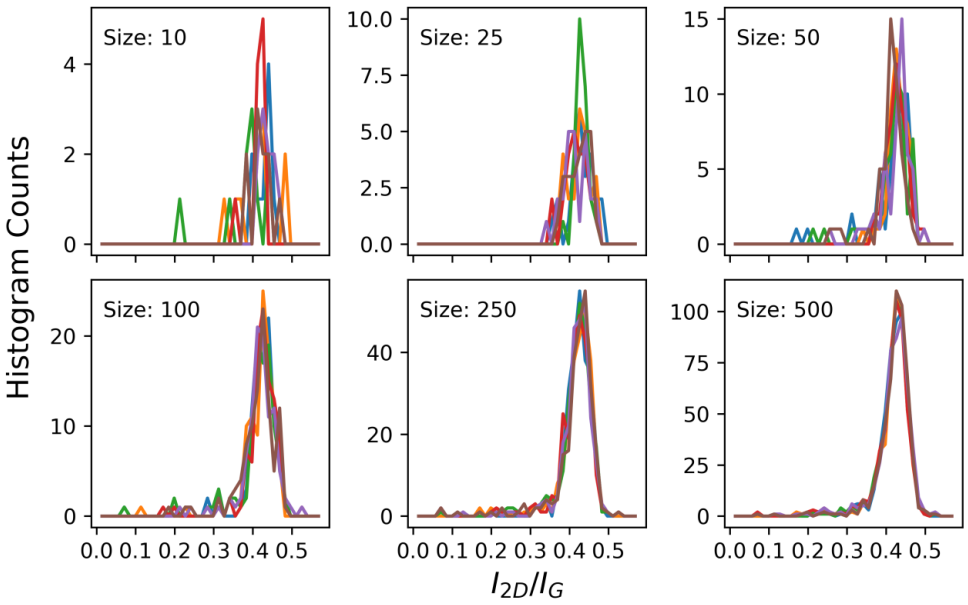

Figure S 185: Panel showing result of bootstrap analysis of graphitized carbon (data set 6), described in detail above.

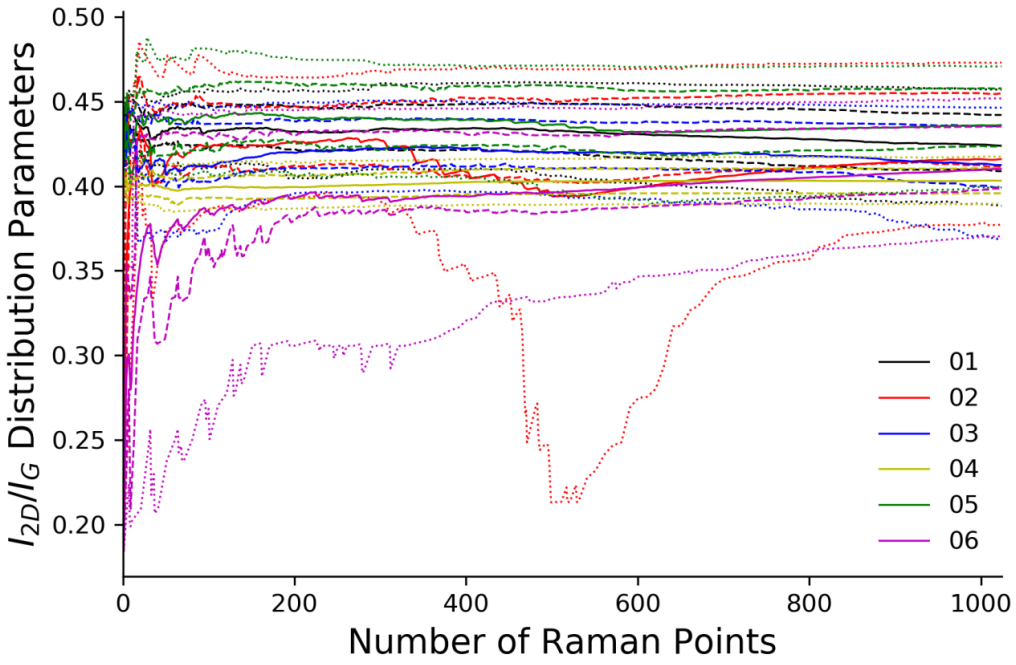

Figure S 186: Plot showing the convergence data of I_{2D}/I_G from all six graphitized carbon data sets. The lines denote the same summary statistics whilst different data sets are shown in different colors.

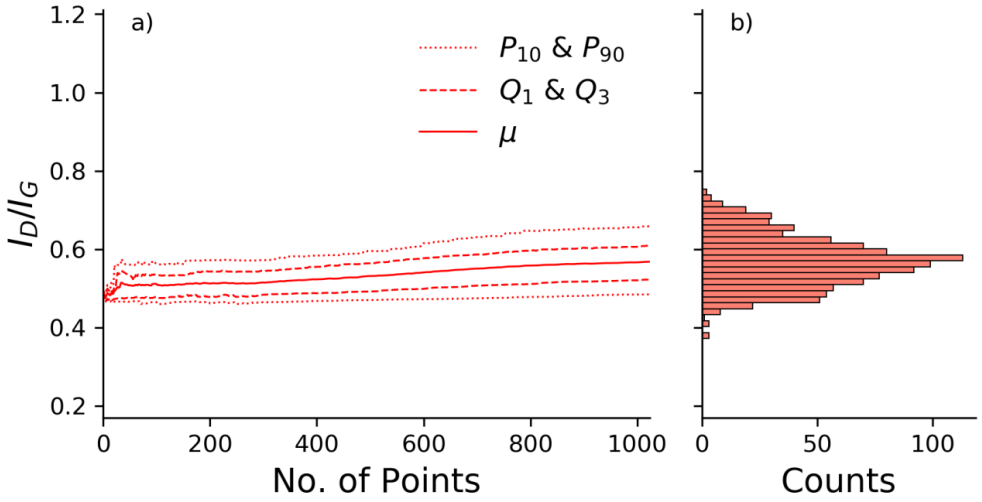

Figure S 187: Convergence plot from graphitized carbon (data set 1) showing a) the change in summary statistics of I_D/I_G as more data points are added to the analysis. b) The final distribution shown as a horizontal histogram, y-axis constant across all plots showing I_D/I_G convergence data from graphite sample.

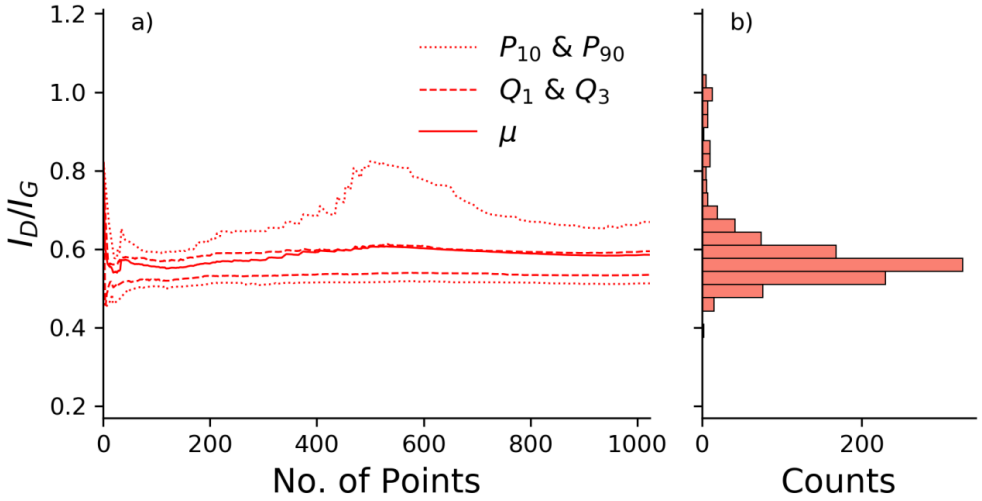

Figure S 188: Convergence plot from graphitized carbon (data set 2) described in detail above.

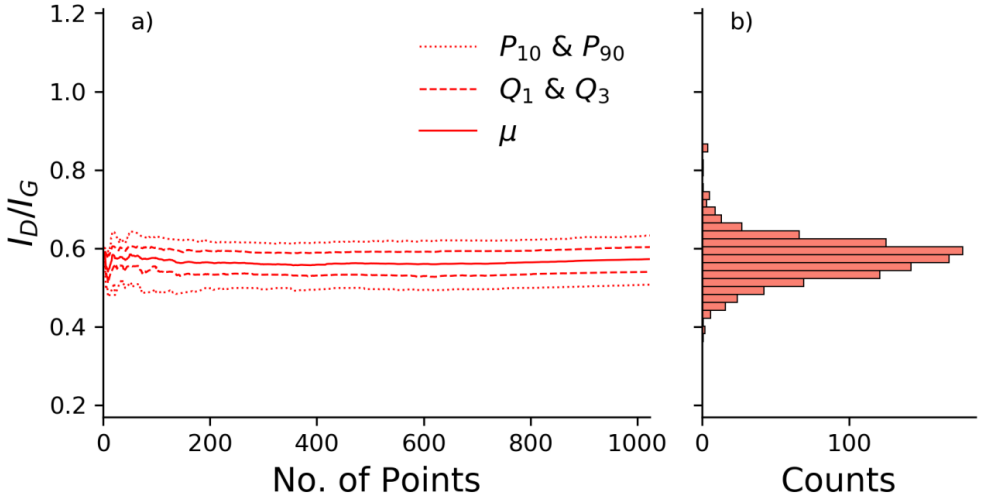

Figure S 189: Convergence plot from graphitized carbon (data set 3) described in detail above.

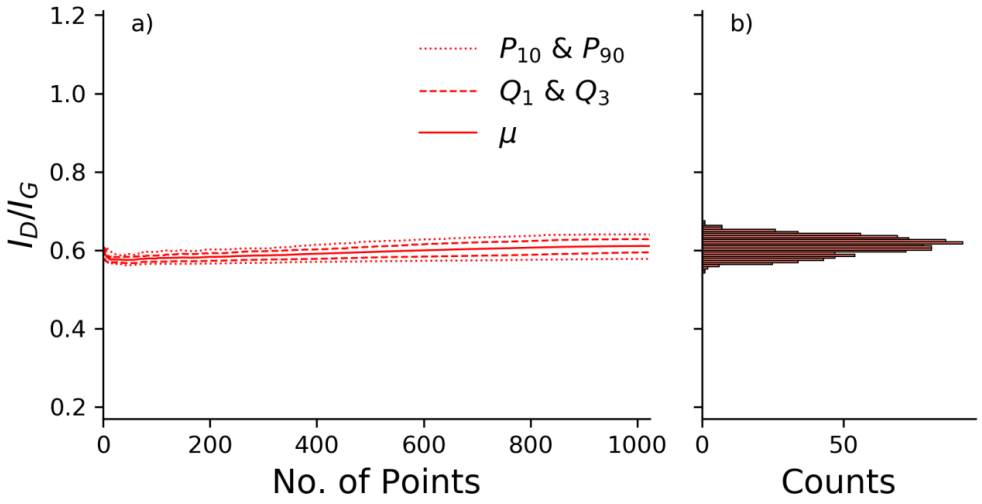

Figure S 190: Convergence plot from graphitized carbon (data set 4) described in detail above.

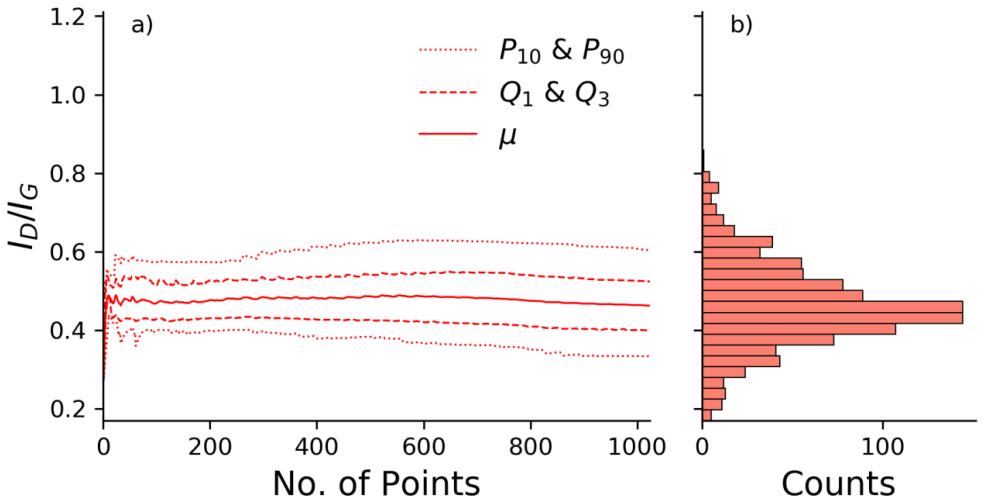

Figure S 191: Convergence plot from graphitized carbon (data set 5) described in detail above.

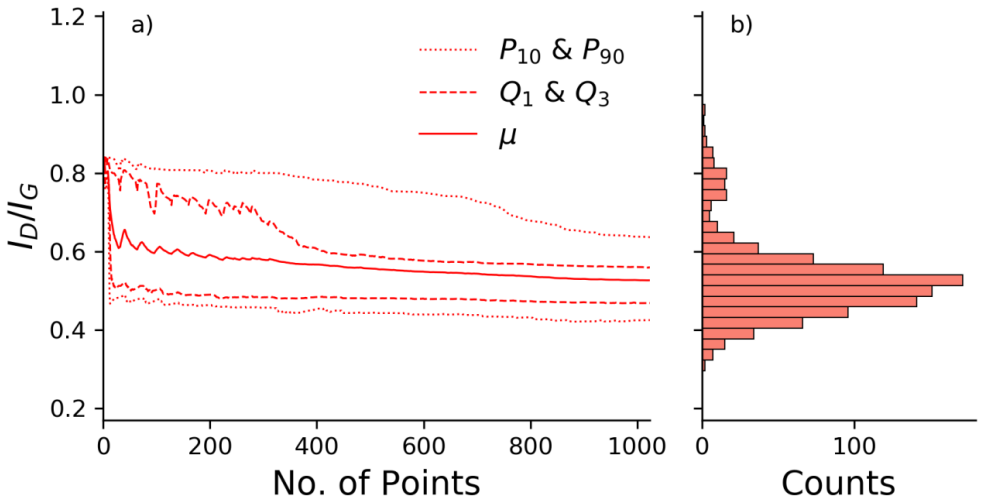

Figure S 192: Convergence plot from graphitized carbon (data set 6) described in detail above.

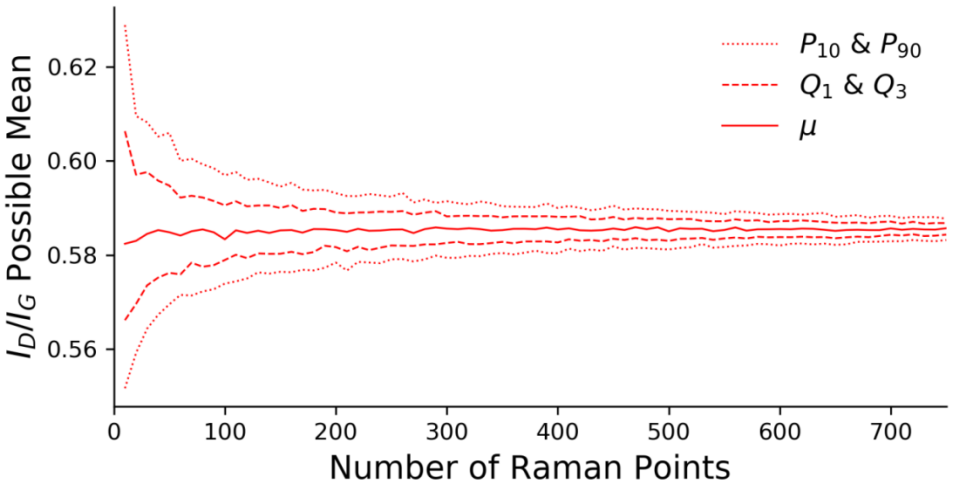

Figure S 193: Bootstrap convergence plot from graphitized carbon (data set 1); this shows the summary statistics (10th and 90th percentiles, 1st and 3rd quartiles, and mean) describing the distribution of mean values obtained from multiple analyses of smaller sub-sets of the sample size shown on the x-axis. This plot can be considered a probability distribution of possible mean values for different sample sizes.

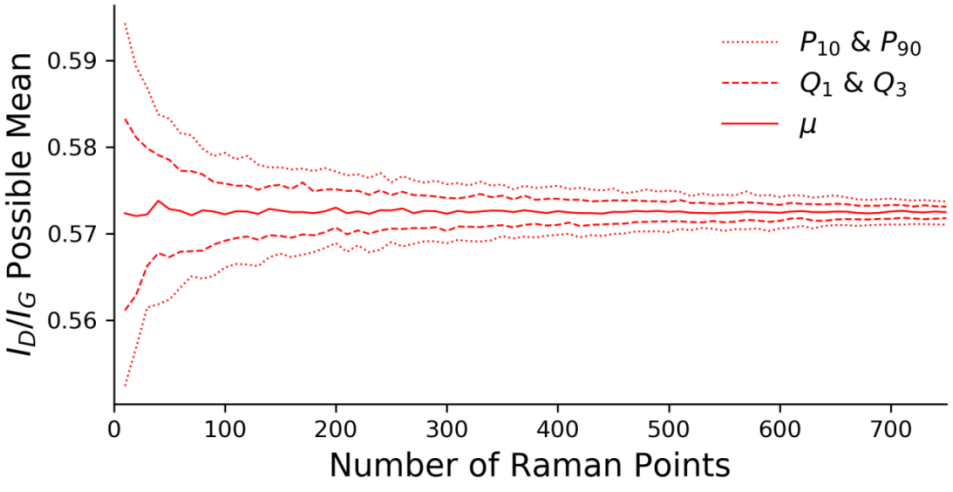

Figure S 194: Bootstrap convergence plot from graphitized carbon (data set 2), described in detail above.

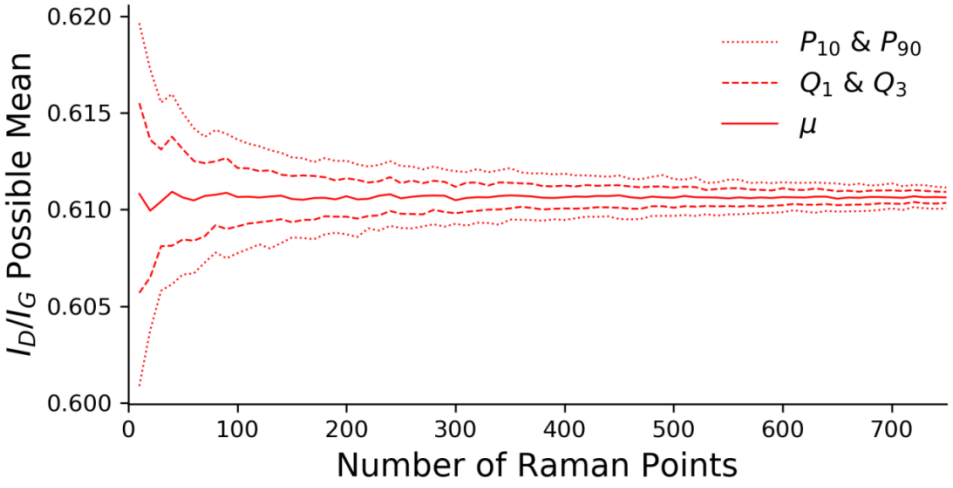

Figure S 195: Bootstrap convergence plot from graphitized carbon (data set 3), described in detail above.

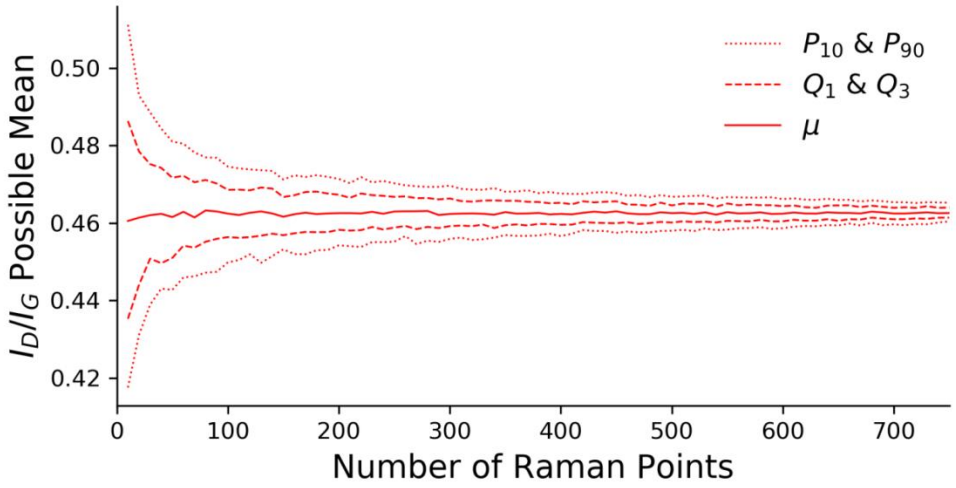

Figure S 196: Bootstrap convergence plot from graphitized carbon (data set 4), described in detail above.

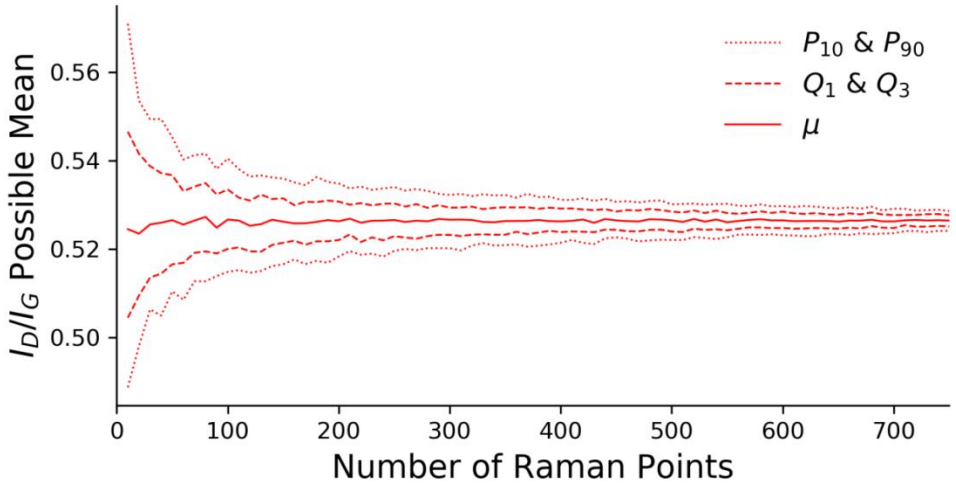

Figure S 197: Bootstrap convergence plot from graphitized carbon (data set 5), described in detail above.

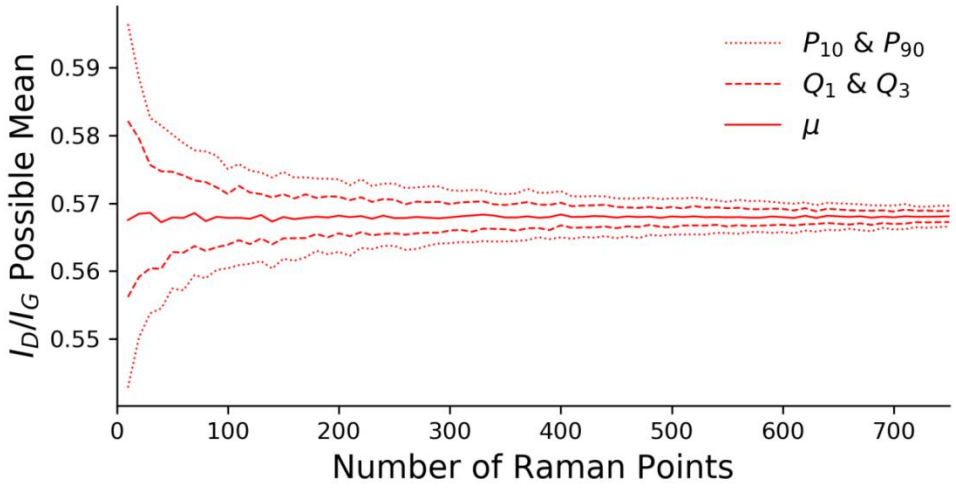

Figure S 198: Bootstrap convergence plot from graphitized carbon (data set 6), described in detail above.

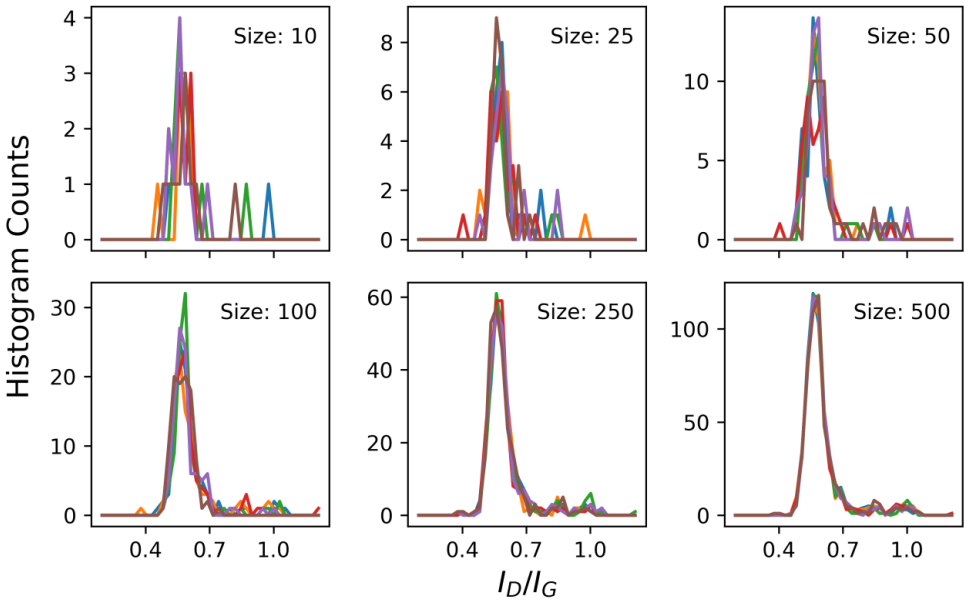

Figure S 199: Panel showing result of bootstrap analysis of graphitized carbon (data set 1). Each panel shows five examples, shown in different colors, of distributions of I_D/I_G produced from sub-sets; the size of these is labelled and the x-axis is common across all I_D/I_G panel plots. These show the convergence to a uniform distribution as the sub-set size increases.

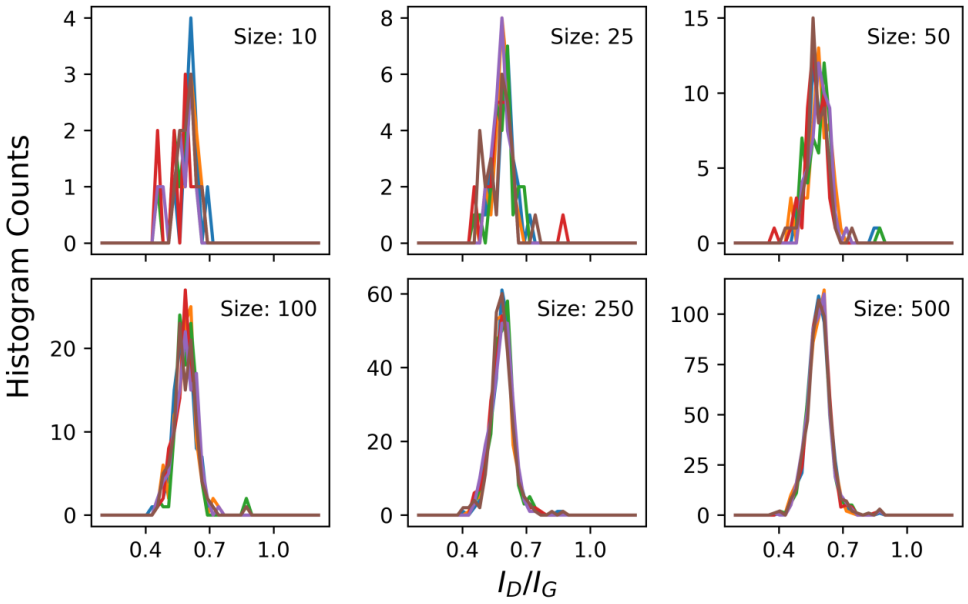

Figure S 200: Panel showing result of bootstrap analysis of graphitized carbon (data set 2), described in detail above.

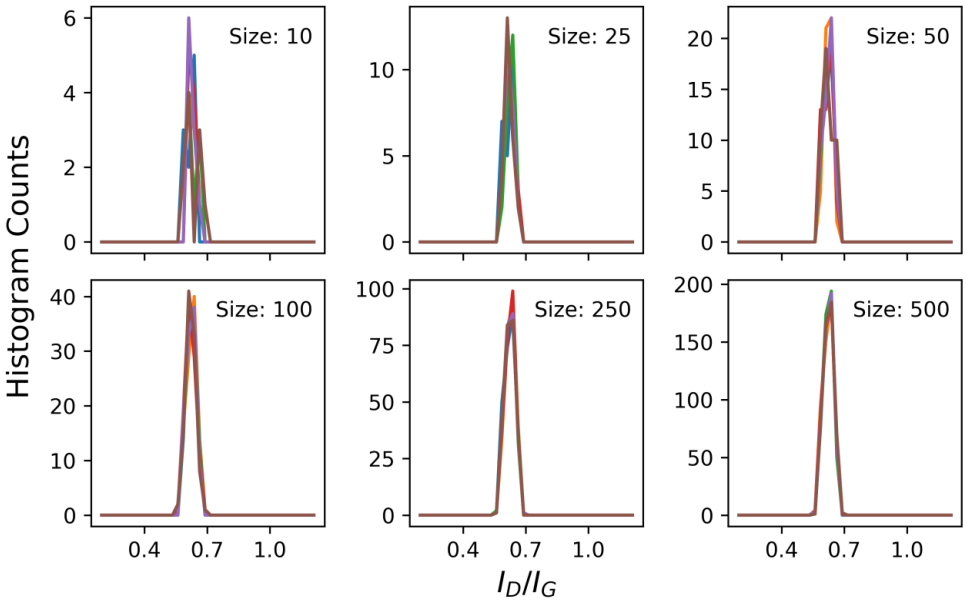

Figure S 201: Panel showing result of bootstrap analysis of graphitized carbon (data set 3), described in detail above.

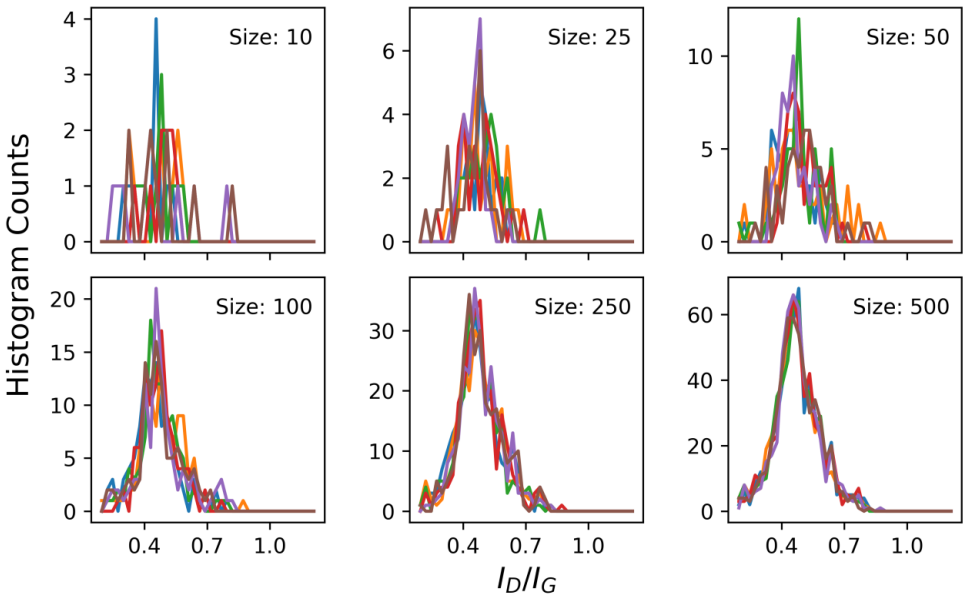

Figure S 202: Panel showing result of bootstrap analysis of graphitized carbon (data set 4), described in detail above.

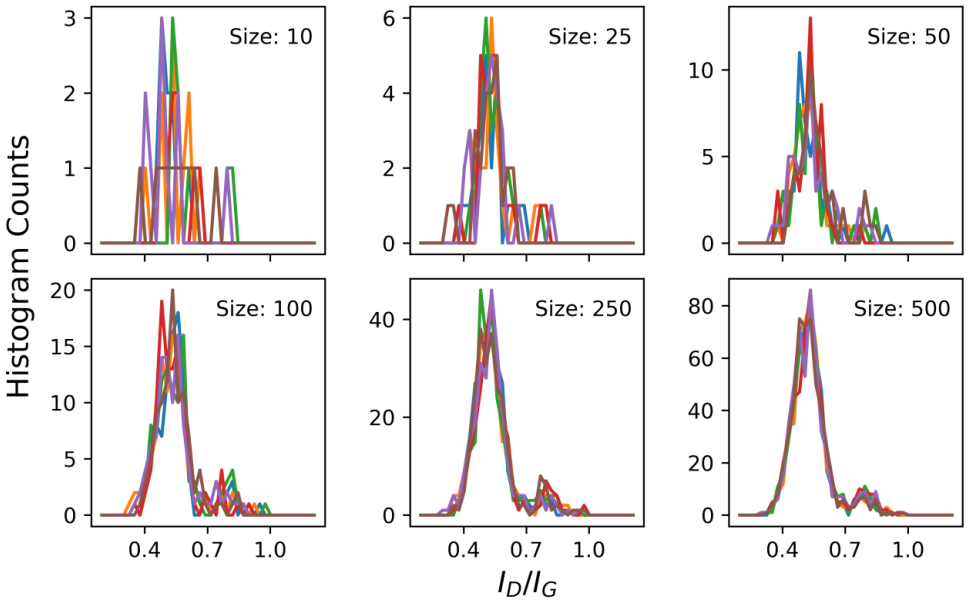

Figure S 203: Panel showing result of bootstrap analysis of graphitized carbon (data set 5), described in detail above.

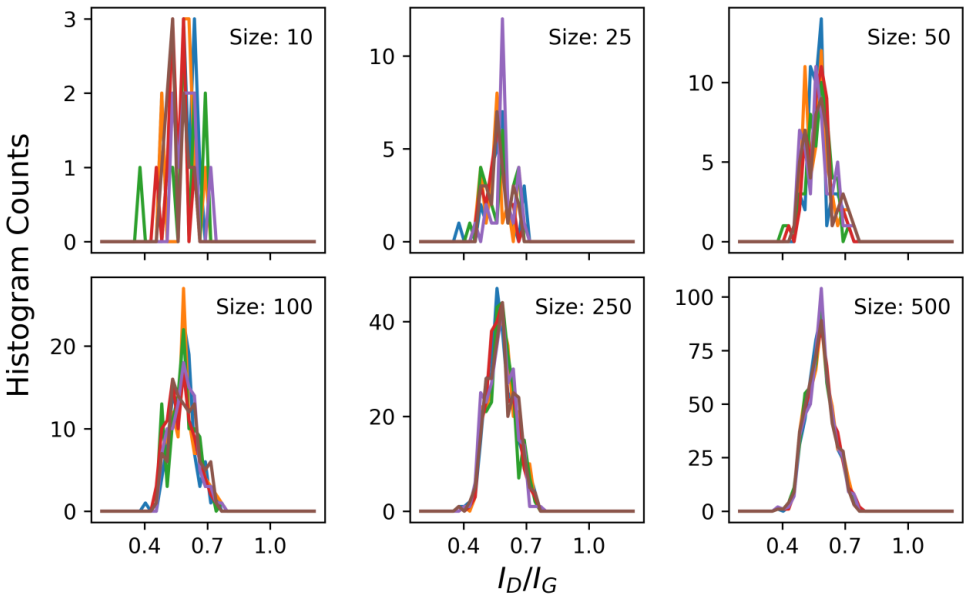

Figure S 204: Panel showing result of bootstrap analysis of graphitized carbon (data set 6), described in detail above.

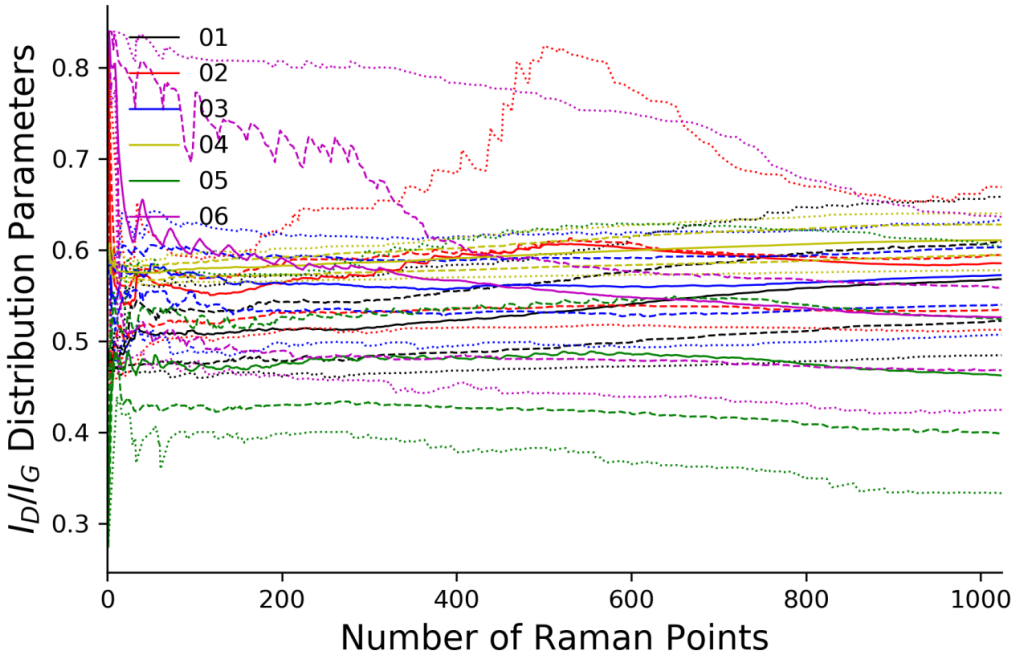

Figure S 205: Plot showing the convergence data of I_D/I_G from all six graphitized carbon data sets. The lines denote the same summary statistics whilst different data sets are shown in different colors.

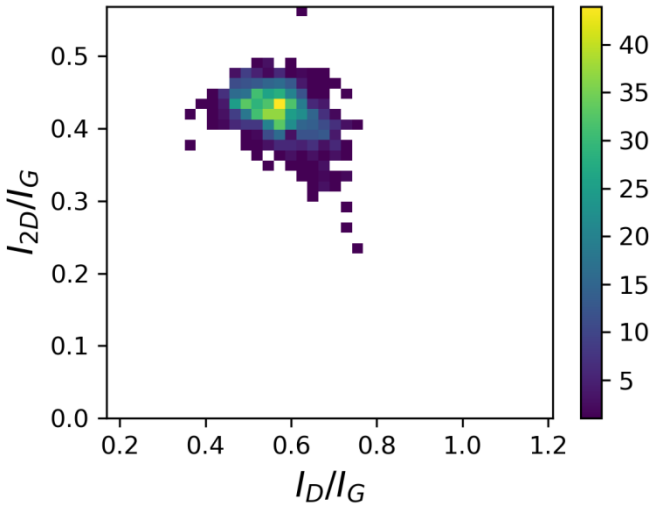

Figure S 206: 3D bivariate histogram showing the distribution of key peak ratios from graphite data (data set 1). The histogram count is shown by the colored heat map (key on right) and the bins are read simultaneously from the x and y axes which are common to all plots.

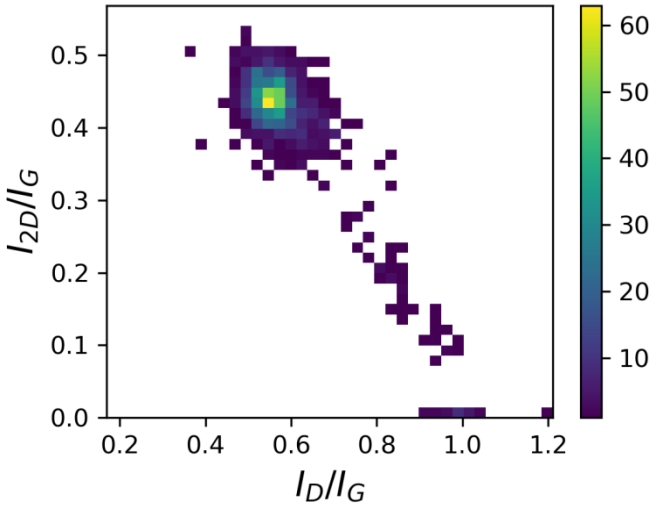

Figure S 207: 3D bivariate histogram showing the distribution of data from graphitized carbon (data set 2).

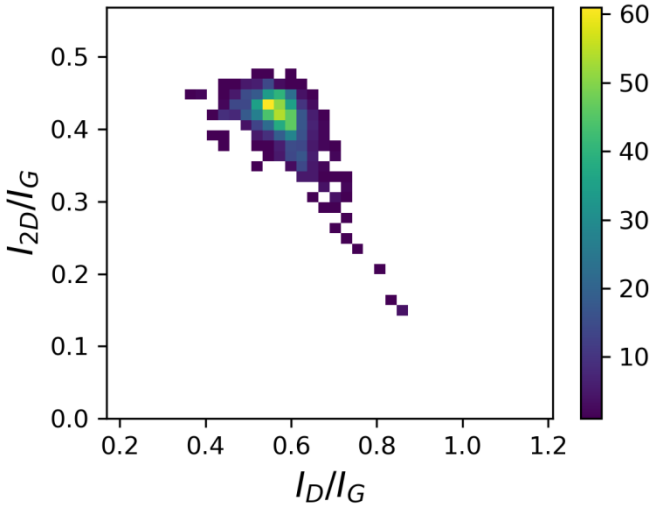

Figure S 208: 3D bivariate histogram showing the distribution of data from graphitized carbon (data set 3).

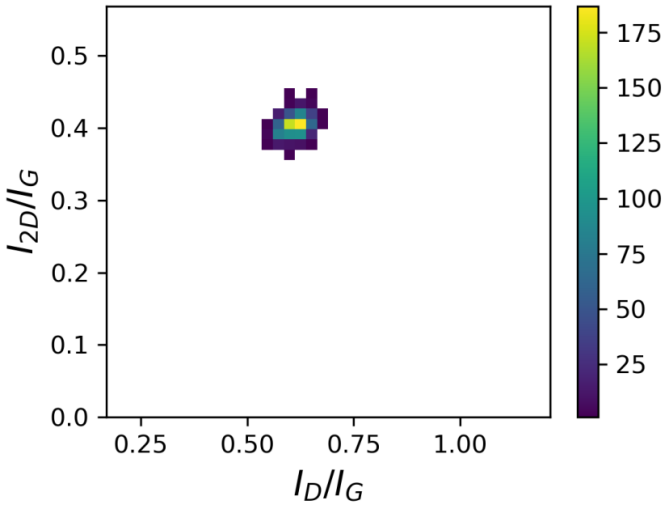

Figure S 209: 3D bivariate histogram showing the distribution of data from graphitized carbon (data set 4).

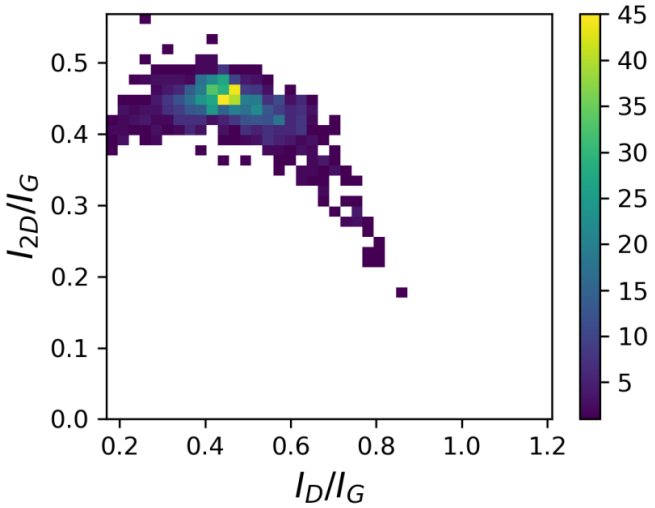

Figure S 210: 3D bivariate histogram showing the distribution of data from graphitized carbon (data set 5).

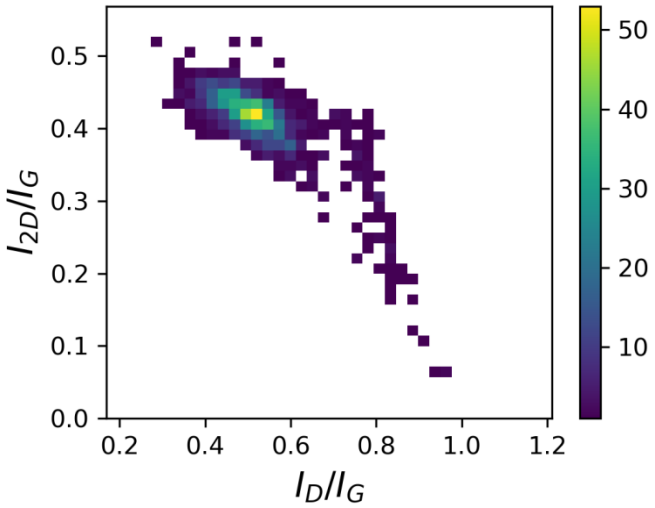

Figure S 211: 3D bivariate histogram showing the distribution of data from graphitized carbon (data set 6).

To consider the overall convergence and trends of the data set, the six different maps recorded from the graphitized sample were combined together and re-arranged into a random order to remove the structure inherent in the data. Whilst not representative of the real maps that would be collected from the material it is useful to ensure the overall trends measured did ultimately converge. Thus the plots below are the same style as above but show the aggregated, randomized data.

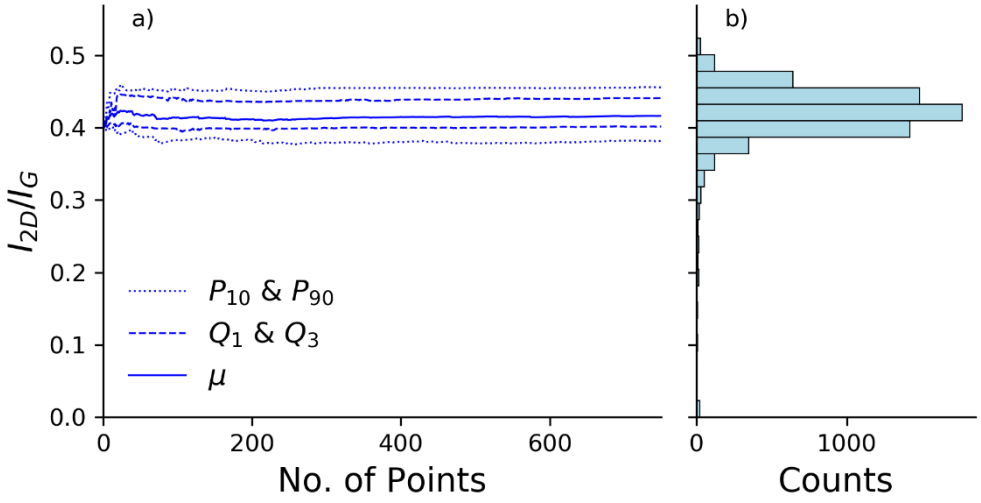

Figure S 212: Convergence plot from graphitized carbon (aggregated data) showing a) the change in summary statistics of I_{2D}/I_G as more data points are added to the analysis. b) The final distribution shown as a horizontal histogram.

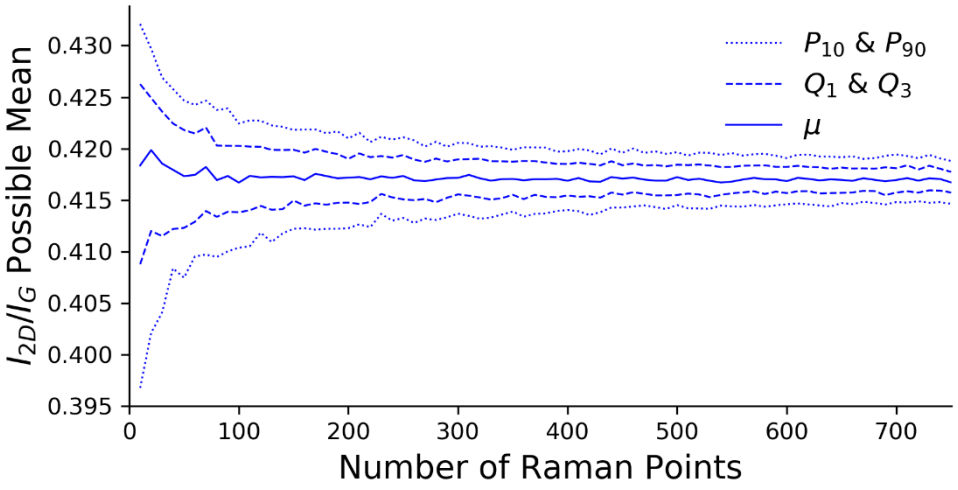

Figure S 213: Bootstrap convergence plot from graphitized carbon (aggregated data); this shows the summary statistics (10th and 90th percentiles, 1st and 3rd quartiles, and mean) describing the distribution of mean values obtained from multiple analyses of smaller sub-sets of the sample size shown on the x-axis. This plot can be considered a probability distribution of possible mean values for different sample sizes.

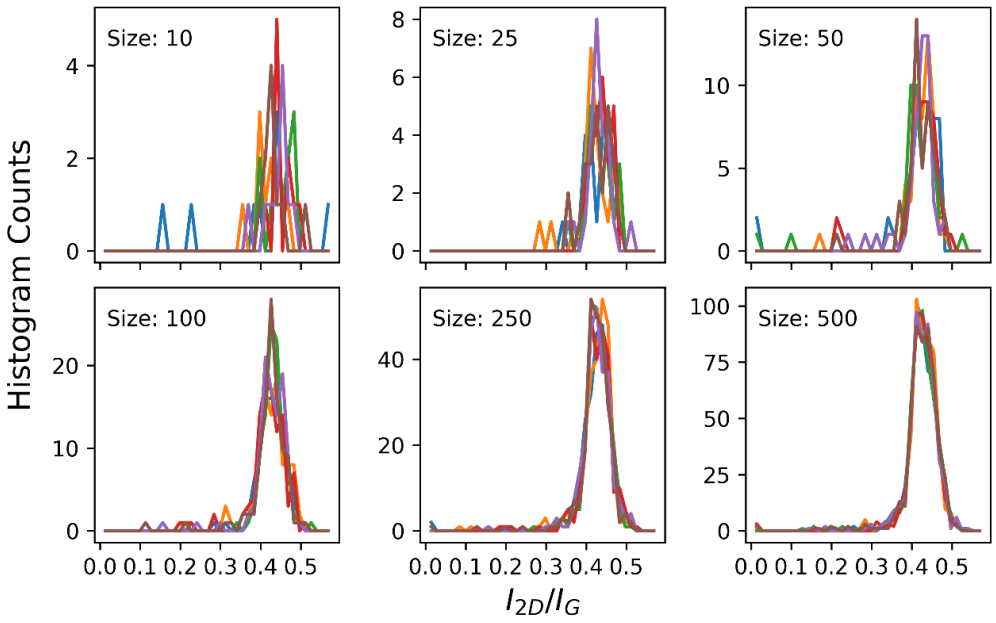

Figure S 214: Panel showing result of bootstrap analysis of graphitized carbon (aggregated data). Each panel shows five examples, shown in different colors, of distributions of I_{2D}/I_G produced from sub-sets; the size of these is labelled and the x-axis is common across all I_{2D}/I_G panel plots. These show the convergence to a uniform distribution as the sub-set size increases.

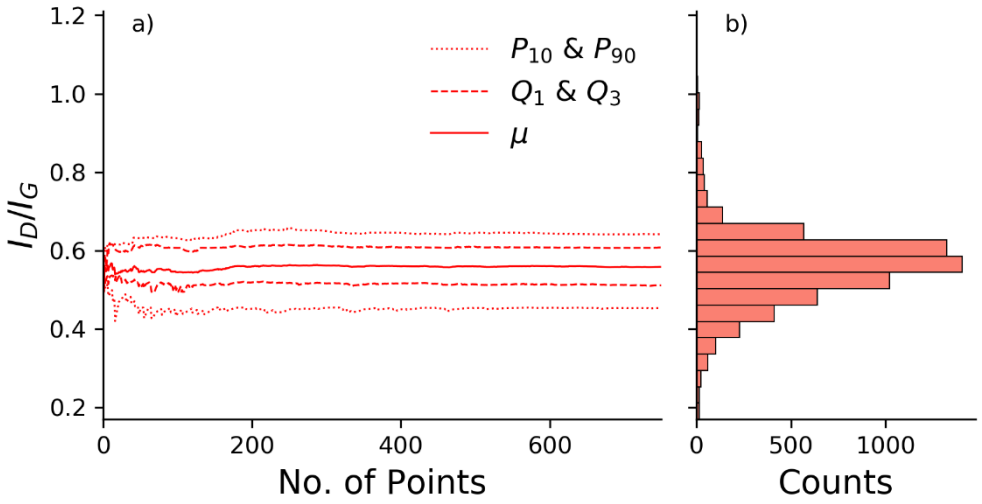

Figure S 215: Convergence plot from graphitized carbon (aggregated data) showing a) the change in summary statistics of I_D/I_G as more data points are added to the analysis. b) The final distribution shown as a horizontal histogram.

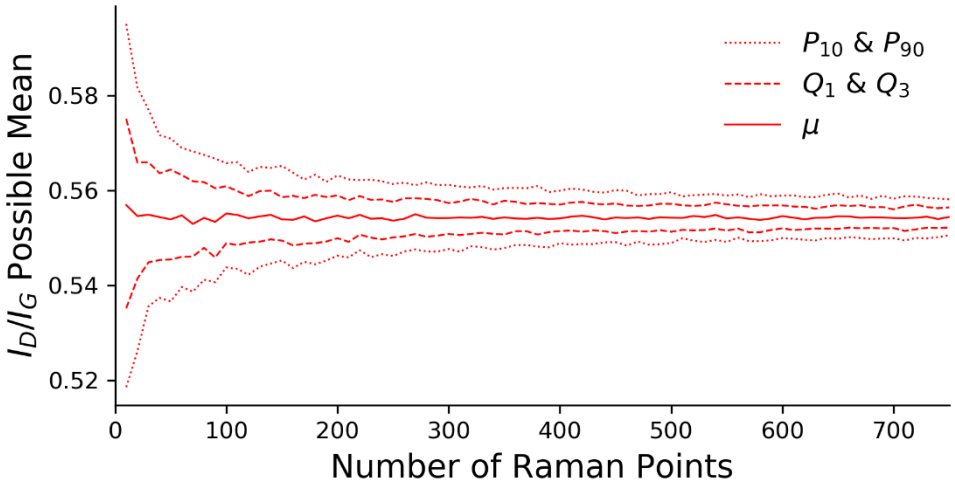

Figure S 216: Bootstrap convergence plot from graphitized carbon (aggregated data); this shows the summary statistics (10th and 90th percentiles, 1st and 3rd quartiles, and mean) describing the distribution of mean values obtained from multiple analyses of smaller sub-sets of the sample size shown on the x-axis. This plot can be considered a probability distribution of possible mean values for different sample sizes.

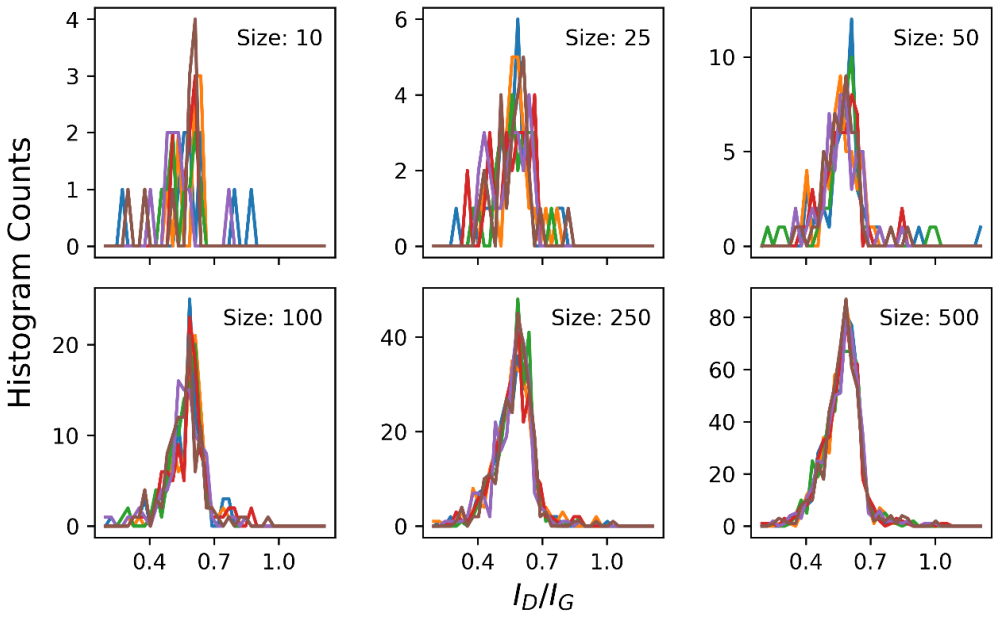

Figure S 217: Panel showing result of bootstrap analysis of graphitized carbon (aggregated data). Each panel shows five examples, shown in different colors, of distributions of I_D/I_G produced from sub-sets; the size of these is labelled and the x-axis is common across all I_D/I_G panel plots. These show the convergence to a uniform distribution as the sub-set size increases.

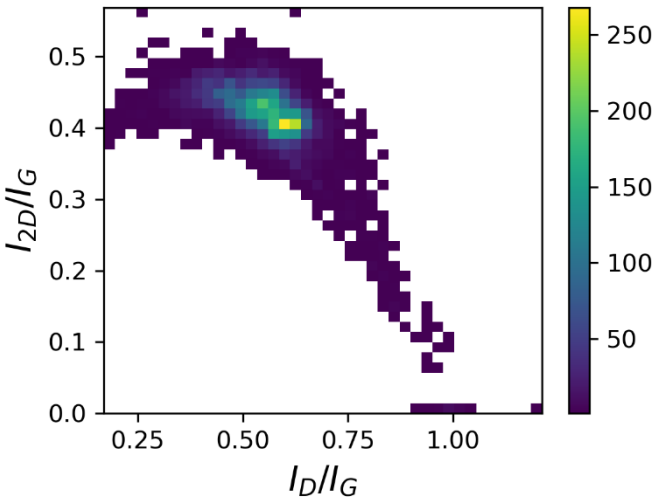

Figure S 218: 3D bivariate histogram showing the distribution of key peak ratios from graphitized carbon (aggregated data). The histogram count is shown by the colored heat map (key on right) and the bins are read simultaneously from the x and y axes.

9.1.8 Raman Fitting Models

When studying different peak models example spectra were fitted with Gaussian, Lorentzian and Voigt functions for comparison. Resulting fits with reduced chi squared shown below.

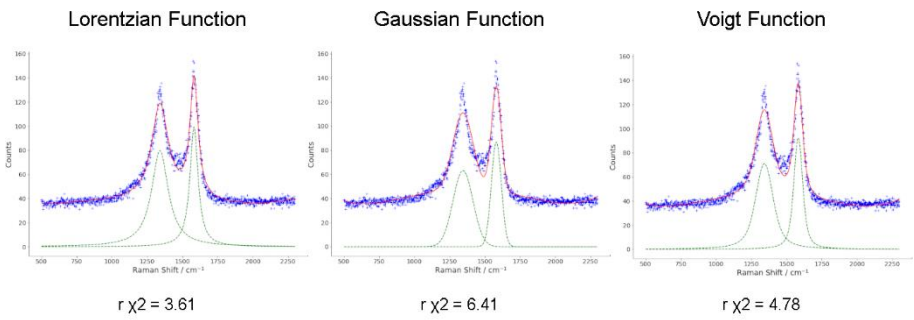

Figure S 219: Example peak fits using three models: Lorentzian, Gaussian and Voight focussed on the D and G peak range. The spectral data is shown in blue, the fitted model shown in red and the individual peak contributions shown in green.

9.2 Dextran Carbonization

9.2.1 Powder x-ray Fitting

The x-ray diffraction patterns collected from the carbonization process were analysed using GSAS-II to complete a Rietveld fitting procedure, confirming the cobalt metal content. CIF files for both hcp and ccp metal phases were taken from the ICSD, instrument parameters and atom positions were fixed whilst the unit cell parameters and thermal parameters were permitted to vary during the fitting.

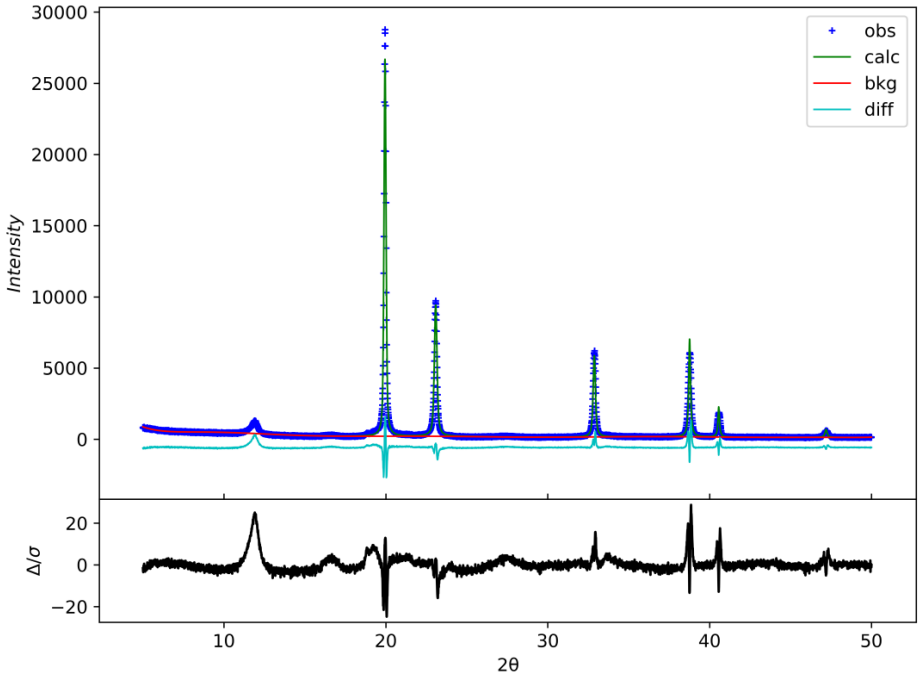

Figure S 220: Fitted powder XRD pattern of $Co(OAc)_2$ showing the calculated pattern of cubic cobalt metal.

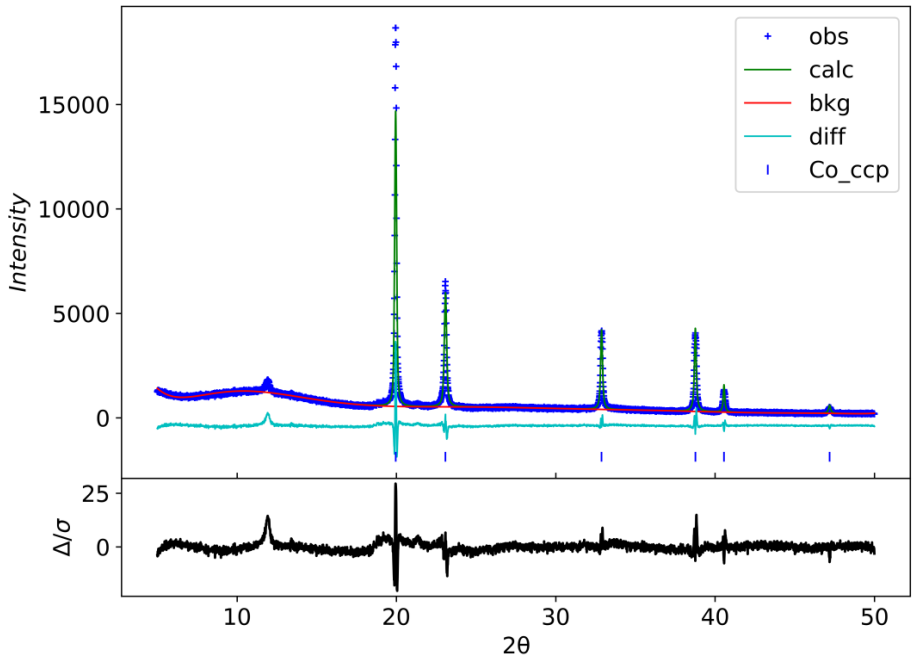

Figure S 221: Fitted powder XRD pattern of $Co(NO_3)_2$ showing the calculated pattern of cubic cobalt metal.

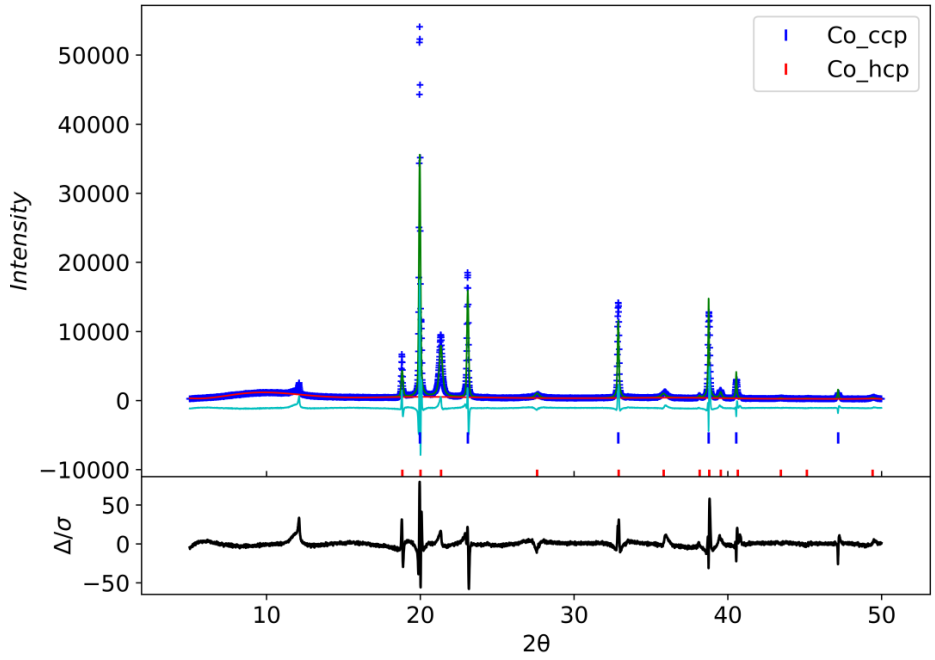

Figure S 222: Fitted powder XRD pattern of $CoCl_2$ showing the two phases of metal present and the calculated pattern.

9.2.2 Thermal Analysis – Derivative Plots

The combustion onset temperature was calculated from the TGA plots according to the standard methodology outlined in chapter 3. The inflection point, or temperature of maximum combustion rate was calculated from the first derivative of the TGA plots.

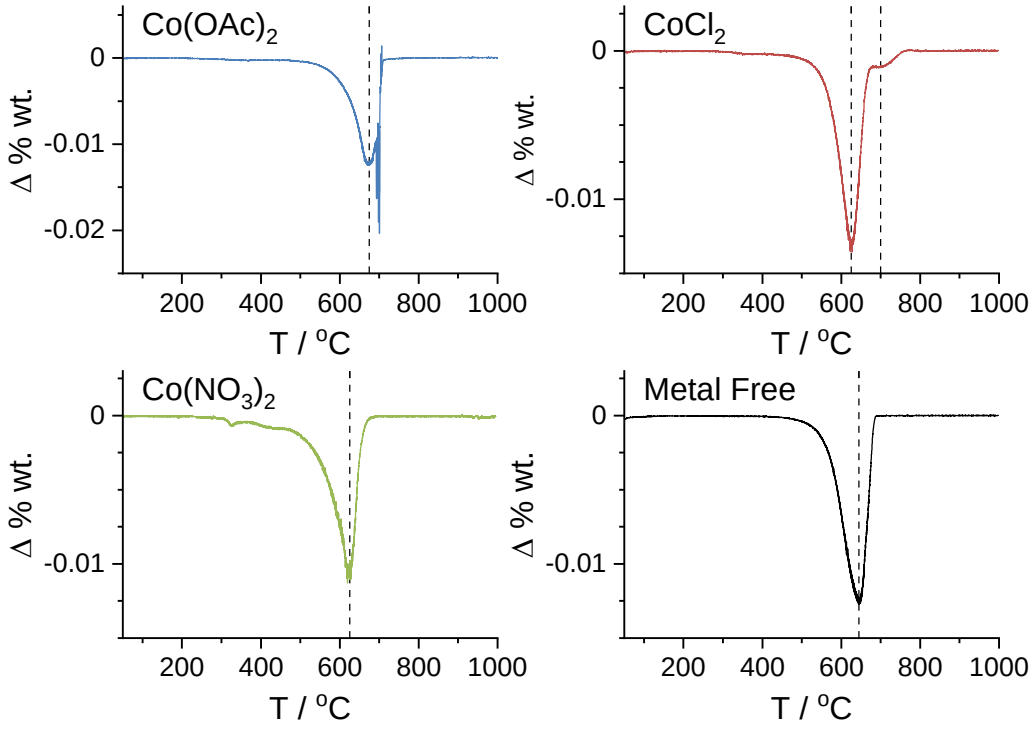

Figure S 223: First derivative plots of thermal gravimetric analysis from each material, labelled top left with the inflection points of maximum combustion marked with dashed lines. The $CoCl_2$ sample has both components marked.

9.2.3 Additional Electron Microscopy

Additional images and analysis from electron microscopy data set.

SEM images of the $Co(NO_3)_2$ and $Co(OAc)_2$ based foams show a difference in morphology, with the nitrate based foam containing many thin flakes and holes with vary narrow wisps of carbon based material extending from the surface. In comparison the acetate based foam, whilst porous has a more solid, smooth surface at this magnification level and does not present any very thin edges extending from the bulk.

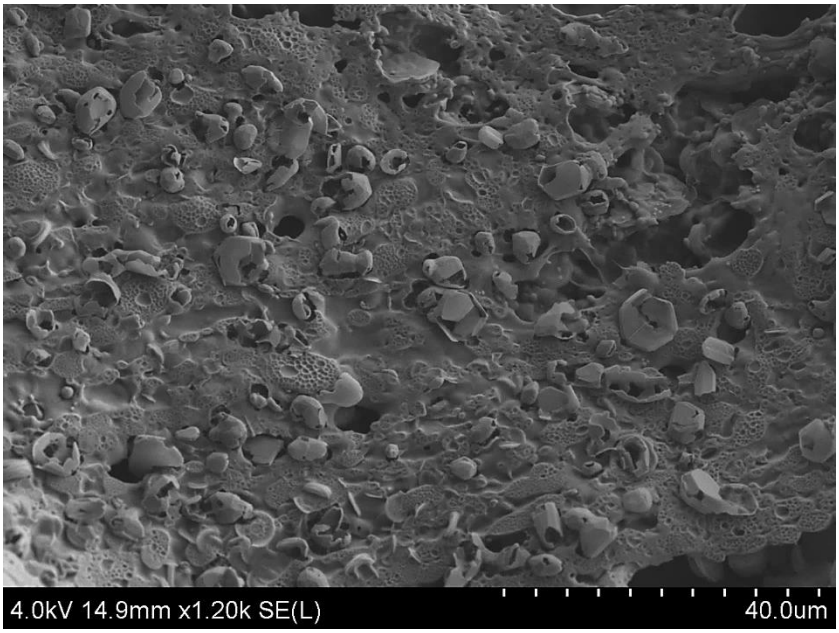

Figure S 224: Wide area SEM image of $CoCl_2$ after acid washing. The surface is covered with hollow carbon shells from graphite growth on crystalline metal particles that have been removed by acid washing.

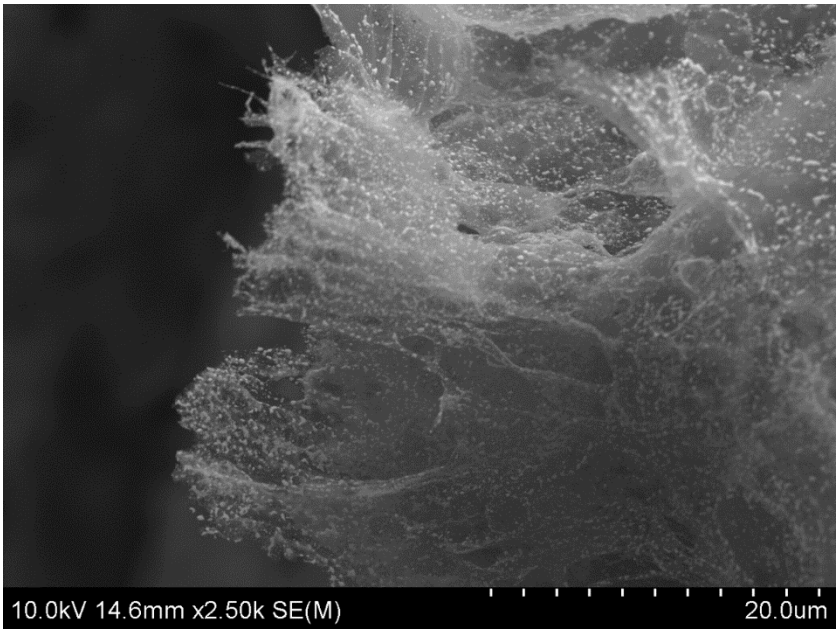

Figure S 225: SEM image of $Co(NO_3)_2$ before acid washing, taken at the edge of a foam. The carbon is made of thin fibrous material and brighter dots of metal particles, many larger than the nanoparticles observed in TEM are visible throughout.

Large area TEM images were used containing a large number of distinct circular particles. These were analysed with ImageJ by first converting them into binary black and white images highlighting only the nanoparticles by their contrast. Using the pixels these shapes were converted into particles sizes and the summary statistics are shown below. The nanoparticles produced from reduction of the acetate are much smaller than the particles from the nitrate;

and the average size of the nitrate nanoparticles are a close match to the size of the holes observed in the structure after acid washing. The images used are included below.

Table S 1: Particle size summary statistics as measured by image analysis of transmission electron micrographs.

Image	P90 / nm	P50 / nm	P10 / nm	Mean / nm	SD / nm
Co(AC)2+M_0005	1.5	2.1	3.2	2.2	0.7
Co(AC)2+M_0001	1.5	2.0	2.9	2.1	0.6
$Co(OAc)_2$	**1.5**	**2.0**	**3.0**	**2.2**	**0.6**
29-1 Co(NO3)2+M_0006	9	10	17	11	3
29-1 Co(NO3)2+M_0005	9	10	16	11	3
Co(NO3)2+M_0005	6	9	14	9	3
$Co(NO_3)_2$	**7**	**10**	**15**	**10**	**3**
$Co(NO_3)_2$ Holes	**8**	**11**	**18**	**12**	**4**

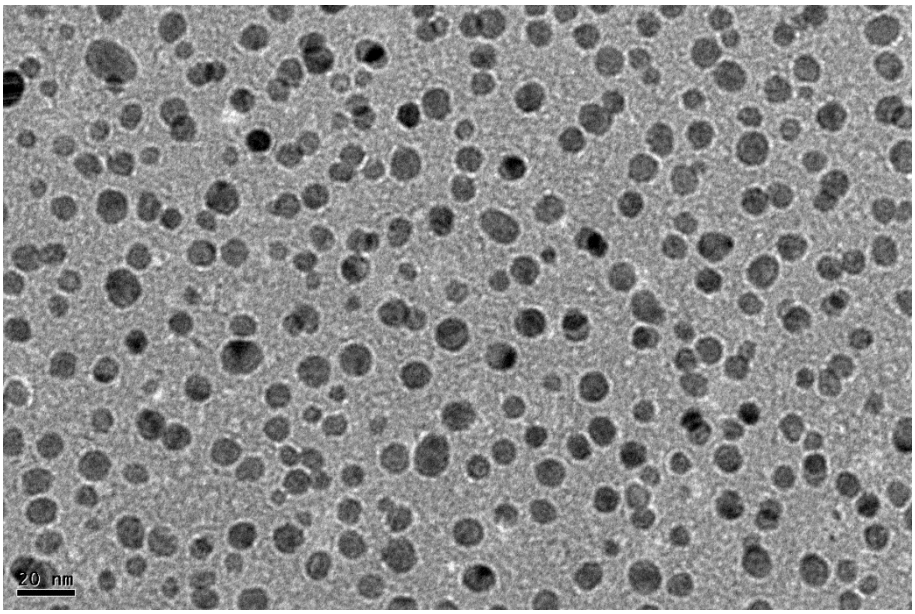

Figure S 226: TEM image of $Co(NO_3)_2$ derived sample used for particle size analysis. (Image label: *Co(NO3)2+M_0005*) Data from this image plotted as darkest bar in Fig 88a.

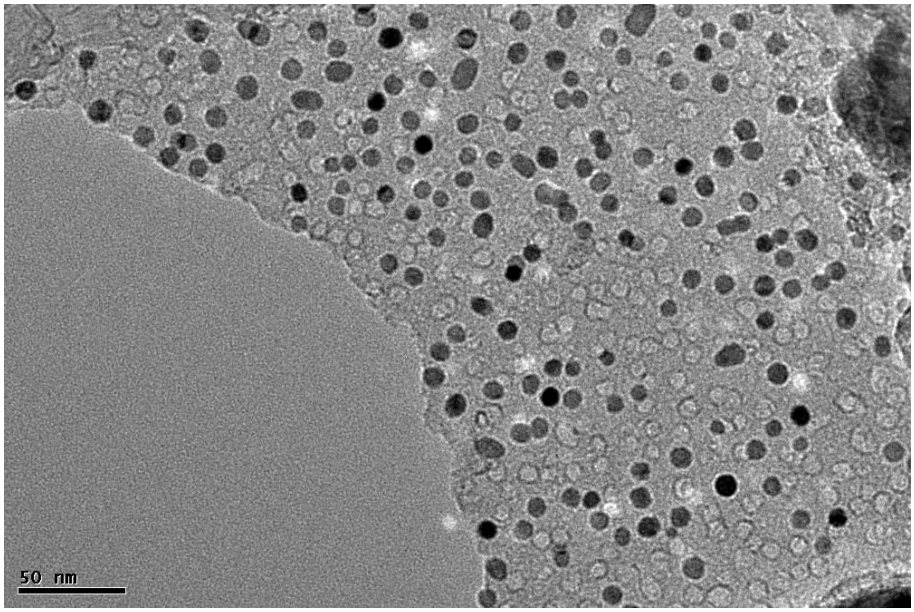

Figure S 227: TEM image of $Co(NO_3)_2$ derived sample used for particle size analysis. (Image label: *29-1 Co(NO3)2+M_0005*) Data from this image plotted as 2nd darkest bar in Fig 88a.

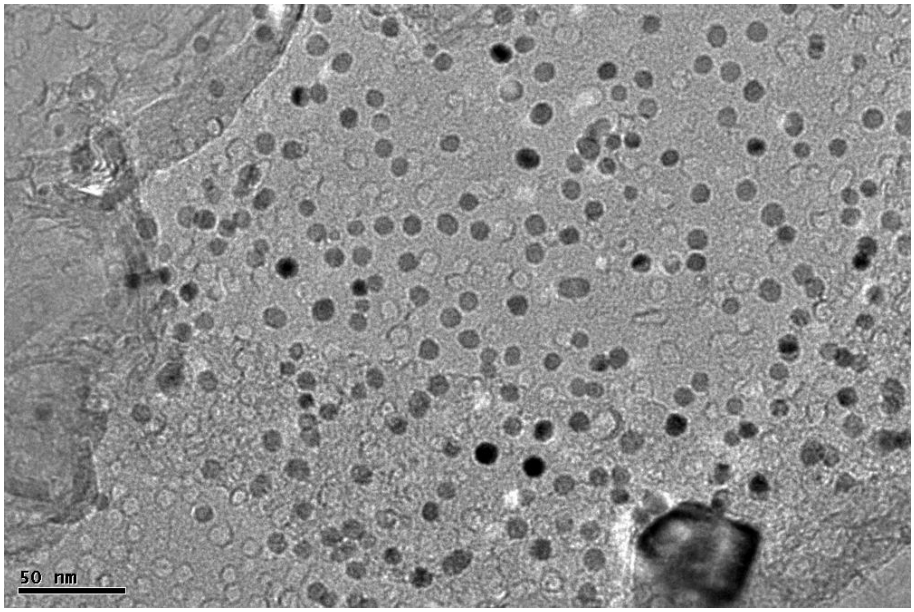

Figure S 228: TEM image of $Co(NO_3)_2$ derived sample used for particle size analysis. (Image label: *29-1 Co(NO3)2+M_0006*) Data from this image plotted as lightest solid bar in Fig 88a.

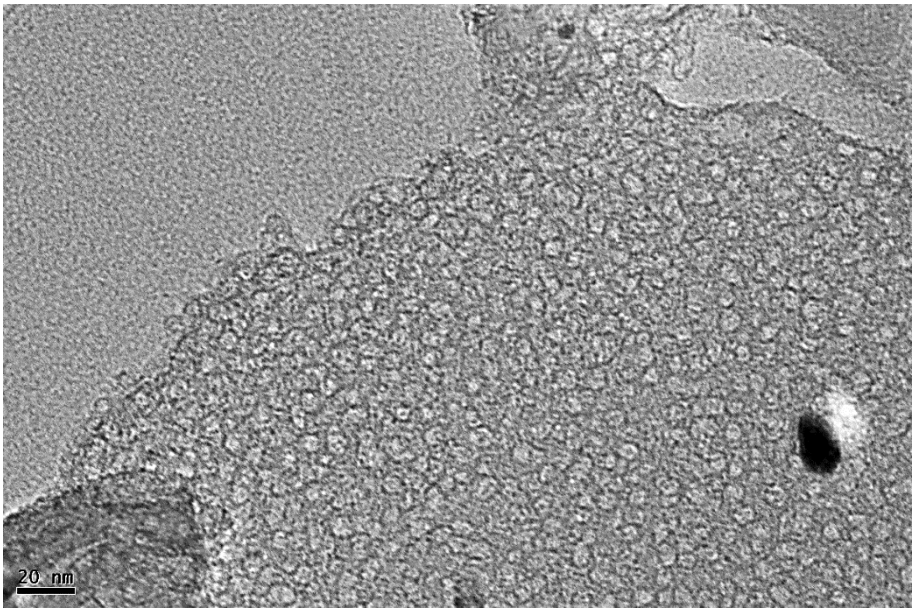

Figure S 229: TEM image of $Co(NO_3)_2$ derived sample used for size analysis of the holes left in the structure, seen as faint pale circles. (Image label: *Co(NO3)2+M_0007 holes*)

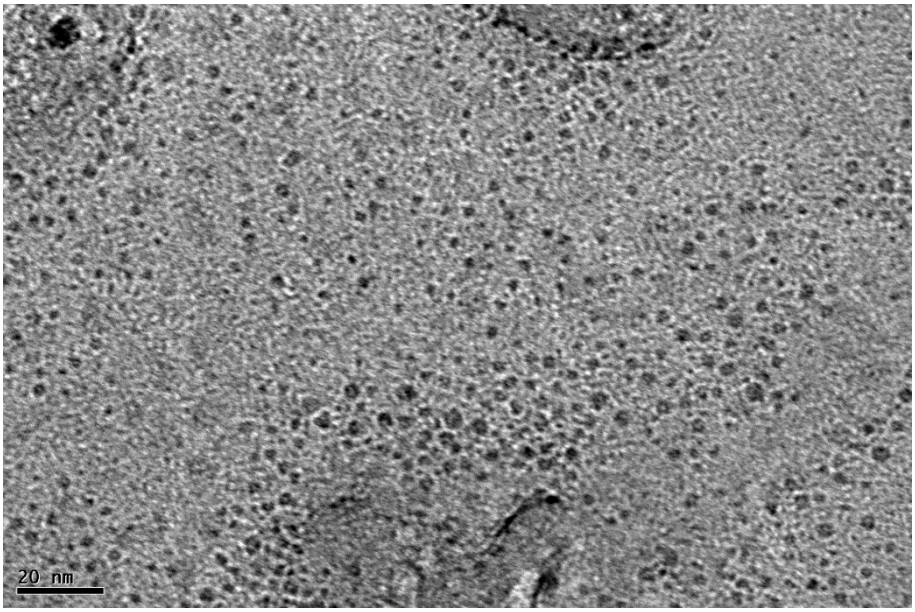

Figure S 230: TEM image of $Co(OAc)_2$ derived sample used for particle size analysis. (Image label: *Co(AC)2+M_0005*) Data from this image plotted lightest bar in Fig 87.

Figure S 231: TEM image of $Co(OAc)_2$ derived sample used for particle size analysis. (Image label: *Co(AC)2+M_0001*) Data from this image plotted as darkest bar in Fig 87.

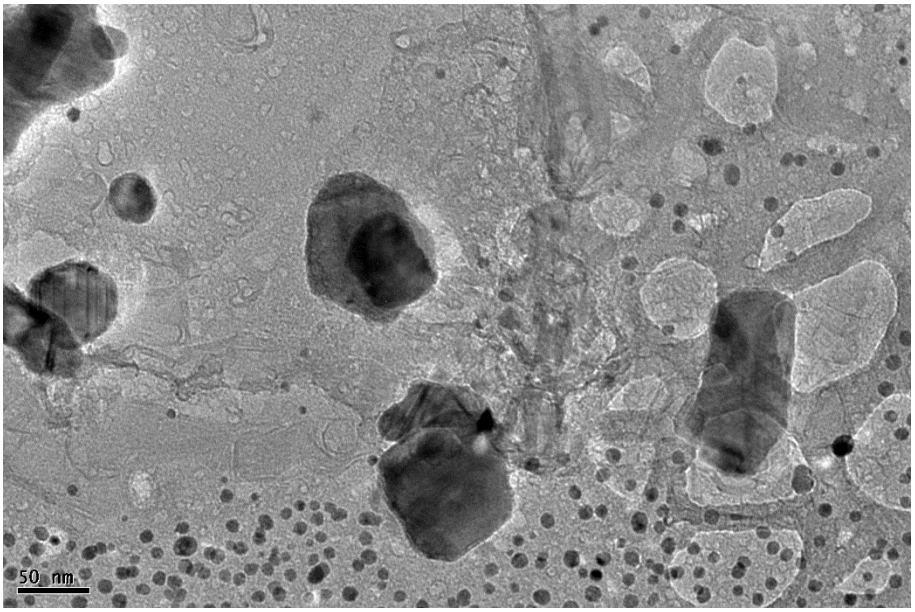

Figure S 232: TEM image of $Co(NO_3)_2$ derived sample used for particle size analysis. (Image label: *Co(NO3)2+M_0006*) Data from this image plotted as darkest bar in Fig 88b.

9.2.4 Gas Chromatography – Mass Spectrometry

9.2.4.1 TritonX™-45 Control

To ensure there is no significant difference with different quantities of Triton present relative to the hydrogen gas flow a number of samples were prepared.

All peaks with intensity greater than 0.5% were assigned.

Table S 2: Summary of gas chromatography peaks and assignment based on mass spectrometry data.

Retention Time / min	% Intensity per mass of TritonX™			Molecular m/z	Structure
	0.8617g	1.3563g	1.6651g		
3.930(0)	-	0.5	0.5	**134**	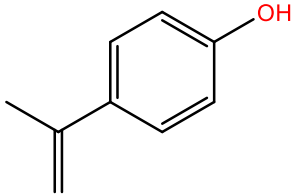
4.323(0)	-	0.7	0.8	**232**	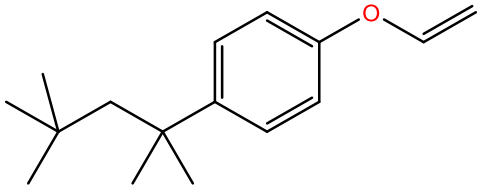

4.593(0)	0.7	1.6	2.1	**206**	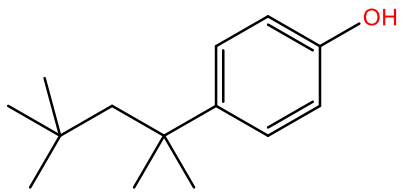
4.663(0)	0.6	0.7	0.8	**218**	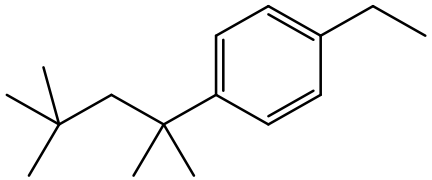
4.973(0)	5.4	3.3	3.9	*Peak present in solvent blank*	
5.213(0)	2.3	2.4	2.6	**250**	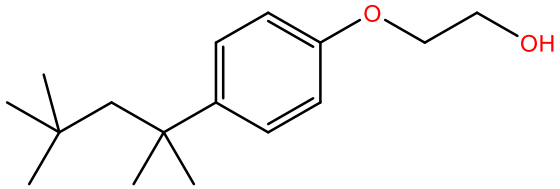
5.410(0)	2.6	1.6	1.9	*Peak present in solvent blank*	

5.793	-	-	0.5	**322**	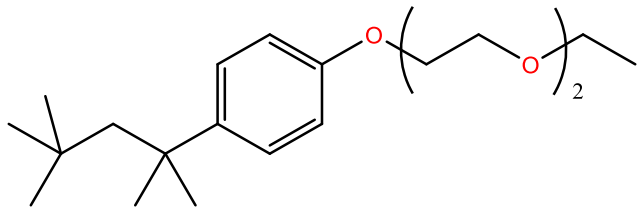
5.842(2)	14.5	13.8	14.5	**294**	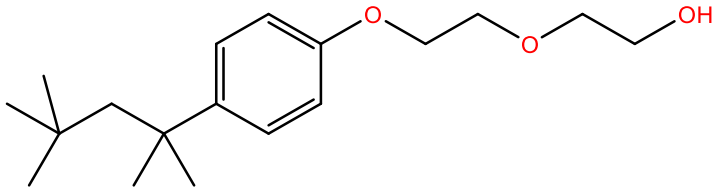
6.399(2)	25.5	22.1	23.4	**338**	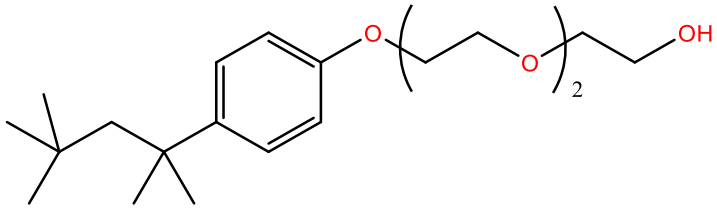
7.009(5)	24.2	25.5	24.8	**382**	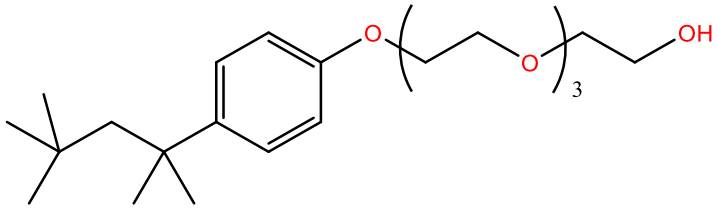

7.997(7)	15.4	18.6	16.6	**426**	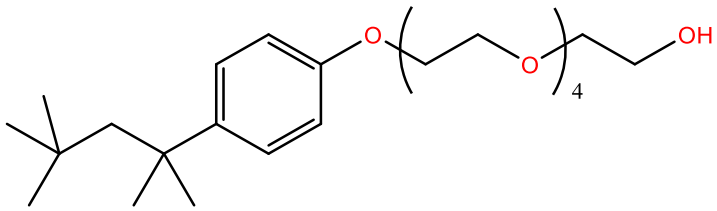
9.513	-	-	0.6	*Mass fragments consistent with TritonX™ decomposition. However, intensity too small for assignment.*	
9.78(1)	6.3	8.2	5.9	**470**	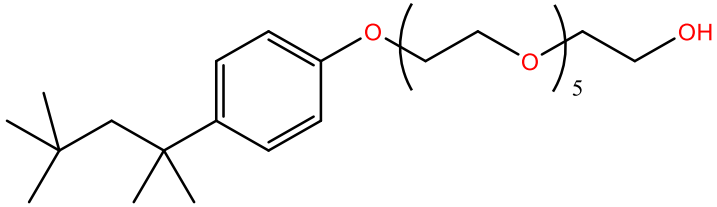
Total	97.5 %	99.0 %	98.9 %		

9.2.4.2 Cobalt Containing Gels

Peaks with intensity greater than 1% listed for comparison with proposed structures consistent with the mass spectrum shown. Not all peaks are observed for every sample. The unsaturated compounds are shown with double bonds at the chain end however it is not possible to assign to double bond exactly.

Table S 3: Summary of gas chromatography data and assignment based on mass spectrometry data for carbonized samples with cobalt salt present.

Retention Time / min	Precursor Used			Present in Control?	Molecular m/z	**Possible Structure**
	$CoAc_2$	$CoCl_2$	$Co(NO_3)_2$			
4.323	1.3%	-	-	✓	**232**	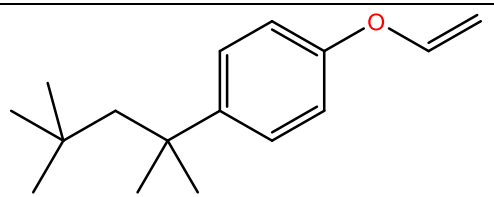
4.593	3.9%	10.6%	11.9%	✓	**206**	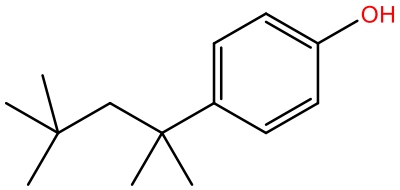
4.613	0.5%	1.1%	-	×	**230**	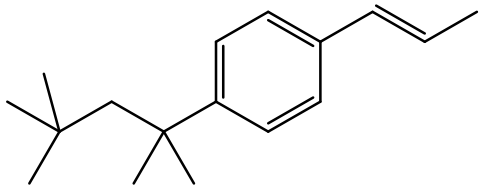

4.847	-	1.6%	-	×	**232**	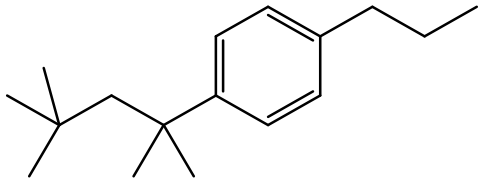
4.883	-	-	1.7%	×	**251**	**?**
4.973	4.0%	5.7%	13.5%	×	*Peak present in solvent blank*	
5.153	-	10.2%	-	×	**268**	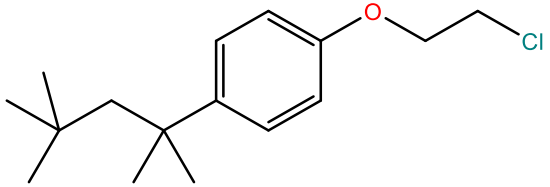
5.213	2.7%	16.7%	14.4%	✓	**250**	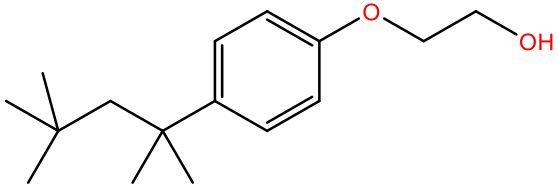
5.350	-	1.0%	1.9%	×	**278**	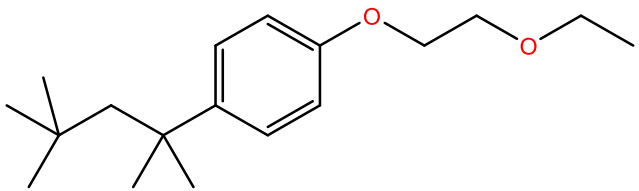

5.410	1.9%	2.8%	6.6%	✓	*Peak present in solvent blank*	
5.48	3.0%	1.2%	-	×	**292**	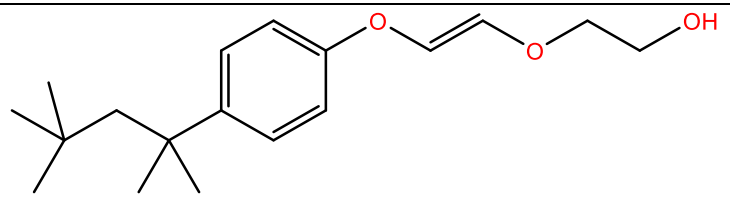
5.840	8.3%	18% OH (10% Cl)	15.1%	✓	**294**	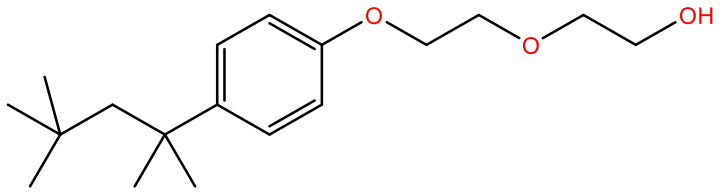
5.973	-	1.6%	2.5%	×	**322**	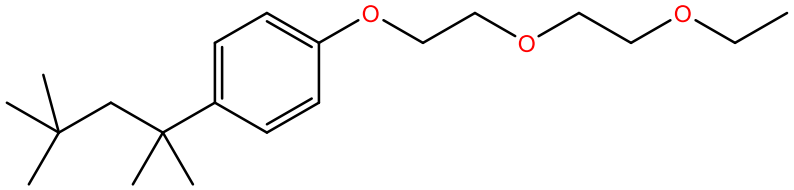
6.08	13.3%	1.2%	-	×	**336**	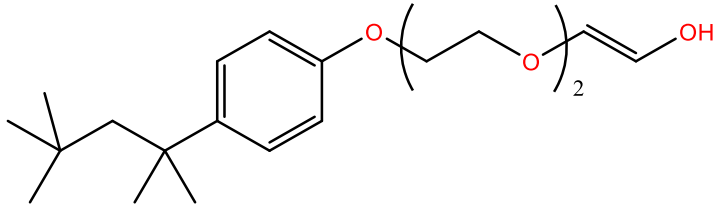

6.373	-	2.8%	-	×	**356**	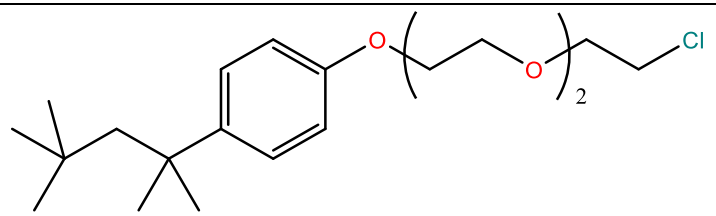
6.399	10.9%	9.4%	15.2%	✓	**338**	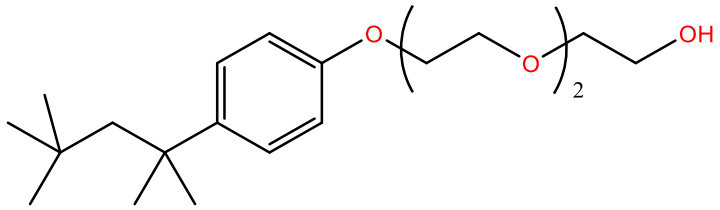
6.500	-	0.7%	2.2%	×	**366**	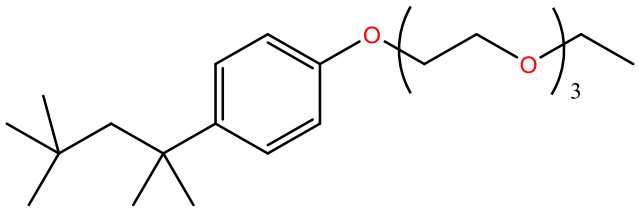
6.603	17.7%	-	-	×	**380**	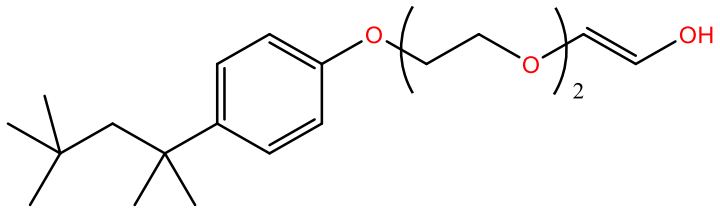

6.995	7.1%	2.9%	6.7%	✓	**382**	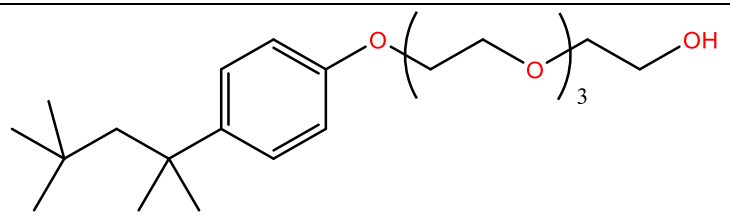
7.300	16.0%	-	-	×	**424**	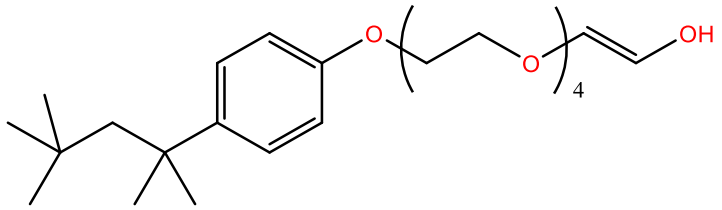
7.997	2.2%	-	1.4%	✓	**426**	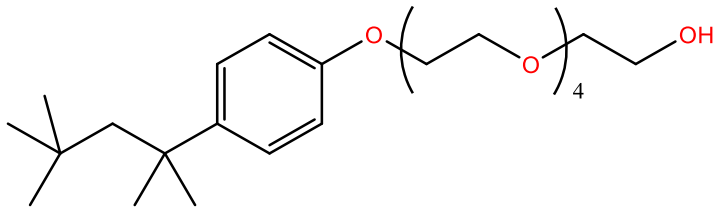
8.490	8.3%	-	-	×	**468**	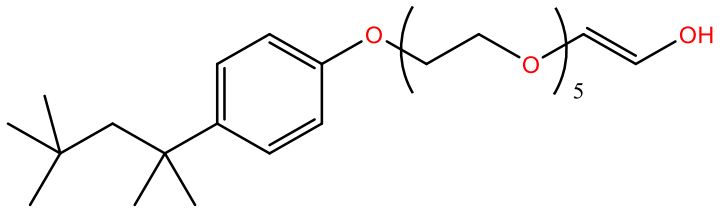
Total	99.8%	97.7%	94.4%			

9.2.4.3 Chromatograms

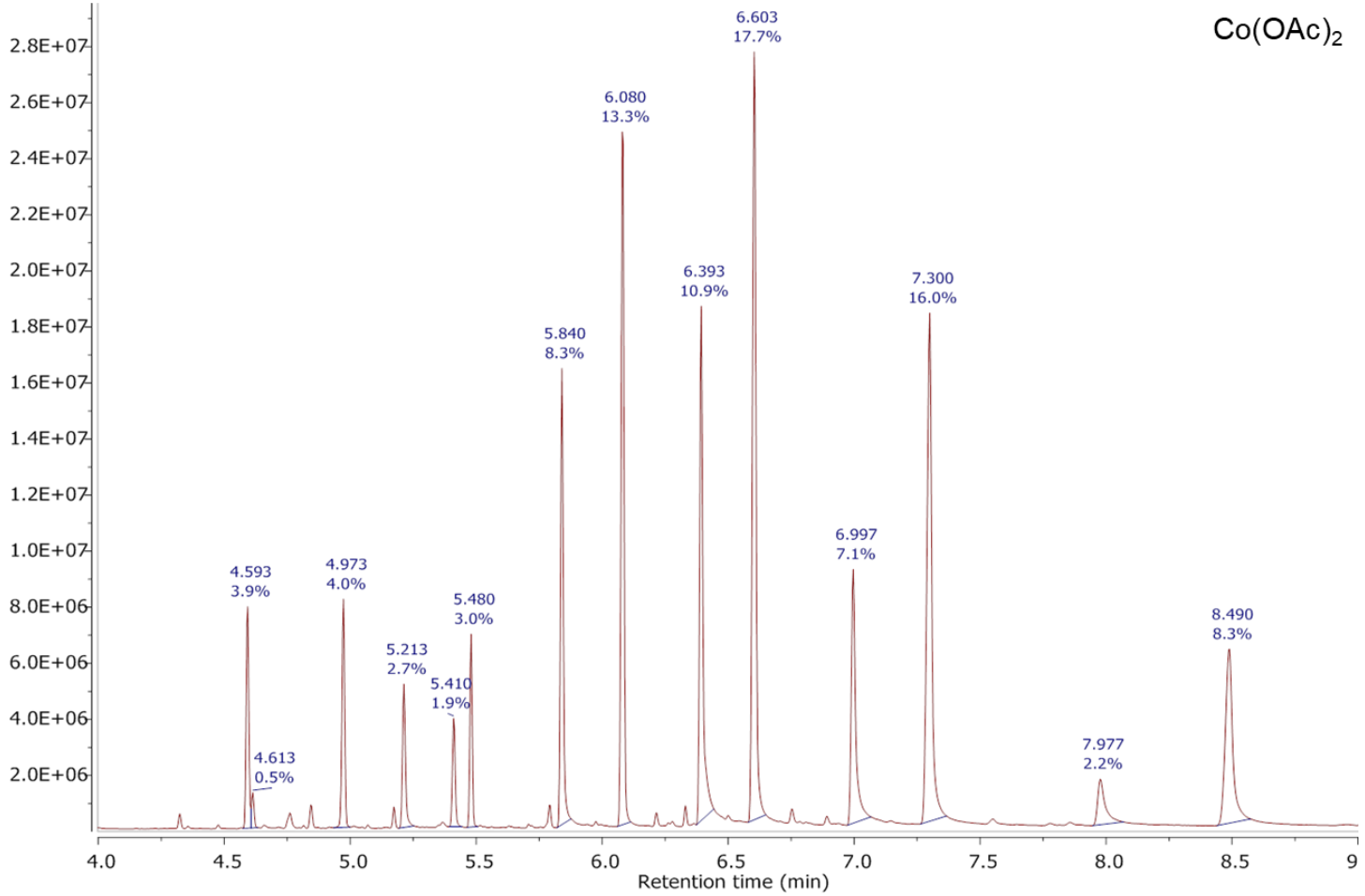

Figure S 233: Gas chromatography trace of the oil extracted from the $Co(OAc)_2$ sample carbonization.

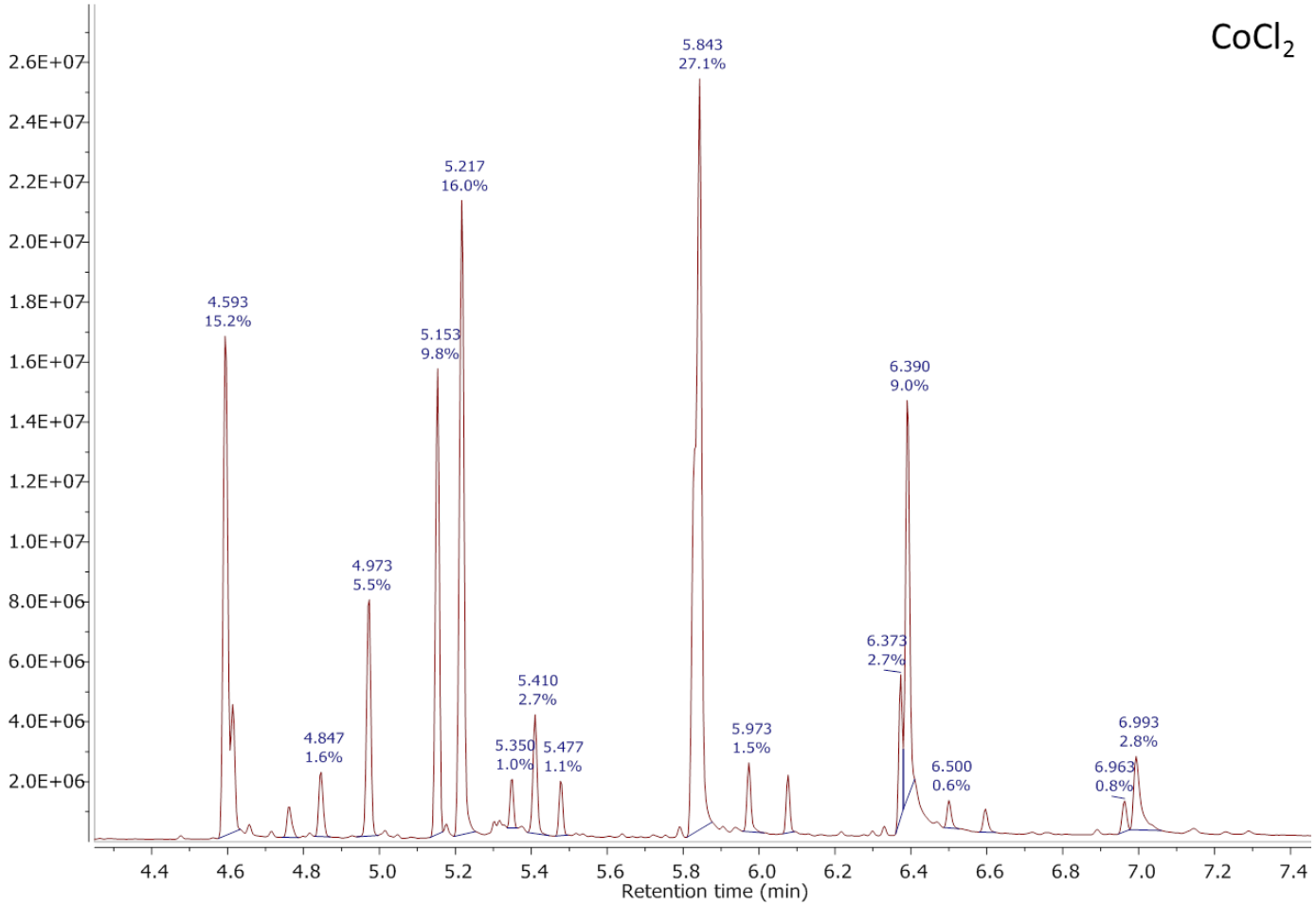

Figure S 234: Gas chromatography trace of the oil extracted from the $CoCl_2$ sample carbonization.

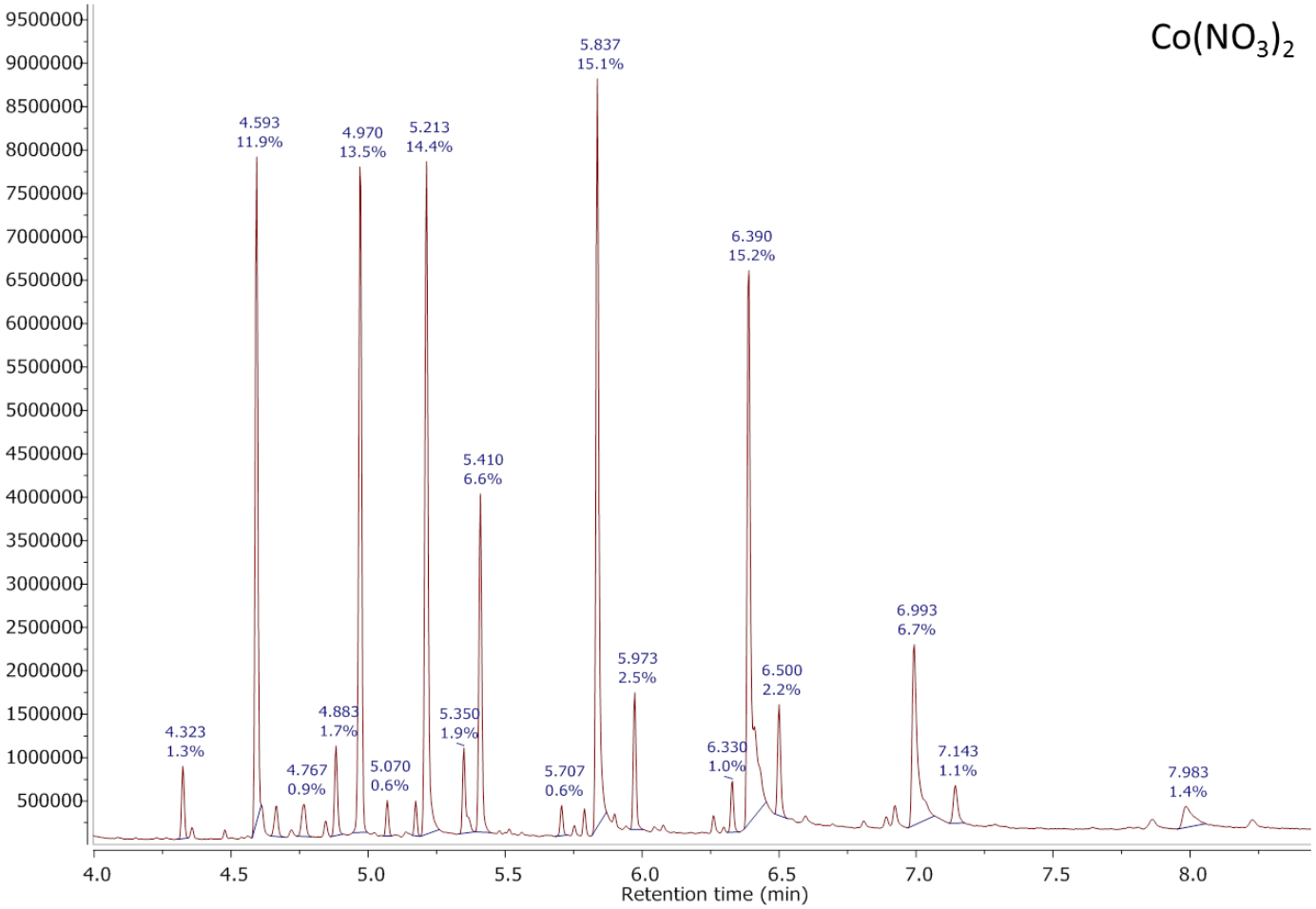

Figure S 235: Gas chromatography trace of the oil extracted from the $Co(NO_3)_2$ sample carbonization.

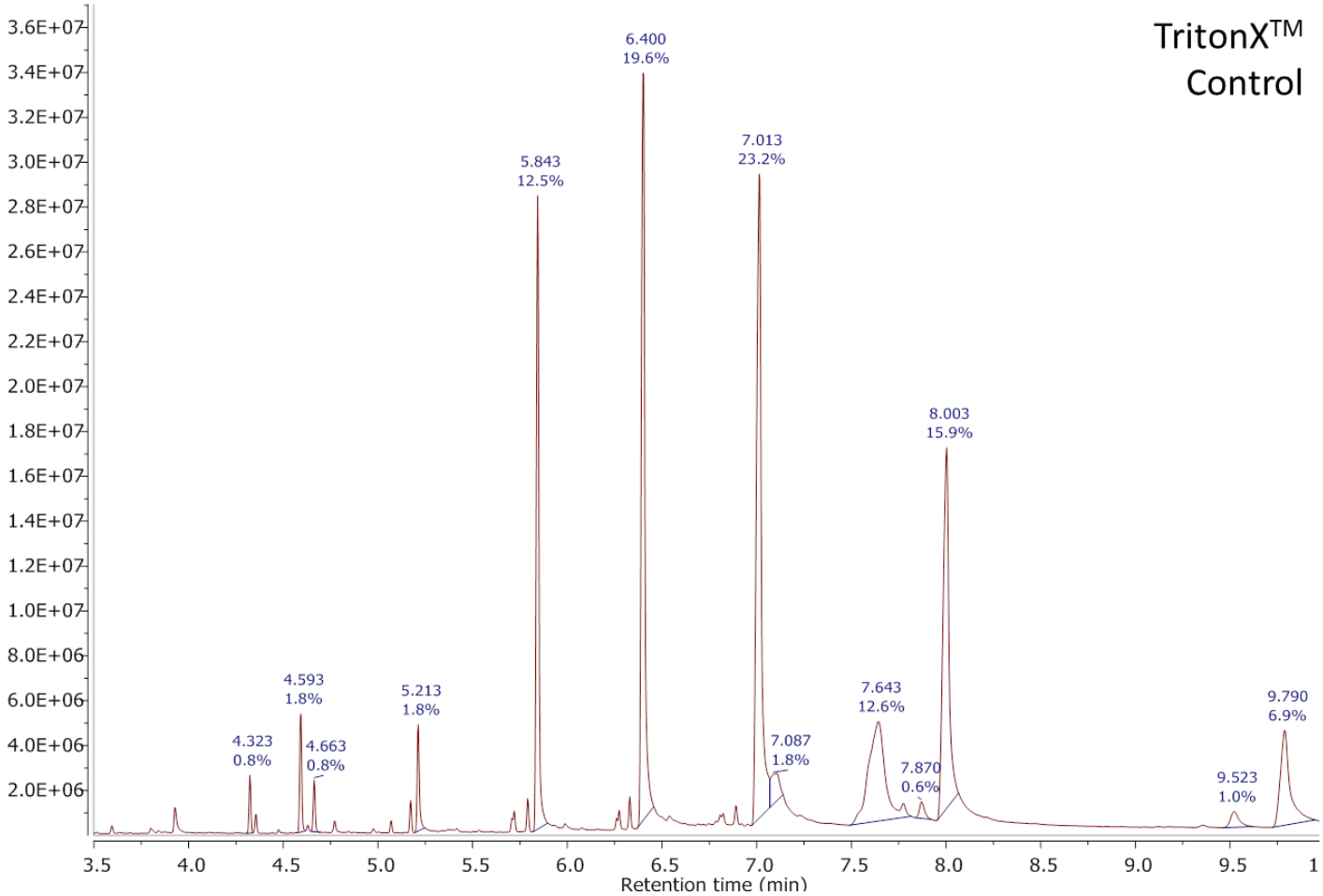

Figure S 236: Gas chromatography trace of the oil extracted from the metal free control carbonization